

Adsorption and Degradation Kinetics of Dyes in Perovskite Dispersion under Visible Light Irradiation

A Thesis

Submitted to the

UNIVERSITY OF KOTA, KOTA

for the degree of

Doctor of Philosophy

In Chemistry

(Faculty of Science)



Submitted by

Kavita Sharma

Under the Supervision of

Dr. Uttra Chandrawat

*Department of Chemistry
Government College Kota
UNIVERSITY OF KOTA
KOTA (RAJ.)*

2018

CERTIFICATE

I feel great pleasure in certifying that the thesis entitled “*Adsorption and Degradation Kinetics of Dyes in Perovskite Dispersion under Visible Light Irradiation*” submitted by *Kavita Sharma* under my guidance.

She has completed the following requirements as per Ph.D. regulation of the University.

- (a) Course work as per the university rules.
- (b) Residential requirements of the university (200 days).
- (c) Regularly submitted annual progress report.
- (d) Presented her work in departmental committee.
- (e) Published/accepted minimum of one research paper in a referred research journal.

I recommend the submission of thesis.

Date:

Dr. Uttra Chandrawat
Associate Professor
Department Of Chemistry
Government College, Kota

ABSTRACT

Owing to extensive manufacturing and widespread uses, synthetic dyes can cause substantial environmental pollution and are severely harmful for human health. Though, the increasing influence of environmental protection on industrial development promotes the development of green technologies which are eco-friendly. The dyes present in water reduce the photosynthetic activity of aquatic plants by interrupting the entering sun rays, resulting in the annihilation of the water ecosystem. As a result, pollution related diseases are becoming more and more prominent. Also, several dyes and their metabolite products are found to be mutagenic and carcinogenic for humans.

Consequently, different chemical biological and physical methods are used for environmental remediation of dyes. Although, thus implied methods are found to be insufficient for the removal of all potentially hazardous dyes and may generate toxic secondary pollutants into ecosystem. Therefore, an effective method is needed for complete mineralization of organic pollutants from waste water.

In recent years, semiconductor photocatalysis as the pioneering purification technology draws attention, because it is able to generate highly reactive transient species for complete mineralization of dyes. But, the efficacy of photocatalysis is limited as most of the catalysts show response in UV light only, and hence, it is necessary to modify photocatalyst to enhance their photocatalytic activity in visible light region.

Perovskites are the mixed metal oxides with the general formula ABO_3 . In the typical crystal structure of perovskite material, the A site is engaged by the larger cation, while the B site is occupied by the smaller cation. Perovskites are one of the most important families of materials exhibiting properties suitable for numerous technological applications. Perovskite materials have been studied for photocatalytic degradation of various pollutants such as phenols, dyes and drugs from waste water. Thus this thesis presents a study of the synthesis of $BaBiO_3$ and $Ba_{0.6}K_{0.4}BiO_3$ perovskites via Pechini method and their subsequent use as a photocatalyst in photodegradation of various dyes i.e. Crystal violet, Malachie green and Congo red. The initial rates of the photo-degradation are calculated for various initial dye concentrations. The Langmuir-Hinshelwood model is used for

interpreting the initial rate data and for the development of a rate equation for degradation of the studied dye. An adsorption study has also been discussed.

The structural, morphological and optical characteristics of the synthesized nanoparticles were studied by Thermo Gravimetric Analysis (TGA), powder X-ray diffraction, Fourier Transform Infra-Red spectroscopy, UV-Vis Diffuse Reflectance Spectroscopy (UV DRS) and Scanning Electron microscopy (SEM).

The XRD patterns suggest that BaBiO_3 crystallizes in the distorted monoclinic structure while $\text{Ba}_{0.6}\text{K}_{0.4}\text{BiO}_3$ crystallizes in the cubic structure. The strong and sharp peaks in the diffractograms indicate the crystalline nature and phase purity of the prepared samples. The phase evolution of both the catalysts with increasing temperature was done by DT-TGA. The TGA curves show that above final calcination temperatures (800°C for BaBiO_3 and 720°C for $\text{Ba}_{0.6}\text{K}_{0.4}\text{BiO}_3$), no weight loss is observed, hence it is concluded above this temperature, the perovskite are stable. FTIR spectrum shows the presence of the bands around 465cm^{-1} in both the catalysts confirming the metal-oxygen bond formation, which is the characteristic property of perovskite materials. The diffuse reflectance spectroscopy showed that the catalysts have a broad absorbance in visible region of light. The onset optical absorption edge was around 600 and 660 nm for barium bismuthate and K doped barium bismuthate respectively. The band gap calculation was done by Tauc's plots through the converted KM functions. The band gap of BaBiO_3 and $\text{Ba}_{0.6}\text{K}_{0.4}\text{BiO}_3$ was found to be 2.07eV and 1.87eV, respectively. Owing to the low band gap, the catalysts were supposed to be promising in displaying their activity in photocatalysis under visible light irradiation. The SEM studies show that both the samples are homogeneous uniform nanoparticles, having 520nm size for BaBiO_3 and 45-101nm for $\text{Ba}_{0.6}\text{K}_{0.4}\text{BiO}_3$. SEM images reveal the nano rod type structure for BaBiO_3 and plate like layered structure for $\text{Ba}_{0.6}\text{K}_{0.4}\text{BiO}_3$.

The feasibility of adsorption and photocatalytic degradation of all the three studied dyes dye using BaBiO_3 and $\text{Ba}_{0.6}\text{K}_{0.4}\text{BiO}_3$ as in the form of aqueous suspension under visible light irradiation has been investigated. Since, the photocatalytic degradation is directly related to the adsorbed quantities of the pollutant, the adsorption properties of all the three studied dye on to BaBiO_3 and $\text{Ba}_{0.6}\text{K}_{0.4}\text{BiO}_3$ are also discussed in terms of Langmuir and Freundlich adsorption

isotherms. The photocatalytic degradation was expressed in terms of LH kinetic model, and the subsequent rate constants are also determined. The effect of different operational parameters such as initial dye concentration, catalyst dose, solution pH and temperature on the rate of photo degradation is studied. Moreover, reusability of these catalysts is studied. Furthermore, to estimate the degree of mineralization, measurements of total organic carbon has also been conducted In the present studies, the percentage removal of three studied dyes through photocatalytic degradation by BaBiO₃ and Ba_{0.6}K_{0.4}BiO₃ was also compared with the TiO₂ (Degussa P-25).

It is to be noted here, that among the three studied dyes, Crystal violet suffers degradation with highest rate followed by Malachite green and then by Congo red in the end. It seems that the triphenyl amine structure of Crystal violet dye is more susceptible to degradation in photocatalytic reaction in comparison to Malachite green having two dimethyl amino group and Congo red having a bulky ensemble, including one central biphenyl group and two symmetric amino substituted naphthalene group.

In summary this work provides better photocatalytic activity of synthesised materials using a green chemistry route for environmental purification.

Declaration

I, hereby, certify that the work, which is being presented in the thesis, entitled “***Adsorption and Degradation Kinetics of Dyes in Perovskite Dispersion under Visible Light Irradiation***” in partial fulfilment of the requirement for the award of the Degree of Doctor of Philosophy, carried under the supervision of Dr. Uttra Chandrawat and submitted to the Department of Chemistry, Government College, Kota, University of Kota, Kota; represents my ideas in my own words and where others ideas or words have been included. I have adequately cited and referenced the original sources. The work presented in this thesis has not been submitted elsewhere for the award of any other degree or diploma from any Institutions. I also declare that I have adhered to all principles of academic honesty and integrity and have not misrepresented or fabricated or falsified any idea/data/fact/source in my submission. I understand that any violation of the above will cause for disciplinary action by the University and can also evoke penal action from the sources which have thus not been properly cited or from whom proper permission has not been taken when needed.

Kavita Sharma

(Registration No: RS/1762/13)

Date:

This is to certify that the above statement made by **Kavita Sharma** (Enrolment No: 06/13023) is correct to the best of my knowledge.

Date:

Dr. Uttra Chandrawat

Research Supervisor

Department Of Chemistry

Government College, Kota

ACKNOWLEDGEMENT

*In the name of most gracious and merciful Lord Shiva! who gave me strength and diligence to complete my work in the best possible manner. I express my heartfelt indebtedness and owe a deep sense of gratitude to my research supervisor **Dr. Uttra Chandrawat**, for her genuine guidance and inspiration in completing this research work. It has been a great opportunity to conduct research under your guidance.*

*I am extremely thankful to **Dr. B.K. Yogi**, Principal Government College, **Dr. Sharda Sharma**, H.O.D., department of Chemistry, for their kind support and cooperation during the work. I owe a great sense of gratitude to **Dr. Ashu Rani**, my post graduate professor, for her invaluable guidance.*

*I would like to thank **Dr. Manju bala Yadav**, **Dr. Loni Lokwani**, **Dr. Monika Dakshene**, **Dr. J. P. Chaudhary**, **Dr Renuka Jain**, **Dr. Bharat Meena**, **Dr. Manju Meena**, **Dr. Dhanraj Meena**, for their generous support during my work.*

*I would also like to acknowledge **Dr. Seema Jain** (Women scientist, UGC), it has been an honour to work with you, and your contribution as co-author is indispensable for my research.*

*I express my gratitude to all the authorities and office staff in the Department of Chemistry specially **Gaurav Sharma** for their help, during the tenure of my work.*

*I consider myself blessed to have **Nakul** and **Yachana** as my best friends forever. I thank you for being beside me in every critical phase of my personal life. I would also like to thank **Arpit**, my friend, from North Carolina (USA) for his help in literature survey throughout my PhD work. I am very grateful to my lab-mates **Preeti**, **Sandeep**, **Rashmi**, **Varsha**, **Ankita**, **Sonal**, for all the support and motivation for my work. I would like to acknowledge **STIC (Cochin)** and **SAIF (Panjab)** and **SAIF (IIT Mumbai)** for providing instrumentation facility for sample analysis.*

*For my family, **Pragya** di and **Maa** and **daddy** thanks for everything, from your generosity to our many dinner chats, after a long tiresome day. My heartfelt*

regards to my **MOTHER** Thanks for listening to my problems and providing perspective. I would not be who am I today without you all. A special thanks to my brother **Dheeraj Sharma**, my sister-in-law **Richa Sharma**, my niece and nephew **Vani, Vinayak and Samriddhi**.

Finally I would like to thank my husband, **Kunal Gaur**, who has been a constant source of support and encouragement during the challenges of Ph.D. and life. Thank you for the every little things you've done for me when I worked late nights. Thank you for those weekends when you sat at the computer, so that my work would go a little quicker. You have been patient with me when I'm frustrated, you celebrate with me when even the littlest things go right, and you are there whenever I need you to just listen.

There are so many others whom I may have inadvertently left out and I sincerely thank all of them for their help.

Kavita Sharma

CONTENTS

Chapters Title	Page No.
1 Introduction and Literature Review	1 - 36
1.1 Dyes and their toxicity	2
1.2 Degradation of dyes	3
1.2.1 Biological treatment methods	3
1.2.2 Physical treatment methods	4
1.2.3 Chemical treatment methods	4
1.2.4 Advanced Oxidation Processes (AOP)	4
1.3 Photocatalysis	7
1.3.1 Homogeneous photocatalysis	8
1.3.2 Heterogeneous photocatalysis	8
1.4 Semiconductor Photocatalysis	9
1.4.1 Mechanism of semiconductor photocatalysis	9
1.4.2 Band gap energy	10
1.4.3 Strategies in the development of semiconductor photocatalysis	12
1.5 Perovskite	15
1.5.1 Structure of perovskite	16
1.5.2 Synthesis of perovskite	18
I. Solid state reaction	18
II. Combustion synthesis	18
III. Microwave synthesis	19
IV. Hydrothermal synthesis	19
V. Sol-gel method	19
a. Alkoxide route	20
b. Alkoxide-salt route	20
c. Pechini method	21
1.5.3 Uses of perovskite	21
1.5.4 Photocatalytic activity of perovskite	23
1.6 Scope of the present study	25
<i>References</i>	27
2 Materials and Methodology	37- 61
2.1 Materials	37
I. Barium nitrate ($\text{Ba}(\text{NO}_3)_2$)	37
II. Bismuth nitrate ($\text{Bi}(\text{NO}_3)_3 \cdot 5\text{H}_2\text{O}$)	37
III. Citric acid ($\text{C}_6\text{H}_8\text{O}_7 \cdot \text{H}_2\text{O}$)	37
IV. Ethylene glycol ($\text{C}_2\text{H}_6\text{O}_2$)	37
V. Hydrochloric Acid (HCl)	38
VI. Nitric acid (HNO_3)	38
VII. Sodium hydroxide (NaOH)	38
VIII. Potassium nitrate (KNO_3)	38
IX. P 25 TiO_2	38
X. Dyes	38

2.2 Apparatus	40
I. Centrifuge	40
II. Crucible	40
III. Cuvettes	40
IV. Electronic Balance	40
V. Filter paper	40
VI. Hot Plate	40
VII. Mini Rotator Flask Shaker	41
VIII. Muffle Furnace	41
IX. pH Meter	41
X. Oven	42
XI. Stirrer	42
XII. TOC analyser	42
XIII. Ultra Pre water purification System	42
XIV. UV Visible spectrophotometer	43
2.3 Synthesis of Catalysts	43
2.4 Characterization of Catalysts	45
I. Thermo-Gravimetric / Differential Thermal Analyses	45
II. X-ray Diffraction	47
III. Fourier Transformed Infrared Spectroscopy	48
IV. UV-Vis. Diffuse reflectance spectroscopy	49
V. Scanning Electron Microscope	51
2.5 Photodegradation of various dyes	53
2.6 Kinetic Modelling	56
I. Adsorption Isotherm	56
a. Langmuir isotherm	57
b. Freundlich isotherm	58
II. Photodegradation kinetic model	59
III. Goodness of fit	60
<i>Reference</i>	61

3 Synthetic Methodology and Characterization 62- 100

3.1 Introduction	62
3.2 Pechini method	64
3.3 Synthesis	66
3.3.1 Synthesis of BaBiO ₃	67
3.3.2 Synthesis of Ba _{0.6} K _{0.4} BiO ₃	69
3.4 Results and discussion	71
3.4.1 Characterization of BaBiO₃	72
3.4.1(A) Thermal Studies	72
3.4.1(B) X-ray diffraction (XRD) patterns	73
3.4.1(C) Fourier Transform infrared spectroscopy	76
3.4.1(D) UV-Vis. Diffuse Reflectance spectroscopy	78
3.4.1 (E) Scanning electron Microscopy	81
3.4.2 Characterization of Ba_{0.6}K_{0.4}BiO₃	83
3.4.2(A) Thermal Studies	83

3.4.2(B) X-ray diffraction (XRD) patterns	84
3.4.2 (C) Fourier Transform infrared spectroscopy	87
3.4.2(D) UV-Vis. Diffuse Reflectance Spectroscopy	89
3.4.2(E) Scanning electron Microscopy	91
3.5 Conclusion	94
<i>References</i>	96

4 Photocatalytic Degradation of Crystal Violet Dye Using BaBiO₃ and Ba_{0.6}K_{0.4}BiO₃ 101-166

4.1 Introduction	101
4.2 Material & Method	105
4.2.1 Chemical reagents	105
4.2.2 Experimental procedure and analytical methods	105
4.3 Results and Discussion	106
4.3.1 UV-VIS spectra of CV dye	106
4.3.2 Photolysis of crystal violet dye	107
4.3.3 Adsorption studies in dark:	108
a. Langmuir isotherm	108
b. Freundlich isotherm	112
4.3.4 Photodegradation studies under visible light irradiation	114
4.3.4.1 Effect of initial dye concentration on photocatalytic degradation of Crystal Violet	115
a. Results with BaBiO ₃	116
b. Results with Ba _{0.6} K _{0.4} BiO ₃	123
4.3.4.2 Effect of catalyst dose on photocatalytic degradation of CV	130
a. Results with BaBiO ₃	131
b. Results with Ba _{0.6} K _{0.4} BiO ₃	135
4.3.4.3 Effect of initial pH on photocatalytic degradation of CV dye	139
a. Results with BaBiO ₃	140
b. Results with Ba _{0.6} K _{0.4} BiO ₃	143
4.3.4.4 Effect of temperature on photocatalytic degradation of CV dye	146
a. Results with BaBiO ₃	147
b. Results with Ba _{0.6} K _{0.4} BiO ₃	150
4.3.4.5 Regeneration of photocatalysis	153
4.4 Comparison of BaBiO ₃ and Ba _{0.6} K _{0.4} BiO ₃ with Degussa p-25 TiO ₂	154
4.5 Visible spectral changes of CV dye	155
4.6 TOC analysis	156
4.7 Proposed mechanism of CV dye photodegradation	157
4.8 Conclusion	158
<i>References</i>	161

5 Photocatalytic Degradation of Malachite Green Dye Using

BaBiO₃ and Ba_{0.6}K_{0.4}BiO₃ 167-231

5.1 Introduction	167
5.2 Material & Method	170
5.2.1 Chemical reagents	170
5.2.2 Experimental procedure and analytical methods	170
5.3 Results and Discussion	172
5.3.1 UV-VIS spectra of MG dye	172
5.3.2 Photolysis of malachite green dye	172
5.3.3 Adsorption studies in dark:	173
a. Langmuir isotherm	174
b. Freundlich isotherm	177
5.3.4 Photodegradation studies under visible light irradiation	179
5.3.4.1 Effect of initial dye concentration on photocatalytic degradation of Malachite Green	180
a. Results with BaBiO ₃	181
b. Results with Ba _{0.6} K _{0.4} BiO ₃	188
5.3.4.2 Effect of catalyst dose on photocatalytic degradation of MG	195
a. Results with BaBiO ₃	196
b. Results with Ba _{0.6} K _{0.4} BiO ₃	200
5.3.4.3 Effect of initial pH on photocatalytic degradation of MG dye	203
a. Results with BaBiO ₃	205
b. Results with Ba _{0.6} K _{0.4} BiO ₃	208
5.3.4.4 Effect of temperature on photocatalytic degradation of MG dye	211
a. Results with BaBiO ₃	212
b. Results with Ba _{0.6} K _{0.4} BiO ₃	215
5.3.4.5 Regeneration of photocatalysis	218
5.4 Comparison of BaBiO ₃ and Ba _{0.6} K _{0.4} BiO ₃ with Degussa p-25 TiO ₂	219
5.5 Visible spectral changes of CV dye	220
5.6 TOC analysis	221
5.7 Proposed mechanism of CV dye photodegradation	222
5.8 Conclusion	223
<i>References</i>	226

6 Photocatalytic Degradation of Congo Red Dye Using

BaBiO₃ and Ba_{0.6}K_{0.4}BiO₃ 232-297

6.1 Introduction	232
6.2 Material & Method	235
6.2.1 Chemical reagents	235
6.2.2 Experimental procedure and analytical methods	236
6.3 Results and Discussion	237
6.3.1 UV-VIS spectra of CR dye	237
6.3.2 Photolysis of Congo red dye	238
6.3.3 Adsorption studies in dark:	238

a.	Langmuir isotherm	239
b.	Freundlich isotherm	243
6.3.4	Photodegradation studies under visible light irradiation	245
6.3.4.1	Effect of initial dye concentration on photocatalytic degradation of Congo Red	246
a.	Results with BaBiO ₃	246
b.	Results with Ba _{0.6} K _{0.4} BiO ₃	253
6.3.4.2	Effect of catalyst dose on photocatalytic degradation of MG	260
a.	Results with BaBiO ₃	261
b.	Results with Ba _{0.6} K _{0.4} BiO ₃	265
6.3.4.3	Effect of initial pH on photocatalytic degradation of MG dye	269
a.	Results with BaBiO ₃	270
b.	Results with Ba _{0.6} K _{0.4} BiO ₃	273
6.3.4.4	Effect of temperature on photocatalytic degradation of MG dye	277
a.	Results with BaBiO ₃	277
b.	Results with Ba _{0.6} K _{0.4} BiO ₃	281
6.3.4.5	Regeneration of photocatalysis	284
6.4	Comparison of BaBiO ₃ and Ba _{0.6} K _{0.4} BiO ₃ with Degussa p-25 TiO ₂	285
6.5	Visible spectral changes of CV dye	286
6.6	TOC analysis	287
6.7	Proposed mechanism of CV dye photodegradation	288
6.8	Conclusion	289
	<i>References</i>	292

7 **Conclusion and Future Work** **298- 303**

7.1	Outcome of the Present Research Work	298
7.2	Future Recommendations	302

Annexure I: Thesis Summary

Annexure II: List of Publications

Publications

LIST OF TABLES

Table No.	Title	Page No.
Table 1.1:	Summary of analytical methods used for the degradation of dyes.	5
Table 1.2:	Photocatalytic activity of modified TiO ₂	13
Table 1.3:	Representative Perovskite materials and their applications	22
Table 1.4:	Promising photocatalytic systems for organic compounds degradation under visible light.	24
Table 2.1:	Physical characteristics and molecular structure of Malachite green, Crystal Violet, and Congo red dyes	39
Table 3.1:	Structural results for BaBiO ₃ nano powder calcined at 800°C/12h	76
Table 3.2:	Interpretation of the peaks obtained by the FTIR spectra of the synthesized BaBiO ₃ /12hours	78
Table 3.3:	Structural results for Ba _{0.6} K _{0.4} BiO ₃ nano-powder calcined at 720°C/12hours	87
Table 3.4:	Interpretation of the peaks obtained by the FTIR spectra of the synthesized Ba _{0.6} K _{0.4} BiO ₃ calcined at 720°C/12hours	89
Table 4.1:	Separation constants (R _L) values for the adsorption of CV dye on BaBiO ₃ and Ba _{0.6} K _{0.4} BiO ₃	112
Table 4.2:	Langmuir and Freundlich constants for the adsorption of CV dye on BaBiO ₃ and Ba _{0.6} K _{0.4} BiO ₃	114
Table 4.3 (a):	Effect of initial dye concentration on degradation of CV	116
Table 4.4 (a):	Effect of initial dye concentration on degradation of CV	117
Table 4.5 (a):	Effect of initial concentration on degradation of CV	117
Table 4.6 (a):	Effect of initial concentration on degradation of CV	118
Table 4.7 (a):	Pseudo-first order apparent rate constant and initial rate values for the different initial concentration of dye	122
Table 4.3 (b):	Influence of initial concentration on degradation of CV	124
Table 4.4 (b):	Influence of initial concentration on degradation of CV	124

Table 4.5 (b):	Influence of initial concentration on degradation of CV	125
Table 4.6 (b):	Influence of initial concentration on degradation of CV	125
Table 4.7 (b):	Pseudo-first order apparent constant values for the different initial dye concentration of dye	129
Table 4.8 (a):	Influence of BaBiO ₃ dose on degradation of CV	132
Table 4.9(a):	Pseudo-first order apparent constant values for the different BaBiO ₃ dose	134
Table 4.8 (b):	Influence of Ba _{0.6} K _{0.4} BiO ₃ dose on degradation of CV	135
Table 4.9 (b):	Pseudo-first order apparent constant values for the different Ba _{0.6} K _{0.4} BiO ₃ dose	137
Table 4.10 (a):	Influence of solution pH on degradation of CV	140
Table 4.11 (a):	Pseudo-first order apparent constant values for the photodegradation of CV at different solution pH	142
Table 4.10 (b):	Effect of solution pH on degradation of CV	143
Table 4.11 (b):	Pseudo-first order apparent constant values for the photodegradation of CV at different solution pH	145
Table 4.12 (a):	Influence of temperature on degradation of CV	147
Table 4.13 (a):	Pseudo-first order apparent constant values for the different temperatures	149
Table 4.12 (b):	Influence of temperature on degradation of CV	150
Table 4.13 (b):	Pseudo-first order apparent constant values for the different temperatures	152
Table 5.1:	Separation constants (R_L) values for the adsorption of MG dye on BaBiO ₃ and Ba _{0.6} K _{0.4} BiO ₃	177
Table 5.2:	Langmuir and Freundlich constants for the adsorption of MG dye on BaBiO ₃ and Ba _{0.6} K _{0.4} BiO ₃	179
Table 5.3 (a):	Effect of initial dye concentration on degradation of MG	181
Table 5.4 (a):	Effect of initial dye concentration on degradation of MG	182
Table 5.5 (a):	Effect of initial dye concentration on degradation of MG	182

Table 5.6 (a):	Effect of initial dye concentration on degradation of MG	183
Table 5.7 (a):	Pseudo-first order apparent rate constant and initial rate values for the different initial concentration of dye	187
Table 5.3 (b):	Influence of initial concentration on degradation of MG	189
Table 5.4 (b):	Influence of initial concentration on degradation of MG	189
Table 5.5 (b):	Influence of initial concentration on degradation of MG	189
Table 5.6 (b):	Influence of initial concentration on degradation of MG	190
Table 5.7 (b):	Pseudo-first order apparent constant values for the different initial dye concentration of dye	194
Table 5.8 (a):	Influence of BaBiO ₃ dose on degradation of MG	197
Table 5.9(a):	Pseudo-first order apparent constant values for the different BaBiO ₃ dose	199
Table 5.8 (b):	Influence of Ba _{0.6} K _{0.4} BiO ₃ dose on degradation of MG	200
Table 5.9 (b):	Pseudo-first order apparent constant values for the different Ba _{0.6} K _{0.4} BiO ₃ dose	202
Table 5.10 (a):	Influence of solution pH on degradation of MG	205
Table 5.11 (a):	Pseudo-first order apparent constant values for the photodegradation of MG at different solution pH	207
Table 5.10 (b):	Influence of solution pH on degradation of MG	208
Table 5.11 (b):	Pseudo-first order apparent constant values for the photodegradation of MG at different solution pH	210
Table 5.12 (a):	Influence of temperature on degradation of MG	212
Table 5.13 (a):	Pseudo-first order apparent constant values for the different temperatures	214
Table 5.12 (b):	Influence of temperature on degradation of MG	215
Table 5.13 (b):	Pseudo-first order apparent constant values for the different temperatures	218
Table 6.1:	Separation constants (R _L) values for the adsorption of MG dye on BaBiO ₃ and Ba _{0.6} K _{0.4} BiO ₃	242
Table 6.2:	Langmuir and Freundlich constants for the adsorption of MG dye on BaBiO ₃ and Ba _{0.6} K _{0.4} BiO ₃	244

Table 6.3 (a):	Effect of initial dye concentration on degradation of CR	247
Table 6.4 (a):	Effect of initial dye concentration on degradation of CR	247
Table 6.5 (a):	Effect of initial dye concentration on degradation of CR	248
Table 6.6 (a):	Effect of initial dye concentration on degradation of CR	248
Table 6.7 (a):	Pseudo-first order apparent rate constant and initial rate values for the different initial concentration of dye	252
Table 6.3 (b):	Influence of initial concentration on degradation of CR	254
Table 6.4 (b):	Influence of initial concentration on degradation of CR	254
Table 6.5 (b):	Influence of initial concentration on degradation of CR	255
Table 6.6 (b):	Influence of initial concentration on degradation of CR	255
Table 6.7 (b):	Pseudo-first order apparent constant values for the different initial dye concentration of dye	259
Table 6.8 (a):	Influence of BaBiO ₃ dose on degradation of CR	262
Table 6.9(a):	Pseudo-first order apparent constant values for the different BaBiO ₃ dose	264
Table 6.8 (b):	Influence of Ba _{0.6} K _{0.4} BiO ₃ dose on degradation of CR	265
Table 6.9 (b):	Pseudo-first order apparent constant values for the different Ba _{0.6} K _{0.4} BiO ₃ dose	267
Table 6.10 (a):	Influence of solution pH on degradation of CR	270
Table 6.11 (a):	Pseudo-first order apparent constant values for the photodegradation of CR at different solution pH	272
Table 6.10 (b):	Influence of solution pH on degradation of CR	274
Table 6.11 (b):	Pseudo-first order apparent constant values for the photodegradation of CR at different solution pH	276
Table 6.12 (a):	Influence of temperature on degradation of CR	278
Table 6.13 (a):	Pseudo-first order apparent constant values for the different temperatures	280
Table 6.12 (b):	Influence of temperature on degradation of CR	281
Table 6.13 (b):	Pseudo-first order apparent constant values for the different temperatures	283

LIST OF FIGURE

Figure No.	Title	Page No.
Figure 1.1:	Indirect transition (left) and direct transition (right)	12
Figure 1.2:	Cubic perovskite unit cell	17
Figure 2.1:	Muffle Furnace	41
Figure 2.2:	Ultra-Pure Water Purification System	42
Figure 2.3:	Double beam spectrophotometer	43
Figure 2.4:	Flow chart for the synthesis of BaBiO ₃ and Ba _{0.6} K _{0.4} BiO ₃ of catalysts	45
Figure 2.5:	Thermogravimetric/differential thermal analyser	46
Figure 2.6:	X-ray Diffractometer	47
Figure 2.7:	FT-IR Spectrometer	49
Figure 2.8:	UV-Vis Spectrophotometer	51
Figure 2.9:	Field emission gun- scanning electron microscope	52
Figure 2.10:	Schematic of the immersion type photocatalytic reactor set up for the degradation of dye solution	54
Figure 2.11:	Flow chart of the photodegradation of studied dyes by the synthesized catalysts	55
Figure 3.1:	Mechanism of Pechini reaction	65
Figure 3.2:	(A) Flowchart for the preparation of BaBiO ₃ (B) BaBiO ₃ powder precursor at 350° C/2h. (C) BaBiO ₃ perovskite at 800 ° C /12h	68
Figure 3.3:	Flowchart for the preparation of Ba _{0.6} K _{0.4} BiO ₃ (B) Ba _{0.6} K _{0.4} BiO ₃ powder precursor at 350° C/2h. (C) Ba _{0.6} K _{0.4} BiO ₃ perovskite at 720 ° C /12h	70
Figure 3.4:	TGA and DTA curves of BaBiO ₃ precursor prepared by Pechini method	73
Figure 3.5:	XRD patterns of BaBiO ₃ at different calcinations temperatures. (a) At 350°C/2 hours (b) at 600°C/5hours (c) at 800°C/12hours	74
Figure 3.6:	Three-dimensional packing diagrams of BaBiO ₃	76

Figure 3.8:	(A) Reflectance and (B) absorption spectrum of BaBiO ₃ calcined at 800°C/12hours	78
Figure 3.9:	Kubelka-Munk converted Tauc plot of BaBiO ₃	79
Figure 3.10:	Scanning electron micrograph of BaBiO ₃ calcined at 800°C/12h at different magnifications.(A) at 10,000 (B) at 5,000, (C) at 2,000 (D) at 10,000	81
Figure 3.11:	TGA and DTA curves of Ba _{0.6} K _{0.4} BiO ₃ precursor prepared by Pechini method	84
Figure 3.12:	XRD patterns of Ba _{0.6} K _{0.4} BiO ₃ at different calcinations temperatures. (A) At 350°C/2 hours (B) at 650°C/6 hours (C) at 720°C/12 hours	85
Figure 3.13:	Three-dimensional packing diagrams of Ba _{0.6} K _{0.4} BiO ₃	87
Figure 3.14:	The FTIR spectra of Ba _{0.6} K _{0.4} BiO ₃ calcined at 720°C/12hours	88
Figure 3.15:	(A) Reflectance and (B) absorption spectrum of Ba _{0.6} K _{0.4} BiO ₃ calcined at 720°C/12 hours	90
Figure 3.16:	Kubelka-Munk converted Tauc plot of Ba _{0.6} K _{0.4} BiO ₃	90
Figure 3.17:	Scanning electron micrograph of Ba _{0.6} K _{0.4} BiO ₃ (calcined at 720°C/12hours) at different magnifications. (A) at 60,000 (B) at 50,000, (C) at 40,000 (D) at 20,000	92
Figure 4.1:	Harmful effects of CV dye	102
Figure 4.2:	UV-VIS spectra of CV dye	107
Figure 4.3:	Photolysis of CV in presence of irradiation	107
Figure 4.4 (a):	Adsorption isotherm from aqueous CV dye solution	110
Figure 4.4 (b):	Adsorption isotherm from aqueous CV dye solution with Ba _{0.6} K _{0.4} BiO ₃ catalyst	110
Figure 4.5 (a):	Langmuir plots for the adsorption of CV on BaBiO ₃	111
Figure 4.5 (b):	Langmuir plots for the adsorption of CV on Ba _{0.6} K _{0.4} BiO ₃	111
Figure 4.6 (a):	Freundlich plots for the adsorption of CV on BaBiO ₃	113
Figure 4.7 (a):	Effect of concentration of CV on its visible light degradation in BaBiO ₃	118

Figure 4.7 (b):	Effect of concentration of CV on its visible light degradation in $\text{Ba}_{0.6}\text{K}_{0.4}\text{BiO}_3$	126
Figure 4.8 (a):	Variation of dye concentration versus time for different CV initial concentration	120
Figure 4.8 (b):	Variation of dye concentration versus time for different CV initial concentration	128
Figure 4.9 (a):	Linear variation of $\ln C_t/C_o$ versus time for the photocatalytic degradation of CV dye at different initial concentration	122
Figure 4.9 (b):	Linear variation of $\ln C_t/C_o$ versus time for the photocatalytic degradation of CV dye at different initial concentration	129
Figure 4.10 (a):	Langmuir-Hinshelwood plot for visible light photodegradation of CV dye by BaBiO_3 photocatalyst	123
Figure 4.10 (b):	Langmuir-Hinshelwood plot for visible light photodegradation of CV dye by $\text{Ba}_{0.6}\text{K}_{0.4}\text{BiO}_3$ photocatalyst	130
Figure 4.11 (a):	Influence of BaBiO_3 dose on visible light degradation of CV dye	132
Figure 4.11 (b):	Influence of $\text{Ba}_{0.6}\text{K}_{0.4}\text{BiO}_3$ dose on visible light degradation of CV dye	136
Figure 4.12(a):	Variation of residual dye concentration at different BaBiO_3	133
Figure 4.12 (b):	Variation of residual dye concentration at different $\text{Ba}_{0.6}\text{K}_{0.4}\text{BiO}_3$	136
Figure 4.13 (a):	Linear variation of $\ln C_t/C_o$ versus time for photocatalytic degradation of CV dye at different BaBiO_3 loading	133

Figure 4.13 (b):	Linear variation of $\ln C_t/C_o$ versus time for photocatalytic degradation of CV dye at different $Ba_{0.6}K_{0.4}BiO_3$ loading	137
Figure 4.14 (a):	Relationship between $\ln K_{app}$ and the amount of $BaBiO_3$	134
Figure 4.14 (b):	Relationship between $\ln K_{app}$ and the amount of $Ba_{0.6}K_{0.4}BiO_3$	138
Figure 4.15 (a):	Effect of initial pH on % degradation of CV	141
Figure 4.15 (b):	Effect of initial pH on % degradation of CV	144
Figure 4.16 (a):	Effect of pH on the residual dye concentration	141
Figure 4.16 (b):	Effect of pH on the residual dye concentration	144
Figure 4.17 (a):	Linear variation of $\ln C_t/C_o$ versus time for photocatalytic degradation of CV dye at different initial solution pH	142
Figure 4.17 (b):	Linear variation of $\ln C_t/C_o$ versus time for photocatalytic degradation of CV dye at different initial solution pH	145
Figure 4.18(a):	Effect of the initial pH on the reaction rate constant for CV dye degradation	143
Figure 4.18 (b):	Effect of the initial pH on the reaction rate constant for CV dye degradation	146
Figure 4.19 (a):	Influence of temperature on % degradation of CV	148
Figure 4.19 (b):	Influence of temperature on % degradation of CV	151
Figure 4.20 (a):	Effects of Temperature on the residual dye fractions	148
Figure 4.20 (b):	Effects of Temperature on the residual dye fractions	151
Figure 4.21 (a):	Linear variation of $\ln C_t/C_o$ versus time for photocatalytic degradation of CV dye at different temperature	149
Figure 4.21 (b):	Linear variation of $\ln C_t/C_o$ versus time for photocatalytic degradation of CV dye at different temperature	152
Figure 4.22 (a):	Plot of $\ln K_{app}$ versus inverse of temperature	150
Figure 4.23:	Regeneration of photocatalyst	154

Figure 4.24:	Comparison of photocatalytic efficiency of as prepared with p25 TiO ₂ under visible light irradiation	155
Figure 4.25:	UV-vis absorbance spectra of CV solution after photocatalytic degradation over as prepared catalysts	156
Figure 4.26:	TOC removal in CV dye solution obtained by photodegradation by as prepared catalysts	157
Figure 5.1:	Harmful effects of MG dye	167
Figure 5.2:	UV-VIS spectra of MG dye	172
Figure 5.3:	Photolysis of MG in presence of irradiation	173
Figure 5.4 (a):	Adsorption isotherm from aqueous MG dye solution	175
Figure 5.4 (b):	Adsorption isotherm from aqueous MG dye solution with Ba _{0.6} K _{0.4} BiO ₃ catalyst	175
Figure 5.5 (a):	Langmuir plots for the adsorption of MG on BaBiO ₃	176
Figure 5.5 (b):	Langmuir plots for the adsorption of MG on Ba _{0.6} K _{0.4} BiO ₃	176
Figure 5.6 (a):	Freundlich plots for the adsorption of MG on BaBiO ₃	178
Figure 5.6 (b):	Freundlich plots for the adsorption of MG on Ba _{0.6} K _{0.4} BiO ₃	178
Figure 5.7 (a):	Effect of concentration of MG on its visible light degradation in BaBiO ₃	183
Figure 5.7 (b):	Effect of concentration of MG on its visible light degradation in Ba _{0.6} K _{0.4} BiO ₃	191
Figure 5.8 (a):	Variation of dye concentration versus time for different MG initial concentration	187
Figure 5.8(b):	Variation of dye concentration versus time for different MG initial concentration	193
Figure-5.9 (b):	Linear variation of $\ln C_t/C_0$ versus time for the photocatalytic degradation of MG dye at different initial concentration	194
Figure 5.10 (a):	Langmuir-Hinshelwood plot for visible light photodegradation of MG dye by BaBiO ₃ photocatalyst	188

Figure 5.10 (b):	Langmuir-Hinshelwood plot for visible light photodegradation of MG dye by Ba _{0.6} K _{0.4} BiO ₃ photocatalyst	195
Figure 5.11 (a):	Influence of BaBiO ₃ dose on visible light degradation of MG dye	197
Figure 5.11 (b):	Influence of Ba _{0.6} K _{0.4} BiO ₃ dose on visible light degradation of MG dye	201
Figure 5.12 (a):	Variation of residual dye concentration at different BaBiO ₃	198
Figure 5.12 (b):	Variation of residual dye concentration at different Ba _{0.6} K _{0.4} BiO ₃	201
Figure 5.13 (a):	Linear variation of $\ln C_t/C_o$ versus time for photocatalytic degradation of MG dye at different BaBiO ₃ loading	198
Figure 5.13 (b):	Linear variation of $\ln C_t/C_o$ versus time for photocatalytic degradation of MG dye at different Ba _{0.6} K _{0.4} BiO ₃ loading	202
Figure 5.14 (a):	Relationship between $\ln K_{app}$ and the amount of BaBiO ₃	199
Figure 5.14 (b):	Relationship between $\ln K_{app}$ and the amount of Ba _{0.6} K _{0.4} BiO ₃	203
Figure 5.15 (a):	Effect of initial pH on % degradation of MG	206
Figure 5.15 (b):	Effect of initial pH on % degradation of MG	209
Figure 5.16 (a):	Effect of pH on the residual dye concentration	206
Figure 5.16 (b):	Effect of pH on the residual dye concentration	209
Figure 5.17 (b):	Linear variation of $\ln C_t/C_o$ versus time for photocatalytic degradation of MG dye at different initial solution pH	210
Figure 5.18 (a):	Effect of the initial pH on the reaction rate constant for MG dye degradation	208
Figure 5.18 (b):	Effect of the initial pH on the reaction rate constant for MG dye degradation	211
Figure 5.19 (a):	Influence of temperature on % degradation of MG	213

Figure 5.19 (b):	Influence of temperature on % degradation of MG	216
Figure 5.20 (a):	Effects of Temperature on the residual dye fractions	213
Figure 5.20 (b):	Effects of Temperature on the residual dye fractions	217
Figure 5.21 (a):	Linear variation of $\ln C_t/C_0$ versus time for photocatalytic degradation of MG dye at different temperature	214
Figure 5.21 (b):	Linear variation of $\ln C_t/C_0$ versus time for photocatalytic degradation of MG dye at different temperature	217
Figure 5.22 (a):	Plot of $\ln K_{app}$ versus inverse of temperature	215
Figure 5.22 (b):	Plot of $\ln K_{app}$ versus inverse of temperature	218
Figure 5.23:	Regeneration of photocatalyst	219
Figure 5.24:	Comparison of photocatalytic efficiency of as prepared with p25 TiO_2 under visible light irradiation	220
Figure 5.25:	UV-vis absorbance spectra of MG solution after photocatalytic degradation over as prepared catalysts	221
Figure 5.26:	TOC removal in MG dye solution obtained by photodegradation by as prepared catalysts	222
Figure 6.1:	Harmful effects of CR dye	233
Figure 6.2:	UV-VIS spectra of CR dye	237
Figure 6.3:	Photolysis of CR in presence of irradiation	238
Figure 6.4 (a):	Adsorption isotherm from aqueous CR dye solution	240
Figure 6.5 (a):	Langmuir plots for the adsorption of CR on $BaBiO_3$	241
Figure 6.5 (b):	Langmuir plots for the adsorption of CR on $Ba_{0.6}K_{0.4}BiO_3$	242
Figure 6.6 (a):	Freundlich plots for the adsorption of CR on $BaBiO_3$	243
Figure 6.6 (b):	Freundlich plots for the adsorption of CR on $Ba_{0.6}K_{0.4}BiO_3$	244
Figure 6.7 (a):	Effect of concentration of CR on its visible light degradation in $BaBiO_3$	249

Figure 6.7 (b):	Effect of concentration of CR on its visible light degradation in $Ba_{0.6}K_{0.4}BiO_3$	257
Figure 6.8 (a):	Variation of dye concentration versus time for different CR initial concentration	251
Figure 6.8 (b):	Variation of dye concentration versus time for different CR initial concentration	258
Figure 6.9 (a):	Linear variation of $\ln C_t/C_o$ versus time for the photocatalytic degradation of CR dye at different initial concentration	252
Figure-6.9 (b):	Linear variation of $\ln C_t/C_o$ versus time for the photocatalytic degradation of CR dye at different initial concentration	259
Figure 6.10 (a):	Langmuir-Hinshelwood plot for visible light photodegradation of CR dye by $BaBiO_3$ photocatalyst	253
Figure 6.10 (b):	Langmuir-Hinshelwood plot for visible light photodegradation of CR dye by $Ba_{0.6}K_{0.4}BiO_3$ photocatalyst	260
Figure 6.11 (a):	Influence of $BaBiO_3$ dose on visible light degradation of CR dye	262
Figure 6.11 (b):	Influence of $Ba_{0.6}K_{0.4}BiO_3$ dose on visible light degradation of CR dye	266
Figure 6.12 (b):	Variation of residual dye concentration at different $Ba_{0.6}K_{0.4}BiO_3$	266
Figure 6.13 (a):	Linear variation of $\ln C_t/C_o$ versus time for photocatalytic degradation of CR dye at different $BaBiO_3$ loading	263
Figure 6.13 (b):	Linear variation of $\ln C_t/C_o$ versus time for photocatalytic degradation of CR dye at different $Ba_{0.6}K_{0.4}BiO_3$ loading	267
Figure 6.14 (a):	Relationship between $\ln K_{app}$ and the amount of $BaBiO_3$	264
Figure 6.14 (b):	Relationship between $\ln K_{app}$ and the amount of $Ba_{0.6}K_{0.4}BiO_3$	268

Figure 6.15 (a):	Effect of initial pH on % degradation of CR	271
Figure 6.15 (b):	Effect of initial pH on % degradation of CR	274
Figure 6.16 (a):	Effect of pH on the residual dye concentration	271
Figure 6.16 (b):	Effect of pH on the residual dye concentration	275
Figure 6.17 (a):	Linear variation of $\ln C_t/C_o$ versus time for photocatalytic degradation of CR dye at different initial solution pH	272
Figure 6.17 (b):	Linear variation of $\ln C_t/C_o$ versus time for photocatalytic degradation of CR dye at different initial solution pH	275
Figure 6.18 (a):	Effect of the initial pH on the reaction rate constant for CR dye degradation	273
Figure 6.18 (b):	Effect of the initial pH on the reaction rate constant for CR dye degradation	276
Figure 6.19 (a):	Influence of temperature on % degradation of CR	278
Figure 6.19 (b):	Influence of temperature on % degradation of CR	282
Figure 6.20 (a):	Effects of Temperature on the residual dye fractions	279
Figure 6.20 (b):	Effects of Temperature on the residual dye fractions	282
Figure 6.21 (b):	Linear variation of $\ln C_t/C_o$ versus time for photocatalytic degradation of CR dye at different temperature	283
Figure 6.22 (a):	Plot of $\ln K_{app}$ versus inverse of temperature	281
Figure 6.22 (b):	Plot of $\ln K_{app}$ versus inverse of temperature	284
Figure 6.23:	Regeneration of photocatalyst	285
Figure 6.24:	Comparison of photocatalytic efficiency of as prepared with p25 TiO ₂ under visible light irradiation	286
Figure 6.25:	UV-vis absorbance spectra of CR solution after photocatalytic degradation over as prepared catalysts	287
Figure 6.26:	TOC removal in CR dye solution obtained by photodegradation by as prepared catalysts	288

List of Abbreviations and Symbols

AOPs: Advanced Oxidation Processes

Ag: Silver

Au: Gold

Ads: Adsorbed

B: Adsorption equilibrium constant

Ba: Barium

Bi: Bismuth

Bi₂O₃: Bismuth (iii) oxide

CA: Citric acid

CB: Conduction band

CdS: Cadmium sulphide

CO₂: Carbon di oxide

Conc: Concentration

Co: Cobalt

C₀: Concentration at time t=0

C_t: Concentration at time t

C_e: Concentration after adsorption-desorption equilibrium

CR: Congo red

CV: Crystal violet

CCl₄: Carbon tetra chloride

DNA: Deoxyribo nucleic acid

e⁻: Electron

EDTA: Ethylene di-amine tetra-acetic acid

EG: Ethylene glycol

E_g: Band gap

eV: Electron Volt

Fe: Iron

FE-SEM: Field-Emission scanning electron microscopy

FTIR: Fourier transform infra-red spectroscopy

g: Gram

h⁺: Positive holes

HOMO: Highest Occupied Molecular Orbital
H₂O: Water
IUPAC: International Union of Pure and Applied Chemistry
i.e.: That is
JCPDS: Joint committee on powder diffraction standards
K: Potassium
kV: Kilo volt
k_{app}: pseudo first order rate constant
K_f: Freundlich constant
K_{LH}: Langmuir Hinshelwood adsorption constant
KM: Kubelka- Munk
K_r: Surface reaction rate constant
La: Lanthanum
LH: Langmuir Hinshelwood
Ln: Lanthanides
LUMO: Lowest Unoccupied Molecular Orbital
mA: milli ampere
mg: Milligram
MG: Malachite green
m: Millilitre
Min.: Minutes
Mol. Wt.: Molecular Weight
Mn: Manganese
mWcm⁻²: Unit representing intensity of light
N: Normality
NHE: Normal hydrogen electrode
nm: Nano meter
Ni: Nickel
N: Nitrogen
Nb: Niobium
O₂: Oxygen
OH°: Hydroxyl radical
OH⁻: Hydroxide anion
Pb: Lead

ppm: Parts per million
Pt: Platinum
 q_e : amount adsorbed
 Q_0 : Maximum adsorption
R: Universal gas constant (8.314 J/mol/K)
 R^2 : Coefficient of determination/correlation coefficient
 R_L : Constant separation factor
 r_0 : initial rate
Ru: Ruthenium
 R_d : Diffused reflectance
SrTiO₃: Strontium titanate
t: Tolerance factor
Ta: Tantalum
Temp.: Temperature
TGA: Thermo-gravimetric analysis
Ti: Titanium
TiO₂: Titanium di oxide
TOC: Total Organic Carbon
UV-DRS: Ultra-violet-diffuse reflectance spectroscopy
V: Vanadium
VB: Valence band
WO₃: Tungsten tri oxide
XRD: X-ray diffraction
ZnO: Zinc Oxide
ZnS: Zinc Sulphide
 $\alpha/\beta/\gamma$ = inter planar angle
a/b/c= lattice parameter
 λ_{max} = Adsorption maxima
s= Scattering coefficient
h= Planck Constants
n= constant related to transition mode
 ν = Oscillation frequency
Å = Angstrom
 2θ = function of the inter planar angle

Chapter 1

Introduction and Literature Review

Dyes are categorized by structural stability and colour stability imparted by their high degree of aromaticity and extensively conjugated chromophore. The manufacture and widespread use of dyes results in their unintended release into the environment, where they pose potential threat to environment [1-2]. The colour of the waste is the most apparent meter of the water pollution and it should be reduced before their drop. The existence of lesser amount of dyes (below 1ppm) is evidently visible and noticeably impacts the water environment. The severely affected water contain significant amount of carcinogenic and mutagenic organic substances. So removal of these dyes is highly desirable like other colourless organic pollutants [3-4].

Conventional treatment processes such as physical, biological and chemical treatments on their own are only able to remove dyes to a certain degree. Furthermore, some of these treatments produce additional problems such as sludge disposal and phase transfer of pollutants [5,6]. Consequently substantial approaches has been mad to develop advanced methods for remediating dye-contaminated water. Among the treatment methods, photocatalytic technologies are commonly useful due to their potential capability for complete mineralisation of organic dye molecule to into CO₂, H₂O and other non-toxic end products. Visible light photocatalysis has attained emergent consideration as one type of photocatalysis. The most significant advantage is it can be driven by visible light rather than UV light which is the only energy source utilized in traditional photocatalysis [7,8]. Perovskite materials are well-known for their narrow band gap and extraordinary photocatalytic activity, and hence have become more noticeable in the field of visible light photocatalysis [9,10].

This chapter delivers the general background and shows an extensive literature review related to dyes and their impact on environment, all the relevant aspects of the photocatalysis and different photocatalysts used in the waste water treatment. It also explains the background information needed to understand the chemistry behind photocatalysis using perovskite oxides as for the degradation of dyes.

1.1 Dyes and their toxicity

Textile dyes are particles designed to impart permanent colours to clothing & textiles. There are several ways of classifying commercial dyes whereby it can be catalogued in terms of its colour, structure and application methods.

Dyes are typically categorized by their Colour Index (CI), established by the **Society of Dyes and Colourist** (1984), which is modified in every three months. It lists dyes firstly by a generic name based on its application and colour, then by assigning a 5-digit CI number based on its chemical structure, if known [11,12]. Dyes could also be classified according to its solubility. Soluble dyes include direct, basic, acid, metal complex, reactive and mordant dyes. On the other hand, insoluble dyes encompass azoic, sulphur, disperse and vat dyes [13,14]. Based on the functional group that constitutes the dyes, dyes are classified as azoic, anthraquinonic, hetero-polyaromatic, aryl methane, indigo, nitro, aryl methane.

Dyes contain two groups; auxochromes and chromophores. Chromophore are the group of atoms which are responsible for the colour of dye. The other group is **auxochrome**, which can be defined as an electron withdrawing or donating substituents that essential for the colour enhancement of the chromophores. The most important chromophores are the azo ($-N=N-$), carbonyl ($-C=O$), methine ($-CH=$) and nitro ($-NO_2$) groups. The most important auxochromes are amine ($-NH_3$), carboxyl ($-COOH$), sulfonate ($-SO_3H$) and hydroxyl ($-OH$) groups. The intensity of the colour of any dye depend upon the number of auxochrome groups [15]. Dye molecules are coloured because they absorbs in the visible range of the solar spectrum at a definite wavelength.

The release of dye-containing effluents into the water bodies impacts water ecosystem adversely. Several studies demonstrated that dyes released in the form of effluents are metabolized into toxic end products which are carcinogenic and mutagenic to humans and other mammalians [16,17]. Also, without appropriate treatment these dyes can exist in the environment persistently.

The major environmental concern with dyes is that they absorb and reflect the incoming sunlight into water bodies. Which further reduces photosynthetic activity of marine plants and thus critically effects the food chain and water ecosystem. The

existence of very small amounts of dyes in the water, which are however extremely noticeable, disturbs the quality and transparency of water bodies such as lakes, rivers and others, which further leading to harm to the water environment. Prolonged human exposure towards coloured effluents resulted in a wide range of immune suppression, cardiovascular, breathing, central nervous and neurobehavioral disorders indications such as vomiting, allergy, salivation, cyanosis, leukaemia and lung edema amongst others [18-20].

In current scenario, environmental pollution can certainly be considered as one of the main problems in established and emerging nations. There are several factors which affects the environment, such as the misuse of natural resources, inefficient legislation and a lack of environmental awareness. Providentially, in current years there has been a trend for change and a sequence of scientific research are being used as a significant tool in the improvement of new treatment methods and even in the application of procedures and ecologically friendly actions.

1.2 Degradation of dyes

Owing to the hazards of dyes in water bodies, inventions of a wide variety of treatment technologies has stimulated a dramatic progress in the scientific society. The available technologies for dye removal can be classified into three categories: physical, biological and chemical. Each method has few advantages and disadvantages.

1.2.1 Biological treatment methods

In biological treatment approaches microorganisms such as bacteria are used, for the decomposition of various effluents to stable end products. More microorganisms, or sludge, are formed and a portion of the waste is transformed to carbon dioxide, water and other end harmless end products. Generally, biological treatment methods can be divided into two parts, **aerobic method** and **anaerobic method**.

These methods are not much effective, as bacteria or fungi cannot efficiently degrade the bulky, and stable dyes, so treatment cannot based on biodegradation alone. Further, aerobic procedures yields huge quantities of biological slurry and

required a huge disposal area. Anaerobic processes do not lower the pollutant content to a proper level [21,22].

1.2.2 Physical treatment methods

These methods are technically easy and low cost process but non-destructive, that is, they just transfer the pollutants from aqueous solution to another phase rather than destroy them. Physical methods such as **coagulation, adsorption, reverse osmosis, nano-filtration, membrane-filtration** and **electro-dialysis** were applicable for textile wastewater treatment [23-25].

Adsorption which is also comes with a few restrictions such as the requirement of regeneration after material exhaustion and the loss of adsorption efficiency following regeneration [26], in addition it requires pre-treatment of the wastewater to lower the suspended solid content before it was fed into the adsorption column and the eco-friendly disposal of the spent adsorbents.

1.2.3 Chemical treatment methods

Processes such as oxidation, sodium hypochlorite (NaOCl) and chemical precipitation (coagulation) are some of the chemical treatment procedures that could be performed on wastewaters containing dyes. Among the chemical methods, the oxidation methods are more efficient and are applicable for large-scale treatment of industrial effluent [27].

1.2.4 Advanced Oxidation Processes(AOP)

Advanced oxidation processes (AOPs), have received great consideration for waste water treatment during the last few years. Advanced Oxidation Processes involve the generation of highly reactive radicals generally hydroxyl radicals ($\cdot\text{OH}$) at ambient temperature and pressure conditions. [28]. Hydroxyl radicals are extremely reactive species that outbreak most of the organic pollutants. The kinetics of reaction is generally first order with respect to the concentration of hydroxyl radicals and to the concentration of the species to be degraded. These processes can be classified as heterogeneous and homogeneous photocatalysis. The semiconductor mediated photocatalysis is known as heterogeneous photocatalysis. The hydroxyl radicals can be generated in different processes, such as **ozonation** (O_3), ultraviolet (UV) [29], hydrogen peroxide combined with ultraviolet radiation

(H₂O₂/UV), **Fenton reagent** (Fe²⁺/H₂O₂) [30], O₃/UV [31], O₃/H₂O₂ and by irradiation of semiconductors such as zinc oxide (ZnO), titanium dioxide (TiO₂) [32-34].

Heterogeneous photocatalysis may be considered a practical alternate for the removal of stable waste organics due to numerous significant advantages such as: complete mineralization or formation of more readily decomposable intermediates when complex organic compounds are treated, no need of auxiliary chemicals, no residual formation, easily operation and maintenance of the equipment [35].

The summary of previously reported analytical methods used for the degradation of dyes has been presented in **Table 1.1**.

Table 1.1 Summary of analytical methods used for the degradation of dyes

S. No.	Technique	Advantage	Disadvantage	Reference
1	Biological Treatment 1. Aerobic method 2. Anaerobic method	<ul style="list-style-type: none"> • Environment friendly • Efficient and cost effective • Low energy demand • Mineralize organic pollutants in relatively nontoxic constituents • Certain dyes have a particular affinity to binding with specific microbial species 	<ul style="list-style-type: none"> • Require extra residence time • Enzyme production has also been shown to be unreliable • Under aerobic conditions Azo dyes are not readily metabolized • Not effective for all dyes 	[36]
2	Chemical Treatment 1. Coagulation /Filtration/Precipitation 2. Oxidative Methods 3. Ion exchange process	<ul style="list-style-type: none"> • Suspended and colloidal particles can be easily separated • Frequently adopted method due to its simplicity of application • Both anionic and cationic dyes can be removed • No loss of absorbent 	<ul style="list-style-type: none"> • Coagulation /Filtration/Precipitation • These agents needs to be activated by some means as UV light • High cost Not effective for disperse dyes 	[37-39]

3	Physical Treatment 1. Adsorption technique 2. Stripping technique 3. Reverse osmosis and filtration	<ul style="list-style-type: none"> • Good removal of wide variety of dyes • High selectivity and efficiency can remove non-biodegradable dyes • Can remove volatile organic Compounds • Favourable for large water stream 	<ul style="list-style-type: none"> • Some of the adsorbents are very expensive • Secondary treatment is needed • Secondary treatment is needed • Energy is needed • Several operational difficulties • High capital difficulties 	[40-42]
4	Advanced Oxidation process 1. Fenton's Reagent 2. Ozonation 3. Ultrasonication	<ul style="list-style-type: none"> • Fenton's reagent is a suitable chemical means • Simplicity of applications • Can Treat Hardly Degradable Organics • Mineralise organic pollutants into relatively non-toxic constituents • Operates at room Conditions and Do not Require Addition of Extra Chemicals 	<ul style="list-style-type: none"> • Not effective for high concentration of certain refractory contaminants • High operational cost • Unstable {Short half Life (20 Min.)} • Substantial Amount of Energy Needed in Generating the radicals 	[43-47]

Thus in search for highly effective methods to degrade the dyes into environmentally compatible non-toxic end products. Alternatively, a photochemical approach has been adopted. In recent times, advanced oxidation processes have been recommended for decontamination of waste water. Among these processes, photocatalysis can play an important role in new technologies of wastewater purification.

In the process of photocatalytic treatment for waste water, holes are generated in Valence band. These holes play the important role in photocatalysis. It induce oxidative decomposition of various organic pollutants. These positive holes (h^+) further react hydroxide ion (OH^-) of water to yield the hydroxyl radical (OH^\bullet). Hydroxyl radical is a strong oxidant with the oxidation potential of 2.8 V (NHE). $^\bullet OH$ rapidly attacks pollutants at the surface and in solution and it directly mineralizes the organic pollutants into simple inorganic species such as CO_2 , H_2O [48,49].

1.3 Photocatalysis

Photocatalysis concerns a sequence of innovative light-induced oxidation routes including the generation and consequent reaction of electron-hole pairs in a photocatalyst which has been excited by photons. This includes a series of redox reactions resulting in the degradation and mineralization of organic pollutants in aqueous solution in the presence of O_2 . As one of the methodologies to chemical solar energy conversion, photocatalysis is an effective technique to remove refractory toxic organic contaminants in our environment, and a promising way to provide clean hydrogen energy via water splitting.

Photocatalytic activity was first popularized by the study of the ‘Honda-Fujishima effect’ on photo-electrochemical water splitting by titania (TiO_2) electrode. Thereafter, it has been broadly used in many application including water cleavage, domestic and industrial wastewater treatment, air cleaning and self-cleaning surfaces. Self-sterilizing tiles to cover the walls of operation rooms in hospital is made of TiO_2 . Sand supported TiO_2 is used in the disinfection of photogenic, microbial contaminated industrial water. Several other application of photocatalysis like antitumor activity, preparation of sound-proofed walls and super-hydrophilic materials for car mirrors are already at or near the stage of application and commercialization [50-54].

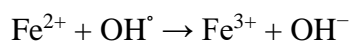
Over the past few spans, photocatalysis has been the focus of widespread research in the elimination of pollutants in air and water streams [55]. Several features, such as ambient operating conditions, complete destruction of compounds and their intermediate compounds, and relatively low operating cost, have

established its applicability to water treatment. In photocatalysis, semiconductor materials are activated by light (generally UV light).

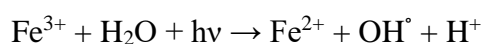
1.3.1. Homogeneous photocatalysis

In homogeneous photocatalysis, the reactants and the photocatalysts are in the same physical state. The most normally used homogeneous photocatalysts comprise ozone and Fenton systems ($\text{Fe}^+/\text{H}_2\text{O}_2$). The reactive species is the OH° which is the key component in the dye degradation process.

The generation of hydroxyl radicals in Fenton reaction take place in the following reaction sequence:



In photo-Fenton type processes, additional sources of OH radicals should be considered: through photolysis of H_2O_2 , and through reduction of Fe^{3+} ions under UV light:



The effectiveness of Fenton type procedures is governed by numerous operating factors like initial concentration of hydrogen peroxide, pH and intensity of UV light. The key advantage of this method is the ability to utilizing sunlight with light sensitivity up to 450 nm. So in this method expensive UV lamps or any other electrical energy is not required. This method is found to be more effective than the other photocatalysis methods. The main drawback of the process are the low pH values which are required for the degradation of pollutants. But at higher pH values iron precipitates, and that iron has to be separated after treatment [56].

1.3.2 Heterogeneous photocatalysis

In heterogeneous catalysis the catalysts and the reactants, both are in the different physical state. Heterogeneous photocatalysis is a discipline which

comprises a large multiplicity of reactions such as: partial or complete oxidations, dehydrogenation, hydrogen transfer, $^{18}\text{O}_2$ - $^{16}\text{O}_2$ and deuterium-alkane isotopic exchange, metal deposition, water detoxification, removal of gaseous pollutant etc.

1.4 Semiconductor Photocatalysis

In the past few years, photocatalytic reactions on semiconductors have been applied for numerous applications, such as air cleaners, self-cleaning materials, and antibacterial materials. The reactions are usually accepted as potential technique, initiating from electrons and holes excited by adsorption of photons with energy greater than the band gap of semiconductors. The holes have a strong ability to eject electrons out of organic and inorganic pollutants, resulting in the total degradation of contaminated substances present in effluents [57].

A semiconductor, by definition, is nonconductive in its un-doped ground state because an energy gap, the band gap, exists between the top of the filled valence band and the bottom of the vacant conduction band. Thus, electron transport between these bands must occur only with appreciable energy change. Semiconductors are particularly useful as photocatalysts because of a favourable combination of electronic structure, light absorption properties, charge transport characteristics and excited-state lifetimes [58].

1.4.1 Mechanism of semiconductor photocatalysis

Usually, a fundamental photocatalytic reaction comprises three basic steps [59-61]: 1) excitation of charge carriers in light irradiation; 2) separation and dispersion of charge carriers to the surface; 3) photocatalytic reaction on the photocatalyst surface.

In the primary step, when semiconductor material absorbs lights with photon energy equal to or higher than its band gaps ($\lambda \geq E_g$), the lone electrons will be excited from valence band to conduction band and, at the same time, an empty valence band holes (h^+) are left behind.

After the electron-hole pairs have been formed under light irradiation, the charge carriers start to dispersed from inside to the surface of photocatalyst molecules. These e^-h^+ pairs are known as surface trapped $e^- - h^+$ pairs.



At the same point, thus prepared charge carriers can be recombined in nanosecond and releasing the heat energy.

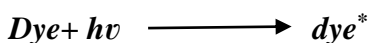


In the presence of absorbed oxygen, the excited photocatalyst, eject an e^- . This e^- is accepted by molecular oxygen (electron acceptor) to form superoxides radical ($O_2^{\circ-}$) which could be further forms hydroperoxyl radical (HO_2°) by accepting one proton, and consequently becoming H_2O_2 .

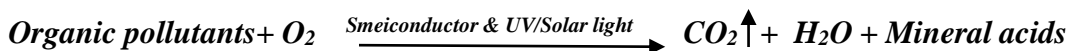
Consequently, hydroxyl radicals (OH°) could not be formed without the presence of adsorbed water molecules. Hence, both $O_2^{\circ-}$ radical and HO_2° radical could extend the recombination time of e^- - h^+ pair in the complete photocatalysis reaction.



The degradation of effluence take place on the surface of photocatalyst by the means of thus prepared OH° radical. Different bulky organic compounds could be completely degraded into non-toxic carbon dioxide and water by OH° . Here, it is worth mentioning that these OH° are generated in the presence of dissolved oxygen and water.



Therefore, the overall process can be summarised as follows



1.4.2 Band gap energy

The electronic energy structure of a semiconductor comprises of three differentiated constituents, i.e. the conduction band (CB), the valence band (VB)

and the forbidden band. The forbidden band symbolises a region in which for an ideal un-doped semiconductor energy state do not exist. Energy state only exists above and below this region. Taking the energy level of the electron in the vacuum as reference and as the uppermost level, the upper band is called the **conduction band** and the lower one the **valence band**. In terms of energy the difference between upper edge of the valence band and the lower edge of the conduction band is called the band gap (E_g) of the semiconductor. If the two levels can be defined with the same wave vector the semiconductor is considered to have a **direct band gap** or otherwise it has an **indirect band gap** [62].

Band gap correspond to difference in potential of CB bottom and VB top. Optical band gap can be estimated from **Kubelka–Munk (K–M) function** which is defined as [63,64]:

$$f(R_d) = \frac{(1-R_d)^2}{2R_d} = \frac{\alpha}{s} \quad \dots (1.1)$$

Where, R_d is diffused reflectance, α is an absorption coefficient and s is scattering coefficient. For samples diluted with a medium of less photo absorption, K–M function can be a measure of sample concentration. The K–M function is often recognized, through this requires assumptions, to be proportional to the absorption coefficient. Usually optical band gap is evaluated from the following relation, where scattering coefficient is supposed to be constant throughout a wavelength range for measurement.

$$\alpha = \frac{(h\nu - E_g)^n}{h\nu} \quad \dots (1.2)$$

In this equation, h is Planck constant, ν is oscillation frequency, E_g is optical band gap and n is constant relating to a mode of transition. The constant n is 1/2, 3/2 or 2 for allowed direct transition, forbidden direct transition and indirect transition. But the forbidden direct transition has often been neglected [64,65].

In indirect transition, the electron cannot shift from the lowest energy state in the conduction band to the highest energy state to valence band without a change in momentum. In this case the band gap energy is analysed from the following relation by extrapolation to $\alpha_{KM} = 0$.

$$(\alpha_{KM} \cdot h\nu)^{1/2} = f(h\nu) \quad \text{--- (1.3)}$$

In the case of the direct transition, the electron can shift from the lowest-energy state in the conduction band to the highest energy state to valence band without a change in momentum (**Figure 1.1**). Here, the band gap energy is analysed from other relation by the same extrapolation as in previous case [64,67].

$$(\alpha_{KM} \cdot h\nu)^2 = f(h\nu) \quad \text{--- (1.4)}$$

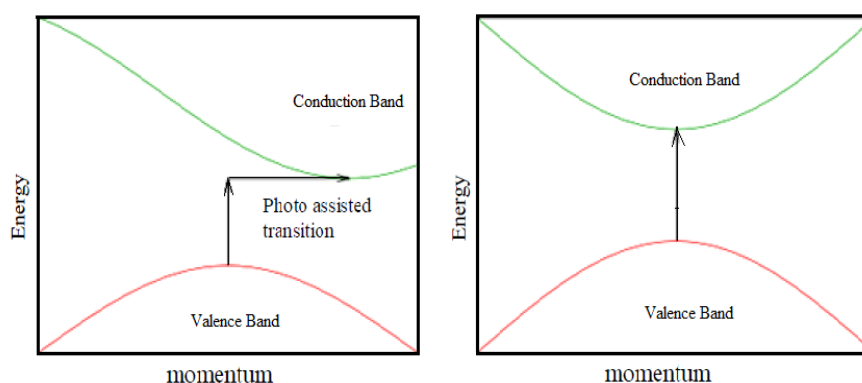


Figure 1.1 Indirect transition (left) and direct transition (right)

1.4.3 Strategies in the development of semiconductor photocatalysis

Several efforts have effectively made extensive range of effective semiconductor based photocatalysts. Being a member of metal-oxide semiconductor photocatalysts family, there is a general agreement among researchers that TiO₂ is more better because of its high photocatalytic activity, large chemical stability and anti-photo corrosion activity, low price, and nontoxicity [68,69].

Numerous approaches have been used to make commercial samples of TiO₂ by changing purity, particle size, and crystal structure and phase configuration to improve photocatalytic efficacy. Degussa P25 grade is one of the best photocatalyst it is the combination of 30% rutile phase and 70% anatase phase of TiO₂ powders [70-72].

Nevertheless, commercial utilisation of this method is insufficient because titania is only active with UV light i.e. radiation with wavelength lower than 387nm.

As the UV light is only a very small portion of the complete solar energy (5%) and the rest is mainly visible light, any apparent shift in the photocatalytic activity of TiO₂ from UV to visible light region would improve its photocatalytic activity. Considerable research has been directed at overcoming this fundamental drawback of TiO₂ besides, other shortcomings such as hassle in separation after synthesis and stirring during complete reaction. Numerous researches have been focused on the synthesis and modification of TiO₂ nanostructured by making composite photocatalysts with ceramics like SiO₂, ZrO₂, Al₂O₃ and TiO₂ coated polymer nanostructures to remove the above mentioned drawbacks of TiO₂ [73-75].

Several reviews on the properties of modified TiO₂ and its photocatalytic behaviour have been presented in **Table 1.2**.

Table 1.2 Photocatalytic activity of modified TiO₂

S.No.	Technique	Photocatalyst	Organic Compound	Light Source	Reference
1	Doping	Ag-TiO ₂	Crystal Violet	Simulated Solar light	[76]
		Au -TiO ₂	Rhodamine-B	500 W halogen Lamp	[77]
		Fe,Co -TiO ₂	Basic Green	Sunlight	[78]
		N-TiO ₂	Orange-G	Visible	[79]
2	Hetero-structuring	TiO ₂ coated FeTiO ₃	Methylene Blue	300 W high pressure Hg Lamp	[80]
		TiO ₂ -CdS	Methyl Violet	Xe Lamp	[81]
		SiO ₂ -TiO ₂	Methyl Orange	Visible Light	[82]
		TiO ₂ -Cement	Aqueous Phenol	UV Light	[83]
3	Sensitization	Tris(4,4'-dicarboxy-2,2'-bipyridyl) ruthenium complex-TiO ₂	CCl ₄	Visible Light	[84]
		Al ₂ O ₃ -TiO ₂	Rhodamine B	Visible Light	[85]

		Reactive Red Dye 198-TiO ₂	Phenol	Visible Light	[86]
--	--	--	--------	---------------	------

However, doping with transition metals decreases the photo excitation energy of TiO₂ to some level, the metal ions also act as the charge recombination centres for the electron-hole-pairs, thus weaken the inclusive efficacy of the doped TiO₂. Furthermore, procedure of doping is generally difficult and involves high temperatures, under which the anatase phase is likely to suffer phase transformation into the less active rutile phase. In addition, a large-scale application of TiO₂ in industrial waste water treatment operations is very non-economic due to its high price and rareness in existence [87,88].

So far, many categories of semiconducting materials have been considered for photocatalysis such as ZnO, ZnS, CdS, WO₃ and Fe₂O₃. Zinc oxide is an outstanding wide band gap, natural n-type semiconducting material. It can absorb wider range of spectrum of radiation which also makes it more applicable for dye sensitized solar cells and solar photovoltaic uses. But, the implementation of ZnO (Band gap=3.2eV) photocatalytic systems has not increased like TiO₂ systems have, because it is unstable in irradiated aqueous solutions [89,90].

CdS, Fe₂O₃ and WO₃ have similar properties and narrow band gaps, 2.25, 2.1 and 2.6eV, respectively. The lowered band gap values of these materials make them proficient for being active in visible light. In the field of photo-electrochemistry, CdS has been the most frequently studied II-IV group semiconductor. But due to the hazardous properties of Cd, it is avoided for industrial purpose [91]. Hematite (α -Fe₂O₃), which is economical, naturally occurring and has low band gap for utilize solar energy. But the main disadvantage of this material is that it undergoes quick e⁻-h⁺ charge recombination and a short charge carrier dispersal distance. As a result of these draw backs, renewed interest in this material has focused on its alteration with cationic dopants such as Cr and Mo to increase its charge transport properties [92,93]. Similarly WO₃ (tungsten trioxide) is also a narrow band gap photocatalyst with band gap value of 2.7 eV, has the drawback of a low electron conduction band. To overcome this

shortcoming, WO_3 coupled with Pt, has been proved to be suitable as alternative multiple-electron reduction processes with lower reduction potentials. This has increased the use of WO_3 as extremely visible-light-active single-phase oxide photocatalyst [91,94].

In addition, to single phase binary photocatalysts, photocatalytic degradation of organic compounds using binary or ternary mixed transition metal oxide in visible light irradiation has also been repeatedly described in the various works. The most interesting characteristic of using these oxides as photocatalysts results from at least two important features: (1) Their ability of absorbing photon in the visible light range ($\lambda > 420\text{nm}$) due to suitably modified electronic band structures, and (2) The huge options of groupings of different elements, thus offering a potential tool in designing of visible-light-driven photocatalysts. Many of these ternary mixed metal oxides have a perovskite structure and behave as semiconductor.

In recent years, perovskite photocatalysts have shown their capability in waste water remediation of waste water. Perovskites and their use in photocatalysis have been elaborated in the coming section.

1.5 Perovskite

The crystal perovskite was discovered and named by Gustav Rose in 1839 from CaTiO_3 samples found in the Ural Mountains. The name perovskite is entitled after Russian mineralogist, Count Lev Aleksevich Von Perovski [95]. The name later was used to define the ABO_3 structure. **A** symbolises a comparatively large cation of with small charge, such as group 3 metals, group 2 metals or alkaline metals. The smaller **B** cations are generally *d* or *f* block metals. **O** is most often a simple anion as oxide or fluoride.

Since the 1980s perovskites have appeared as fascinating nanomaterials for wide applications in catalysis, fuel cells, and electrochemical sensing. In catalysis application, mixed oxides of transition and rare earth metals possessing perovskite structure appear to be suitable for such high-temperature processes as catalytic combustion, methane reforming, ammonia oxidation, sulfur dioxide reduction, etc [96-98].

The origin of such novel photo-physical and electronic properties lies in the crystal structure of perovskites. Properties such as electron and hole effective mass, excited state lifetime and diffusion length, binding energy affect the electron-hole separation and transport within the lattice. These properties are known to strongly influence the performance (kinetics/efficiency) of the photocatalytic reactions. Defects in the lattice, defect-induced energy states, localization of electrons on specific defect sites could determine the fate of the photo-excited electron-hole pair. Finally, the electron transfer across semiconductor-electrolyte interface is significantly affected by surface states, surface band structure (depletion region induced electric field), and band bending. Such electronic properties of materials could be altered to suit specific photocatalytic applications [99,100].

For this purpose, perovskites have shown excellent promise for efficient photocatalysis under visible light irradiation, as their crystal structure offers an excellent framework to tune the band gap values to enable visible light absorption and band edge potentials to suit the needs of specific photocatalytic reactions.

1.5.1 Structure of perovskite

The simplest case of the perovskite structure is that of a simple cubic cell with one ABO_3 formula unit per unit cell. In the ABO_3 form, B is a transition metal ion with small radius, larger A ion is an alkali earth metals or lanthanides with larger radius, and O is the oxygen ion with the ratio of 1:1:3. In the cubic unit cell of ABO_3 perovskite, atom A is situated at the body center, atom B is located at the cube corner site, and oxygen atoms are located at face-centered positions (**Figure 1.2**). The 6-fold coordination of B cation (octahedron) and the 12-fold coordination of the A cation resulted in the stabilization of the perovskite structure. The perfect perovskite structure was described by Hines et al. as corner linked BO_6 octahedra with interstitial A cations [101-104].

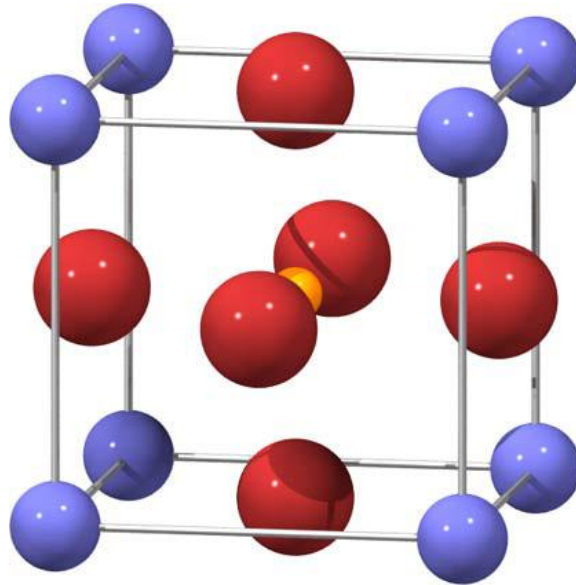


Figure 1.2 *Cubic perovskite unit cell.*

(Blue spheres represent the A cations, yellow spheres represent the B cations, and red spheres represent oxygen anions forming an octahedra.)

(Source: <https://www.intechopen.com/source/html/49438/media/fig1.png>)

Certain distortions may occur in the perfect cubic arrangement of perovskite giving rise to several transformations such as orthorhombic, hexagonal, rhombohedral, hexagonal, and tetragonal structures. Generally, all perovskite distortions keeping the A- and the B-site oxygen coordination is attained by the leaning of the BO_6 octahedra and an related dislocation of the A cation [105].

V.M. Goldschmidt first established the principle of the tolerance factor t , which is valid to the experimental ionic radii at room temperature [106-108]:

$$t = \frac{r_A + r_O}{\sqrt{2}(r_B + r_O)} \quad \text{--- (1.5)}$$

where, r_A is the radius of the A-site cation, r_B is the radius of the B-site cation, and r_O is the radius of oxygen ion O^{2-} [109].

The tolerance factor can be used to determine the suitability of the incorporation of different cations in the perovskite structure. It is an actual extent of the degree of the distortion of perovskite from the ideal cubic structure. The structure of these different perovskite is based on the value of their tolerance factor value. The tolerance factor value $1.00 < t < 1.13$, $0.9 < t < 1.0$, and $0.75 < t < 0.9$, is assigned to the perovskite structure is hexagonal, cubic, and orthorhombic, respectively.

1.5.2 Synthesis of perovskite

The distinct features of perovskites and their photocatalytic activity are extremely influenced by their method of synthesis, calcination temperature, and duration, and doping at A- and/or B-sites in the perovskite structure. Upon doping A- and/or B-sites in ABO_3 perovskite oxides, the catalytic activity (through oxidation state modification, the generation of oxygen vacancies, the mobility of oxygen lattice, and the formation of structural defects [110-113] ionic and electronic conductivity, and flexible physical and chemical properties can be improved for application in numerous applications [114,115].

Several methods can be used to synthesize perovskite materials, comprising solid state reaction, co-precipitation, hydrothermal, spray and freeze drying, and sol-gel process. The choice of the synthesis technique is very significant for the performance of the compounds.

I. Solid state reaction

The solid state synthesis method is the most extensively used in preparation of different solid materials. It involves direct heating of starting materials, which are generally solid metal oxides. One of the advantages of the solid state reaction is that the starting materials react in absence of any solvent. In this process, predetermined quantities of commercially available starting materials such as carbonates and oxides are precisely weighed out, followed by mixing and subsequent heating. However, this method has several drawbacks such as elongated processing time, low surface area, large particle size of the final product and limited degree of chemical uniformity [116-117].

II. Combustion synthesis

The combustion synthesis of nano materials are classified on the physical nature of the initial reaction medium: (I) Conventional, solvo-thermal synthesis of nanoscale materials, i.e. initial reactants are in solid state (condensed phase combustion). (II) Solution-combustion synthesis (SCS) of nanosized powders, i.e. initial reaction medium is aqueous solution. (III) Synthesis of nanoparticles in flame, i.e. gas-phase combustion.

However, the list of compound synthesised by this method is comparatively small and low efficacy of this technology currently orders high cost of the final products [118].

III. Microwave synthesis

The microwave irradiation process (MIP), is extensively applied in food drying, inorganic/organic mixture, plasma chemistry, and microwave-induced catalysis. This method show some interesting features such as: fast reaction rate and clean energy. This method is recently used to synthesise perovskites nanomaterials with relatively lower calcination temperature and lower calination period [119,120]. Although, several expensive pre-treatments are required.

IV. Hydrothermal synthesis

Amongst the low temperature methods, the hydrothermal method is extensively used for the synthesis of nano-phase materials. When water is used as a solvent, the process is called hydrothermal process and when any solvent including water or organic solvents such as methanol, ethanol polyol, etc. are used, the process is termed **solvothermal processes**. Thus the latter term encompasses all solvents including water. This method, leads to homogeneous and low crystalline products at relatively low temperatures, but they usually require expensive initial compounds and/or complicated synthesis procedures [121,122].

V. Sol-gel method

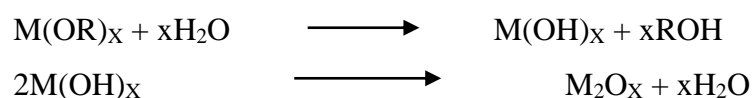
The sol-gel technique can be classified in two general routes. The first one consists in the colloid chemistry of aqueous media, whereas the second one consists in the formation of polymeric chains connected with the metal ions in solution. Basically, the first step is the formation of a sol by the mixture of molecular precursors that are either metal salts or metal organics. Condensation reactions are carried out in the sol stage, forming colloids or clusters, which lead to the formation of a gel when they agglomerate and cross-link each other. After the gel stage, there is a heat treatment stage when drying and calcination steps take place. The heat treatment stage determines the nature of the perovskite, since the used temperature may lead to a material containing residual organics (80-350 °C). The following step

is the calcinations process in which densification occurs and the final perovskite is formed. The best significant benefits of this method is the low temperature required for the comparatively low calcination process, high purity and precise control of the composition of the final product [123].

A range of sol-gel methods are utilized for synthesizing perovskites, comprising alkoxide, alkoxide-salt, and Pechini methods.

a. Alkoxide route

Metal alkoxides are used as precursors in this route. The incompatibility of water with a non-polar solvent gives rise to regions where the concentration of water is very high resulting in reactions of hydrolysis and condensation with formation of hydroxides or oxides [36]. Organic by-products are easily removed by volatilization resulting in very pure products. In this method hydrolysis and subsequent condensation reaction takes place in the following manner:



Various perovskites materials have been prepared by this procedure, showing lower reaction temperatures (around 100 °C) when compared to other conventional methods, as well as calcination temperatures [124].

b. Alkoxide-salt route

This variance of the alkoxide route uses metal salts, or hydroxides, of some of the starting materials instead of metal alkoxides, since metal alkoxides of groups I and II are solid and non-volatile, making their purification challenging. Furthermore, metal salts are easily converted to metal hydroxides and oxides and these are more soluble in organic solvents. A solution with the metal alkoxides is prepared followed by the addition of metal salts in either alcoholic solution or in aqueous solution, which can be used to enhance the hydrolysis reaction. Compounds dissolved in the system are uniformly distributed throughout the volume and gelation immobilizes them in a rigid network [123].

c. Pechini method

The Pechini method is a route associated to the sol-gel route (Pechini, 1967) named after its American discoverer, Maggio Pechini. It has been shown to be an operative method for mixture of multicomponent oxide materials [124].

Basically, the procedure involves of three main stages as follows:

- (i) The complexation of metal ions with citric acid in water without regulating pH,
- (ii) The polymerization, where the designed chelates undergo polyesterification when they are treated with a poly hydroxyalcohol, such as ethylene glycol, with the formation of a stable polymeric network, and finally,
- (iii) The decay of the formed organic linkage to attain the powder precursor after boiling at moderate temperature (~ 363 K). On removal of the excess solvent, a transparent resin containing the metals in solid solution was made.

The temperature has been proved to be very important: at temperatures higher than 363 K, the solution becomes turbid in time, generating nontransparent final resin, which can be explained by the formation of insoluble precipitates from the rapid hydrolysis of the metal-citrate species. At lower temperatures, a longer time is needed to obtain the stable polyester network.

An advantage of the Pechini method is providing single-phase, homogeneous synthesized powders at low crystallization temperature with high surface area. Several researchers had synthesized perovskite via the Pechini method. [125,126]

1.5.3 Uses of perovskite

The physical and compositional flexibility of perovskite materials delivers the option to synthesize new photocatalysts with preferred properties. Therefore perovskite materials have attracted widespread attention in many functional and important area of solid state chemistry, physics, advanced materials, and catalysis [127-140].

Table 1.3 shows the usefulness of the perovskite materials, and the extensive series of properties and resulting technical applications.

Table 1.3 Representative Perovskite materials and their applications.

S.No.	Material	Application	Reference
1	Er ³⁺ , Ho ³⁺ doped YLaO ₃	Optical laser	[127]
2	Rh doped BaTiO ₃	Photorefractive materials, First generation harmonic generator	[128]
3	(La,Sr)(Ga,Mg)O _{3-δ}	Solid electrolyte for ionic conductivity	[129]
4	SrTiO ₃ , KTaO ₃	Tunable microwave devices	[130]
5	LaFeO ₃	NO _x sensors	[131]
6	LaMnO _{3+δ}	Potentiometric sensors response	[132]
7	BaTiO ₃	Capacitors PTC for hair dryer	[133]
8	[(Li _{0.04} Na _{0.44} K _{0.52})(NbO _{0.86} Ta _{0.1} Sb _{0.04})]O ₃	Lead-free high temperature piezoelectric ceramic	[134]
9	Eu ³⁺ MnSO ₃	Light emitting device	[134]
10	LaBO ₃ B= Fe,Co,Ni	Direct conversion of methane to C ₂ hydrocarbon via Oxidative coupling	[135]
11	NaBiO ₃	Degradation of 2-Propanol	[136]
12	La _{0.75} Sr _{0.25} Mn _{0.95-x} Co _x Ni _{0.005} O _{3+δ}	Solid oxide fuel	[137]
13	LaNiO ₃	Electrode for fatigue-free ferroelectric random access memories Solid oxide fuel cells Methane reforming reaction	[138]
14	CH ₃ NH ₃ PX ₃ X=Cl,Br,I	Light harvesters for solar cell	[139]
15	CH ₃ NH ₃ Pb (I _{1-x} Br _x) ₃	Colourful solar cells	[140]

1.5.4 Photocatalytic activity of perovskite

Amongst several photocatalysts that have been investigated, perovskite based photocatalysts have attained much importance because of their high photocatalytic activities therefore the preparation, characterization and photocatalytic activity of perovskite related compounds have been extensively studied. To improve their photocatalytic performance; there are 3 fundamental approaches: 1) variation of band gap; 2) creation of semiconductor composites; and 3) alteration of morphology.

Transition metals such as Ti(IV), Nb(V), Ta(V) based perovskite photocatalysts are found to be effective photocatalysts for complete water splitting and photodegradation of dyes and other contaminants. Though, the comparatively large band gaps of these compounds (3.8-4 eV) are not fit for visible light-induced photocatalysis [141,142].

Initially, various materials such as SrTiO₃, and KTaO₃ were reported as potential UV-light-active photocatalysts. SrTiO₃ as a photosensitive material could be used to produce hydrogen under UV light. Transition metals such as Fe, Co, Mn, Pt, Ru have been substituted into SrTiO₃ to allow visible light absorption [143, 144].

ATaO₃ i.e. Alkali metal tantalates are mostly known for effective total water splitting reaction under UV irradiation as they possess both valence bond and conduction band abilities appropriate for water splitting reaction [145]. Also, Niobium (Nb)-based perovskites such as KNbO₃ (Eg 3.14eV) and NaNbO₃ (Eg 3.08eV) are UV-responsive, though appropriate alterations of the band structure have caused in visible light photocatalysis [146,147].

Most of the Ti-based perovskites (BaTiO₃, PbTiO₃) have band gap energy (Eg) value more than 3.0eV, nevertheless they have shown outstanding photocatalytic properties under UV radiation [144,148].

For the complete consumption of solar energy i.e. to prolong the photosensitive absorption of the UV- sensitive photocatalysts into the profound

visible light range, several researchers have contributed to developing novel visible light active photocatalysts.

Most of the Fe- based perovskites have lower band gaps and they have shown activity in the visible light region. Pt- doped LaFeO₃ is prepared by So-gel method, showed complete mineralization of contaminants under visible light. Mn doped LaFeO₃ has also been studied, and it shows advanced photocatalytic activity. New studies has revealed that BiFeO₃ (E_g=3.2eV) could be used as a visible light photocatalyst. The ferroelectric assets of BiFeO₃ could be used to increase the electron-hole separation and improved photocatalytic activity in visible region of light [149-153].

Along with the above mentioned perovskite, several other metal oxide exhibit potential for visible light photocatalysis, which are summarised in **Table 1.4**.

Table 1.4: Promising photocatalytic systems for organic compounds degradation under visible light.

S.No.	Perovskite Material	Photocatalytic Reaction	Band Gap	Reference (Year)
1.	PrFeO ₃	Hydrogen Evolution from Ethanol		[154]
2.	YFeO ₃	RhB Degradation	2.43 eV	[155]
3.	GaFeO ₃	Water Splitting		[156]
4.	Na doped NaNbO ₃	2-propanol Degradation & Water Splitting		[157]
5.	AgNbO ₃	O ₂ Evolution Reaction	2.7 eV	[158]
6.	AgVO ₃	RhB Degradation	2.4 eV	[159]
7.	NiTiO ₃	Degradation of Nitrobenzene	2.16 eV	[160]
8.	PbTiO ₃	Photodegradation of Methyl orange dye	2.75 eV	[161]

9.	CdTiO ₃	Photodegradation of Rhodamine 6G Dye	2.8 eV	[162]
10.	FeTiO ₃	2-Propenol Degradation	2.8 eV	[163]

Several bismuth based compounds such as Bi(III) containing oxides such as BiVO₄, Bi₂WO₆, KBiO₃, LiBiO₃ and BiPO₄ as well as have been reported to be promising photocatalysts under visible light irradiation. In particular, application of perovskite photocatalysts in visible-light-driven photocatalysis has been in lime light during recent years, although the choice of applicable materials for direct photocatalytic degradation processes is still limited [163-167].

For above said purpose, therefore, the present research work is being conducted to develop newer materials, with lowered band gap and good absorption properties to fully harness the solar light.

1.6 Scope of the present study

In the search of alternative green photocatalysts we propose in this work to develop Barium, Bismuth and potassium containing novel visible-light-driven mixed metal oxides by Pechini method. The structural analysis of thus prepared photocatalysts through various characterization techniques such as X-ray diffraction (XRD), Ultra-violet visible spectroscopy (UV-DRS), Scanning electron microscopy (SEM), Fourier transform infrared spectroscopy (FTIR) and Thermo gravimetric analysis (TGA) has helped in evaluation of photo-absorption properties, particle morphology with size, bonding and phase evolution. This approach has been quite effective and instrumental in utilizing solar and indoor lamp energy besides engineering a novel visible light sensitive photocatalysts with enhanced photocatalytic activity.

In the present work, three dyes; Crystal violet, Malachite green and Congo red are utilized to undergo photocatalytic processes through heterogeneous photocatalytic reactions using prepared catalysts. The kinetics related to the adsorption and degradation phenomena during photocatalytic degradation of dyes are also investigated using a batch reactor in visible light irradiation. Effect of

different experimental parameters like, effect of initial dye concentration, reaction temperature, catalyst loading and temperature was studied. At the same time, a systematic study is carried out to achieve the optimum operating conditions for different dye degradation.

Therefore, the synthesis via a green chemistry route, characterization of thus prepared photocatalyst and the photocatalytic properties via the degradation of organic dyes have paved a new path in the field of tailoring and designing new visible-light-active photocatalyst.

References

- [1] C. Wang, A. Yediler, D. Linert, Z. Wang, A. Kettrup, *Chemosphere* 46, (2002), 339.
- [2] R. Vinu, G. Madras *Journal of the Indian Institute of Science* 90, (2010), 189.
- [3] T. Yahagi, Y. Seino, T. Matsushima, M. Nago, T. Sugimura, Y. Hasshimoto, *Cancer Lett.* 1, (1975), 91.
- [4] S. Gita, A. Hussan, T.G. Choudhury, *Ecol. Environ.* 35, (2016), 2349.
- [5] R. Tim, M. Roger, M. Nigam, *Bioresour. Tech.* 77, (2001), 247.
- [6] S.T. Ong, P.S. Keng, W.N. Lee, S.T. Ha, Y.T. Hung, *Water* 3, (2011), 157.
- [7] R. Asahi, T. Morikawa, T. Ohwaki, K. Aoki, Y. Taga, *Science* 293, (2001), 269.
- [8] T.P. Yoon, M.A. Ischay, J. Du, *Nat. Chem.* 2, (2010), 527.
- [9] F. Gao, X. Chen, K. Yin, S. Dong, Z. Ren, F. Yuan, T. Yu, Z. Zou, J.M. Liu, *Adv. Mater.* 19, (2007), 2889.
- [10] T. Takata, Y. Furuni, K. Shinohara, A. Tanaka, M. Hara, J.N. Kondo, K. Domen, *Chem. Mater.* 9, (1997), 1063.
- [11] D.M. Stevenson, D.G. Duff, D.J. Kirkwood, *Color. Technol.* 97, (1981), 13.
- [12] J.A. Kiernan, *Biotech. Histochem.* 76, (2002), 261.
- [13] R.S. Shertate, P. Thorat, *Am. J. Environ. Sci.* 10, (2014), 489.
- [14] M. F. Comelo, *Control of the adsorption of dyes on cotton*. Ph.D. Thesis, 2002, University of Leeds, Leeds, U.K.
- [15] A.R. Khataee, M. B. Kasiri, *J. Mol. Catal. A: Chem.* 328, (2010), 8.
- [16] K.T. Chung, S.E. C.E. Cerniglia, *Crit. Rev. Biotechnol.* 18, (1992), 175.
- [17] V. Fessard, T. Godard, S. Huet, A. Mourot, J.M. Poul, *J. Appl. Toxic.* 19, (1999), 421.
- [18] S.J. Culp, F.A. Beland, *Int. J. Toxic.* 15, (1996), 219.

-
- [19] H. Hagiwara, M. Nagatomo, C. Seto, S. Ida, and T. Ishihara, *J. Photochem. Photobiol. A* 272, (2013), 41.
- [20] W. Au, T. C. Hsu, *Environ. Mol. Mutagen.* 1, (1979), 27.
- [21] T.W. Ng, Q. Cai, C.K. Wong, A.T. Chow, P.K. Wong, *J. Hazard. Mater.* 182, (2010), 792.
- [22] G. Prabakaran, R. Pugalvendhan, M. Jayaseelan, *Pollut. Res.* 28, (2009), 555.
- [23] X. Ren, T. Wang, C. Zhou, S. Du, Z. Luan, J. Wang, D. Hou, *Fresenius Environ. Bull.* 19, (2010), 1441.
- [24] M. Tekere, A.Y. Mswaka, R. Zvauya, J.S. Read, *Enzyme Microb. Technol.* 28, (2001), 420.
- [25] S. Prakash, A.M. Rajesh, V.K. Shahi, *Chem. Eng. J.* 168, (2011), 108.
- [26] S. Rosa, M.C.M. Laeranjeira, H.G. Riela, V.T. Favere, *J. Hazard. Mater.* 155, (2008), 253.
- [27] S. Chakrabarti, B.K. Dutta, R. Apak, *Water Sci. Tech.* 60, (2009), 3017.
- [28] W.H. Glaze, *Environ. Sci. Technol.* 21, (1987), 224.
- [29] H. Valdes, H.P. Godoy, C.A. Zaror, *J. Int. Assoc. Water Pollut. Res.* 61, (2010), 2973.
- [30] P.K. Malik, S.K. Saha, *Sep. Purif. Technol.* 31, (2003), 241.
- [31] L.L. Hsieh, H.J. Kang, H.L. Shyu, C.Y. Chang, *Water Sci. Technol.* 60, (2009), 1295.
- [32] N. Daneshvar, D. Salari, A.R. Khataee, *J. Photochem. Photobiol. A: Chem.* 162, (2004).
- [33] T. Xu, L. Zhang, H. Cheng, Y. Zhu, *Appl. Catal. B* 101, (2011), 382.
- [34] K. Hashimoto, H. Irie, A. Fujishima, *Jpn. J. Appl. Phys.* 44, (2005), 8269.
- [35] A. O. Ibhaddon, P. Fitzpatrick, *Catalysts* 3, (2013), 189.
- [36] S. Seshadri, P.L. Bishop, A.M. Agha, *Waste Manage.* 14, (1994), 127.

-
- [37] E.A. de Lara, S.B. Damas, E.Z. Agusti, M.I.A. Miranda, M.I.I. Clar, *Sep. Pur. Technol.* 129, (2014), 96.
- [38] S. Mondal, *Environ. Eng. Sci.* 25, (2008), 383.
- [39] R. sangeetha, C.A. Basha, *J. Hazard. Mater.* 149, (2007), 324.
- [40] G. Crini, *Bioresour. Technol.* 97, (2006), 1061.
- [41] A. Teichmann, U. Jacobi, M. Ossandik, H. Ritcher, S. Koch, W. Sterry, J. Lademann, *J. Gen. Internal Med.* 20, (2005), 264.
- [42] S.K. Nataraj, K. M. Hosamani, T.M. Aminabhavi, *Desalination*, 249, (2009), 12.
- [43] M. S. Lucas, J. A. Peres, *Dyes Pigm.* 71, (2006), 236.
- [44] S.P. Sun, C.J. Li, J.H. Sun, S.H Shi, M. H. Fan, Q. Zhou, *J. Hazard. Mater.* 161, (2009), 1052.
- [45] M. Punzi, F. Nilsson, A. Anbalagan, B. M Svensson, K. Jönsson, B. Mattiasson, M. Jonstrup, *J. Hazard. Mater.* 292, (2015), 52.
- [46] R.B.P. Marcelino, M.M.D. Leão, R.M. Lago, C.C. Amorim, *J. Environ. Manage.* 195, (2017), 110.
- [47] M. Saad, H. Tahir, J. Khan, U. Hameed, A. Saud, *Ultrason. Sonochem.* 34, (2017), 600.
- [48] K. Yu, S. Yang, C. Liu, H. Chen, H. Li, C. Sun, S.A. Boyd, *Environ. Sci. Technol.* 20, (2012), 7318.
- [49] M.A. Barakat, H. Schaeffer, G. Hayes, S.I. Shah, *Appl. Catal. B: Environ.* 57, (2004), 23.
- [50] U.G. Akpan, B.H. Hameed, *J. Hazard. Mater.* 170, (2009), 520.
- [51] D.A.H. Hanaor, C.C. Sorrell, *Adv. Eng. Mater.* 16, (2014), 248.
- [52] E. Grabowska, A. Zaleska, S. Sorgues, M. Kunst, A. Etcheberry, C.C. Justin, H. Remita, *J. Phys. Chem. C* 117, (2013), 1955.

-
- [53] J.M. Herrmann, *Catal. Today* 53, (1999), 115.
- [54] N. Arjunan, C.M. Singaravelu, J. Kulanthaivel, J. Kandasamy, *Int. J. Biol. Macromol.* 104, (2017), 1774.
- [55] F. Akira, T. Rao, D. Tryk, *J. Photochem. Photobiol. C* 1, (2000), 1.
- [56] H.J. Fan, S. T. Huang, W. H. Chung, J. L. Jan, W. Y. Lin, C.C. Chen, *J. Hazard. Mater.* 171, 2009, 1032.
- [57] A. Fujishima, K. Honda, *Nature* 238, (1972), 37.
- [58] Z.F. Huang, J.J. Zou, L. Pan, S. Wang, X. Zhang, and L. Wang, *Appl. Catal. B* 147, (2014), 167.
- [59] H. U. Lee, G. Lee, J. C. Park et al., *Chem. Eng. J.* 240, (2014), 91.
- [60] H. G. Cha, H. S. Noh, M. J. Kang, and Y. S. Kang, *New J. Chem.* 37, (2013), 4004.
- [61] B. Pare, P. Singh, S.B. Jonnalagadda, *Ind. J. Chem.* 48, (2009), 1364.
- [62] J. Robertson, *J. Vac. Sci. Technol. B* 18, (2000), 1785.
- [63] J.C. Tauc, *Amorphous and Liquid Semiconductor*, (Plenum, New York, 1974).
- [64] Z. Zhang, P. Wu, K.P. Ong, L. Lu, C. Shu, *Phy. Rev. B* 76, (2007), 125102-1.
- [65] I.E. Castelli, J.M.G. Lastra, K.S. Thygesen, K.W. Jacobsen, *Appl. Mater.* 2, (2014), 081514.
- [66] J. Tang, Z. Zou, J. Ye, *J. Phys. Chem. C* 111, (2007), 12779.
- [67] J. Tang, Z. Zou, J. Ye, *Phys. Chem. B* 107, (2003), 14256.
- [68] V.K. Gupta, R. Jain, A. Mittal, T. A. Saleh, A. Nayak, S. Agarwal, S. Sikarwar, *Mater. Sci. Eng. C* 32, (2012), 12.
- [69] M. Saquib, M. Muneer, *Dyes Pigm.* 56, (2003), 37.
- [70] S. Sakthivel, M.V. Shankar, M. Palanichamy, B. Arabindoo, D.W. Bahnemann, V. Murugesan *Water Res.* 38, (2004), 3001.

-
- [71] D. Wu, F. Mao, Z. Yang, S. Wang, Z. Zhou, *Mater. Sci. Semicond. Process.* 23, (2014), 72.
- [72] A.P. Toor, N. Yadav, R.K. Wanchoo, *Mater. Sci. Forum* 757, (2013), 271.
- [73] X. Sun, C. Li, L. Ruan, Z. Peng, J. Jhang, J. Zhao, Y. Li, *J. Alloys Comp.* 585, (2014), 800.
- [74] J.L. Gong, B. Wang, G.M. Zeng, C.P. Yeng, C.G. Niu, Q.Y. Niu, W.J. Zhou, Y. Liang *J. Hazard. Mater.* 164, (2009), 1517.
- [75] Y. Tian, Y. Song, M. Dou, J. Ji, F. Wang, *Appl. Surf. Sci.* 430, (218), 466.
- [76] V. Gunasekar, B. Divya, K. Brinda, J. Vijakrishnan, V. Ponnusami, K. S. Rajan, *J. Sol-Gel Sci. Technol.* 68, (2013), 60.
- [77] Z. Xiong, L. Zhang, X. Zhao, *Chem. Euro. J.* 20, (2014), 10.
- [78] L. S. Andrade, L. A. M. Ruotolo, R. C. Rocha-Filho, *Chemosphere* 66, (2007), 2035.
- [79] T. Ohno, T. Mitsui, M. Matsumura, *Chem. Lett.* 32, (2003), 364.
- [80] H. Meng, B. Wang, S. Liu, R. Jiang, H. Long, *Ceram. Int.* 39, (2013), 5785.
- [81] G. Yang, B. Yang, T. Xiao, Z. Yan, *Appl. Surf. Sci.* 283, (2013), 402.
- [82] L. Zhou, W. Zang, X. Han, H. Hongbo, *Asian J. Chem.* 26, (2014), 3837.
- [83] L. Sopyan, N. Hafizah, P. Jamal, *Ind. J. Chem. Tech.* 18, (2011), 263.
- [84] Y. Cho, W. Choi, C. H. Lee, T. Hyeon, H.I. Lee, *Environ. Sci. Technol.* 35, (2001), 966.
- [85] D. Zhao, C. Chen, Y. Wang, W. Ma, J. Zhao, T. Rajh, L. Zang, *Environ. Sci. Technol.* 42, (2008), 308.
- [86] S. Kaur, V. Singh, *Ultrason. Sonochem.* 14, (2007), 531.
- [87] E. Bae, W. Choi, *Environ. Sci. Technol.* 37, (2003), 147.
- [88] J. J. He, A. Hagfeldt, S.I. Lindquist, *Langmuir* 17, (2001), 2743.

-
- [89] M.A Habib, M. T. Shahadat, N.M. Bahadur, IM.I. Ismail, A.J. Mahmood, *Int. Nano Lett.* 3, (2013), 1.
- [90] C. Wang, X. Zhang, B. Yuan, *Chem. Eng. J.* 237, (2014), 29.
- [91] N. Strataki, M. Antoniadou, V. Dracopoulos, P. Lianos, *Catal. Today* 151, (2010), 53.
- [92] M. Mishra, D. M. Chun, *Appl. Catal, A. Gen.* 498, (2015), 126.
- [93] C. Zhu, Y. Li, Q. Su, *J. Alloys Compd.*, 575, (2013), 333.
- [94] C. Wang, X. Zhang, B. Yuan, Y. Wang, P. Sun, D. Wang, Y. Wei Y. Liu, *Chem. Eng. J.* 237, (2014), 29.
- [95] J.M. Rondinelli, S.J. May, J.W. Freeland, *MRS Bull.* 37, (2012), 261.
- [96] C. Vijayakumar, H.P. Kumar, S. Solomon, J.K. Thomas, P.R.S. Warriar, J. Koshy, *Bull. Mater. Sci.* 31, (2008), 719.
- [97] N. Hur, S. Park, P.A. Sharma, J.S. Ahn, S. Guha, S.W. Cheong, *Nature* 429, (2004), 392.
- [98] S. Kanagesan, C. Kumar, R. Velmurugan, S. Jesurani, *Mater. Sci. –Poland*, 28, (2010), 647.
- [99] D. Damjanovic, *Ann. Chim.-Sci. Mat.* 26, (2001), 99.
- [100] A.S. Bhalla, R. Guo, R. Roy, *Mat. Res. Innov.* 4, (2000), 3.
- [101] E. Grabowska, *Appl. Catal., B: Environ.* 186, (2016), 97.
- [102] R. W. Schwartz, *Chem. Mater.* 9, (1997), 2325.
- [103] B. Reihl, J.G. Muller, Y. Junget G. Landgren, J.F. Morar, *Phys. Rev. B* 30, (1984), 803.
- [104] V. Subramanam, R.K. Roeder, E.E. Wolf, *Ind. Eng. Chem. Res.* 45, (2006), 2187.

-
- [105] Y Teraoka, M. Yoshimatsu, N. Yamazoe, T. Seiyama, *Chem. Lett.* (1984), 893.
- [106] W. Travis, E.N.K. Glover, H. Bronstein, D.O. Scanlon, R.G. Palgrave, *Chem. Sci.* 7, (2016), 4548.
- [107] V. M. Goldschmidt, *Naturwissenschaften* 14, (1926), 477.
- [108] E. Beurer, J. Grimm, P. Gerner and H. U. Guedel, *Inorg. Chem.* 45, (2006), 9901.
- [109] C. Frontera, J.L. Garcia-Munoz, A. Llobet, M.A.G. Aranda, *Phys. Rev. B* 65, (2002), 180405.
- [110] D. D. Athayde, D.F. Souza, A.M.A. Silva, D. Vasconcelos, E.H.M. Nunes, J.C.D. Decosta, W.L. Vasconcelos, *Ceram. Int.* 42, (2016), 6555.
- [111] Y. Mao, H. Zou, S.S. Wong, *Mat. Mater.* 5, (2010), 50.
- [112] C. Liu, B. Zou, J. Zhang, *J. Am. Ceram. Soc.* 123, (2001), 1344.
- [113] D.M. Smyth, *Curr. Opin. Solid State Mater. Sci.* 5, (1996), 692.
- [114] S. Li, H. Nie, X. Chen, F. Cao, G. Wang, X. Dong, *J. Alloys Compd.* 732, (2018), 306.
- [115] F. Dogan, H. Lin, M. G. Viry, O. Pefia, *Sci. Technol. Adv. Mater.* 16, (2015), 020301.
- [116] Y. Luo, X. Li, X. Liu, *Adv. Mater. Sci. Eng.* 10, (2009), 1.
- [117] T. Hatakeyama, S. Takeda, F. Ishikawa, A. Ohmura, A. Nakayama, Y. Yamada, A. Matsushita, J. Yea, *J. Ceram. Soc. Jpn.* 118, (2010), 91.
- [118] J.J. Kingsley, L.R. Pederson, *Mat. Lett.* 18, (1993), 89.
- [119] M. Abulikemu, M. Neophytou, J.M. Barbé, M. T. Tietze, A.E. Labban, D.H. Anjum, A. Amassian, I. McCulloh, S.D. Gobbo, *J. Mater. Chem.* 5, (2017), 7759.
- [120] P. Tang, H. Chen, C. Lv, K. Wang, Y. Wang, *Integr. Ferroelectr.* 181, (2017), 49.

-
- [121] H. Li, Y. Yan, G. Wang, Q. Li, Y. Gu, J. Huang, *J. Mater. Sci.: Mat. Elec.* 29, (2018), 746.
- [122] C. T. Nam, W.D. Yang, L.M. Duc, *Bull. Mater. Sci.* 36, (2013), 779.
- [123] L.X. Zhu, Z.H. Zhao, X.Y. Yue, J.M. Fan, *J. Mol. Catal.* 27, (2013), 467.
- [124] M.P. Pechini, *United States Patents*, 3,330,697.
- [125] P.D. Spagnol, J. A Varela, M.A.Z. Bertochi, B.D. Stojanovic, S.M. Tebcherani, *Thin solid Films* 410, (2002), 177.
- [126] G. K. Chuah, S. Jaenicke, K.S. Chan, S. T Khor, J.O. Hill, *J. Therm. Anal.* 40, (1993), 1157.
- [127] Y. Sun, Q. Hang, H. Wang, Y. Saho, *J. Lumin.* 194, (2018), 50.
- [128] S. Nishioka, K. Maeda, *RSC Adv.* 5, (2015), 100123.
- [129] S. N. Shkerin, D.I. Bronin, S.A. Kovyazina, V.P. Gorelov, A.V. Kuz'min, Z.S. Martem'yahova, S.M. Beresnev, *J. Struct. Chem.* 44, (2003), 216.
- [130] X.X. Xi, H.C. Li, W. Si, A.A. Sirenko, I.A. Akimov, J.R. Fox, A.M. Clark, J. Hao, *J. Electroceram.* 4, (2000), 393.
- [131] E.N. Armstrong, T. Striker, V. Ramaswamy, J.A. Ruud, E.D. Wachsman, *Sens. Actuators B: Chem.* 158, (2011), 159.
- [132] J. J. Urban, W. S. Yun, Q. Gu, H. Park, *J. Am. Chem. Soc.* 124, (2002), 1186.
- [133] J. Yoo, K. Lee, K. Chung, S. Lee, K. Kim, J. Hong, S. Ryu C. Lhee, *Jpn. J. Appl. Phys., Part 1* 45, (2006), 1347.
- [134] L. Liu, H. Li, P. Su, Z. Zhang, G. Fu, B. li, X. Lu, *J. Mater. Chem. C*, 5, (2017), 4780.
- [135] M. J. Lee, H. Jun, J. S. Jung, Y. R. Kim, S.H. Lee, *Bull. Korean Chem. Soc.* 26, (2005), 1591.
- [136] T. Kako, Z. Zou, M. Katagiri, J. Ye, *Chem. Mater.* 19, (2007), 198.

-
- [137] A. Petric, P. Hang, F. Tietz, *Solid State Ionics* 135, (2000), 719.
- [138] R. P. Forslund, J.T. Mefford, W.G. Hardin, C.T. Alexander, K.P. Johnston, K.J. Stevenson, *ACS Catal.* 6, (2016), 5014.
- [139] L. Etgar, *Mater. (Basel)* 6, (2013), 445.
- [140] N.J. Jeon, J.H. Noh, W.S. Yang, Y.C. Kim, S. Ryu, J. Seo, S.I. Seok, *Nature* 517, (2015), 476.
- [141] J.W. Liu, G. Chen, Z.H. Li, Z.G. Zhang, *Int. J. Hydrog. Energy* 32, (2007), 2269.
- [142] H. Zhang, G. Chen, Y. Li, Y. Teng, *Int. J. Hydrog. Energy* 35, (2010), 2713.
- [143] H.C. Chen, C.W. Huang, J.C.S. Wu, S.T. Lin, *J. Phys. Chem. C* 116, (2012), 7897.
- [144] S. Piskunov, E. Heifets, R.I. Eglitis, G. Borstel, *Comput. Mat. Sci.* 29, (2004), 165.
- [145] L. Ni, M. Tanabe, H. Irie, *Chem. Commun.* 49, (2013), 10094.
- [146] R. Wang, Y. Zhu, Y. Qiu, C.F. Leung, J. He, G. Liu, T.C. Lau, *Chem. Eng. J.* 226, (2013), 123.
- [147] G. Liu, S. Ji, L. Yin, G. Xu, G. Fei, C. Ye, *J. Appl. Phys.* 109, (2011), 063103.
- [148] K. Maeda, *ACS App. Mater. Interfaces* 6, (2014), 2167.
- [149] Z. X. Wei, Y. Wang, J.P. Liu, W.W. Zeng, *Mater. Chem. Phys.* 136, (2012), 755.
- [150] C. Zhang, Y. Li, M. Chu, N. Rong, P. Xiao, Y. Zhang, *RSC Adv.* 6, (2016), 24760.
- [151] P. Kanhere, Z. Chen, *Molecules* 19, (2014), 19995.
- [152] Y. Si, Y. Li, J. Zou, X. Xiong, X. Zeng, J. Zhou, *Materials* 10, (2017), 1161.
- [153] S.N. Tijare, M.V. Joshi, P.S. Padole, P.A. Mangrulkar, S.S. Rayalu, N.K. Labhsetwar, *Int. J. Hydrog. Energy* 37, (2012), 10451.

-
- [154] S.N. Tijare, S. Bakardjieva, J. Subrt, M.V. Joshi, S.S. Rayalu, S. Hishita, N. Labhsetwar, *J. Chem. Sci.* 126, (2014), 517.
- [155] P. Tang, H. Chen, F. Cao, G. Pan, *Catal. Sci. Technol.* 1, (2011), 1145.
- [156] P. Dhanasekaran, N.M. Gupta, *Int. J. Hydrog. Energy* 37, (2012) 4897.
- [157] H. Shi, X. Li, H. Iwai, Z. Zou, J. Ye, *J. Phys. Chem. Solids* 70, (2009), 931.
- [158] D. Wang, T. Kako, J. Ye, *J. Phys. Chem. C* 113, (2009), 3785.
- [159] Y. Sang, L. Kuai, C. Chen, Z. Fang, B. Geng, *ACS App. Mater. Interfaces* (6), 2014, 5061.
- [160] Y. Qu, W. Zhou, Z. Ren, S. Du, X. Meng, G. Tian, K. Pan, G. Wang, H. Fu, *J. Mater. Chem.* 22, (2012), 16471.
- [161] L. Li, Y. Zhang, A.M. Schultz, X. Liu, P.A. Salvador, G.S. Rohrer, *Catal. Sci. Technol.* 2, (2012), 1945.
- [162] M.A. Hassan, T. Amna, M.S. Khil, *Ceram. Int.* 40, (2014), 423.
- [163] Y. J. Kim, B. Gao, B. S.Y. Han, M.H. Jung, A.K. Chakraborty, T. Ko, C. Lee, W.I. Lee, *J. Phys. Chem. C* 113, (2009), 19179.
- [164] R. Ramachandran, M. Sathiya, K. Ramesha, A.S. Prakash, G. Madras, A.K. Shukla, *J. Chem. Sci.* 4, (2011), 517.
- [165] H. Fu, C. Pan, W. Yao, Y. Zhu, *J. Phys. Chem. B* 109, (2005), 22432.
- [166] Y. Zhang, R. Selvaraj, M. Sillanpää, Y. Kim, C.W. Tai, *Chem. Eng. J.* 245, (2014), 117.
- [167] N.A.S.A. Areqi, A.A. Alas, A.S.N.A. Kamali, K.A.S. Ghaleb, K.A. Mureish, *J. Mater. Catal.* 381, (2014), 1.

Chapter 2

Materials and Methodology

In this chapter, a detailed description of the experimental procedures adopted for the present research work are presented. This chapter provides the experimental-related issues, including the lists of chemicals and apparatus employed during catalyst preparation and characterization as well as reaction studies. Moreover, the theoretical fundamentals and operational dealings of the catalyst characterization instruments are also be discussed. Finally, a detailed description of procedure for studying adsorption and photodegradation kinetics is also presented.

2.1 Materials

This section gives all the materials used in the research work. In this research, all materials were used as received without further purification unless otherwise noted. All the reagents were purchased from Merck, India.

i. Barium nitrate ($\text{Ba}(\text{NO}_3)_2$)

The molecular mass of barium nitrate is 261.337g mol^{-1} . 1M solution of barium nitrate was prepared by dissolving 26.13g of barium nitrate into 100mL of distilled water. Further dilutions were made accordingly.

ii. Bismuth nitrate ($\text{Bi}(\text{NO}_3)_3 \cdot 5\text{H}_2\text{O}$)

The molecular mass of bismuth nitrate is 485.07g mol^{-1} . 1M solution of bismuth nitrate was prepared by dissolving 48.5g of bismuth nitrate into 100mL of 5N HNO_3 solution.

iii. Citric acid ($\text{C}_6\text{H}_8\text{O}_7 \cdot \text{H}_2\text{O}$)

The molecular mass of citric acid is 210.14g mol^{-1} . 1M solution of citric acid was prepared by dissolving 210.47g of citric acid into 100mL of distilled water.

iv. Ethylene glycol ($\text{C}_2\text{H}_6\text{O}_2$)

The molecular mass of ethylene glycol is 62.07g mol^{-1} . It is taken by weighing appropriate amount of Ethylene glycol in w/w ratio. In this work, the CA: EG ratio was fixed to 3:2.

v. Hydrochloric Acid (HCl)

0.1N HCl was used to adjust the pH in acidic range. 0.87mL of HCl was added in 100mL of distilled water to obtain 0.1NHCl solution.

vi. Nitric acid (HNO₃)

5N HNO₃ was used to dissolve Bismuth nitrate. 31.5mL of HNO₃ was taken in 100mL of water to prepare 5N HNO₃ solution.

vii. Sodium hydroxide (NaOH)

0.1N NaOH was used to adjust the pH in basic medium. 0.4g of NaOH was dissolved in 100mL of distilled water to obtain 0.1NNaOH solution.

viii. Potassium nitrate (KNO₃)

The molecular mass of potassium nitrate is 101.103gmol⁻¹. 1M solution of potassium nitrate was prepared by dissolving 10.11 gm of potassium nitrate into 100mL of distilled water.

ix. P 25 TiO₂

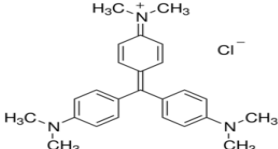
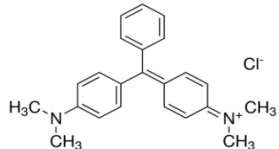
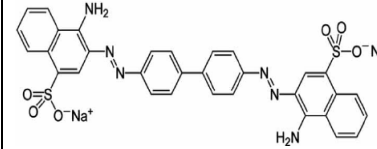
The molecular mass of p 25 TiO₂ is 79.87 gmol⁻¹. The particle size of this commercial photocatalyst is 21nm.

x. Dyes

In the present work, three dyes; Malachite green, Crystal Violet, and Congo red are utilized to undergo photocatalytic processes through heterogeneous photocatalytic reactions using prepared catalysts. A stock solution of 100ppm was prepared by dissolving 0.1gm of dye into 1000mL of distilled water. Further dilutions were made by this stock solution.

The structures and properties of these dyes are given in **Table 2.1**.

Table 2.1: Physical characteristics and molecular structure of Malachite green, Crystal Violet, and Congo red dyes.

Dye	Crystal Violet	Malachite Green	Congo red
Structure			
Alternate Names	Aniline violet, Basic violet, Hexamethyl- <i>p</i> -rosaniline chloride	Aniline green, Basic green4, Diamond green B	C.I. Direct red 28, direct red 28, Hemorrhagyl
IUPAC name	Tris(4-(dimethylamino)phenyl)methylium chloride	4-[[4-(dimethylamino)phenyl](phenyl)methylidene]- <i>N,N</i> -dimethylcyclohexa-2,5-dien-1-iminium chloride	disodium 4-amino-3-[4-[4-(1-amino-4-sulfonato-naphthalene-2-yl) diazenylphenyl] phenyl] diazenyl-naphthalene-1-sulfonate
Molecular Formula	C ₂₅ N ₃ H ₃₀ Cl	C ₂₃ H ₂₅ N ₂	C ₃₂ H ₂₂ N ₆ Na ₂ O ₆ S ₂
Color	Violet	Green	Brownish red
Molecular weight	407.99 gmol ⁻¹	364.911 gmol ⁻¹	696.66 gmol ⁻¹
λ_{\max}	590nm	618nm	500nm

2.2 Apparatus

This section includes the list of various apparatus employed during the whole experimental procedure.

i. Centrifuge

After the photodegradation treatment of the dye sample, the suspended photocatalyst particles were separated from the de sample before measuring its absorbance. The photocatalyst were separated by LABPRO digital bench top centrifugal machine.

ii. Crucible

A silica crucible is used for the calcination of polymeric precursor used for the preparation of catalysts.

iii. Cuvettes

Thoroughly cleaned quartz cuvettes (M labs, MCQ-104) are used for the observation of the transmittance of the colored dye solution.

iv. Electronic Balance

Citizen Electronic balance, C x 200 is used for weighing purpose. The least count of balance is 0.0001mg.

v. Filter paper

After photocatalytic degradation treatment suspended photocatalyst was filtered using Whatman filter paper grade- 4.

vi. Hot Plate

LABPRO (Temperature-500°C) hot plate is used for heating purposes.

vii. Mini Rotator Flask Shaker

Mac mini rotator flask shaker (MSW 303) is used for shaking solution.

viii. Muffle Furnace

Unitech sales, muffle furnace is used for heat treatment during catalyst synthesis procedure (**Figure 2.1**).



Figure 2.1: Muffle Furnace

ix. pH Meter

In our study, the pH of the collected samples is measured using a Eutech-pH meter (EC-pH 6500 42S Model). The pH meter is calibrated before each measurement using standard buffer solution at pH 4.00, 7.00 and 10.00. The samples are placed in a 35°C water bath then pH is measured.

x. Oven

LABPRO hot air oven is used for drying purpose.

xi. Stirrer

Remi 2 LH stirrer is used for stirring purpose at a fixed and suitable rpm.

xii. TOC analyzer

Total organic carbon (TOC) was measured using a multi N/C 3000 TOC analyzer (Analytik jena AG, Germany) to evaluate the mineralization of studied dyes.

xiii. Ultra Pre water purification System

Ultra-pure water purification system (Elix UV 3 model) is used to obtain de-ionized ultra-pure water (**Figure 2.2**).



Figure 2.2: *Ultra-Pure Water Purification System.*

xiv. UV Visible spectrophotometer

Computer based Systronics double beam spectrophotometer 166 is used for the determination of remaining concentration of dye (**Figure 2.3**).



Figure 2.3: Double beam spectrophotometer.

2.3 Synthesis of catalysts

This section describes the main steps taken to synthesize the BaBiO_3 and K- doped BaBiO_3 .

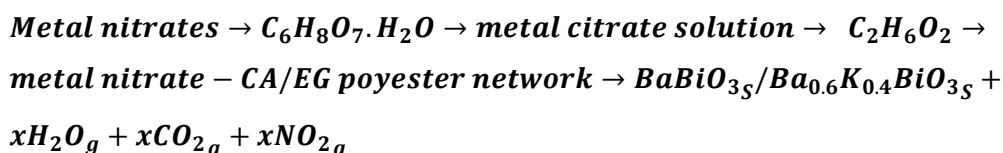
The physicochemical properties and hence the activity, of a photocatalyst strongly depend on the preparation method [1,2]. Since catalyst preparation and design are a major part of this work, careful attention was devoted to the preparation of all catalysts including monitoring and controlling related variables such as mixing speed, timing

and temperature. In this work we adopted Pechini method for the synthesis of both the catalysts [3].

Figure 2.4 shows the flow chart of the Pechini process for preparing barium bismuthate and potassium doped bismuthate powders. Both the catalysts were prepared under identical conditions other than the calcination temperature. Stoichiometric amounts of analytical grade metal nitrates were dissolved in distilled water and while bismuth nitrate is dissolved in dil. HNO_3 solution under continues stirred with a magnetic stir bar. Quantities of citric acid, in a 4:1 molar ratio with respect to the total amount of cations, and ethylene glycol in a 3:2 molar ratio with respect to CA was added to the above solution under constant strong stirring. Thus obtained solution is transferred to a hot plate where it is heated up to 90°C resulting in the formation of brown resin.

After this resin is pulverized at 350°C . Thus obtained precursor material is powdered with an agate mortar. Further, to fully evaporate highly combustion species in the mass and to burn down most of the organic constituents, the powder is calcined in a furnace at different temperatures (6 hours at 600°C and 12hours at 850°C for BaBiO_3 and 6 hours at 650°C and 12 hours at 720° for $\text{Ba}_{0.6}\text{K}_{0.4}\text{BiO}_3$).

Overall chemical reaction of the above procedure can be written as follows



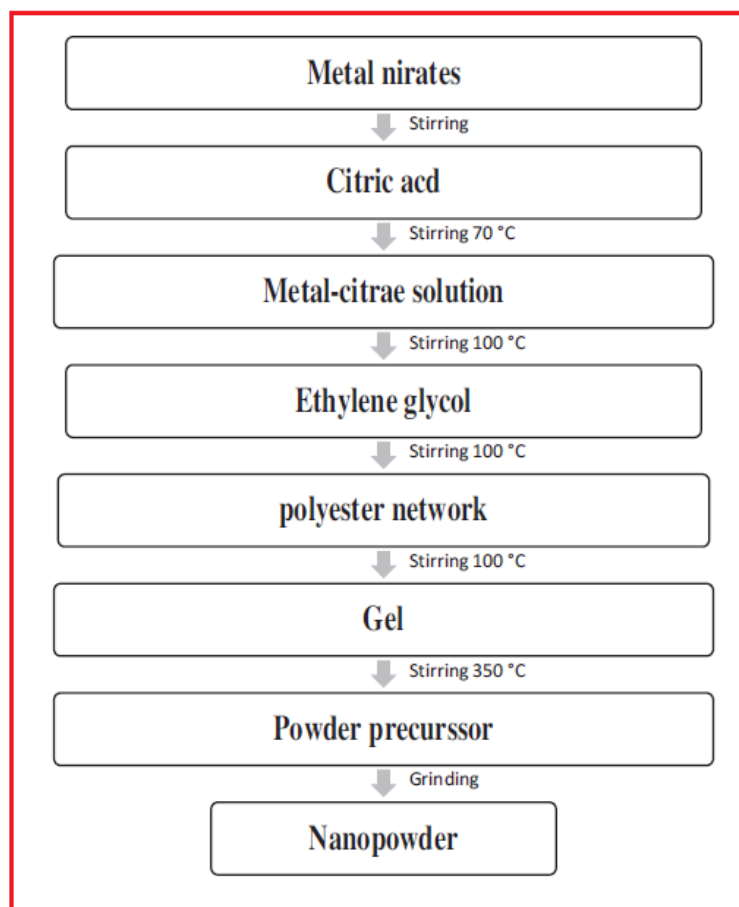


Figure 2.4: Flow chart for the synthesis of BaBiO₃ and Ba_{0.6}K_{0.4}BiO₃ of catalysts.

2.4 Characterization of catalysts

In this section, the as-synthesized samples are characterized using the different characterization techniques as mentioned in the third part.

i. Thermo-Gravimetric / Differential Thermal Analyses (TGA/DTA)

The as-synthesized sample was first subjected to thermal analysis in order to find the decomposition, stability and phase formation of the material using Perkin Elmer, Diamond Thermo-gravimetric /differential analysis (TG/DTA) 6300 thermal analyzer [Figure 2.5]. The TGA curve was recorded in the range from 40 to 850 °C

with a heating rate of 20 °C/min under nitrogen atmosphere at Sophisticated Analytical Instrument Facility (SAIF) at STIC, Kochi.

TGA/DTA is a characterization technique that is performed on samples to determine changes in weight in relation to change in temperature. TGA/DTA is commonly used to determine the degradation temperatures, absorbed moisture content of materials, the level of inorganic and organic components in materials, decomposition points of explosives, and solvent residues. TGA/DTA is carried out by raising the temperature of the sample and reference gradually and measuring weight and temperature difference between the sample and the reference [4]. The sample and reference pan are heated and the temperature difference is measured by a thermocouples which are embedded into the bottom of the two pan holders. To the sample pan is also attached a laser which shoots a light beam onto a photo-diode array. As the sample and reference are heated, changes in weight are recorded by measuring the relative deflection of the beam in relation to the diodes. Since TGA/DTA enables both the weight loss and the temperature difference to be recorded simultaneously, the nature of the thermal events associated with the weight loss can be obtained [5].



Figure 2.5: Thermogravimetric/differential thermal analyzer

Source: (<http://www.uop.edu.pk/labs/crl/?q=Facilities&r=Thermo-Gravimetric-and-Differential-Thermal-Analyzer>)

ii. X-ray Diffraction (XRD)

X-ray diffraction (XRD) technique is used to characterize the phase components, structure, and phase symmetry and lattice parameters of the materials prepared in this work. Powder X-Ray diffraction analysis (XRD) was carried out for the calcined samples with a Panalytical's Xpert Pro model (**Figure 2.6**) at Sophisticated Analytical Instrument Facility (SAIF) at Chandigarh. The X-ray diffraction pattern is obtained from 10° to 90° and was inspected using JCPDS data (if available) to identify the crystallographic phases.

X-rays are generated by using a cathode ray tube in which electrons are accelerated towards a Cu target that will be the source of the X-ray radiation. When the cathode ray strikes the target, penetrating electrons eject other electrons out of core atomic orbitals, specifically from the inner most (K) shell. An electron from a higher energy (L) orbital relaxes to fill the lower energy orbital while emitting its excess energy in the form of an intense X-ray beam. Since the energies of the shells are well defined, each transition produces a monochromatic wavelength of radiation [6].



Figure 2.6: X-ray Diffractometer

Source: (<https://www.cenimat.fct.unl.pt/services/laboratory-electronic-and-optoelectronic-materials-and-devices/x-ray-diffraction-panalytical-xpert-pro>)

iii. Fourier Transformed Infrared Spectroscopy (FT-IR)

Infrared Spectroscopy is one of the most common and powerful techniques used by organic and inorganic chemists. The FT-IR measurements have been performed in the potassium bromide mode (KBr) using the model Thermo Nicolet, Avatar 370 FT-IR spectrophotometer in the spectral range of 400-4000 cm^{-1} with a resolution of 4cm^{-1} at Sophisticated Analytical Instrument Facility (SAIF) at STIC, Kochi (**Figure 2.7**).

Basically, it is the absorption measurement of the IR electromagnetic waves within different frequencies. Electromagnetic waves used in infrared spectroscopy have frequencies ranging from 1.9×10^{13} to 1.2×10^{14} Hz, corresponding to photon energies ranging from 0.078 to 0.5 eV from the Plank relation

$$E = h\nu \quad \text{--- (2.1)}$$

Where h is the Planck constant and ν the frequency. This level of energy is inadequate to excite electrons but may induce vibration excitation of covalently bonded atoms or groups. The frequencies that absorption happens are closely related to the structure of the molecules, i.e. atom species, bonding types and ways of possible vibration (stretching, scissoring, rocking and twisting). For a typical IR spectrum, studied samples are exposed to a beam of infrared light and transmitted light is collected which reveals the absorption of the samples. From their characteristic absorption frequencies, different functional groups can be quickly identified [7].



Figure 2.7: FT-IR Spectrometer

Source: (<http://www.sticindia.com/images/LARGE/14.jpg>)

iv. UV-Vis. Diffuse reflectance spectroscopy (UVDRS)

Diffuse reflectance spectroscopy (DRS) is one of the most powerful spectroscopic techniques for the powdered or crystalline materials in mid-IR and near IR region. It is also known as Elastic Scattering Spectroscopy (ESS) in which the characteristic reflectance spectrum is measured, which is produced when light passed through the medium. In UV/Vis spectroscopy, the change in transmittance of light is determined when it passes through a solution. It is well known that when a light passes through a sample it may get reflected transmitted or absorbed. The diffuse reflection reveals the part of the incident light beam scattered within the sample and comes back to the surface. The incident light beam scattered in different directions belongs to diffuse reflection, while light beam reflected symmetrically is associated to specular reflection. In this project, the UV-Vis transmission spectra of the as-synthesized catalysts are recorded at Sophisticated Analytical Instrument Facility (SAIF), STIC, Kochi, with HP Hewlett Packard 8452A Diode Array Spectrophotometer over the

wavelength range of 200-800nm, in order to determine the proper wavelength of the incoming light source (**Figure 2.8**).

The UV-Vis spectra not only uniquely define the material, but also identify the possibility of using the materials for photocatalytic studies either in the UV or visible light range. To be more specific, the UV-Vis Spectra give the information necessary to decide the maximum wavelength (minimum frequency and energy) required in the incoming light source in order to excite the photocatalyst. The spectra generated here is due to the optical transitions from the ground state to an excited state of the catalyst molecules, i.e. a transition of electrons from valence band to conduction band [8].

According to Wood and Tauc studies, estimation of the optical band gap energy (E_g) of a crystalline material can be done by a graphical method. The following relation expression is used

$$(h\nu\alpha)^{1/n} = A (h\nu - E_g) \quad \text{--- (2.2)}$$

Where, h , ν , α , A and E_g are plank constant, vibrational frequency, absorption coefficient, proportionality coefficient, respectively. Here, value of n is taken $\frac{1}{2}$ considering the direct allowed transition. [9]

A plot of $(\alpha h\nu)^2$ as a function of $h\nu$ (photon energy), where the optical band gap energy (E_g) is obtained by extrapolation of the linear portion (absorption edge) till interception with the $h\nu$ axis for $(\alpha h\nu) = 0$ [10].



Figure 2.8: UV-Vis Spectrophotometer

Source: (<https://cdn.labx.com/labvista/2018/01/28/www-bidservice-com/39852e21-8715-4ac0-8de1-51d1802ae5a6.jpg>.)

v. Scanning Electron Microscope (SEM)

Diffraction techniques are powerful and irreplaceable in crystallography; however atomic arrangements are obtained indirectly by analyzing diffraction patterns and subsequent Rietveld analysis. Furthermore diffraction is insensitive to atoms in amorphous phase. Imaging of samples at reasonable magnification provides valuable complementary information. A Scanning Electron Microscope (SEM) is a powerful magnification tool that utilizes focused beams of electrons to obtain high-resolution, three-dimensional images for topographical and morphological information. Most SEM instruments are equipped with Energy Dispersive Spectroscopy (EDS) detectors which can also provide compositional information for a selected area in the SEM image. Scanning electron microscopy (SEM) is commonly used for study of atmospheric chemical species. It gives us a better insight about the morphology and

origin of aerosol particles that whether emitted from anthropogenic or the natural processes.

Scanning electron microscopy (SEM) is a method for high resolution surface imaging. The SEM uses an electron beam for surface imaging. Different elements and surface topographies emit different quality of electrons, due to which the contrast in a SEM micrograph (picture) is representative of the surface topography and distribution of elemental composition on the surface [11].

Atmospheric samples of free fall particulates matter are analyzed by SEM at Sophisticated Analytical Instrument Facility (SAIF) at STIC, Kochi. The particles size and morphology of the synthesized sample has been studied by The SEM analysis is carried out with the help of computer controlled field emission scanning electron microscope JEOL JSM 7600F FEG SEM equipment (**Figure 2.9**). The working conditions are set at an accelerating voltage of 0.5 kV to 30kV, resolution: 4 nm (30kV), magnification: 300,000.



Figure 2.9: Field emission gun- scanning electron microscope.

Source: (<http://www.rsic.iitb.ac.in/IMG/feg-sem1.jpg>)

2.5 Photodegradation of various dyes

This section gives the experimental set-up and the procedures used for studying photodegradation experiments.

The photocatalytic activities of the synthesized BaBiO_3 and $\text{Ba}_{0.6}\text{K}_{0.4}\text{BiO}_3$ samples were quantified by measuring the rates of photo degradation of different dyes. The experiments were performed in indigenously prepared immersion type photocatalytic reactor for the photodegradation of dyes. The schematic diagram of reactor is depicted in **Figure 2.10**. The reactor consists of a jacketed glass tube, which houses the radiation source. A 500 W Xe arc lamp with intensity of 137mW cm^{-2} was used for the emission of visible light radiation. The mixture of dye and catalyst is taken in the outer borosilicate reactor. Cold water was circulated in the outer reactor to maintain the solution temperature at 308K. The inner glass tube is immersed in the solution of dye and photocatalyst. In all the studies the mixture was magnetically stirred before enduring illumination at specific time interval, 5mL of the sample was collected and centrifuged prior to the absorbance measurement. The residual concentration of dye was monitored by change in absorbance using Systronics double beam spectrophotometer 166. Before irradiation, the suspension was stirred in the dark for 30 min to obtain a state of sorption equilibrium. Controlled experiments, without the catalyst were performed to demonstrate the extent of photocatalysis. Therefore A preliminary control experiment was carried out to examine the effect of visible light on dye, by illuminating dye solution without photocatalyst.

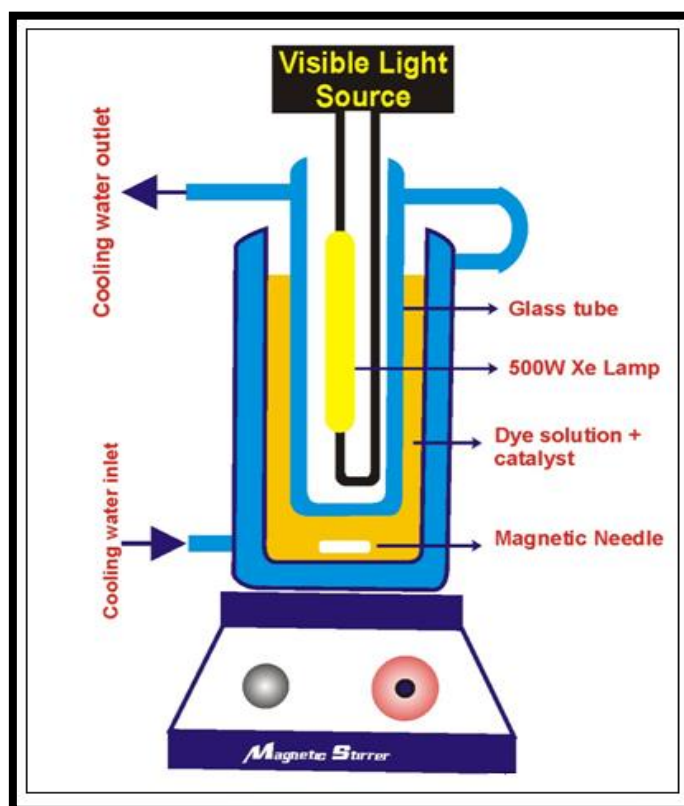


Figure 2.10: Schematic of the immersion type photocatalytic reactor set up for the degradation of dye solution.

A flow chart of photodegradation of dyes is shown in **Figure 2.11**.

The degradation efficiency was observed in terms of change in intensity of the dye before and after light irradiation. Photocatalytic performance was quantified by the degradation of crystal violet as a model organic pollutant under visible light irradiation.

$$\frac{C_0 - C_t}{C_0} \times 100 \quad \text{--- (2.3)}$$

Where, C_0 = concentration of dye solution before photo irradiation (mgL^{-1}), C_t = Concentration of dye solution after photo irradiation (mg L^{-1}).

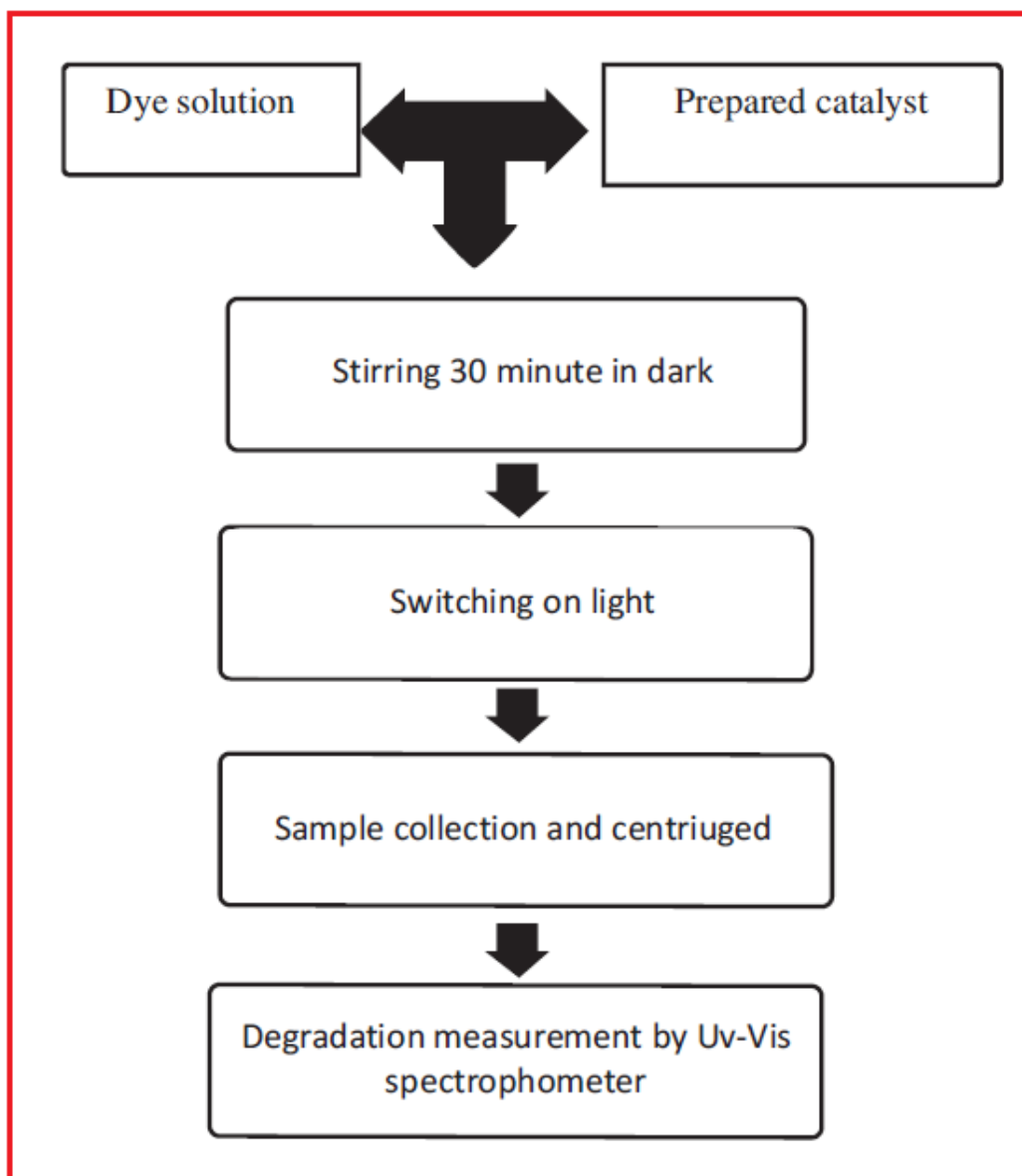


Figure 2.11: Flow chart of the photodegradation of studied dyes by the synthesized catalysts.

2.6 Kinetic modeling

This section describes the various kinetic model (Adsorption isotherms, and photodegradation kinetic model) to provide theoretical support for evaluating the photocatalytic efficiency of the samples.

i. Adsorption Isotherm

Since, the photo-assisted degradation of the dyes occurs predominantly on the photocatalyst surface. Therefore, adsorption of the dye is an important parameter in determining photocatalytic degradation rate. Experiments of adsorption of dyes on both the catalysts were conducted in the reactor at a temperature of 308K. Operating conditions for the reactor were the same as in the photodegradation experiments. First, the reactor was filled with certain dye initial concentration (20, 40, 60 and, 80mgL⁻¹). One sample was taken at this point in order to measure the actual concentration of the dye (C₀). Then, 0.75gL⁻¹ of the respective catalysts was added to the solution. The reacting solution, with the catalyst, was left running for 30 minutes in order to reach adsorption equilibrium. After this period of time, a sample was taken in order to measure the concentration in the liquid at equilibrium (C_e). With these two concentration values, the adsorption capacity at equilibrium time has been determined.

Analysis of the adsorption isotherm is of fundamental importance to describe how adsorbate molecules interact with the adsorbent surface. Equilibrium studies determine the capacity of the adsorbent and describe the adsorption isotherm by contents whose values express the surface properties and affinity of the adsorbents. The relationship between equilibrium data and either theoretical or practical equations is essential for interpretation and prediction of the adsorption.

Several adsorption isotherms have been investigated for the adsorption process of organic pollutants, out of them, the Langmuir and Freundlich models are the most common isotherm due to their simplicity and capability to describe experimental results in wide range of concentration [12].

a) Langmuir isotherm

Langmuir model is valid for single layer adsorption [13]. It is based on the assumption that all adsorption sites have equal affinity for molecules of the adsorbate in the plain surface. The Langmuir description of adsorption provides the most common equation, and is applied to kinetic modelling for quantitative analysis of the adsorption-desorption process due to its simplicity and its ability to fit a variety of adsorption data. It is based on four major assumptions:

- All of the adsorption sites are equivalent and each site can only accommodate one molecule.
- The surface is energetically homogeneous and adsorbed molecules do not interact.
- There are no phase transitions.
- At the maximum adsorption, only a monolayer is formed. Adsorption only occurs at localized sites on the surface, and not with other adsorbates.

The Langmuir isotherms are represented by the following equations.

$$q_e = \frac{Q_0bc}{1+bc} \quad \text{--- (2.4)}$$

$$\frac{C_e}{q_e} = \frac{1}{Q_0b} + \frac{C_e}{Q_0} \quad \text{--- (2.5)}$$

Where C_e is the concentration of the adsorbate (mg/l) at equilibrium, q_e is the amount of adsorbate per unit mass of adsorbent at equilibrium in mgg^{-1} , Q_0 is the maximum adsorption at monolayer coverage in mgg^{-1} , b is the adsorption equilibrium constant related to the energy of adsorption in Lmg^{-1} .

The adsorbate uptake q_e (mgg^{-1}), can be calculated as

$$q_e = \frac{(C_0 - C_e)V}{w} \quad \text{--- (2.6)}$$

Where C_0 is the initial adsorbate concentration (mgL^{-1}), V is the volume of solution (L), W is the mass of adsorbate (g). The value of Q_0 and b was found from the intercept and slope of the C_0/q_e vs C_e curve respectively.

b) Freundlich models

The equilibrium removal of dye was mathematically expressed in terms of adsorption isotherm. The adsorption isotherm is a function of expression for the variation of adsorption with concentration of adsorbate in bulk solution at constant temperature. The relation between the dye uptake capacity of the adsorbent q_e (mgg^{-1}) and the residual dye concentration at equilibrium C_e (mgL^{-1}) is given by equation 9 which will have a straight line with a slope of $1/n$ and an intercept of $\log(K_F)$ when $\log(q_e)$ is plotted against $\log(C_e)$, where K_F and $1/n$ are empirical constants dependent on several environmental factors [14].

Here the intercept $\log K_F$ is a measure of adsorbent capacity and the slope $1/n$, is the sorption intensity. The value of $1/n$ is less than 1, indicates a favorable adsorption.

A plot of C_0/q_e versus C_e indicates a straight line of slope $1/q_m$ and an intercept of $1/(K_L q_m)$.

$$\mathbf{\log(q_e) = \frac{1}{n} \log(C_e) + \log K_F} \quad \text{--- (2.7)}$$

$$\frac{C_e}{q_e} = \frac{1}{q_{\max.} K_L} + \frac{1}{q_{\max.}} C_e \quad \text{--- (2.8)}$$

$$\mathbf{q_e = \frac{q_{\max.} K_L C_e}{1 + K_L C_e}} \quad \text{--- (2.9)}$$

The essential characteristics of Langmuir equation can be expressed in terms of dimensionless separation factor R_L .

$$\mathbf{R_L = \frac{1}{1 + K_L C_0}} \quad \text{--- (2.10)}$$

ii. Photodegradation kinetic model (Langmuir- Hinshelwood kinetics)

Consider that only two reactants take part in the reaction on the surface of photocatalyst.

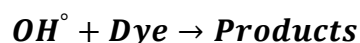
The most common surface reaction mechanism is that where both reactants are adsorbed on the surface and subsequently they collide and create products. This is known as the Langmuir -Hinshelwood mechanism. It was derived from ideas proposed by Hinshelwood based on Langmuir's principles for adsorption [15].

This mechanism is based on the following hypotheses

- Surface is homogeneous
- Adsorption occurs only on the specific places of surface
- Each active center use only one molecule of adsorbed reactant
- Adsorbed molecules do not react with each other
- Only monolayer is formed during the adsorption process

Analysis of heterogeneous kinetics of photocatalytic reaction can be simply quantified by the rate equation; by Langmuir-Hinshelwood equation.

Assuming that the hydroxyl radical OH° is the primary oxidant for the degradation of dye, a chemical kinetics for the process may be written as:



The rate of degradation of dye can be expressed as:

$$r = \frac{dC}{dt} = \frac{kKC}{1+KC} \quad \text{--- (2.11)}$$

Where r is the rate of degradation of reactant ($\text{mgL}^{-1}\text{min}^{-1}$), C concentration of the reactant (mgL^{-1}), t the illumination time (min.) and k is the reaction rate constant (min^{-1}) and K is the adsorption coefficient of the reactant (Lmg^{-1}).

When the reactant concentration is avoidable, equation (2) can be simplified to an apparent-first-order equation:

$$\ln \frac{C_o}{C} = kK_t = K_{app} \quad \text{--- (2.12)}$$

A plot of $\ln(C_0/C_t)$ against time represents approximately linear straight lines, showing the case of first-order reaction. The slope of the line equals the apparent first-order rate constant K_{app} .

iii. Goodness of fit

Goodness of fit is a fundamentally key parameter that approximate how well the predicted curve correlates with the experimental data [16]. Usually least squares method is used to measure the degree of the goodness of fit. Previously, nonlinear data would be transformed into a linear form and accordingly analyzed the data by the least squares fit method (i.e. conversion of C_t into $\ln C_t$). The coefficient of determination, R^2 gives the proportion of the variance of one variable that is predictable from the other variable. The coefficient of determination is such that $0 < R^2 < 1$, and indicates the strength of the linear association between experimental data. In all the kinetic modelling (adsorption isotherms and LH kinetics) linear and non-linear regression were applied using MS Excel spreadsheet.

References

- [1] D.C. Bradley, *Chem. Rev.* 89, (1989), 1317
- [2] J.J. Urban, W.S. Yun, Q. Gu, H. Park, *J. Am. Chem. Soc.* 124, (2002), 1186.
- [3] M.P. Pechini, *United States Patents*, 3,330,697.
- [4] P.K. Gallagher, *Encyclopedia Mater. : Sci. Technol.* 2, (2001), 9141.
- [5] A.W. Coats, J.P. Redfern, *Analyst* 88, (1963), 906.
- [6] C. Vijaykumar, H.P. Kumar, S. Solomon, J.K. Thomas, P.R.S. Warrior, J. Koshy, *Bull. Mater. Sci.* 31, (2008), 719.
- [7] M.A.P. Osorio, R.L. Milot, M.R. Filip, J.B. Patel, L.M. Herz, M.B. Johnston, F. Giustino, *J. Phys. Chem. C* 119, (2015), 25703.
- [8] J. Tauc, R. Grigorovici, A. Vancu, *Phys. Stat. Sol.* 15, (1966), 627.
- [9] J. Tang, Z. Zou, J. Ye, *J. Phys. Chem. C* 111, (2007), 12779.
- [10] A. Ibrahim, S.K.J. Al-Ani, *Czech. J. Phys.* 44, (1994), 785.
- [11] O. Klemperer, *Rep. Prog. Phys.* 7, (1940), 107.
- [12] S. Jain, R. Yamgar, R.V. Jayaram, *Chem. Eng. J.* 148, (2009), 342.
- [13] L. Largetitte, R. Pasquier, *Chem. Eng. Res. Des.* 109, (2016), 495.
- [14] M.T. Yagub, T.K. Sen, S.A. Afroze, H.M. Ang, *Adv. Colloid Interface Sci.* 209, (2014), 172.
- [15] D.F. Ollis, *J. Phys. Chem. B* 109, (2005), 2439
- [16] M. Verz, A.Z. Moghaddam, S. Alijani, *Ind. Eng. Chem Res.* 51, (2012), 4199.

Chapter 3

Synthetic Methodology and Characterization Techniques

3.1 Introduction

A large number of metal oxides have been examined as photocatalysts for environmental application in dye degradation. There is a majority of the simple metal oxide photocatalysts; however, they are primarily active under UV irradiation, utilizing only a small portion of solar light. Till now, TiO_2 has been used, for the above said purpose, which has wide band-gap energy 3.0~3.2eV which prevents the utilization of visible-light that accounts for most of solar spectrum [1,2]. In recent times, significant efforts have also been made to develop new semiconductor photocatalyst with visible light photocatalytic activity. For this purpose, many approaches have been used which includes metal ion doping, nonmetallic element doping, coupling with other photocatalysts, sensitization with organic dyes. [3-5].

The increasing necessity of stable and durable visible light active photocatalyst (green photocatalyst) has been the motivation of many investigations in order to develop new materials with a more efficient use of natural sunlight [6-8].

The perovskite type oxides (ABO_3), where A and B represent 12-coordination and 6-coordination metal cations, respectively, own special physical and chemical features because of their stable crystal structure, electromagnetic behavior, magneto-resistive properties and high catalytic activity. They have been applied in environmental protection and industrial catalysis [9-10]. Most of the metal cations are known to be stably incorporated in the perovskite structure. One of the major characteristics of perovskites is the possibility for substitutions at the position of cations. As a result, there are large groups of compounds with different cations in A position $\{\text{A}_y\text{A}'_{1-y}\text{BO}_3\}$ [11-12] and with different cations in B position $\{\text{AB}_y\text{B}'_{1-y}\text{O}_3\}$ [13-14] and with substitution in positions of both the cations $\{\text{A}_x\text{A}'_{1-x}\text{B}_y\text{B}'_{1-y}\text{O}_3\}$ [15-16]. Perovskite exhibits much higher activity compared to TiO_2 for the decomposition of various dyes and phenolic compounds under visible light [17,18].

Owing to the novel physical properties and potential applications, perovskites have been studied intensively. Many of these like LaNiO_3 , PbTiO_3 , and LnVO_3 which

are commonly used in waste water treatment are synthesized from costly and complicated methods [19-21].

It is to be noted that the photocatalyst synthesized during this research work can be prepared at laboratory level through Pechini method besides being synthesized in a very cost effective manner. In the present research work, perovskite BaBiO₃ is selected with Ba at 'A' site and Bi at 'B' site along with a new catalyst i.e. K doped BaBiO₃ (Ba_{0.6}K_{0.4}BiO₃) for photodegradation studies.

There is a major advantage for using barium owing to its properties related to fixed valance band state (Ba²⁺) and large ionic radius (1.60Å) [22]. These combined properties are very attractive, thus favoring the creation of large lattice spacing and facilitating the desired tailoring of the photocatalyst being synthesized. To complement barium, bismuth was chosen as a cation dopant since it has ionic radius variability at different valance states (Bi³⁺ and Bi⁵⁺) and coordination numbers which allowed flexible incorporation of bismuth in A-site and/or B-site [23]. Many Bi³⁺ containing oxides exhibit photocatalytic properties due to the hybridized O (2*p*) and Bi (6*s*) valence bands [24,25].

Hence, in the search for alternative green photocatalysts, this work takes the advantage of these combined features of barium (as discussed above) with the flexibility of bismuth in the manipulation of the perovskite structure.

The present research works aims at synthesizing a novel visible light active photocatalyst (independent of TiO₂) BaBiO₃ through Pechini method. Furthermore, different photochemical and physical properties of as synthesized BaBiO₃ are studied in detail. Besides that, to improve the physical and absorption properties of parent BaBiO₃ perovskite compound while retaining its ideal properties, efforts were taken to develop a newly designed perovskite through partial substitution of Ba by K at 'A' site. In addition, the photo degradation properties of thus prepared BaBiO₃ and Ba_{0.6}K_{0.4}BiO₃ photocatalysts are studied to degrade the three dyes viz Crystal violet, Malachite green and Congo red.

As the physicochemical properties of different photocatalysts and hence their activity are potentially influenced by, calcination conditions (temperature, time and atmosphere) , substitution of A and B sites and the synthesis methods [26], therefore, many routes have been used to synthesize perovskite materials, such as solid state reaction, co-precipitation, hydrothermal, spray and freeze drying, and sol-gel process [27-31].

The sol-gel process is a very useful technique for preparing many materials in a variety of shapes and forms. Applying the sol-gel process, it is possible to fabricate ultrafine oxide material at relatively low temperatures with high purity and nano-scale powder along with accurate control of the composition of the final material [32]. The Pechini method is based on rigorous mixing of positive ions in a solution, precise alteration of the solution into a polymer gel, elimination of the polymer matrix and development of an oxide precursor with a high degree of uniformity [33, 34].

3.2 Pechini method

In the present research work we have adopted the Pechini method to achieve a good crystallized, single phase, under 100 nm size, mono disperse and homogeneous morphology compound which is ideal for a semiconductor material in order to be an efficient and chemically stable photocatalyst.

The Pechini method is a widely used option for the synthesis of many mixed oxides. It has been idealized on the ability of some compounds, such as, lactic, glycolic, citric, and ethylene diamine tetra acetic (EDTA) acids, to form polybasic acid chelates with cations dissolved in the system [35]. Chelating agents are used to prevent the partial segregation of metals in the final compound, which may be caused by different interactions between metal ions present in the solution [36]. A subsequent step may be performed with the addition of a polyol, such as ethylene glycol, promoting the polymerization with the chelating agent. It has been reported that the use of ethylene glycol can result in a material with increased homogeneity and high surface area when compared to samples prepared using only chelating agents, since polyester net can

minimize further segregations of particular metals during the decomposition process at the required temperatures in the heat treatment. [35,37]. The addition of a poly-hydroxy alcohol (here EG), allied with heating the solution, leads to the poly-esterification of the chelates, creating a cross-linked chain of metal atoms bonded to organic radicals. The heat treatment, which requires lower temperatures than conventional methods, leads to the removal of organic material and formation of the mixed oxides (**Figure 3.1**). These oxides are finely divided and exhibit high purity as well as high homogeneity. As a consequence, the system is in a highly desirable state for successfully synthesizing a good photocatalyst for degradation of dyes.

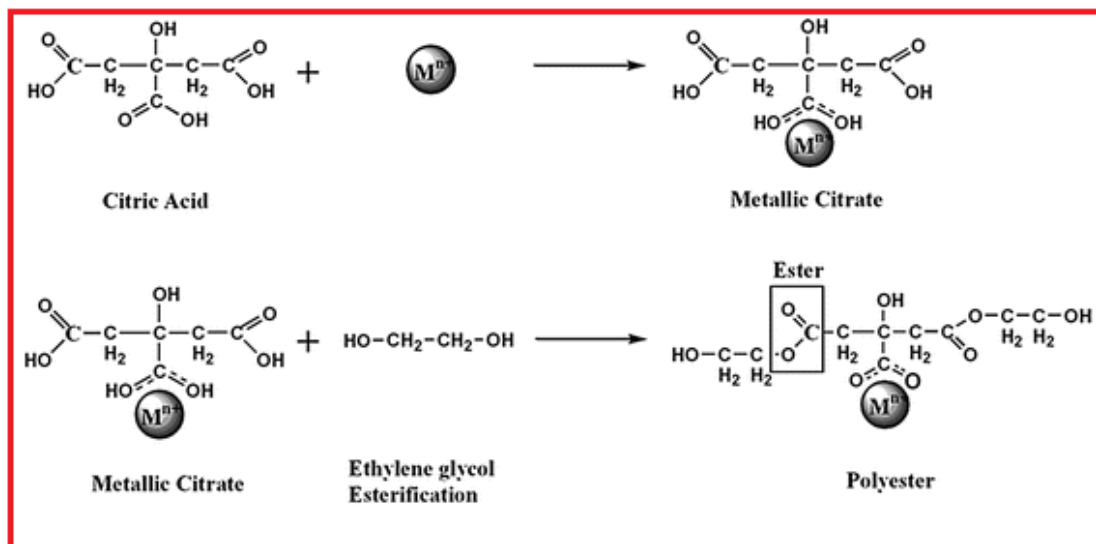


Figure 3.1: Mechanism of Pechini reaction

(Source: https://media.springernature.com/lw785/springer-static/image/chp%3A10.1007%2F978-3-319-19454-7_123-1/MediaObjects/339104_0_En_123-1_Fig2_HTML.gif)

BaBiO₃ perovskite, an indirect semiconductor material that was discovered by Cox et al in 1976 [38]. As far as our knowledge, the earlier studies on the use of BaBiO₃ as photocatalyst has not been reported much except its use in a recent study where it was synthesized through soft chemical technique [39]. In all the research work, emphasis has been given to its superconductivity and magneto-electric properties, and

dielectric properties, where it was synthesized via vapor phase synthesis, solid state reaction and microwave assisted hydrothermal reaction [40-43], rather than their utilization in photodegradation of organic pollutants.

Potassium doped BaBiO₃ perovskite semiconductor material was discovered by Mattheiss et al. in 1988 [44]. Conventionally, potassium doped BaBiO₃ powders have been prepared by a traditional solid state reaction [45] and powder sintering technique [46] which needs high temperature and may lead to the presence of impure phases like Bi₂O₃ in the prepared catalyst [47].

In order to overcome these disadvantages, we used Pechini method (sol-gel technique) [34] which is simple and economical, low processing temperature and wide range of possibility to change the properties by varying the composition of the solution [35].

It is to be noted that the synthesis of Ba_{0.6}K_{0.4}BiO₃ via Pechini method followed by its utilization in photodegradation of dyes is being reported for the first time. In this chapter, we report on the successful synthesis of crystalline and single-phase BaBiO₃ and Ba_{0.6}K_{0.4}BiO₃ photocatalysts using Pechini method.

3.3 Synthesis

Synthesizing uniform, mono disperse particles with reliable reproducibility with control over nanostructure phase, size and morphology is experimentally challenging. Moreover, elimination of impurities associated with the final nano materials is also difficult. In this section, we report on the successful preparation of crystalline and single-phase BaBiO₃ and Ba_{0.6}K_{0.4}BiO₃ photocatalysts

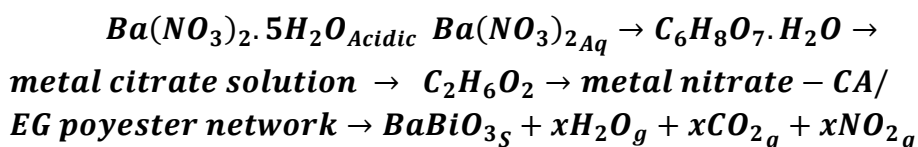
3.3.1 Synthesis of BaBiO₃

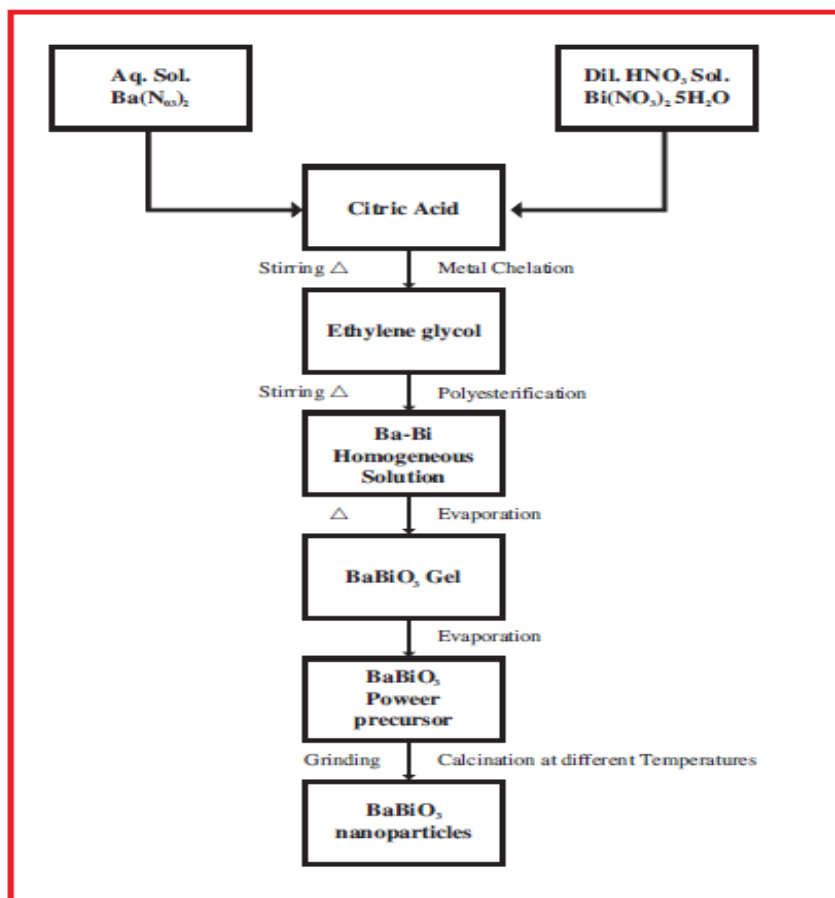
BaBiO₃ perovskite is prepared by the Pechini method as depicted in flow diagram in **Figure 3.2 (A)**. All the reagent materials are carefully weighed to calculated values of mass (g) in order to achieve stoichiometric products. In a typical procedure, the starting material barium nitrate {Ba(NO₃)₂} is dissolved in 100 ml distilled water applying strong stirring for 15 min., while bismuth nitrate {Bi(NO₃)₂.5H₂O} is dissolved in dil.HNO₃ solution, to avoid the precipitate of the bismuth ions [48]. These Barium nitrate and bismuth nitrate solutions are used as starting materials. Both the above solutions are mixed and then magnetically stirred to get a uniform solution. Once the starting materials are dissolved, 1M citric acid (C₆H₈O₇.H₂O) is added to above solution as complexing agent under constant stirring for next 30 minutes.

After homogenization of the solution containing the Ba and Bi cations, ethylene glycol (C₂H₆O₂) was added to promote mixed citrate polymerization by the poly-esterification reaction. Upon continued heating at 80–90 °C, the solution became more viscous, without any visible phase separation.

The solution was heated for several hours to evaporate the excess water and subsequently to accelerate poly-esterification reactions between citric acid and ethylene glycol results in the formation a viscous, bubbly mass that formed a brown resin upon cooling. Here, citric acid and ethylene glycol are used as complexing agents. The molar ratio among Barium, Bismuth cations is 1:1. The citric acid/metal ratio is fixed at 4.0 while keeping the citric acid/ethylene glycol ratio as 3:2. This resin is pulverized at 350 °C {**Figure3.2 (B)**} and then calcined at 600 °C for 5 hours and then finally at 800 °C for 12 hours to obtain distorted monoclinic BaBiO₃ perovskite. In the end, the calcined compound {**Figure3.2 (C)**} is ground to fine powder once more for further characterization.

The chemical reaction taking place during the process is given below:





(A)



(B)



(C)

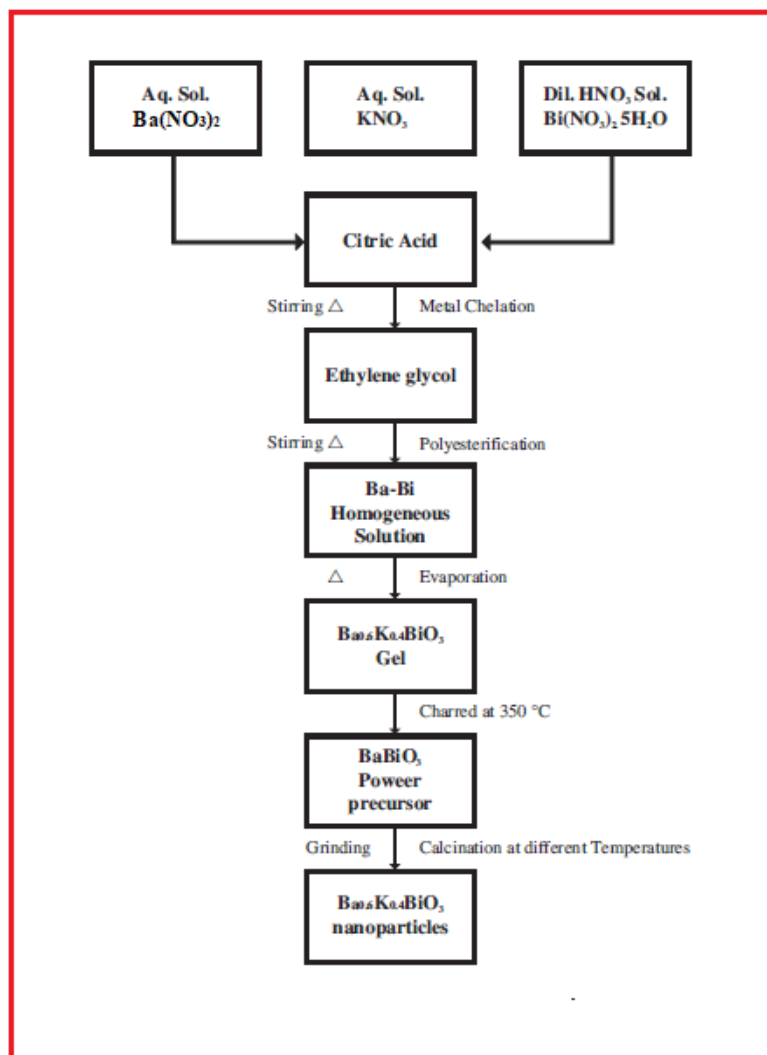
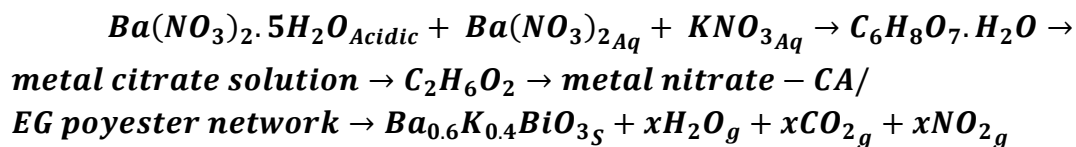
Figure 3.2: (A) Flowchart for the preparation of BaBiO₃ (B) BaBiO₃ powder precursor at 350° C/2h. (C) BaBiO₃ perovskite at 800° C/12h

3.3.2 Synthesis of $\text{Ba}_{0.6}\text{K}_{0.4}\text{BiO}_3$

Potassium doped BaBiO_3 i.e. $\text{Ba}_{0.6}\text{K}_{0.4}\text{BiO}_3$ is prepared by Pechini method as depicted in flow diagram **Figure 3.3 (A)** and the structural properties of $\text{Ba}_{0.6}\text{K}_{0.4}\text{BiO}_3$ are examined by various characterization techniques. This process is based on metallic citrate polymerization with the use of ethylene glycol. A hydro carboxylic acid (such as citric acid), is used to chelate cations in aqueous solution. Polymerization is promoted by heating the mixture, and it results in the formation of homogeneous resin in which metal ions are uniformly distributed.

All the reagent materials are carefully weighed to calculated values of mass (g) in order to achieve stoichiometric products. For the preparation of $\text{Ba}_{0.6}\text{K}_{0.4}\text{BiO}_3$ particles, barium nitrate $\{\text{Ba}(\text{NO}_3)_2\}$, potassium nitrate (KNO_3) and bismuth nitrate $\{\text{Bi}(\text{NO}_3)_2 \cdot 5\text{H}_2\text{O}\}$ are used as starting materials. Atomic ratio of barium nitrate, potassium nitrate and bismuth nitrate is 3:2:5. First, barium nitrate and potassium nitrate are dissolved in deionized water under stirring condition. Bismuth nitrate is separately dissolved in minimum amount of dilute HNO_3 to avoid precipitation of Bi ions, then it is added drop wise to the barium nitrate and potassium nitrate solution [48]. Citric acid ($\text{C}_6\text{H}_8\text{O}_7 \cdot \text{H}_2\text{O}$) is then added proportionally to the above metal solution, followed by the addition of ethylene glycol ($\text{C}_2\text{H}_6\text{O}_2$) as a chelating agent. The citric acid/ethylene glycol ratio is kept as 3:2. The solution thus prepared, while being stirred with a magnetic stirrer, is heated up to 90°C to remove excess water and subsequently to accelerate poly esterification reaction between citric acid and ethylene glycol. During the evaporation of solvent, reddish brown gas corresponding to NO_2 comes out of the solution [49]. This produces a viscous, bubbly mass that forms a resin upon cooling. This precursor is burned at 350°C for 2 hours followed by grinding in mortar to achieve fine powder **{Figure3.3 (C)}**. Further, to fully evaporate highly combustion species in the mass and to burn down most of the organic constituents, the powder is calcined in a furnace at 650°C for 6 hours and then at 720°C for 12 hours **{Figure3.3 (C)}**. The calcination removes most of the residual carbon and thus cubic phase perovskite is finally obtained which is then ground to fine powder once more for

further characterization. The chemical reaction taking place during the process is given below:



(A)

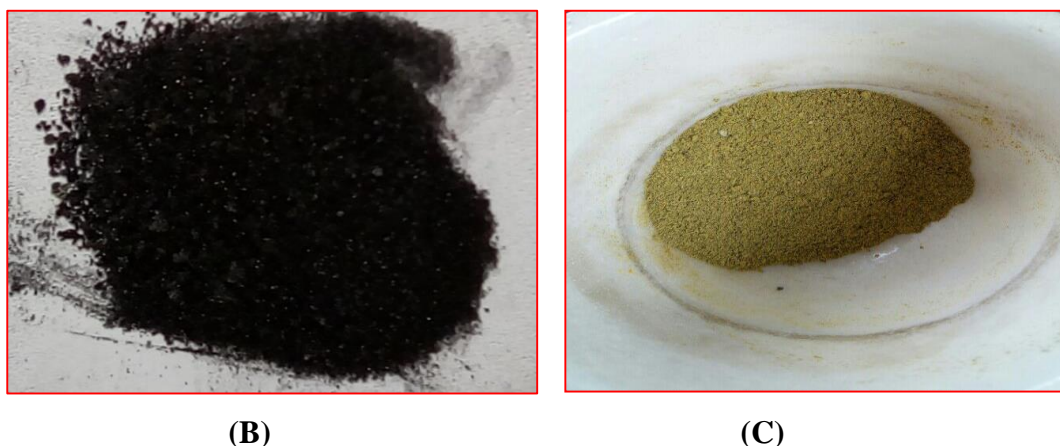


Figure 3.3: (A) Flowchart for the preparation of $Ba_{0.6}K_{0.4}BiO_3$ (B) $Ba_{0.6}K_{0.4}BiO_3$ powder precursor at $350^\circ C/2h$. (C) $Ba_{0.6}K_{0.4}BiO_3$ perovskite at $720^\circ C/12h$.

3.4. Results and discussion

In the consecutive sections, the techniques used in this work to characterize the compounds through their structural, morphological and optical analysis, are described followed by their results and discussion.

The as-synthesized sample was first subjected to thermal analysis in order to find the decomposition, stability and phase formation of the material using Perkin Elmer, Diamond TG/DTA 6300 thermal analyzer. The TGA curve was recorded in the range from 40 to $850^\circ C$ with a heating rate of $20^\circ C/min$ under nitrogen atmosphere. Powder X-Ray diffraction analysis (XRD) was carried out for the annealed samples with a Panalytical's Xpert Pro model 1 kV, and $30mA$. The X-ray diffraction pattern is obtained from 10° to 90° and was inspected using JCPDS data (if available) to identify the crystallographic phases. The FT-IR measurements have been performed in the potassium bromide mode (KBR) using the model Thermo Nicolet, Avatar 370 FT-IR spectrophotometer in the spectral range of $400-4000\text{ cm}^{-1}$ with a resolution of 4 cm^{-1} . The particles size and morphology of the synthesized sample has been studied by JEOL JSM 7600F FEG SEM microscope operated at 20 kV . The optical absorption study of the synthesized sample has been carried out in the range of $200-800\text{ nm}$ using Cary

5000 high resolution spectrophotometer. The band gap calculations are done with the help of KM function and corresponding Tauc's plot.

3.4.1. Characterization of BaBiO₃

3.4.1 (A) Thermal Studies

To determine the best annealing conditions and to evaluate the crystallization temperature necessary to obtain a single phase BaBiO₃ by the Sol-gel method, thermal analyses were performed using TG-DTA analyses of BaBiO₃ powder obtained by heating of polymeric precursor at 90° C. It can be seen that the decomposition of BaBiO₃ precursor resin takes place in three distinct steps. The first weight loss region (31°C -185 °C) corresponds to the loss of physio-absorbed water and accompanied by 8.9% weight [50]. The second weight loss (60.80%) region is in temperature range of 186 °C - 416 °C, which can be attributed to the pyrolysis and combustion of organic compounds and the degradation of intermediate species formed during the polymerization process. The next weight loss around 13.0 % lies in the range of 417 °C - 440 °C and can be attributed to the decomposition of nitrates and nitrites residue. The DTA curve shows three weak exothermic peaks at 200 °C, 259 °C, 292 °C and one strong exothermic peak at 456 °C, which are correlated to the weight loss mentioned above and subsequent crystallization of the residual amorphous phase. The DTA curve shows a strong exothermic peaks around 459°C, which is correlated to the weight loss that must be considered as the crystallization of the residual amorphous phase [51]. This observation is supported by powder X-ray diffraction (XRD) of the sample obtained from calcinations of the precursor at 350°C, 600°C and 800°C (**Figure 3.4**).

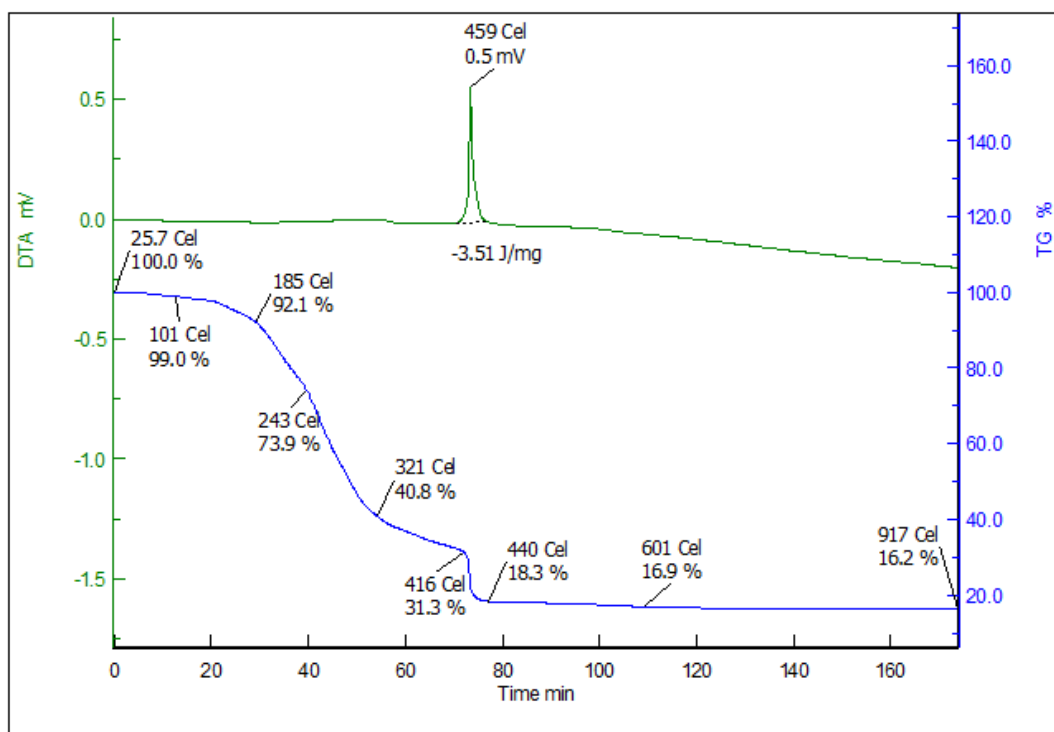
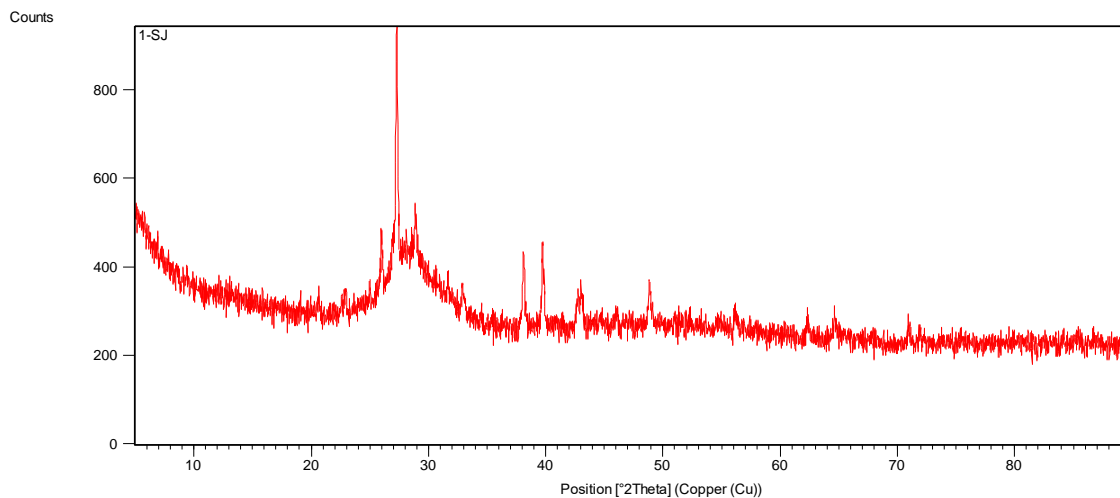


Figure 3.4: TGA and DTA curves of BaBiO_3 precursor prepared by Pechini method

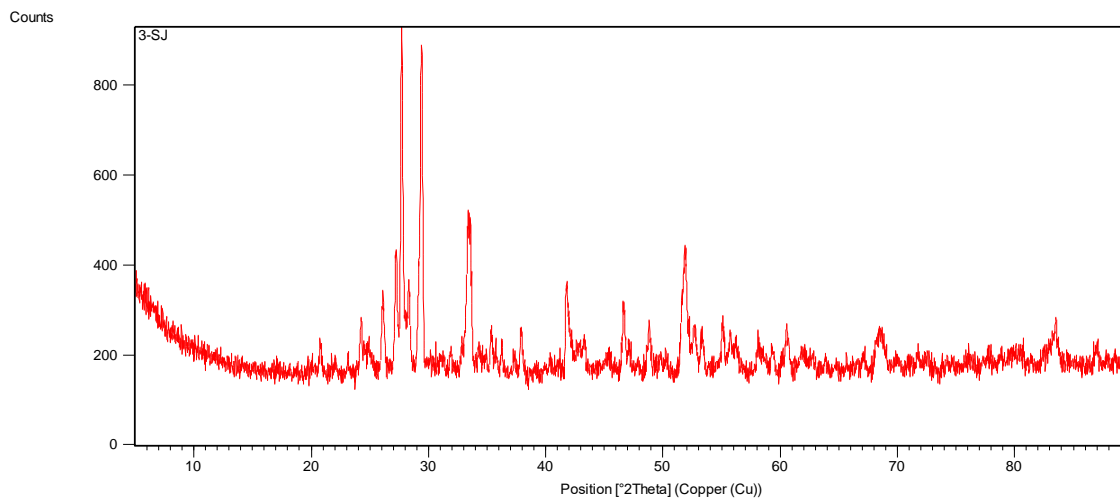
3.4.1 (B) X-ray diffraction (XRD) patterns

The XRD pattern of the characterized BaBiO_3 samples was measured within the range (5° - 90°) with scan rate of 5°min^{-1} . The XRD patterns of a given material consist of the intensity of the light diffracted by the lattice of the material as a function of the angle 2θ , resulting in a plot of narrow peaks with different intensities. Crystalline structure evolution of pure BaBiO_3 as a function of calcinations temperature i.e. 350°C , 600°C & 800°C is shown in **Figure 3.5(a)**, **3.5(b)** and **3.5(c)**, respectively, which indicates that well crystallized monoclinic BaBiO_3 can be synthesized by calcination at 800°C . On the other hand, at lower calcinations temperatures (350°C & 600°C) intense and well defined diffraction peaks are absent, suggesting the compound have an amorphous structure. As **Figure 3.5** shows, BaBiO_3 exhibits a crystalline perovskite phase with relevant diffraction peaks properly indexed. In the XRD pattern we can identify the presence of (110), (112), (220), (312), (240), (332) and (316) crystal planes. All the diffraction peaks are found to be in accordance with the distorted monoclinic

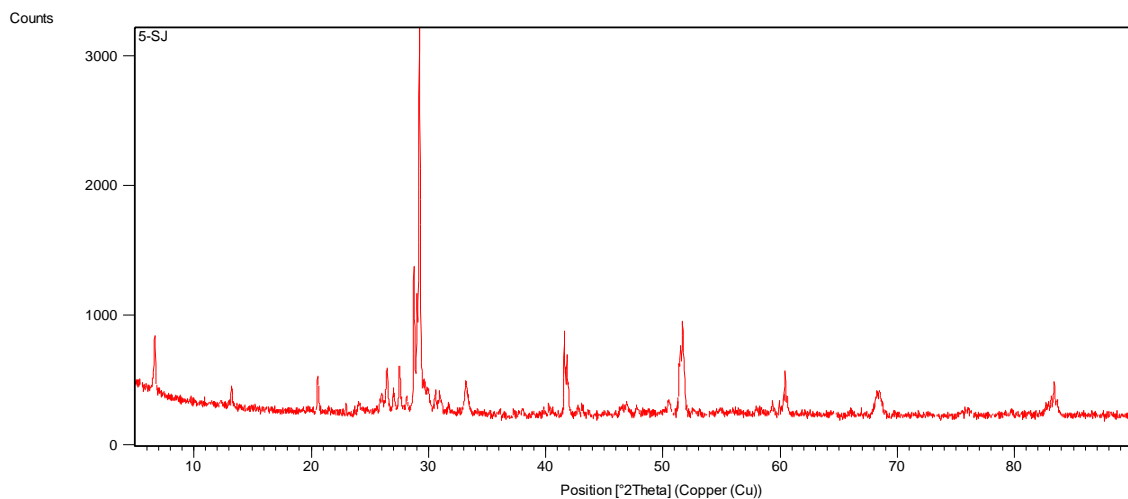
BaBiO₃ phase having space group I2/m, with the lattice parameters $a = 6.18 \text{ \AA}$, $b = 6.14 \text{ \AA}$, $c = 8.67 \text{ \AA}$, $\beta = 90.17^\circ$. These values match well with the JCPDS data card 79-1864 [52]. **Table 3.1** reports the parameters of BaBiO₃ crystals prepared by Pechini method, calcined at 800°C for 12 hours. This table summarizes the lattice parameters, space group and structure of the prepared compound.



(A)



(B)



(C)

Figure 3.5: XRD patterns of $BaBiO_3$ at different calcinations temperatures. (A) At $350^\circ C/2$ hours (B) at $600^\circ C/5$ hours (C) at $800^\circ C/12$ hours.

Thus, $BaBiO_3$ crystallizes in distorted monoclinic perovskite structure [39], and this distortion is attributed to the coexistence of two valence states, Bi^{3+} ($6s^2$) and Bi^{5+} ($6s^0$) [23]. The resulting distortion contained an ordered alternation of Bi^{3+} and Bi^{5+} sites. A schematic illustration of the crystal structure of $BaBiO_3$ is shown in **Figure 3.6**, where BiO_6 octahedra connect by sharing corners with each other, forming a diamond tunnel, and Ba is located in the tunnel. Earlier reports indicate the material's structure contains two kinds of distorted BiO_6 octahedra: Bi^1O_6 and Bi^2O_6 . In other words, structurally, this is manifested as two distinctly different Bi–O distances the shorter Bi^{+5} -O (2.12\AA) and the larger Bi^{+3} -O (2.31\AA) which result in alternately expanded and contracted BiO_6 octahedra, which further leads to the distortion in the symmetry of the compound [53,54].

Crystallographic parameters of powder calcined at $800^\circ C/12$ hours are listed in **Table 3.1**.

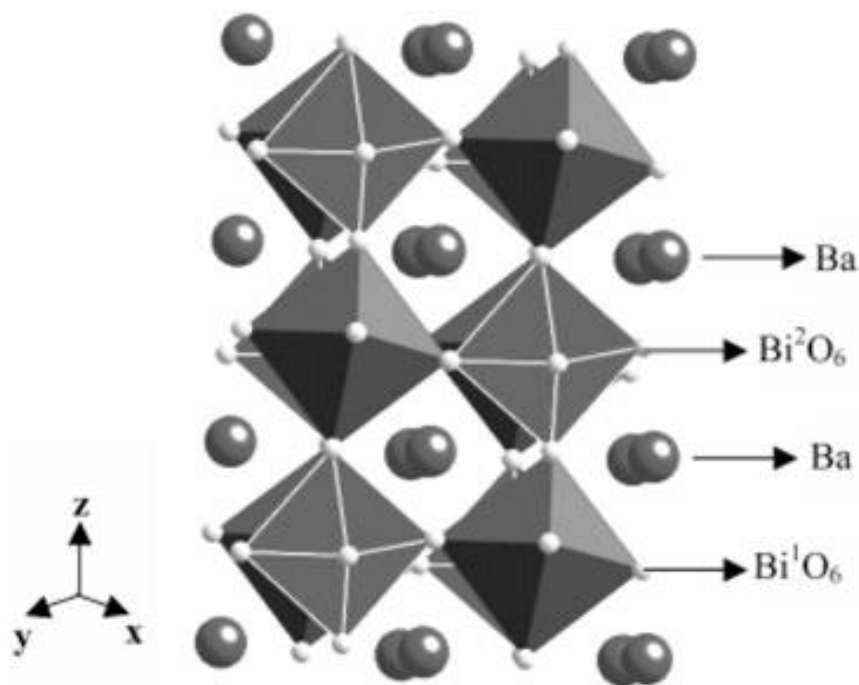


Figure 3.6: Three-dimensional packing diagrams of $BaBiO_3$ [39].

Table 3.1: Structural results for $BaBiO_3$ nano powder calcined at $800^\circ\text{C}/12\text{h}$.

$2\theta^\circ$	(hkl)	Structure	Lattice Parameter	Space Group
20.53	(110)	Distorted Monoclinic	a=6.18Å b=6.14Å c=8.67Å $\alpha=90.17^\circ$	I2/m
29.23	(112)			
41.57	(220)			
51.68	(312)			
60.41	(240)			
68.28	(332)			
83.37	(316)			

3.4.1(C) Fourier Transform infrared spectroscopy

FTIR was used to study the purity and functional group composition of the $BaBiO_3$. The dried $BaBiO_3$ particles were mixed with KBr to form pellets and then characterized with FTIR. The different functional groups existing in $BaBiO_3$ calcined

at 800°C/12hours sample are analyzed using FTIR spectra given in **Figure 3.7**. Absorption bands around 3496cm⁻¹ and 1697cm⁻¹ can be assigned to OH and HOH bending motion which are caused by surface adsorbed water [55]. Band, produced by acetate groups, are observed at 1548cm⁻¹ (asymmetrical stretching vibration of COO⁻) [56]. In addition, the medium bands at 1082cm⁻¹ can be attributed to the stretching vibration of CO₃²⁻ [57], which is in accordance with the results obtained from TGA analysis showing the carbonates generated by the decomposition of organics and nitrates. The FTIR spectrum of pure BaBiO₃ also shows two more bands at 799.11cm⁻¹ and 459.30cm⁻¹ which is considered to be a characteristic feature of the sample and is attributed to the vibration of Ba-O and Bi-O bond respectively [58,59]. A small broad peak around 924cm⁻¹ is related to vibration of Bi-O bonds in BiO₆ octahedra.

The observed band frequencies and their corresponding assignment of the functional groups are given in **Table 3.2**.

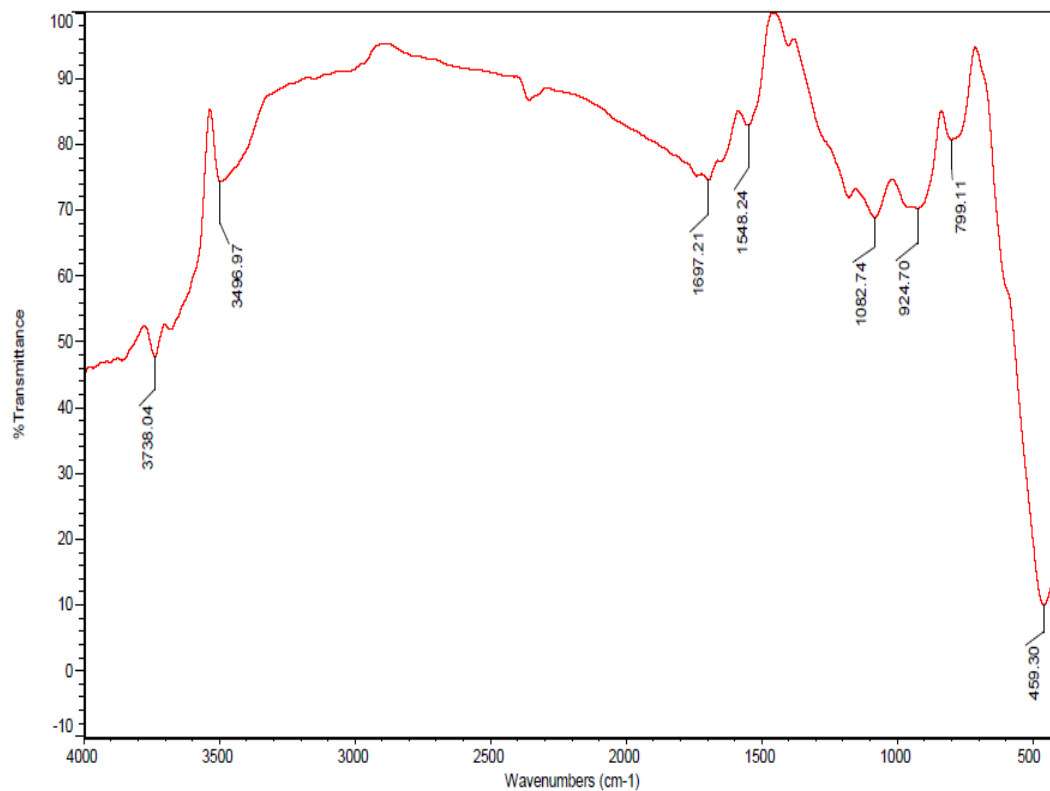


Figure 3.7: The FTIR spectra of BaBiO₃ calcined at 800°C/12hours.

Table 3.2: Interpretation of the peaks obtained by the FTIR spectra of the synthesized BaBiO₃/12hours.

Wave number (cm ⁻¹)	Intensity	Significance
459.30	Sharp and intense	Bi-O bond vibration
799.11	small	Ba-O bond vibration
924.70	Small and broad	Vibration in BiO ₆ octahedra
1082.74	small	Stretching vibration of CO ₃ ²⁻
1548.24	small	Asymmetric vibration of COO ⁻
1697.21	weak	HOH bending motion
3496.97	small	OH bending motion

3.4.1(D) UV-Vis. Diffuse Reflectance spectroscopy

The diffuse reflectance spectra of BaBiO₃ showed in **Figure 3.8** shows a strong fundamental absorption edge at 600nm, which indicates the photocatalytic activity in the visible light as well as in the solar light. The optical band gap E_g of prepared compound can be determined by its absorption and reflectance spectrum shown in this **Figure 3.8**.

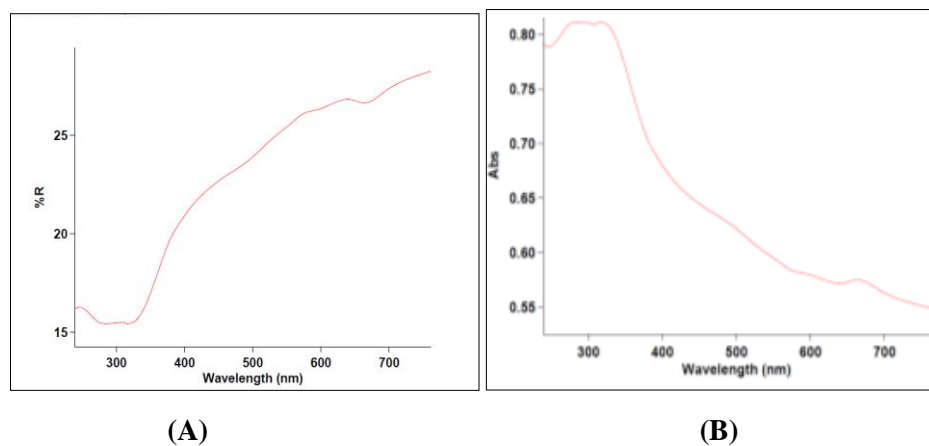


Figure 3.8: (A) Reflectance and (B) absorption spectrum of BaBiO₃ calcined at 800°C/12hours.

The optical absorption near the band edge was determined from Tauc's formula [60],

$$\alpha h\nu \propto (h\nu - E_g)^n$$

Where, $\alpha=4\pi\kappa/\lambda$ is the absorption coefficient, E is the photon energy, and n decides the characteristics of the transition in a semiconductor is a constant. Since semiconductor shows allowed indirect transition for which the value of n is decided 2 [61].

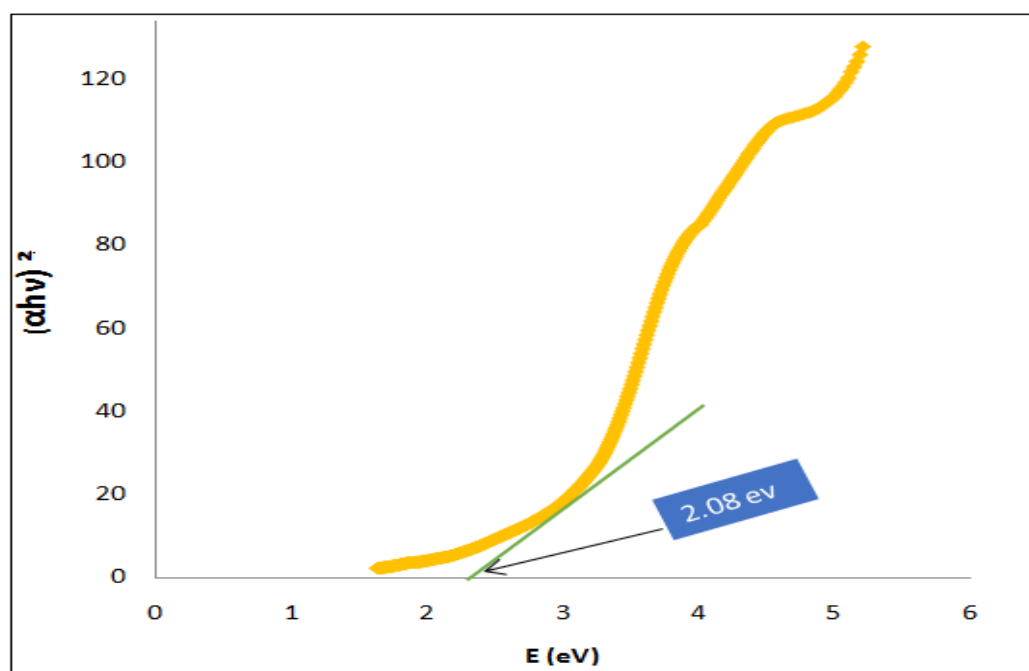


Figure 3.9: Kubelka-Munk converted Tauc plot of BaBiO₃

To calculate the band gap, the $(\alpha h\nu)^2$ is plotted against energy (Tauc's plot) given in **Figure 3.9**. The value associated with the point of intersection of the line is tangent to the plotted curve inflection point with the horizontal axis becomes the band gap energy. The value of band gap is found to be 2.08eV which is slightly greater than

the one previously published by **Tang** et al. in which the band gap energy is about $\sim 2.05\text{eV}$ for BaBiO_3 powder prepared by Soft chemical technique [39].

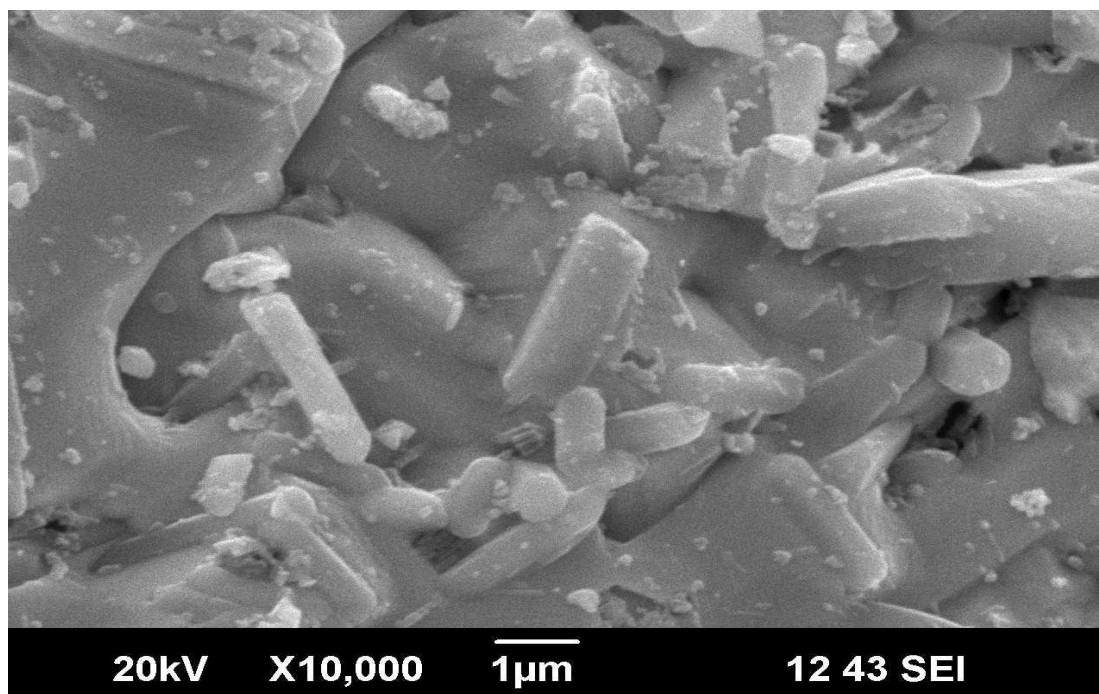
In many Bi based oxides the VB are composed of Bi $6s$ and O $2p$ orbitals and the CB are composed of d orbitals or p orbital. While in BaBiO_3 both VB and CB contains Bi $6s$ orbitals.(top of the VB is mainly composed of Bi^{3+} $6s$ and O $2p$ and the bottom of the CB is Bi^{5+} $6s$ and Bi $6p$) This unique band structure is responsible for its enhanced photocatalytic property. The photo-generated electrons usually transfer from the top of the VB (HOMO) to the bottom of the CB. There are four predominant bands near the Fermi level; Ba $5p$ orbital, VB (comprised of O $2p$, Bi $6s$ and Bi $6p$), CB (comprised of Bi $6s$, Bi $6p$ and O $2p$), and a hybridized orbital comprised of Bi $6p$ and Ba $6s$, as reported earlier [62,63].

As we know, to be an efficient photocatalyst with a narrow band gap, it is important to control the position of VB. As reported, enhanced visible light activity of Bi based oxides is due to the transfer of photoelectrons from the $6s$ orbital of Bi^{3+} to $6s$ orbital of Bi^{5+} during the light exposure. The feasibility of e^- transfer is affected by three dimensional alignment of the orbitals. Since, s orbitals have spherical symmetry so, s to s transition might have the lowest barrier which further increases the mobility of charge carriers as this may lead to the suppression of the recombination of e^- hole pair and therefore, relatively higher photooxidation potential the material, which allow them to easily reach the surface of the photocatalyst. Besides this under strong dispersion e^- excited by irradiation possess a small effective mass which causes high mobility of e^- towards the surface, hence higher photooxidation [64].

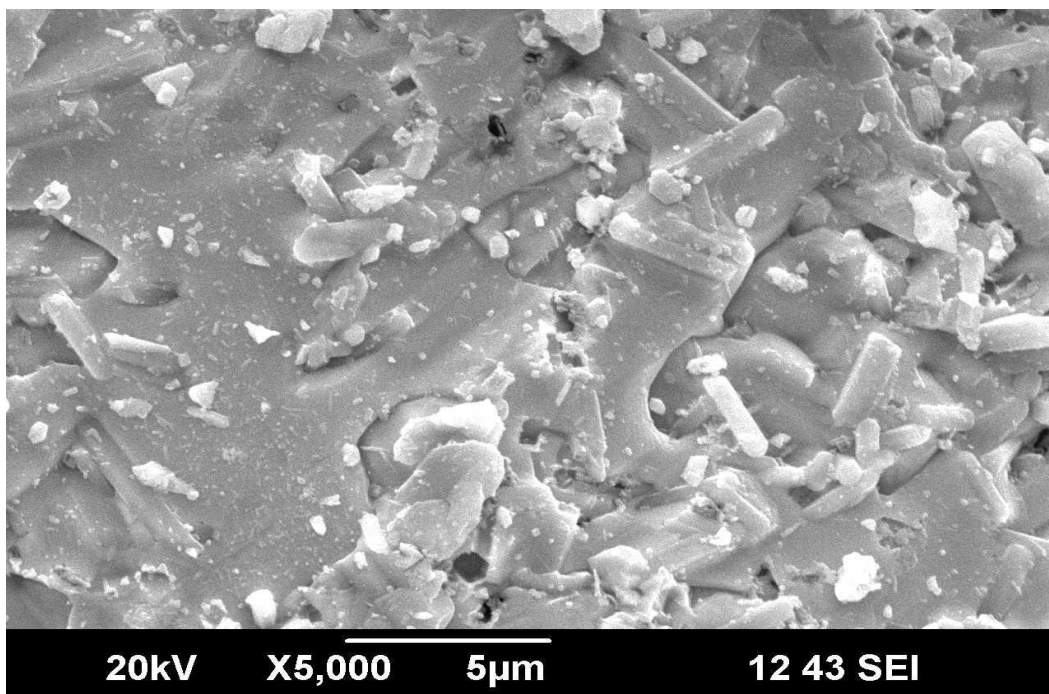
Therefore, it is concluded that the large contribution of s orbitals in both VB and CB, increases the feasibility of electron transition through the reduction of band gap thereby resulting in the synthesis of a highly efficient photocatalyst under visible light irradiation.

3.4.1 (E) Scanning electron Microscopy

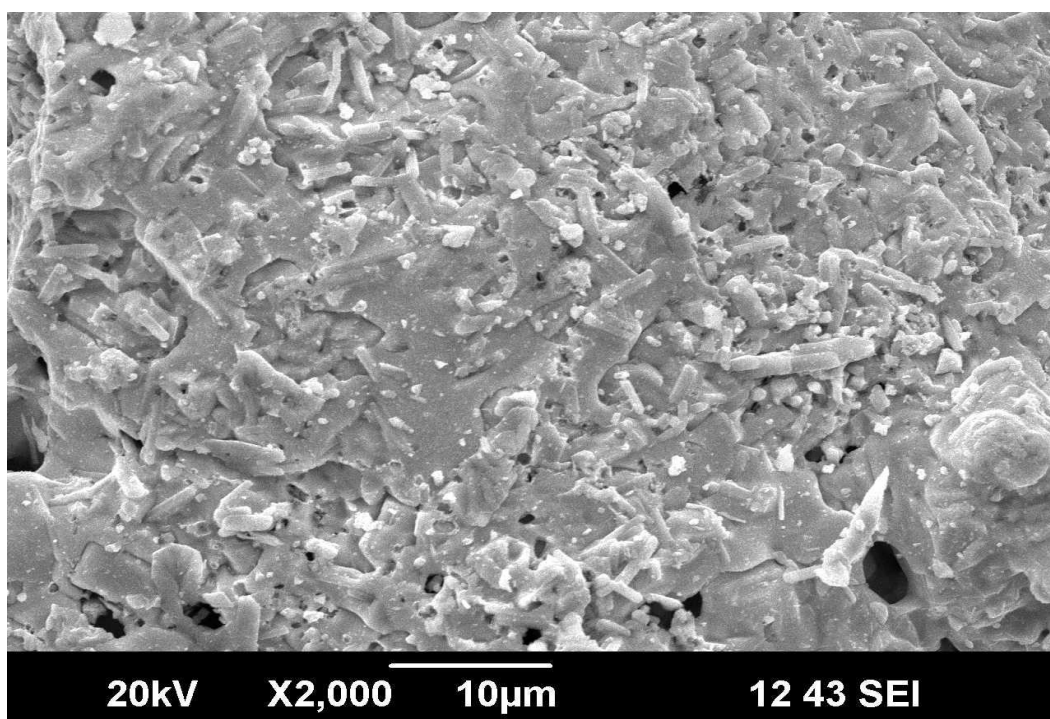
The scanning electron micrograph of BaBiO₃ sample was taken at different magnifications and shown in **Figure 3.10**. As seen in the micrographs, morphology of the BaBiO₃ particles were rods like with average width 520 nm and length up to 2.55μm. SEM was used to study the surface morphology for the prepared powders. The scanning electron micrograph of BaBiO₃ sample prepared at 800°C/12h was taken at different magnifications and shown in **Figure 3.10(a-d)**. As seen from the SEM images all the samples have high degree of crystalline, homogeneously distributed rod like shape. The low magnification micrograph shown in **Figure 3.10(a)** demonstrates homogeneous morphology with uniform particle distribution. As seen in the high magnification micrograph {**Figure 3.10(d)**}, morphology of the BaBiO₃ particles were in nano-range having rods like shape, with average width 520 nm and length up to 2.55μm.



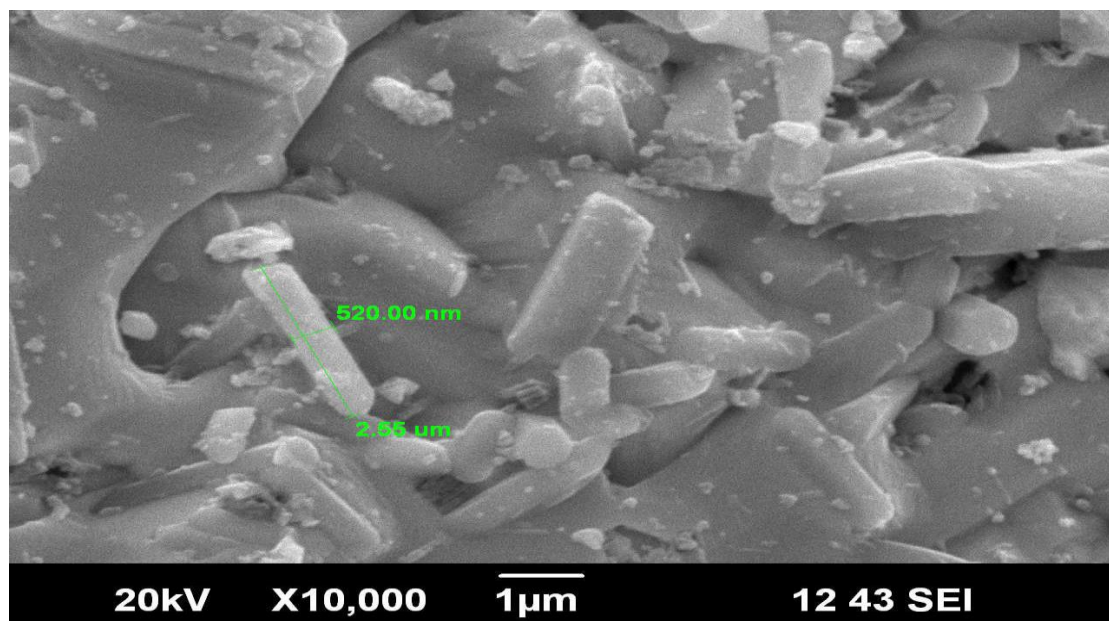
(A)



(B)



(C)



(D)

Figure 3.10: Scanning electron micrograph of $BaBiO_3$ calcined at $800^\circ C/12h$ at different magnifications. (A) at 10,000 (B) at 5,000, (C) at 2,000 (D) at 10,000

3.4.2. Characterization of $Ba_{0.6}K_{0.4}BiO_3$

3.4.2 (A) Thermal Studies

Simultaneous TG and DTA investigations are carried out to evaluate the crystallization temperature. **Figure 3.11** shows DTA-TGA curve of polymeric resin for $Ba_{0.6}K_{0.4}BiO_3$ indicating evolution of perovskite phase with increasing temperature. TGA curve shows a four step decomposition of resin precursor to form the perovskite material. We observed a slight weight loss of $\sim 6\%$ up to $200^\circ C$ accompanied by a weak exothermic peak at $190^\circ C$. This weight loss is caused by elimination of residual water adsorbed due to the storage of the preheated sample in ambient atmosphere [50]. The second weight loss region (42%) is observed in the range of $210-300^\circ C$ is because of combustion of light organic matter and acetates as indicated by an exothermic peak around $240^\circ C$ in DTA curve. The third weight loss around 23% in the temperature

range of 310-580°C corresponds to decomposition of the nitrates and nitrites residue. This observation is supported by the well resolved exothermic peak at 550°C in DTA curve. The final small weight loss on the TGA curve observed above 560°C to 900°C corresponds to the crystallization and formation of perovskite phase (at 720°C) which is also confirmed by XRD (**Figure 3.12**) and FTIR (**Figure 3.14**) analysis. The total weight loss of this powder is 72.51% [51].

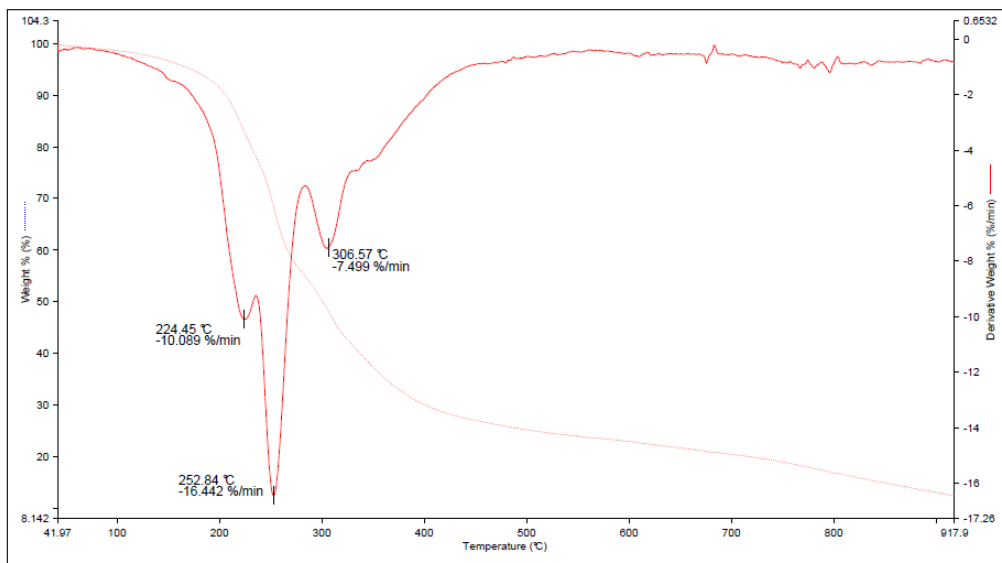


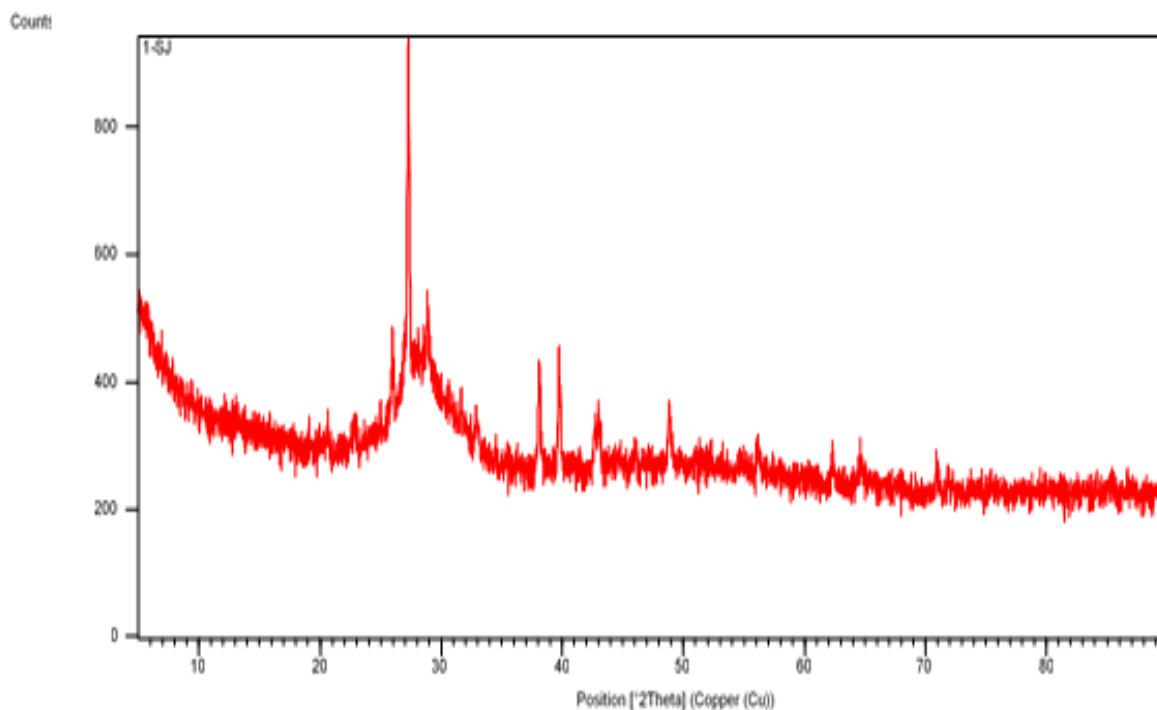
Figure 3.11: TGA and DTA curves of $Ba_{0.6}K_{0.4}BiO_3$ precursor prepared by Pechini method

3.4.2(B) X-ray diffraction (XRD) patterns

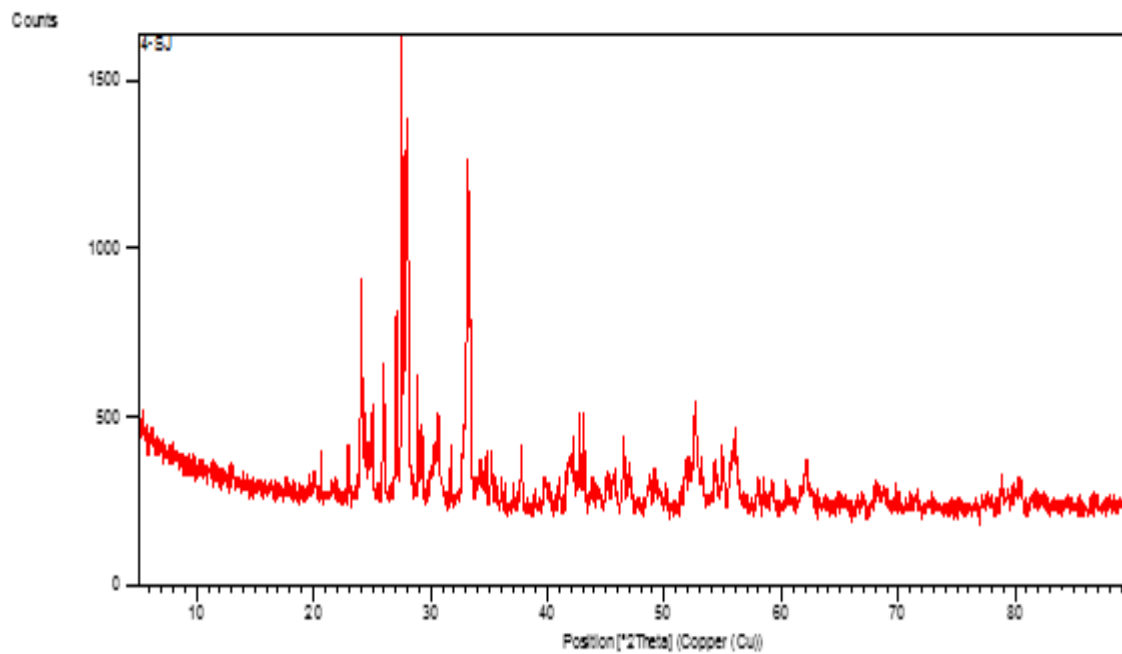
The as-prepared $Ba_{0.6}K_{0.4}BiO_3$ nanoparticles synthesized by using Pechini method at 720°C for 12 hours were used for structural measurement with XRD technique. **Figure 3.12** depicts the XRD patterns of the as-obtained $Ba_{0.6}K_{0.4}BiO_3$ nanoparticles. The peak is very strong and narrow, demonstrating a high degree of crystallinity of the prepared catalyst. Moreover, there are no other distinct peaks from impurities detected, indicating that the product is very pure. It is observed that all the diffraction peaks are in good agreement with the standard $Ba_{0.6}K_{0.4}BiO_3$ cubic crystalline structure, with measured lattice constants ($a = b = c = 3.2498 \text{ \AA}$) being the same as the indexed ones.

Patterns in **Figure 3.12 (a)** reveal that the sample burned at 350°C is amorphous in nature. Upon calcination at 600°C the sample becomes more crystalline. {**Figure**

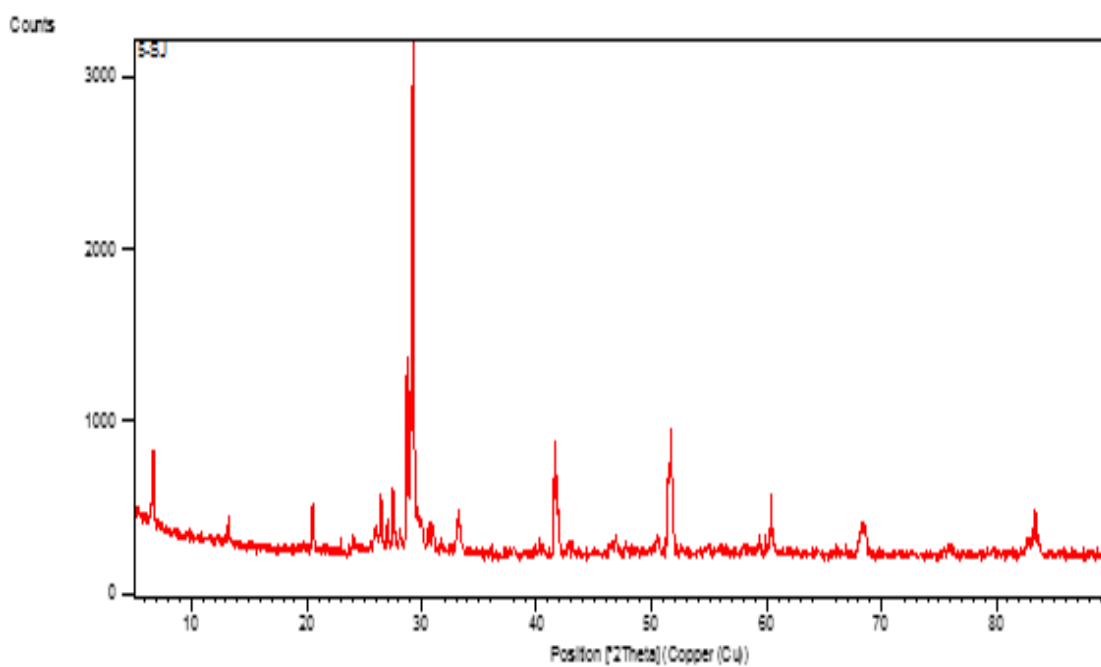
3.12(b)}. The sample calcined at 720°C for 12 hours is highly crystalline with predominantly perovskite structure. **{Figure 3.12(c)}** Though, its JCPDS card is not available, it could be seen that the diffraction peaks can be well indexed to cubic phase $\text{Ba}_{0.6}\text{K}_{0.4}\text{BiO}_3$ (pm3m space group and lattice parameter of 3.2498 Å) which are in accordance with the earlier studies [65]. In the **Figure 3.12(c)** main diffraction peaks are observed at 20.53°, 29.33°, 36.66°, 42.74°, 51.33°, 60.41°, 68.280°, 76.04° and 83.37° which can be assigned to 100, 110, 111, 200, 201, 220, 310 and 321 planes, respectively. Diffraction peak related to Bi_2O_3 are not observed in XRD pattern confirming the purity of the synthesized compound [47]. **Table 3.3** reports the parameters of $\text{Ba}_{0.6}\text{K}_{0.4}\text{BiO}_3$ crystals prepared by Pechini method, calcined at 720°C for 12 hours. This table summarizes the lattice parameters, space group and structure of the prepared compound.



(A)



(B)



(C)

Figure 3.12: XRD patterns of $Ba_{0.6}K_{0.4}BiO_3$ at different calcinations temperatures. (A) At 350°C/2 hours (B) at 650°C/6 hours (C) at 720°C/12 hours.

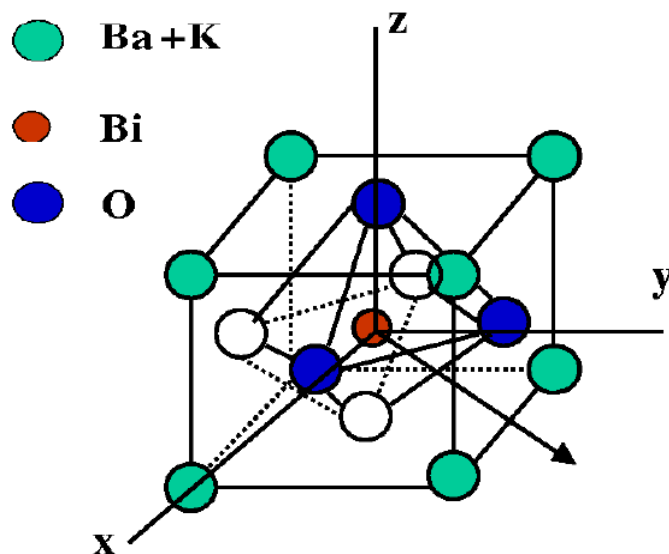


Figure 3.13 Three-dimensional packing diagrams of $Ba_{0.6}K_{0.4}BiO_3$ [66].

Table 3.3: Structural results for $Ba_{0.6}K_{0.4}BiO_3$ nano-powder calcined at $720^\circ C/12$ hours.

$2\theta^\circ$	(hkl)	Structure	Lattice Parameter	Space Group
20.53	(110)	Perfect Cubic	$a=4.284\text{\AA}$ $\alpha=90^\circ$	Pm3m
29.23	(112)			
41.57	(220)			
51.68	(312)			
60.41	(240)			
68.28	(332)			
83.37	(316)			

3.4.2 (C) Fourier Transform infrared spectroscopy

Figure 3.14 shows the FTIR spectra of $Ba_{0.6}K_{0.4}BiO_3$. The band at nearly 465cm^{-1} is related to Bi-O bending mode vibrations. The strong peak at 615cm^{-1} is related to anisotropic oxygen motions, which depends on the potassium ion distribution in the crystal lattice [67]. For the Pechini method, as ethylene glycol is used for polyesterification with citric acid to form a rigid polymer network, a strong band around 1105cm^{-1} is attributed to the C-C-O structure confirming the polymerization process

[68]. The FTIR results thus confirm that complex formation between citric acid and metallic ions occurred in the sol-gel route, and that poly- esterification of ethylene glycol and citric acid and complexation with metallic ions occurred in the Pechini Method. It is seen from the **Figure 3.14** that the peak at 1425cm^{-1} is attributed to Ba-O bending vibrations [69]. Thus, the bands at 615cm^{-1} and 1425cm^{-1} are due to creation of new active sites in the photocatalyst, which results in the higher activity of $\text{Ba}_{0.6}\text{K}_{0.4}\text{BiO}_3$ photocatalyst.

The observed band frequencies and their corresponding assignment of the functional groups are given in **Table 3.4**.

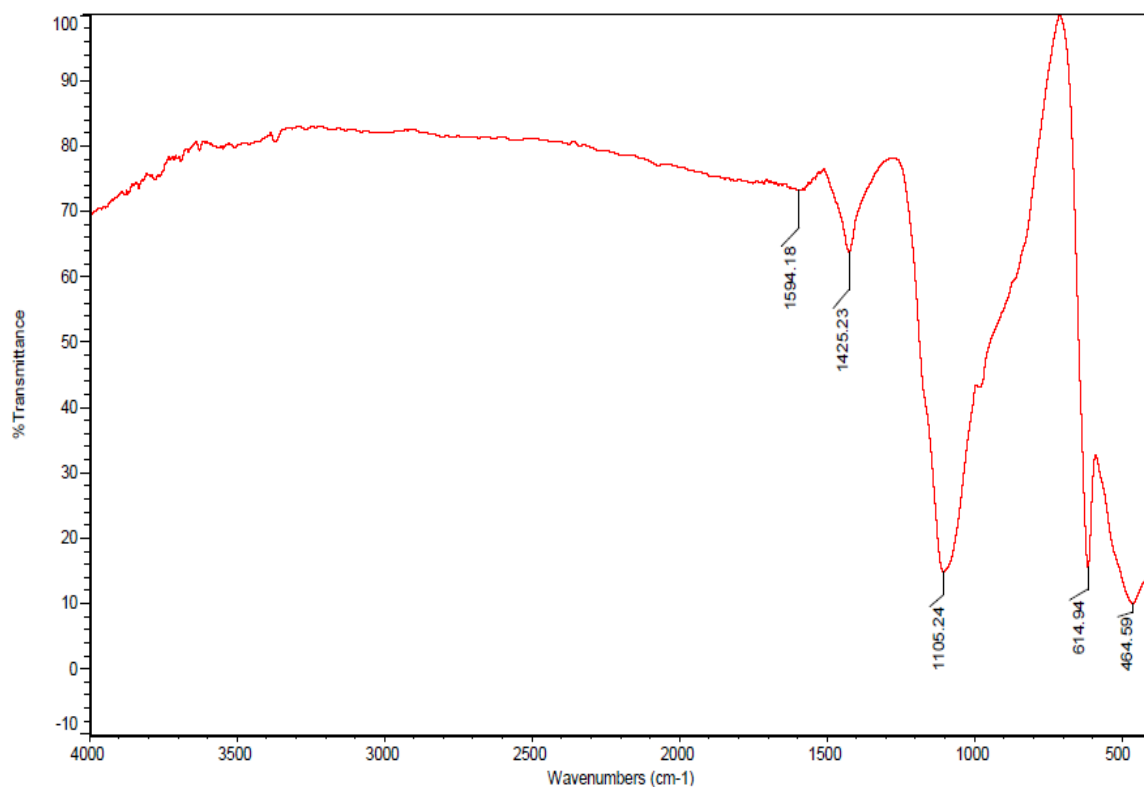


Figure 3.14: The FTIR spectra of $\text{Ba}_{0.6}\text{K}_{0.4}\text{BiO}_3$ calcined at $720^\circ\text{C}/12\text{hours}$.

Table 3.4: Interpretation of the peaks obtained by the FTIR spectra of the synthesized Ba_{0.6}K_{0.4}BiO₃ calcined at 720°C/12hours.

Wave number (cm ⁻¹)	Intensity	Significance
464.59	Sharp	Bi-O bond vibration
614.94	Sharp	Anisotropic oxygen bending vibration (owing to K ion distribution)
1105.24	Sharp and intense	C-C-O bending motion
1425.23	Weak	Ba-O bond vibration
1594.18	Very weak	Asymmetrical vibration of COO ⁻

3.4.2(D) UV-Vis. Diffuse Reflectance Spectroscopy

The diffuse reflectance spectra of Ba_{0.6}K_{0.4}BiO₃ (calcined at 720°C/12 hours) { **Figure 3.15** } show a strong fundamental absorption edge at 600nm, which indicates the photocatalytic activity in the visible light as well as the solar light. Further, the optical band gap E_g was determined from Tauc's formula.

The optical absorption near the band edge was determined from Tauc's formula,

$$\alpha h\nu \propto (h\nu - E_g)^n$$

Where, $\alpha=4\pi\kappa/\lambda$ is the absorption coefficient, E is the photon energy, and n decides the characteristics of the transition in a semiconductor is a constant. Since semiconductor shows allowed indirect transition for which the value of n is decided 2. (Ref)

Figure 3.16 shows the Tauc plot i.e. $(\alpha h\nu)^2$ versus $h\nu$, whose intercept on energy axis gives the direct band gap energy E_g of the prepared sample. The value of band gap is found to be 1.87eV.

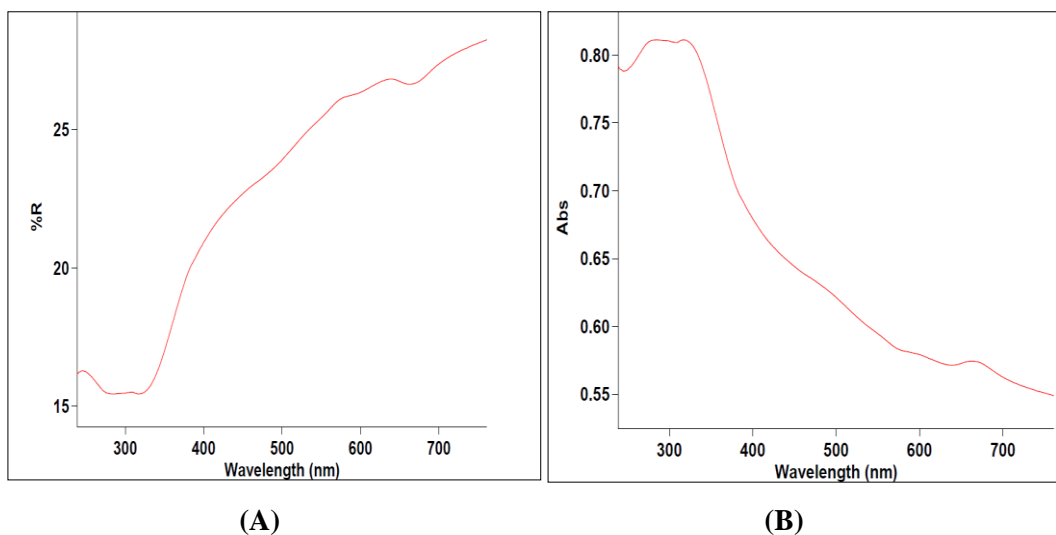


Figure 3.15: (A) Reflectance and (B) absorption spectrum of $Ba_{0.6}K_{0.4}BiO_3$ calcined at $720^\circ C/12$ hours.

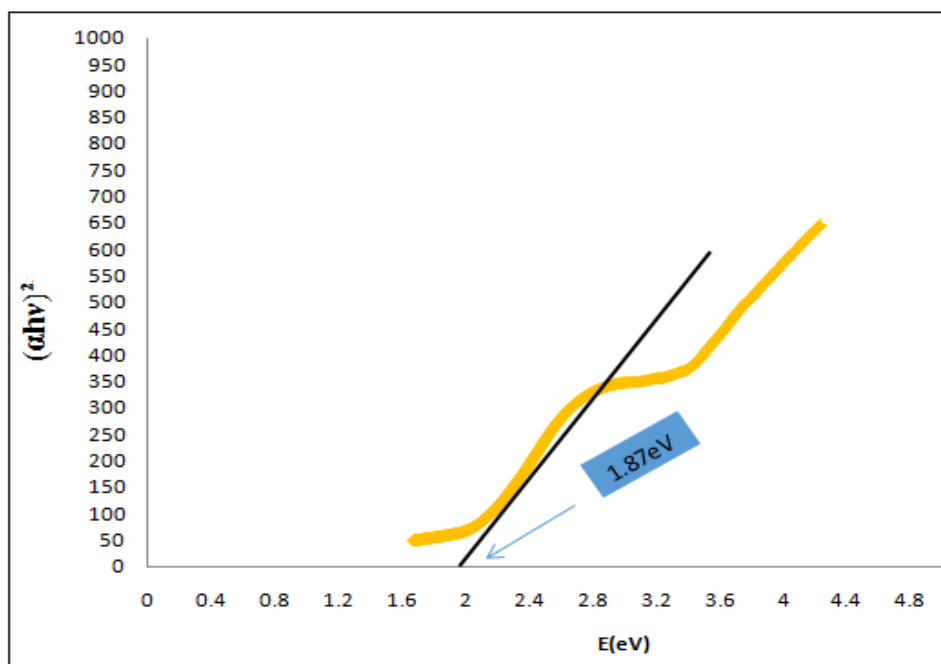


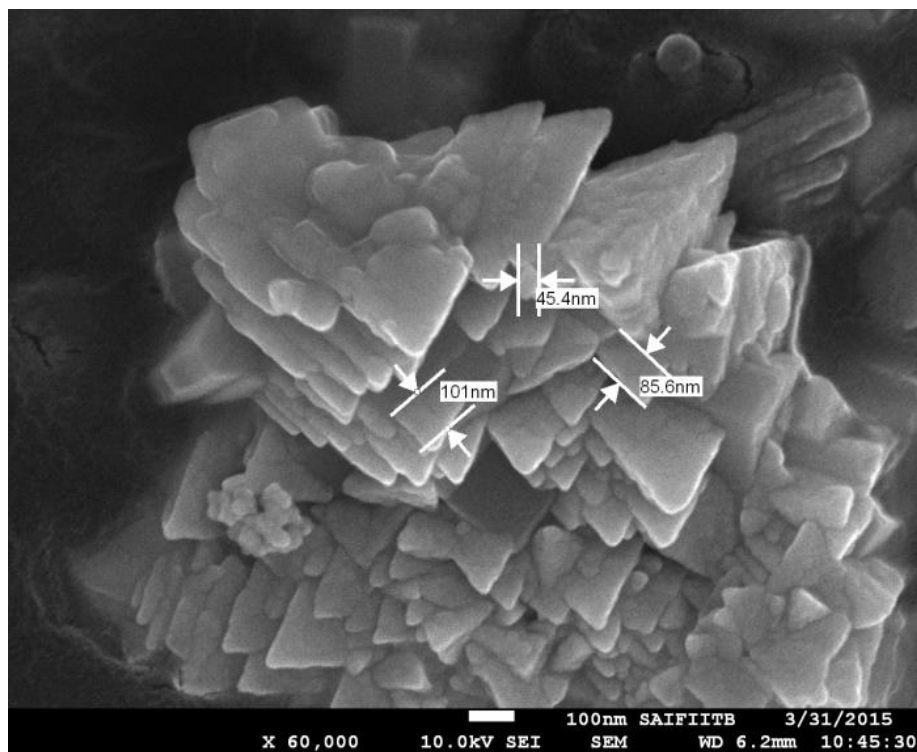
Figure 3.16: Kubelka-Munk converted Tauc's plot of $Ba_{0.6}K_{0.4}BiO_3$

The value of band gap for K doped BaBiO₃ is found to be lower than the parent compound. The chemical substitution of monovalent alkali K⁺ at the divalent Ba²⁺ site introduces free charge carriers. Since K⁺ ion has one valence electron rather than the two of the Ba²⁺ ion, the substitution of each set of two Ba²⁺ for two K⁺ ions produces hole pair in Bi6s-O2pσ* which produces an additional unoccupied energy level between HOMO and LUMO. This newly created unoccupied e⁻ donor level contains freed e⁻ which further increases the degradation potential of thus prepared compound by inducing a red shift of light absorption towards higher wavelength of visible region.

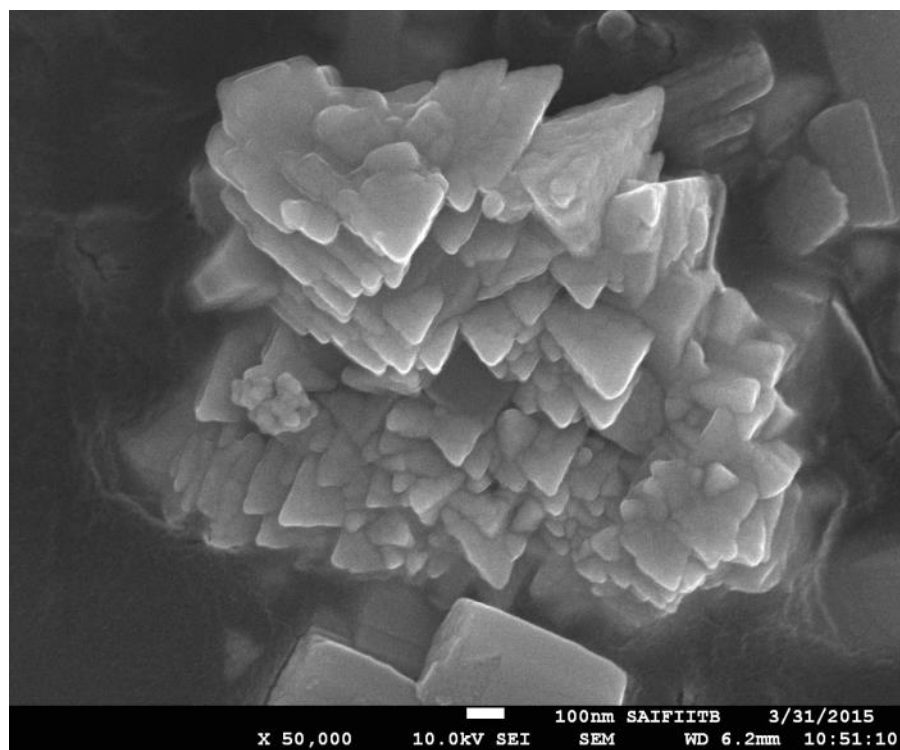
3.4.2(E) Scanning electron Microscopy

To investigate the morphology of the as-obtained product, we carried out scanning electron microscopy SEM analysis. The scanning electron micrograph of BaBiO₃ sample prepared at 720°C/12h was taken at different magnifications and shown in **Figure 3.17(a-d)**. All the SEM images show well packed plate-like crystals of different size assembled into textured structure. The layered plate-like morphology is a characteristic feature of the bismuth and potassium containing compounds [70]. **Figure 3.17(a)** is the low magnification micrograph of Ba_{0.6}K_{0.4}BiO₃ showing agglomerated non uniform particle distribution. SEM image at higher magnification {**Figure 3.17(d)**} shows the morphology of the sample having step-like-triangular-platy- nano-scale particles.

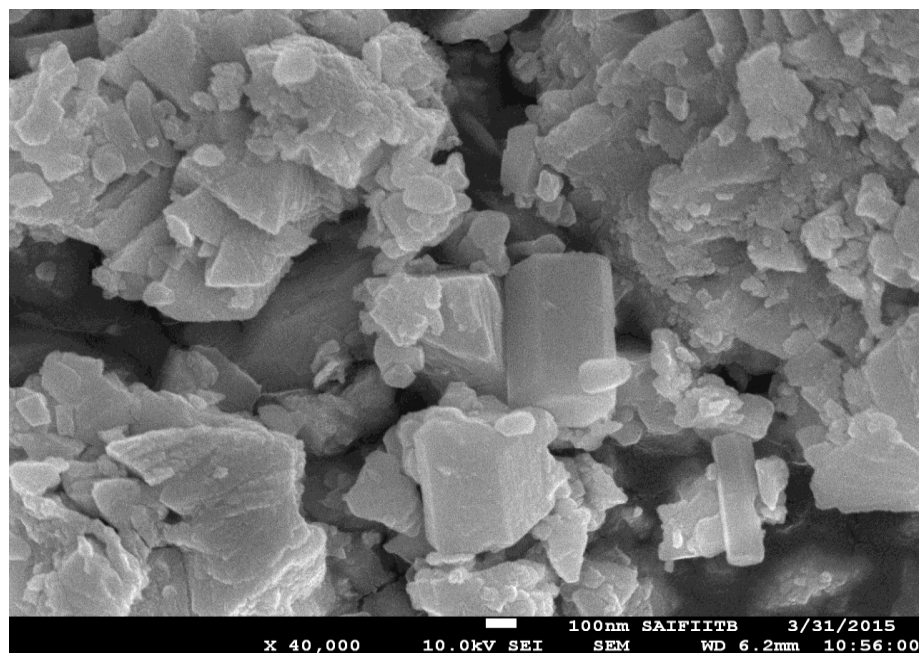
Micrographs show weakly bound agglomeration process, which is attributed to Vander-Waals forces. In order to reduce the surface energy, the primary particles tend to form agglomerates with a minimum surface to volume ratio. This type of structure is common in oxides, ferrites, and titanate ceramics prepared by sol gel procedure [71]. The nano-particles have an average size in the range of 45-101 nm.



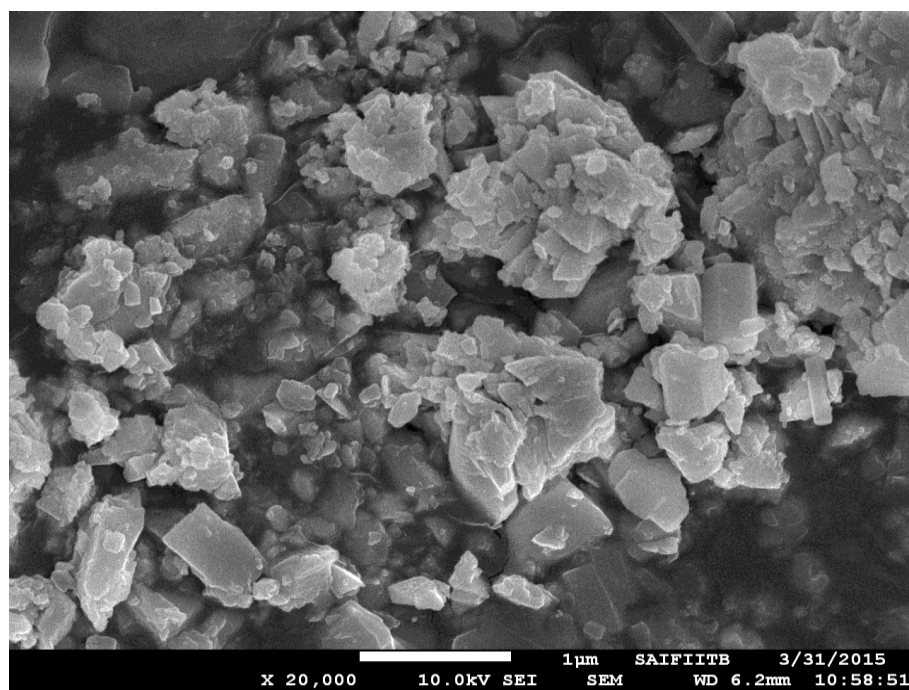
(A)



(B)



(C)



(D)

Figure 3.17: Scanning electron micrograph of $Ba_{0.6}K_{0.4}BiO_3$ (calcined at 720°C/12hours) at different magnifications. (A) at 60,000 (B) at 50,000, (C) at 40,000 (D) at 20,000.

3.5 Conclusion

The present work aimed at synthesizing pure and doped barium bismuthate nanoparticles using Pechini method. Herein, BaBiO_3 and $\text{Ba}_{0.6}\text{K}_{0.4}\text{BiO}_3$ nanopowders were prepared at comparatively low temperature (800°C and 720°C) by Pechini method using ethylene glycol, citric acid and metal nitrates as raw materials. The structural, morphological and optical characteristics of the synthesized nanoparticles were studied by Thermo Gravimetric Analysis (TGA), powder X-ray diffraction, Fourier Transform Infra-Red spectroscopy, UV-Vis Diffuse Reflectance Spectroscopy (UV DRS) and Scanning Electron microscopy (SEM).

The XRD patterns suggest that BaBiO_3 crystallizes in the distorted monoclinic structure while $\text{Ba}_{0.6}\text{K}_{0.4}\text{BiO}_3$ crystallizes in the cubic structure. The distortion in the structure of BaBiO_3 is attributed to the coexistence of two different types of Bi-O bond. Further, by the incorporation of K, the resulting material gets transformed to perfect cubic structure. The strong and sharp peaks in the diffractograms indicate the crystalline nature and phase purity of the prepared samples.

The phase evolution of both the catalysts with increasing temperature was done by DT-TGA. The TGA curves show that above final calcination temperatures (800°C for BaBiO_3 and 720°C for $\text{Ba}_{0.6}\text{K}_{0.4}\text{BiO}_3$), no weight loss is observed, hence it is concluded above this temperature, the perovskite are stable.

FTIR spectrum shows the presence of the bands around 465cm^{-1} in both the catalysts confirming the metal-oxygen bond formation, which is the characteristic property of perovskite materials. In the FTIR spectra, there was no peak observed related to nitrate and carbonate group, showing the total decomposition and subsequent formation of pure desired product.

The diffuse reflectance spectroscopy showed that the catalysts have a broad absorbance in visible region of light. The onset optical absorption edge was around 600 and 660 nm for barium bismuthate and K doped barium bismuthate respectively. The band gap calculation was done by Tauc plots through the converted KM functions. The band gap of BaBiO_3 and $\text{Ba}_{0.6}\text{K}_{0.4}\text{BiO}_3$ was found to be 2.07eV and 1.87eV,

respectively. Owing to the low band gap, the catalysts were supposed to be promising in displaying their activity in photocatalysis under visible light irradiation. Incorporation of K ion partially at Ba site creates a new level between HOMO and LUMO of the parent BaBiO_3 which further decreases the band gap of $\text{Ba}_{0.6}\text{K}_{0.4}\text{BiO}_3$.

The SEM studies show that both the samples are homogeneous uniform nanoparticles, having 520nm size for BaBiO_3 and 45-101nm for $\text{Ba}_{0.6}\text{K}_{0.4}\text{BiO}_3$. SEM images reveal the nano rod type structure for BaBiO_3 and plate like layered structure for $\text{Ba}_{0.6}\text{K}_{0.4}\text{BiO}_3$.

The photocatalytic activity of as-synthesized BaBiO_3 and $\text{Ba}_{0.6}\text{K}_{0.4}\text{BiO}_3$ nanoparticles was demonstrated over degradation of dyes viz. Crystal violet, Malachite green and Congo red under visible light irradiation and are fully described in Chapter 4, 5 and 6 respectively.

References

- [1] S. Samira, A.P. Raja, C. Mohan, J.M. Modak, *J. Thermodynam. Cat.* 3, (2012), 1.
- [2] J. Q. Chen, D. Wang, M.X. Zhu, C.J. Gao, *Desalination* 207, (2007), 87.
- [3] A. Zaleska, *Recent Patents on Eng.* 2, (2008), 157.
- [4] G. Song, F. Xin, J. Chen, X. Yin, *App. Catal. A: Gen.* 473, (2014), 90.
- [5] M. A. habib, M. T. Shahadat, N. M. Bahadur, I.M. Ismail, A. J. Mahmood, *Int. Nano. Lett.* 3, (2015), 1.
- [6] D. Saha, S. Mahapatra, T.N. G. Row, G. Madras, *Ind. Eng. Chem. Res.* 48, (2009), 7489.
- [7] Y. Wang, X. Bai, C. Pan, J. He, Y. Zhu, *J. Mater. Chem.* 22, (2012), 11568.
- [8] V. Subramanian, R.K. Roeder, EE. Wolf, *Ind. Eng. Chem. Res.* 45, (2006), 2187.
- [9] T. Kako, Z. Zou, M. Katagiri, J. Ye, *Chem Mater.* 19, (2007), 198.
- [10] R. Ramachandran, M. Sathiya, K. Ramesha, A.S. Prakash, G. Madras, A.K. Shukla, *J. Chem. Soc.* 123, (2011), 517.
- [11] B. Bushan, Z. Wang, J. V. Tol, N. S. Dalal, A. Basumallick, N. Y. Vasanthacharya, S. Kumar, D. Das, *Solid State Sci.* 12,(2010), 1063.
- [12] S. Kanagesan, C. Kumar, R. Velmurugan, S. *Mater. Sci. Poland* 28, (2010), 647.
- [13] Y. Zhang, J. Hao, C.L. Mak, X Wei, *Opt. Express* 19,(2011), 1824.
- [14] Z. Zhang, P. Wu, K.P. Ong, L. Lu, C. Shu, *Phy. Rev. B* 76, (2007), 125102.
- [15] K.B. Lee, H.S. Lee, S.K. Cho, *J. Kor. Phy. Soc.* 31, (1997), 532.
- [16] D. Klavana, J. Vaillancourt, J. Kirchnerova, J. Chaouki, *Appl. Catal., A*, 109, (1994), 181.

-
- [17] P. Kanhere, Z. Chen, *Molecules* 19, (2014), 19995.
- [18] H. Shi, X. Li, H. Iwai, Z. Zou, J. Ye, *J. Phys. Chem. Solids* 70, 2009, 931.
- [19] P. Tang, H. Sun, F. Cao, J. Yang, S. Ni, H. Chen, *Adv. Mater. Res.* 279, (2011), 83.
- [20] L. Li, Y. Zhang, A. M. Schultz, X. Liu, P.A Salvador, G. S. Rohrer, *Catal. Sci. Technol.* 2, (2012), 1945.
- [21] D. Saha, S. Mahapatra, T. N. G. Row, G. Madras, *Ind. Eng. Chem. Res.* 48, (2009), 7489.
- [22] S. Yaowen, Z. Zizhong, H. Meichun, *Commun. Theor Phys.* 30, (1998), 387.
- [23] R.P.S.M. Lobo, F. Gervais, *Phys. Rev.* 52, (1995), 294.
- [24] N. Kikugawa, L. Yang, T. Matsumoto, J. Ye, *J. Mater. Res.* 25, (2010), 177.
- [25] A.K. Ganguli, T. Ahmad, P.R Arya, P. Jha, *J. Phys.* 65, (2005), 937.
- [26] R. Zenati, C. Bernard, C. Calmet, S. Guillemet, G. Fantozzi, B. Durand, *J. Eur. Ceram. Soc.* 25, (2005), 935.
- [27] R.E. Moore, H. Sang, *Bol. Soc. Esp. Ceram.* 32, (1996), 369.
- [28] A. Civera, M. Pavese, G. Saracco, V. Specchia, *Catal. Today* 83, (2003), 199.
- [29] G. Biasotto, A. Z. Simões, C.R. Foschini, S. G. Antônio, M. A. Zaghete, J. A. Varela., *Process. App. Ceram.* 5, (2011), 171.
- [30] S.H. Lee, J. Y. Lee, Y.M. Park, J.H. Wee, K.Y. Lee, *Catal. Today* 117, (2006), 376.
- [31] M. Yazdanbakhsh, H. Tavakkoli, S.M. Hosseini, *S. Afr. J. Chem.* 64 (2011), 71.
- [32] R. D. Toro, P. Hernández, Y. Díaz, J.L. Brito, *Mater. Lett.* 107 (2013), 231.
- [33] M.P. Pechini, *United States Patents*, 3,330,697.

-
- [34] D. A. Kumar, S. Selvasekarapandian, H. Niitya, J. Leiro, Y. Masuda, S.D. Kim, S.K. Woo, *Pow. Tech.* 235, (2013), 140.
- [35] P.D. Spagnol, J. A Varela, M.A.Z. Bertochi, B.D. Stojanovic, S.M. Tebcherani, *Thin solid Films* 410, (2002), 177.
- [36] K. Huang, M. Feng, J. B. Goodenough, *J. Am. Ceram. Soc.* 79, (1996), 1100.
- [37] X. Lu, T.S. Pine, D.R. Mumm, J. Brouwer, *Solid State Ionics* 178, (2007), 1195.
- [38] D.E. Cox, A.W. Sleight, *Solid State Commun.* (1976), 969.
- [39] J. Tang, Z. Zou, J. Ye, *J. Phy. Chem. C* 111, (2007), 12779.
- [40] A. Bansil, S. Kaprzyk, *Phys. Rev. B* 43, (1991), 10335.
- [41] L. A. Klinkova, V.I. Nikolaichik, N. V. Barkovskii, V.K. Fedotov, *J. Solid State Chem.* 146, (1993), 439.
- [42] J. Ge, W. J. Yin, Y. Yan, *Chem. Mater.* 30, (2018), 4880.
- [43] S. Tajima, M. Yoshida, N. Koshizuka, *Phys. Rev. B* 46, (1992), 1232.
- [44] L.E. Mattheiss, E. M. Gyorgy D.W.J. Johanson, *Phys. Rev. B* 37, (1988), 3745.
- [45] A.N. Baranov, J.S. Kim, D.C. Kim, D.S. Suh, Y.W. Park, E.V. Antipov, *Physica C* 383, (2002), 95.
- [46] A. N. Baranov, D. C. Kim, J.S. Kim, H. R. Kang, B.J. Kim, Y.C. Kim, J.S. Pshirkov, E.V. Antipov, *Phys. C* 414, (2001), 357.
- [47] R.M. Fleming, R.J. Cava, J.J. Krajewski, *Phys. Rev. B* 38,(1988), 7026.
- [48] Y. Hu, L. Fei, Y. Zhang, J. Yuan, Y. Wang, H. Gu, *J. Nanomater.* 10, (2011), 1.
- [49] S. W. Kwona, S. B. Parkb, G. Seoc, S.T. Hwanga, *J. Nucl. Mater.* 257, (1998), 172.
- [50] S.M. Selbach, G. Wang, M. A. Einarsrud, T. Grande, *J. Am. Ceram. Soc.* 90, (2007), 2649.

-
- [51] F.C.D. Lemos, E. Longo, E.R. Leite, D.M.A. Melo, A.O. Silva, *J. Sol. State Chem.* 177, (2004).
- [52] D. Bhatnagar, R. Chatterjee, *Adv. Mater. Lett.* 7, (2016), 604.
- [53] D. Zhu, Y. H. Zhang, *J. Phys.: Condns. Mater* 14, (2002), 519.
- [54] A.P. Menushenkov, K.V. Klementev, *J. Phys.: Condns. Mater* 12 (2000), 3767.
- [55] J. Shao, Y. Tao, J. Wang, C. Xu, W. G. Wang, *J. Alloys Compd.* 484, (2009), 263.
- [56] G.R.O. Silva, J.C. Santos, D.M.H. Martinell, A.M.G. Pedrosa, M.J.B.D. Souja, D.M.A. Melo, *Mater. Sci. Appl.* 1, (2010), 39.
- [57] A. Abdolrahmani, M. Parvari, M. Habibpoor, *Iran. J. Chem. Eng.* 9, (2012), 31.
- [58] G. K. Chuah, S. Jaenicke, K.S. Chan, S. T Khor, J.O. Hill, *J. Therm. Anal.* 40, (1993), 1157.
- [59] W. Zhong, T. Jiang, Y. Dang, J. He, S. Y. Chen, C. H. Kuo, D Kriz, Y. Meng, A.G. Meguerdichian, S.L. Suib, *Appl. Catal. A: Gen.* 549, (2018), 302.
- [60] P. Kubelka, F. Munk, *Z. Tech. Phys.* 12, (1931), 593.
- [61] J. Tang, Z. Zou, J. Ye, *J. Phys. Chem. B* 107, (2003), 14265.
- [62] D.A. Papaconsantopoulos, *Phys. Rev. B* 40, (1989), 8848.
- [63] L.F. Mattheiss, D.R. Hamann, *Phys. Rev. Lett.* 60, (1988), 2681.
- [64] P.B. Allen, I.B. Biscofs, *Phys. Rev.B* 65, (2002), 115113.
- [65] H.T. Kim, K.Y. Kang, W.J Kim, Y.N. Choi, B.J. Kim, Y.C. Kim, *J. Korean Chem. Soc.* 39, (2011), 1013.
- [66] B.A. Baumer, *J. Supercond.* 8, (1995), 175.
- [67] C.Y. Lee, K.Y. Song, R.P. Sperline, *Korean j. Mater. Res.* 6, (1996), 555.

- [68] M. Gupta, P. Yadav, W. Khan, A. Azam, A. H. Naqvi, R.K. Kotnala, *Adv. Mat. Lett.* 3 (2012), 220.
- [69] F. Legesse, K. Sreenu, S. Kena, K. Legesse, *Sci. Tech. Arts Res.* 4, (2015) 80.
- [70] F.R. Marcos, J. J. Romero, J. F. Fernandez, *J. Nanopart. Res.* 12, (2010), 2495.
- [71] M.R. Cesàrio, D. A. Macedo, R.M.P.B. Oliveira, P.M. Pimntel, R. L. Moreira, D.M.A. Melo, *J. Ceram. Process. Res.* 12, (2011), 102.

Chapter 4

Photocatalytic Degradation of Crystal Violet Dye Using BaBiO_3 and $\text{Ba}_{0.6}\text{K}_{0.4}\text{BiO}_3$

4.1 Introduction

Synthetic dyes comprise an important part of industrial water effluents, as they are discharged in abundance by many manufacturing and textile industries. The impact of these dyes on the environment is a major concern because of the potentially carcinogenic properties of these chemicals [1-4]. Organic dyes can undergo transformation in aquatic media and can form harmful carcinogenic and mutagenic intermediates, this way causing a serious risk for survival of microorganisms, aquatic life and environmental media – water and soil [5, 6]. The effect of such contamination on human health may be unpredictable hazard inflicting different diseases like immune-suppression, respiratory, central nervous, neuro-behavioral disorders, allergy, tissue necrosis, skin or eye infections and irritation and even lung edema [7, 8].

Triarylmethane dyes, part of a group trivially named aniline dyes, are among the first ones to be produced and marketed, Mauvein, being the first synthetic aniline dye to be synthesized in 1856 by William Perkin [9]. Due to their high coloring power and relatively inexpensive production methods, these aniline dyes initially gained great popularity [10].

Crystal violet or gentian violet is a triarylmethane cationic dye and widely used as a purple dye for textiles such as cotton and silk, for paints and as printing ink on papers. It is a component of navy blue and black inks for printing, ball-point pens and ink-jet printers. It is also used to colorize diverse products such as fertilizers, anti-freezes, detergents, and leather jackets [11-14]. The dye is also used as a histological stain, particularly in Gram's Method for classifying bacteria [15]. Crystal violet has antibacterial, antifungal, and anthelmintic properties. When conducting DNA gel electrophoresis, crystal violet can be used as a non-toxic DNA stain as an alternative to fluorescent, intercalating dyes such as ethidium bromide [16, 17]. Used in this manner, it may be either incorporated into the agar-rose gel or applied after the electrophoresis process is finished. Used at a 0.001% concentration and allowed to stain a gel after electrophoresis for 30 minutes, it can detect as little as of DNA. When crystal violet is used as an alternative to fluorescent

stains, it is not necessary to use ultraviolet illumination; this has made crystal violet popular as a means of avoiding UV-induced DNA destruction when performing DNA cloning in-vitro [18].

Apart from its versatile uses in different areas, CV has some harmful effects on environment and human health (**Figure 4.1**). It is a mutagen and mitotic poison [19]. Therefore, there are both environmental and health concerns of this particular dye. Like malachite green (MG), crystal violet (CV) is readily absorbed into fish tissue from water exposure and is reduced metabolically by fish. Several studies by the National Toxicology Program reported the carcinogenic and mutagenic effects of crystal violet in rodents [20, 21].

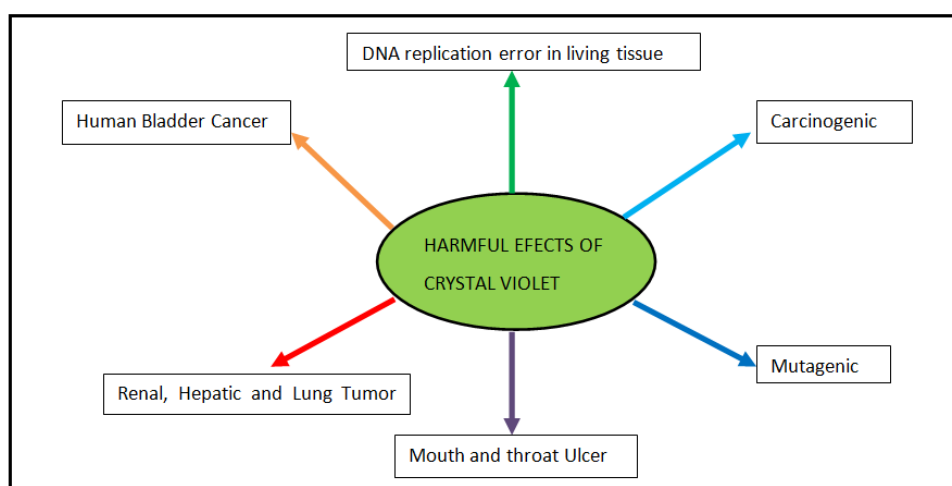


Figure 4.1. Harmful effects of CV dye.

The release of waste water containing this dye poses a dramatic source of water pollution, eutrophication and perturbation of aquatic life. Therefore, it is treated as a serious pollutant in waste water and difficult to remove by common removal methods. Many techniques have been developed to remove the pollutant from wastewater such as, coagulation, flocculation combined with floatation [22], ozonation [23], chemical oxidation [24], membrane separation process [25], electrochemical treatment [26,], biological degradation including ,aerobic and anaerobic microbial degradation [27-29], precipitation [30], adsorption [31-34] , advanced oxidation processes (AOPs) such as Fenton reaction [35,36], and photocatalytic degradation [37-40].

Among these methods, photodegradation has been extensively studied as low-cost and simple technology during past decades [41-43].

Despite the good removal of CV dye by the above mentioned methods it is found that most of the photocatalysts used above are not visible light active, following which various doping methods were invented for the conventionally used photocatalysts [44,45]. Under this category, perovskite-type oxides have attracted a great interest for the development of environment friendly catalytic materials. Perovskites are the class of compounds presenting the general formula ABO_3 . Generally, in this crystal structure, the A site is occupied by the larger cation, while the B site is occupied by the smaller cation. Perovskites are one of the most important families of materials exhibiting properties suitable for numerous technological applications [46].

They have been used in processes such as catalytic combustion for the automotive control emission and catalytic destruction of chlorinated compounds [47]. These metal oxides are known for their narrow band gap and high photocatalytic activity and hence have become prominent in the field of visible light photocatalysis [48,49]. Perovskite like metal oxides have also been reported to possess oxygen storage capacity that can be successfully utilized for direct oxidation of environmental contamination [50, 51].

However, application of perovskite catalyst in the field of water treatment is still limited. The present study attempts to investigate the performance of barium, bismuth and potassium containing binary and ternary perovskite oxides for the treatment of crystal violet dye solution under visible light irradiation.

In this chapter, doped and undoped Barium bismuthate, used for the degradation of CV dye from aqueous solution, have been synthesized by Pechini method, details of which have been elaborated in chapter 3. The degradation potential of these catalysts has been evaluated by different characterization methods such as TG-TGA, XRD, UV-DRS, SEM and FTIR, results of which have been described in chapter 3.

FTIR spectrum shows the presence of a band around 465cm^{-1} in both the catalysts conforming the metal-oxygen bond formation, which is the characteristic

property of perovskite materials. The SEM studies show that both the samples are homogeneous uniform nanoparticles, having size 520 nm and between 45-101nm for the BaBiO_3 and $\text{Ba}_{0.6}\text{K}_{0.4}\text{BiO}_3$, respectively. SEM images reveal the nano rod type structure and plate like layered structure of BaBiO_3 and for $\text{Ba}_{0.6}\text{K}_{0.4}\text{BiO}_3$, respectively. The XRD patterns suggest that BaBiO_3 crystallizes in the monoclinic structure while $\text{Ba}_{0.6}\text{K}_{0.4}\text{BiO}_3$ crystallizes in cubic structure. XRD patterns exhibit the typical pattern corresponding to perovskite structure. The phase evolution of both the catalysts with increasing temperature was done by DT-TGA.

The diffuse reflectance spectroscopy showed that the catalysts have a broad absorbance around 600 and 660 nm with a band gap of 2.07 and 1.87eV for barium bismuthate and K doped barium bismuthate respectively. Due to the low band gap, the catalysts are supposed to be promising in displaying their visible light activity and hence they are tested further for the degradation of CV dye under visible light irradiation.

The objective of this work is to study the photodegradation of CV dye using the prepared catalysts. The photodegradation rates and efficiency of the photocatalytic system are highly dependent on a number of operational parameters that govern the photodegradation of the organic molecule [52] such as initial dye concentration catalyst dose, solution pH and temperature. Optimization of such conditions will greatly help in the development of industrial-scale dye removal treatment process.

Therefore, herein, the dependence of the photodegradation rate on various parameters viz. initial dye concentration, catalyst dose, pH and temperature is studied. The reaction kinetics was studied and the applicability of the first order kinetic model is also discussed. The agreement of the experimental results with the Langmuir-Hinshelwood kinetic model has been examined which led to the determination of both photo-reaction kinetics and adsorption equilibrium constants [53]. In addition, photolysis and adsorption study of dye on prepared catalyst is also discussed. The adsorption experiment data is fitted to Langmuir isotherm model and Freundlich isotherm model [54]. Furthermore, to estimate the degree of mineralization, measurements of total organic carbon has also been conducted

4.2. Material & Method

4.2.1. Chemical reagents

The reagents used for the synthesis of BaBiO₃ and Ba_{0.6}K_{0.4}BiO₃ are Barium nitrate, Bismuth nitrate, potassium nitrate as starting materials while, citric acid and ethylene glycol are used as complexing agents. Details of synthesis procedure are given in chapter 3. Crystal violet dye (Mol. Wt. = 407.9 mgmol⁻¹) is purchased from Sigma-Aldrich Company (India). A solution of 100 mgL⁻¹ CV dye solution was prepared as stock solution. Different dye solutions of various concentrations are made from the stock solution (100mgL⁻¹) by appropriate dilutions. Ultra-pure water (18.2 MΩcm⁻¹) was used to prepare all solutions in this study. The pH of the solutions is adjusted using 0.1N NaOH and 0.1N HCl. All the chemicals except CV dye is purchased from Merck (India). Analytical grade p 25TiO₂ is purchased from Sigma-Aldrich Company (India). The chemicals used in this experiment are of the analytical grade and are used without further purification.

4.2.2. Experimental procedure and analytical methods

An experimental setup for the photocatalytic activity test has been explained in chapter 2. The visible light irradiation experiments are carried out in an indigenously prepared immersion type photocatalytic reactor. A 500W Xe arc lamp (intensity=137 mWcm⁻²) is used as a visible light source. This lamp is placed in a quartz tube which is sealed from one side. This tube is then immersed in a cylindrical borosilicate reactor (capacity 1L). In this, mixture of catalyst and dye solution are taken following which the mixture is placed in a water bath circulated at a constant speed to keep the above suspension homogenous. Only in experiments dealing with the effect of pH on the dye degradation, initial pH was adjusted with buffer solutions and measured with pH meter.

Since some dyes can be degraded by direct UV or visible irradiation without the assist from catalysts [53], it is important to find out the extent to which the degradation of CV dye in aqueous solution takes place directly by the visible light or in other words, to find out the extent of direct photolysis of CV dye. So, some

control experiments are carried out in the absence of the catalysts, while holding all other parameters the same. Following this, their respective photodegradation rates are measured to evaluate their photolysis.

Since, the photo-assisted degradation of the dyes occurs predominantly on the surface. Therefore, adsorption of the dye is an important parameter in determining photocatalytic degradation rate. Photocatalysts, dispersed into CV dye solution is allowed to reach adsorption-desorption equilibrium under continuous magnetic stirring at 600 rpm for 30 min in the dark, before illumination. Irradiation was then provided. Dye samples are withdrawn at 5 min time intervals and then centrifuged to remove the suspended catalyst. The clear supernatant fluid followed by filtration is then analysed by a spectrophotometer (Double beam spectrophotometer-2203, Systronics) at $\lambda_{\max} = 590\text{nm}$ with a calibration curve based on Beer Lambert's law [55].

The degradation efficiency is observed in terms of change in intensity of the dye before and after light irradiation. Photocatalytic performance is quantified by the degradation of CV dye under visible light irradiation.

$$\% \textit{degradation} = \frac{C_0 - C_t}{C_0} \times 100 \quad \text{--- (4.1)}$$

Where, C_0 = concentration of dye solution after adsorption-desorption equilibrium (mgL^{-1}), C_t = concentration of dye solution after photo irradiation (mg L^{-1}).

4.3. Results and Discussion

4.3.1. UV-VIS spectra of CV dye

Crystal violet is a basic tri phenyl methane dye with high water solubility, and its molecular formula is $\text{C}_{25}\text{H}_{30}\text{N}_3$. The UV-vis. absorbance spectrum of CV is drawn to determine its absorption maxima. **Figure 4.2** shows the typical time dependent UV-vis spectrum of CV dye. It is clear that CV dye has an intensive absorbance at 590nm. The rate of degradation was investigated with respect to change in absorption maxima of CV dye ($\lambda_{\max.} = 590\text{nm}$).

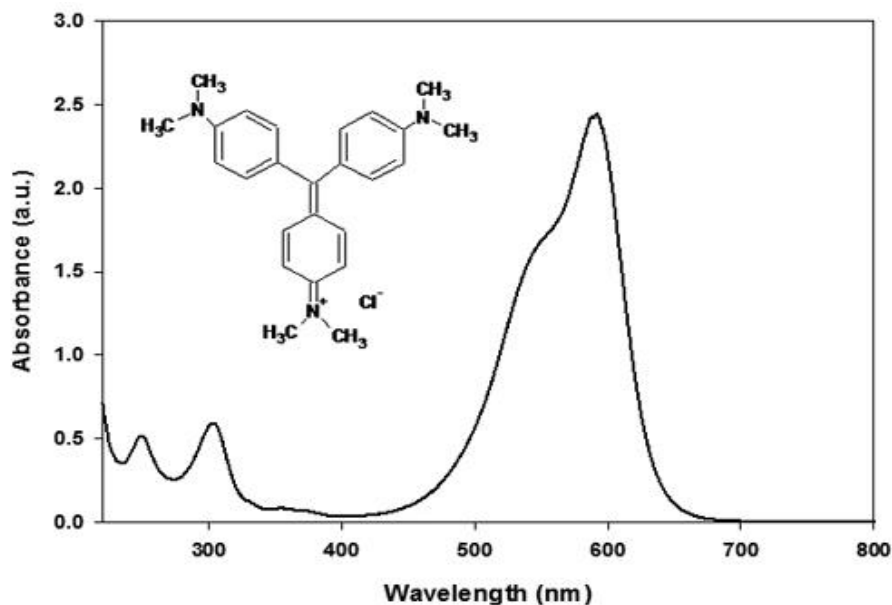


Figure 4.2. UV-VIS spectra of CV dye. ($\lambda_{max}=590\text{nm}$)

4.3.2. Photolysis of crystal violet dye

Photolysis is the process of decomposition of dyes in the presence of light radiation only. Direct photolysis of the dye in the absence of photocatalysts showed no considerable degradation even after 1 hour. **Figure 4.3** shows the results of photocatalysis in terms of % degradation.

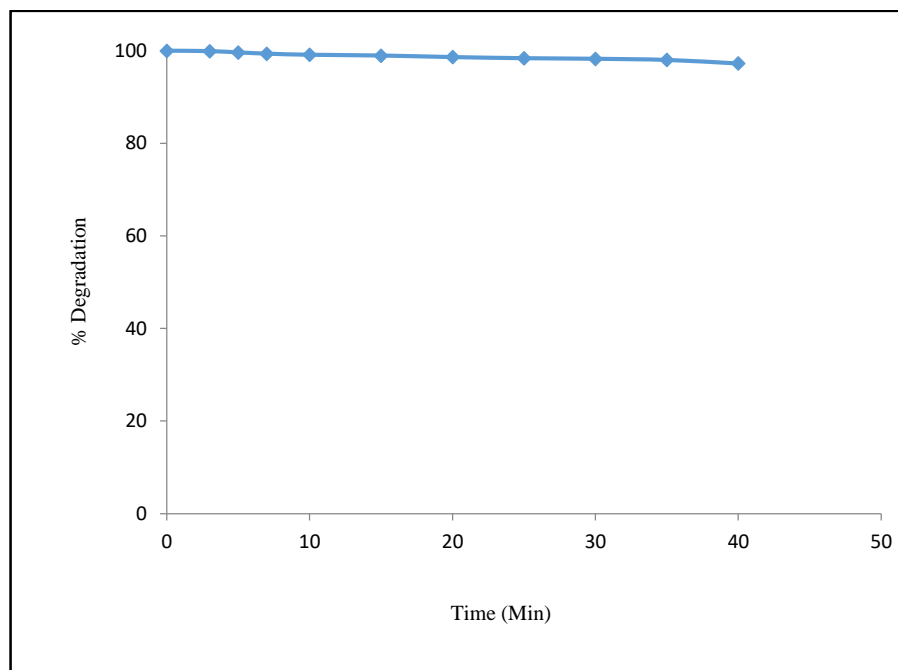


Figure 4.3 Photolysis of CV in presence of irradiation. (Experimental condition: [CV] = 40mgL^{-1} ; pH=6.0; Temp.= 308K).

The constant absorbance with time verifies that CV dye is not homogeneously degraded by light. Therefore, the self-degradation of the dye by visible light irradiation can be ignored. Similar results are obtained in the study of CV dye under UV-Vis irradiation in earlier reports [56].

4.3.3. Adsorption studies in dark:

Since, the photo-assisted degradation of the dyes occurs predominantly on the surface. Therefore, adsorption of the dye is an important parameter in determining photocatalytic degradation rate. The adsorbed dye on the surface of the semiconductor particles act as an electron donor, injecting electrons from its excited state to the conduction band of the semiconductor under light irradiation, so in the heterogeneous photocatalytic degradation process, adsorption of dye on the catalytic surface was assumed to be a primary step of the reaction [57-59] The adsorption experiments are carried out to evaluate the experiments the equilibrium quantity of adsorbent. The equilibrium adsorption isotherm is fundamental in describing the interactive behaviour between adsorbates and adsorbent and is important in the design and analysis of adsorption systems. For the sake of convenience, explicit and simple models are preferred and commonly used [60] Equilibrium adsorption data collected in this study could be fitted to both Langmuir and Freundlich isotherms.

A. Langmuir isotherm

Langmuir isotherm [53, 61] model was used to interpret the experimental data. The Langmuir isotherms are represented by the following equations.

$$q_e = \frac{Q_0bc}{1+bc} \quad \text{--- (4.2)}$$

$$\frac{C_e}{q_e} = \frac{1}{Q_0b} + \frac{C_e}{Q_0} \quad \text{--- (4.3)}$$

Where C_e is the concentration of the adsorbate (mgL^{-1}) at equilibrium, q_e is the amount of adsorbate per unit mass of adsorbent at equilibrium in mgg^{-1} , Q_0 is the maximum adsorption at monolayer coverage in mgg^{-1} , b is the adsorption equilibrium constant related to the energy of adsorption in Lmg^{-1} .

The adsorbate uptake q_e (mgg^{-1}), can be calculated as

$$q_e = \frac{(C_0 - C_e)V}{W} \quad \text{--- (4.4)}$$

Where C_0 is the initial adsorbate concentration (mgL^{-1}), V is the volume of solution (L), W is the mass of adsorbate (g).

The essential characteristic of the Langmuir isotherm can be described by a separation factor which is called the equilibrium constant, R_L

The equilibrium factor thus is defined as:

$$R_L = \frac{1}{1 + K_{LH}} \times \frac{1}{C_0} \quad \text{--- (4.5)}$$

Where, K_{LH} is the affinity constant (mg^{-1}), C_0 is the initial concentration of the adsorbate (mg/L). The R_L value is to be favourable at $0 < R_L < 1$ [62].

Adsorption experiments are carried out in the same experimental setup, taking dye solutions of different initial concentration. The constants of isotherm are obtained by least square fitting of the adsorption equilibrium data. Adsorption experiments for the dye CV dye are carried out by selecting a concentration range of 20mgL^{-1} to 80mgL^{-1} with an adsorbent dosage of 0.75g of both the adsorbents i.e. BaBiO_3 and $\text{Ba}_{0.6}\text{K}_{0.4}\text{BiO}_3$ at 308K {**Figure 4.4 (a & b)**}. The effect of initial dye concentration depends on the immediate relation between the concentration of the dye and the available sites on an adsorbent surface. In general, the percentage of dye removal increases with increase in initial dye concentration because it will cause an increase in the capacity of the adsorbent and this may be due to the high driving force for mass transfer at a high initial dye concentration [62].

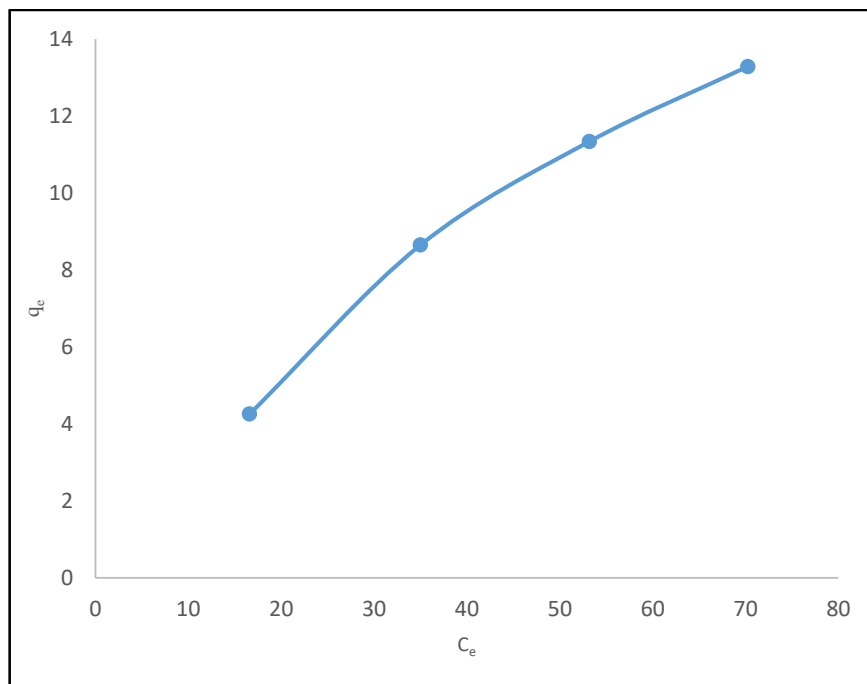


Figure 4.4 (a): Adsorption isotherm from aqueous CV dye solution

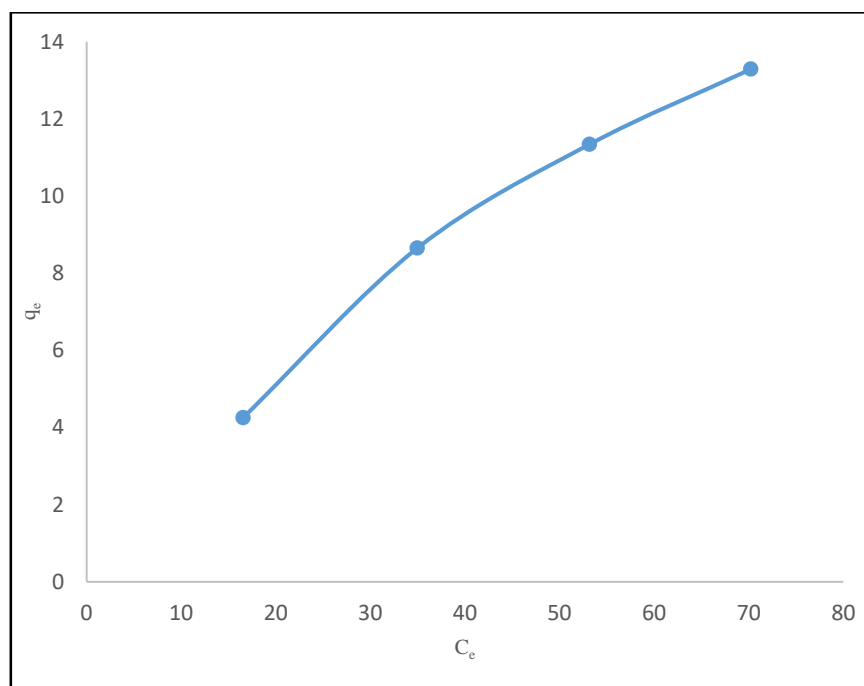


Figure 4.4 (b): Adsorption isotherm from aqueous CV dye solution with $Ba_{0.6}K_{0.4}BiO_3$ catalyst.

The plot of C_e/q_e versus C_e are linear and represented in **Figure 4.5(a)** and **4.5(b)** for $BaBiO_3$ and $Ba_{0.6}K_{0.4}BiO_3$ respectively. The value of Q_0 and b was found from the intercept and slope of the C_e/q_e vs C_e curve respectively.

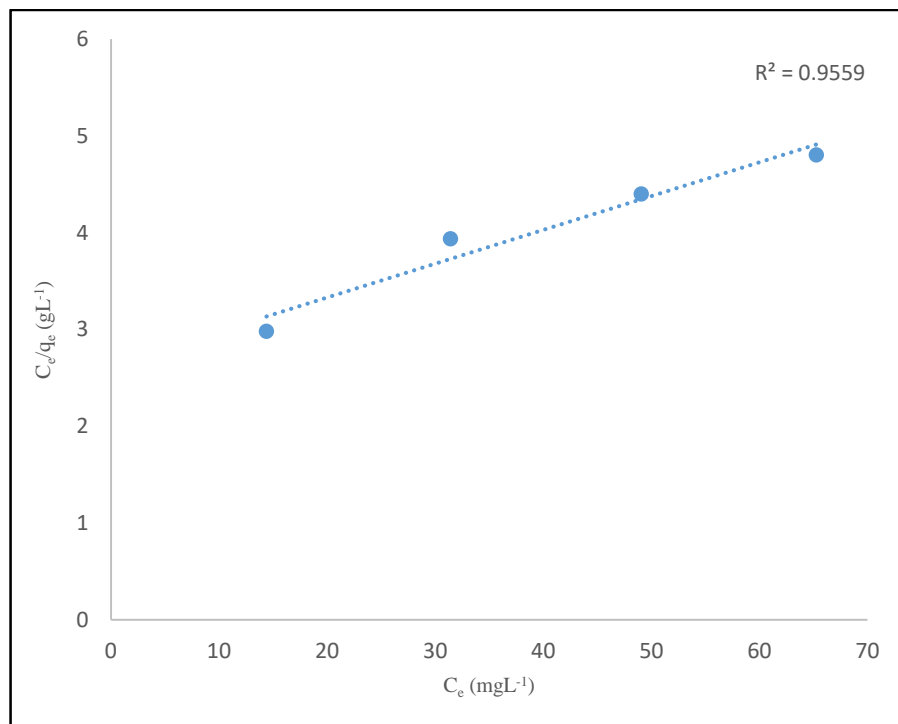


Figure 4.5(a): Langmuir plots for the adsorption of CV on BaBiO₃. (Experimental condition: BaBiO₃ = 0.75g/L; Temp. = 308K; pH=6.0).

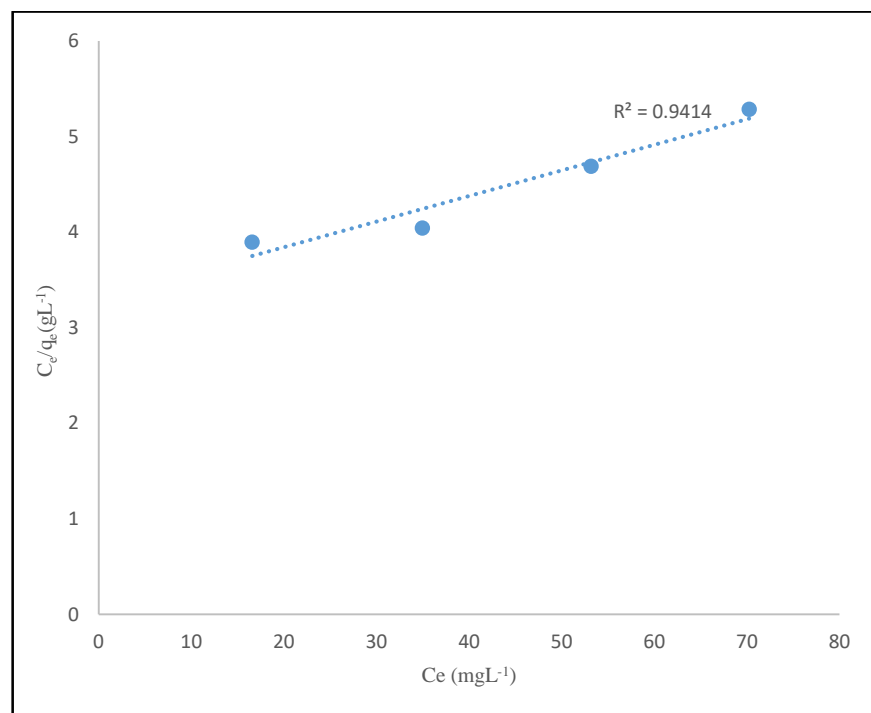


Figure 4.5(b): Langmuir plots for the adsorption of CV on Ba_{0.6}K_{0.4}BiO₃. (Experimental condition: Ba_{0.6}K_{0.4}BiO₃ = 0.75g/L; Temp. = 308K; pH=6.0).

The maximum absorbable dye quantity (Q_0) and Langmuir adsorption constant (b) are calculated from the **Figures 4.5(a)** and **4.5(b)** as 0.052 mgg^{-1} , 0.030 mgg^{-1} for BaBiO_3 and 0.05 Lmg^{-1} , 1.325 Lmg^{-1} for $\text{Ba}_{0.6}\text{K}_{0.4}\text{BiO}_3$, respectively.

The value of separation constants for different initial concentration are determined from equation 4.5 and found to be in range of 0.0526-0.0131 and 0.051-0.0128 for BaBiO_3 and $\text{Ba}_{0.6}\text{K}_{0.4}\text{BiO}_3$ catalysts and are listed in **Table 4.1**.

Table 4.1: Separation constants (R_L) values for the adsorption of CV dye on BaBiO_3 and $\text{Ba}_{0.6}\text{K}_{0.4}\text{BiO}_3$

$C_0 \longrightarrow$	20mgL^{-1}	40mgL^{-1}	60mgL^{-1}	80mgL^{-1}
BaBiO₃	0.0526	0.0263	0.0175	0.0131
Ba_{0.6}K_{0.4}BiO₃	0.0515	0.025	0.0171	0.0128

The values of R_L are found in the range of $0 < R_L < 1$, indicating that the adsorption is favoured.

B. Freundlich isotherm

The Freundlich isotherm equation assumes a heterogeneous adsorption surface with sites that have different energies of adsorption and are not equally available [54, 60]. The Freundlich exponential equation is given as-

$$q_e = K_f C_e^{1/n} \quad \text{--- (4.6)}$$

Where, q_e is the amount adsorbed (mgg^{-1}), C_e is the equilibrium concentration of the adsorbate (mgL^{-1}), K_f (Lg^{-1}) and n are Freundlich constants related to the adsorption capacity and adsorption intensity, respectively.

The linear logarithmic form of Freundlich equation is mathematically given by

$$\log q_e = \log K_f + \frac{1}{n} \log C_e \quad \text{--- (4.7)}$$

The value of $1/n$ represents the favourable adsorption conditions.

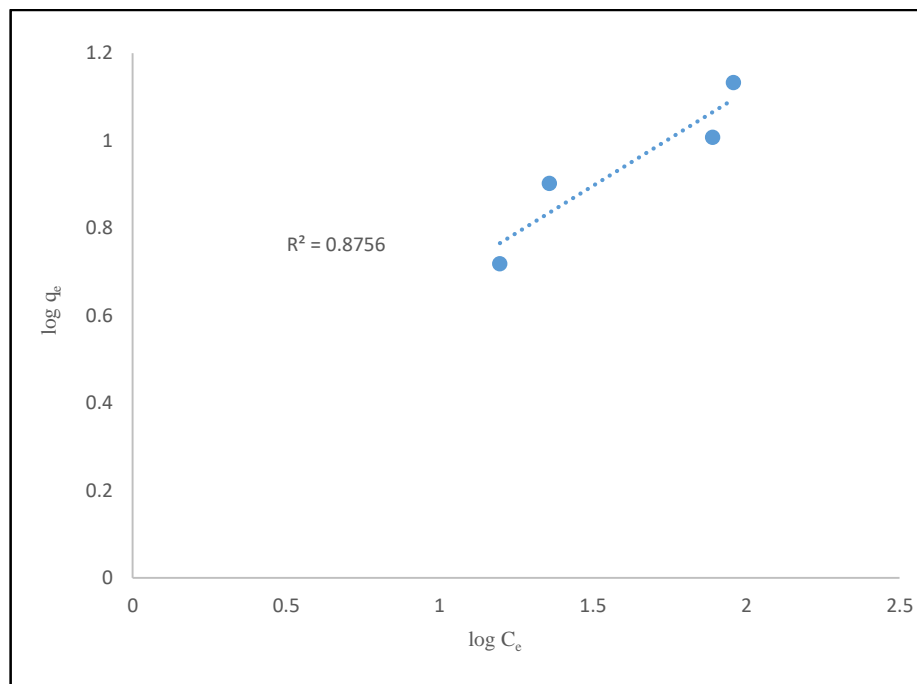


Figure 4.6(a): Freundlich plots for the adsorption of CV on $BaBiO_3$. (Experimental condition; $BaBiO_3 = 1gL^{-1}$; Temp. = 308K; pH = 6.0).

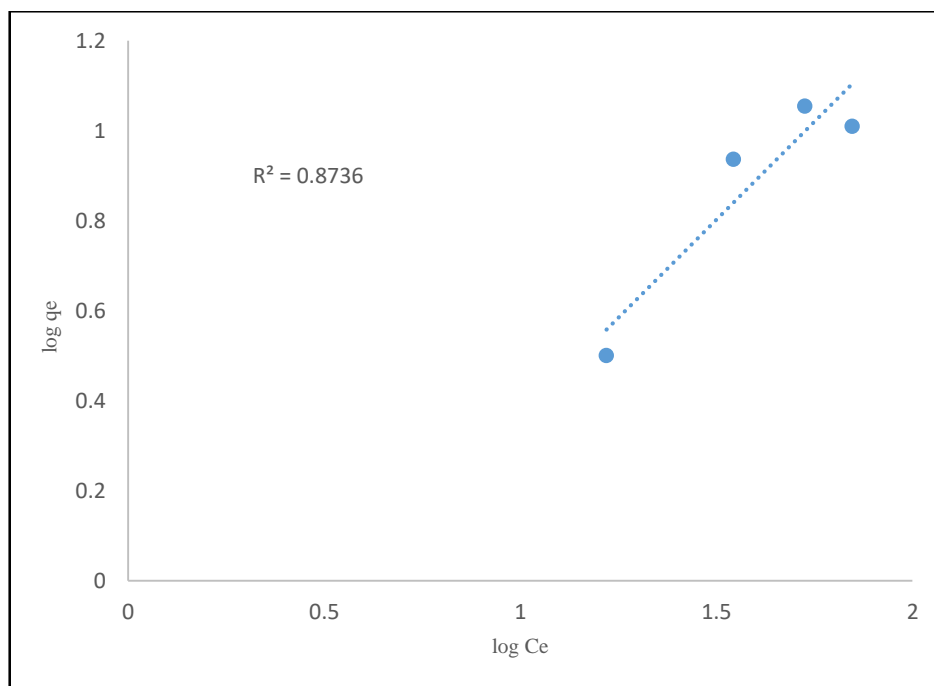


Figure 4.6(b): Freundlich plots for the adsorption of CV on $Ba_{0.6}K_{0.4}BiO_3$. (Experimental condition: $Ba_{0.6}K_{0.4}BiO_3 = 1gL^{-1}$; Temp. = 308K; pH = 6.0).

K_f and n can be calculated from the intercept and slope of the plots in **Figures 4.6(a)** and **4.6(b)** for BaBiO_3 and $\text{Ba}_{0.6}\text{K}_{0.4}\text{BiO}_3$ respectively.

Langmuir and Freundlich constants for the adsorption of CV dye on $\text{Ba}_{0.6}\text{K}_{0.4}\text{BiO}_3$ has been represented in **Table 4.2**.

Table 4.2: Langmuir and Freundlich constants for the adsorption of CV dye on BaBiO_3 and $\text{Ba}_{0.6}\text{K}_{0.4}\text{BiO}_3$

Adsorbent catalyst	Langmuir Constants			Freundlich Constants		
	Q_0 (mgg ⁻¹)	b (Lmg ⁻¹)	R^2	K_f (Lg ⁻¹)	n	R^2
BaBiO₃	0.052	0.05	0.977	1.97	2.975	0.8677
Ba_{0.6}K_{0.4}BiO₃	0.0307	1.325	0.929	7.74	1.68	0.717

Since the R^2 values are fairly close to 1, both the models describe the system well but Langmuir isotherm model is considered to be best fit because for this model R^2 was ~ 0.9 as comparison to $R^2 \sim 0.87$ for Freundlich isotherm.

4.3.4. Photodegradation studies under visible light irradiation

In order to assess the rate of photocatalytic degradation of dyes over BaBiO_3 and $\text{Ba}_{0.6}\text{K}_{0.4}\text{BiO}_3$, the observed dye degradation results are kinetically analysed by Langmuir-Hinshelwood kinetic equation [53,63]. Langmuir-Hinshelwood kinetic equation describes the following relationship between the initial rate constant and initial concentration of the organic substrate.

$$r_o = -\frac{dC}{dt} = \frac{K_r K_{LH} C_o}{1 + K_r C_o} \quad \text{--- (4.8)}$$

$$r_o = \frac{1}{K_r} + \frac{1}{K_r K_{LH} C_o} \quad \text{--- (4.9)}$$

Where C_o is the initial concentration of organic substrate (mgL⁻¹), r_o is initial rate (mgL⁻¹min⁻¹), K_{LH} is the Langmuir-Hinshelwood adsorption equilibrium constant (Lmg⁻¹) and K_r is the rate constant of surface reaction (mgL⁻¹min⁻¹).

The degradation of organic pollutants over catalysts follows the pseudo-first-order kinetics with respect to the initial concentration of the pollutant [64].

$$r_o = -\frac{dC}{dt} = K_{app} \quad \text{--- (4.10)}$$

Following equation was used to determine the initial rate by multiplying the apparent first-order rate constant K_{app} with the initial concentration of dye, C_o

$$\ln\left(\frac{C_t}{C_o}\right) = K_{app} \cdot C_o \quad \text{--- (4.11)}$$

In which K_{app} is the apparent pseudo-first-order rate constant in min^{-1} . The apparent reaction rate constant K_{app} (min^{-1}) is given by the slope of the graph of $\ln C_t/C_o$ versus time (minutes).

As we have seen that in the absence of catalyst, the concentration of CV dye shows no significant variation indicating that CV cannot be degraded by photolysis. Hence, any change in the CV concentration can be attributed to the adsorption/photocatalytic process. The pseudo-first-order kinetic model is usually used to fit all data sets (dye concentration, photocatalyst dose, initial pH solution, and temperature) [65].

4.3.4.1 Effect of initial dye concentration on photocatalytic degradation

It is important from both mechanistic and application point of view to study the dependence of the photocatalytic reaction rate on the substrate concentration. It is generally noted that the degradation rate increases with the increase in dye concentration to a certain level and a further increase in dye concentration leads to decrease the degradation rate of the dye. The effect of the initial dye concentration of dye on the rate of degradation is studied by varying the initial dye concentration from 20 to 80 mgL^{-1} initial pH 6.0, with a constant catalyst dose of 0.75 gL^{-1} (for both the catalysts). It is observed that up to 40 mgL^{-1} the degradation efficiency increases due to the greater availability of dye molecules for excitation and consecutive degradation; hence there is an increase in the rate. After this, as the dye concentration is increased, the equilibrium adsorption of dye on catalyst surface increases; hence competitive adsorption of OH^- on the same site decreases, which further decreases the rate of formation of OH^\bullet radical, which is the principal oxidant necessary for a high degradation efficiency. Our results are in accordance with an earlier research work [66]. The corresponding results with both the catalysts have been described below.

On the other hand, considering **Beer-Lambert law**, as the initial dye concentration increases, the path length of photon entering the solution decreases, resulting in the lower photon adsorption on the catalyst particles and consequently a lower photodegradation rate [66]. Also, the high concentration of dye would have acted as a filter for the incident light, which ultimately reduces the degradation efficiency [67,68].

a. Results with BaBiO₃

The experimental results shows that the rate of photocatalytic degradation increases with increase in concentration of dye up to 40mgL⁻¹. The rate of reaction was then, found to decrease with further increase in the concentration of dye. It is clear from the **Table 4.3(a)** to **4.6(a)**, initially % degradation of dye increases rapidly and thereafter slowly attains the limiting value.

Figure 4.7.a (A-D) shows the plots of change in % degradation with time for various concentration of dye at various amount of catalyst.

Table 4.3(a): Effect of initial dye concentration on degradation of CV
(Experimental Condition: [BaBiO₃] = 0.25g/L; pH=6.0; Temp. = 308K)

Dye Concentration	20 mgL ⁻¹	40 mgL ⁻¹	60 mgL ⁻¹	80 mgL ⁻¹
Time (min)	%Degradation	%Degradation	%Degradation	%Degradation
0	0.00	0.00	0.00	0.00
3	8.59	12.20	6.69	4.89
5	15.00	21.58	12.81	9.87
7	23.34	30.36	20.57	13.92
10	33.54	39.58	29.38	21.65
15	46.27	55.70	40.57	35.02
20	57.65	68.54	51.24	43.90
25	67.14	76.10	61.24	54.96
30	73.50	81.54	70.41	64.82
35	81.39	85.67	78.83	71.58
40	83.41	87.14	80.35	79.08
∞	83.67	87.45	81.45	80.50

Table 4.4 (a): Effect of initial dye concentration on degradation of CV
(Experimental Condition: $[\text{BaBiO}_3] = 0.75\text{gL}^{-1}$; $\text{pH}=6.0$; $\text{Temp.}=308\text{K}$)

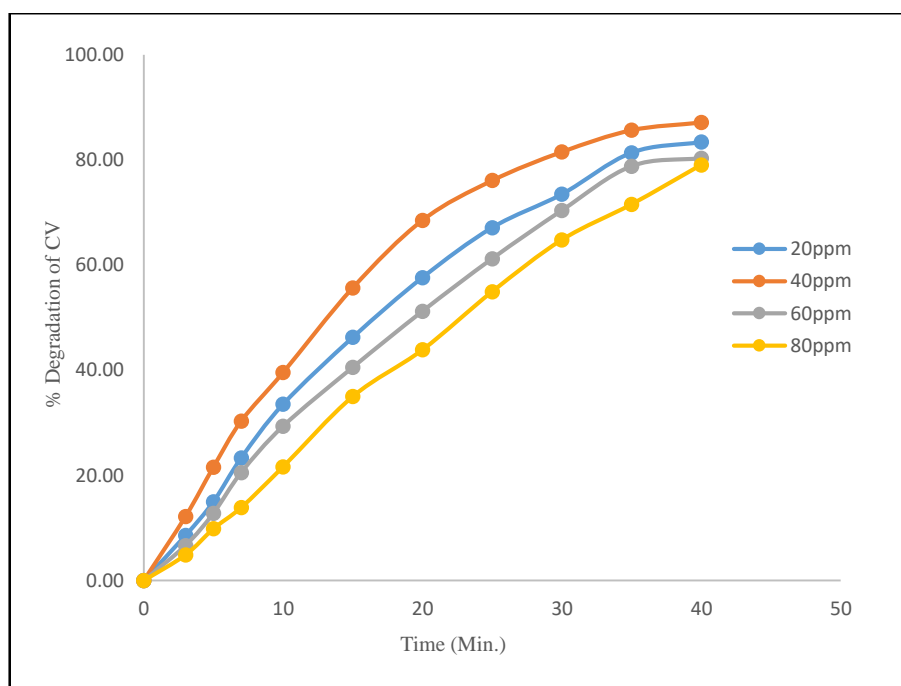
Dye Concentration	20 mgL^{-1}	40 mgL^{-1}	60 mgL^{-1}	80 mgL^{-1}
Time (min)	%Degradation	%Degradation	%Degradation	%Degradation
0	0.00	0.00	0.00	0.00
3	17.81	20.98	14.22	11.07
5	26.39	32.75	21.15	16.89
7	35.56	40.17	30.58	24.87
10	46.29	54.12	40.75	36.87
15	63.59	68.57	57.95	51.23
20	77.48	81.69	70.47	63.29
25	84.59	89.67	80.55	74.58
30	87.69	92.89	83.59	80.39
35	90.36	95.27	87.26	85.85
40	91.57	95.89	89.21	88.62
∞	91.66	95.90	89.21	89.25

Table 4.5 (a): Effect of initial concentration on degradation of CV
(Experimental Condition: $[\text{BaBiO}_3] = 1.00\text{gL}^{-1}$; $\text{pH}=6.0$; $\text{Temp.}=308\text{K}$)

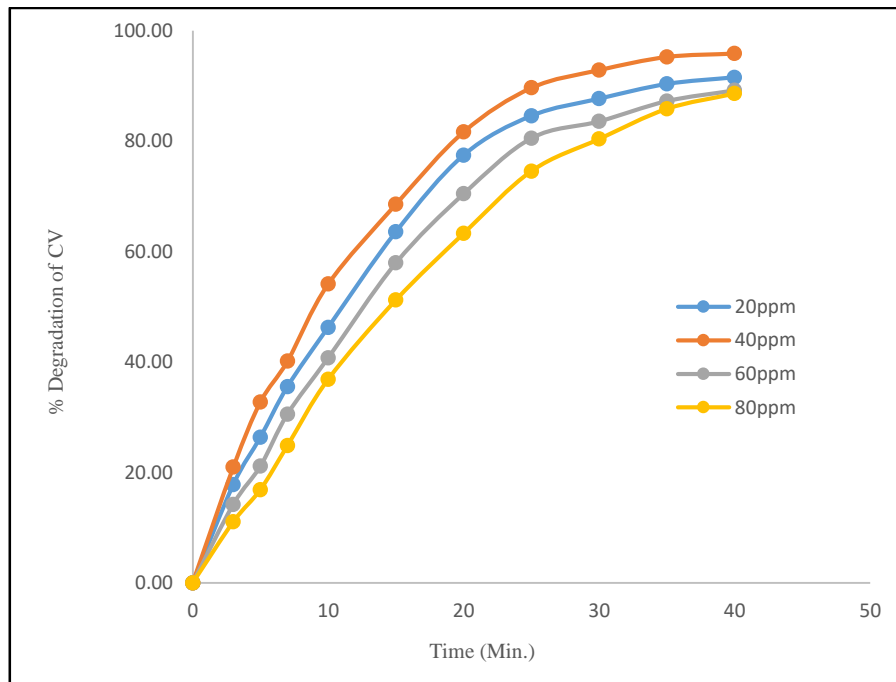
Dye Concentration	20 mgL^{-1}	40 mgL^{-1}	60 mgL^{-1}	80 mgL^{-1}
Time (min)	%Degradation	%Degradation	%Degradation	%Degradation
0	0.00	0.00	0.00	0.00
3	13.27	15.56	11.61	9.25
5	23.81	26.88	20.52	15.69
7	31.81	35.72	25.83	21.51
10	38.73	44.88	35.51	31.73
15	54.21	64.06	46.72	41.98
20	67.61	75.74	59.84	53.83
25	76.78	85.75	71.93	66.49
30	82.83	90.36	78.26	75.89
35	85.36	91.11	82.41	80.47
40	87.61	93.57	85.55	83.66
∞	87.78	93.65	85.9	83.75

Table 4.6 (a): Effect of initial concentration on degradation of CV
 (Experimental Condition: $[\text{BaBiO}_3] = 1.25\text{gL}^{-1}$; $\text{pH}=6.0$; $\text{Temp.} = 308\text{K}$)

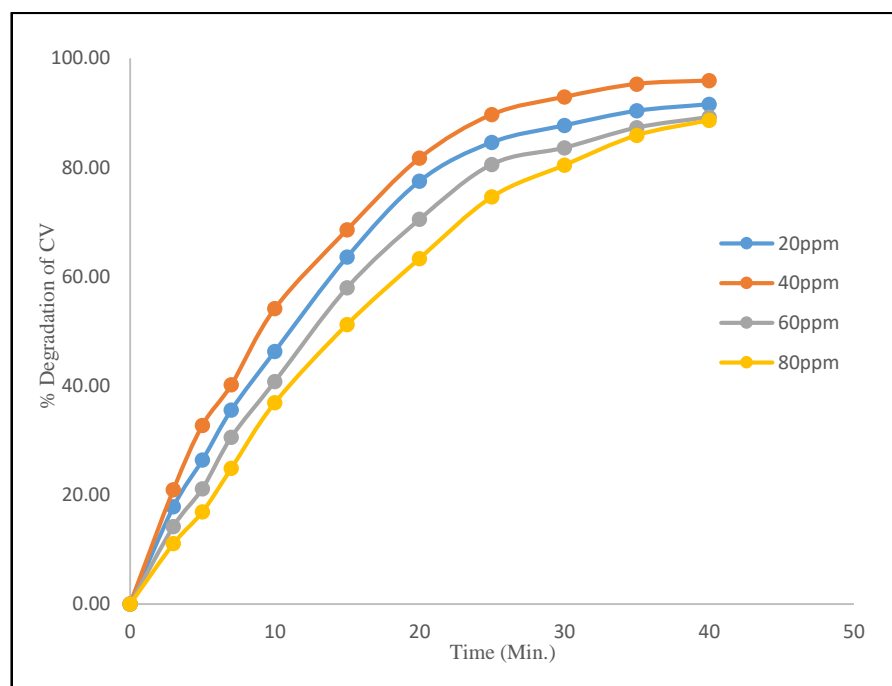
Dye Concentration	20 mgL^{-1}	40 mgL^{-1}	60 mgL^{-1}	80 mgL^{-1}
Time (min)	%Degradation	%Degradation	%Degradation	%Degradation
0	0.00	0.00	0.00	0.00
3	11.36	14.57	8.29	5.74
5	21.29	23.22	17.42	10.60
7	27.53	30.28	22.24	15.83
10	34.29	38.34	30.42	25.19
15	50.91	57.55	47.09	40.14
20	63.11	72.47	58.81	50.85
25	72.59	81.26	65.79	57.66
30	78.15	85.10	74.90	66.94
35	84.69	90.90	82.69	76.47
40	87.96	93.06	84.06	79.88
∞	88.01	93.01	84.01	79.78



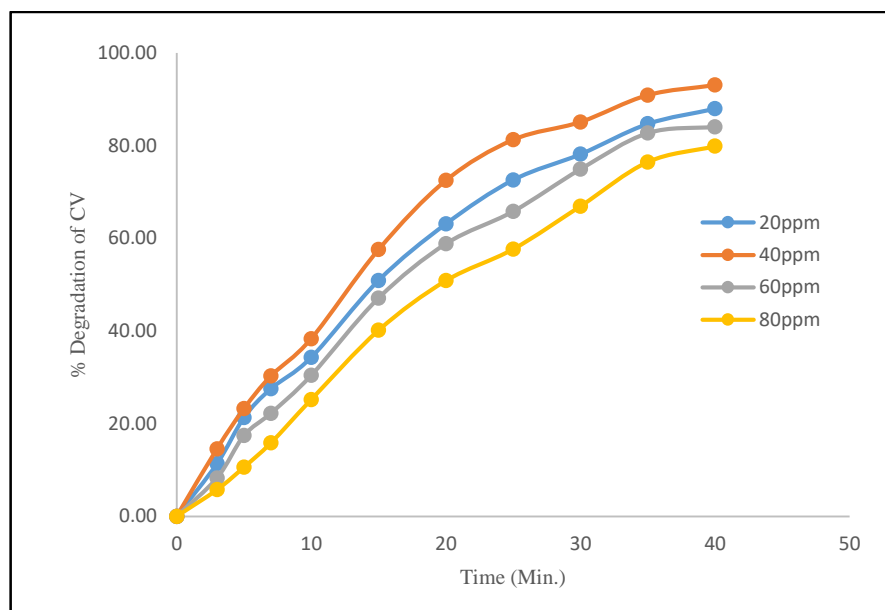
(A)



(B)



(C)



(D)

Figure 4.7 (a): Effect of concentration of CV on its visible light degradation in $BaBiO_3$ [(A) Catalyst dose: 0.25gL^{-1} ; (B) Catalyst dose: 0.75gL^{-1} ; (C) Catalyst dose: 1.00gL^{-1} ; (D) Catalyst dose: 1.25gL^{-1} ; $\text{pH}=6.0$; $\text{Temp.} = 308\text{K}$].

The photodegradation kinetics of initial dye concentration is illustrated in **Figure 4.8(a)**, which depicts the dark adsorption-desorption equilibrium and the additional decrease in CV concentration caused by visible light irradiation at optimum catalyst dose i.e. 0.75gL^{-1} .

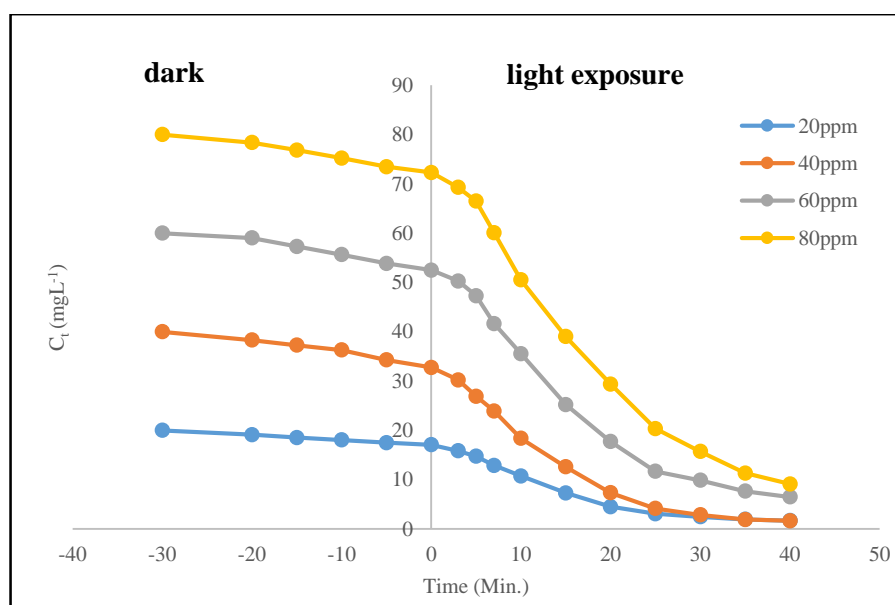


Figure 4.8(a): Variation of dye concentration versus time for different CV initial concentration. (Experimental condition: $BaBiO_3 = 0.75\text{gL}^{-1}$; $\text{pH}=6.0$, $\text{Temp.} = 308\text{K}$).

With respect to initial concentration, the rate expression is given by equation:

$$\frac{-d[CV]}{dt} = K_{app}[C]_o \quad \text{--- (4.12)}$$

Integration of the above equation yields:

$$\ln \frac{C_o}{C_t} = K_{app} \cdot t \quad \text{--- (4.13)}$$

Where, K_{app} is a pseudo first order rate constant (min^{-1}). $[C]_o$ is the equilibrium concentration of the CV dye solution after adsorption, and it is taken as the concentration of the dye solution at visible light irradiation time ' $t=0$ ' for kinetic analysis.

Initial rate (r_o) is determined by the following equation

$$r_o = K_{app}[C]_o \quad \text{--- (4.14)}$$

Where, r_o is initial rate ($\text{mgL}^{-1}\text{min}^{-1}$).

The plot of $\ln C_t/C_o$ versus t with different initial concentration of CV is shown in **Figure 4.9(a)**. The figure shows that the photocatalytic degradation follows perfectly the pseudo-first order kinetic with respect to CV concentrations.

It is found that a plot between $\ln C_t/C_o$ versus time represents a straight line, the slope of linear regression equals the apparent first order rate constant K_{app} which is consistent with the reported first order reaction [69].

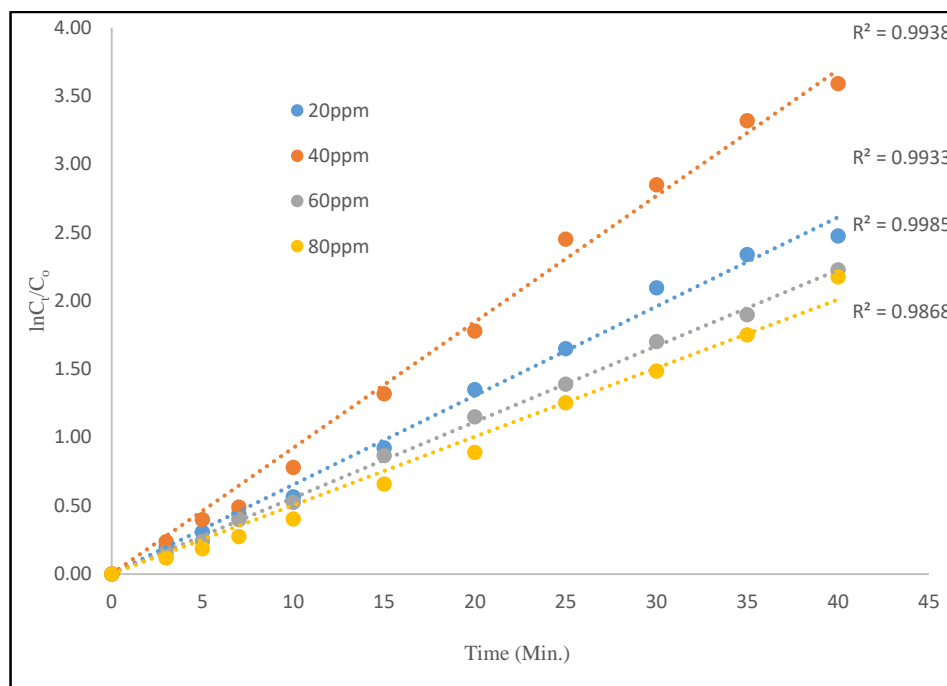


Figure-4.9 (a): Linear variation of $\ln C_t/C_0$ versus time for the photocatalytic degradation of CV dye at different initial concentration. (Experimental condition: $[\text{BaBiO}_3] = 0.75\text{gL}^{-1}$; $\text{pH}=6.0$; $\text{Temp.} = 308\text{K}$).

The values of rate constants K_{app} , which corresponds to different initial concentration, along with the initial rate (r_0) and corresponding regression constants, are listed in **Table 4.7(a)**.

Table 4.7 (a): Pseudo-first order apparent rate constant and initial rate values for the different initial concentration of dye

(Experimental condition: $[\text{BaBiO}_3] = 0.75\text{gL}^{-1}$; $\text{pH} = 6.0$; $\text{Temp.} = 308\text{K}$)

S. No.	Initial concentration (mgL^{-1})	Rate constant K_{app} (min^{-1})	Initial rate $r_0 \times 10^{-3}$ ($\text{mgL}^{-1}\text{min}^{-1}$)	R^2
1	20	0.0653	1.306	0.993
2	40	0.0922	3.68	0.994
3	60	0.0556	2.61	0.998
4	80	0.0302	2.41	0.986

The rate of degradation increases with the initial concentration of CV dye then finds a tendency towards independent values with the higher initial concentrations.

According to the **equation 4.9** the plot of $1/r_0$ versus $1/C_0$ represented in **Figure 4.10(a)** shows a linear variation, confirming the Langmuir-Hinshelwood relationship for the initial rates of photodegradation. The values of K_r and K_{LH}

calculated from the intercept ($1/ K_r \cdot K_{LH}$) and the slope ($1/ K_r$) of the straight line ($R^2=0.95$) are $6.90 \text{ mgL}^{-1}\text{min}^{-1}$ and 2.76 Lmg^{-1} respectively.

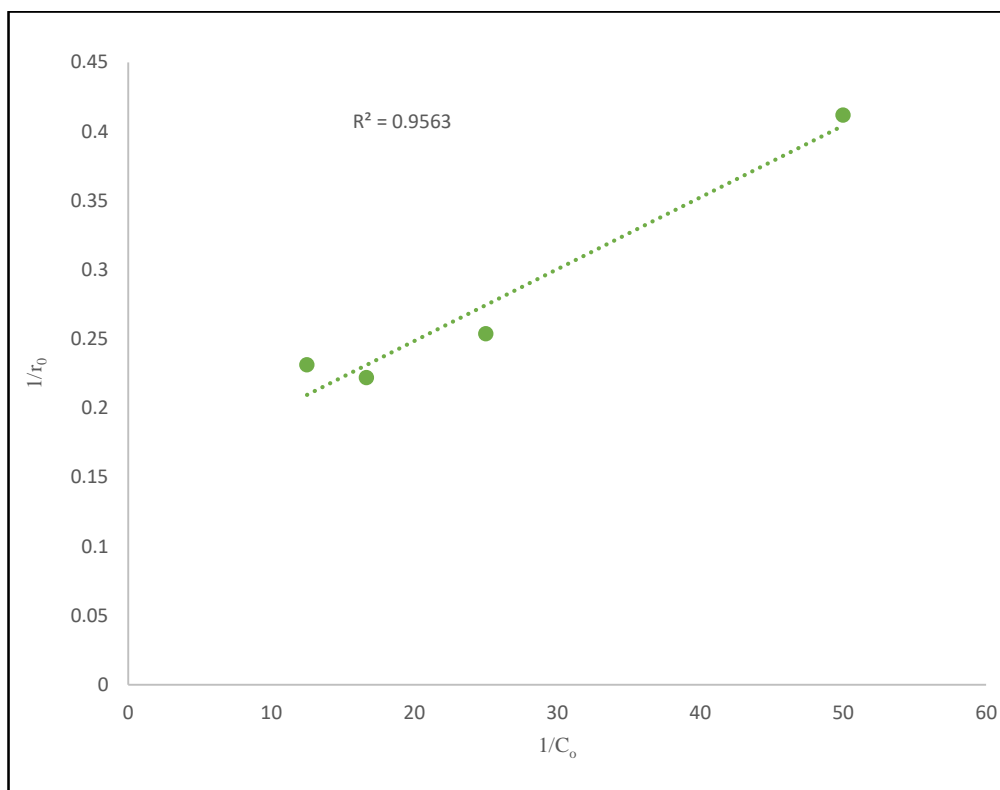


Figure-4.10(a): Langmuir-Hinshelwood plot for visible light photodegradation of CV dye by BaBiO_3 photocatalyst. (Experimental condition: $[\text{BaBiO}_3] = 0.75 \text{ gL}^{-1}$; $\text{pH} = 6.0$; $\text{Temp.} = 308 \text{ K}$).

b. Results with $\text{Ba}_{0.6}\text{K}_{0.4}\text{BiO}_3$

The experimental results shows that the rate of photocatalytic degradation increases with increase in concentration of dye up to 40 mgL^{-1} . The rate of reaction was then, found to decrease with further increase in the concentration of dye. It is clear from the **Table 4.3(b)** to **4.6 (b)**, initially % degradation of dye increases rapidly and thereafter slowly attains the limiting value. **Figure 4.7.b. (A-D)** shows the plots of change in % degradation with time for various concentration of dye at various amount of catalyst.

Table 4.3 (b): Influence of initial concentration on degradation of CV
 (Experimental Condition: $[\text{Ba}_{0.6}\text{K}_{0.4}\text{BiO}_3] = 0.25\text{gL}^{-1}$; $\text{pH}=6.0$; $\text{Temp.}=308\text{K}$)

Dye Concentration	20 mgL^{-1}	40 mgL^{-1}	60 mgL^{-1}	80 mgL^{-1}
Time (min)	%Degradation	%Degradation	%Degradation	%Degradation
0	0.00	0.00	0.00	0.00
3	8.33	10.42	6.35	5.29
5	16.14	21.13	15.88	11.29
7	25.44	30.21	21.59	15.23
10	37.39	41.26	31.38	25.60
15	49.77	58.61	41.80	36.50
20	58.99	69.87	52.00	45.68
25	71.66	78.78	68.15	57.76
30	78.31	84.78	75.36	68.11
35	83.12	90.24	81.11	75.09
40	87.00	93.09	84.52	80.46
∞	87.02	93.11	84.55	80.57

Table 4.4 (b): Influence of initial concentration on degradation of CV
 (Experimental Condition: $[\text{Ba}_{0.6}\text{K}_{0.4}\text{BiO}_3] = 0.75\text{gL}^{-1}$; $\text{pH}=6.0$; $\text{Temp.}=308\text{K}$)

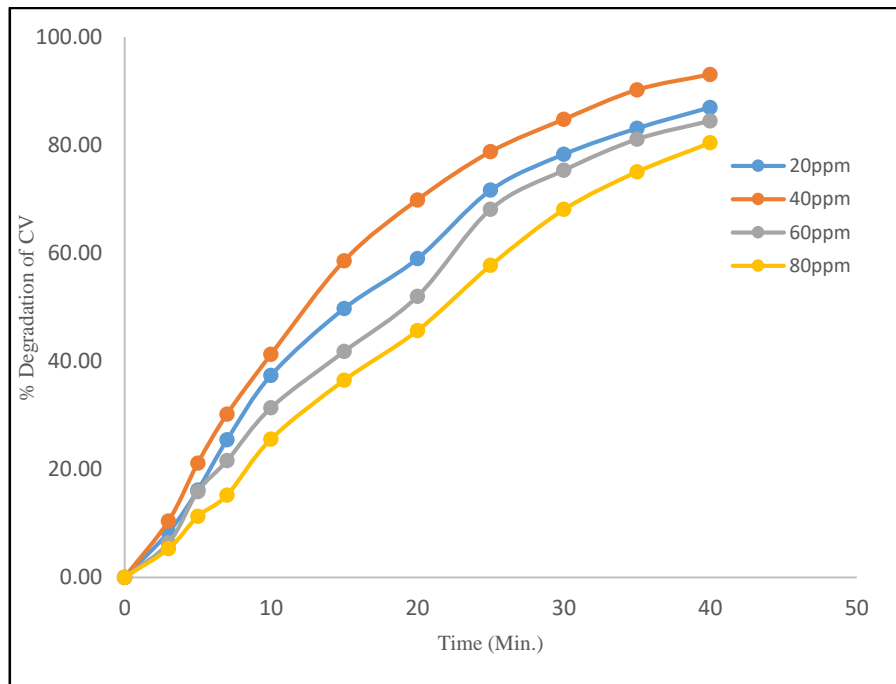
Dye Concentration	20 mgL^{-1}	40 mgL^{-1}	60 mgL^{-1}	80 mgL^{-1}
Time (min)	%Degradation	%Degradation	%Degradation	%Degradation
0	0	0	0	0
3	20.36	25.59	16.80	14.26
5	29.20	37.73	25.36	19.53
7	37.84	44.59	35.48	27.93
10	48.29	58.42	44.03	36.49
15	63.98	75.35	59.16	50.23
20	80.19	84.24	70.27	62.03
25	87.19	95.73	83.29	73.02
30	91.64	97.60	86.39	80.70
35	96.41	98.27	91.29	89.43
40	95.17	98.89	93.12	90.88
∞	95.20	99.90	93.15	90.9

Table 4.5 (b) Influence of initial concentration on degradation of CV
 (Experimental Conditions: $[\text{Ba}_{0.6}\text{K}_{0.4}\text{BiO}_3] = 1.00\text{gL}^{-1}$; $\text{pH}=6.0$; $\text{Temp.}=308\text{K}$)

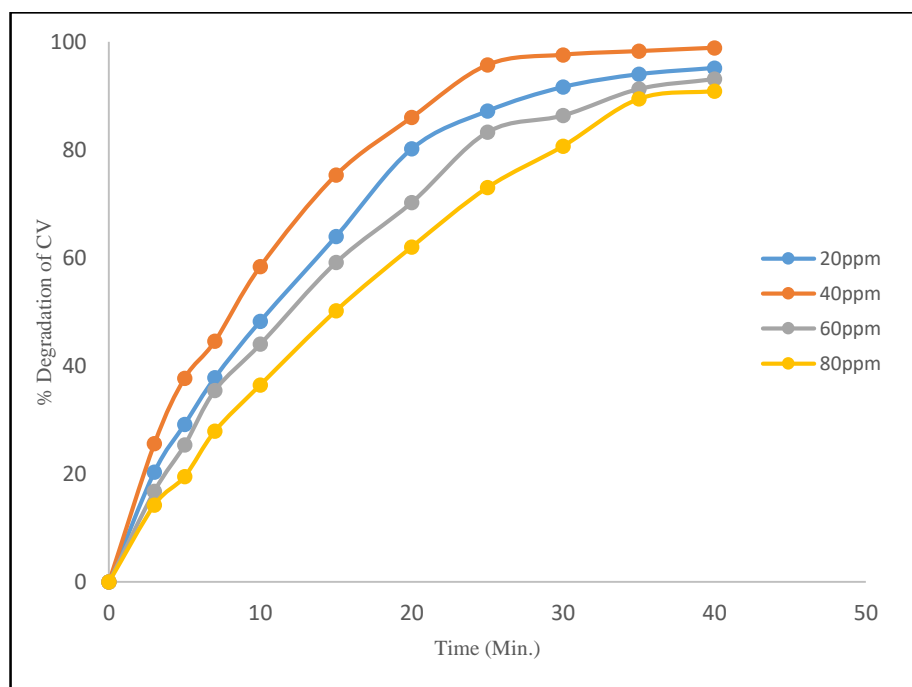
Dye Concentration	20 mgL^{-1}	40 mgL^{-1}	60 mgL^{-1}	80 mgL^{-1}
Time (min)	%Degradation	%Degradation	%Degradation	%Degradation
0	0	0	0	0
3	18.95	22.06	15.18	11.65
5	28.60	30.39	24.12	17.30
7	34.59	38.50	29.57	22.39
10	42.02	47.25	37.59	32.29
15	58.63	65.62	50.29	43.35
20	71.43	81.51	65.33	54.91
25	80.96	87.28	77.01	68.23
30	84.84	93.57	81.29	78.37
35	88.02	95.81	86.47	83.49
40	92.95	96.57	89.50	86.05
∞	92.97	96.61	89.52	86.07

Table 4.6 (b): Influence of initial concentration on degradation of CV
 (Experimental Conditions: $[\text{Ba}_{0.6}\text{K}_{0.4}\text{BiO}_3] = 1.25\text{gL}^{-1}$; $\text{pH}=6.0$; $\text{Temp.}=308\text{K}$)

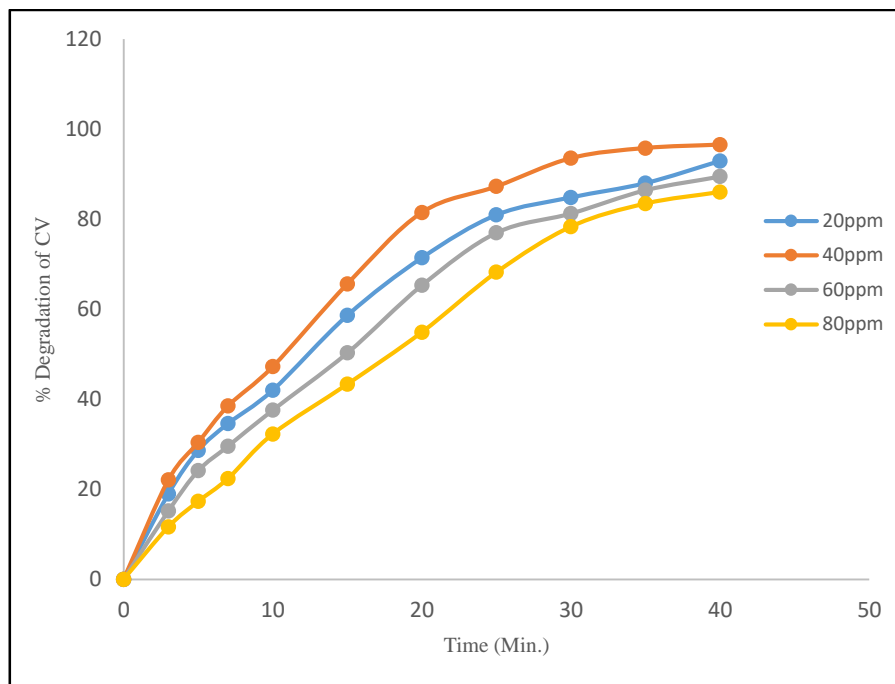
Dye Concentration	20 mgL^{-1}	40 mgL^{-1}	60 mgL^{-1}	80 mgL^{-1}
Time (min)	%Degradation	%Degradation	%Degradation	%Degradation
0	0	0	0	0
3	12.47	17.89	10.51	8.91
5	22.14	28.98	19.57	13.54
7	27.79	32.29	23.67	17.90
10	36.69	41.30	31.46	27.86
15	52.10	61.08	45.49	40.91
20	67.78	75.03	60.84	54.80
25	75.18	84.55	67.80	60.02
30	80.40	88.85	76.24	68.31
35	85.74	94.01	82.71	79.88
40	89.80	95.78	86.65	83.32
∞	89.83	95.81	86.68	83.35



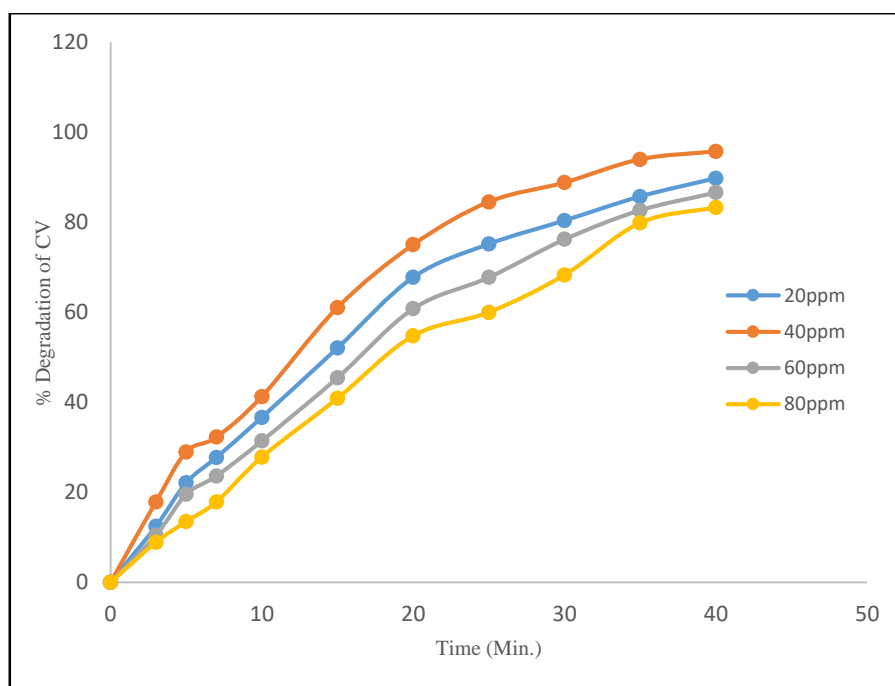
(A)



(B)



(C)



(D)

Figure 4.7 (b): Effect of concentration of CV on its visible light degradation in $Ba_{0.6}K_{0.4}BiO_3$ [(A) Catalyst dose: $0.25gL^{-1}$; (B) Catalyst dose: $0.75gL^{-1}$; (C) Catalyst dose: $1.00gL^{-1}$; (D) Catalyst dose: $1.25gL^{-1}$; pH=6.0; Temp. =308K].

The photodegradation kinetics of initial dye concentration is illustrated in **Figure 4.8(b)**, which depicts the dark adsorption-desorption equilibrium and the additional decrease in CV concentration caused by visible light irradiation at optimum catalyst dose i.e. 0.75gL^{-1} .

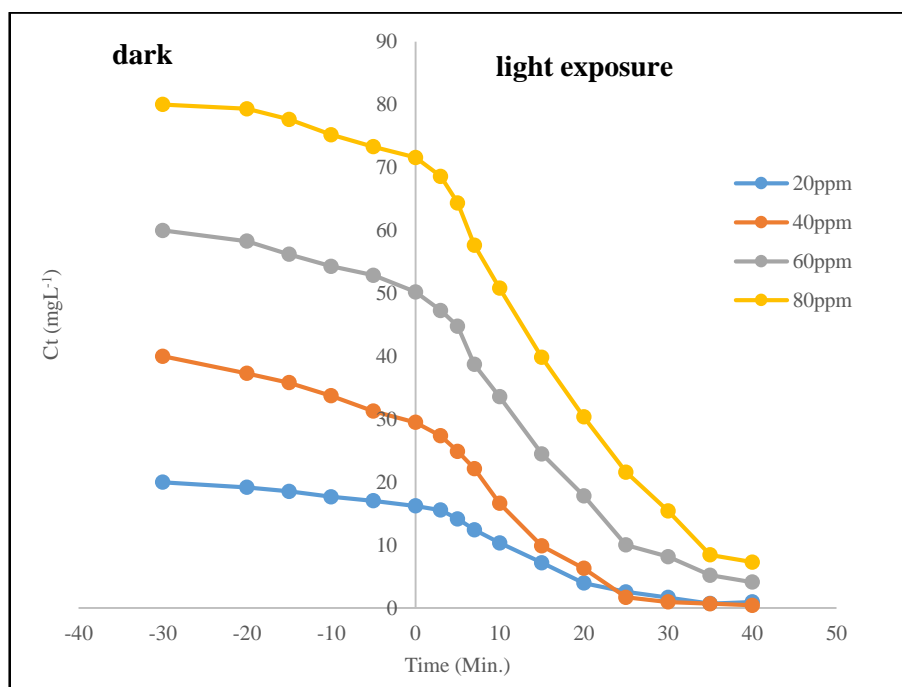


Figure 4.8(b): Variation of dye concentration versus time for different CV initial concentration. (Experimental condition: $[\text{Ba}_{0.6}\text{K}_{0.4}\text{BiO}_3] = 0.75\text{gL}^{-1}$ at initial $\text{pH}=6.0$, $\text{Temp.}=308\text{K}$).

Keeping the rate expression with respect to initial concentration given in **equation 4.12 to 4.14** in mind, graphs are plotted between $\ln C_t/C_0$ and time.

The plot of $\ln C_t/C_0$ versus t with different initial concentration of CV is shown in **Figure 4.9(b)**. The figure shows that the photocatalytic degradation follows perfectly the pseudo-first order kinetic with respect to CV concentrations.

It is found that a plot between $\ln C_t/C_0$ versus time represents a straight line, the slope of linear regression equals the apparent first order rate constant K_{app} which is consistent with the reported first order reaction [69].

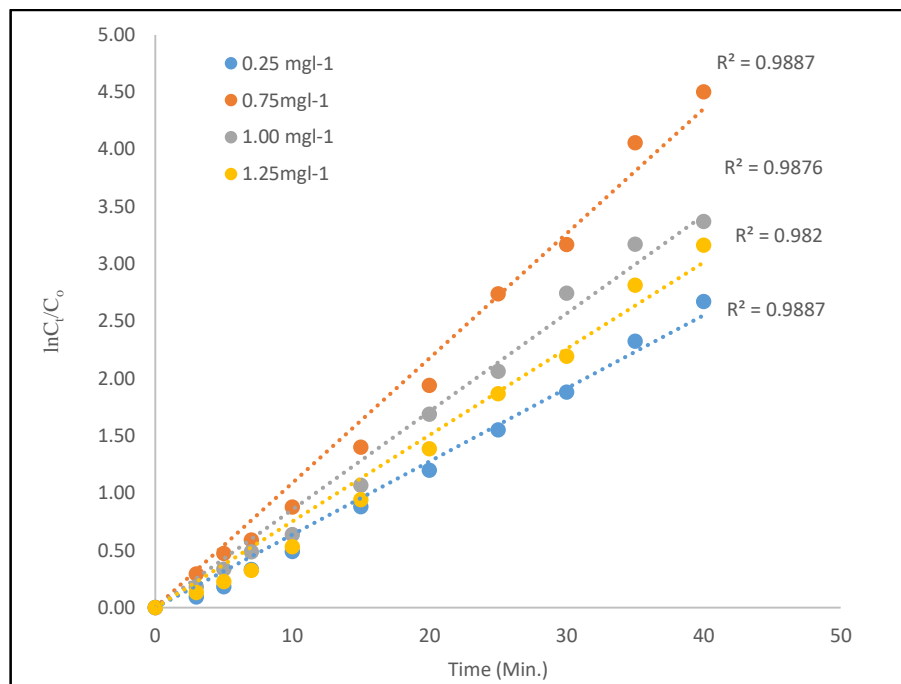


Figure 4.9(b): Linear variation of $\ln C_t/C_0$ versus time for photocatalytic degradation of CV at different initial dye concentration.

The values of rate constants K_{app} , which corresponds to different initial concentration, along with the initial rate (r_0) and corresponding regression constants, are listed in **Table 4.7 (b)**.

Table 4.7 (b): Pseudo-first order apparent constant values for the different initial dye concentration of dye
(Experimental condition: $[Ba_{0.6}K_{0.4}BiO_3] = 0.75g/L$; $pH = 6.0$; $Temp. = 308K$)

S. No.	Initial concentration (mgL^{-1})	Rate constant K_{app} (min^{-1})	Initial rate $r_0 \times 10^{-3}$ ($mgL^{-1}min^{-1}$)	R^2
1	20	0.785	1.57	0.99
2	40	0.113	4.52	0.988
3	60	0.0665	3.96	0.994
4	80	0.0413	3.28	0.985

The rate of degradation increases with the initial concentration of CV dye then finds a tendency towards independent values with the higher initial concentrations.

According to equation 4.9, the plot of $1/r_0$ against $1/C_0$ as shown in **Figure 4.10(b)** gives linear relationship between $1/r_0$ and $1/C_0$ confirming the Langmuir-Hinshelwood relationship for the initial rate of photodegradation. The values of K_r

and K_{LH} calculated from the slope ($1/K_r$) and intercept ($1/K_r \cdot K_{LH}$) of the above figure are found to be, $7.14 \text{ mgL}^{-1}\text{min}^{-1}$ and 1.5 Lmg^{-1} , respectively.

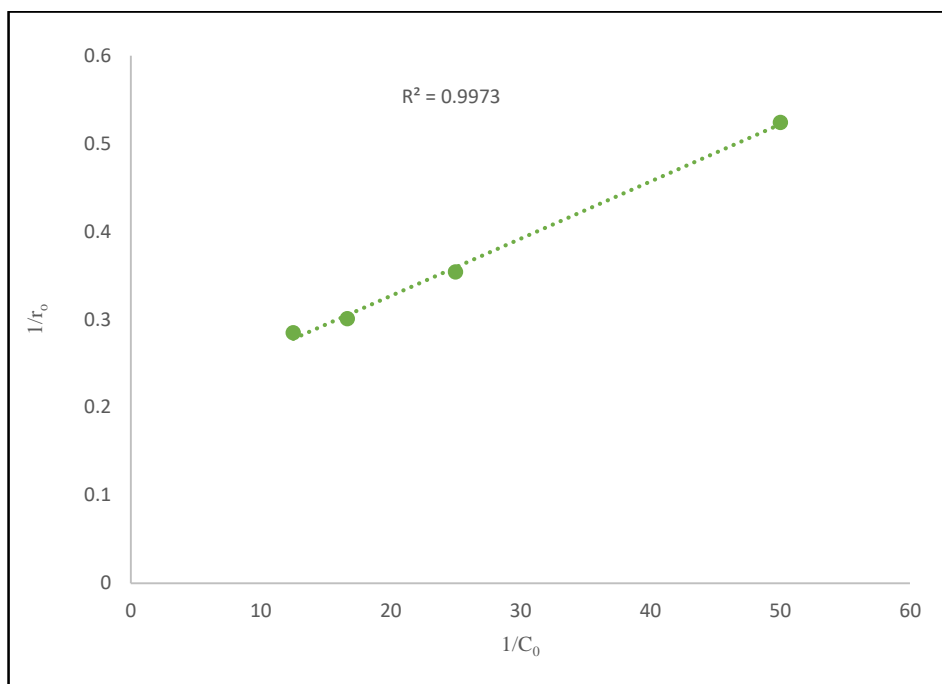


Figure-4.10 (b): Langmuir-Hinshelwood plot for visible light photodegradation of CV dye by $Ba_{0.6}K_{0.4}BiO_3$. (Experimental condition: $[Ba_{0.6}K_{0.4}BiO_3] = 0.75 \text{ gL}^{-1}$; $pH = 6.0$ Temp. = 308 K).

Here, for both the catalysts adsorption equilibrium constant i.e. K_{LH} obtained from the linearization of inverse of initial rate ($1/r_0$) and initial concentration ($1/C_0$), is different to the constant obtained from the dark adsorption (b). This is due to the photo adsorption and very rapid photoreaction of the dyes on the catalyst surface. These results are consistent with the earlier studies on photodegradation of dyes [70].

4.3.4.2 Effect of catalyst dose on photocatalytic degradation of CV

The optimization of catalyst dose is an important issue that is significant for avoiding the use of excessive catalyst and ensuring the maximum absorption of photon light. Hence, a series of experiments is carried out by varying the amount of both the catalysts from 0.25 to 1.25 gL^{-1} at $pH 6.0$ and 40 mgL^{-1} CV dye concentration at 308 K . The degradation is studied till the maximum degradation is achieved.

It is observed that for both the cases, up to 0.75 gL^{-1} doses of photocatalysts, degradation rate increases and then with further increase in dose, the rate decreases. The enhancement of removal rate may be due to the increase in the availability of active sites on the surface of the photocatalysts, which in turn increases the adsorption of dye species and, hence, the proportion of the excited species by the incoming photons. Larger amount of the catalyst favours the degradation efficiency due to the generation of free radicals O_2° and OH° . Therefore, the rate of degradation increases with the increase of catalysts from 0.25 to 0.75 gL^{-1} . A further increase in catalyst dose beyond the optimum will result in non-uniform light intensity distribution, so that the reaction rate would, indeed, be lowered with increased catalyst dosage. The tendency toward agglomeration (particle-particle interaction) increases at high solids concentration, resulting in a reduction in surface area available for light absorption and hence a drop in photocatalytic degradation rate. Although the number of active sites in solution will increase with catalyst dose, a point will be appeared to reach where light penetration is to be compromised because of excessive particle concentration. Thus, the trade-off between these two opposing phenomena results in an optimum catalyst dose for the photocatalytic reaction [71,72] Since the maximum degradation of CV dye is observed with 0.75 gL^{-1} , the other experiments are performed using the same catalyst dose. Similar results have been obtained in the earlier reports on photodegradation of dyes [66,73-76]. The corresponding results with both the catalysts (BaBiO_3 and $\text{Ba}_{0.6}\text{K}_{0.4}\text{BiO}_3$) have been elaborated below:

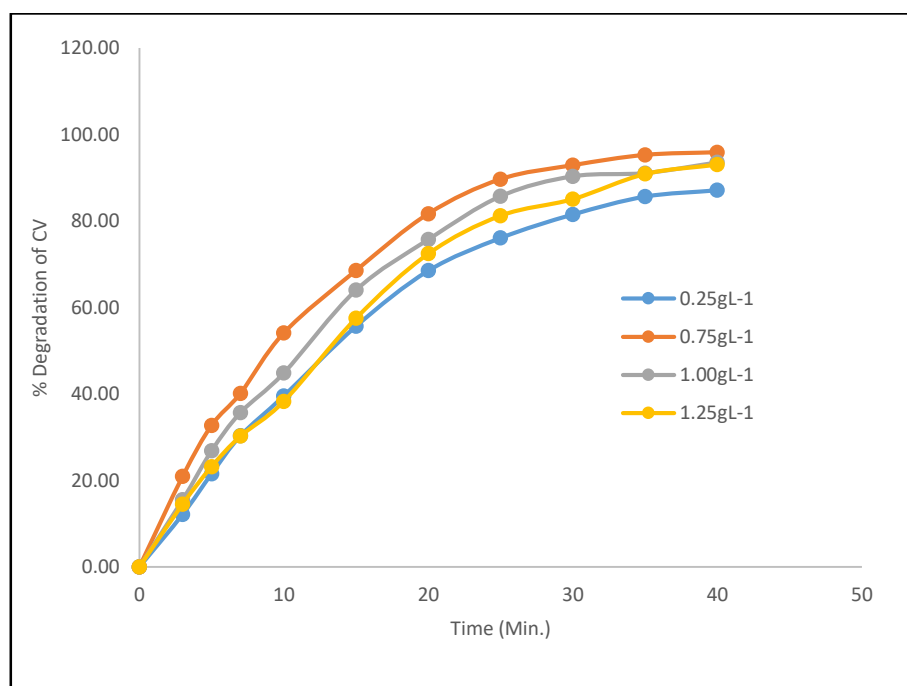
(a) Results with BaBiO_3

A series of experiments is carried out by varying the amount of catalyst from 0.25 to 1.25 gL^{-1} at pH 6.0 and 40 mgL^{-1} CV dye concentration. The degradation is studied till the maximum degradation is achieved.

Table 4.8 (a) shows the influence of the catalyst dose on the % photodegradation of CV under visible light irradiation and the corresponding graphs is shown in **Figure 4.11(a)**.

Table 4.8 (a): Influence of BaBiO₃ dose on degradation of CV(Experimental Conditions: [CV] = 40mgL⁻¹; pH=6.0; Temp. =308K)

Catalyst dose	0.25gL ⁻¹	0.75gL ⁻¹	1.00gL ⁻¹	1.25gL ⁻¹
Time (min)	% Degradation	% Degradation	% Degradation	% Degradation
0	0.00	0.00	0.00	0.00
3	12.20	20.98	15.56	14.57
5	21.58	32.75	26.88	23.22
7	30.36	40.17	35.72	30.28
10	39.58	54.12	44.88	38.34
15	55.70	68.57	64.06	57.55
20	68.54	81.69	75.74	72.47
25	76.10	89.67	85.75	81.26
30	81.54	92.89	90.36	85.10
35	85.67	95.27	91.11	90.90
40	87.14	95.89	93.57	93.06
∞	87.25	96.91	93.61	93.08

**Figure 4.11(a): Influence of BaBiO₃ dose on visible light degradation of CV dye.**
(Experimental condition: [CV] = 40mgL⁻¹pH=6, Temp. =308K)

The photodegradation kinetics at different catalyst loading is illustrated in **Figure 4.12(a)**, which depicts the dark adsorption-desorption equilibrium and the additional decrease in CV concentration caused by visible light irradiation.

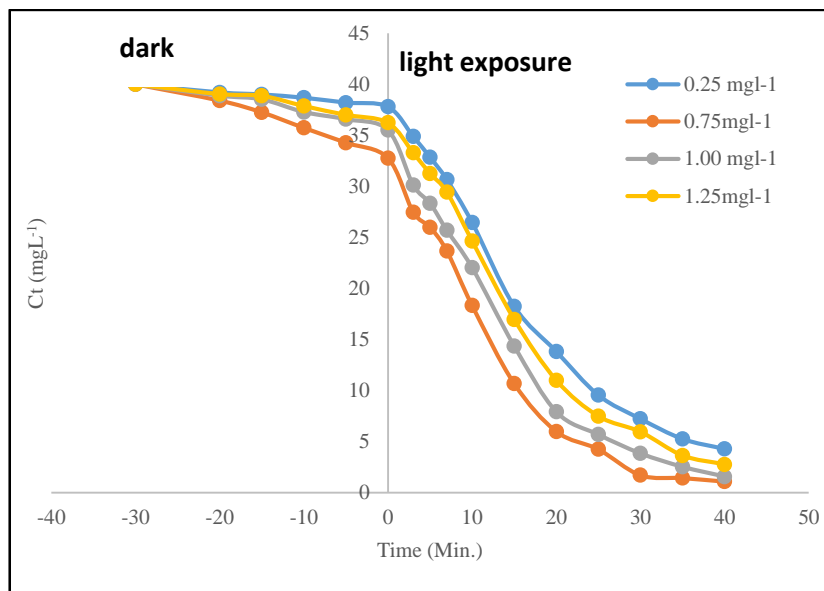


Figure 4.12(a): Variation of residual dye concentration at different BaBiO_3 . (Experimental conditions: $[\text{CV}] = 40 \text{ mgL}^{-1}$, $\text{pH}=6.0$, $\text{Temp.} = 308\text{K}$).

For the calculation of the rate constant (K_{app}) the logarithm of remaining concentration of CV is fitted to the Langmuir Hinshelwood kinetic model (given by **equation 4.11**) by plotting $\ln C_t/C_0$ against the irradiation time at different catalyst dose, which has been shown in **Figure 4.13(a)**.

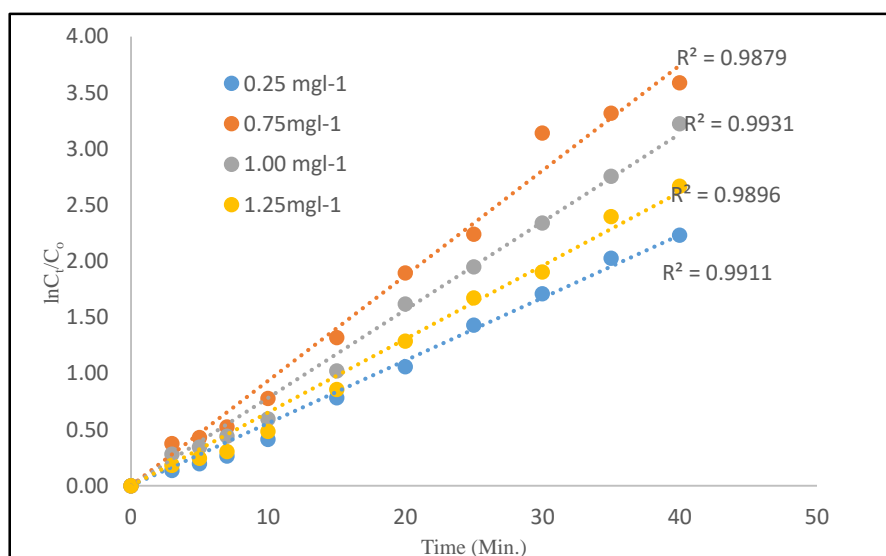


Figure 4.13(a): Linear variation of $\ln C_t/C_0$ versus time for photocatalytic degradation of CV dye at different BaBiO_3 loading. (Experimental condition: $[\text{CV}] = 40\text{mgL}^{-1}$; $\text{pH}=6.0$; $\text{Temp.} = 308\text{K}$).

The pseudo-first-order rate constants, K_{app} (Min^{-1}), are calculated from the slopes of the above **Figure 4.13(a)** and are listed in **Table 4.9(a)**.

Table 4.9(a): Pseudo-first order apparent constant values for the different BaBiO_3 dose (Experimental condition: $[\text{CV}] = 40\text{mgL}^{-1}$; $\text{pH} = 6.0$; $\text{Temp.} = 308\text{K}$)

S.No.	Catalyst Dose (gL^{-1})	Rate Constant K_{app} (min^{-1})	R^2
1	0.25	0.0558	0.991
2	0.75	0.0935	0.988
3	1.00	0.0783	0.993
4	1.25	0.0653	0.989

An empirical relationship between the catalyst dose and initial dye concentration has been reported by Galindo et al ($r_0 \propto [\text{catalyst}]^n [\text{dye}]$), where n is an exponent less than 1 for all the dyes studied relative to low concentration of catalyst. [29]

Figure 4.14(a) shows the log-log plots of rate constant against the catalyst dose which results in a straight line with a slope of 0.62 (equal to reaction order with respect to photocatalyst and intercept of -2.29. {**Figure 4.14(a)**} thus the initial degradation rate can be expressed by **equation 4.15**.

$$r_0 \propto [\text{BaBiO}_3]^{0.62} [\text{CV}] \quad \text{--- (4.15)}$$

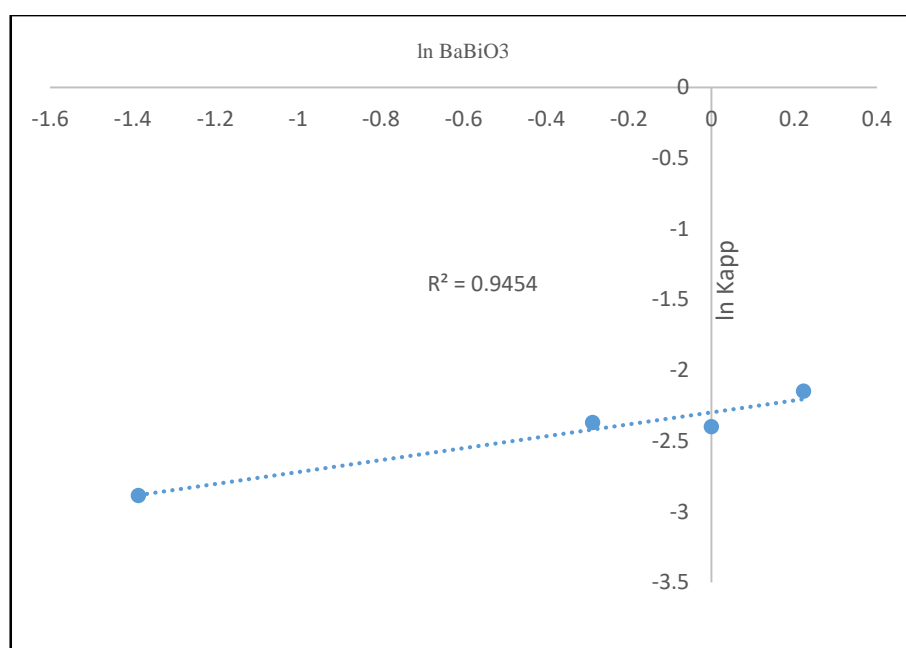


Figure 4.14(a): Relationship between $\ln K_{app}$ and the amount of BaBiO_3 . (Experimental condition: $[\text{CV}] = 40\text{mgL}^{-1}$; $\text{pH} = 6.0$; $\text{Temp.} = 308\text{K}$).

(b) Results with Ba_{0.6}K_{0.4}BiO₃

The catalyst loading was varied from 0.25gL⁻¹ to 1.5gL⁻¹ with an initial dye concentration of 40mgL⁻¹, initial pH 6.0 at 308K. The degradation is studied till the maximum degradation is achieved. **Table 4.8(b)** shows the influence of the catalyst dose on the % photodegradation of CV under visible light irradiation and the corresponding graphs is shown in **Figure 4.11(b)**.

Table 4.8 (b): Influence of Ba_{0.6}K_{0.4}BiO₃ dose on degradation of CV (Experimental Conditions: [CV] = 40mgL⁻¹; pH=6.0; Temp. =308K)

Catalyst dose	0.25gL ⁻¹	0.75gL ⁻¹	1.00gL ⁻¹	1.25gL ⁻¹
Time (min)	% Degradation	% Degradation	% Degradation	% Degradation
0	0.00	0.0	0.00	0.00
3	10.42	25.59	22.06	17.89
5	21.13	37.73	30.39	28.98
7	30.21	44.59	38.50	32.29
10	41.26	58.42	47.25	41.30
15	58.61	75.35	65.62	61.08
20	69.87	84.24	81.51	75.03
25	78.78	95.73	87.28	84.55
30	84.78	97.60	93.57	88.85
35	90.24	98.27	95.81	94.01
40	93.09	98.89	96.57	95.78
∞	93.10	98.90	96.60	95.98

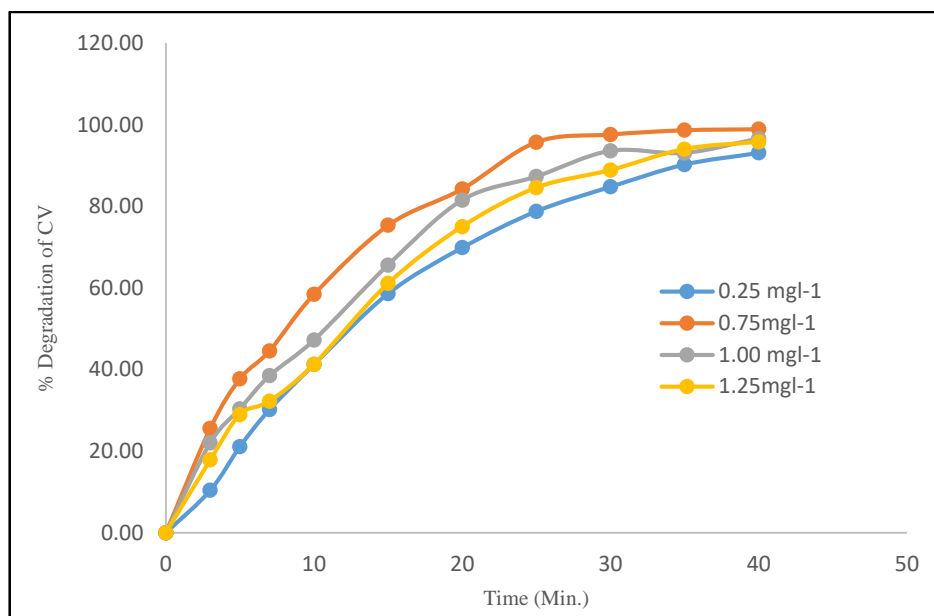


Figure 4.11(b): Influence of $Ba_{0.6}K_{0.4}BiO_3$ dose on visible light degradation of CV dye. (Experimental condition: $[CV] = 40\text{mgL}^{-1}$; $pH=6.0$; $Temp. = 308\text{K}$).

The photodegradation kinetics at different catalyst loading is illustrated in **Figure 4.12(b)**, which depicts the dark adsorption-desorption equilibrium and the additional decrease in CV concentration caused by visible light irradiation.

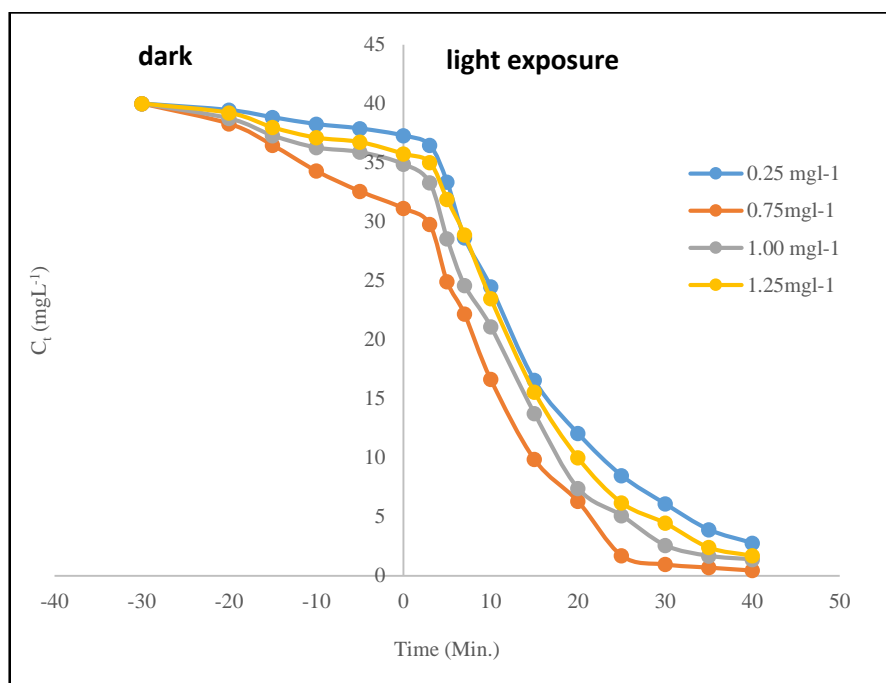


Figure 4.12(b): Variation of residual dye concentration at different $Ba_{0.6}K_{0.4}BiO_3$. (Experimental conditions: $[CV] = 40\text{mgL}^{-1}$ $pH=6.0$, $Temp. = 308\text{K}$).

For the calculation of the rate constant (K_{app}) the logarithm of remaining concentration of CV is fitted to the Langmuir Hinshelwood kinetic model by plotting $\ln C_t/C_0$ against the irradiation time at different catalyst dose, which has been shown in **Figure 4.13(b)**.

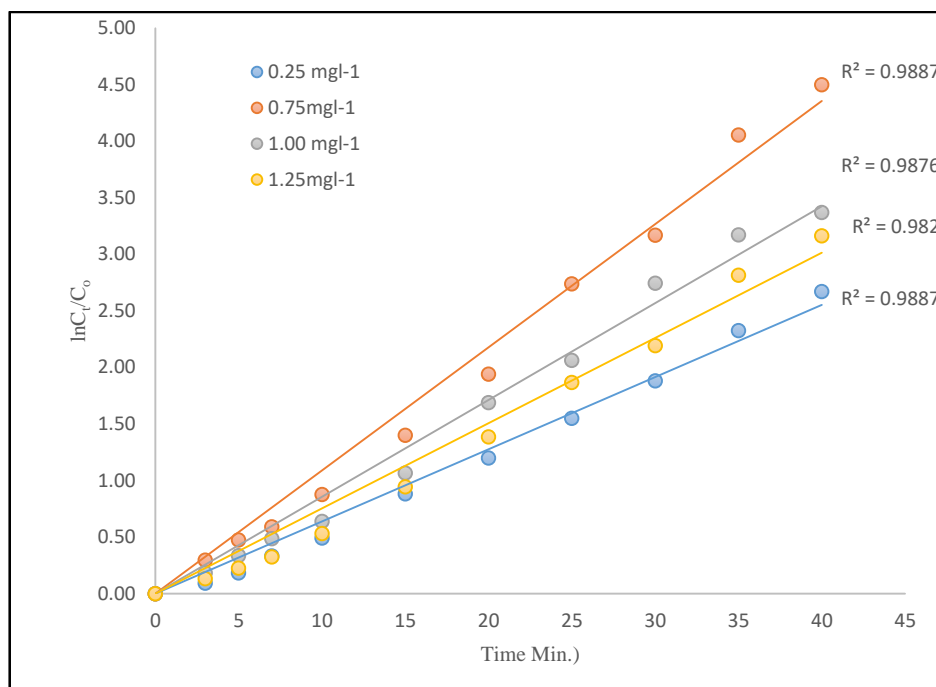


Figure 4.13(b): Linear variation of $\ln C_t/C_0$ versus time for photocatalytic degradation of CV dye at different $Ba_{0.6}K_{0.4}BiO_3$ loading (Experimental condition: $[CV] = 40\text{mgL}^{-1}$; $\text{pH}=6.0$; $\text{Temp.} = 308\text{K}$).

The pseudo-first-order rate constants, K_{app} (min^{-1}), are calculated from the slopes of the above **Figure 4.13(b)** and are listed in **Table 4.9(b)**.

Table 4.9 (b): Pseudo-first order apparent constant values for the different $Ba_{0.6}K_{0.4}BiO_3$ dose (Experimental condition: $[CV] = 40\text{mgL}^{-1}$; $\text{pH}=6.0$; $\text{Temp.} = 308\text{K}$)

S.No.	Catalyst Dose gL^{-1}	Rate Constant K_{app} (min^{-1})	R^2
1	0.25	0.0638	0.988
2	0.75	0.1089	0.988
3	1.00	0.0856	0.987
4	1.25	0.0754	0.982

Also, an empirical relationship between the initial dye concentration has been reported by Galindo et al ($r_0 a [\text{catalyst}]^n [\text{dye}]$), where n is an exponent less than 1 for all the dyes studied relative to low concentration of catalyst. [29]

Figure 4.14(b) shows the log-log plots of rate constant against the catalyst dose which results in a straight line with a slope of 0.82 (equal to reaction order with respect to photocatalyst) and intercept of -1.84. **{Figure 4.14(b)}** thus the initial degradation rate can be expressed by **equation 4.16**.

$$r_0 \propto [\text{Ba}_{0.6}\text{K}_{0.4}\text{BiO}_3]^{0.82} [\text{CV}] \quad \text{--- (4.16)}$$

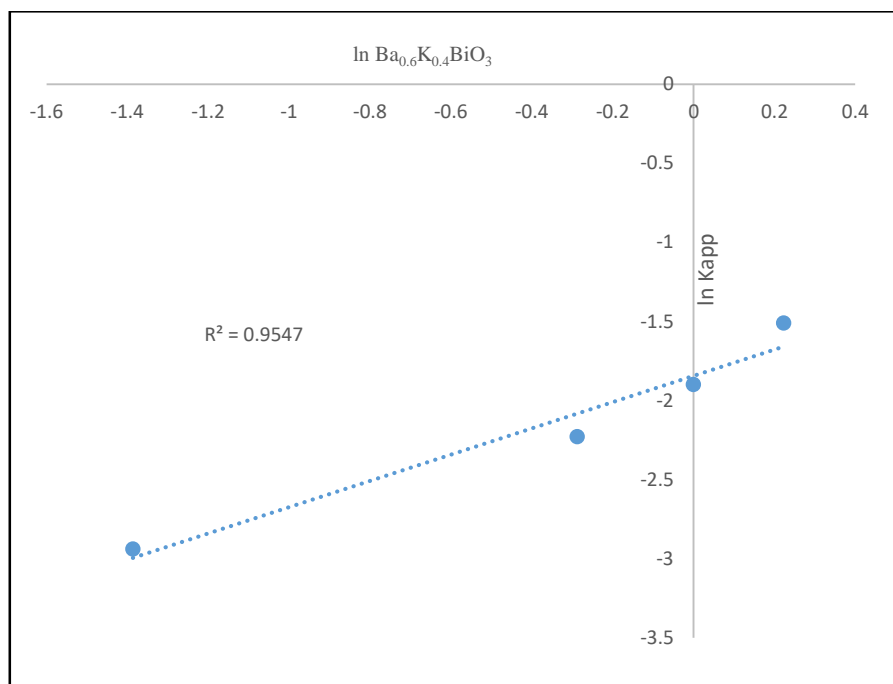


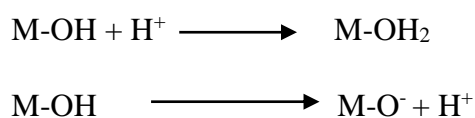
Figure 4.14(b): Relationship between $\ln K_{app}$ and the amount of $\text{Ba}_{0.6}\text{K}_{0.4}\text{BiO}_3$. (Experimental condition: $[\text{CV}] = 40\text{mgL}^{-1}$; $\text{pH} = 6.0$; $\text{Temp.} = 308\text{K}$).

From the experimental results, it was observed that the increase in catalyst dose from 0.25gL^{-1} to 0.75gL^{-1} increased the rate and with further increase in the catalyst dose the reaction rate decreases which is the characteristics of heterogeneous photocatalysis and results are in a good agreement with the earlier studies [77,78]. In order to have a better dye removal efficiency, we used 0.75gL^{-1} BaBiO_3 or $\text{Ba}_{0.6}\text{K}_{0.4}\text{BiO}_3$ suspension concentration for the rest of the experimental runs. The photocatalytic destruction of other organic pollutants has also exhibited the same dependency over the catalyst dose [79,80].

4.3.4.3 Effect of initial pH on photocatalytic degradation of CV dye

Organic compounds in wastewater differ greatly in several parameters, particularly in their speciation behaviour, solubility in water and hydrophobicity. While some compounds are uncharged at common pH conditions typical of natural water or wastewater, other compounds exhibit a wide variation in speciation (or charge) and physico-chemical properties. Besides, because of the amphoteric behaviour of most semiconductor oxides, an important parameter governing the rate of reaction taking place on semiconductor particle surfaces is the pH of the dispersions [73,81,82]. Since, pH influences the surface-charge-properties of the photocatalysts; therefore, the effect of pH on the rate of degradation needs to be considered. The interpretation of pH effects on the efficiency of the photocatalytic degradation process is a very difficult task because of its multiple roles. Most significantly, it is related to the acid base property of the metal-oxide surface as explained above on the basis of their amphoteric nature [83,84].

In the present research work also, both the catalysts despite having status of p-type (BaBiO_3) and n-type ($\text{Ba}_{0.6}\text{K}_{0.4}\text{BiO}_3$) semiconductors are supposed to be electrically neutral, making them amphoteric in nature [85]. It is known that the metal oxide particles suspended in water behave similarly to diprotic acids. The adsorption of water molecules at sacrificial metal sites is followed by the dissociation of OH^- charged groups leading to coverage with chemically equivalent metal hydroxyl group (M-OH) due to amphoteric behaviour of most metal hydroxides, the following 2 equilibrium reactions are considered [86]:



Experiments are carried out at pH values in the range of 4.0-8.0, using 40mgL^{-1} CV solution and 0.75gL^{-1} BaBiO_3 dose. For CV, the extent of photocatalysis increases with increase in pH up to 6.0 and with further increase in pH the degradation efficiency decreases. An increase in the rate of degradation with increase in the pH is due to the generation of more OH^- ions. These ions loose an

electron to the hole generated at the semiconductor surface and OH[•] free radicals are formed. These formed free radicals cause oxidation of the dye. On further increase in pH above 6.0, a decrease is observed because at very high pH, CV becomes negatively charged and so it repels negatively charged OH⁻ ions. This repulsive force does not allow the approach of OH⁻ ions to the surface of catalyst and free radical generation is retarded. Similar results have been obtained in the earlier reports of photodegradation of dyes by semiconductor photocatalysts [87,88].

(a) Results with BaBiO₃

The influence of the initial pH of the solution on the % photocatalytic degradation of CV is depicted in **Table 4.10 (a)** and corresponding graphs are shown in **Figure 4.15(a)**.

Table 4.10 (a): Influence of solution pH on degradation of CV
(Experimental Conditions: [CV]=40mgL⁻¹; [BaBiO₃]=0.75 gL⁻¹; Temp.=308K)

pH	pH=4.0	pH=5.0	pH=6.0	pH =7.0	pH = 8.0
Time (min)	% Degradation				
0	0.00	0.00	0.00	0.00	0
3	11.40	14.14	20.98	19.79	16.03
5	18.86	22.72	32.75	28.71	26.15
7	28.73	30.21	38.71	35.91	33.15
10	43.39	45.15	54.12	51.44	47.60
15	62.87	66.25	73.27	70.94	69.50
20	72.01	73.39	83.09	79.28	75.98
25	86.12	87.77	94.41	90.48	88.84
30	89.71	90.73	95.68	94.56	93.43
35	84.91	87.79	96.38	93.03	90.90
40	88.50	91.49	97.24	93.95	92.88
∞	88.61	91.56	97.35	93.98	92.90

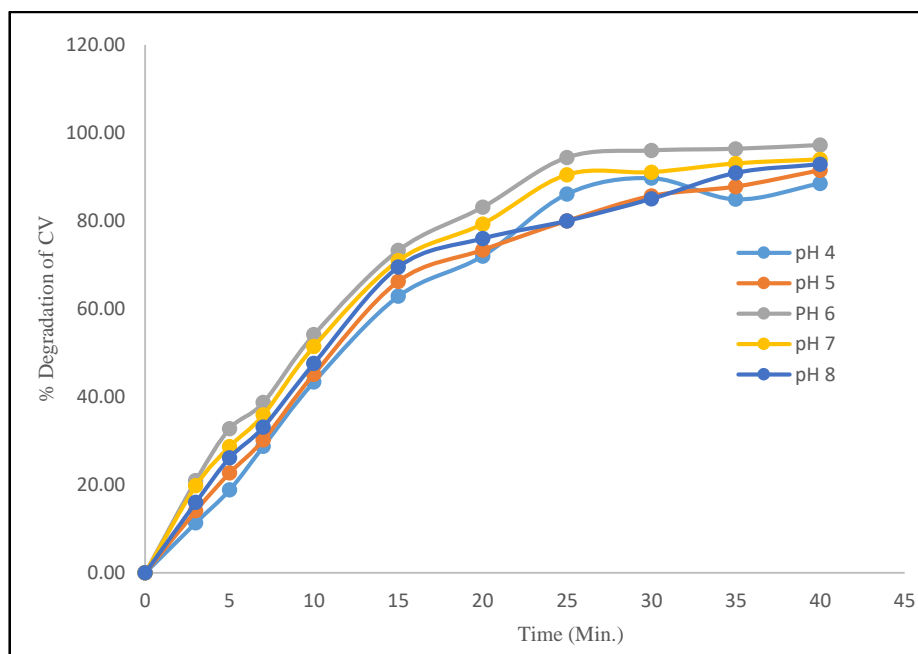


Figure 4.15(a): Effect of initial pH on % degradation of CV. (Experimental condition: $[CV] = 40 \text{ mg L}^{-1}$; $[BaBiO_3] = 0.75 \text{ g L}^{-1}$; Temp. = 308 K).

The photodegradation kinetics of different pH loading is illustrated in **Figure 4.16(a)**, which depicts the dark adsorption-desorption equilibrium and the additional decrease in CV concentration caused by visible light irradiation

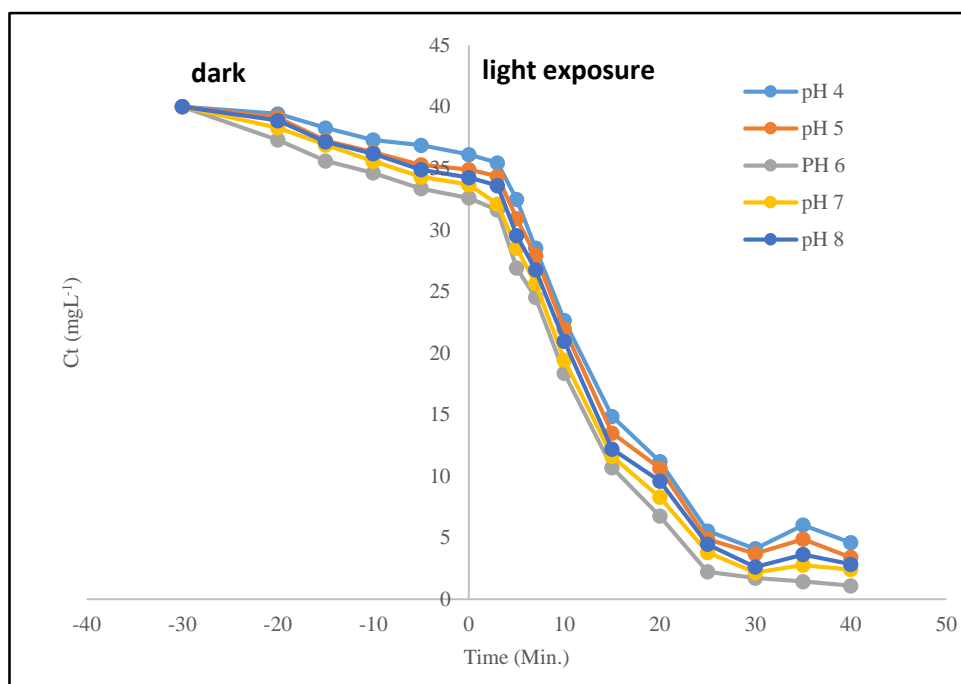


Figure 4.16 (a) Effect of pH on the residual dye concentration. (Experimental conditions: $[CV] = 40 \text{ mg L}^{-1}$; $[BaBiO_3] = 0.75 \text{ g L}^{-1}$; Temp. = 308 K).

The photocatalytic degradation of CV under a wide range of pH values was fitted to the Langmuir-Hinshelwood model by plotting $\ln(C_t/C_0)$ versus irradiation time which has been shown in **Figure 4.17(a)**.

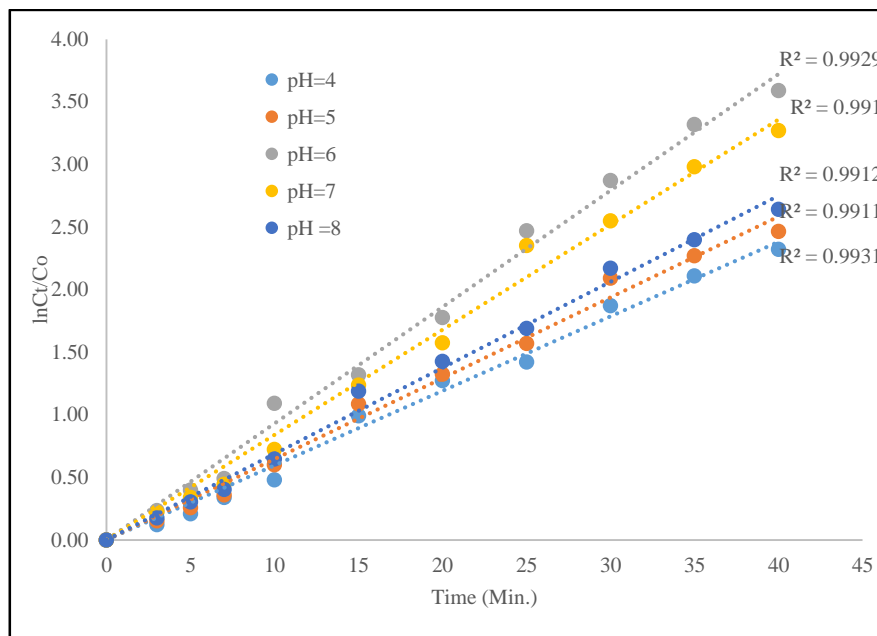


Figure 4.17 (a) Linear variation of $\ln C_t/C_0$ versus time for photocatalytic degradation of CV dye at different initial solution pH. (Experimental condition: $[CV] = 40\text{mgL}^{-1}$; $[\text{BaBiO}_3] = 0.75\text{gL}^{-1}$; $\text{Temp.} = 308\text{ K}$).

The pseudo-first-order rate constant, K_{app} (min^{-1}), are calculated from the slopes of the plots {**Figure 4.17(a)**} and are presented in **Table 4.11(a)**.

Table 4.11(a): Pseudo-first order apparent constant values for the photodegradation of CV at different solution pH (Experimental condition: $[CV] = 40\text{mgL}^{-1}$; $[\text{BaBiO}_3] = 0.75\text{gL}^{-1}$ $\text{Temp.} = 308\text{ K}$)

S. No.	pH	Rate Constant $K_{\text{app.}} (\text{min}^{-1})$	R^2
1	4.0	0.0595	0.991
2	5.0	0.0646	0.991
3	6.0	0.0931	0.993
4	7.0	0.0840	0.991
5	8.0	0.0687	0.993

The pseudo-first-order rate constant (K_{app}) values of dye degradation obtained by performing photodegradation reactions under different initial pH are reported in **Figure 4.18(a)**. These K_{app} values indicate that the highest degradation is achieved at neutral pH i.e. pH 6.0.

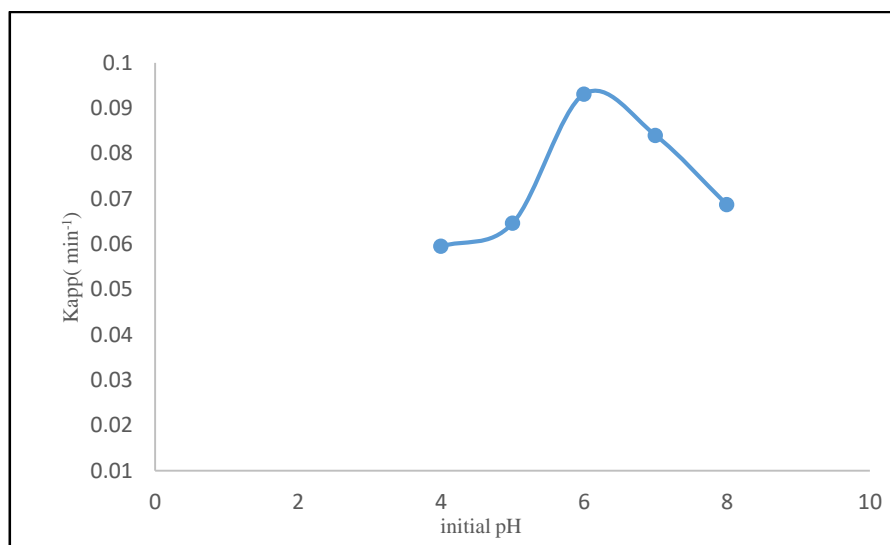


Figure 4.18 (a) Effect of the pH on the reaction rate constant for CV dye degradation (Experimental condition: [CV] = 40mgL⁻¹; [BaBiO₃] = 0.75gL⁻¹; Temp.= 308K).

(b) Results with Ba_{0.6}K_{0.4}BiO₃

The influence of the initial pH of the solution on the % photocatalytic degradation of CV is depicted in **Table 4.10(b)** and corresponding graphs are shown in **Figure 4.15(b)**. For CV dye degradation, the extent of photocatalysis increases with increase in pH up to 6.0 and with further increase in pH the degradation efficiency decreases.

Table 4.10(b): Effect of solution pH on degradation of CV
(Experimental Conditions: [CV]= 40mgL⁻¹; [Ba_{0.6}K_{0.4}BiO₃] = 0.75gL⁻¹;Temp.= 308K)

pH	pH=4.0	pH =5.0	pH=6.0	pH=7.0	pH = 8.0
Time (min)	% Degradation				
0	0.00	0.00	0	0.00	0
3	16.87	18.44	25.59	23.42	21.25
5	30.05	31.70	37.73	35.96	34.19
7	36.95	39.29	44.59	43.38	42.17
10	48.05	50.08	58.42	55.61	52.80
15	67.23	69.59	75.35	73.54	71.74
20	75.63	77.89	84.24	82.21	80.17
25	87.02	89.07	95.73	93.79	91.86
30	90.92	93.29	97.60	96.53	95.47
35	88.55	90.83	98.27	95.74	93.22
40	91.43	92.96	98.89	97.37	95.86
∞	91.50	92.99	98.99	97.42	95.90

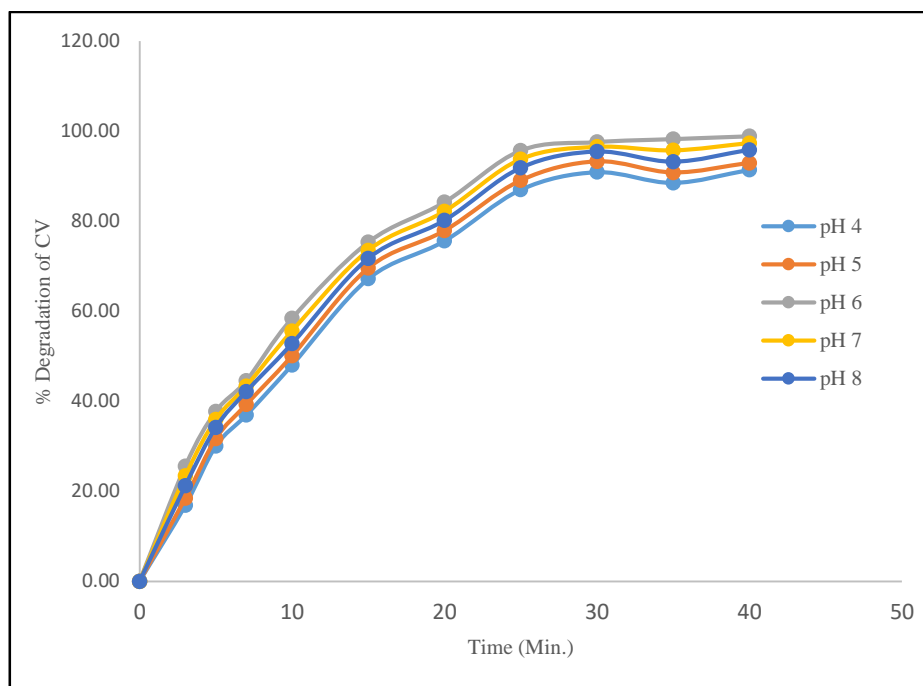


Figure 4.15 (b) Influence of solution pH on % degradation of CV. (Experimental condition: $[CV] = 40 \text{ mg L}^{-1}$, $[Ba_{0.6}K_{0.4}BiO_3] = 0.75 \text{ g L}^{-1}$, Temp. = 308K).

The photodegradation kinetics of different pH loading is illustrated in **Figure 4.16(b)**, which depicts the dark adsorption-desorption equilibrium and the additional decrease in CV concentration caused by visible light irradiation.

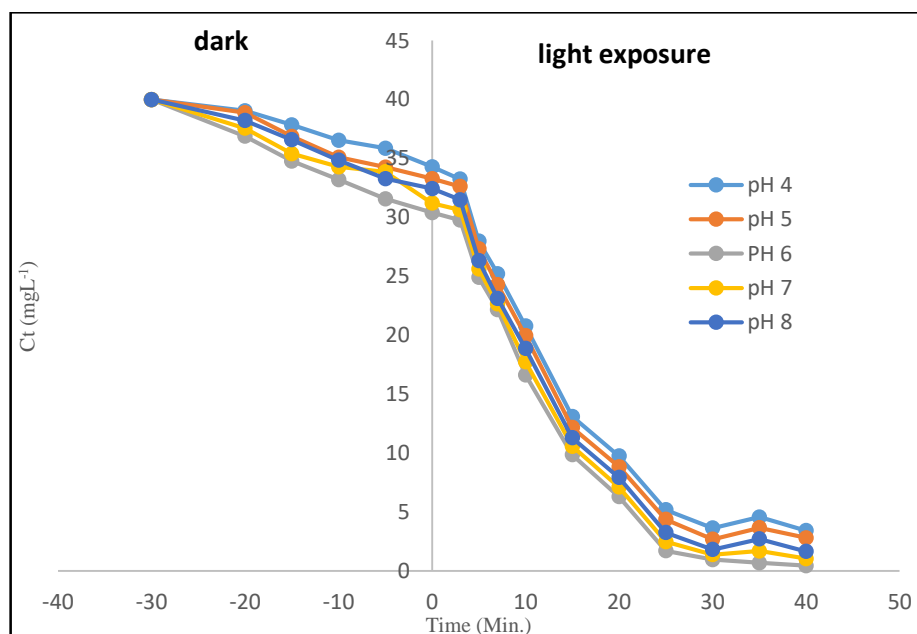


Figure 4.16 (b) Effects of solution pH on the residual dye fractions. (Experimental conditions: $[CV] = 40 \text{ mg L}^{-1}$; $[Ba_{0.6}K_{0.4}BiO_3] = 0.75 \text{ g L}^{-1}$ Temp. = 308K).

A plot between $\ln(C_t/C_0)$ versus irradiation time (t) was fitted to the Langmuir–Hinshelwood model. The pseudo-first-order rate constants, K_{app} (min^{-1}), are calculated from the slopes of the plots { **Figure 4.17(b)** }.

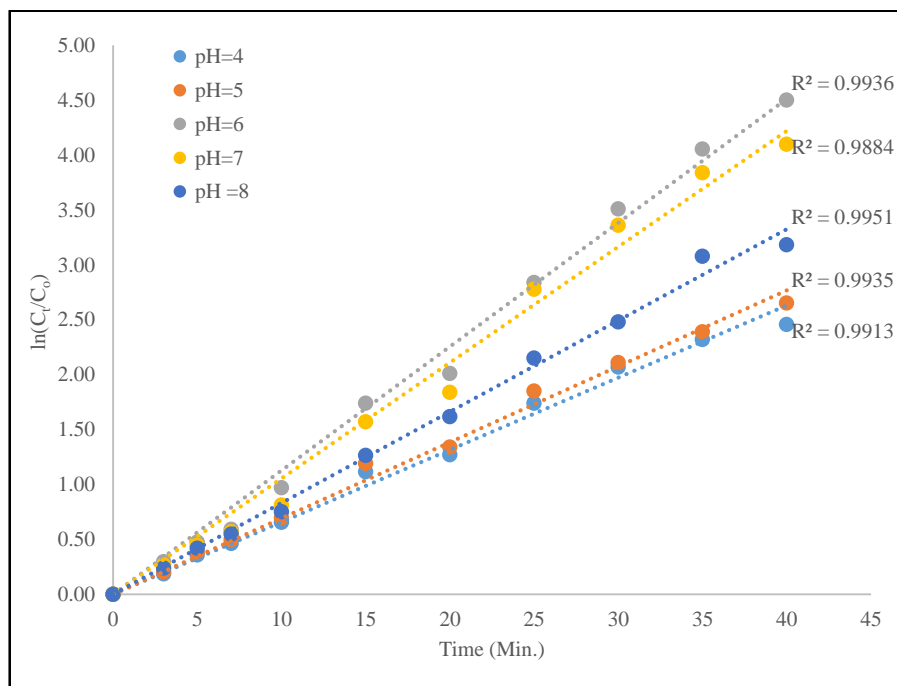


Figure 4.17 (b) Linear variation of $\ln C_t/C_0$ versus time for photocatalytic degradation of CV dye at different initial pH. (Experimental condition: $[CV] = 40\text{mgL}^{-1}$; $[Ba_{0.6}K_{0.4}BiO_3] = 0.75\text{gL}^{-1}$; Temp. = 308K)

The pseudo-first-order rate constant, K_{app} (min^{-1}), are calculated from the slopes of the plots { **Figure 4.17(b)** } and are presented in **Table 4.11(b)**.

Table 4.11(b): Pseudo-first order apparent constant values for the photodegradation of CV at different solution pH (Experimental condition: $[CV] = 40\text{mgL}^{-1}$; $[Ba_{0.6}K_{0.4}BiO_3] = 0.75\text{gL}^{-1}$; Temp. = 308K).

S.No.	pH	Rate Constant K_{app} (min^{-1})	R^2
1	4.0	0.0658	0.991
2	5.0	0.0692	0.993
3	6.0	0.1128	0.993
4	7.0	0.1055	0.988
5	8.0	0.0831	0.995

The pseudo-first-order rate constant (K_{app}) values of dye degradation obtained by performing photodegradation reactions under different initial pH are

reported in **Figure 4.18(b)**. These K_{app} values indicate that the highest degradation is achieved at neutral pH i.e. pH 6.0.

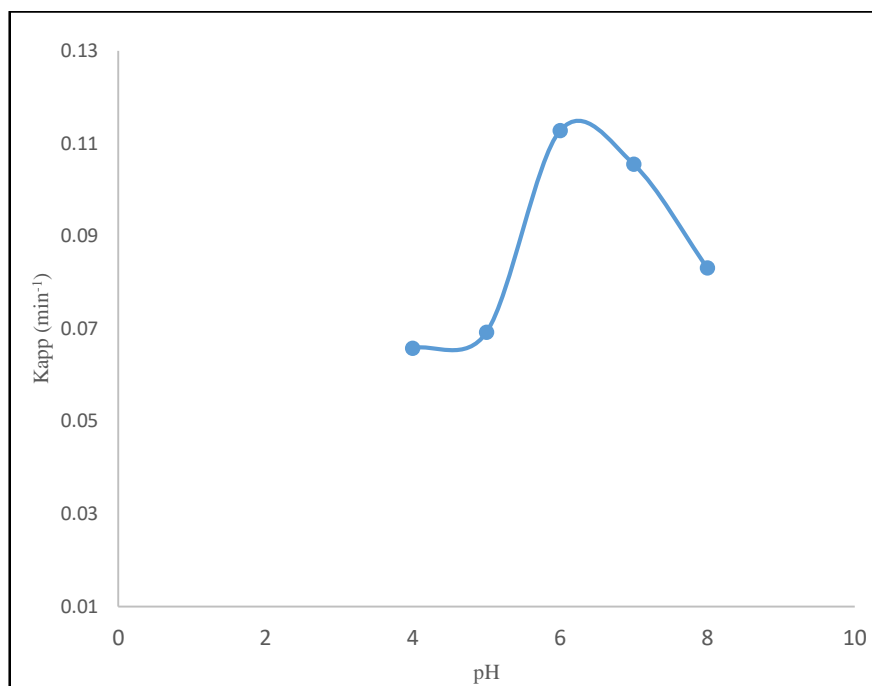


Figure 4.18(b) Effect of the initial pH on the reaction rate constant for CV dye degradation (Experimental condition: $[CV] = 40\text{mgL}^{-1}$; $[Ba_{0.6}K_{0.4}BiO_3] = 0.75\text{gL}^{-1}$; Temp. = 308K).

4.3.4.4 Effect of temperature on photocatalytic degradation of CV dye

Generally, photocatalysis is not temperature dependent. However, an increase in temperature can affect the amount of adsorption and helped the reaction to complete more efficiently with e^-h^+ recombination [72,89]. An increase in temperature helps the reaction to compete more efficiently with e^-/h^+ recombination as a result of increased collision frequency of molecules; leading to an enhancement of the degradation activity [90]. Several previous research work indicate that the rate of the photocatalytic degradation is temperature dependent and is favoured with the increase of solution temperature [91,92]. The apparent activation energy (E_a) has been calculated from the **Arrhenius equation** [93]:

$$K_{app} = A \exp \left[-\frac{E_a}{RT} \right] \quad \text{--- (4.17)}$$

Where, A is a temperature independent factor (min^{-1}), E_a is the apparent activation energy of the photocatalytic degradation (J/mol), R is the gas constant (8.31 J/K mol) and T is the solution temperature. The linear transform of $\ln(K_{\text{app}}) = f(1/T)$, gives a straight line whose slope is equal to $-E_a/R$.

The effect of temperature was investigated by studying the photocatalytic degradation at different solution temperatures (298-308 K) under the same operating conditions i.e. $[\text{CV}] = 40\text{mgL}^{-1}$; Catalyst dose = 0.75gL^{-1} and initial $\text{pH}=6.0$.

(a) Results with BaBiO_3

The influence of solution temperature on the % photodegradation of CV dye as a function of time is depicted in **Table 4.12(a)** and the corresponding graph is shown in **Figure 4.19(a)**. The figure indicates that the rate of the photocatalytic degradation is temperature dependent and is favoured with the increase of solution temperature.

Table 4.12(a): Influence of temperature on degradation of CV
(Experimental condition: $[\text{CV}] = 40\text{mgL}^{-1}$; $[\text{BaBiO}_3] = 0.75\text{gL}^{-1}$; Temp.=308K).

Temperature	298K	303K	308K
Time (min)	%Degradation	%Degradation	%Degradation
0	0.00	0.00	0.00
3	12.32	15.69	20.98
5	17.37	26.59	32.75
7	24.80	32.93	38.71
10	39.64	48.85	54.12
15	63.69	66.84	73.27
20	72.38	76.61	83.09
25	77.74	88.44	94.41
30	76.54	89.31	95.68
35	78.94	89.90	96.38
40	79.54	91.95	97.24
∞	79.80	92.05	97.34

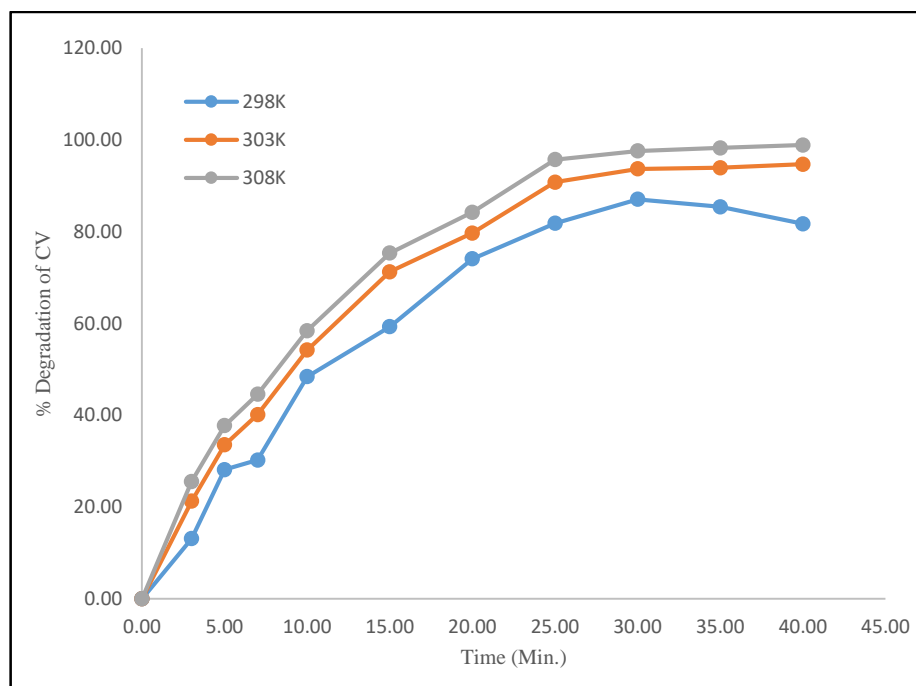


Figure 4.19 (a) Influence of temperature on % degradation of CV. (Experimental condition: $[CV] = 40 \text{ mg L}^{-1}$, $[BaBiO_3] = 0.75 \text{ g L}^{-1}$, $pH=6.0$).

The photodegradation kinetics at different temperature is illustrated in **Figure 4.20(a)**, which depicts the dark adsorption-desorption equilibrium and the additional decrease in CV concentration caused by visible light irradiation.

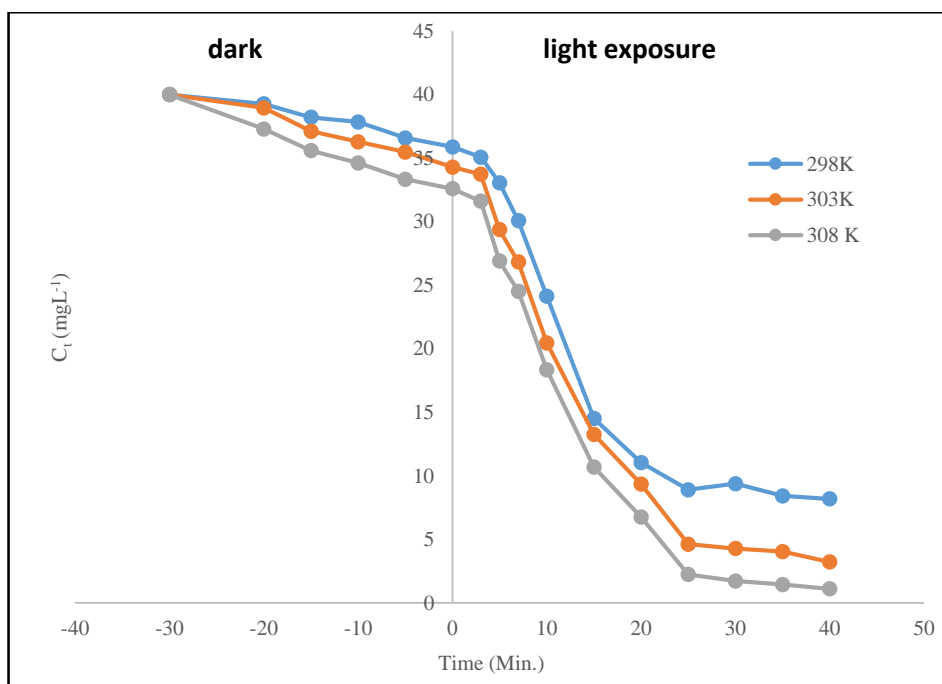


Figure 4.20(a) Effects of Temperature on the residual dye fractions. (Experimental conditions: $[CV] = 40 \text{ mg L}^{-1}$; $[BaBiO_3] = 0.75 \text{ g L}^{-1}$; $pH=6.0$).

The photodegradation of CV dye at different temperature was fitted to Langmuir Hinshelwood model by plotting $\ln C_t/C_0$ versus time, which has been shown in **Figure 4.21(a)**.

The pseudo-first-order rate constants, K_{app} (min^{-1}), are calculated from the slopes obtained by the curves plotted between $\ln C_t/C_0$ and irradiation time at different temperatures { **Figure 4.21(a)** } and are presented in **Table 4.13(a)**.

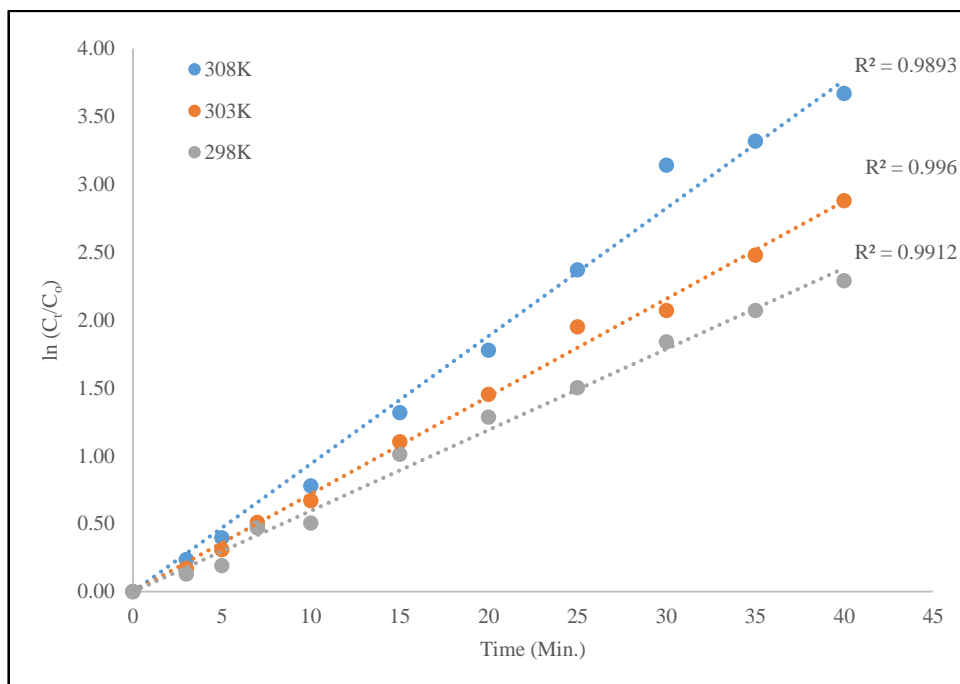


Figure 4.21 (a) Linear variation of $\ln C_t/C_0$ versus time for photocatalytic degradation of CV dye at different temperature. (Experimental condition: $[CV] = 40 \text{ mg L}^{-1}$, $[BaBiO_3] = 0.75 \text{ g L}^{-1}$, $pH=6.0$).

Table 4.13(a): Pseudo-first order apparent constant values for the different temperatures.

Experimental condition: $[CV] = 40 \text{ mg L}^{-1}$; $[Ba_{0.6}K_{0.4}BiO_3] = 0.75 \text{ g L}^{-1}$; $pH = 6.0$

S. No.	Temperature (K)	Rate Constant K_{app} (Min^{-1})	R^2
1	298	0.0596	0.991
2	303	0.0719	0.996
3	308	0.0942	0.989

Figure 4.22(a) shows the plot of $\ln K_{app}$ versus Temperature, gives a linear relationship whose slope gives the apparent activation energy which equals to $34.89 \text{ kJ mol}^{-1}$. This apparent energy represents the total activation energy of both adsorption and photocatalytic degradation of dye. [59,89].

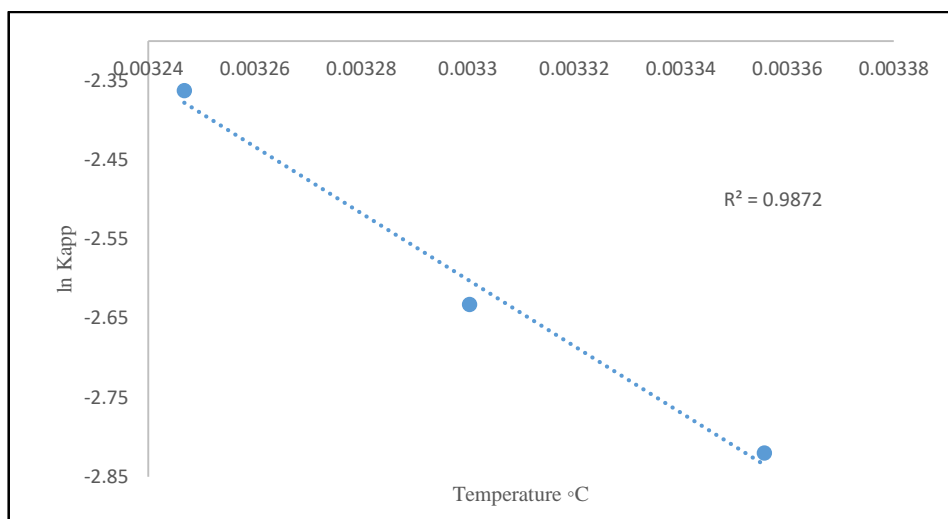


Figure 4.22 (a): Plot of $\ln K_{app}$ versus inverse of temperature (Experimental condition: $[CV] = 40 \text{ mg L}^{-1}$; $[BaBiO_3] = 0.75 \text{ g L}^{-1}$; $pH = 6.0$).

(b) Results with $Ba_{0.6}K_{0.4}BiO_3$

The influence of solution temperature on the % photodegradation of CV dye as a function of time is depicted in **Table 4.12(b)** and the corresponding graphs is shown in **Figure 4.19(b)**. The figure indicates that the rate of the photocatalytic degradation is temperature dependent and is favoured with the increase of solution temperature.

Table 4.12(b): Influence of temperature on degradation of CV (Experimental conditions: $[CV] = 40 \text{ mg L}^{-1}$; $[Ba_{0.6}K_{0.4}BiO_3] = 0.75 \text{ g L}^{-1}$; $pH=6.0$)

Temperature	298K	303K	308K
Time (min)	%Degradation	%Degradation	%Degradation
0	0.00	0.00	0.00
3	13.12	21.27	25.59
5	28.14	33.55	37.73
7	30.25	40.14	44.59
10	48.41	54.23	58.42
15	59.29	71.26	75.35
20	74.10	79.71	84.24
25	81.84	90.81	95.73
30	87.09	93.69	97.60
35	85.43	93.94	98.27
40	81.72	94.71	98.89
∞	82.07	94.85	98.95

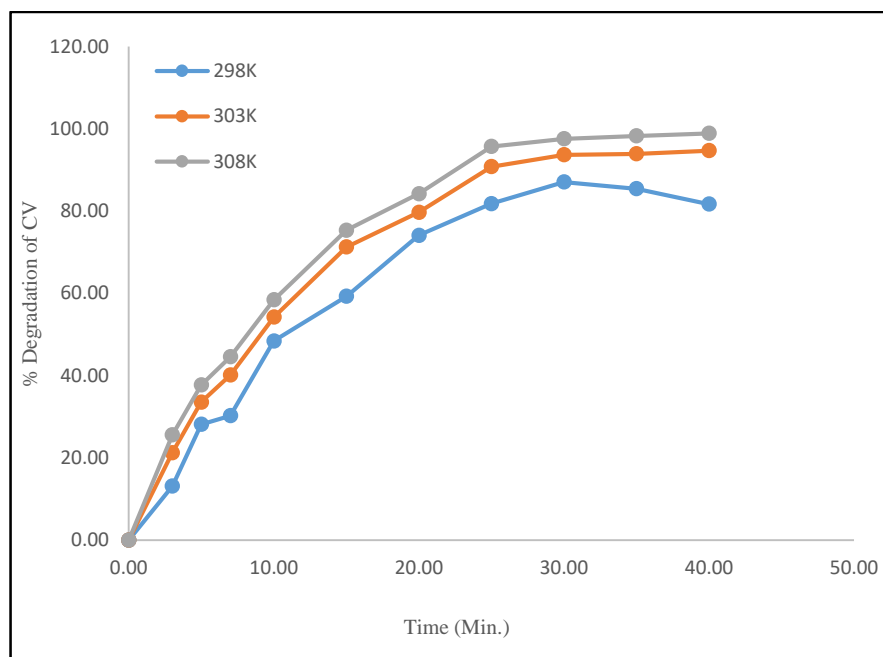


Figure 4.19(b): Influence of temperature on % degradation of CV. (Experimental condition: $[CV] = 40 \text{ mg L}^{-1}$, $[B_{0.6}K_{0.4}BiO_3] = 0.75 \text{ g L}^{-1}$, $pH = 6.0$).

The photodegradation kinetics at different temperature is illustrated in **Figure 4.20(b)**, which depicts the dark adsorption-desorption equilibrium and the additional decrease in CV concentration caused by visible light irradiation.

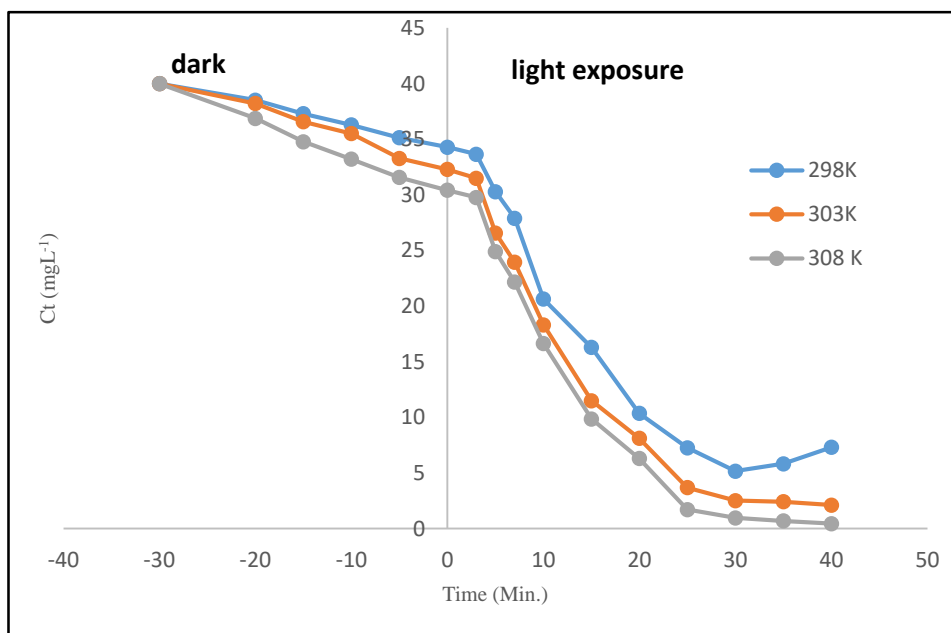


Figure 4.20(b): Variation of CV dye concentration versus time at different temperature. (Experimental condition: $[CV] = 40 \text{ mg L}^{-1}$, $[Ba_{0.6}K_{0.4}BiO_3] = 0.75 \text{ g L}^{-1}$; $pH = 6.0$).

The photodegradation of CV dye at different temperature was fitted to Langmuir Hinshelwood model by plotting $\ln C_t/C_0$ versus time, which has been shown in **Figure 4.21(b)**. The pseudo-first-order rate constants, K_{app} (min^{-1}), are calculated from the slopes obtained by the curves plotted between $\ln C_t/C_0$ and irradiation time at different temperatures { **Figure 4.21(b)** } and are presented in **Table 4.13(b)**.

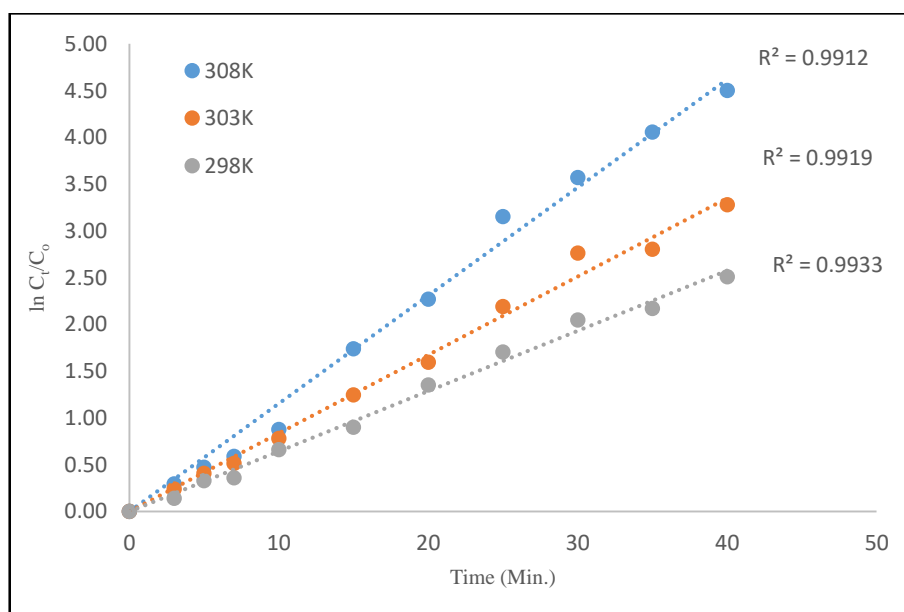


Figure 4.21 (b): Linear variation of $\ln C_t/C_0$ versus time for photocatalytic degradation of CV dye at different temperature. (Experimental condition: $[CV] = 40 \text{ mg L}^{-1}$, $[Ba_{0.6}K_{0.4}BiO_3] = 0.75 \text{ g L}^{-1}$; $\text{pH}=6.0$).

Table 4.13(b): Pseudo-first order apparent constant values for the different temperatures.

(Experimental condition: $[CV] = 40 \text{ mg L}^{-1}$; $[Ba_{0.6}K_{0.4}BiO_3] = 0.75 \text{ g L}^{-1}$; $\text{pH} = 6.0$)

S. No.	Temperature (K)	Rate Constant K_{app} (Min^{-1})	R^2
1	298	0.0644	0.993
2	303	0.0837	0.991
3	308	0.1150	0.991

Figure 4.22(b) shows the plot of $\ln K_{app}$ versus Temperature, gives a linear relationship whose slope gives the apparent activation energy equals to $44.55 \text{ kJ mol}^{-1}$. This apparent energy represents the total activation energy of both adsorption and photocatalytic degradation of dye [59].

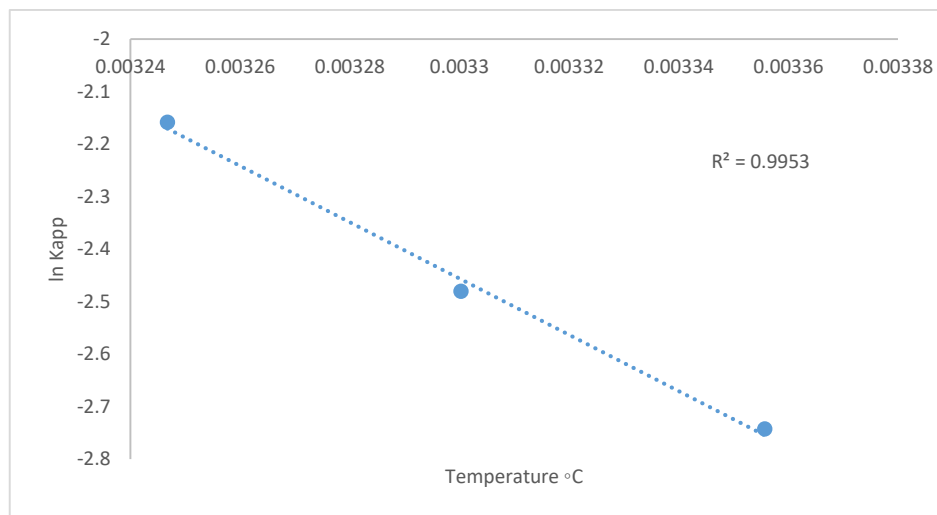


Figure 4.22 (b): Plot of $\ln K_{app}$ versus inverse of temperature (Experimental condition: $[CV] = 40 \text{ mg L}^{-1}$; $[Ba_{0.6}K_{0.4}BiO_3] = 0.75 \text{ g L}^{-1}$; $pH=6.0$).

4.3.4.5 Regeneration of photocatalysts

Photocatalysis is a clean technology, which normally does not involve any waste disposal problem. The catalyst can be recycled. The economy of the photocatalytic process depends upon how many times a catalyst can be reused without sacrificing its efficiency and the type of regeneration it requires [93].

To evaluate the stability of the as prepared, three recycling experiments are performed. The used catalyst was regenerated by treating it with boiling distilled water till a colourless filtrate was obtained and then by drying it in a hot air oven at a temperature of 90° to 100°C . After this, the catalyst was heated in a muffle furnace at about 500°C . As shown in **Figure 4.23**, after being used 3 times for CV dye degradation, the % degradation of dye declined from 95.74% to 93.12 for $BaBiO_3$ and 98.89 to 95.01% for $Ba_{0.6}K_{0.4}BiO_3$ under the same experimental condition. ($[CV] = 40 \text{ mg L}^{-1}$, $[Ba_{0.6}K_{0.4}BiO_3/BaBiO_3] = 0.75 \text{ g L}^{-1}$, $pH=6.0$, $Temp.=308\text{K}$).

These results indicate that as prepared catalyst is photo-stable during the photocatalytic degradation. The slight decrease in the efficiency of the recycled catalyst may be attributed to the deposition of photo-insensitive hydroxides on the catalyst surface, blocking its active sites [73].

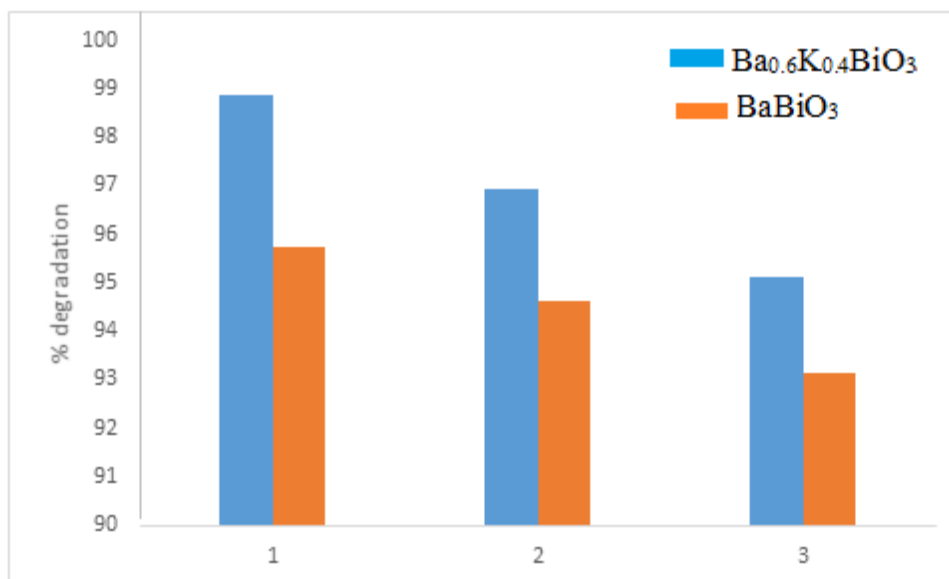


Figure 4.23: Regeneration of photocatalyst. (Experimental condition: $[CV] = 40 \text{ mg mL}^{-1}$, $[Ba_{0.6}K_{0.4}BiO_3]/[BaBiO_3] = 0.75 \text{ g L}^{-1}$, $pH = 6.0$, $Temp. = 308 \text{ K}$).

4.4 Comparison of BaBiO₃ and Ba_{0.6}K_{0.4}BiO₃ with Degussa p-25 TiO₂

Effectiveness of BaBiO₃ and Ba_{0.6}K_{0.4}BiO₃ has been compared with commercially available Degussa p25 TiO₂ under above mentioned identical optimum experimental conditions (i.e. $[CV] = 40 \text{ mg L}^{-1}$, $[Catalysts] = 0.75 \text{ g L}^{-1}$, $pH = 6.0$, $Temperature = 308 \text{ K}$). As shown in **Figure 4.24**, photocatalytic degradation potential of the as synthesized photocatalysts is found to be much better than the commercially available TiO₂ owing to their much narrower band gap in comparison to the $\sim 3.2 \text{ eV}$ band gap of TiO₂ [94]. Also, Degussa p-25 adsorbs more CV dye than BaBiO₃ and Ba_{0.6}K_{0.4}BiO₃. As the amount of dye absorbed increases, thereby the active sites are covered with dye ions, thus decreases the formation of $^{\circ}\text{OH}$ ions which further decreases the degradation efficiency.

Thus, it proved the worth of this research work in the direction of tailoring new visible light active photocatalysts.

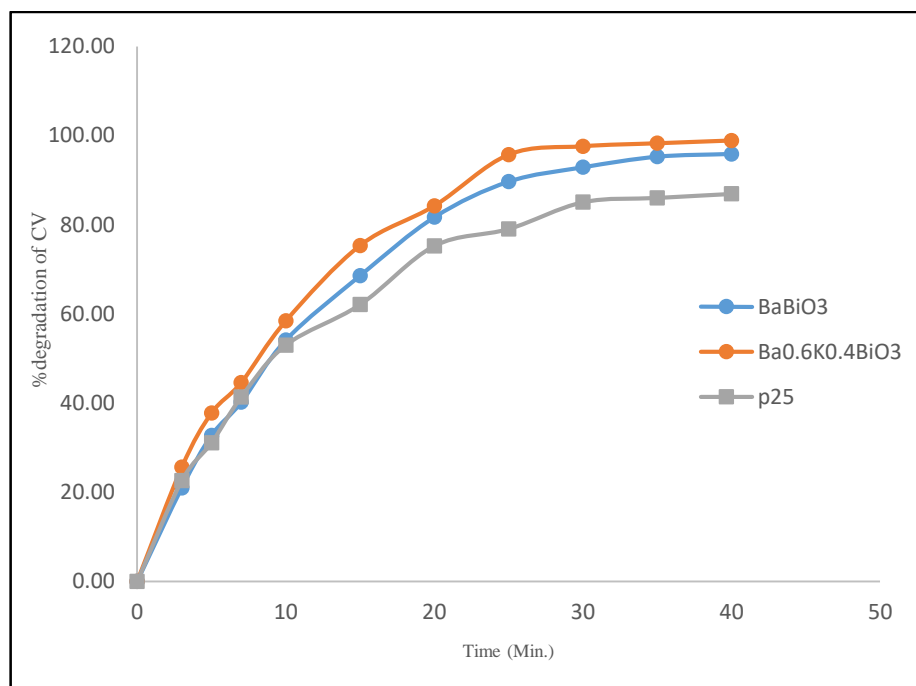


Figure 4.24: Comparison of photocatalytic efficiency of as prepared with p25 TiO₂ under visible light irradiation (Experimental condition: [CV] = 40 mg L⁻¹, [Ba_{0.6}K_{0.4}BiO₃] / [BaBiO₃] / [p25 TiO₂] = 0.75 g L⁻¹, pH = 6.0, Temp. = 308 K).

4.5 Visible spectral changes of CV dye

The degradation of CV dye is monitored by UV/vis. spectrophotometry. Figure 4.25 depicts the UV-vis spectrum of CV dye degradation in the presence of BaBiO₃, Ba_{0.6}K_{0.4}BiO₃ and p25TiO₂ under visible light irradiation. The rate of degradation is recorded with respect to the change in the intensity of absorption peak in visible light.

It can be seen by the **Figure 4.25** with all the catalysts, light irradiation leads to the prominent decrease in the characteristic band of CV dye at 590 nm after 40 minutes of visible light irradiation. This also indicates that CV dye has been effectively degraded by Ba_{0.6}K_{0.4}BiO₃ and BaBiO₃. The decrease in intensity of absorption peak is associated with the discoloration of the dye. The decrease in absorption peaks at 590 nm, indicates the removal of -N=N- bond chromophoric group from the azo dye. The almost disappearance of the peaks in the spectrum reveals that dye is eliminated in the presence of Ba_{0.6}K_{0.4}BiO₃ after 40 min of irradiation. The absorption spectra reveal no evidence of the existence of new intermediates or products formed in the visible region at the end of the reaction. It

is clear from the Figure 4.25 that the maximum degradation efficiency is shown by $\text{Ba}_{0.6}\text{K}_{0.4}\text{BiO}_3$ owing to its lowest band gap value (1.87eV) in comparison to BaBiO_3 (2.07eV) {as discussed in Chapter 3}. P-25TiO_2 has shown least degradation efficiency which is due to its highest band gap.

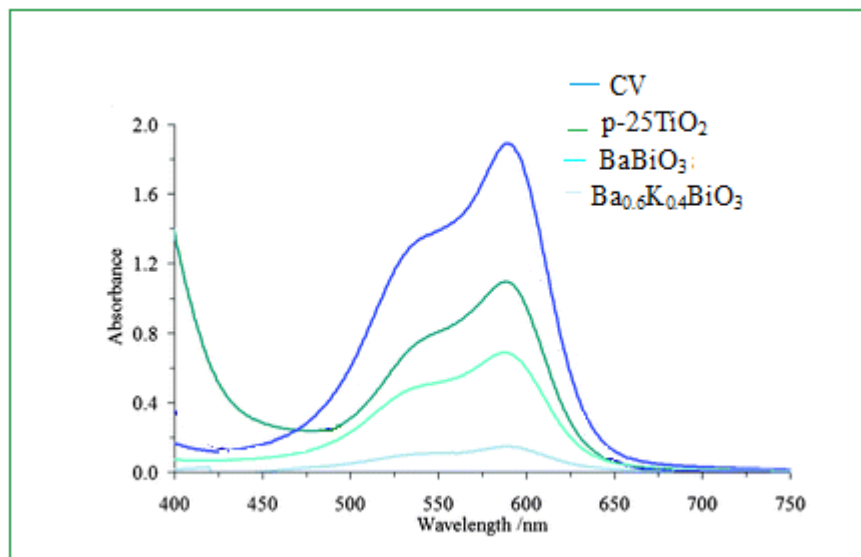


Figure 4.25: UV-vis absorbance spectra of CV solution after photocatalytic degradation over as prepared catalysts. Experimental Conditions: $[\text{CV}] = 40\text{mgL}^{-1}$; $[\text{Ba}_{0.6}\text{K}_{0.4}\text{BiO}_3] / [\text{BaBiO}_3] / [\text{p25TiO}_2] = 0.75\text{gL}^{-1}$, $\text{pH} = 6.0$, $\text{Temp.} = 308\text{K}$.

4.6 TOC analysis

The complete mineralization of the studied dye is confirmed from the analysis of total organic carbon (TOC) content. The CV dye degradation takes place through the oxidative cleavage of the chromophore $-\text{N}=\text{N}-$ bond resulting in the production of primary reaction by-products which are then oxidized and ultimately yielding carbon di oxide and water [95]. The TOC concentration is of importance as it is the best parameter to indicate the ultimate mineralization of the target compound. **Figure 4.26** shows the TOC reduction of CV dye by as prepared BaBiO_3 and $\text{Ba}_{0.6}\text{K}_{0.4}\text{BiO}_3$ at optimum reaction conditions. It can be seen that the % TOC removal values for $\text{Ba}_{0.6}\text{K}_{0.4}\text{BiO}_3$ is higher than BaBiO_3 . As shown in Figure 4.26, %TOC removal for photodegradation (following adsorption) in the presence of as prepared photocatalysts is higher than that obtained by the commercially available p25 TiO_2 , thus indicating the greater reactivity of synthesized photocatalysts (BaBiO_3 and $\text{Ba}_{0.6}\text{K}_{0.4}\text{BiO}_3$).

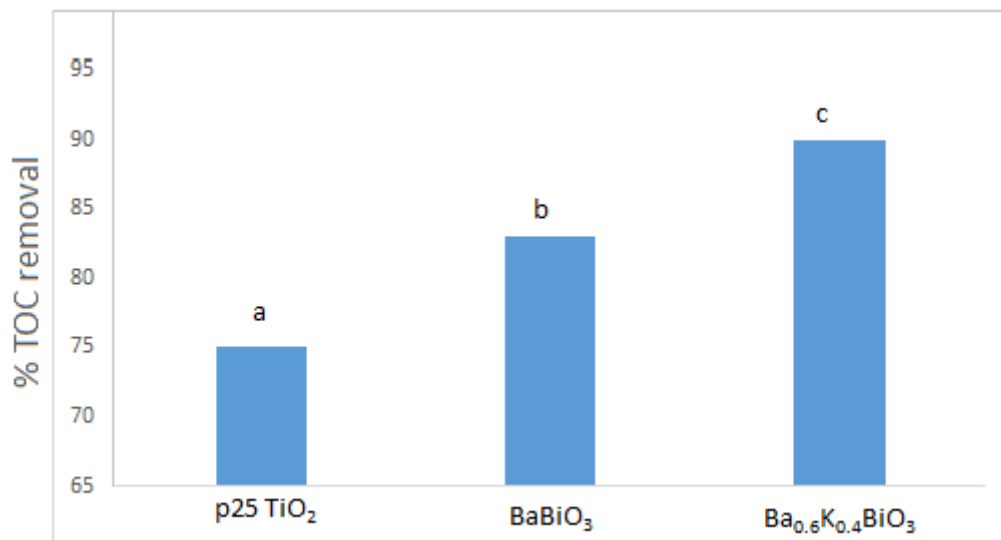


Figure 4.26: TOC removal in CV dye solution obtained by photodegradation by as prepared catalysts. (Experimental Conditions: [CV] = 40mgL⁻¹; catalyst dose=0.75gL⁻¹, pH=6.0, Temperature =308K). (a) for p25 TiO₂ (b) for BaBiO₃ (c) for Ba_{0.6}K_{0.4}BiO₃.

4.7 Proposed mechanism of CV dye photodegradation

Organic pollutants like dyestuffs have the ability to absorb visible light. Initially the dye molecules are adsorbed on catalyst surface and get excited through the absorption of light. Thus excited dye (Dye^{*}) injects an electron to the conduction band of the photocatalyst where it is scavenged by O₂ to form active oxygen radicals. The consequence of electron-ejection into the conduction band results in the charge separation and thus e-hole pairs are generated. Holes are generated in conduction band while e⁻ are generated in valance band. These electron-hole pair are responsible of generating other reactive species like [•]OH, HO₂, H₂O₂ and [•]O₂⁻. These active radicals carry out photodegradation or mineralization of organic compounds. Proposed mechanism of CV dye degradation by BaBiO₃ and Ba_{0.6}K_{0.4}BiO₃ under visible light irradiation is as follows:





$CV^{\circ} + HO_2^{\circ} / ^{\circ}OH / O_2^{\circ} \longrightarrow$ peroxyated or hydroxylated degraded or mineralized end products {CO₂, Nitrates, H₂O, Sulphates}

4.8 Conclusion

In summary, BaBiO₃ and Ba_{0.6}K_{0.4}BiO₃ successfully synthesized by Pechini method resulted in the formation of, mono phase crystalline nano-sized particles which proved their potential in visible light owing to their low band gap (2.07eV and 1.87eV respectively). The feasibility of adsorption and photocatalytic degradation of CV dye using BaBiO₃ and Ba_{0.6}K_{0.4}BiO₃ as in the form of aqueous suspension under visible light irradiation has been investigated. Since, the photocatalytic degradation is directly related to the adsorbed quantities of the pollutant, the adsorption properties of CV on to BaBiO₃ and Ba_{0.6}K_{0.4}BiO₃ are also discussed in terms of Langmuir and Freundlich adsorption isotherms. The photocatalytic degradation was expressed in terms of LH kinetic model, and the subsequent rate constants are also determined. The effect of different operational parameters such as initial dye concentration, catalyst dose, solution pH and temperature on the rate of photo degradation is studied. Moreover, reusability of these catalysts is studied. Furthermore, to estimate the degree of mineralization, measurements of total organic carbon has also been conducted In the present studies, the percentage removal of CV through photocatalytic degradation by BaBiO₃ and Ba_{0.6}K_{0.4}BiO₃ was also compared with the one through TiO₂ (Degussa P-25).

Controlled experiments (photolysis) demonstrated that both visible light and catalyst are needed for the effective destruction of dye. The data obtained from the adsorption experiments are fitted into Langmuir and Freundlich isotherms. They are found to be linear, indicating the formation of mono layer of adsorbate on the outer surface of adsorbent. Langmuir adsorption model is found to be fit for both the catalysts. Thus, obtained results argue that a slow adsorption is noticed on both the catalyst surface, followed by strong photocatalytic degradation.

The study of parameters influencing the degradation process allowed us to find the operating conditions for achieving the highest CV dye degradation rate. The optimization studies revealed the optimum operating conditions: pH value 6.0, catalyst concentration 0.75gL^{-1} , dye concentration 40mgL^{-1} .

The dependence of catalyst concentration on the reaction rate can be explained as $r_0 \propto [\text{BaBiO}_3]^{0.62} [\text{CV}]$ and $r_0 \propto [\text{Ba}_{0.6}\text{K}_{0.4}\text{BiO}_3]^{0.82} [\text{CV}]$ for BaBiO_3 and $\text{Ba}_{0.6}\text{K}_{0.4}\text{BiO}_3$, respectively, when the catalyst concentration is less than 1gL^{-1} .

The Langmuir–Hinshelwood kinetic model showed a good agreement for the initial rates of degradation with the appropriate reaction rate constant (K_r) and the substrate adsorption constant (K_{LH}) values. Here, $K_r = 6.90\text{mgL}^{-1}\text{min}^{-1}$ and $K_{LH} = 2.76\text{Lmg}^{-1}$ are found for BaBiO_3 while for $\text{Ba}_{0.6}\text{K}_{0.4}\text{BiO}_3$ they are: $K_r = 7.14\text{mgL}^{-1}\text{min}^{-1}$ and $K_{LH} = 1.5\text{Lmg}^{-1}$. The value of adsorption coefficient (K_{LH}) in kinetic model is found to be different to that found in dark (b) due to the photo-adsorption and very rapid photoreaction of CV dye on the catalyst surface.

The photocatalytic degradation was temperature dependent with apparent activation energy for CV dye of 34.89kJmol^{-1} and 44.55kJmol^{-1} while using BaBiO_3 and $\text{Ba}_{0.6}\text{K}_{0.4}\text{BiO}_3$ as photocatalyst, respectively.

Good reusability of our photocatalyst is obtained after separation from the reaction solution by filtration and washing followed by re-calcination without an clear reduced photocatalytic activity for at least 3rd run.

Thus, it can be concluded that both BaBiO_3 and $\text{Ba}_{0.6}\text{K}_{0.4}\text{BiO}_3$ are efficient recoverable in CV dye degradation. The complete mineralization of the studied dye is confirmed from the analysis of total organic carbon (TOC) content. On analysing the UV–vis spectrum of CV dye degradation in the presence of both the catalysts under visible light irradiation leads to prominent decrease in the characteristic band of CV dye at 590nm after 40 minutes. The proposed mechanism indicates the participation of various active species like $^{\circ}\text{OH}$, HO_2 , H_2O_2 and $^{\circ}\text{O}_2^-$ in the degradation of CV dye.

Our results prove that the photocatalytic efficiency of $\text{Ba}_{0.6}\text{K}_{0.4}\text{BiO}_3$ is shown to be greater than that of BaBiO_3 in degradation of CV dye. The higher

activity of $\text{Ba}_{0.6}\text{K}_{0.4}\text{BiO}_3$ was attributed to its narrower band gap in comparison to the parent compound (BaBiO_3).

The photocatalytic degradation potential of the as synthesized photocatalysts is found to be much better than the commercially available Degussa P-25 TiO_2 owing to their much narrower band gap in comparison to the wider band gap ($\sim 3.2\text{eV}$) of the later.

Therefore, exploring higher catalytic activity of such perovskite structures may pave the way for designing useful photocatalytic material.

References

- [1] K. Tanaka, K. Padermpole, T. Hisanaga, *Water Res.* 34, (2000), 327.
- [2] R.M. Gong, M. Li, C. Wang, Y. Z. Sun, J. Chen, *J. Hazard. Mater. B* 121, (2005), 247.
- [3] C. Wang, A. Yediler, D. Lienert, Z. Wang, A. Kettrup, *Chemosphere* 46, (2002), 339.
- [4] D. Partelová, A. Šušnovská, J. Marešová, M. Horník, M. Pipíška, S.A. Hostin, *Nova Biotechnologica et Chimica* 14, (2015), 212.
- [5] R. Kant *Nat. Sci.* 4, (2012), 220.
- [6] A.A. Bergwerff, P. Scherpenisse, *J. Chromatogr. B* 788, (2003), 351.
- [7] G.M. Colonna, T. Caronna, B. Marcandalli, *Dyes Pigm.* 41, (1999), 211.
- [8] D. Wang, *Pol. J. Chem. Tech.* 14, (2012), 42.
- [9] W. Johnston, *J. Biotechnol. Histochem.* 83, (2008), 83.
- [10] M. Sankar, G. Sekaran, S. Sadulla, T. Ramasami, *J. Chem. Technol. Biotechnol.* 74, (1999), 337.
- [11] H. He, S. Yang, K. Yu, Y. Ju, C. Sun, L. Wang, *J. Hazard. Mater.* 173, (2010), 393.
- [12] R.K. Sani, U.C. Banerjee, *Enzyme Microbiol. Technol.* (1999), 433.
- [13] M. Zahoor, *Tenside surf. Det.* 49, (2012), 107.
- [14] https://en.wikipedia.org/wiki/Crystal_violet, visited *July 2015*.
- [15] S. Halebian, B. Harris, S.M. Finegold, R.D. Rolfe, *J. Clin. Microbiol.* 13, (1981), 444.
- [16] J. Hed, *FEMS Microbiol. Lett.* 1, (1977), 357.
- [17] K. Saotome, H. Morita, M. Umeda, *Toxicol. in Vitro* 3, (1989), 317.

-
- [18] M. Ishiyama, H. Tominaga, M. Shiga, K. sasamoto, Y. Ohkura, K. Ueno, *Biol. Pharm. Bull.* 19, (1996), 1518.
- [19] M. Saquib, M. Muneer, *Dyes Pigm.* 56, (2003), 37.
- [20] W. Au, M. A. Butler, S. E. Bloom, T. S. Matmeyer, *Mutat. Res.* 66, (1979), 103.
- [21] S. Mani, R.N. Bhargava, *Res. Environ. Contam. Toxicol.* 237, (2016), 71.
- [22] V. Sabna, S.G. Thampi, S. Chandrakaran, *Ecotoxicol. Environ. Saf.* 134, (2016), 390.
- [23] H.Y. Shu, C.R. Huang, *Chemosphere* 31, (1995), 3815.
- [24] Y. Benjelloun, A. Lahrichi, S. Boumchita, M. Idrissi, Y. Miyah, K. Anis, V. Nenov, F. Zerrouq, *J. Mater. Environ.* 8, (2017), 2259.
- [25] T. Tsuchido, K. Katsui, A. Takeuchi, M. Takano, I. Shibasaki, *Appl. Environ. Microbiol.* 50, (1985), 298.
- [26] R.E.P. Goyea, F.L.G. Duque, G. Peñuela, I. González, J.L. Nava, R.A.T. Palma, *Chemosphere* 81, (2010), 26.
- [27] J.A. Bumpus, B.J. Brock, *Appl. Environ. Microbiol.* 84, (2018), 1143.
- [28] C. Yatome, S. Yamada, T. Ogawa, M. Matsui, *App. Microbiol. Biotechnol.* 38, (1993), 565.
- [29] E. Forgaes, T. Cserhádi, G. Oros, *Environ. Int.* 30, (2004), 953.
- [30] M. Mittal, M. Sharma, O.P. Pandey, *Sol. Energy* 110, (2014), 386.
- [31] A. Mittal, J. Mittal, A. Malviya, D. Kaur, V.K. Gupta, *J. Colloid Interface Sci.* 343, (2010), 463.
- [32] S. Chakraborty, S. Chowdhury, P.D. Saha, *Carbohydr. Polym.* 86, (2011), 1533.
- [33] R. Ahmad, *J. Hazard. Mater.* 171, (2009), 767.
- [34] M.R. Kulkarni, T. Revanth, A. Acharya, P. Bhat, *Resour.-Efficient Technol.* 3, (2017), 71.

-
- [35] H.J. Fan, S.T. Huang, W.H. Chung, J.L. Jan, W.Y. Lin, C.C. Chen, *J. Hazard. Mater.* 171, (2009), 1032.
- [36] J. Wu, H. Gao, S. Yao, L. Chen, Y. Gao, H. Zhang, *Sep. Purif. Technol.* 147, (2015), 179.
- [37] A.D. Bokare, R.C. Chikate, C.V. Rode, K.M. Paknikar, *Appl. Catal. B: Environ.* 79, (2008), 2701.
- [38] Y. Li, W. Qu, L. Huang, P. Li, F. Zhang, D. Yuan, Q. Wang, H. Xu, H. Li, *J. Inor. Organomet. Polym. Mater.* 27, (2017), 1674.
- [39] M.T.N. Le, B.K. Lee, *Catal. Today* 297, (2017), 228.
- [40] W. Raza, D. Bahnemann, M. Muneer, *Catal. Today* 300, (2018), 89.
- [41] S. Senthilkumar, K. Porkodi, *J. Colloid Interface Sci.* 288, (2005), 184.
- [42] A. Fujishima, K. Honda, *Nature* 238, (1972), 37.
- [43] Y.H.B. Liao, J.X. Wang, J.S. Lin, W.H. Chung, W.Y. Lin, C.C. Chen, *Catal. Today* 174, (2011), 148.
- [44] T. Begum, P.K. Gogoi, U. Bora, *Ind. J. Chem. Technol.* 24, (2017), 97.
- [45] S.R. Couto, A. Domínguez, A. Sanromán, *Chemosphere* 46, (2002), 83.
- [46] V. Prashant, V. Kamat, J. Bisquert, J. Buriak, *ACS Energy Lett.* 2, (2017), 904.
- [47] F. Deganello, G. Marci, G. Daganello, *J. Europ. Ceram. Soc.* 29, (2009), 439.
- [48] J. Chena, Z. Hea, G. Li, T. Ana., H. Shi, Y. Li, *App. Catal. B: Environ.* 209, (2017), 146.
- [49] Y. Ebina, T. Sasaki, M. Harada, M. Watanabe, *Chem. Mater.* 29, (2002), 4390.
- [50] N. Guilhame, M. Primet, *Stud. Surf. Sci. Catal.* 116, (1998), 581.
- [51] S. Royerr, H. Alamdari, D. Duprez, S. Kaliaguine, *Appl. Catal. B: Environ.* 58, (2005), 273.

-
- [52] N. Daneshvar, D. Salari, A.R. Khatee, *J. Photochem. Photobiol. A: Chem.* 157, (2003), 111.
- [53] K.V. Kumar, K. Porkodi, F. Rocha, *Catal. Commun.* 9, (2008), 82.
- [54] R.A. Shawabkeh, M.T. Tutnji, *Appl. Clay Sci.* 24, (2003), 111.
- [55] N. Soltani, E. Saion, M.Z. Hussein, M. Erfani, A. Abedini, G. Bahmanrokh, M. Navasery, P. Vaziri, *J. Photochem. Photobiol. A: Chem.* 267, (2013), 6.
- [56] S. Samira, P.R. Akash, C. Mohan, J.M. Modak, *J. Thermodynam. Cat.* 3, (2012), 1.
- [57] M.A. Rauf, M. A. Meetani, S. Hisaindee, *Desalination* 276, (2011), 13.
- [58] Z. Xiong, L.L. Zhang, J. Ma, X.S. Zhao, *Chem. Commun.* 46, (2010), 6099.
- [59] L. Lucarelli, V. Nadtochenko, J. Kiwi, *Langmuir* 16, (2010), 1102.
- [60] S. Jain, R. Yamgar, R.V. Jayaram, *Chem. Eng. J.* 148, (2009), 342.
- [61] A.P. Toor, A. Verma, C.K. Jotshi, P.K. Bajpai, V. Singh, *Dyes Pigm.* 68, (2006) 53.
- [62] W.S.W. Ngah, L.C. Teong, MA.K.M. Hanafiah, *Carbo. Polym.* 83, (2011), 1446.
- [63] F. Zhang, J. Zhao, T. Shen, H. Hidaka, E. Pelizzeti, N. Serpone, *Appl. Catal. B: Environ.* 15, (1998), 147.
- [64] M.A Habib, M. T. Shahadat, N.M. Bahadur, I.M.I. Ismail, A.J. Mahmood, *Int. Nano Lett.* 3, (2013), 1.
- [65] I.K. Konstantinou, T.A. Albanis, *Appl. Catal. B: Environ.* 49, (2004), 1.
- [66] J.C. D'Oliveira, G.A. Sayyed, P. Pichat, *Environ. Sci. Tech.* 24, (1990), 990.
- [67] S. Ameen, M.S. Akhtar, M. Nazim, H.S. Shin, *Mater Lett.* 96, (2013), 228.
- [68] C. Hachem, F. Bocquilon, O. Zahraa, M. Bouchy, *Dyes Pigm.* 49, (2001), 117.
- [69] T. Yetim, T. Tekin, *Period. Polytech. Chem. Eng.* 61, (2017), 102.

-
- [70] E. Kusuvrana, A. Samil, O.M. Atanur, O. Erbatur, *Appl. Catal. B: Environ.* 58, (2005), 211.
- [71] J. V. Tolia, M. Chakraborty, Z.V.P. Murthy, *Pol. J. Chem. Tech.* 14, (2012), 16.
- [72] J.C.S. Wu, C.H. Chen, *J. Photochem. Photobiol. A: Chem.* 163, (2004), 509.
- [73] U.G. Akpan, B.H. Hameed, *J. Hazard. Mater.* 170, (2009), 520.
- [74] D.S. Kim, Y.S. Park, *Chem. Eng. J.* 116, (2006), 133.
- [75] C. Galindo, P. Jacques, A. Kalt, *Chemosphere* 45, (2001), 997.
- [76] S. Khezrianjoo, H.D. Revanasiddappa, *Chem. Sci. J.* 85, (2012), 1.
- [77] L. Karimi, S. Zohoori, M. E. Yazdanshernas, *J. Saud. Chem. Soc.* 18, (2014), 581.
- [78] S. Song, L. Xu, Z. He, H. Ying, J. Chen, X. Xiao, B. Yan, *J. Hazard. Mater.* 152, (2008), 1301.
- [79] S. Lathasree, R. Nageswara, B. Sivasankar, V. Sadasivam, K. Rengaraj, *J. Mole. Catal A: Chem* 223, (2004), 101.
- [80] C.H. Wu, W.H.W. Chang, J.M. Chern, *J. Hazard. Mater.* 137, (2006), 336.
- [81] C. Sahoo, A.K. Gupta, A. Pal, *Dyes Pigm.* 66, (2005), 189.
- [82] L.M.A. Fayoumi, M.A. Ezzedine, H.H. Akel, M.M.E. Jamal, *Portugal. Electrochimica Acta* 30, (2012), 121.
- [83] S.S. Jamali, D. Singh, H. Tavakkoli, F. Kaveh, T. Tabari, *Mater. Sci. Semi. Process.* 64, (2017), 47.
- [84] A. Boukhenoufa, M. Bouhelassa, A. Zoulalian, *J. Adv. Chem. Eng.* 1, (2001), 1.
- [85] D. Bhatnagar, R. Chatterjee, *Adv. Mater. Lett.* 7, (2016), 604.
- [86] B. A. Baumert, *J. Supercond.* 8, (1995), 175.
- [87] S. Chakrabarti, B.K. Dutta *J. Hazard. Mater.* 112, (2004), 269.

-
- [88] S. Dafare, P.S. Deshpande, R.S. Bhavsar, *Ind. J. Chem. Tech.* 20, (2013), 406.
- [89] H. Qi, L. Baoshun, Z. Zhengzhong, S. Mingxia, Z. Xinjia, *J. Wuhan Univ. Tech- Mater. Sci. Ed.* 25, (2010), 210.
- [90] M.H. Habibi, A. Hassanzadeh, S. Mahdavi, *J. Photochem. Photobiol. A: Chem.* 172, (2005), 89.
- [91] M.A. Behnajady N. Modirshala, R. Hamzavi, *J. Hazard. Mater.* 133, (2006), 216.
- [92] N. Barka, S. Qourzal, A. Assabbane, A. Nounah, Y.A. Ichou, *Arab. J. Chem.* 3, (2010), 279.
- [93] N. Daneshvar, M. Rabbani, N. Modirshala, M. A. Behnajady, *J. Photobiol. Photochem. A: Chem.* 168, (2004), 39.
- [94] A. Hu, X. Zhang, K.D. Oakes, P. Peng, Y.N. Zhou, M. R. Servos, *J. Hazard. Mater.* 189, (2011), 278.
- [95] W. Zhu, X. Qiu, V. Iancu, X.Q. Chen, H. Pan, W. Wang, N.M. Dimitrijevic, T. Rajh, H.M. Meyer, M. P. Paranthaman, G.M. Stocks, H.H. Weitering, B. Gu, G. Eres, Z. Zhang, *Phys. Rev. Lett.* 103, (2009), 226401.

Chapter 5

Photocatalytic Degradation of Malachite Green Dye Using BaBiO_3 and $\text{Ba}_{0.6}\text{K}_{0.4}\text{BiO}_3$

5.1 Introduction

Synthetic dyes are widely used in many industries, such as in textile industry, as colouring additives in food technology, in leather tanning industry, in paper production, in agricultural research, in light-harvesting ranges in photo-electrochemical cells and for hair colouring purposes. Due to large-scale production and extensive application, synthetic dyes can cause substantial environmental pollution and are stern health-risk factors. Though, the increasing influence of environmental protection on industrial development promotes the development of green technologies which are eco-friendly [1-3].

MG was introduced in aquaculture in 1933, and extensively used in the fish industry due to its low cost and efficacy [4]. Several studies show that MG is metabolically reduced to leuco-malachite green [LMG] which is lipophilic and can be stored in fish tissues for several years [5,6]. Thus, MG has become highly controversial compound due to the risks it poses to the consumers of treated fish where it has been detected, since it introduces to DNA causing carcinogenesis, mutagenesis and teratogenicity. Though, the use of this dye has been banned in several countries and not approved by US Food and Drug Administration, it is still being used in many parts of the world due to its low cost, easy availability and efficacy [7,8] and to lack of a proper alternative. Several harmful effects of MG dye on environment and human health are depicted in **Figure 5.1**.

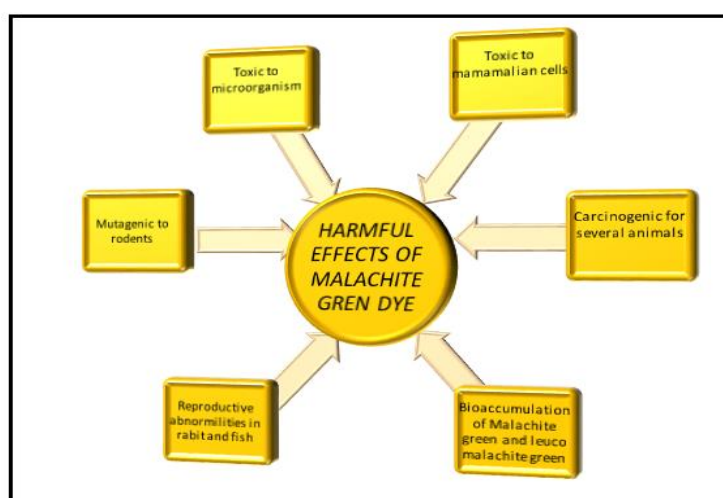


Figure 5.1: Harmful effects of MG dye

The dyes present in water reduce the photosynthetic activity of aquatic plants by interrupting the entering sun rays, resulting in the demolition of the water ecosystem [9,10]. These dyes have properties that make it difficult to remove from aqueous solutions and also toxic to major microorganisms. Various waste water techniques such as chemical treatment, physical treatment and biological treatment methods are used in waste water purification. Further, these methods produce huge amount of toxic slurry so secondary treatments are needed [11-13]. So efforts are carried out to effectively remove the dyes from wastewaters, for this purpose, researchers have investigated a variety of photo-induced green treatments which consumes the least amount of chemicals and solar energy.

Advanced oxidation processes (AOPs) compose significant, promising, effective green methods is a relatively newer, more powerful, and very promising approach called advanced oxidation processes (AOPs) [14-16]. AOPs are a set of techniques which normally utilize a strong oxidizing species such as $\cdot\text{OH}$ radicals produced in situ, which causes a sequence of reactions to break down the complex aromatic structure into smaller and less harmful end products such as CO_2 and H_2O [17,18].

The emergence and application of solar energy in waste water treatment is being intensively studied worldwide [19]. Till date TiO_2 -based and other simple oxide materials are studied for photocatalytic degradation of organic pollutants [20-24]. Although, use of these in photocatalysts is obstructed by the lower absorption in visible region of light. The efficiency of doped TiO_2 photocatalyst for photocatalytic degradation is low because of the recombination of photo-generated charge carriers, less stability of as prepared doped photocatalyst and the back reaction of intermediate chemical species [25-30]. So from the viewpoint of solar energy utilization, it is very urgent to develop photocatalysts with visible light response.

Due to their distinct photo-absorption and photo-physical properties perovskite materials are extensively studied in the past few years [31,32]. Perovskite materials are the mixed metal oxides with the general formula ABO_3 . In the typical crystal structure of perovskite material, the A site is engaged by the larger cation, while the B site is occupied by the smaller cation [33,34]. Perovskites are one of the most important families of materials exhibiting properties suitable for numerous

technological applications [35-37]. Perovskite materials have been studied for photocatalytic degradation of various pollutants such as phenols, dyes and drugs from waste water [38-40]. But most of the studied perovskites show the photocatalytic properties under UV light irradiation due to their large band gap energy [41-43]. Many efforts are made to develop new perovskite materials which can efficiently utilize solar light [44,45].

In this chapter, doped and undoped Barium bismuthate, used for the degradation of MG dye from aqueous solution, have been synthesized by Pechini method, details of which have been elaborated in chapter 3. The degradation potential of these catalysts has been evaluated by different characterization methods such as TG-TGA, XRD, UV-DRS, SEM and FTIR, results of which have been described in chapter 3.

FTIR spectrum shows the presence of a band around 465cm^{-1} in both the catalysts conforming the metal-oxygen bond formation, which is the characteristic property of perovskite materials [46]. The SEM studies show that both the samples are homogeneous uniform nanoparticles, having size 520 nm and between 45-101nm for the BaBiO_3 and $\text{Ba}_{0.6}\text{K}_{0.4}\text{BiO}_3$, respectively. SEM images reveal the nano rod type structure and plate like layered structure of BaBiO_3 and for $\text{Ba}_{0.6}\text{K}_{0.4}\text{BiO}_3$, respectively. The XRD patterns suggest that BaBiO_3 crystallizes in the monoclinic structure while $\text{Ba}_{0.6}\text{K}_{0.4}\text{BiO}_3$ crystallizes in cubic structure. XRD patterns exhibit the typical pattern corresponding to perovskite structure. The phase evolution of both the catalysts with increasing temperature is done by DT-TGA.

The diffuse reflectance spectroscopy showed that the catalysts have a broad absorbance around 600 and 660 nm with a band gap of 2.07 and 1.87eV for barium bismuthate and K doped barium bismuthate respectively. Due to the low band gap, the catalysts are supposed to be promising in displaying their visible light activity and hence they are tested further for the degradation of MG dye under visible light irradiation.

The objective of this work is to study the photodegradation of MG dye using the prepared catalysts. The photodegradation rates and efficiency of the photocatalytic system are highly dependent on a number of operational parameters that govern the photodegradation of the organic molecule [47] such as catalyst dose,

solution pH, temperature, and initial dye concentration. Optimization of such conditions will greatly help in the development of industrial-scale dye removal treatment process.

Therefore, herein, the dependence of the photodegradation rate on various parameters viz. initial dye concentration, catalyst dose, pH and temperature is studied. The reaction kinetics is studied and the applicability of the first order kinetic model is also discussed. The agreement of the experimental results with the Langmuir-Hinshelwood kinetic model has been examined which led to the determination of both photo-reaction kinetics and adsorption equilibrium constants [48]. In addition, photolysis and adsorption study of dye on prepared catalyst is also discussed. The adsorption experiment data is fitted to Langmuir isotherm model and Freundlich isotherm model [49,50]. Furthermore, to estimate the degree of mineralization, measurements of total organic carbon has been conducted.

5.2. Material & Method

5.2.1. Chemical reagents

The reagents used for the synthesis of BaBiO_3 and $\text{Ba}_{0.6}\text{K}_{0.4}\text{BiO}_3$ are Barium nitrate, Bismuth nitrate, potassium nitrate as starting materials while, citric acid and ethylene glycol are used as complexing agents. Details of synthesis procedure are given in chapter 3. MG dye (Mol. Wt. = $364.911 \text{ gmol}^{-1}$) dye is purchased from Sigma-Aldrich Company (India). A solution of 100 mgL^{-1} MG dye solution is prepared as stock solution. Different dye solutions of various concentrations are made from the stock solution (100 mgL^{-1}) by appropriate dilutions. Ultra-pure water ($18.2 \text{ M}\Omega\text{cm}^{-1}$) is used to prepare all solutions in this study. The pH of the solutions is adjusted using 0.1 N NaOH and 0.1 N HCl . All the chemicals except MG dye is purchased from Merck (India). Analytical grade $\text{p}25\text{TiO}_2$ is purchased from Sigma-Aldrich Company (India). The chemicals used in this experiment are of the analytical grade and are used without further purification.

5.2.2. Experimental procedure and analytical methods

An experimental setup for the photocatalytic activity test has been explained in chapter 2. The visible light irradiation experiments are carried out in an

indigenously prepared immersion type photocatalytic reactor. A 500W Xe arc lamp (intensity=137 mWcm⁻²) is used as a visible light source. This lamp is placed in a quartz tube which is sealed from one side. This tube is then immersed in a cylindrical borosilicate reactor (capacity 1L). In this, mixture of catalyst and dye solution are taken following which the mixture is placed in a water bath circulated at a constant speed to keep the above suspension homogenous. Only in experiments dealing with the effect of pH on the dye degradation, initial pH is adjusted with buffer solutions and measured with pH meter.

Since some dyes can be degraded by direct UV or visible irradiation without the assist from catalysts [51], it is important to find out the extent to which the degradation of MG dye in aqueous solution takes place directly by the visible light or in other words, to find out the extent of direct photolysis of MG dye. So, some control experiments are carried out in the absence of the catalysts, while holding all other parameters the same. Following this, their respective photodegradation rates are measured to evaluate their photolysis.

Since, the photo-assisted degradation of the dyes occurs predominantly on the surface. Therefore, adsorption of the dye is an important parameter in determining photocatalytic degradation rate. Photocatalysts, dispersed into MG dye solution is allowed to reach adsorption-desorption equilibrium under continuous magnetic stirring at 600 rpm for 30 minutes in the dark, before illumination. Irradiation is then provided. Samples are withdrawn at 5 minutes' time intervals and then centrifuged to remove the suspended catalyst. The clear supernatant fluid followed by filtration is then analysed by spectrophotometer (Double beam spectrophotometer-2203, Systronics) at λ_{\max} = 618nm with a calibration curve based on Beer Lambert's law [52]

The degradation efficiency is observed in terms of change in intensity of the dye before and after light irradiation. Photocatalytic performance is quantified by the degradation of MG dye under visible light irradiation.

$$\%degradation = \frac{C_0 - C_t}{C_0} \times 1000 \quad \text{--- (5.1)}$$

Where, C_0 = concentration of dye solution after adsorption-desorption equilibrium (mgL^{-1}), C_t = concentration of dye solution after photo irradiation (mg L^{-1}).

5.3. Results and Discussion

5.3.1. UV-VIS spectra of MG dye

Malachite Green is a basic tri phenyl methane dye with high water solubility, and its molecular formula is $\text{C}_{23}\text{H}_{25}\text{N}_2$. The UV-vis. absorbance spectrum of MG is drawn to determine its absorption maxima. **Figure 5.2** shows the typical time dependent UV-vis spectrum of MG dye. It is clear that MG dye has an intensive absorbance at 618 nm. The rate of degradation is investigated with respect to change in absorption maxima of MG dye ($\lambda_{\text{max}}=618\text{nm}$).

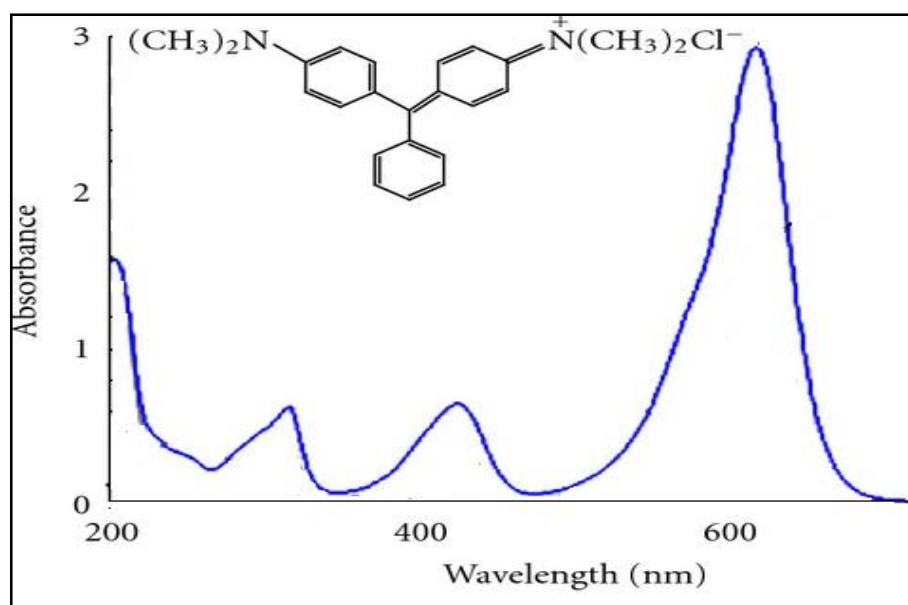


Figure 5.2: UV-VIS spectra of MG dye. ($\lambda_{\text{max}}= 618\text{nm}$)

5.3.2. Photolysis of Malachite green dye

Photolysis is the process of decomposition of dyes in the presence of light radiation only. Direct photolysis of the dye in the absence of photocatalyst showed no considerable degradation even after 1 hour. **Figure 5.3** shows the results of photocatalysis in terms of % degradation.

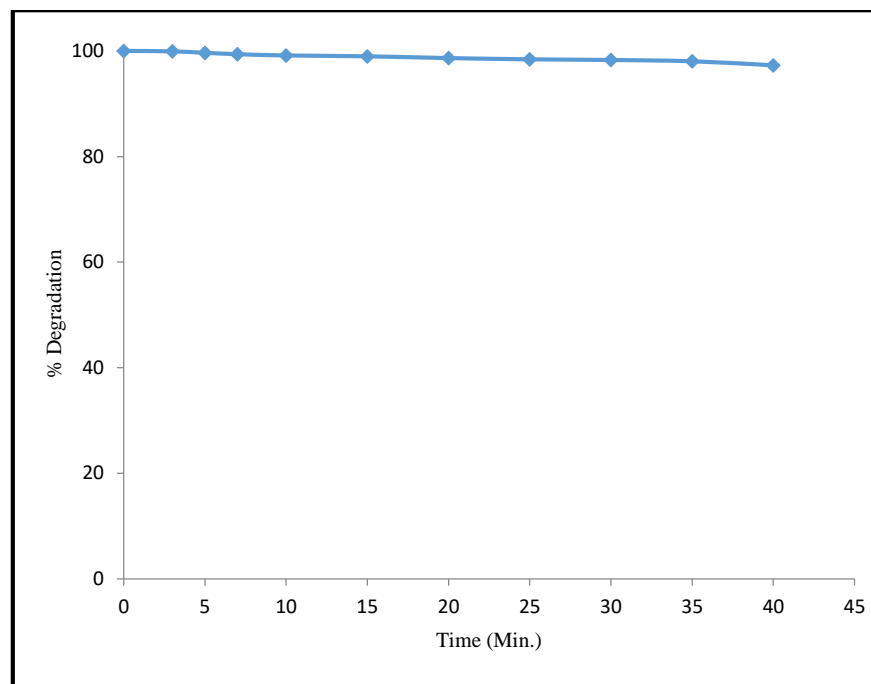


Figure 5.3: Photolysis of MG in presence of irradiation. (Experimental condition: $[MG] = 40\text{mgL}^{-1}$; $\text{pH}=6.0$; $\text{Temp.}= 308\text{K}$)

The constant absorbance with time verifies that MG dye is not homogeneously degraded by light. Therefore, the self-degradation of the dye by visible light irradiation can be ignored. Similar results are obtained in the study of MG dye under UV-Vis irradiation in earlier reports [53].

5.3.3 Adsorption studies in dark:

Since, the photo-assisted degradation of the dyes occurs predominantly on the surface. Therefore, adsorption of the dye is an important parameter in determining photocatalytic degradation rate. The adsorbed dye on the surface of the semiconductor particles act as an electron donor, injecting electrons from its excited state to the conduction band of the semiconductor under light irradiation, so in the heterogeneous photocatalytic degradation process, adsorption of dye on the catalytic surface is assumed to be a primary step of the reaction [54-56]. The adsorption experiments are carried out to evaluate the experiments the equilibrium quantity of adsorbent. The equilibrium adsorption isotherm is fundamental in describing the interactive behaviour between adsorbates and adsorbent and is important in the design and analysis of adsorption systems. For the sake of convenience, explicit and simple models are preferred and commonly used [57].

Equilibrium adsorption data collected in this study could be fitted by both Langmuir and Freundlich isotherms.

A. Langmuir isotherm

Langmuir isotherm [58] model is used to interpret the experimental data. The Langmuir isotherms are represented by the following equations.

$$q_e = \frac{Q_0 bc}{1+bc} \quad \text{--- (5.2)}$$

$$\frac{C_e}{q_e} = \frac{1}{Q_0 b} + \frac{C_e}{Q_0} \quad \text{--- (5.3)}$$

Where C_e is the concentration of the adsorbate (mgL^{-1}) at equilibrium, q_e is the amount of adsorbate per unit mass of adsorbent at equilibrium in mgg^{-1} , Q_0 is the maximum adsorption at monolayer coverage in mgg^{-1} , b is the adsorption equilibrium constant related to the energy of adsorption in Lmg^{-1} .

The adsorbate uptake $q_e(\text{mgg}^{-1})$, can be calculated as

$$q_e = \frac{(C_0 - C_e)V}{W} \quad \text{--- (5.4)}$$

Where C_0 is the initial adsorbate concentration (mgL^{-1}), V is the volume of solution (L), W is the mass of adsorbate (g).

The essential characteristic of the Langmuir isotherm can be described by a separation factor which is called the equilibrium constant, R_L

The equilibrium factor thus is defined as:

$$R_L = \frac{1}{1+K_{LH}} \times \frac{1}{C_0} \quad \text{--- (5.5)}$$

Where, K_{LH} is the affinity constant (mg^{-1}), C_0 is the initial concentration of the adsorbate (mgL^{-1}). The R_L value is to be favourable at $0 < R_L < 1$ [59,60].

Adsorption experiments are carried out in the same experimental setup, taking dye solutions of different initial concentration. The constants of isotherm are obtained by least square fitting of the adsorption equilibrium data. Adsorption experiments for the dye MG dye are carried out by selecting a concentration range of 20mgL^{-1} to 80mgL^{-1} with an adsorbent dosage of 0.75g of both the adsorbents i.e. BaBiO_3 and $\text{Ba}_{0.6}\text{K}_{0.4}\text{BiO}_3$ at 308K {**Figure 4.4 (a & b)**}. The effect of initial

dye concentration depends on the immediate relation between the concentration of the dye and the available sites on an adsorbent surface. In general, the percentage of dye removal increases with increase in initial dye concentration because it will cause an increase in the capacity of the adsorbent and this may be due to the high driving force for mass transfer at a high initial dye concentration [61].

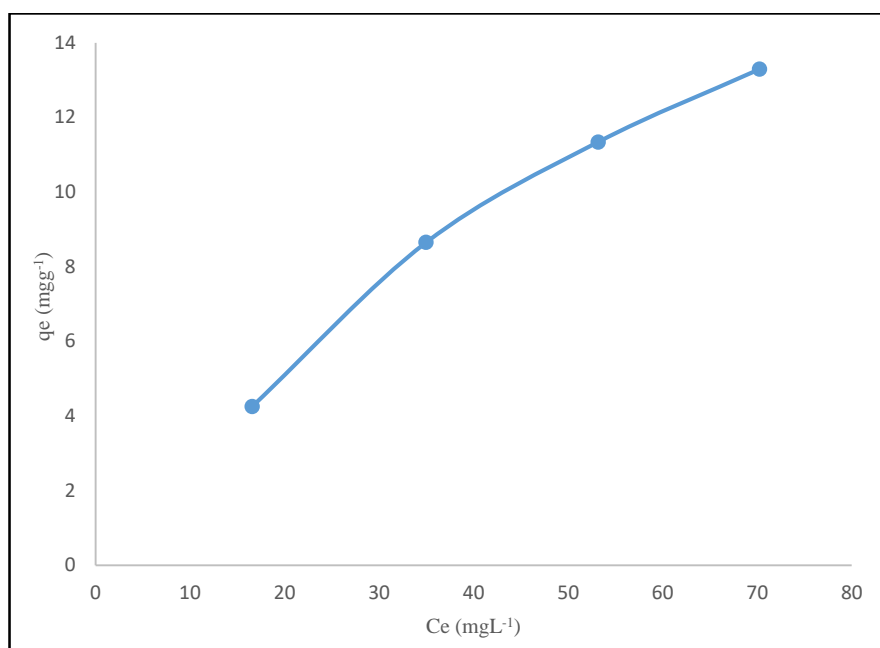


Figure 5.4(a): Adsorption isotherm from aqueous MG dye solution on BaBiO₃ catalyst

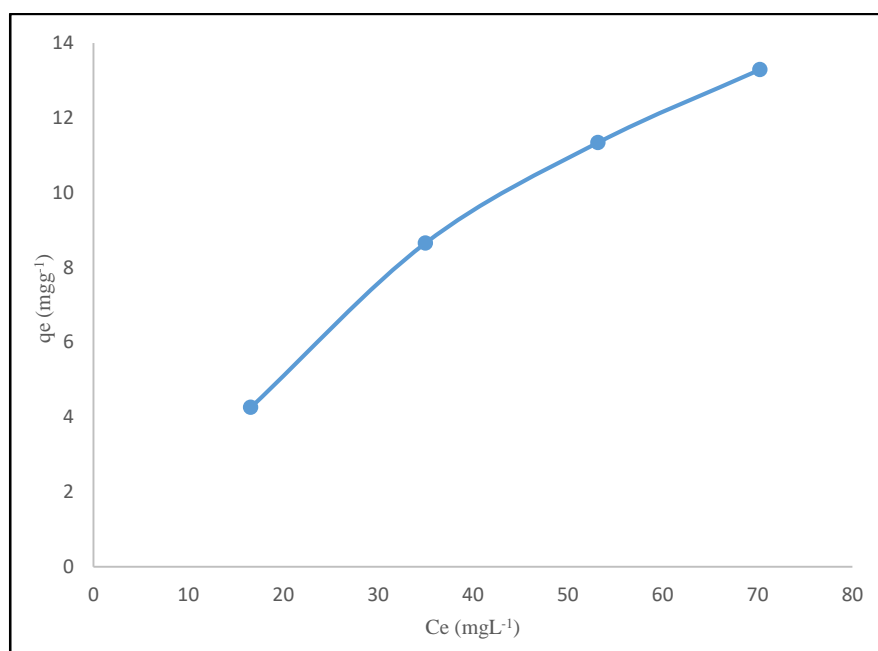


Figure 5.4(b): Adsorption isotherm from aqueous MG dye solution Ba_{0.6}K_{0.4}BiO₃ catalyst

The plot of C_e/q_e versus C_e are linear and represented in **Figure 5.5(a)** and **5.5(b)** for BaBiO_3 and $\text{Ba}_{0.6}\text{K}_{0.4}\text{BiO}_3$ respectively. The value of Q_0 and b is found from the intercept and slope of the C_e/q_e vs C_e curve respectively.

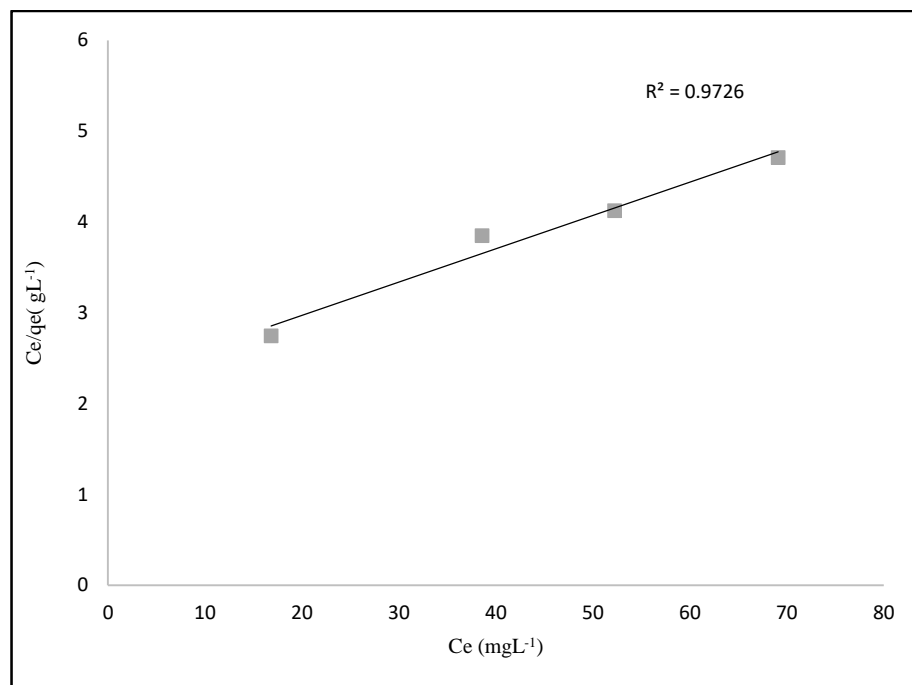


Figure 5.5(a): Langmuir plots for the adsorption of MG on BaBiO_3 . (Experimental condition: $\text{BaBiO}_3 = 0.75\text{gL}^{-1}$; $\text{pH} = 6.0$; $\text{Temp.} = 308\text{K}$)

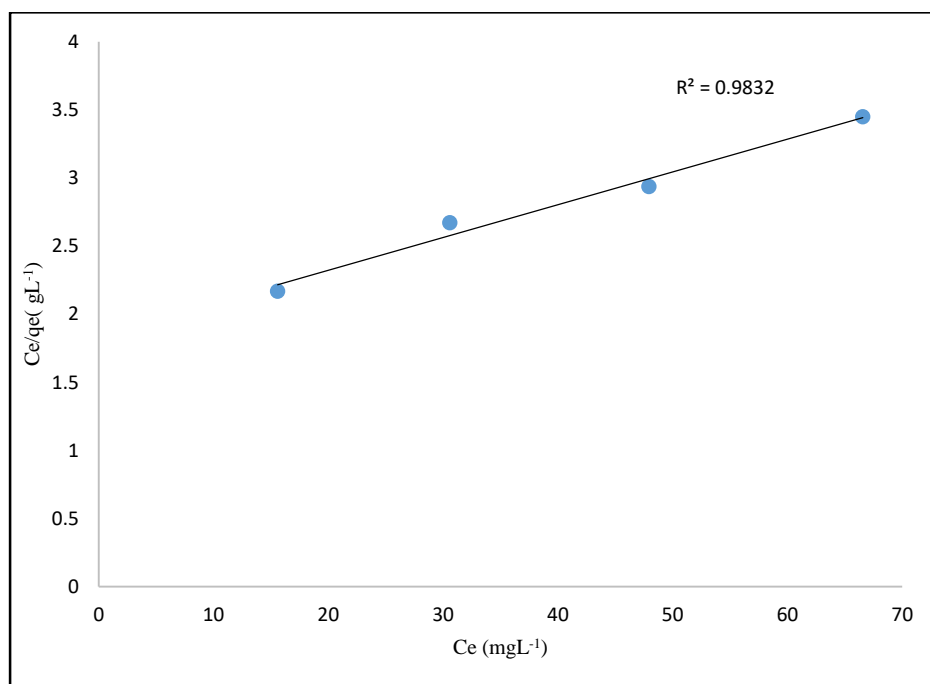


Figure 5.5(b): Langmuir plots for the adsorption of MG on $\text{Ba}_{0.6}\text{K}_{0.4}\text{BiO}_3$. (Experimental condition: $\text{Ba}_{0.6}\text{K}_{0.4}\text{BiO}_3 = 0.75\text{gL}^{-1}$; $\text{pH} = 6.0$; $\text{Temp.} = 308\text{K}$).

Langmuir adsorption constant (b) and the maximum adsorbable dye quantity (Q_0) are calculated from the **Figures 5.5(a)** and **5.5(b)** as 2.663mgg^{-1} , 0.0349Lmg^{-1} for BaBiO_3 and, 3.305mgg^{-1} , 0.0268Lmg^{-1} for $\text{Ba}_{0.6}\text{K}_{0.4}\text{BiO}_3$.

The value of separation constants for different initial concentration are determined from equation 5.5 and found to be in range of 0.45-0.183 and 0.053-0.215 for BaBiO_3 and $\text{Ba}_{0.6}\text{K}_{0.4}\text{BiO}_3$ catalysts and are listed in **Table 5.1**.

Table 5.1: Separation constants (R_L) values for the adsorption of MG dye on BaBiO_3 and $\text{Ba}_{0.6}\text{K}_{0.4}\text{BiO}_3$

$C_0 \longrightarrow$	20mgL^{-1}	40mgL^{-1}	60mgL^{-1}	80mgL^{-1}
BaBiO₃	0.183	0.0915	0.0610	0.0457
Ba_{0.6}K_{0.4}BiO₃	0.215	0.1076	0.07177	0.0538

The values of R_L are found in the range of $0 < R_L < 1$ for both the catalysts, indicating that the adsorption is favoured.

B. Freundlich isotherm

The Freundlich isotherm equation assumes a heterogeneous adsorption surface with sites that have different energies of adsorption and are not equally available [62]. The Freundlich exponential equation is given as-

$$q_e = K_f C_e^{1/n} \quad \text{--- (5.6)}$$

Where, q_e is the amount adsorbed (mgg^{-1}), C_e is the equilibrium concentration of the adsorbate (mgL^{-1}), K_f (Lg^{-1}) and n are Freundlich constants related to the adsorption capacity and adsorption intensity, respectively.

The linear logarithmic form of Freundlich equation is mathematically given by

$$\log q_e = \log K_f + \frac{1}{n} \log C_e \quad \text{--- (5.7)}$$

The value of $1/n$ represents the favourable adsorption conditions.

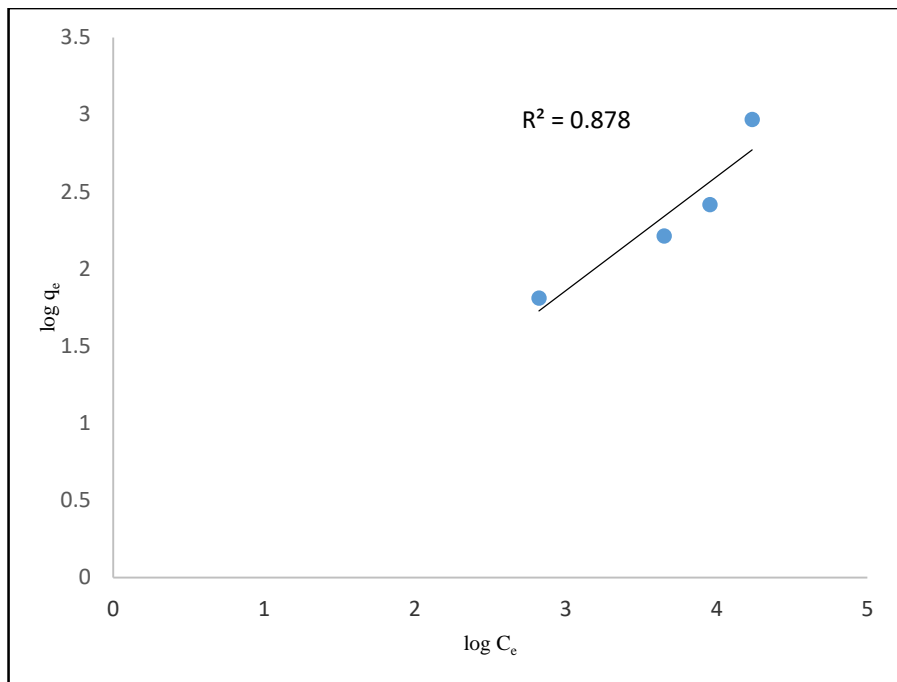


Figure 5.6(a): Freundlich plots for the adsorption of MG on $BaBiO_3$. (Experimental condition: $BaBiO_3 = 1g L^{-1}$; $pH = 6.0$; $Temp. = 308K$)

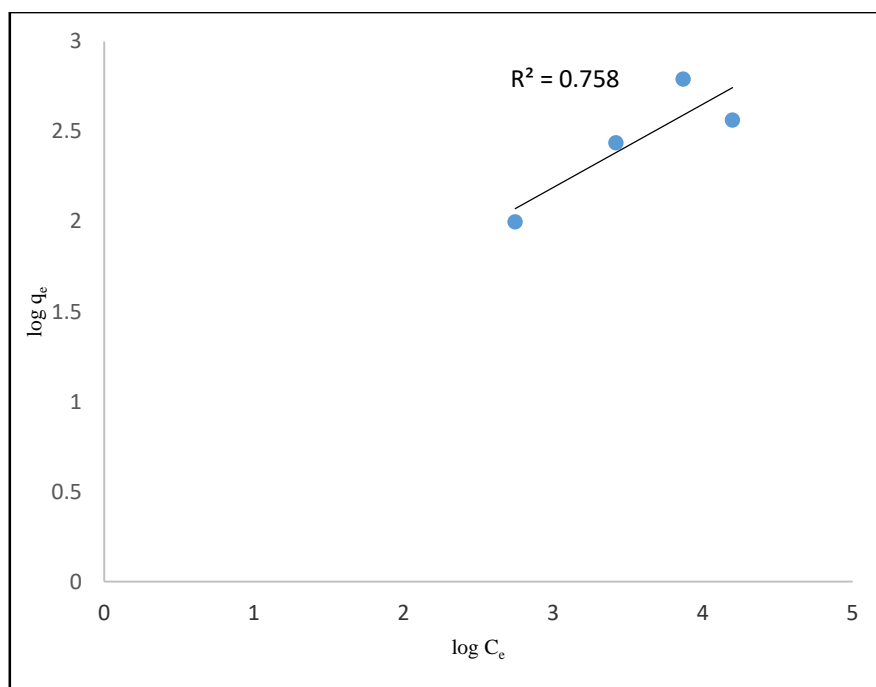


Figure 5.6(b): Freundlich plots for the adsorption of MG on $Ba_{0.6}K_{0.4}BiO_3$. (Experimental condition: $Ba_{0.6}K_{0.4}BiO_3 = 1g L^{-1}$; $pH = 6.0$; $Temp. = 308K$)

K_f and n can be calculated from the intercept and slope of the plots in **Figures 5.6(a)** and **5.6(b)** for BaBiO_3 and $\text{Ba}_{0.6}\text{K}_{0.4}\text{BiO}_3$ respectively. Langmuir and Freundlich constants for the adsorption of MG dye on $\text{Ba}_{0.6}\text{K}_{0.4}\text{BiO}_3$ has been represented in **Table 5.2**.

Table 5.2: Langmuir and Freundlich constants for the adsorption of MG dye on BaBiO_3 and $\text{Ba}_{0.6}\text{K}_{0.4}\text{BiO}_3$

Adsorbent catalyst	Langmuir Constants			Freundlich Constants		
	$Q_0(\text{mgg}^{-1})$	$b(\text{Lmg}^{-1})$	R^2	$K_f(\text{Lg}^{-1})$	n	R^2
BaBiO_3	2.663	0.0349	0.955	1.77	2.313	0.875
$\text{Ba}_{0.6}\text{K}_{0.4}\text{BiO}_3$	3.305	0.0268	0.941	0.313	1.147	0.870

Since the R^2 values are fairly close to 1, both the models describe the system well but Langmuir isotherm model is considered to be best fit because for this model R^2 is ~ 0.955 & 0.941 as comparison to $R^2 \sim 0.875$ & 0.870 for Freundlich isotherm.

5.3.4 Photodegradation studies under visible light irradiation

In order to assess the rate of photocatalytic degradation of dyes over BaBiO_3 and $\text{Ba}_{0.6}\text{K}_{0.4}\text{BiO}_3$, the observed dye degradation results are kinetically analysed by Langmuir-Hinshelwood kinetic equation [63]. Langmuir-Hinshelwood kinetic equation describes the following relationship between the initial rate constant and initial concentration of the organic substrate.

$$r_o = -\frac{dC}{dt} = \frac{K_r K_{LH} C_o}{1 + K_r C_o} \quad \text{--- (5.8)}$$

$$r_o = \frac{1}{K_r} + \frac{1}{K_r K_{LH} C_o} \quad \text{--- (5.9)}$$

Where C_o is the initial concentration of organic substrate (mgL^{-1}), r_o is initial rate ($\text{mgL}^{-1}\text{min}^{-1}$), K_{LH} is the Langmuir-Hinshelwood adsorption equilibrium constant (Lmg^{-1}) and K_r is the rate constant of surface reaction ($\text{mgL}^{-1}\text{min}^{-1}$).

The degradation of organic pollutants over catalysts follows the pseudo-first-order kinetics with respect to the initial concentration of the pollutant.

$$r_o = -\frac{dC}{dt} = K_{app} \quad \dots (5.10)$$

Following equation is used to determine the initial rate by multiplying the apparent first-order rate constant K_{app} with the initial concentration of dye, C_o

$$\ln\left(\frac{C_t}{C_o}\right) = K_{app} \cdot C_o \quad \dots (5.11)$$

In which K_{app} is the apparent pseudo-first-order rate constant in min^{-1} . The apparent reaction rate constant $K_{app}(\text{min}^{-1})$ is given by the slope of the graph of $\ln C_t/C_o$ versus time (minutes).

As we have seen that in the absence of catalyst, the concentration of MG dye shows no significant variation indicating that MG cannot be degraded by photolysis. Hence, any change in the MG concentration can be attributed to the adsorption/photocatalytic process. The pseudo-first-order kinetic model is usually used to fit all data sets (dye concentration, photocatalyst dose, initial pH solution, and temperature) [64].

5.3.4.1 Effect of initial dye concentration on photocatalytic degradation

It is important from both mechanistic and application point of view to study the dependence of the photocatalytic reaction rate on the substrate concentration. It is generally noted that the degradation rate increases with the increase in dye concentration to a certain level and a further increase in dye concentration leads to decrease the degradation rate of the dye. The effect of the initial dye concentration of dye on the rate of degradation is studied by varying the initial dye concentration from 20 to 80 mgL^{-1} initial pH 6.0, with a constant catalyst dose of 0.75 gL^{-1} (for both the catalysts). It is observed that up to 40 mgL^{-1} the degradation efficiency increases due to the greater availability of dye molecules for excitation and consecutive degradation; hence there is an increase in the rate. After this, as the dye concentration is increased, the equilibrium adsorption of dye on catalyst surface increases; hence competitive adsorption of OH^- on the same site decreases, which further decreases the rate of formation of OH^\bullet radical, which is the principal oxidant necessary for a high degradation efficiency. Our results are in accordance with an

earlier research work [65]. The corresponding results with both the catalysts have been described below.

On the other hand, considering **Beer-Lambert law**, as the initial dye concentration increases, the path length of photon entering the solution decreases, resulting in the lower photon adsorption on the catalyst particles and consequently a lower photodegradation rate [66]. Also, the high concentration of dye would have acted as a filter for the incident light, which ultimately reduces the degradation efficiency [67].

(a) Results with BaBiO₃

The experimental results shows that the rate of photocatalytic degradation increases with increase in concentration of dye up to 40mgL⁻¹. The rate of reaction was then, found to decrease with further increase in the concentration of dye. It is clear from the **Table 5.3(a)** to **5.6(a)**, initially % degradation of dye increases rapidly and thereafter slowly attains the limiting value.

Figure 5.7.a (A-D) shows the plots of change in % degradation with time for various concentration of dye at various amount of catalyst

Table 5.3 (a): Effect of initial dye concentration on degradation of MG (Experimental Condition: [BaBiO₃] = 0.25gL⁻¹; pH=6.0; Temp.=308K).

Dye Concentration	20 mgL ⁻¹	40 mgL ⁻¹	60 mgL ⁻¹	80 mgL ⁻¹
Time (min)	% Degradation	% Degradation	% Degradation	% Degradation
0	0.00	0.00	0.00	0.00
3	6.41	4.67	3.70	3.00
5	12.30	11.67	9.75	7.11
7	18.30	19.69	16.83	11.22
10	27.97	32.11	25.49	18.24
15	40.50	48.23	38.88	30.14
20	51.08	61.26	48.11	40.11
25	62.08	70.91	60.42	51.44
30	69.97	73.41	67.28	61.14
35	78.41	83.84	76.11	69.22
40	80.74	84.25	78.19	75.25
∞	81.15	84.88	78.59	75.75

**Table 5.4 (a): Effect of initial dye concentration on degradation of MG
(Experimental Condition: $[\text{BaBiO}_3] = 0.75\text{gL}^{-1}$; $\text{pH}=6.0$; $\text{Temp.}=308\text{K}$).**

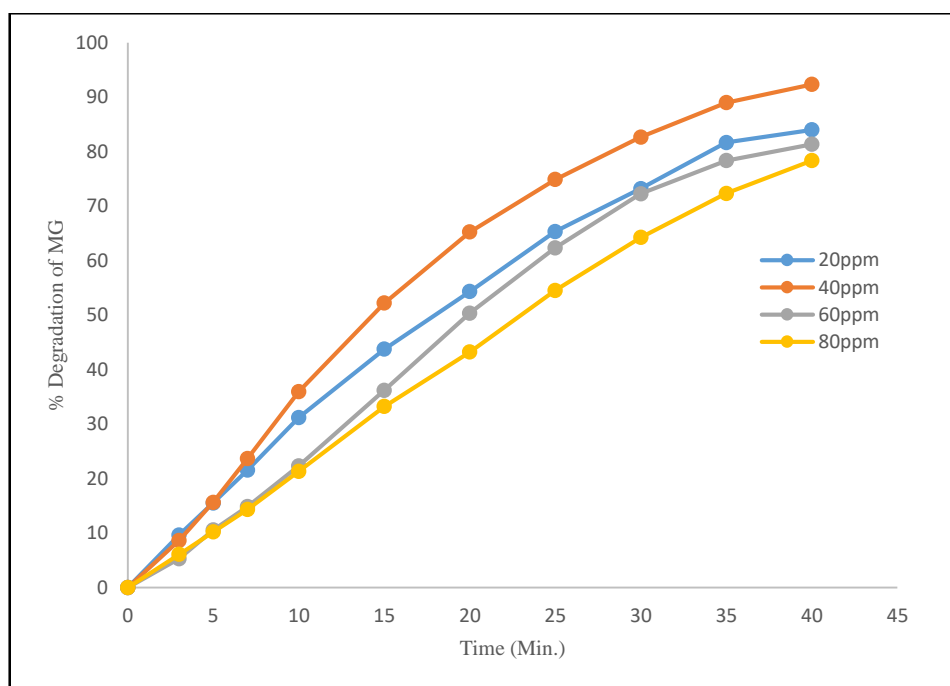
Dye Concentration	20 mgL^{-1}	40 mgL^{-1}	60 mgL^{-1}	80 mgL^{-1}
Time (min)	% Degradation	% Degradation	% Degradation	% Degradation
0	0.00	0.00	0.00	0.00
3	10.40	15.09	7.77	8.85
5	20.52	27.20	17.37	15.44
7	27.17	35.14	23.61	22.24
10	40.23	49.42	39.08	31.18
15	57.47	66.67	52.95	45.02
20	71.16	79.21	68.21	57.16
25	79.54	88.12	76.12	66.73
30	84.36	93.56	79.29	75.19
35	87.25	95.25	83.90	81.13
40	89.35	95.29	88.02	84.35
∞	89.74	95.29	88.54	84.85

**Table 5.5 (a): Effect of initial dye concentration on degradation of MG
(Experimental Condition: $[\text{BaBiO}_3] = 1.00\text{gL}^{-1}$; $\text{pH}=6.0$; $\text{Temp.}=308\text{K}$).**

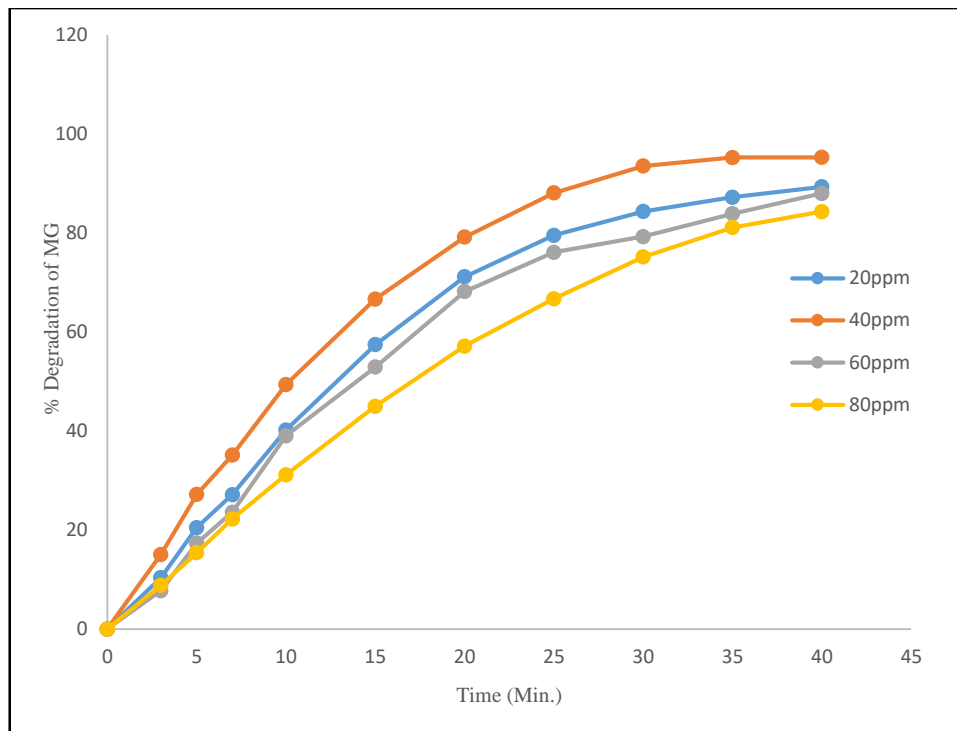
Dye Concentration	20 mgL^{-1}	40 mgL^{-1}	60 mgL^{-1}	80 mgL^{-1}
Time (min)	% Degradation	% Degradation	% Degradation	% Degradation
0	0.00	0.00	0.00	0.00
3	9.12	11.13	2.35	7.25
5	17.65	20.90	9.64	12.36
7	24.30	30.09	16.09	18.48
10	35.50	42.20	29.65	27.74
15	50.97	59.82	40.62	40.47
20	64.41	74.20	57.10	52.28
25	74.57	82.22	63.85	63.25
30	81.11	88.90	71.15	71.11
35	84.59	89.65	77.77	77.27
40	86.86	90.00	77.82	81.25
∞	87.23	90.58	78.14	81.87

Table 5.6 (a): Effect of initial dye concentration on degradation of MG
 (Experimental Condition: $[\text{BaBiO}_3] = 1.25\text{gL}^{-1}$; $\text{pH}=6.0$; $\text{Temp.}=308\text{K}$).

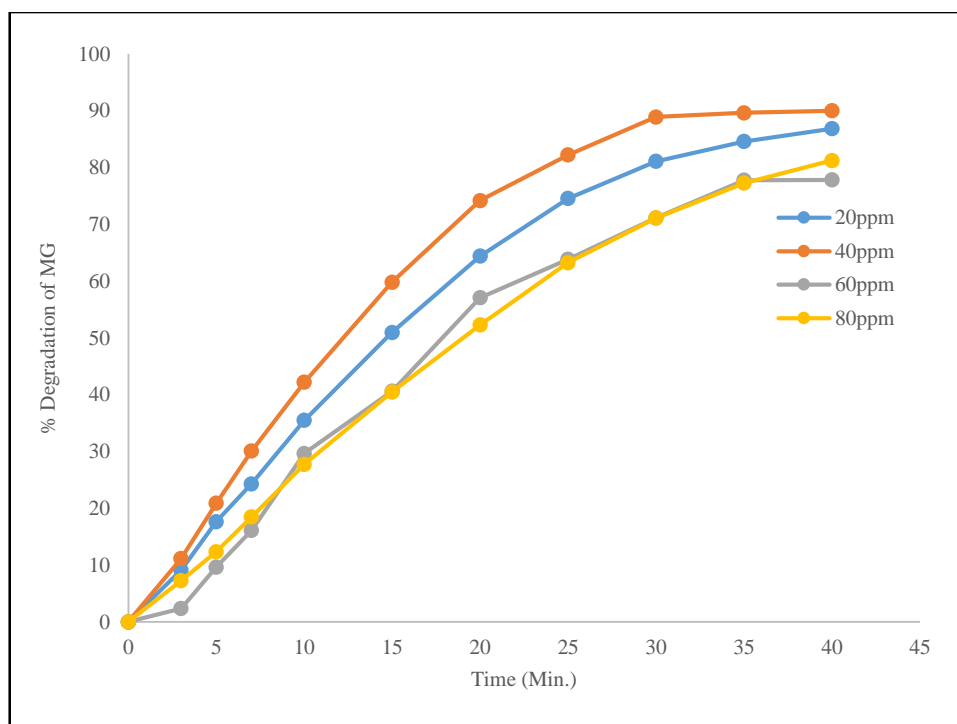
Dye Concentration	20 mgL^{-1}	40 mgL^{-1}	60 mgL^{-1}	80 mgL^{-1}
Time (min)	% Degradation	% Degradation	% Degradation	% Degradation
0	0.00	0.00	0.00	0.00
3	8.08	7.90	6.01	5.21
5	15.50	17.20	12.64	10.43
7	21.27	24.42	18.87	15.43
10	30.63	36.42	26.40	23.73
15	45.41	54.09	42.10	36.40
20	57.08	67.82	53.70	47.13
25	67.30	76.39	64.30	57.24
30	75.65	84.09	72.72	66.51
35	81.54	88.12	77.50	73.20
40	84.97	89.65	81.91	77.67
∞	85.24	89.97	82.11	77.89



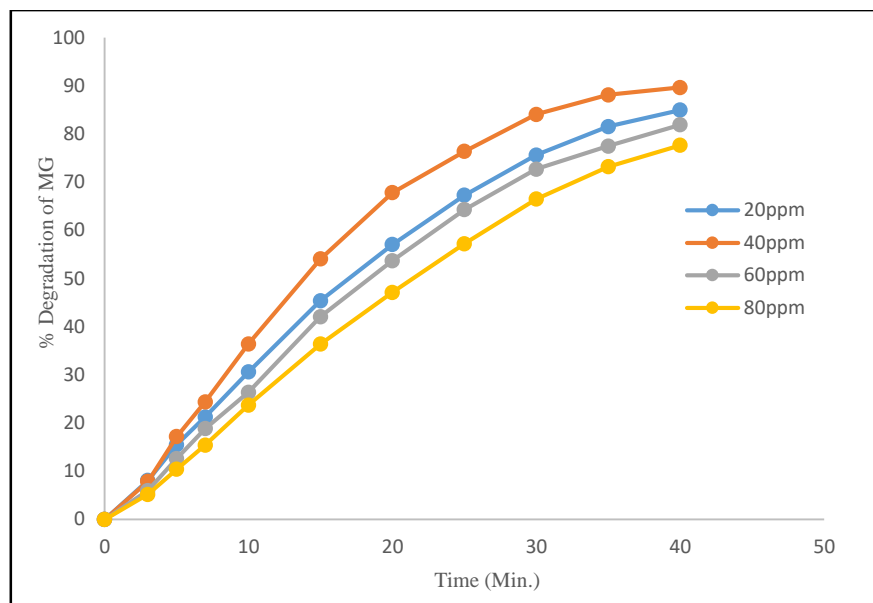
(A)



(B)



(C)



(D)

Figure 5.7(a): Effect of concentration of MG on its visible light degradation in BaBiO_3 [(A) Catalyst dose: 0.25gL^{-1} ; (B) Catalyst dose: 0.75gL^{-1} ; (C) Catalyst dose: 1.00gL^{-1} ; (D) Catalyst dose: 1.25gL^{-1} , $\text{pH}=6.0$, $\text{Temp.}=308\text{K}$].

The photodegradation kinetics of initial dye concentration is illustrated in **Figure 5.8(a)**, which depicts the dark adsorption-desorption equilibrium and the additional decrease in MG concentration caused by visible light irradiation at optimum catalyst dose i.e. 0.75gL^{-1} .

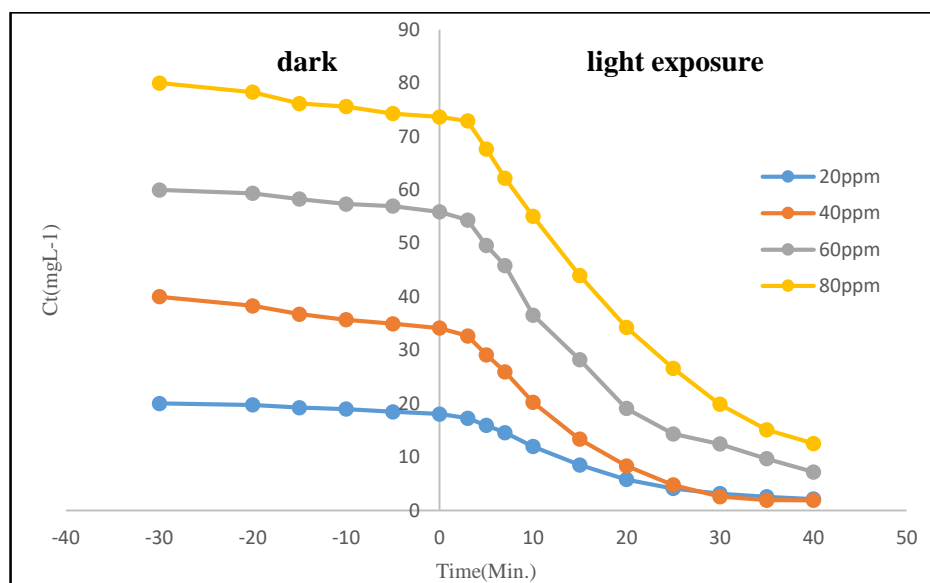


Figure 5.8(a): Variation of dye concentration versus time for different MG initial concentration. (Experimental condition: $\text{BaBiO}_3=0.75\text{gL}^{-1}$; $\text{pH}=6.0$, $\text{Temp.}=308\text{K}$).

With respect to initial concentration, the rate expression is given by equation:

$$\frac{-d[C]}{dt} = K_{app}[C]_o \quad \text{--- (5.12)}$$

Integration of the above equation yields:

$$\ln \frac{C_o}{C_t} = K_{app} \cdot t \quad \text{--- (5.13)}$$

Where, K_{app} is a pseudo first order rate constant (min^{-1}). $[C]_o$ is the equilibrium concentration of the MG dye solution after adsorption, and it is taken as the concentration of the dye solution at visible light irradiation time 't=0' for kinetic analysis.

Initial rate (r_o) is determined by the following equation

$$r_o = K_{app}[MG]_o \quad \text{--- (5.14)}$$

Where, r_o is initial rate ($\text{mgL}^{-1}\text{min}^{-1}$).

The plot of $\ln C_t/C_o$ versus t with different initial concentration of MG is shown in **Figure 5.9(a)**. The figure shows that the photocatalytic degradation follows perfectly the pseudo-first order kinetic with respect to MG concentrations.

It is found that a plot between $\ln C_t/C_o$ versus time represents a straight line, the slope of linear regression equals the apparent first order rate constant K_{app} which is consistent with the reported first order reaction [68].

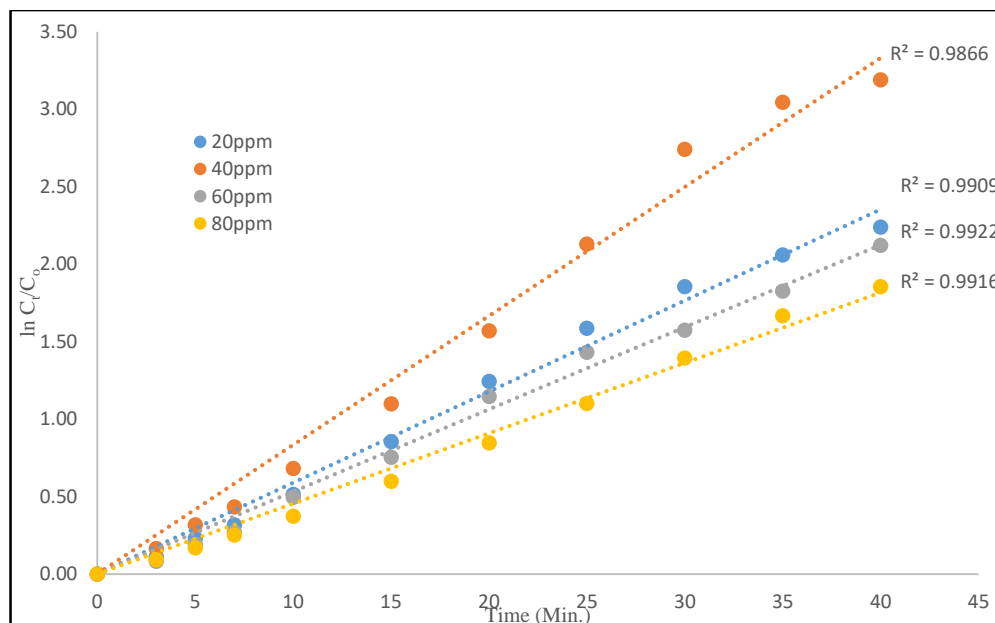


Figure 5.9(a): Linear variation of $\ln C/C_0$ versus time for the photocatalytic degradation of CMG dye at different initial concentration. (Experimental condition: $[BaBiO_3] = 0.75gL^{-1}$; $pH=6.0$; $Temp. = 308K$).

The values of rate constants K_{app} , which corresponds to different initial concentration, along with the initial rate (r_0) and corresponding regression constants, are listed in **Table 5.7 (a)**.

Table 5.7(a): Pseudo-first order apparent rate constant and initial rate values for the different initial concentration of dye
(Experimental condition: $[Catalyst] = 0.75gL^{-1}$; $pH = 6.0$; $Temp. = 308K$)

S.No.	Initial dye concentration (gL^{-1})	Rate Constant K_{app} (min^{-1})	Initial rate $r_0 \times 10^{-3}$ ($mgL^{-1}min^{-1}$)	R^2
1	0.02	0.0588	1.17	0.986
2	0.04	0.0868	3.47	0.990
3	0.06	0.0481	2.88	0.992
4	0.04	0.0404	3.23	0.99

The rate of degradation increases with the initial concentration of MG dye then finds a tendency towards independent values with the higher initial concentrations.

According to the **equation 5.9** the plot of $1/r_0$ versus $1/C_0$ represented in **Figure 5.10(a)** shows a linear variation, confirming the Langmuir-Hinshelwood relationship for the initial rates of photodegradation. The values of K_r and K_{LH}

calculated from the intercept and the slope of the straight line ($R^2=0.928$) are $1.1 \text{ mgL}^{-1}\text{min}^{-1}$ and 4.5Lmg^{-1} respectively.

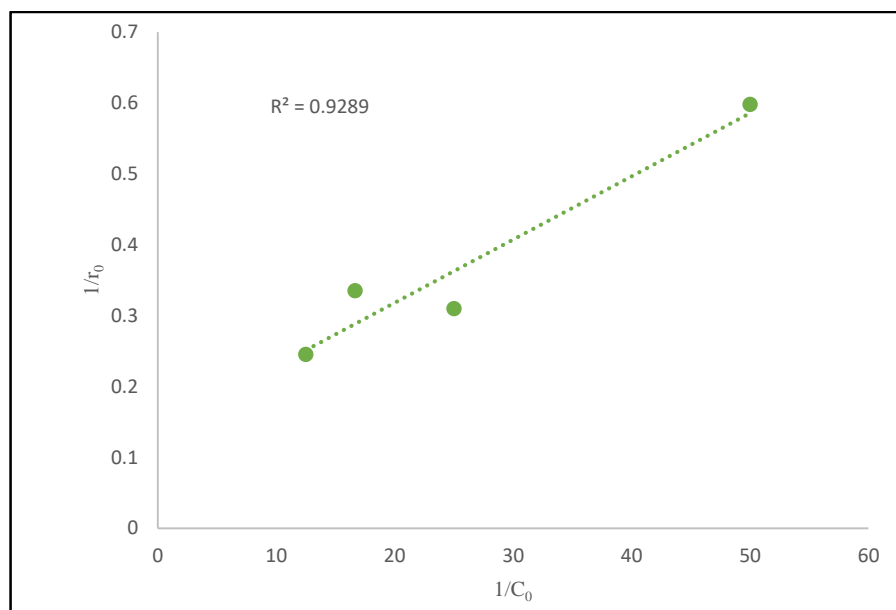


Figure-5.10(a): Langmuir-Hinshelwood plot for visible light photodegradation of MG dye by BaBiO_3 photocatalyst. (Experimental condition: $[\text{BaBiO}_3] = 0.75\text{gL}^{-1}$; $\text{pH} = 6.0$; $\text{Temp.} = 308\text{K}$).

(b) Results with $\text{Ba}_{0.6}\text{K}_{0.4}\text{BiO}_3$

The experimental results shows that the rate of photocatalytic degradation increases with increase in concentration of dye up to 40mgL^{-1} . The rate of reaction was then, found to decrease with further increase in the concentration of dye. It is clear from the **Table 5.3 (b)** to **5.6(b)**, initially % degradation of dye increases rapidly and thereafter slowly attains the limiting value.

Figure 5.7.b. (A-D) shows the plots of change in % degradation with time for various concentration of dye at various amount of catalyst

Table 5.3 (b): Influence of initial concentration on degradation of MG
 (Experimental Condition: $[\text{Ba}_{0.6}\text{K}_{0.4}\text{BiO}_3] = 0.25\text{gL}^{-1}$; $\text{pH}=6.0$; $\text{Temp.} = 308\text{K}$)

Dye Concentration	20 mgL^{-1}	40 mgL^{-1}	60 mgL^{-1}	80 mgL^{-1}
Time (min)	% Degradation	% Degradation	% Degradation	% Degradation
0	0	0	0	0
3	9.65	8.65	5.32	6.1
5	15.54	15.65	10.57	10.21
7	21.54	23.67	14.84	14.32
10	31.21	35.98	22.35	21.34
15	43.74	52.21	36.21	33.24
20	54.32	65.24	50.35	43.21
25	65.32	74.89	62.35	54.54
30	73.21	82.67	72.25	64.24
35	81.65	88.98	78.35	72.32
40	83.98	92.32	81.35	78.35
∞	84.14	92.87	81.78	78.88

Table 5.4(b): Influence of initial concentration on degradation of MG
 (Experimental Condition: $[\text{Ba}_{0.6}\text{K}_{0.4}\text{BiO}_3] = 0.75\text{gL}^{-1}$; $\text{pH}=6.0$; $\text{Temp.} = 308\text{K}$)

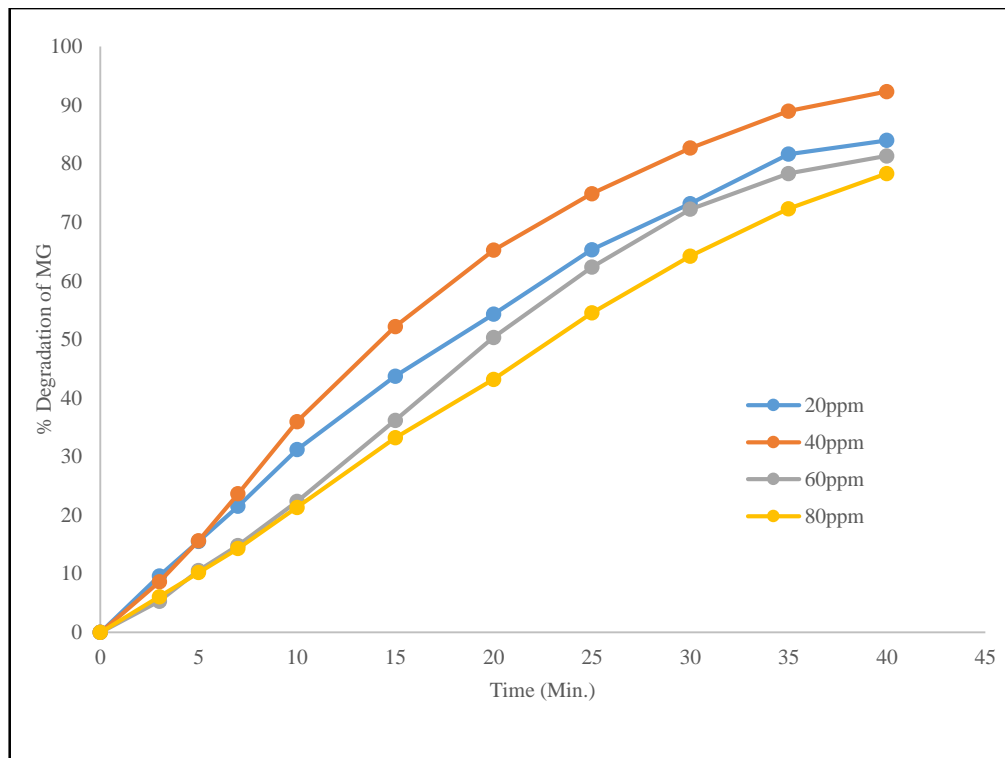
Dye Concentration	20 mgL^{-1}	40 mgL^{-1}	60 mgL^{-1}	80 mgL^{-1}
Time (min)	% Degradation	% Degradation	% Degradation	% Degradation
0	0	0	0	0
3	13.52	18.54	12.63	11.95
5	23.64	30.65	22.56	18.54
7	30.29	38.59	28.69	25.34
10	43.35	52.87	39.25	34.28
15	60.59	70.12	53.58	48.12
20	74.28	82.66	64.98	60.26
25	83.97	91.57	77.31	69.83
30	90.22	97.01	82.81	78.29
35	93.55	97.89	88.39	84.23
40	94.12	98.74	91.60	87.45
∞	94.66	98.75	91.90	87.88

Table 5.5 (b): Influence of initial concentration on degradation of MG
 (Experimental Conditions: $[\text{Ba}_{0.6}\text{K}_{0.4}\text{BiO}_3] = 1.00\text{gL}^{-1}$; $\text{pH}=6.0$; $\text{Temp.} = 308\text{K}$)

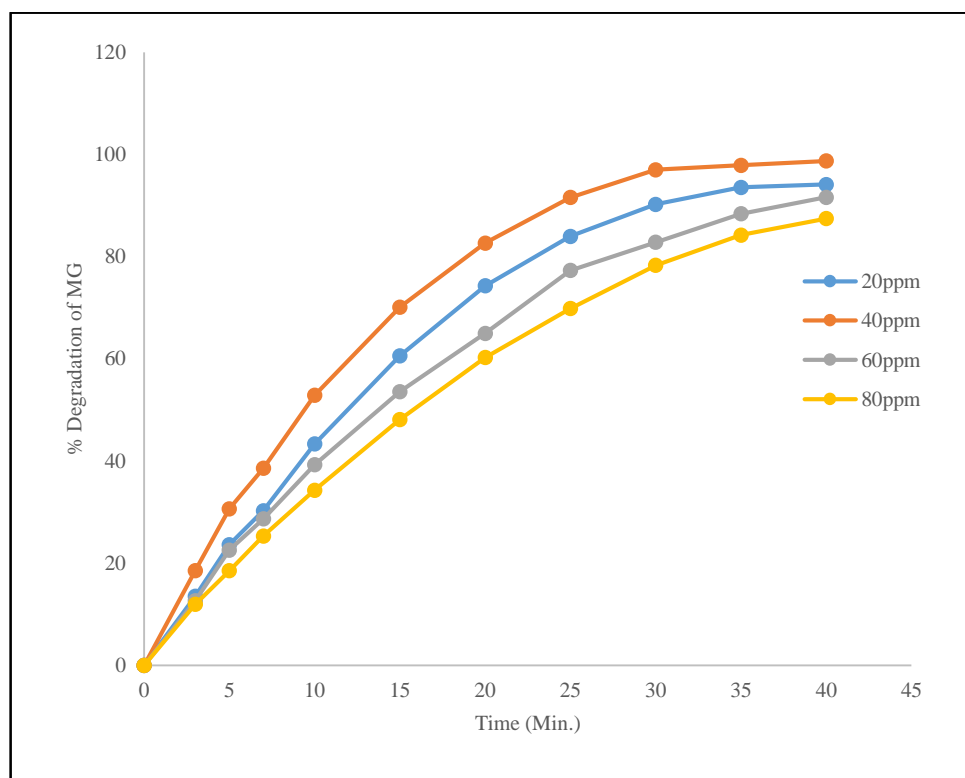
Dye Concentration	20 mgL^{-1}	40 mgL^{-1}	60 mgL^{-1}	80 mgL^{-1}
Time (min)	% Degradation	% Degradation	% Degradation	% Degradation
0	0	0	0	0
3	12.36	14.58	10.32	10.35
5	20.89	24.35	16.35	15.46
7	27.54	33.54	23.67	21.58
10	38.74	45.65	34.21	30.84
15	54.21	63.27	48.57	43.57
20	67.65	77.65	60.32	55.38
25	77.81	85.67	72.59	66.35
30	84.35	92.35	80.32	74.21
35	89.21	95.00	85.32	80.37
40	90.10	95.57	88.65	84.35
∞	90.54	95.89	89.10	84.94

Table 5.6(b): Influence of initial concentration on degradation of MG
 (Experimental Conditions: $[\text{Ba}_{0.6}\text{K}_{0.4}\text{BiO}_3] = 1.25\text{gL}^{-1}$; $\text{pH}=6.0$; $\text{Temp.} = 308\text{K}$)

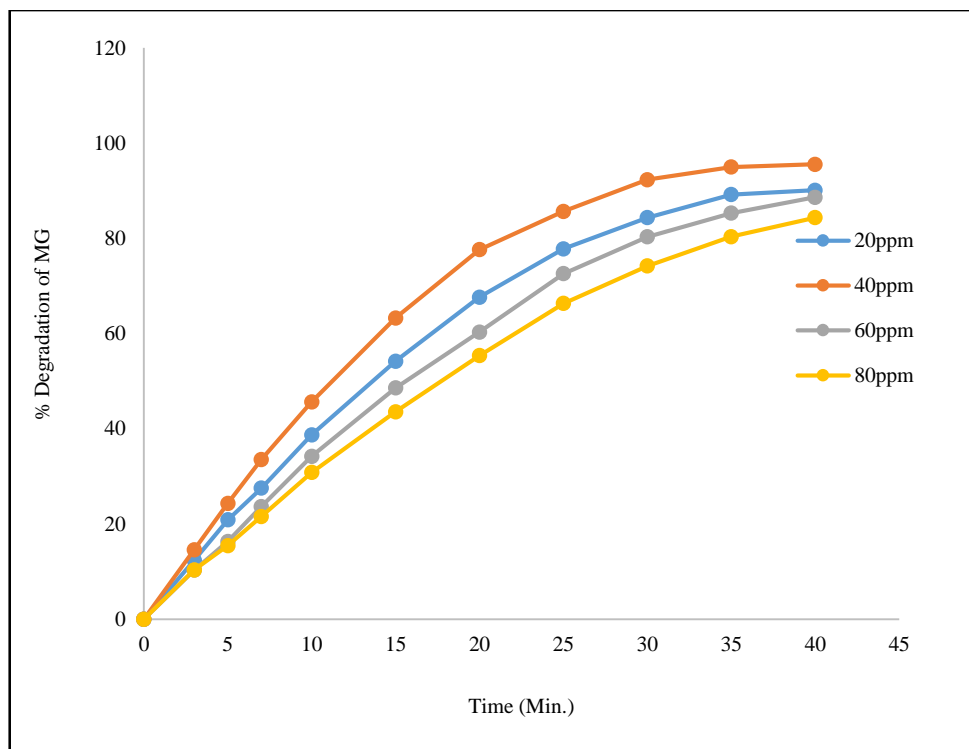
Dye Concentration	20 mgL^{-1}	40 mgL^{-1}	60 mgL^{-1}	80 mgL^{-1}
Time (min)	% Degradation	% Degradation	% Degradation	% Degradation
0	0	0	0	0
3	11.32	11.35	7.38	8.35
5	18.74	20.65	13.68	13.57
7	24.51	27.87	19.65	18.57
10	33.87	39.87	28.89	26.87
15	48.65	57.54	42.35	39.54
20	60.32	71.27	55.68	50.27
25	70.54	79.84	67.54	60.38
30	78.89	87.54	76.87	69.65
35	84.78	91.57	82.35	76.34
40	88.21	93.89	85.32	80.81
∞	88.70	94.19	85.69	81.26



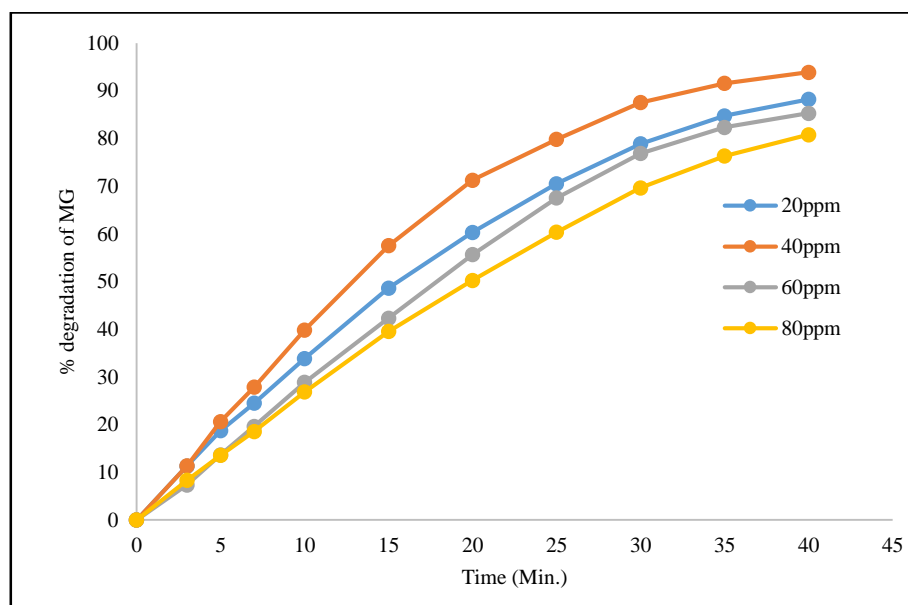
(A)



(B)



(C)



(D)

Figure 5.7(b): Effect of concentration of MG on its visible light degradation in $Ba_{0.6}K_{0.4}BiO_3$ [(A) Catalyst dose: $0.25gL^{-1}$; (B) Catalyst dose: $0.75gL^{-1}$; (C) Catalyst dose: $1.00gL^{-1}$; (D) Catalyst dose: $1.25gL^{-1}$; $pH=6.0$; $Temp. =308K$].

The photodegradation kinetics of initial dye concentration is illustrated in **Figure 5.8(b)**, which depicts the dark adsorption-desorption equilibrium and the

additional decrease in MG concentration caused by visible light irradiation at optimum catalyst dose i.e. 0.75gL^{-1} .

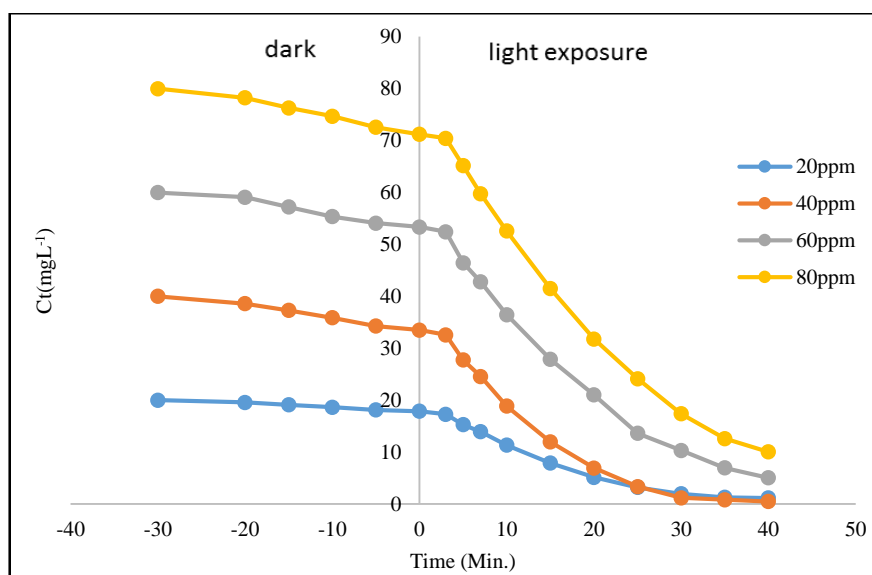


Figure 5.8(b): Variation of dye concentration versus time for different MG initial concentration. (Experimental condition: $[\text{Ba}_{0.6}\text{K}_{0.4}\text{BiO}_3] = 0.75\text{gL}^{-1}$; $\text{pH}=6.0$, $\text{Temp.}=308\text{K}$).

Keeping the rate expression with respect to initial concentration given in **equation 5.12** to **5.14** in mind, graphs are plotted between $\ln C_t/C_0$ and time.

The plot of $\ln C_t/C_0$ versus t with different initial concentration of MG is shown in **Figure 5.9(b)**. The figure shows that the photocatalytic degradation follows perfectly the pseudo-first order kinetic with respect to MG concentrations.

It is found that a plot between $\ln C_t/C_0$ versus time represents a straight line, the slope of linear regression equals the apparent first order rate constant K_{app} which is consistent with the reported first order reaction [68].

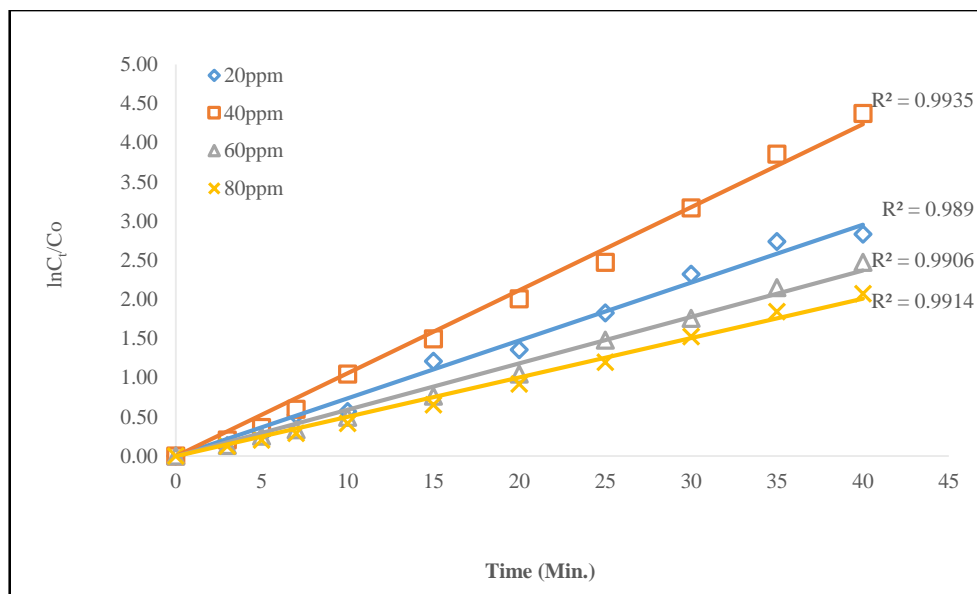


Figure 5.9(b): Linear variation of $\ln C_t/C_0$ versus time for photocatalytic degradation of at different initial dye concentration.

The values of rate constants K_{app} , which corresponds to different initial concentration, along with the initial rate (r_0) and corresponding regression constants, are listed in **Table 5.7(b)**.

Table 5.7(b): Pseudo-first order apparent constant values for the different initial dye concentration of dye
(Experimental condition: $[Ba_{0.6}K_{0.4}BiO_3] = 0.75g/L$; $pH = 6.0$; $Temp. = 308K$)

S.No.	Initial concentration (mg/L)	Rate constant K_{app} (min^{-1})	Initial rate $r_0 \times 10^{-3}$ ($mg/L \cdot min^{-1}$)	R^2
1	0.02	0.0739	1.47	0.989
2	0.04	0.126	5.04	0.993
3	0.06	0.0491	2.94	0.990
4	0.04	0.0501	4.008	0.991

According to **equation 5.9**, the plot of $1/r_0$ against $1/C_0$ as shown in **Figure 5.10(b)** gives linear relationship between $1/r_0$ and $1/C_0$ confirming the Langmuir-Hinshelwood relationship for the initial rate of photodegradation. The values of K_r and K_{LH} calculated from the slope ($1/K_r$) and intercept ($1/K_r \cdot K_{LH}$) of the above figure are found to be, $5.06 mg/L \cdot min^{-1}$ and $3.2 Lmg^{-1}$, respectively.

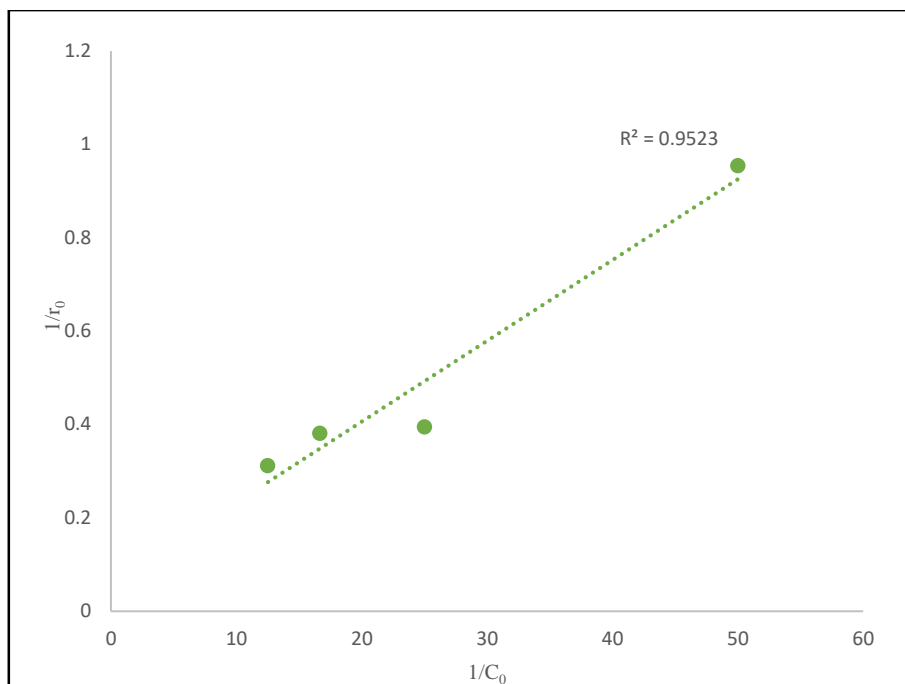


Figure-5.10(b): Langmuir-Hinshelwood plot for visible light photodegradation of MG dye by $Ba_{0.6}K_{0.4}BiO_3$. (Experimental condition: $[Ba_{0.6}K_{0.4}BiO_3] = 0.75 gL^{-1}$; $pH=6.0$; $Temp. = 308K$).

Here, for both the catalysts adsorption equilibrium constant i.e. K_{LH} obtained from the linearization of inverse of initial rate ($1/r_0$) and initial concentration ($1/C_0$) is different to the constant obtained from the dark adsorption (b). This is due to the photo adsorption and very rapid photoreaction of the dyes on the catalyst surface. These results are consistent with the earlier studies on photodegradation of dyes [65,66].

5.3.4.2 Effect of catalyst dose on photocatalytic degradation of MG

The optimization of catalyst dose is an important issue that is significant for avoiding the use of excessive catalyst and ensuring the maximum absorption of photon light. Hence, a series of experiments is carried out by varying the amount of both the catalysts from 0.25 to 1.25 gL^{-1} at pH 6.0 and 40 mgL^{-1} MG dye concentration at 308K. The degradation is studied till the maximum degradation is achieved.

It is observed that for both the cases, up to 0.75 gL^{-1} doses of photocatalysts, degradation rate increases and then with further increase in dose, the rate decreases. The enhancement of removal rate may be due to the increase in the availability of

active sites on the surface of the catalyst which in turn increases the adsorption of dye species and, hence, the proportion of the excited species by the incoming photons. Larger amount of the catalyst favours the degradation efficiency due to the generation of free radicals O_2° and OH° . Therefore, the rate of degradation increases with the increase of catalysts from 0.25 to 0.75gL^{-1} . A further increase in catalyst dose beyond the optimum will result in non-uniform light intensity distribution, so that the reaction rate would, indeed, be lowered with increased catalyst dosage. The tendency toward agglomeration (particle-particle interaction) increases at high solids concentration, resulting in a reduction in surface area available for light absorption and hence a drop in photocatalytic degradation rate. Although the number of active sites in solution will increase with catalyst dose, a point will be appeared to reach where light penetration is to be compromised because of excessive particle concentration. Thus, the trade-off between these two opposing phenomena results in an optimum catalyst dose for the photocatalytic reaction [69,70]. Since the maximum degradation of MG dye is observed with 0.75gL^{-1} , the other experiments are performed using the same catalyst dose. Similar results have been obtained in the earlier reports on photodegradation of dyes [66,71,72].

The corresponding results with both the catalysts (BaBiO_3 and $\text{Ba}_{0.6}\text{K}_{0.4}\text{BiO}_3$) have been elaborated below:

(a) Results with BaBiO_3

A series of experiments is carried out by varying the amount of catalyst from 0.25 to 1.25gL^{-1} at pH 6.0 and 40mgL^{-1} MG dye concentration. The degradation is studied till the maximum degradation is achieved.

Table 5.8(a) shows the influence of the catalyst dose on the % photodegradation of MG under visible light irradiation and the corresponding graphs are given in **Figure 5.11(a)**.

Table 5.8 (a): Influence of BaBiO₃ dose on degradation of MG
 (Experimental Conditions: [MG] = 40mgL⁻¹; pH=6.0; Temp.= 308K)

Catalyst dose	0.25gL ⁻¹	0.75gL ⁻¹	1.00gL ⁻¹	1.25gL ⁻¹
Time (min)	% Degradation	% Degradation	% Degradation	% Degradation
0	0.00	0.00	0.00	0.00
3	4.67	15.09	11.13	7.90
5	11.67	27.20	20.90	17.20
7	19.69	35.14	30.09	24.42
10	32.11	49.42	42.20	36.42
15	48.23	66.67	59.82	54.09
20	61.26	79.21	74.20	67.82
25	70.91	88.12	82.22	76.39
30	73.41	93.56	88.90	84.09
35	83.84	95.25	89.65	88.12
40	84.25	95.29	90.00	89.65
∞	84.76	95.74	90.23	89.98

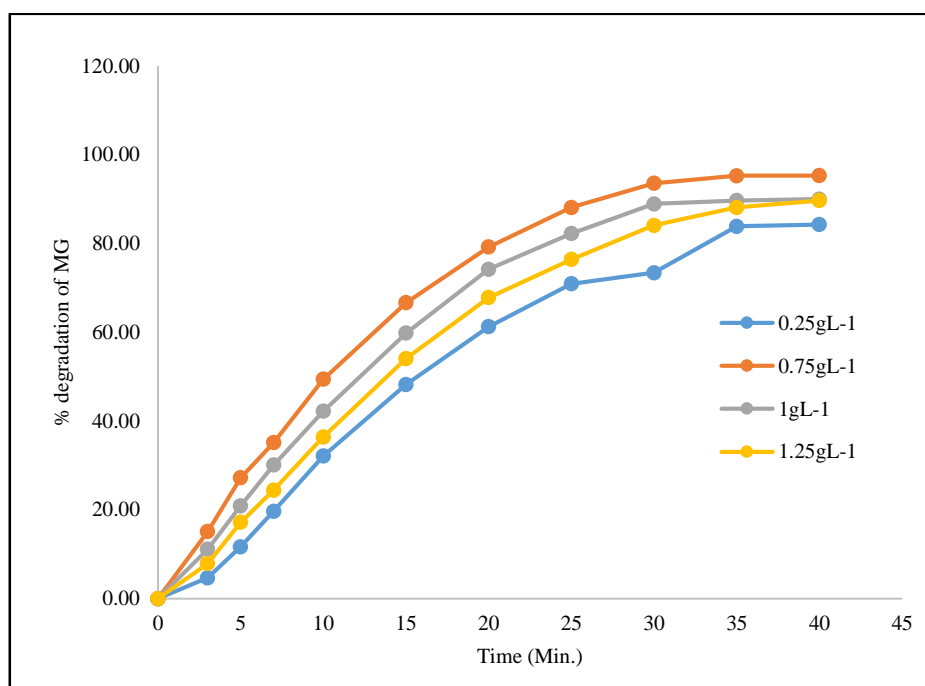


Figure 5.11(a): Influence of BaBiO₃ dose on visible light degradation of MG dye.
 (Experimental condition: [MG] = 40mgL⁻¹; pH=6; Temp. =308K)

The photodegradation kinetics at different catalyst loading is illustrated in **Figure 5.12(a)**, which depicts the dark adsorption-desorption equilibrium and the additional decrease in MG concentration caused by visible light irradiation.

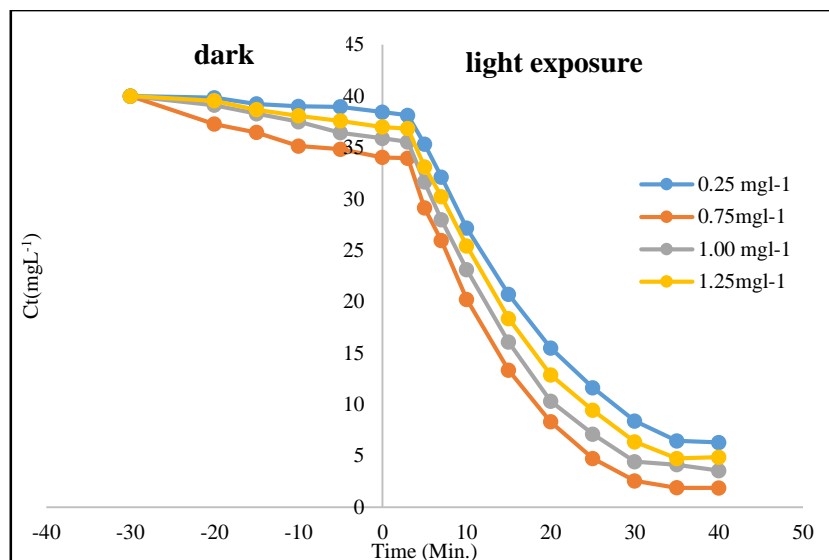


Figure 5.12(a): Variation of residual dye concentration at different $BaBiO_3$. (Experimental conditions: $[MG] = 40 \text{ mgL}^{-1}$; $pH=6.0$; $Temp. = 308K$).

For the calculation of the rate constant (K_{app}) the logarithm of remaining concentration of MG is fitted to the Langmuir Hinshelwood kinetic model (given by **equation 5.11**) by plotting $\ln C_t/C_0$ against the irradiation time at different catalyst dose, which has been shown in **Figure 5.13(a)**.

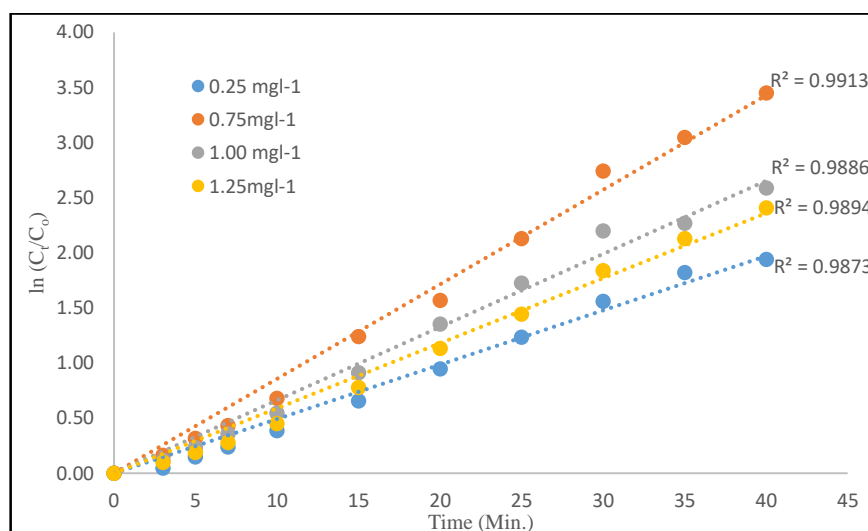


Figure 5.13(a): Linear variation of $\ln C_t/C_0$ versus time for photocatalytic degradation of MG dye at different $BaBiO_3$ loading. (Experimental condition: $[MG] = 40 \text{ mgL}^{-1}$; $pH=6.0$; $Temp. = 308K$).

The pseudo-first-order rate constants, $K_{app}(\text{min}^{-1})$, are calculated from the slopes of the above **Figure 5.13(a)** and are listed in **Table 5.9(a)**.

Table 5.9(a): Pseudo-first order apparent constant values for the different BaBiO₃ dose
 (Experimental condition: [MG] = 40mgL⁻¹; pH =6.0; Temp. = 308K)

S.No.	Catalyst Dose (gL ⁻¹)	Rate Constant K _{app.} (min ⁻¹)	R ²
1	0.25	0.0493	0.987
2	0.75	0.0857	0.991
3	1.00	0.066	0.989
4	1.25	0.059	0.987

An empirical relationship between the catalyst dose and initial dye concentration has been reported by Galindo et al ($r_0 \alpha [\text{catalyst}]^n [\text{dye}]$), where n is an exponent less than 1 for all the dyes studied relative to low concentration of catalyst. [29,73]

Figure 5.14(a) shows the log-log plots of rate constant against the catalyst dose which results in a straight line with a slope of 0.75 (equal to reaction order with respect to photocatalyst and intercept of -2.21 { **Figure 5.14(a)** } thus the initial degradation rate can be expressed by **equation 5.15**.

$$r_0 \alpha [\text{BaBiO}_3]^{0.75} [\text{MG}] \quad \text{--- (5.15)}$$

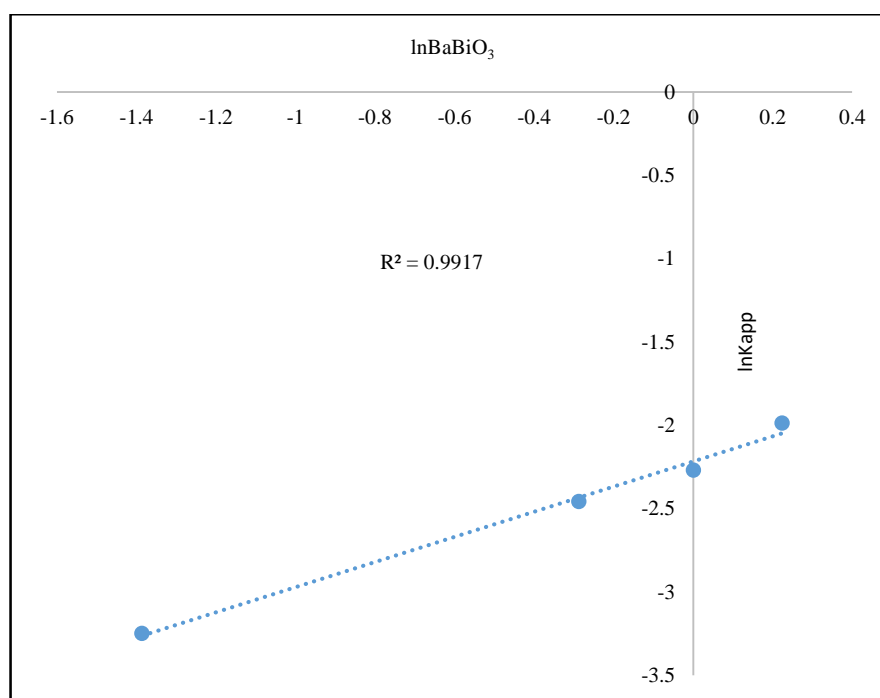


Figure 5.14(a): Relationship between $\ln K_{app}$ and the amount of BaBiO₃. (Experimental condition: [MG] = 40mgL⁻¹; pH =6.0; Temp. = 308K).

(b) Results with Ba_{0.6}K_{0.4}BiO₃

The catalyst loading was varied from 0.25gL⁻¹ to 1.5gL⁻¹ with an initial dye concentration of 40mgL⁻¹, initial pH 6.0 at 308K. The degradation is studied till the maximum degradation is achieved.

Table 5.8(b) shows the influence of the catalyst dose on the % photodegradation of MG under visible light irradiation and the corresponding graphs are given in **Figure 5.11(b)**.

Table 5.8(b): Influence of Ba_{0.6}K_{0.4}BiO₃ dose on degradation of MG (Experimental Conditions: [MG] = 40mgL⁻¹; pH=6.0; Temp. = 308K)

Catalyst dose	0.25gL ⁻¹	0.75gL ⁻¹	1.00gL ⁻¹	1.25gL ⁻¹
Time (min)	% Degradation	% Degradation	% Degradation	% Degradation
0	0	0	0	0
3	8.65	18.54	14.58	11.35
5	15.65	30.65	24.35	20.65
7	23.67	38.59	33.54	27.87
10	35.98	52.87	45.65	39.87
15	52.21	70.12	63.27	57.54
20	65.24	82.66	77.65	71.27
25	74.89	91.57	85.67	79.84
30	82.67	97.01	92.35	87.54
35	88.98	97.89	95.00	91.57
40	92.32	98.74	95.57	93.89
∞	92.74	99.89	95.98	94.14

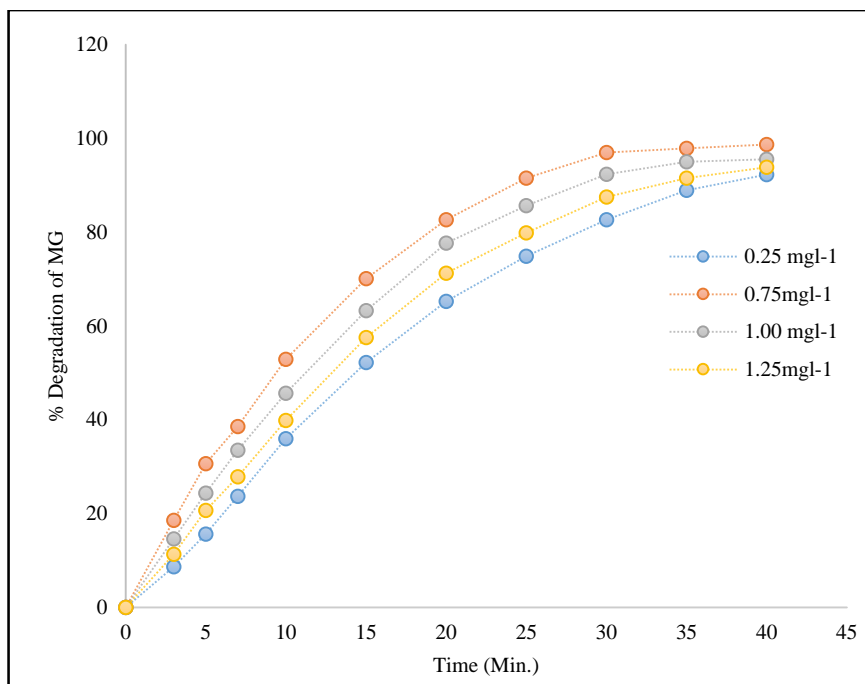


Figure 5.11(b): Influence of $Ba_{0.6}K_{0.4}BiO_3$ dose on visible light degradation of MG dye. (Experimental condition: $[MG]=40\text{mgL}^{-1}$; $pH=6.0$; $Temp.=308\text{K}$).

The photodegradation kinetics at different catalyst loading is illustrated in **Figure 5.12(b)**, which depicts the dark adsorption-desorption equilibrium and the additional decrease in MG concentration caused by visible light irradiation.

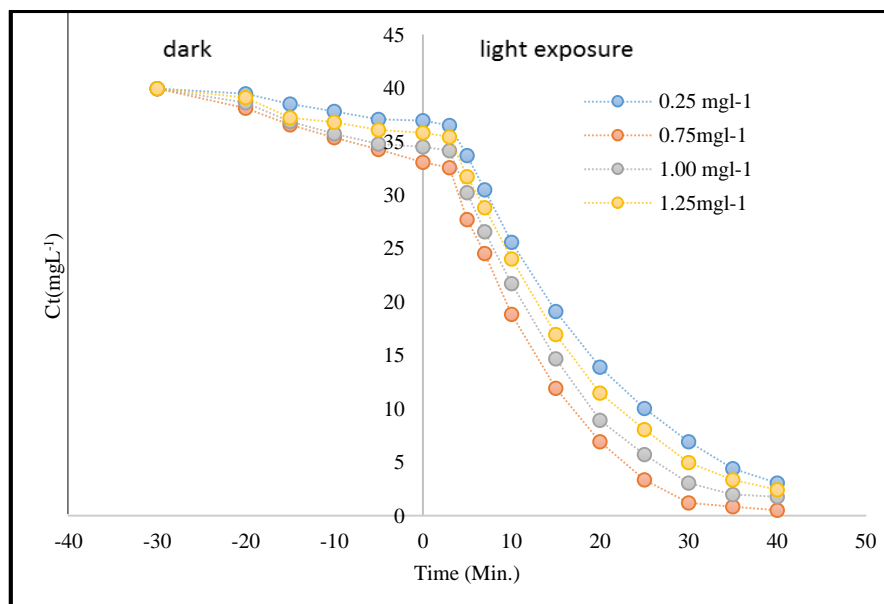


Figure 5.12(b): Variation of residual dye concentration at different $Ba_{0.6}K_{0.4}BiO_3$ (Experimental conditions: $[MG]=40\text{mgL}^{-1}$; $pH=6.0$, $Temp.=308\text{K}$).

For the calculation of the rate constant (K_{app}) the logarithm of remaining concentration of MG is fitted to the Langmuir Hinshelwood kinetic model by plotting $\ln(C_t/C_0)$ against the irradiation time at different catalyst dose, which has been shown in **Figure 5.13(b)**.

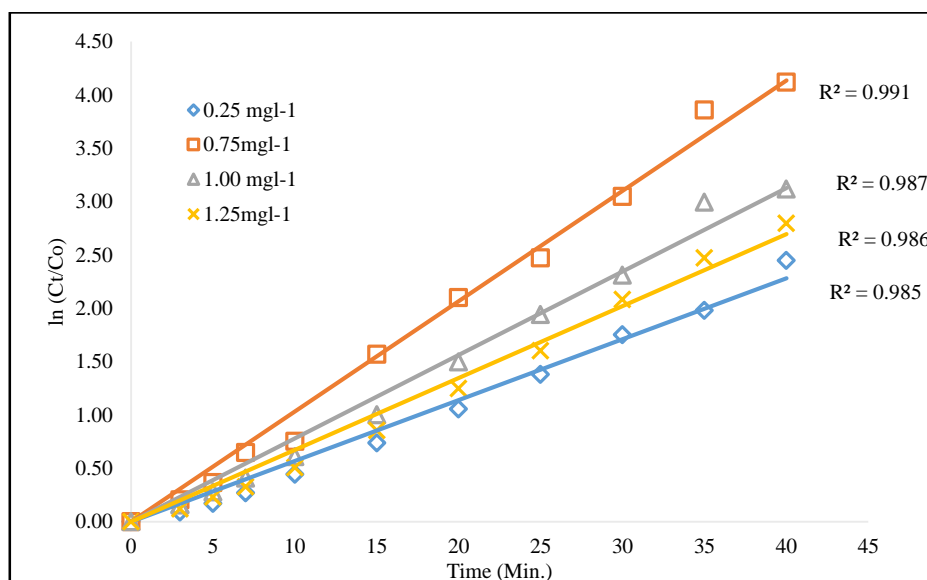


Figure 5.13(b): Linear variation of $\ln C_t/C_0$ versus time for photocatalytic degradation of MG dye at different $Ba_{0.6}K_{0.4}BiO_3$ loading. (Experimental condition: $[MG] = 40\text{mgL}^{-1}$; $pH=6.0$; $Temp. = 308K$).

The pseudo-first-order rate constants, $K_{app}(\text{min}^{-1})$, are calculated from the slopes of the above **Figure 5.13(b)** and are listed in **Table 5.9(b)**.

Table 5.9(b): Pseudo-first order apparent constant values for the different $Ba_{0.6}K_{0.4}BiO_3$ dose

(Experimental condition: $[MG] = 40\text{mgL}^{-1}$; $pH = 6.0$; $Temp. = 308K$)

S.No.	Catalyst Dose (gL^{-1})	Rate Constant $K_{app.}(\text{min}^{-1})$	R^2
1	0.25	0.067	0.985
2	0.75	0.103	0.991
3	1.00	0.078	0.987
4	1.25	0.057	0.986

Also, an empirical relationship between the initial dye concentration has been reported by Galindo et al ($r_0 a [\text{catalyst}]^n [\text{dye}]$), where n is an exponent less than 1 for all the dyes studied relative to low concentration of catalyst. [29,73]

Figure 5.14(b) shows the log-log plots of rate constant against the catalyst dose which results in a straight line with a slope of (equal to reaction order with respect

to photocatalyst) and intercept of -2.25. {Figure 5.14(b)} thus the initial degradation rate can be expressed by equation 5.16.

$$r_o \propto [\text{Ba}_{0.6}\text{K}_{0.4}\text{BiO}_3]^{0.48} [\text{MG}] \quad \text{---(5.16)}$$

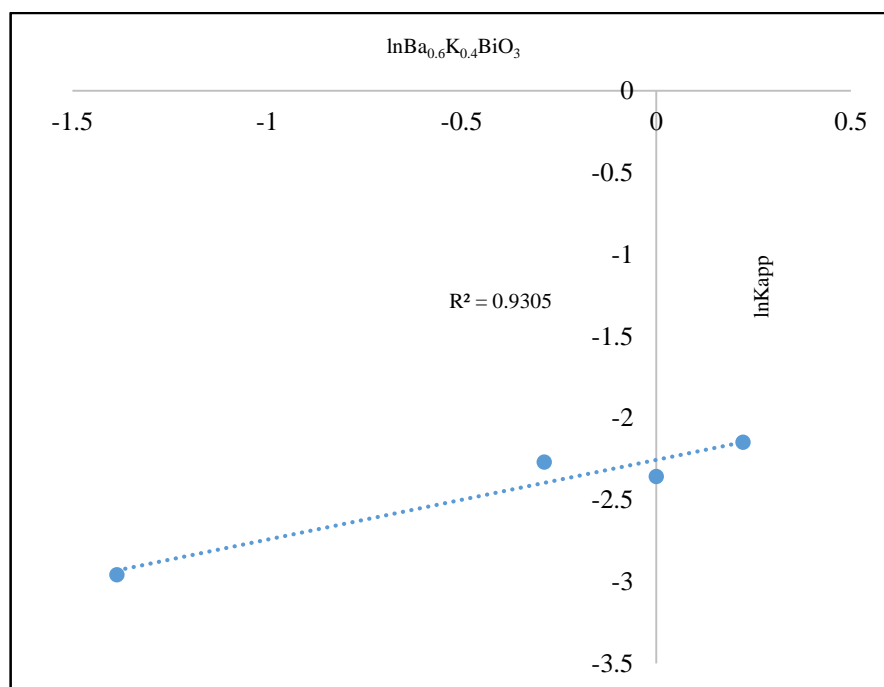


Figure 5.14(b): Relationship between $\ln K_{app}$ and the amount of $\text{Ba}_{0.6}\text{K}_{0.4}\text{BiO}_3$. (Experimental condition: $[\text{MG}] = 40\text{mgL}^{-1}$; $\text{pH} = 6.0$; $\text{Temp.} = 308\text{K}$).

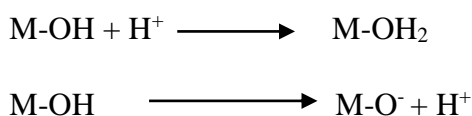
From the experimental results, it was observed that the increase in catalyst dose from 0.25gL^{-1} to 0.75gL^{-1} increased the rate and with further increase in the catalyst dose the reaction rate decreases, which is the characteristics of heterogeneous photocatalysis and results are in a good agreement with the earlier studies [74,75]. In order to have a better dye removal efficiency, we used 0.75gL^{-1} BaBiO_3 or $\text{Ba}_{0.6}\text{K}_{0.4}\text{BiO}_3$ suspension concentration for the rest of the experimental runs. The photocatalytic destruction of other organic pollutants has also exhibited the same dependency over the catalyst dose [76].

5.3.4.3 Effect of initial pH on photocatalytic degradation of MG dye

Organic compounds in wastewater differ greatly in several parameters, particularly in their speciation behaviour, solubility in water and hydrophobicity. While some compounds are uncharged at common pH conditions typical of natural

water or wastewater, other compounds exhibit a wide variation in speciation (or charge) and physico-chemical properties. Besides, because of the amphoteric behaviour of most semiconductor oxides, an important parameter governing the rate of reaction taking place on semiconductor particle surfaces is the pH of the dispersions [77,78]. Since, pH influences the surface-charge-properties of the photocatalysts; therefore, the effect of pH on the rate of degradation needs to be considered. The interpretation of pH effects on the efficiency of the photocatalytic degradation process is a very difficult task because of its multiple roles. Most significantly, it is related to the acid base property of the metal-oxide surface as explained above on the basis of their amphoteric nature [79].

In the present research work also, both the catalysts despite having status of p-type (BaBiO_3) and n-type ($\text{Ba}_{0.6}\text{K}_{0.4}\text{BiO}_3$) semiconductor are supposed to be electrically neutral, making them amphoteric in nature [80,81]. It is known that the metal oxide particles suspended in water behave similarly to diprotic acids. The adsorption of water molecules at sacrificial metal sites is followed by the dissociation of OH^- charged groups leading to coverage with chemically equivalent metal hydroxyl group (M-OH) due to amphoteric behaviour of most metal hydroxides, the following 2 equilibrium reactions are considered [82]:



Experiments are carried out at pH values in the range 4.0-8.0, using 40mgL^{-1} MG solution and $0.75\text{gL}^{-1}\text{BaBiO}_3$ dose. For MG, the extent of photocatalysis increases with increase in pH up to 6.0 and with further increase in pH the degradation efficiency decreases. An increase in the rate of degradation with increase in the pH is due to the generation of more OH^- ions. These ions loose an electron to the hole generated at the semiconductor surface and OH^\bullet free radicals are formed. These formed free radicals cause oxidation of the dye. On further increase in pH above 6.0, a decrease is observed because at very high pH, MG becomes negatively charged and so it repels negatively charged OH^- ions. This repulsive force does not allow the approach of OH^- ions to the surface of catalyst and free radical generation is retarded. Similar results have been obtained in the

earlier reports of photodegradation of dyes by semiconductor photocatalysts [83,84].

(a) Results with BaBiO₃

The influence of the initial pH of the solution on the % photocatalytic degradation of MG is depicted in **Table 5.10(a)** and corresponding graphs are shown in **Figure 5.15(a)**.

Table 5.10 (a): Influence of solution pH on degradation of MG
(Experimental Conditions: [MG] = 40mgL⁻¹; [BaBiO₃] = 0.75 gL⁻¹; Temp: 308K)

pH	pH=4.0	pH=5.0	pH=6.0	pH =7.0	pH = 8.0
Time (min)	% Degradation				
0	0.00	0.00	0.00	0.00	0
3	9.46	10.69	15.09	13.16	11.93
5	20.00	21.96	27.20	25.88	23.92
7	29.12	30.53	35.14	33.35	31.94
10	41.29	43.38	49.42	47.58	45.48
15	58.22	60.25	66.67	64.31	62.28
20	72.69	74.27	79.21	77.43	75.85
25	80.65	82.47	88.12	86.11	84.29
30	88.40	89.50	93.56	91.70	90.60
35	86.57	88.66	95.25	92.85	90.75
40	86.81	88.82	95.29	93.27	90.84
∞	86.80	88.83	95.28	93.26	90.83

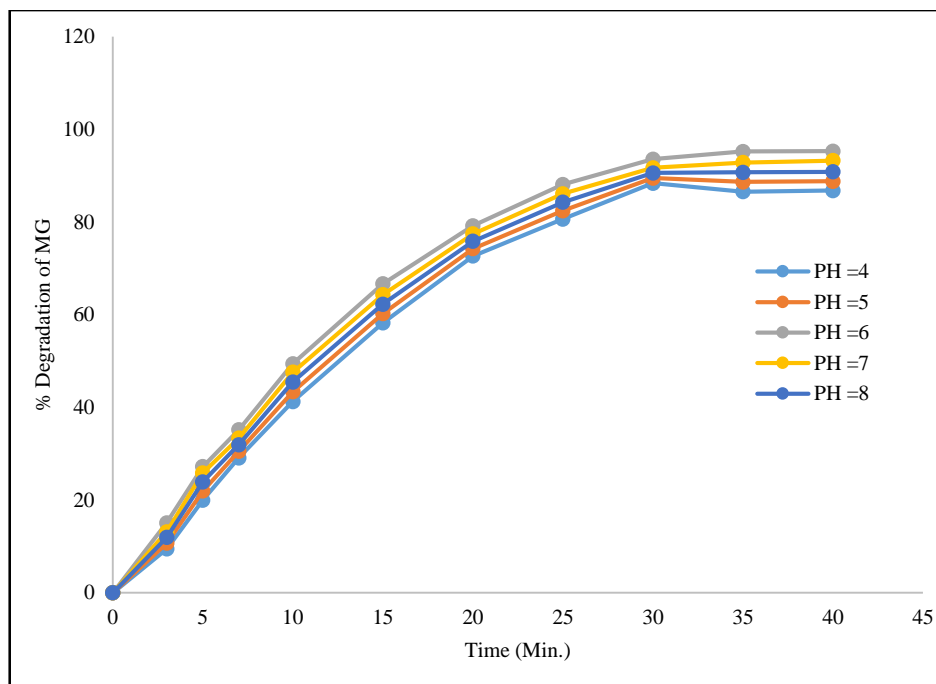


Figure 5.15(a): Effect of initial pH on % degradation of MG. (Experimental condition: $[MG] = 40 \text{ mg L}^{-1}$; $[BaBiO_3] = 0.75 \text{ g L}^{-1}$; Temp. = 308K).

The photodegradation kinetics of different pH loading is illustrated in **Figure 5.16(a)**, which depicts the dark adsorption-desorption equilibrium and the additional decrease in MG concentration caused by visible light irradiation.

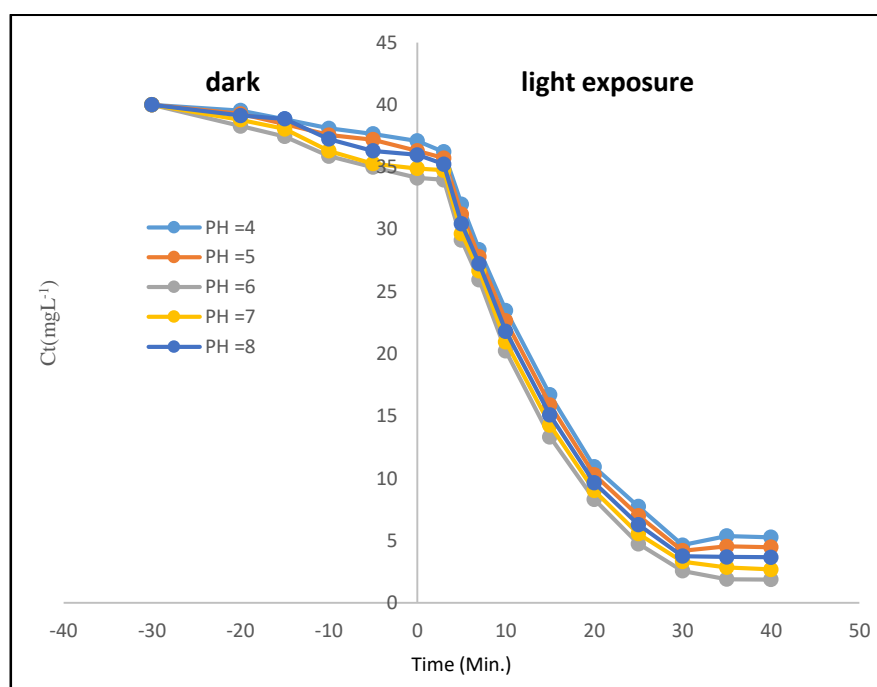


Figure 5.16(a): Effect of pH on the residual dye concentration. (Experimental conditions: $[MG] = 40 \text{ mg L}^{-1}$; $[BaBiO_3] = 0.75 \text{ g L}^{-1}$; Temp. = 308K).

The photocatalytic degradation of MG under a wide range of pH values was fitted to the Langmuir-Hinshelwood model by plotting $\ln(C_t/C_0)$ versus irradiation time which has been shown in **Figure 5.17(a)**.

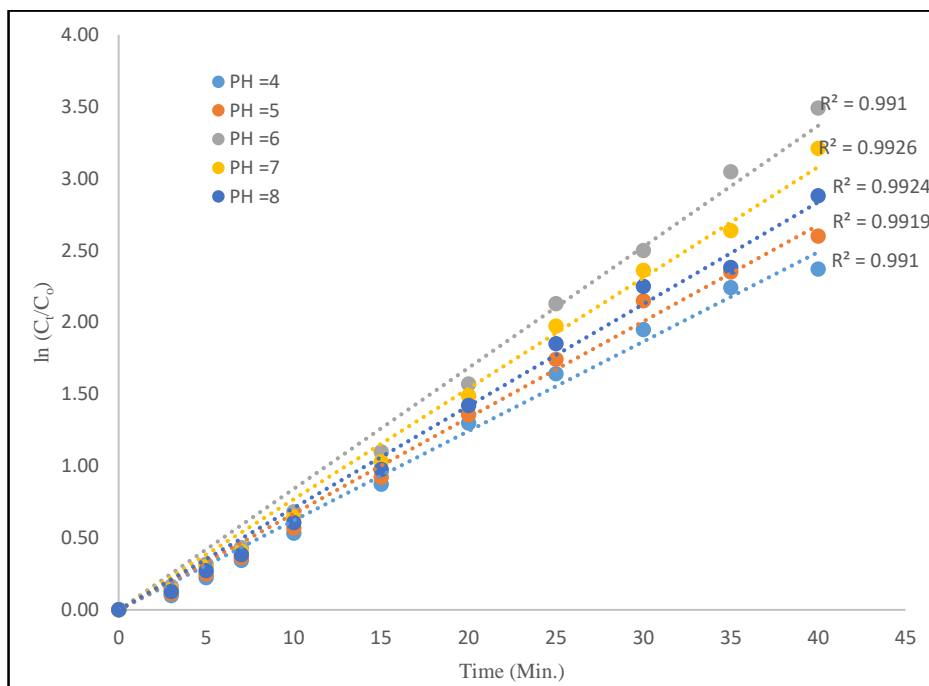


Figure 5.17 (a): Linear variation of $\ln C_t/C_0$ versus time for photocatalytic degradation of MG dye at different initial solution pH. (Experimental condition: $[MG] = 40\text{mgL}^{-1}$; $[BaBiO_3] = 0.75\text{gL}^{-1}$; Temp. = 308K).

The pseudo-first-order rate constant, K_{app} (min^{-1}), are calculated from the slopes of the plots { **Figure 5.17(a)** } and are presented in **Table 5.11(a)**.

Table 5.11(a): Pseudo-first order apparent constant values for the photodegradation of MG at different solution pH (Experimental condition: $[MG] = 40\text{mgL}^{-1}$; $[BaBiO_3] = 0.75\text{gL}^{-1}$; Temp. = 308K)

S.No.	pH	Rate Constant K_{app} (min^{-1})	R^2
1	4.0	0.0709	0.992
2	5.0	0.0699	0.991
3	6.0	0.0842	0.991
4	7.0	0.077	0.992
5	8.0	0.0622	0.991

The pseudo-first-order rate constant (K_{app}) values of dye degradation obtained by performing photodegradation reactions under different initial pH are

reported in **Figure 5.18(a)**. These K_{app} values indicate that the highest degradation is achieved at neutral pH i.e. pH 6.0.

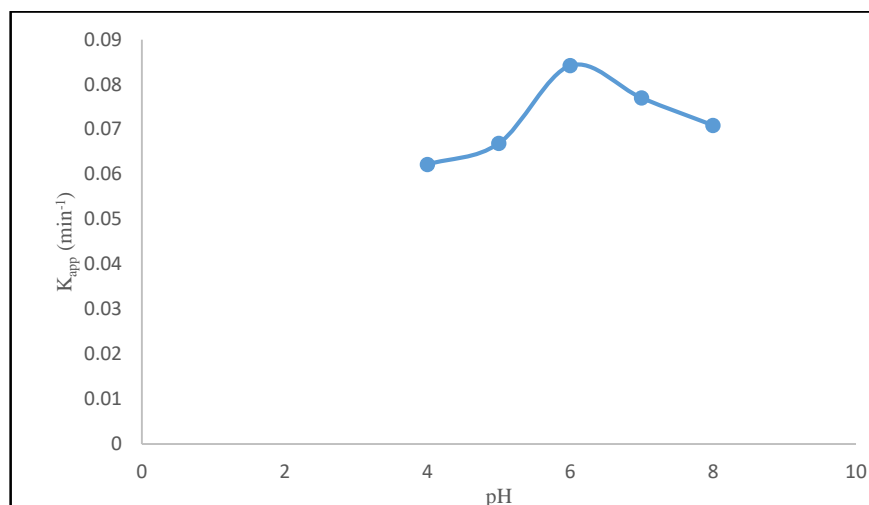


Figure 5.18(a): Effect of the pH on the reaction rate constant for MG dye degradation (Experimental condition: $[MG] = 40\text{mgL}^{-1}$; $[BaBiO_3] = 0.75\text{gL}^{-1}$; Temp= 308K).

(b) Results with $Ba_{0.6}K_{0.4}BiO_3$

The influence of the initial pH of the solution on the % photocatalytic degradation of MG is depicted in **Table 5.10(b)** and corresponding graphs are shown in **Figure 5.15(b)**. For MG dye degradation, the extent of photocatalysis increases with increase in pH up to 6.0 and with further increase in pH the degradation efficiency decreases.

Table 5.10(b): Effect of solution pH on degradation of MG (Experimental Conditions: $[MG]= 40\text{mgL}^{-1}$; $[Ba_{0.6}K_{0.4}BiO_3] = 0.75\text{gL}^{-1}$; Temp.= 308K)

pH	pH=4.0	pH=5.0	pH=6.0	pH =7.0	pH = 8.0
Time (min)	% Degradation				
0	0.00	0.00	0	0.00	0
3	10.98	13.72	18.54	17.29	15.15
5	23.31	26.04	30.65	29.48	27.17
7	30.37	32.49	38.59	36.58	33.75
10	44.87	47.60	52.87	51.45	48.85
15	62.07	64.18	70.12	68.15	65.38
20	74.02	76.76	82.66	80.32	78.17
25	83.94	86.17	91.57	90.03	87.21
30	88.67	90.91	97.01	95.00	92.33
35	90.54	93.01	97.89	96.48	94.08
40	91.05	93.66	98.74	97.73	94.78
∞	91.06	93.66	98.73	97.71	94.77

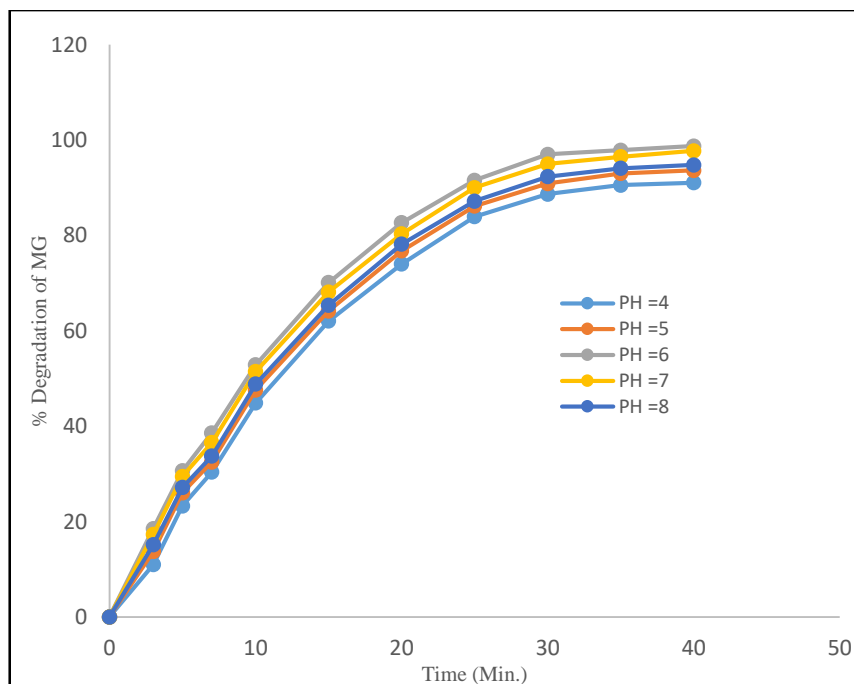


Figure 5.15(b): Influence of solution pH on % degradation of MG. (Experimental condition: $[MG] = 40 \text{ mg L}^{-1}$, $[Ba_{0.6}K_{0.4}BiO_3] = 0.75 \text{ g L}^{-1}$, Temp. = 308K).

The photodegradation kinetics of different pH loading is illustrated in **Figure 5.16(b)**, which depicts the dark adsorption-desorption equilibrium and the additional decrease in MG concentration caused by visible light irradiation.

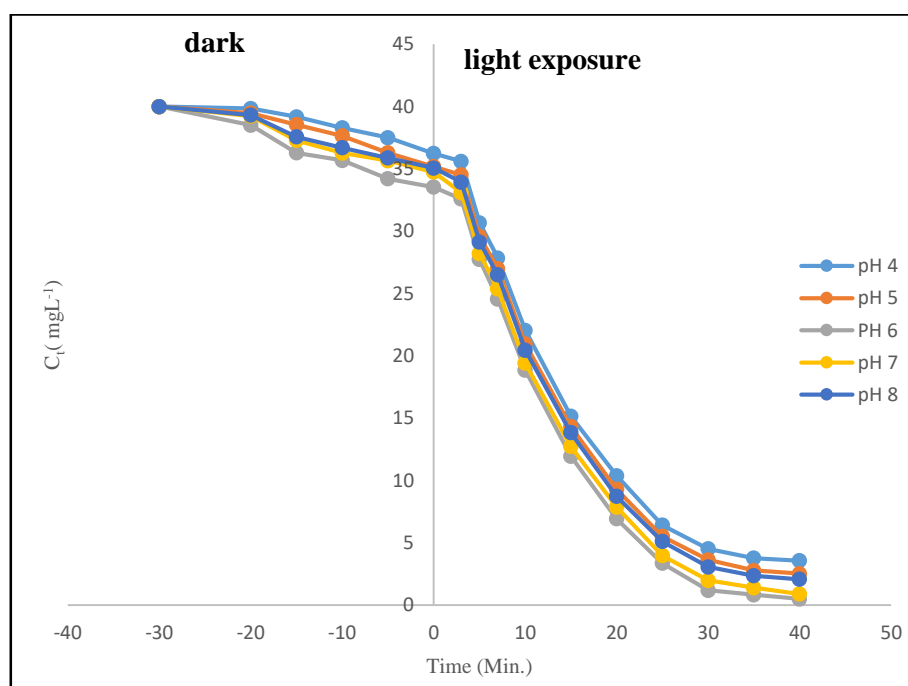


Figure 5.16(b): Effects of solution pH on the residual dye fractions. (Experimental conditions: $[MG] = 40 \text{ mg L}^{-1}$; $[Ba_{0.6}K_{0.4}BiO_3] = 0.75 \text{ g L}^{-1}$; Temp. = 308K).

A plot between $\ln(C_t/C_o)$ versus irradiation time (t) was fitted to the Langmuir–Hinshelwood model. The pseudo-first-order rate constants, K_{app} (min^{-1}), are calculated from the slopes of the plots { **Figure 5.17(b)** }.

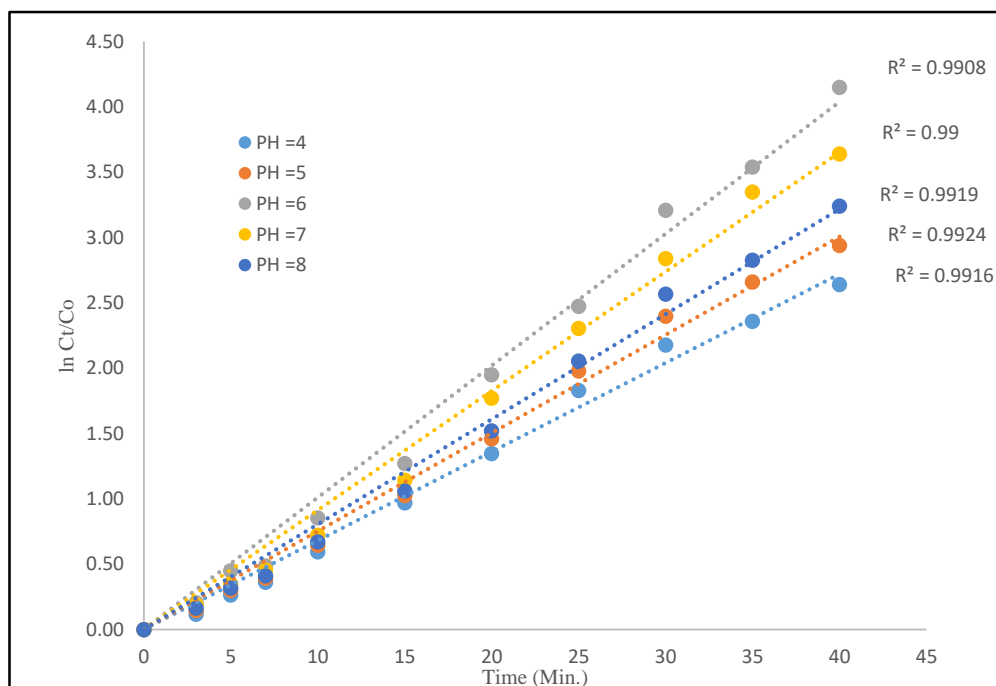


Figure 5.17(b): Linear variation of $\ln C_t/C_o$ versus time for photocatalytic degradation of MG dye at different initial solution pH. (Experimental condition: $[MG] = 40\text{mgL}^{-1}$; $[Ba_{0.6}K_{0.4}BiO_3] = 0.75\text{gL}^{-1}$; Temp. = 308K)

The pseudo-first-order rate constant, K_{app} (min^{-1}), are calculated from the slopes of the plots { **Figure 5.17(b)** } and are presented in **Table 5.11(b)**.

Table 5.11(b): Pseudo-first order apparent constant values for the photodegradation of MG at different solution pH

(Experimental condition: $[MG] = 40\text{mgL}^{-1}$; $[Ba_{0.6}K_{0.4}BiO_3] = 0.75\text{gL}^{-1}$; Temp. = 308K).

S.No.	pH	Rate Constant K_{app} (min^{-1})	R^2
1	4.0	0.068	0.9916
2	5.0	0.0752	0.992
3	6.0	0.101	0.990
4	7.0	0.0913	0.99
5	8.0	0.0805	0.991

The pseudo-first-order rate constant (K_{app}) values of dye degradation obtained by performing photodegradation reactions under different initial pH are

reported in **Figure 5.18(b)**. These K_{app} values indicate that the highest degradation is achieved at neutral pH i.e. pH 6.0.

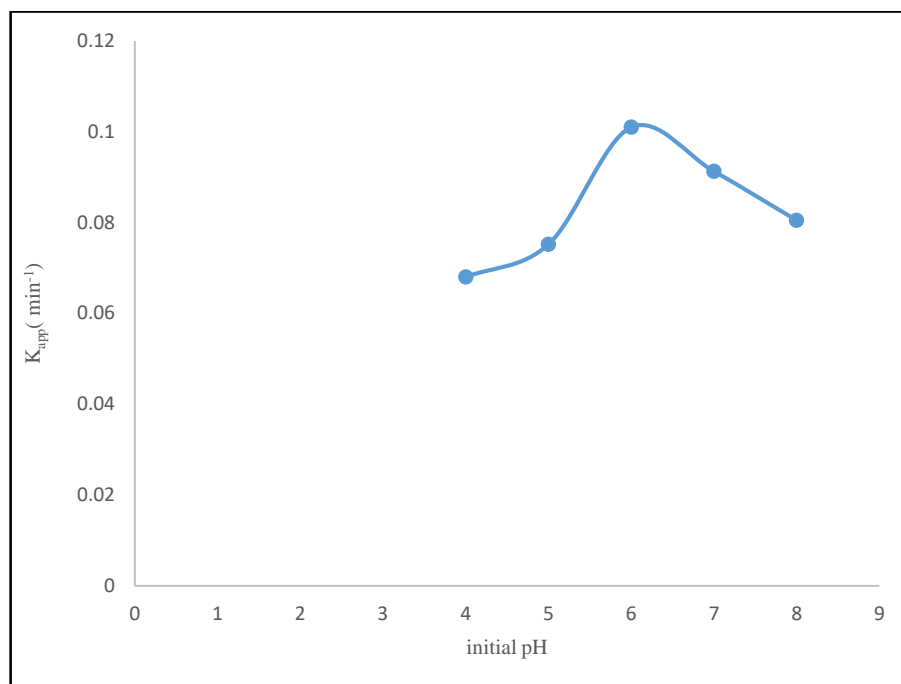


Figure 5.18(b): Effect of the initial pH on the reaction rate constant for MG dye degradation (Experimental condition: $[MG] = 40\text{mgL}^{-1}$; $[Ba_{0.6}K_{0.4}BiO_3] = 0.75\text{gL}^{-1}$; Temp. = 308K).

5.3.4.4 Effect of temperature on photocatalytic degradation of MG dye

Generally, photocatalysis is not temperature dependent. However, an increase in temperature can affect the amount of adsorption and helped the reaction to complete more efficiently with e^-h^+ recombination [85]. An increase in temperature helps the reaction to compete more efficiently with e^-/h^+ recombination as a result of increased collision frequency of molecules; leading to an enhancement of the degradation activity [86,87]. Several previous research work indicate that the rate of the photocatalytic degradation is temperature dependent and is favoured with the increase of solution temperature [88]. The apparent activation energy (E_a) has been calculated from the **Arrhenius equation** [89]:

$$K_{app} = A \exp \left[-\frac{E_a}{RT} \right] \quad \text{--- (5.17)}$$

Where, A is a temperature independent factor (min^{-1}), E_a is the apparent activation energy of the photocatalytic degradation (J/mol), R is the gas constant (8.31 J/K

mol) and T is the solution temperature. The linear transform of $\ln(K_{app}) = f(1/T)$, gives a straight line whose slope is equal to $-E_a/R$.

The effect of temperature is investigated by studying the photocatalytic degradation at different solution temperatures (298-308 K) under the same operating conditions i.e. $[MG] = 40\text{mgL}^{-1}$; Catalyst dose = 0.75gL^{-1} and initial $\text{pH}=6.0$.

(a) Results with BaBiO_3

The influence of solution temperature on the % photodegradation of MG dye as a function of time is depicted in **Table 5.12(a)** and the corresponding graph is shown in **Figure 5.19(a)**. The figure indicates that the rate of the photocatalytic degradation is temperature dependent and is favoured with the increase of solution temperature.

Table 5.12(a): Influence of temperature on degradation of MG
(Experimental conditions: $[MG] = 40\text{mgL}^{-1}$; $[\text{BaBiO}_3] = 0.75\text{gL}^{-1}$; Temp. =308K)

Temperature	298K	303K	308K
Time (min)	%Degradation	%Degradation	%Degradation
0	0.00	0.00	0.00
3	7.30	9.85	15.09
5	16.18	20.05	27.20
7	24.39	30.53	35.14
10	38.24	42.02	49.42
15	59.13	61.76	66.67
20	70.84	76.48	79.21
25	76.37	81.95	88.12
30	83.38	89.01	93.56
35	84.56	89.05	95.25
40	81.98	88.00	95.29
∞	81.99	88.02	95.28

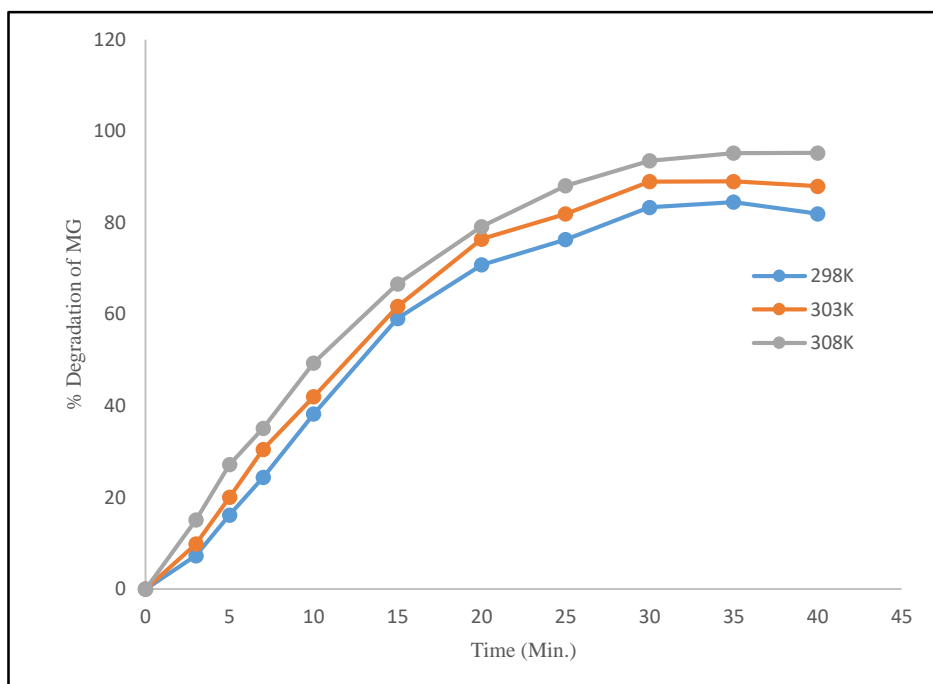


Figure 5.19(a): Influence of temperature on % degradation of MG. (Experimental condition: $[MG] = 40 \text{ mg L}^{-1}$, $[BaBiO_3] = 0.75 \text{ g L}^{-1}$; $\text{pH}=6.0$).

The photodegradation kinetics at different temperature is illustrated in **Figure 5.20**, which depicts the dark adsorption-desorption equilibrium and the additional decrease in MG concentration caused by visible light irradiation.

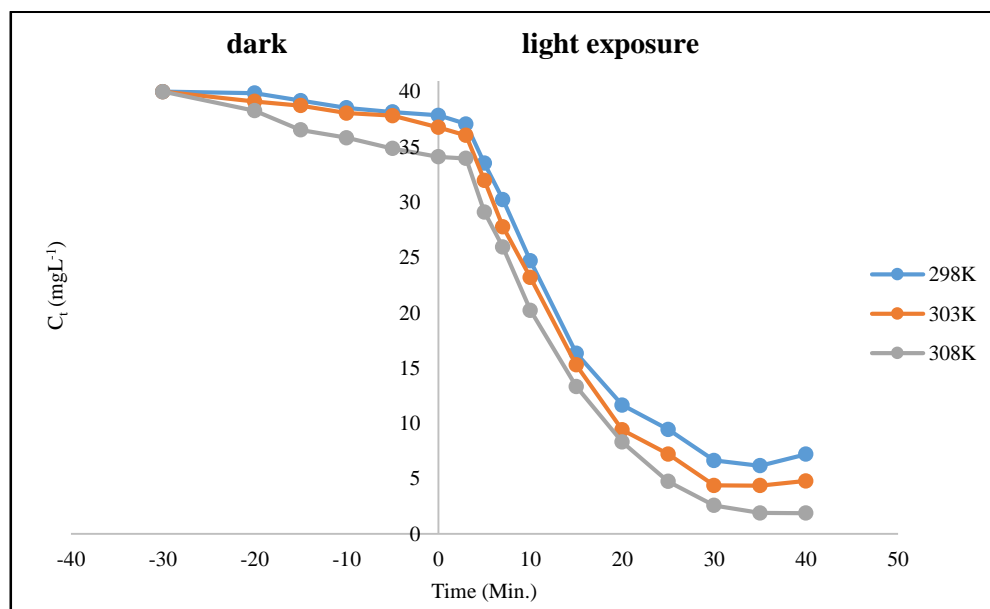


Figure 5.20(a): Effects of Temperature on the residual dye fractions. (Experimental conditions: $[MG] = 40 \text{ mg L}^{-1}$; $[BaBiO_3] = 0.75 \text{ g L}^{-1}$; $\text{pH}=6.0$).

The photodegradation of MG dye at different temperature was fitted to Langmuir Hinshelwood model by plotting $\ln C_t/C_0$ versus time, which has been shown in **Figure 5.21(a)**.

The pseudo-first-order rate constants, K_{app} (min^{-1}), are calculated from the slopes obtained by the curves plotted between $\ln C_t/C_0$ and irradiation time at different temperatures { **Figure 5.21(a)** } and are presented in **Table 5.13(a)**.

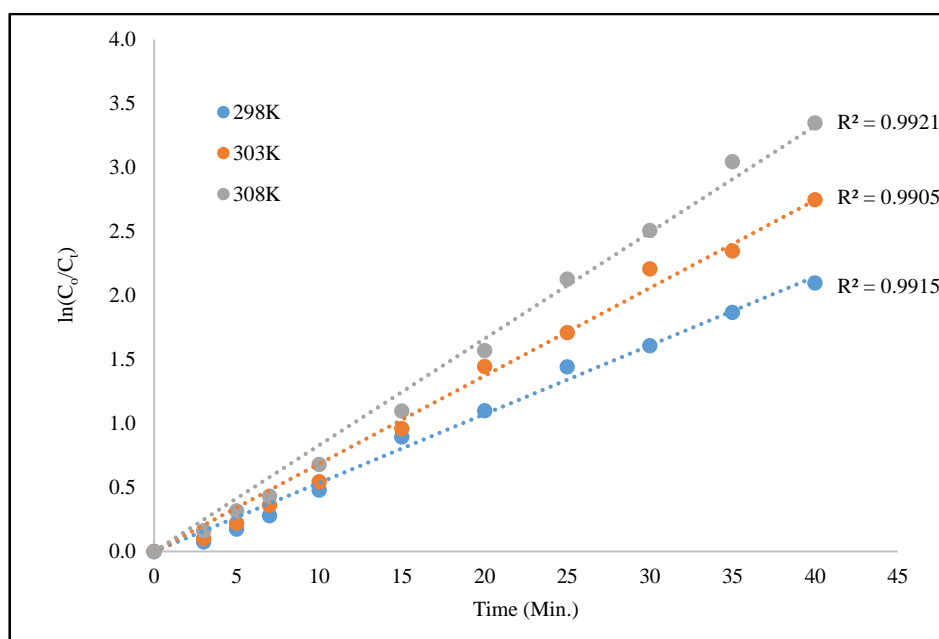


Figure 5.21(a): Linear variation of $\ln C_t/C_0$ versus time for photocatalytic degradation of MG dye at different temperature. (Experimental condition: $[MG] = 40 \text{ mg L}^{-1}$, $[BaBiO_3] = 0.75 \text{ g L}^{-1}$, $\text{pH} = 6.0$).

Table 5.13(a): Pseudo-first order apparent constant values for the different temperatures (Experimental condition: $[MG] = 40 \text{ mg L}^{-1}$; $\text{pH} = 6.0$; Temp. = 308K)

S. No.	Temperature (K)	Rate Constant $K_{app}(\text{Min}^{-1})$	R^2
1	298	0.0537	0.991
2	303	0.0687	0.990
3	308	0.0832	0.992

Figure 5.22(a) shows the plot of $\ln K_{app}$ versus Temperature, gives a linear relationship whose slope gives the apparent activation energy which equals to 33.34

kJmol^{-1} . This apparent energy represents the total activation energy of both adsorption and photocatalytic degradation of dye [90].

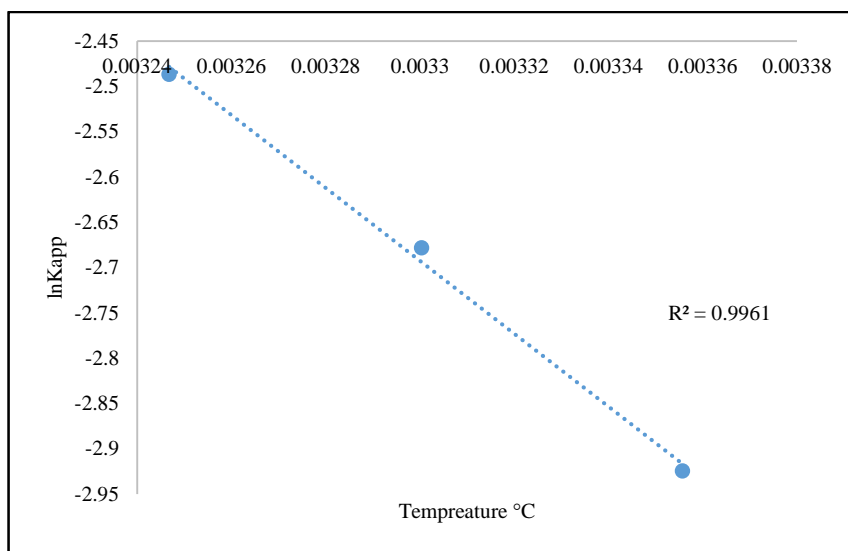


Figure 5.22(a): Plot of $\ln K_{app}$ versus inverse of temperature (Experimental condition: $[MG] = 40 \text{ mg L}^{-1}$; $[\text{BaBiO}_3] = 0.75 \text{ g L}^{-1}$; $\text{pH} = 6.0$).

(b) Results with $\text{Ba}_{0.6}\text{K}_{0.4}\text{BiO}_3$

The influence of solution temperature on the % photodegradation of MG dye as a function of time is depicted in **Table 5.12(b)** and the corresponding graphs is shown in **Figure 5.19(b)**. The figure indicates that the rate of the photocatalytic degradation is temperature dependent and is favoured with the increase of solution temperature.

Table 5.12(b) Influence of temperature on degradation of MG

(Experimental conditions: $[MG] = 40 \text{ mg L}^{-1}$; $[\text{Ba}_{0.6}\text{K}_{0.4}\text{BiO}_3] = 0.75 \text{ g L}^{-1}$)

Temperature	298K	303K	308K
Time (min)	%Degradation	%Degradation	%Degradation
0	0.00	0.00	0.00
3	1.93	11.78	18.54
5	20.94	25.97	30.65
7	24.69	33.27	38.59
10	41.33	46.53	52.87
15	56.70	65.17	70.12
20	71.45	77.66	82.66

25	83.29	88.86	91.57
30	85.31	91.13	97.01
35	86.99	93.27	97.89
40	87.67	93.61	98.74
∞	87.7	93.62	98.73

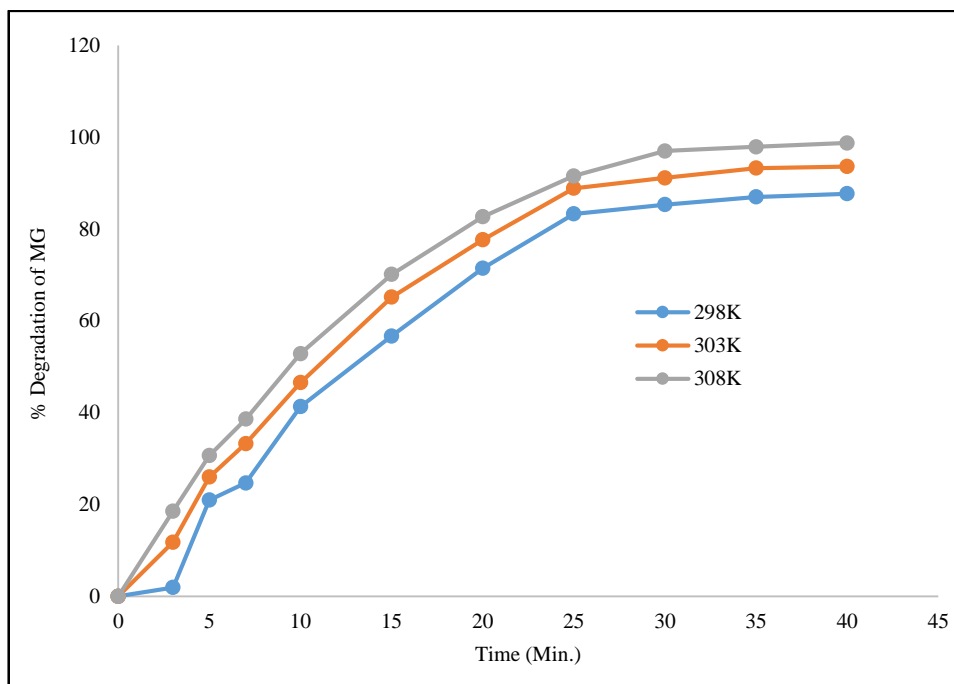


Figure 5.19(b): Influence of temperature on % degradation of MG. (Experimental condition: $[MG] = 40 \text{ mg L}^{-1}$; $[B_{0.6}K_{0.4}BiO_3] = 0.75 \text{ g L}^{-1}$; $pH = 6.0$).

The photodegradation kinetics at different temperature is illustrated in **Figure 5.20(b)**, which depicts the dark adsorption-desorption equilibrium and the additional decrease in MG concentration caused by visible light irradiation.

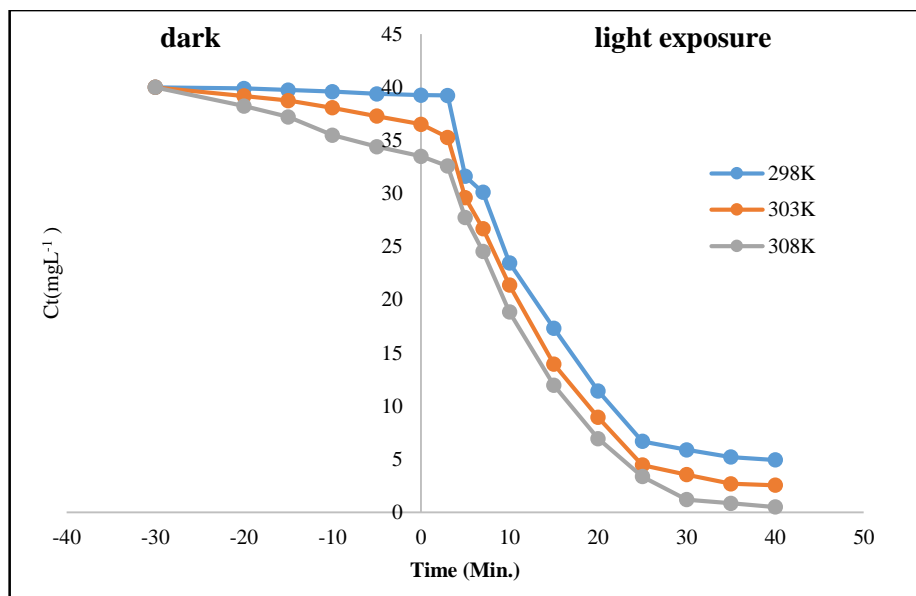


Figure 5.20(b): Variation of MG dye concentration versus time at different temperature. (Experimental condition: $[MG] = 40 \text{ mg L}^{-1}$; $[Ba_{0.6}K_{0.4}BiO_3] = 0.75 \text{ g L}^{-1}$; $pH=6.0$).

The photodegradation of MG dye at different temperature was fitted to Langmuir Hinshelwood model by plotting $\ln C_t/C_0$ versus time, which has been shown in **Figure 5.21(b)**.

The pseudo-first-order rate constants, K_{app} (min^{-1}), are calculated from the slopes obtained by the curves plotted between $\ln C_t/C_0$ and irradiation time at different temperatures {**Figure 5.21(b)**} and are presented in **Table 5.13(b)**.

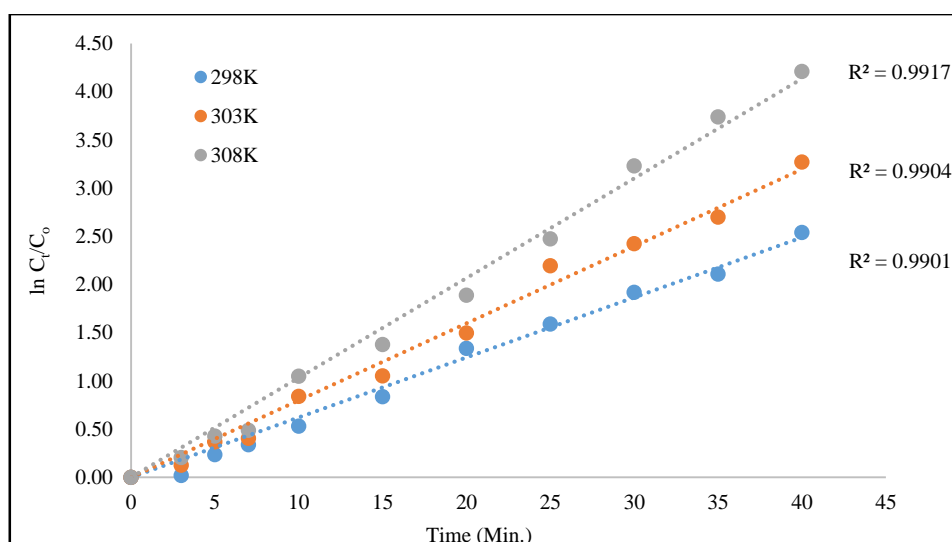


Figure 5.21(b): Linear variation of $\ln C_t/C_0$ versus time for photocatalytic degradation of MG dye at different temperature. (Experimental condition: $[MG] = 40 \text{ mg L}^{-1}$; $[Ba_{0.6}K_{0.4}BiO_3] = 0.75 \text{ g L}^{-1}$; $pH=6.0$).

Table 5.13(b): Pseudo-first order apparent constant values for the different temperatures

(Experimental condition: $[MG] = 40\text{mgL}^{-1}$; $\text{pH} = 6.0$; $\text{Temp.} = 308\text{K}$)

S. No.	Temperature (K)	Rate Constant $K_{\text{app}}(\text{Min}^{-1})$	R^2
1	298	0.0622	0.990
2	303	0.0799	0.990
3	308	0.1034	0.991

Figure 5.22(b) shows the plot of $\ln K_{\text{app}}$ versus Temperature, gives a linear relationship whose slope gives the apparent activation energy equals to 38.77 kJmol^{-1} . This apparent energy represents the total activation energy of both adsorption and photocatalytic degradation of dye [91].

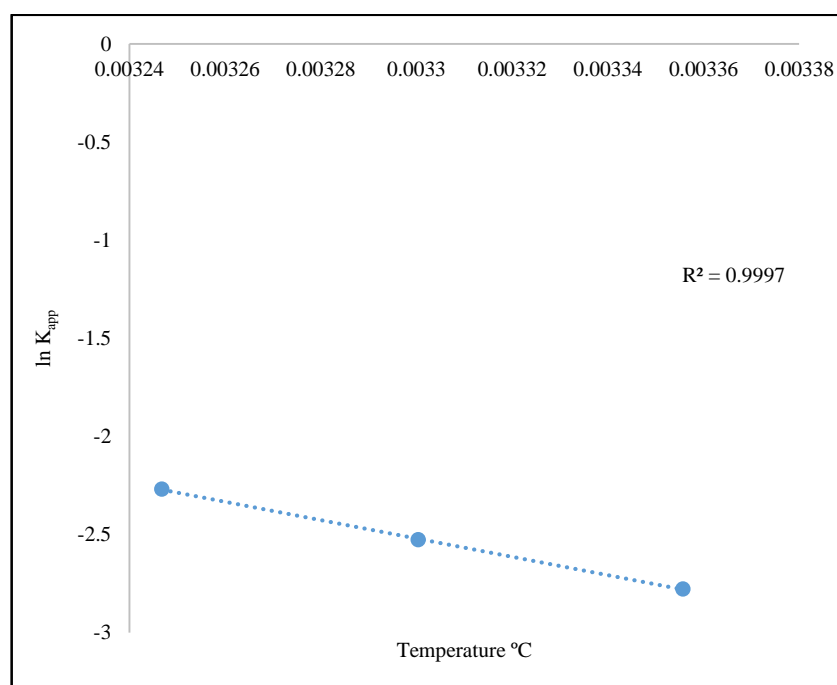


Figure 5.22(b): Plot of $\ln K_{\text{app}}$ versus inverse of temperature (Experimental condition: $[MG] = 40\text{ mg L}^{-1}$; $[Ba_{0.6}K_{0.4}BiO_3] = 0.75\text{gL}^{-1}$; $\text{pH} = 6.0$).

5.3.4.5 Regeneration of photocatalysts

Photocatalysis is a clean technology, which normally does not involve any waste disposal problem. The catalyst can be recycled. The economy of the photocatalytic process depends upon how many times a catalyst can be reused without sacrificing its efficiency and the type of regeneration it requires [92].

To evaluate the stability of the as prepared, three recycling experiments are performed. The used catalyst was regenerated by treating it with boiling distilled

water till a colourless filtrate was obtained and then by drying in it a hot air oven at a temperature of 90° to 100°C. After this, the catalyst was heated in a muffle furnace at about 500°C. As shown in **Figure 5.23**, after being used 3 times for MG dye degradation, the % degradation of dye declined from 95.6% to 94.67% for BaBiO₃, and 98.7 to 95.01% for Ba_{0.6}K_{0.4}BiO₃ under the same experimental condition. ([MG] = 40mgL⁻¹, [catalyst] = 0.75gL⁻¹, pH=6.0, Temp.=308K).

These results indicate that as prepared catalyst is photo-stable during the photocatalytic degradation. The slight decrease in the efficiency of the recycled catalyst may be attributed to the deposition of photo-insensitive hydroxides on the catalyst surface, blocking its active sites [93].

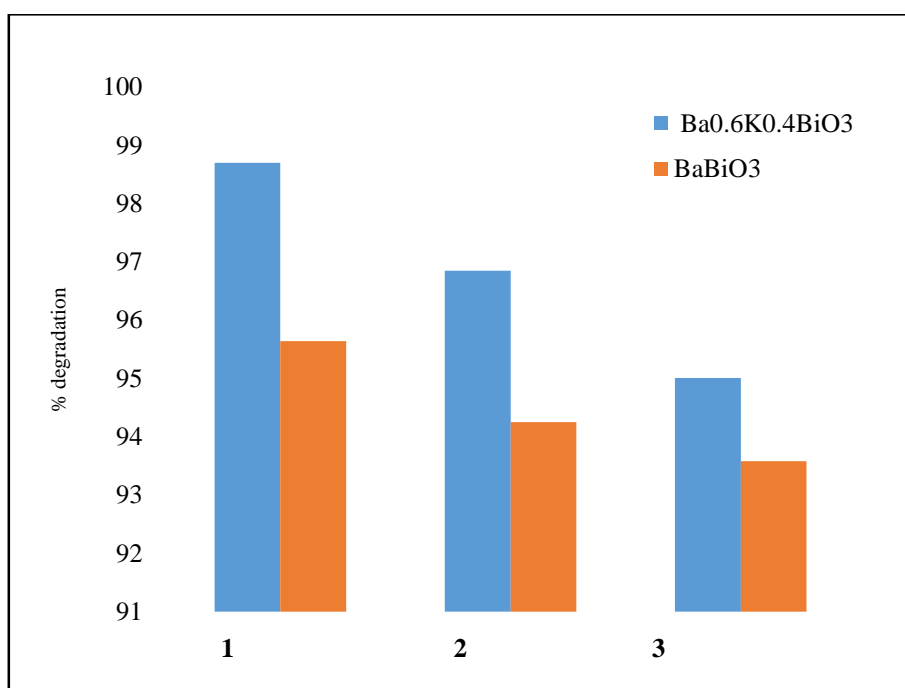


Figure 5.23: Regeneration of photocatalyst. (Experimental condition: [MG] =40mgL⁻¹, [Ba_{0.6}K_{0.4}BiO₃]/[BaBiO₃] =0.75gL⁻¹; pH=6.0; Temp=308K).

5.4 Comparison of BaBiO₃ and Ba_{0.6}K_{0.4}BiO₃ with Degussa p-25 TiO₂

Effectiveness of BaBiO₃ and Ba_{0.6}K_{0.4}BiO₃ has been compared with commercially available Degussa p25 TiO₂ under above mentioned identical optimum experimental conditions (i.e. [MG] =40mgL⁻¹, [Catalysts]=0.75gL⁻¹, pH=6.0, Temp.=308K). As shown in **Figure 5.24**, photocatalytic degradation potential of the as synthesized photocatalysts is found to be much better than the

commercially available TiO_2 owing to their much narrower band gap in comparison to the $\sim 3.2\text{eV}$ band gap of TiO_2 [94]. Also, Degussa p-25 adsorbs more MG dye than BaBiO_3 and $\text{Ba}_{0.6}\text{K}_{0.4}\text{BiO}_3$. As the amount of dye absorbed increases, thereby the active sites are covered with dye ions, thus decreases the formation of $^\circ\text{OH}$ ions which further decreases the degradation efficiency.

Thus, it proved the worth of this research work in the direction of tailoring new visible light active photocatalyst.

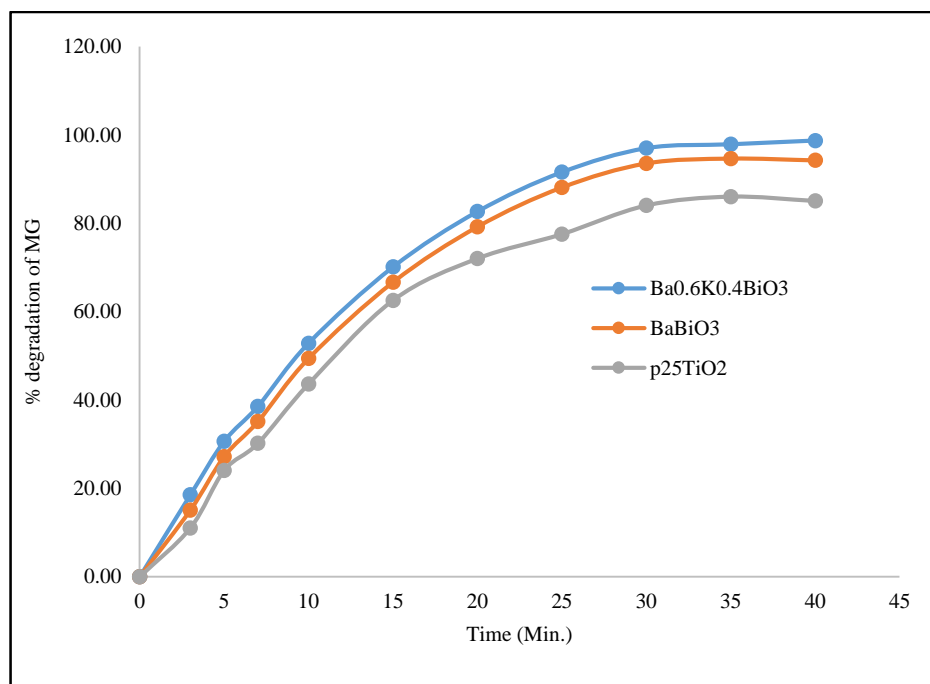


Figure 5.24: Comparison of photocatalytic efficiency of as prepared with p25 TiO_2 under visible light irradiation (Experimental condition: $[\text{MG}] = 40\text{mgL}^{-1}$, $[\text{Ba}_{0.6}\text{K}_{0.4}\text{BiO}_3]/[\text{BaBiO}_3]/[\text{p25 TiO}_2] = 0.75\text{gL}^{-1}$; $\text{pH} = 6.0$; $\text{Temp} = 308\text{K}$).

5.5 Visible spectral changes of MG dye

The degradation of MG dye is monitored by UV/vis. Spectrophotometry **Figure 5.25** depicts the UV–vis spectrum of MG dye degradation in the presence of BaBiO_3 , $\text{Ba}_{0.6}\text{K}_{0.4}\text{BiO}_3$ and p25TiO_2 under visible light irradiation. The rate of degradation is recorded with respect to the change in the intensity of absorption peak in visible light.

It can be seen by the **Figure 5.25** with all the catalysts, light irradiation leads to the prominent decrease in the characteristic band of MG dye at 618 nm after 40 minutes of visible light irradiation. This also indicates that MG dye has been effectively degraded by $\text{Ba}_{0.6}\text{K}_{0.4}\text{BiO}_3$ and BaBiO_3 . The decrease in intensity of

absorption peak is associated with the discoloration of the dye. The decrease in absorption peaks at 618 nm, indicates the removal of $-N=N-$ bond chromophoric group from the azo dye. The almost disappearance of the peaks in the spectrum reveals that dye is eliminated in the presence of $Ba_{0.6}K_{0.4}BiO_3$ after 40 minutes of irradiation. The absorption spectra reveal no evidence of the existence of new intermediates or products formed in the visible region at the end of the reaction. It is clear from the **Figure 5.25** that the maximum degradation efficiency is shown by $Ba_{0.6}K_{0.4}BiO_3$. Owing to its lowest band gap value (1.87 eV) in comparison to $Ba_{0.6}K_{0.4}BiO_3$ (2.07 eV) {as discussed in Chapter 3}. $P-25TiO_2$ has shown least degradation efficiency which is due to its highest band gap.

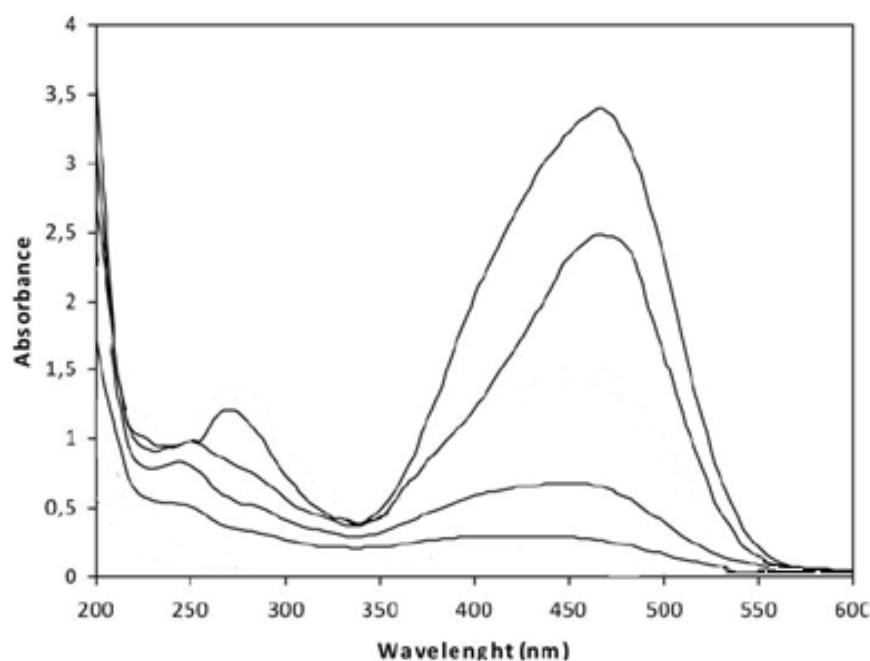


Figure 5.25: UV-vis absorbance spectra of MG solution after photocatalytic degradation over as prepared catalysts. Experimental Conditions: $[MG] = 40\text{mgL}^{-1}$; $[Ba_{0.6}K_{0.4}BiO_3]/ [BaBiO_3] / [p25TiO_2] = 0.75\text{gL}^{-1}$; $pH=6.0$; $Temp. =308\text{K}$.

5.6 TOC analysis

The complete mineralization of the studied dye is confirmed from the analysis of total organic carbon (TOC) content. The MG dye degradation takes place through the oxidative cleavage of the chromophore $-N=N-$ bond resulting in the production of primary reaction by-products which are then oxidized and ultimately yielding carbon di oxide and water [95]. The TOC concentration is of importance as it is the best parameter to indicate the ultimate mineralization of the

target compound. **Figure 5.26** shows the TOC reduction of MG dye by as prepared BaBiO_3 and $\text{Ba}_{0.6}\text{K}_{0.4}\text{BiO}_3$ at optimum reaction conditions. It can be seen that the % TOC removal values for $\text{Ba}_{0.6}\text{K}_{0.4}\text{BiO}_3$ is higher than BaBiO_3 . As shown in **Figure 5.26 (a)**, %TOC removal for photodegradation (following by adsorption) in the presence of as prepared photocatalysts is higher than that obtained by the commercially available p25 TiO_2 , thus indicating the greater reactivity of synthesized photocatalysts (BaBiO_3 and $\text{Ba}_{0.6}\text{K}_{0.4}\text{BiO}_3$).

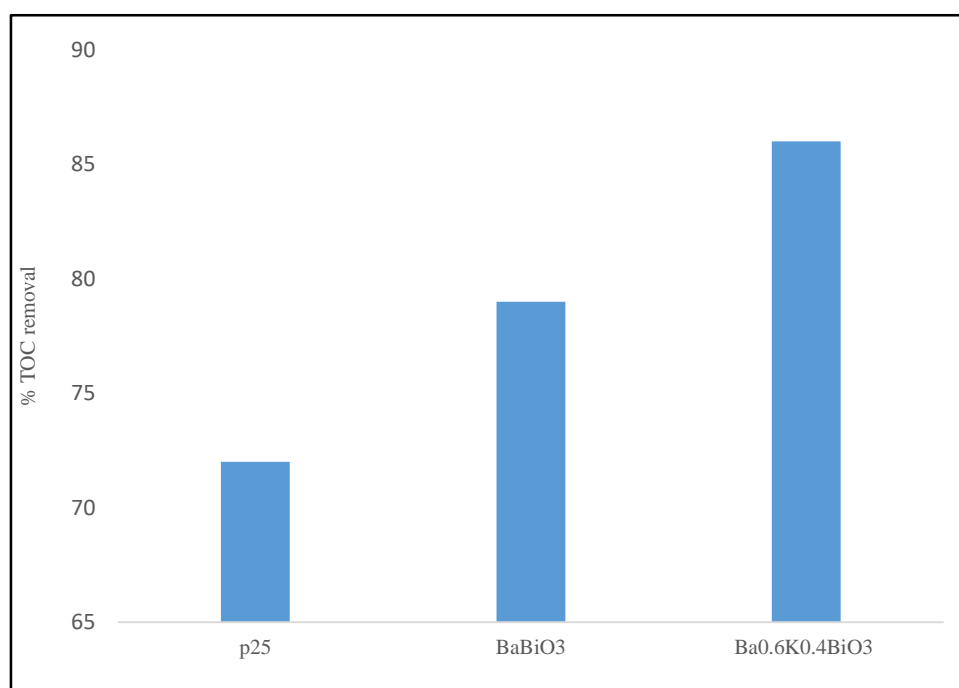
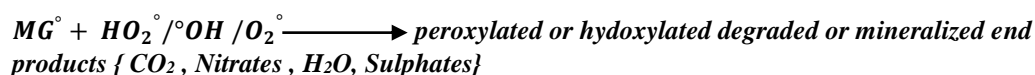


Figure 5.26: TOC removal in MG dye solution obtained by photodegradation by as prepared catalysts. (Experimental Conditions: $[\text{MG}] = 40\text{mgL}^{-1}$; catalyst dose= 0.75gL^{-1} , pH=6.0, Temp. =308K). (a) for p25 TiO_2 (b) for BaBiO_3 (c) for $\text{Ba}_{0.6}\text{K}_{0.4}\text{BiO}_3$.

5.7 Proposed mechanism of MG dye photodegradation

Organic pollutants like dyestuffs have the ability to absorb visible light. Initially the dye molecules are adsorbed on catalyst surface and get excited through the absorption of light. Thus excited dye (Dye^*) injects an electron to the conduction band of the photocatalyst where it is scavenged by O_2 to form active oxygen radicals. The consequence of electron-ejection into the conduction band results in the charge separation and thus e-hole pairs are generated. Holes are generated in

conduction band while e^- are generated in valance band. These electron-hole pair are responsible of generating other reactive species like $^{\circ}\text{OH}$, HO_2 , H_2O_2 and $^{\circ}\text{O}_2^-$. These active radicals carry out photodegradation or mineralization of organic compounds. Proposed mechanism of MG dye degradation by BaBiO_3 and $\text{Ba}_{0.6}\text{K}_{0.4}\text{BiO}_3$ under visible light irradiation is as follows:



5.8 Conclusion

In summary, BaBiO_3 and $\text{Ba}_{0.6}\text{K}_{0.4}\text{BiO}_3$ successfully synthesized by Pechini method resulted in the formation of, mono phase crystalline nano-sized particles which proved their potential in visible light owing to their low band gap (2.07eV and 1.87eV respectively). The feasibility of adsorption and photocatalytic degradation of MG dye using BaBiO_3 and $\text{Ba}_{0.6}\text{K}_{0.4}\text{BiO}_3$ as in the form of aqueous suspension under visible light irradiation has been investigated. Since, the photocatalytic degradation is directly related to the adsorbed quantities of the pollutant, the adsorption properties of MG on to BaBiO_3 and $\text{Ba}_{0.6}\text{K}_{0.4}\text{BiO}_3$ are also discussed in terms of Langmuir and Freundlich adsorption isotherms. The photocatalytic degradation was expressed in terms of LH kinetic model, and the subsequent rate constants are also determined. The effect of different operational parameters such as initial dye concentration, catalyst dose, solution pH and temperature on the rate of photo degradation is studied. Moreover, reusability of these catalysts is studied. Furthermore, to estimate the degree of mineralization,

measurements of total organic carbon has also been conducted. In the present studies, the percentage removal of MG through photocatalytic degradation by BaBiO₃ and Ba_{0.6}K_{0.4}BiO₃ was also compared with the one through TiO₂ (Degussa P-25).

Controlled experiments (photolysis) demonstrated that both visible light and catalyst are needed for the effective destruction of dye. The data obtained from the adsorption experiments are fitted into Langmuir and Freundlich isotherms. They are found to be linear, indicating the formation of mono layer of adsorbate on the outer surface of adsorbent. Langmuir adsorption model is found to be fit for both the catalysts. Thus, obtained results argue that a slow adsorption is noticed on both the catalyst surface, followed by strong photocatalytic degradation.

The study of parameters influencing the degradation process allowed us to find the operating conditions for achieving the highest MG dye degradation rate. The optimization studies revealed the optimum operating conditions: pH value 6.0, catalyst concentration 0.75gL⁻¹, dye concentration 40mgL⁻¹.

The dependence of catalyst concentration on the reaction rate can be explained as $r_0 \alpha [\text{BaBiO}_3]^{0.75} [\text{MG}]$ and $r_0 \alpha [\text{Ba}_{0.6}\text{K}_{0.4}\text{BiO}_3]^{0.48} [\text{MG}]$ for BaBiO₃ and Ba_{0.6}K_{0.4}BiO₃, respectively, when the catalyst concentration is less than 1gL⁻¹.

The Langmuir–Hinshelwood kinetic model showed a good agreement for the initial rates of degradation with the appropriate reaction rate constant (K_r) and the substrate adsorption constant (K_{LH}) values. Here, $K_r = 1.1 \text{ mgL}^{-1}\text{min}^{-1}$ and $K_{LH} = 4.5 \text{ Lmg}^{-1}$ are found for BaBiO₃ while for Ba_{0.6}K_{0.4}BiO₃ they are: $K_r = 5.06 \text{ mgL}^{-1}\text{min}^{-1}$ and $K_{LH} = 3.2 \text{ Lmg}^{-1}$. The value of adsorption coefficient (K_{LH}) in kinetic model is found to be different to that found in dark (b) due to the photo-adsorption and very rapid photoreaction of MG dye on the catalyst surface.

The photocatalytic degradation was temperature dependent with apparent activation energy for MG dye of 33.34kJmol⁻¹ and 38.77 kJmol⁻¹ while using BaBiO₃ and Ba_{0.6}K_{0.4}BiO₃ as photocatalyst, respectively.

Good reusability of our photocatalyst is obtained after separation from the reaction solution by filtration and washing followed by re-calcination without an obviously reduced photocatalytic activity for at least 3rd run.

Thus, it can be concluded that both BaBiO_3 and $\text{Ba}_{0.6}\text{K}_{0.4}\text{BiO}_3$ are efficient recoverable in MG dye degradation. The complete mineralization of the studied dye is confirmed from the analysis of total organic carbon (TOC) content. On analysing the UV–vis spectrum of MG dye degradation in the presence of both the catalysts under visible light irradiation leads to prominent decrease in the characteristic band of MG dye at 618 nm after 40 minutes. The proposed mechanism indicates the participation of various active species like OH° , HO_2 , H_2O_2 and $^\circ\text{O}_2^-$ in the degradation of MG dye.

Our results prove that the photocatalytic efficiency of $\text{Ba}_{0.6}\text{K}_{0.4}\text{BiO}_3$ is shown to be greater than that of BaBiO_3 in degradation of MG dye. The higher activity of $\text{Ba}_{0.6}\text{K}_{0.4}\text{BiO}_3$ was attributed to its narrower band gap in comparison to the parent compound (BaBiO_3).

The photocatalytic degradation potential of the as synthesized photocatalysts is found to be much better than the commercially available Degussa P-25 TiO_2 owing to their much narrower band gap in comparison to the wider band gap ($\sim 3.2\text{eV}$) of the later.

Therefore, exploring higher catalytic activity of such perovskite structures may pave the way for designing useful photocatalytic material and could be useful for the large scale mineralization of the industrial effluents. Also, the degradation of water would enable the recycling of waste water.

References

- [1] M. S. Tsuboy, J. P. F. Angeli, M. S. Mantovani, S. Knasmiiller, G. A. Limbuzerio, L. R. Ribeiro, *Toxicol. in vitro.* 21, (2007), 1650.
- [2] J. S. Bae, H. S. Freeman, S. D. Kim, *Fibers Polym.* 7, (2006), 30.
- [3] M.A. Shannon, P.W. Bohn, M. Elimelech, J.G. Georgiadis, B.J. Mariñs, A.M. Mayes, *Nature* 452, (2008), 301.
- [4] P. Matpang, M. Sriuttha, N. Piwpuan, *Agric. Nat. Resour.* 51, (2017), 96.
- [5] S. Srivastava, R. Sinha, D. Roy, *Aquat. Toxicol.* 66, (2004), 319.
- [6] E. Sudova, J. Machova, Z. Svobodova, T. Vesely, *Veterinarni Medicina*, 52, (2007), 527.
- [7] C.R. Nelson, R.A. Hites, *Environ. Sci. Technol.* 14, (1980), 147.
- [8] https://en.wikipedia.org/wiki/Malachite_green , visited **December 2016**.
- [9] J.-S. Bae, H.S. Freeman, *Dyes Pigm.* 73, (2007), 81.
- [10] F.I. Vacchi, J.A.D.S. Vendemiatti, B.F. daSilva, M.V.B. Zanoni, G.D.A. Umbuzeiro, *Sci. Total Environ.* 601, (2017), 230.
- [11] E. Forgacs, T. Cserháti, G. Oros, *Environ. Int.* 30, (2004), 953.
- [12] C. R. Holkar, A. J. Jadhav, D. V. Pinjari, N. M. Mahamuni, A. B. Pandit, *J. Environ. Manag.* 182, (2016), 351.
- [13] M. S. Nawaz, M. Ahsan, *Alexandria. Eng. J.* 53, (2014), 717.
- [14] I. Arslan, I. A. Balcioglu, *Dyes pigm.* 43, (1999), 95.
- [15] J. He, X. Yang, B. Men, D. Wang, *J. Environ. Sci.* 39, (2016), 97.
- [16] R. Aplin, T. D. Waite, *Water Sci. Technol.* 2000, 42,345.
- [17] A. Zuorro, R. Lavecchia, *Desalination Water Treat.* 52, (2014), 15711.
- [18] A. E. Nemr, M. Hassaan, F. F. Madkour, *Environ. Process.* 5, (2016), 95.

- [19] G. Zhang, G. Liu, L. Wang, *Chem. Soc. Rev.* 45 , (2016), 5951.
- [20] K. Nagaveni, G. Sivalingam, M.S. Hegde, G. Madras, *Appl. Catal. B: Environ.* 48, (2004), 83.
- [21] F. Han, V.S.R. Kambala, M. Srinivasan, D. Rajarathnam, R. Naidu, *Appl. Catal. A: Gen.* 359, (2009), 25.
- [22] H. Zangeneh, A.A.L zinatizadeh, M. Habibi, M. Akia, M.H. Isa, *J. Indus. Eng. Chem.* 26, (2015), 1.
- [23] X. Chen, Z. Wu, D. Liu, Z. Gao, *Nano. Res. Lett.* 143, (12), 2017.
- [24] W. Liu, M. Wang, C. Xu, X. Fu, *J. Nanosci. Nanotechnol.* 13, (2013), 657.
- [25] P. Ellappan, L.R. Miranda, *Int. J. Photoenergy* 2014, (2014), 1.
- [26] H. Dong, G. Zeng, L. Tang, C. Fan, C. Zhang, X. He, Y. He, O. Le, *Water Res.* 79, (2015), 128.
- [27] O. Legrini, E. Oliveros, A.M. Braun, *Chem. Rev.* 93, (1993), 671.
- [28] J. Yu, H. Yu, C.H. Ao, S.C. Lee, J.C. Yu, W. Ho, *Thin Solid Films* 496, (2006), 273.
- [29] C. Galindo, P. Jacques, A. Kalt, *Chemosphere* 45, (2007), 997.
- [30] Y. Liu, J.H. Wei, R. Xiong, C.X. Pan, J. Shi, *Appl. Surf. Sci.* 257, (2011), 8121.
- [31] J. Shi, L. Gu, *Prog. Nat. Sci. Mater. Int.* 22, (2012), 592.
- [32] J. S. Lee, *Catal. Surveys Asia.* 9, (200), 217.
- [33] A. S. Bhalla, R. Guo, R. Roy, *Mat. Res. Innovat.* 4, (2000), 3.
- [34] K. Miura, M. Azuma, H. Funakubo, *Materials*, 4, (2011), 260.
- [35] W. Li, W. Zhang, S. V. Reenen, R. J. Sutton, J. Fan, A. H. Haghighirad, M. B. Johnston, L. Wang, H. J. Snaith, *Energy Environ. Sci.* 9, (2016), 490.
- [36] M. Petrovi, V. Chellappan, S. Ramakrishna, *Solar Energy*, 122, (2015), 678.
- [37] K.-H. Kim, S.-K. Ihm, *J. Hazard. Mater.* 186, (2011), 16.

- [38] J.L. Sotelo, G. Ovejero, F. Martínez, J.A. Melero, A. Milieni, *Appl. Catal. B: Environ.* 47, (2004), 281.
- [39] O.P. Taran, A.B. Ayusheev, O.L. Ogorodnikova, I.P. Prosvirin, L.A. Isupova, V. N. Parmon, *Appl. Catal. B: Environ.* 180, (2016), 86.
- [40] B. Yang, O. Dyck, W. Ming, M.H. Du, S. Das, C.M. Rouleau, G. Duscher, D.B. Geohegan, K. Xiao, *ACS Appl. Mater. Interfaces* 8, (2016), 32333.
- [41] T. Leijters, G. E. Eperson, S. Pathak, A. Abate, M. M. Lee, H. J. Snaith, *Nature Commun.* 4, (2013), 2885.
- [42] W. F. Zhang, J. Tang, J. Ye, *Chem. Phys. Lett.* 418, (2006), 174.
- [43] H.G. Kim, D.W. Hwang, J. Kim, Y.G. Kim, J.S. Lee, *Chem. Commun.* 12, (1999), 1077.
- [44] D. Wang, T. Kako, J. Ye, *J. Am. Ceram. Soc.* 130, (2008), 2724.
- [45] P. Tang, Y. Tong, H. Chen, F. Cao, G. Pan, *Curr. Appl. Phys.* 13, (2013), 340.
- [46] K. Wakino, M. Murata, H. Tamura, *J. Am. Ceram. Soc.* 69, (1986), 34.
- [47] V. A. Sakkas, M. A. Islam, C. Stalikas, T. A. Albanis, *J. Hazard. Mater.* 175, (2010), 33.
- [48] D. Wang, *Chin. J. Catal.* 31, (2010), 972
- [49] A. M. Aljeboree, A. N. Alshirfi, A. F. Alkain, *Arab. J. Chem.* 10, (2017), 53.
- [50] Y. Yu, J. C. Yu, C. Y. Chan, Y. R. Che, J. C. Zhao, L. Ding, W. K. Ge, P. K. Wong, *Appl. Catal. B: Environ.* 61, (2005), 1.
- [51] A. R. Fischer, P. Werner, K. U. Goss, *Chemosphere* 82, (2011), 210.
- [52] N. Soltani, E. Saion, M. Z. Hussein, M. Erfani, A. Abedini, G. Bahmanrokh, M. Navasery, P. Vaziri, *Int. J. Mol. Sci.* 13, (2012), 12242.
- [53] L.A.P. Estrada, A. Agüera, M.D. Hernando, S. Malato, A.R.F. Alba, *Chemosphere* 70, (2008), 2068.
- [54] S. Chowdhury, R. Mishra, P. Saha, P. Kushwaha, *Desalination*, 265, (2011), 159.

- [55] L. Chabane, B. Cheknane, F. Zermane, O. Bouras, *Chem. Eng. Res. Des.* 120, (2017), 291.
- [56] X. P. Lou, S. Y. Fu, Y. M. Du, J. Z. Guo, B. Li, *Microporous Mesoporous Mater.* 237, (2017), 268.
- [57] S. Jain, R. Yamgar, R.V. Jayaram, *Chem. Eng. J.* 148, (2009), 342.
- [58] B. A. Fil, *Part. Sci. Tehnol.* 118. 34, (2016).
- [59] A. S. Sartape, A. M. Mandhare, V. K. Jadhav, P. D. Raut, M. A. Anuse, S. S. Kolekar, *Arab. J. Chem.* 10, (2017), 3229.
- [60] F. Naseeruteen, N. S. A. Hamid, F. B. M. Suah W. S. W. Ngah, F. S. Mehamod, *Int. J. Biol. Macromol.* 107, (2018), 1270.
- [61] M. Rajabi, B. Mirza, K. Mahanpoor, M. Mirjalili, F. Najafi, O. Moradi, H. Sadegh, R.S. Ghoshekandi, M. Asif, I. Tyagi, S. Agarwal, V.K. Gupta, *J. Ind. Eng. Chem.* 34, (2016), 130.
- [62] K.V. Kumar, *Dyes Pigm.* 74, (2007), 595.
- [63] Y. Liu, Y. Ohko, R. Zhang, Y. Yang, Z. Zhang, *J. Hazard. Mater.* 184, (2010), 386.
- [64] M.A. Behnajady, N. Modirshala, M. Shokri, B. Vahid, *Ultrason. Sonochem.* 15, (2008), 1009.
- [65] M.A. Rauf, S.S. Ashraf, *Chem. Eng. J.* 151, (2009), 10.
- [66] Y. Ju, S. Yang, Y. Ding, C. Sun, A. Zhang, L. Wang, *J. Phys. Chem. A* 112, (2008), 11172.
- [67] Y. Panahian, N. Arsalani, *J. Phys. Chem. A* 121, (2017), 5614.
- [68] A. Pandurangan, P. Kamala, S. Uma, M. Palanichamy, V. Murugesan, *Ind. J. Chem. Technol.* 8, (2001), 496.
- [69] M. Asiltürk, F. Sayilkan, E. Arpaç *J. Photochem. Photobiol. A: Chem.* 203, (2009), 64.
- [70] S. Saha, J.M. Wang, A. Pal, *Sep. Purif. Technol.* 89, (2012), 147.

- [71] T.A. Gad-allah, M.E. Ali, M.I. Badawy, *J. Hazard. Mater.* 186, (2011), 751.
- [72] S. Kaniou, K. Pitarakis, K. Barlagianni, I. Barlagianni, I. Poullos, *Chemosphere* 60, (2005), 372.
- [73] S. Senthilkumaar, K. Porkodi, *J. Colloid Interface Sci.* 288, (2005), 184.
- [74] M. Salehi, H. Hashemipour, M. Mirzaee, *Am. J. Environ. Eng.* 2, (2012), 1.
- [75] X. Li, G. Liu, J. Zhao, *New J. Chem.* 23, (1999), 1193.
- [76] L. Yu, Y. Huang, Y. Yang, Y. Xu, G. Wang, S. Yang, *Int. J. Photo.* 812376, (2013), 1.
- [77] A. Boukhenoufa, M. Bouhelassa, A. Zoulalian, *J. Adv. Chem. Eng.* 1, (2011), 1.
- [78] E. Zhang, J. Zhao, T. Shen, H. Hidaka, E. Pelizzetti, N. Serpone, *Appl. Catal. B Environ.* 15, (1998), 147.
- [79] W.Z. Tang, Z. Zhang, H. An, M.O. Quintama, D.F. Torres Environ. *Technol.* 18, (1997), 1.
- [80] D. Bhatnagar, R.Chatterjee, *Adv. Mater. Lett.* 7, (2016), 604.
- [81] B. A. Baumert, *J. Supercond.* 8, (1995), 175.
- [82] C. Guillard, H. Lachheb, A. Houas, M. Ksibi, E. Elaloni, J.M. Herrmann, *J. Photochem. Photobiol. A: Chem.* 158, (2003), 27.
- [83] S.J. Vajapara, S.J. Patel, C.P. Bhasin, *Int. J. Nano. Chem.* 3, (2017), 33.
- [84] C. C. Chen, C.S. Lu, Y.C. Chung, J.L. Jan, *J. Hazard. Mater.* 141, (2007), 520.
- [85] Y. Bessekhoud, D. Robert, J. V. Weber, *J. Photochem. Photobiol. A: Chem.* 157, (2003), 47.
- [86] C. Berberidou, I. Poullos, N.P. Xekoukoulotakis, D. Mantzavinos, *Appl. Catal. B: Environ.* 74, (2007), 63.
- [87] A.S. Hussein, N.Y. Fairouz, *J. Babylon Univ./ Pure Appl. Chem.* 24, (2016), 2510.

[88] R.A. Raheem, H.Y. Al-gubury, A.M. Aljeboree, A.F. Alkai, *J. Chem. Pharma. Sci.* 9, (2016), 1134.

[89] N. Daneshvar, M. Rabbani, N. Modirshala, M. A. Behnajady, *J. Photochem. Photobiol. A: Chem* 168, (2004), 39.

[90] A. Hu, X. Zhang, K.D. Oakes, P. Peng, Y.N. Zhou, M. R. Servos, *J. Hazard. Mater.* 189, (2011), 278.

[91] Q. Hu, B. Liu, Z. Zhang, M. Song, X. Zhao, *J. Wuhan Univ. Technol. –Mater. Sci. Edit.* 25, (2010), 210.

[92] E.S. Baeissa, *J. Alloy Comp.* 672, (2016), 564.

[93] A.G.S. Pardo, L.L. Costa, *J. Hazard. Mater.* 169, (2009), 297.

[94] C. Dette, M.A.P. Osorio, C.S. Kley, P. Punke, C.E. Patrick, P. Jacobson, F. Giustino, S.J. Jung, K. Kern, *Nano Lett.* 14, (2014), 6533.

[95] L. Yong, G. Zhanqi, J. Yuefei, H. Xiaobin, S. Cheng, Y. Shaogui, W. Lianhong, W. Qingeng, F. Die, *J. Hazard. Mater.* 285, (2015), 127.

Chapter 6

Photocatalytic Degradation of Congo Red Dye Using BaBiO_3 and $\text{Ba}_{0.6}\text{K}_{0.4}\text{BiO}_3$

6.1 Introduction

Everyday dye factories across the world are dumping a huge amount of dye effluents into the water bodies thereby, polluting the water ecosystem. High concentrations of textile dyes in water bodies stop the re-oxygenation capacity of the receiving water and cut-off sunlight, thereby disturbing biological activity in aquatic life and also the photosynthesis process of aquatic plants [1-3]. These contamination may cause different diseases like immune-suppression, respiratory, central nervous, neuro-behavioral disorders, allergy, tissue necrosis, skin or eye infections and irritation in humans [3,4].

Azo dyes symbolises a main class of synthetic dyes that are widely used for dyeing in the textile industry. Azo dyes are categorized by the presence of one or more azo ($-N=N-$) groups and sulphonate substituted aromatic rings [6,7]. These dyes are highly stable to light, heat, water, detergents, bleach and dampness due to their resonance and π -conjugated azo bond characteristics. These properties make them highly suitable for use in the textile, paper, pharmaceutical, cosmetic and various chemical industries [8,9].

Congo red is a benzidine-based diazo dye, which was first synthesised by **Paul Böttiger** in 1883 [10]. It is commonly used in textile industries for dyeing purposes as it is highly water soluble, as well as in molecular biology laboratories for staining [11,12]. The aqueous solution of CR dye is used as secondary gamma-ray dosimeter. Congo red is used as acid-base indicator, histology for staining of amyloid in the cell wall of fungi, plants and several other gram-negative bacteria. Congo red has been used as an anti-amyloid agent in curing Alzheimer's disease by obstructing amyloid- β peptide aggregation [13-15].

Many studies prove that Congo red is found to be toxic to daphnids (planktonic crustaceans) [16]. Congo red have been known to cause an allergic reaction and to be metabolized to benzidine, which is a human carcinogen compound [17]. Congo Red (CR) can also restrict the replication of the infectious agent and delay the onset of clinical disease when administered directly into the brain or peritoneum at or near the time of infection of mice or hamsters [18,19]. Considering the potential adverse effects of CR dye, it should be removed from the environment.

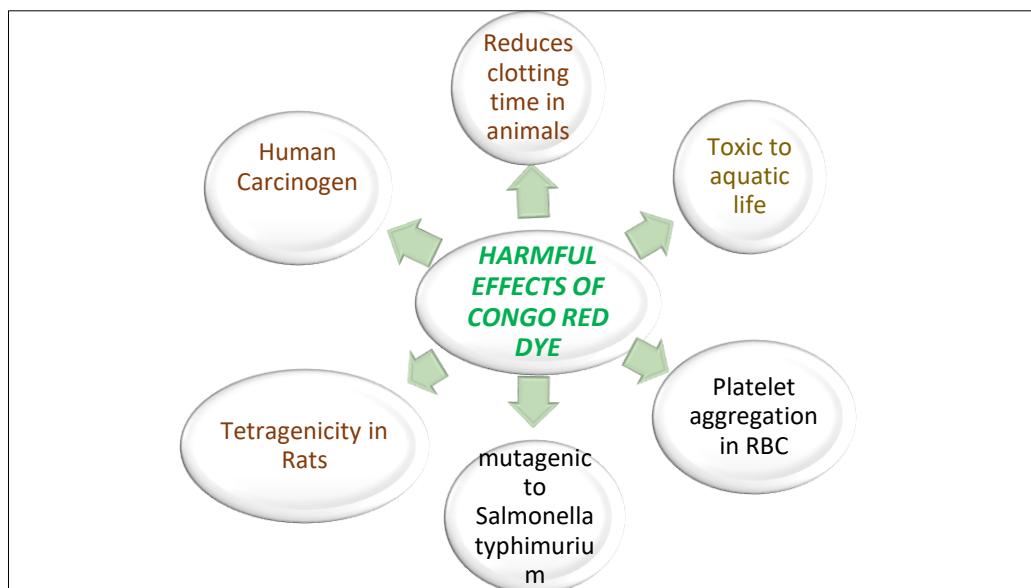


Figure 6.1: Harmful effects of CR dye

Synthetic dyes are highly stable as they have complex aromatic structure, therefore it is very tough to eliminate them from waste water. It is difficult to eliminate impurities containing large, stable and refractory compounds of dyes from waste water. A wide range of approaches have been applied for removal of CR dye from waste water has been studied by several biological, physical and chemical treatment methods [20-22]. Though the overall high treatment cost, lower extent of dye removal, and generation of secondary pollutants, are some of inherent limitations of these conventional methods [23,24].

Advanced oxidation process has been widely studied as an innovative technique, because it can effectively purifies the polluted water [25]. In this process the organic pollutants are completely mineralized into simple oxides converted to less or more harmful compounds based on the stability of that intermediates [26,27]. For this purpose, TiO_2 semiconductor has been extensively employed as a photocatalyst in waste water treatment [28-30]. Although, TiO_2 has shown excellent photocatalytic performance, nevertheless its large band gap ($\sim 3.2\text{eV}$) is a limitation for its visible light photo-catalysis applications [31-33].

Perovskite materials covers a big family of promising photocatalysts. The ideal perovskite structure has a cubic arrangement with common formula of ABO_3 [34,35]. The A and B sites can accommodate most of the metal elements of the

periodic table. The ideal cubic structure of these materials can be altered by multiple metal cation substitutions at A site or B site which leads to structural distortion which further can change the physical and photocatalytic properties of these materials [36,37]. However, most of the perovskite materials have large band gap causing lack of photo-catalytic activity under visible light irradiation [38-40]. Therefore, many new efforts are made to reduce optical band gaps of perovskite materials [41-43].

Though, several perovskites have been studied for photocatalytic applications in waste water remediation [44,45]. Nevertheless, application of perovskite catalyst in the field of water treatment is still limited. The present study attempts to investigate the performance of barium, bismuth and potassium containing binary and ternary perovskite oxides for the treatment of crystal violet dye solution under visible light irradiation.

In this chapter, doped and undoped Barium bismuthate, used for the degradation of CR dye from aqueous solution, have been synthesized by Pechini method, details of which have been elaborated in chapter 3. The degradation potential of these catalysts has been evaluated by different characterization methods such as TG-TGA, XRD, UV-DRS, SEM and FTIR, results of which have been described in chapter 3.

FTIR spectrum shows the presence of a band around 465cm^{-1} in both the catalysts conforming the metal-oxygen bond formation, which is the characteristic property of perovskite materials. The SEM studies show that both the samples are homogeneous uniform nanoparticles, having size 520 nm and between 45-101nm for the BaBiO_3 and $\text{Ba}_{0.6}\text{K}_{0.4}\text{BiO}_3$, respectively. SEM images reveal the nano rod type structure and plate like layered structure of BaBiO_3 and for $\text{Ba}_{0.6}\text{K}_{0.4}\text{BiO}_3$, respectively. The XRD patterns suggest that BaBiO_3 crystallizes in the monoclinic structure while $\text{Ba}_{0.6}\text{K}_{0.4}\text{BiO}_3$ crystallizes in cubic structure. XRD patterns exhibit the typical pattern corresponding to perovskite structure. The phase evolution of both the catalysts with increasing temperature is done by DT-TGA.

The diffuse reflectance spectroscopy showed that the catalysts have a broad absorbance around 600 and 660 nm with a band gap of 2.07 and 1.87eV for barium bismuthate and K doped barium bismuthate respectively. Due to the low band gap,

the catalysts are supposed to be promising in displaying their visible light activity and hence they are tested further for the degradation of CR dye under visible light irradiation.

The objective of this work is to study the photodegradation of CR dye using the prepared catalysts. The photodegradation rates and efficiency of the photocatalytic system are highly dependent on a number of operational parameters that govern the photodegradation of the organic molecule [46] such as catalyst dose, solution pH, temperature, and initial dye concentration. Optimization of such conditions will greatly help in the development of industrial-scale dye removal treatment process.

Therefore, herein, the dependence of the photodegradation rate on various parameters viz. initial dye concentration, catalyst dose, pH and temperature is studied. The reaction kinetics is studied and the applicability of the first order kinetic model is also discussed. The agreement of the experimental results with the Langmuir-Hinshelwood kinetic model [47] has been examined which led to the determination of both photo-reaction kinetics and adsorption equilibrium constants. In addition, photolysis and adsorption study of dye on prepared catalyst is also discussed. The adsorption experiment data is fitted to Langmuir isotherm model and Freundlich isotherm model [48,49]. Furthermore, to estimate the degree of mineralization, measurements of total organic carbon has been conducted.

6.2. Material & Method

6.2.1. Chemical reagents

The reagents used for the synthesis of BaBiO_3 and $\text{Ba}_{0.6}\text{K}_{0.4}\text{BiO}_3$ are Barium nitrate, Bismuth nitrate, potassium nitrate as starting materials while, citric acid and ethylene glycol are used as complexing agents. Details of synthesis procedure are given in chapter 3. CR dye (Mol. Wt. = 696.66 gmol^{-1}) dye is purchased from Sigma-Aldrich Company (India). A solution of 100 mgL^{-1} CR dye solution is prepared as stock solution. Different dye solutions of various concentrations are made from the stock solution (100 mgL^{-1}) by appropriate dilutions. Ultra-pure water ($18.2 \text{ M}\Omega\text{cm}^{-1}$) is used to prepare all solutions in this study. The pH of the solutions

is adjusted using 0.1N NaOH and 0.1N HCl. All the chemicals except CR dye is purchased from Merck (India). Analytical grade $\text{p}25\text{TiO}_2$ is purchased from Sigma-Aldrich Company (India). The chemicals used in this experiment are of the analytical grade and are used without further purification.

6.2.2. Experimental procedure and analytical methods

An experimental setup for the photocatalytic activity test has been explained in chapter 2. The visible light irradiation experiments are carried out in an indigenously prepared immersion type photocatalytic reactor. A 500W Xe arc lamp (intensity= 137 mWcm^{-2}) is used as a visible light source. This lamp is placed in a quartz tube which is sealed from one side. This tube is then immersed in a cylindrical borosilicate reactor (capacity 1L). In this, mixture of catalyst and dye solution are taken following which the mixture is placed in a water bath circulated at a constant speed to keep the above suspension homogenous. Only in experiments dealing with the effect of pH on the dye degradation, initial pH is adjusted with buffer solutions and measured with pH meter.

Since some dyes can be degraded by direct UV or visible irradiation without the assist from catalysts [50], it is important to find out the extent to which the degradation of CR dye in aqueous solution takes place directly by the visible light or in other words, to find out the extent of direct photolysis of CR dye. So, some control experiments are carried out in the absence of the catalysts, while holding all other parameters the same. Following this, their respective photodegradation rates are measured to evaluate their photolysis.

Since, the photo-assisted degradation of the dyes occurs predominantly on the surface. Therefore, adsorption of the dye is an important parameter in determining photocatalytic degradation rate. Photocatalysts, dispersed into CR dye solution is allowed to reach adsorption-desorption equilibrium under continuous magnetic stirring at 600 rpm for 30 minutes in the dark, before illumination. Irradiation is then provided. Samples are withdrawn at 5 minutes time intervals and then centrifuged to remove the suspended catalyst. The clear supernatant fluid followed by filtration is then analysed by spectrophotometer (Double beam

spectrophotometer-2203, Systronics) at λ_{\max} = 500nm with a calibration curve based on Beer Lambert's law [51]

The degradation efficiency is observed in terms of change in intensity of the dye before and after light irradiation. Photocatalytic performance is quantified by the degradation of CR dye under visible light irradiation.

$$\% \text{degradation} = \frac{C_0 - C_t}{C_0} \times 100 \quad \text{--- (6.1)}$$

Where, C_0 = concentration of dye solution after adsorption-desorption equilibrium (mgL^{-1}), C_t = concentration of dye solution after photo irradiation (mg L^{-1}).

6.3. Results and Discussion

6.3.1. UV-vis spectra of CR dye

Congo red {(3,3'- ([1,1'-biphenyl] -4,4'- diyl) bis (4-aminonaphthalene-1-sulfonic acid))} is an acidic azo dye. Which is water soluble and its molecular formula is $\text{C}_{32}\text{H}_{22}\text{N}_6\text{Na}_2\text{O}_6\text{S}_2$. The UV-vis. absorbance spectrum of Congo red (CR) is drawn to determine its absorption maxima. **Figure 6.2** shows the typical time dependent UV-vis. spectrum of CR dye. It is clear from the spectrum that CR has an intense absorbance at 510 nm. The rate of degradation is investigated with respect to change in absorption maxima of CR dye (λ_{\max} = 510 nm)

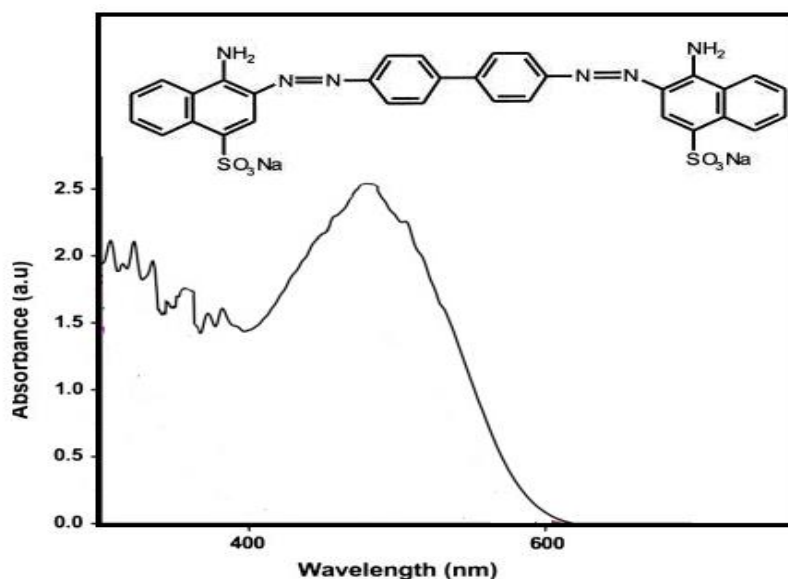


Figure 6.2: UV-VIS spectra of CR dye. (λ_{\max} = 510nm).

6.3.2. Photolysis of Congo red dye

Photolysis is the process of decomposition of dyes in the presence of light radiation only. Direct photolysis of the dye in the absence of photocatalyst showed no considerable degradation even after 1 hour. **Figure 6.3** shows the results of photocatalysis in terms of % degradation.

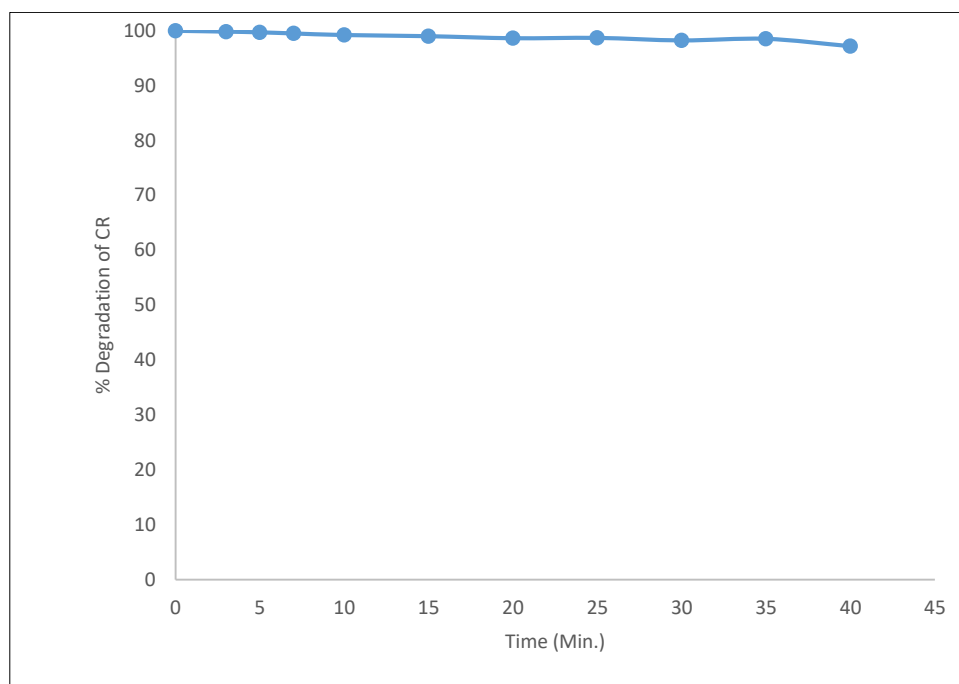


Figure 6.3: Photolysis of CR in presence of irradiation. (Experimental condition: [CR] =40 mgL⁻¹; pH=5.0; Temp. = 308K)

The constant absorbance with time verifies that CR dye is not homogeneously degraded by light. Therefore, the self-degradation of the dye by visible light irradiation can be ignored. Similar results are obtained in the study of CR dye under UV-Vis irradiation in earlier reports [52].

6.3.3. Adsorption studies in dark:

Since, the photo-assisted degradation of the dyes occurs predominantly on the surface. Therefore, adsorption of the dye is an important parameter in determining photocatalytic degradation rate. The adsorbed dye on the surface of the semiconductor particles act as an electron donor, injecting electrons from its excited state to the conduction band of the semiconductor under light irradiation, so in the

heterogeneous photocatalytic degradation process, adsorption of dye on the catalytic surface is assumed to be a primary step of the reaction [53,54]. The adsorption experiments are carried out to evaluate the experiments the equilibrium quantity of adsorbent. The equilibrium adsorption isotherm is fundamental in describing the interactive behaviour between adsorbates and adsorbent and is important in the design and analysis of adsorption systems. For the sake of convenience, explicit and simple models are preferred and commonly used [55]. Equilibrium adsorption data collected in this study could be fitted by both Langmuir and Freundlich isotherms.

A. Langmuir isotherm

Langmuir isotherm [48,56] model is used to interpret the experimental data. The Langmuir isotherms are represented by the following equations.

$$q_e = \frac{Q_0 b c}{1 + b c} \quad \text{--- (6.2)}$$

$$\frac{c_e}{q_e} = \frac{1}{Q_0 b} + \frac{c_e}{Q_0} \quad \text{--- (6.3)}$$

Where C_e is the concentration of the adsorbate (mgL^{-1}) at equilibrium, q_e is the amount of adsorbate per unit mass of adsorbent at equilibrium in mgg^{-1} , Q_0 is the maximum adsorption at monolayer coverage in mgg^{-1} , b is the adsorption equilibrium constant related to the energy of adsorption in Lmg^{-1} .

The adsorbate uptake q_e (mgg^{-1}), can be calculated as

$$q_e = \frac{(C_0 - C_e)V}{W} \quad \text{--- (6.4)}$$

Where C_0 is the initial adsorbate concentration (mgL^{-1}), V is the volume of solution (L), W is the mass of adsorbate (g).

The essential characteristic of the Langmuir isotherm can be described by a separation factor which is called the equilibrium constant, R_L

The equilibrium factor thus is defined as:

$$R_L = \frac{1}{1 + K_{LH}} \times \frac{1}{C_0} \quad \text{--- (6.5)}$$

Where, K_{LH} is the affinity constant (mg^{-1}), C_0 is the initial concentration of the adsorbate (mgL^{-1}). The R_L value is to be favourable at $0 < R_L < 1$ [57].

Adsorption experiments are carried out in the same experimental setup, taking dye solutions of different initial concentration. The constants of isotherm are obtained by least square fitting of the adsorption equilibrium data. Adsorption experiments for the dye CR dye are carried out by selecting a concentration range of 20mgL^{-1} to 80mgL^{-1} with an adsorbent dosage of 0.75g of both the adsorbents i.e. BaBiO_3 and $\text{Ba}_{0.6}\text{K}_{0.4}\text{BiO}_3$ at 308K {**Figure 4.4 (a & b)**}. The effect of initial dye concentration depends on the immediate relation between the concentration of the dye and the available sites on an adsorbent surface. In general, the percentage of dye removal increases with increase in initial dye concentration because it will cause an increase in the capacity of the adsorbent and this may be due to the high driving force for mass transfer at a high initial dye concentration [58].

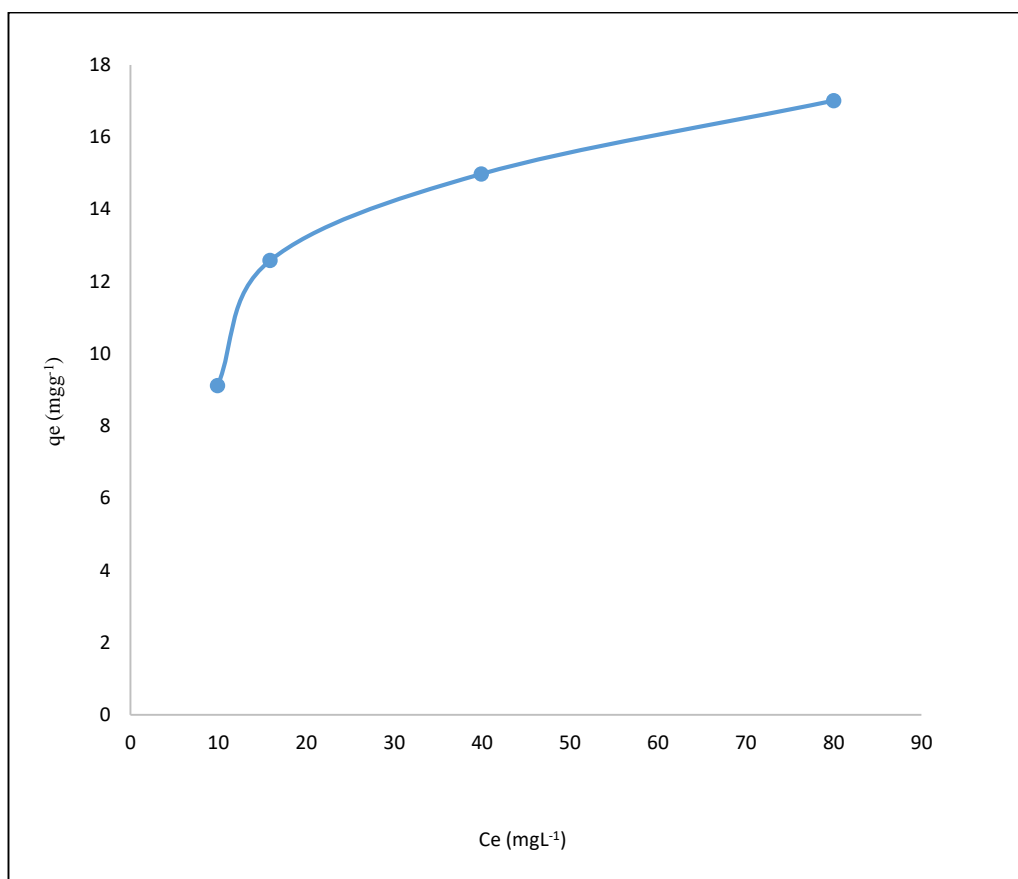


Figure 6.4 (a): Adsorption isotherm from aqueous CR dye solution

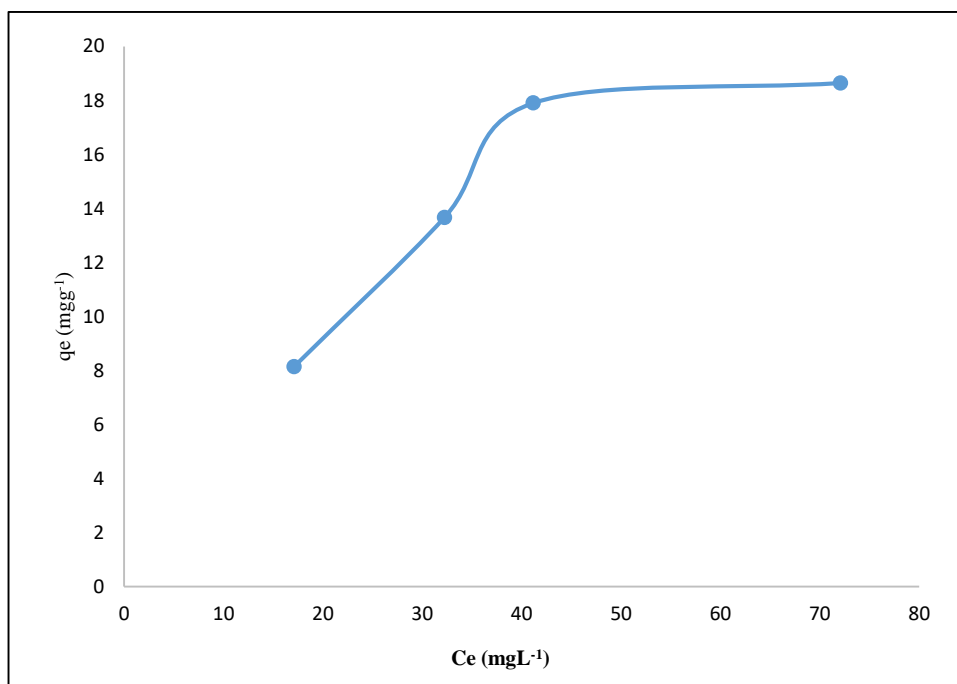


Figure 6.4 (b): Adsorption isotherm from aqueous CR dye solution

The plot of C_e/q_e versus C_e are linear and represented in **Figure 6.5(a)** and **6.5(b)** for $BaBiO_3$ and $Ba_{0.6}K_{0.4}BiO_3$ respectively. The value of Q_0 and b is found from the intercept and slope of the C_e/q_e vs C_e curve respectively.

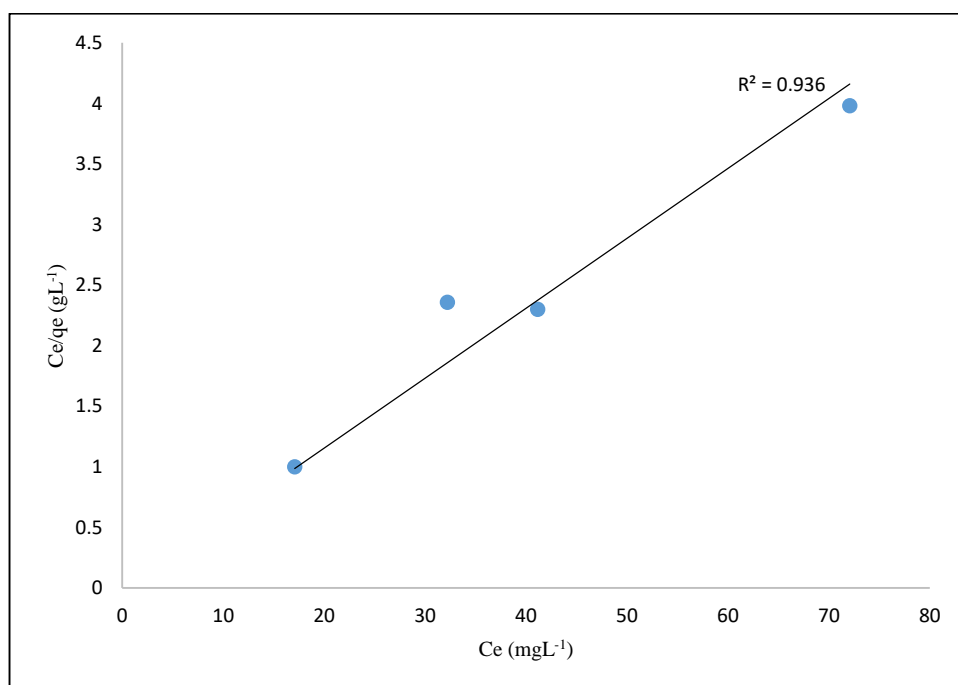


Figure 6.5 (a): Langmuir plots for the adsorption of CR on $BaBiO_3$. (Experimental condition: $BaBiO_3 = 0.75 \text{ g/L}$; $\text{pH} = 5.0$; $\text{Temp.} = 308 \text{ K}$).

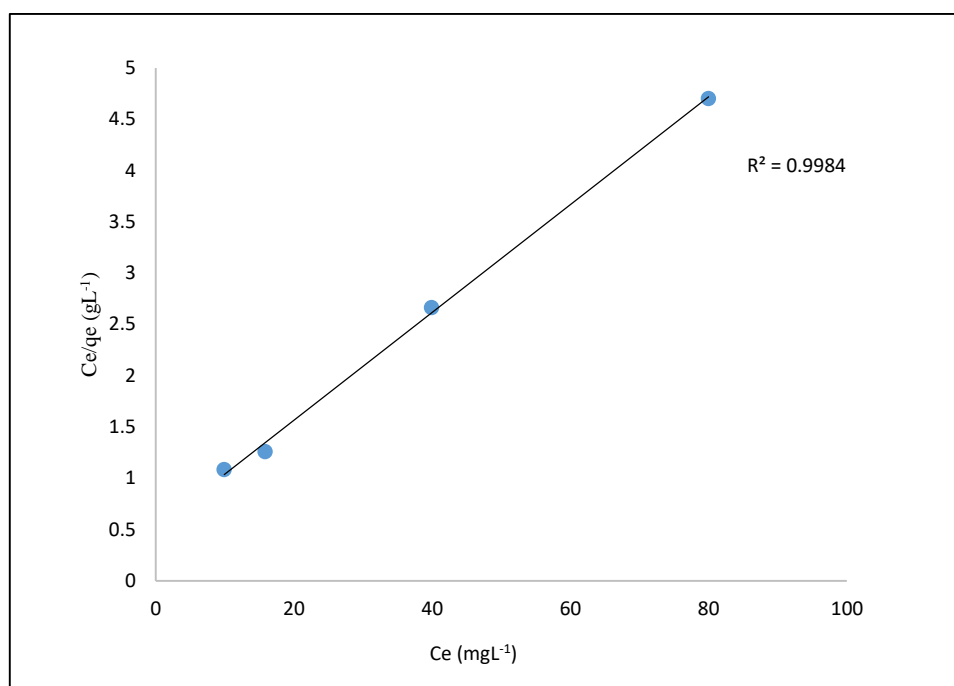


Figure 6.5 (b): Langmuir plots for the adsorption of CR on $Ba_{0.6}K_{0.4}BiO_3$. (Experimental condition: $Ba_{0.6}K_{0.4}BiO_3 = 0.75gL^{-1}$; $pH=5.0$; $Temp.= 308K$).

Langmuir adsorption constant (b) and the maximum adsorbable dye quantity (Q_0) are calculated from the **Figures 6.5(a)** and **6.5(b)** as $2.237mgg^{-1}$, $0.0367Lmg^{-1}$ for $BaBiO_3$ and, $0.0315mgg^{-1}$, $1.644Lmg^{-1}$ for $Ba_{0.6}K_{0.4}BiO_3$.

The value of separation constants for different initial concentration are determined from equation 6.5 and found to be in range of 0.040-0.1618 and 0.128-0.0515 for $BaBiO_3$ and $Ba_{0.6}K_{0.4}BiO_3$ catalysts and are listed in **Table 6.1**.

Table 6.1: Separation constants (R_L) values for the adsorption of CR dye on $BaBiO_3$ and $Ba_{0.6}K_{0.4}BiO_3$

$C_0 \longrightarrow$	$20mgL^{-1}$	$40mgL^{-1}$	$60mgL^{-1}$	$80mgL^{-1}$
BaBiO₃	0.1618	0.0809	0.0539	0.0404
Ba_{0.6}K_{0.4}BiO₃	0.0515	0.0257	0.01719	0.0128

The values of R_L are found in the range of $0 < R_L < 1$ for both the catalysts, indicating that the adsorption is favoured [57].

B. Freundlich isotherm

The Freundlich isotherm equation assumes a heterogeneous adsorption surface with sites that have different energies of adsorption and are not equally available [49,59]. The Freundlich exponential equation is given as-

$$q_e = K_f C_e^{1/n} \quad \text{--- (6.6)}$$

Where, q_e is the amount adsorbed (mgg^{-1}), C_e is the equilibrium concentration of the adsorbate (mgL^{-1}), K_f (Lg^{-1}) and n are Freundlich constants related to the adsorption capacity and adsorption intensity, respectively.

The linear logarithmic form of Freundlich equation is mathematically given by

$$\log q_e = \log K_f + \frac{1}{n} \log C_e \quad \text{--- (6.7)}$$

The value of $1/n$ represents the favourable adsorption conditions.

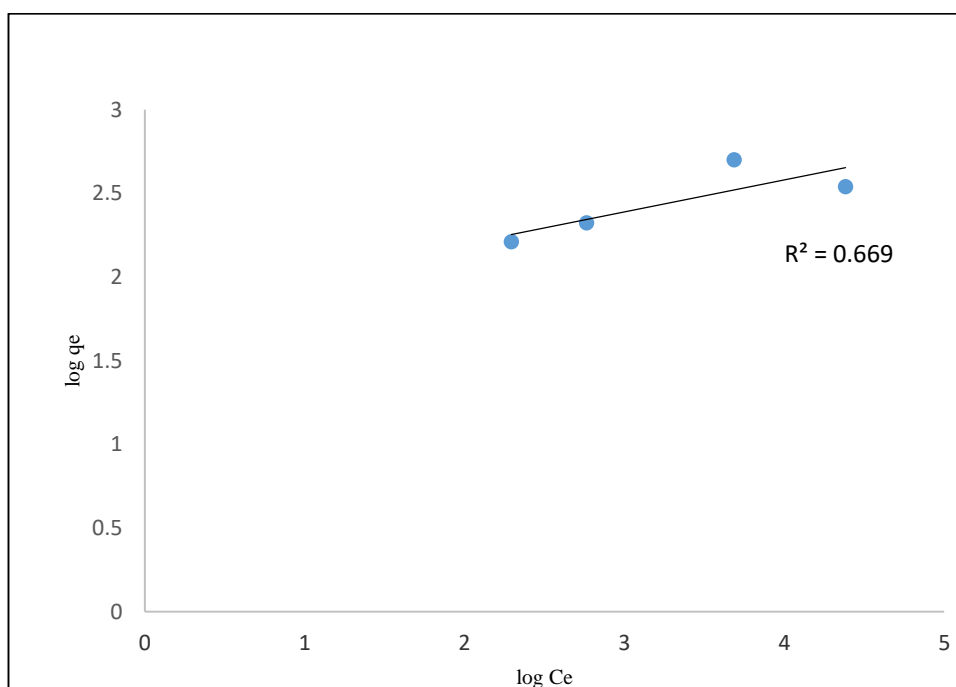


Figure 6.6 (a): Freundlich plots for the adsorption of CR on BaBiO₃. (Experimental condition: BaBiO₃= 1gL⁻¹; pH= 5.0; Temp.= 308K).

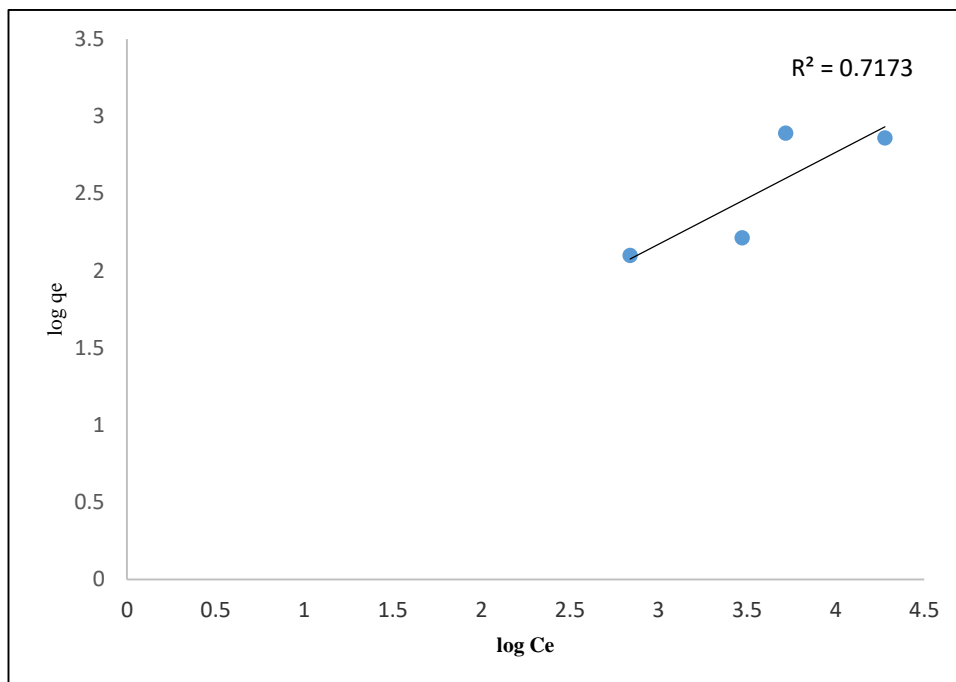


Figure 6.6 (b): Freundlich plots for the adsorption of CR on $Ba_{0.6}K_{0.4}BiO_3$. (Experimental condition: $Ba_{0.6}K_{0.4}BiO_3 = 1g L^{-1}$; $pH=5.0$; $Temp. = 308K$).

K_f and n can be calculated from the intercept and slope of the plots in **Figures 6.6 (a) and 6.6(b)** for $BaBiO_3$ and $Ba_{0.6}K_{0.4}BiO_3$ respectively.

Langmuir and Freundlich constants for the adsorption of CR dye on $Ba_{0.6}K_{0.4}BiO_3$ has been represented in **Table 6.2**.

Table 6.2: Langmuir and Freundlich constants for the adsorption of CR dye on $BaBiO_3$ and $Ba_{0.6}K_{0.4}BiO_3$

Adsorbent catalyst	Langmuir Constants			Freundlich Constants		
	$Q_0 (mg g^{-1})$	$b (L mg^{-1})$	R^2	$K_f (L g^{-1})$	n	R^2
$BaBiO_3$	2.237	0.0367	0.972	1.258	1.68	0.843
$Ba_{0.6}K_{0.4}BiO_3$	0.0315	1.644	0.983	1.807	1.578	0.798

Since the R^2 values are fairly close to 1, both the models describe the system well but Langmuir isotherm model is considered to be best fit because for this model R^2 is ~ 0.972 & 0.983 as comparison to $R^2 \sim 0.843$ & 0.798 for Freundlich isotherm.

6.3.4. Photodegradation studies under visible light irradiation

In order to assess the rate of photocatalytic degradation of dyes over BaBiO₃ and Ba_{0.6}K_{0.4}BiO₃, the observed dye degradation results are kinetically analysed by Langmuir-Hinshelwood kinetic equation [47,60]. Langmuir-Hinshelwood kinetic equation describes the following relationship between the initial rate constant and initial concentration of the organic substrate.

$$r_o = -\frac{dC}{dt} = \frac{K_r K_{LH} C_o}{1 + K_r C_o} \quad \text{--- (6.8)}$$

$$r_o = \frac{1}{K_r} + \frac{1}{K_r K_{LH} C_o} \quad \text{--- (6.9)}$$

Where C_o is the initial concentration of organic substrate (mgL⁻¹), r_o is initial rate (mgL⁻¹min⁻¹), K_{LH} is the Langmuir-Hinshelwood adsorption equilibrium constant (Lmg⁻¹) and K_r is the rate constant of surface reaction (mgL⁻¹min⁻¹).

The degradation of organic pollutants over catalysts follows the pseudo-first-order kinetics with respect to the initial concentration of the pollutant.

$$r_o = -\frac{dC}{dt} = K_{app} \quad \text{--- (6.10)}$$

Following equation was used to determine the initial rate by multiplying the apparent first-order rate constant K_{app} with the initial concentration of dye, C_o

$$\ln\left(\frac{C_t}{C_o}\right) = K_{app} \cdot C_o \quad \text{--- (6.11)}$$

In which K_{app} is the apparent pseudo-first-order rate constant in min⁻¹. The apparent reaction rate constant K_{app} (min⁻¹) is given by the slope of the graph of ln C_t/C_o versus time (minutes).

As we have seen that in the absence of catalyst, the concentration of CR dye shows no significant variation indicating that CR cannot be degraded by photolysis. Hence, any change in the CR concentration can be attributed to the adsorption/photocatalytic process. The pseudo-first-order kinetic model is usually used to fit all data sets (dye concentration, photocatalyst dose, initial pH solution, and temperature) [61].

6.3.4.1 Effect of initial dye concentration on photocatalytic degradation

It is important from both mechanistic and application point of view to study the dependence of the photocatalytic reaction rate on the substrate concentration. It is generally noted that the degradation rate increases with the increase in dye concentration to a certain level and a further increase in dye concentration leads to decrease the degradation rate of the dye. The effect of the initial dye concentration of dye on the rate of degradation is studied by varying the initial dye concentration from 20 to 80 mgL⁻¹ initial pH 5.0, with a constant catalyst dose of 0.75 gL⁻¹ (for both the catalysts). It is observed that up to 40 mgL⁻¹ the degradation efficiency increases due to the greater availability of dye molecules for excitation and consecutive degradation; hence there is an increase in the rate. After this, as the dye concentration is increased, the equilibrium adsorption of dye on catalyst surface increases; hence competitive adsorption of OH⁻ on the same site decreases, which further decreases the rate of formation of OH[•] radical, which is the principal oxidant necessary for a high degradation efficiency [62]. Our results are in accordance with an earlier research work [63,64]. The corresponding results with both the catalysts have been described below.

On the other hand, considering **Beer-Lambert law**, as the initial dye concentration increases, the path length of photon entering the solution decreases, resulting in the lower photon adsorption on the catalyst particles and consequently a lower photodegradation rate [51]. Also, the high concentration of dye would have acted as a filter for the incident light, which ultimately reduces the degradation efficiency [65].

(a) Results with BaBiO₃

The experimental results shows that the rate of photocatalytic degradation increases with increase in concentration of dye up to 40 mgL⁻¹. The rate of reaction was then, found to decrease with further increase in the concentration of dye. It is clear from the **Table 6.3(a)** to **6.6(a)**, initially % degradation of dye increases rapidly and thereafter slowly attains the limiting value.

Figure 6.7.a (A-D) shows the plots of change in % degradation with time for various concentration of dye at various amount of catalyst.

Table 6.3(a): Effect of initial dye concentration on degradation of CR

(Experimental Condition: $[\text{BaBiO}_3] = 0.25\text{gL}^{-1}$; $\text{pH}=5.0$; $\text{Temp.}= 308\text{K}$).

Dye Concentration	20 mgL^{-1}	40 mgL^{-1}	60 mgL^{-1}	80 mgL^{-1}
Time (min)	%Degradation	%Degradation	%Degradation	%Degradation
0	0.00	0.00	0.00	0.00
3	2.14	3.24	1.14	1.00
5	6.39	8.57	4.37	3.54
7	12.98	13.57	10.87	9.84
10	22.72	28.46	21.16	16.93
15	36.94	40.76	30.82	25.27
20	48.43	56.00	46.75	34.16
25	59.73	65.00	56.93	48.48
30	66.03	71.40	63.50	58.40
35	72.02	74.89	69.98	64.80
40	76.14	79.89	73.62	72.63
∞	76.15	79.90	73.63	72.64

Table 6.4 (a): Effect of initial dye concentration on degradation of CR

(Experimental Condition: $[\text{BaBiO}_3] = 0.75\text{gL}^{-1}$; $\text{pH}=5.0$; $\text{Temp.}=308\text{K}$).

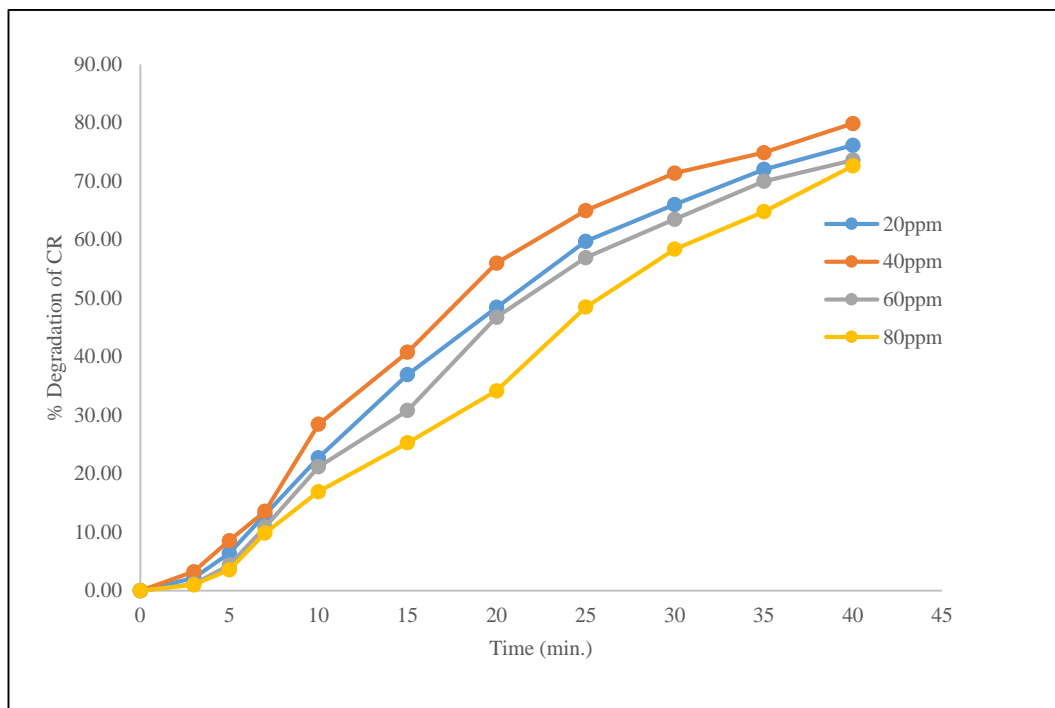
Dye Concentration	20 mgL^{-1}	40 mgL^{-1}	60 mgL^{-1}	80 mgL^{-1}
Time (min)	%Degradation	%Degradation	%Degradation	%Degradation
0	0.00	0.00	0.00	0.00
3	8.54	11.05	6.59	4.54
5	14.65	20.84	12.41	11.46
7	25.67	30.39	21.65	19.80
10	32.17	39.00	30.19	26.52
15	48.10	60.57	44.29	39.14
20	62.00	69.36	59.26	51.72
25	69.82	73.59	66.96	63.93
30	76.09	80.24	74.54	69.59
35	79.42	82.36	78.29	77.14
40	82.78	85.55	81.06	80.54
∞	82.79	85.56	81.07	80.54

Table 6.5 (a): Effect of initial concentration on degradation of CR(Experimental Condition: $[\text{BaBiO}_3] = 1.00\text{gL}^{-1}$; $\text{pH}=5.0$; $\text{Temp.}=308\text{K}$).

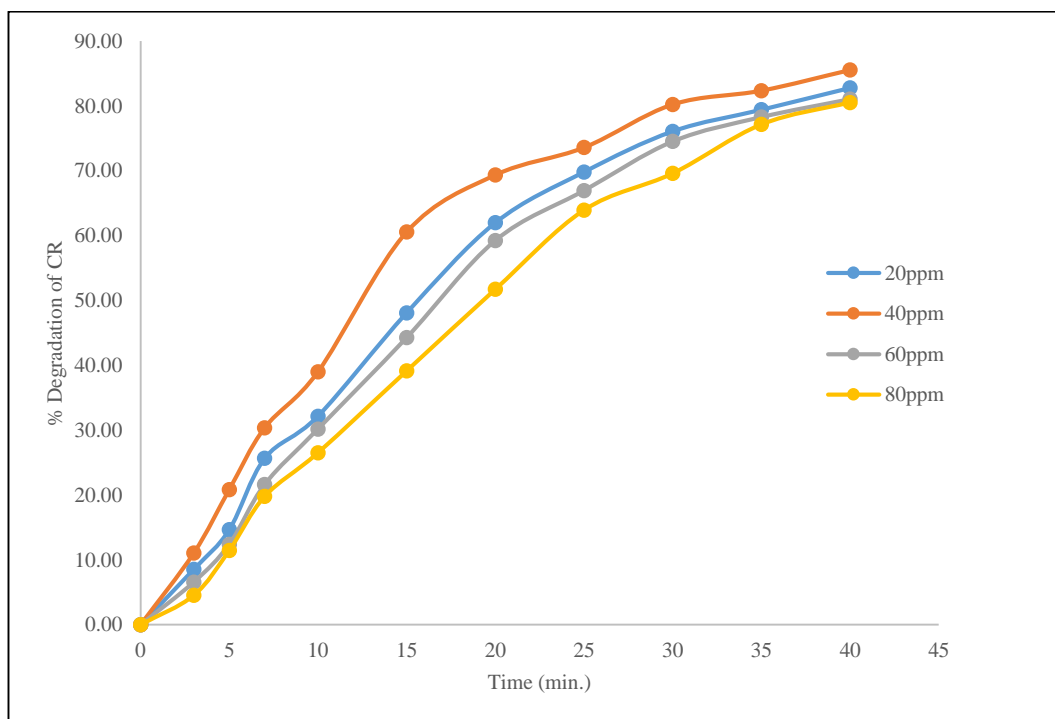
Dye Concentration	20 mgL^{-1}	40 mgL^{-1}	60 mgL^{-1}	80 mgL^{-1}
Time (min)	%Degradation	%Degradation	%Degradation	%Degradation
0	0	0	0	0
3	4.59	7.85	2.35	1.18
5	12.09	19.48	9.64	7.73
7	18.12	28.62	15.09	13.29
10	31.84	38.38	29.65	24.40
15	44.58	57.10	40.62	39.06
20	57.15	68.80	54.36	52.55
25	67.25	73.56	63.85	58.45
30	74.28	77.36	71.15	69.54
35	78.47	80.98	77.77	73.85
40	81.51	84.58	79.27	76.35
∞	81.52	84.59	79.28	76.35

Table 6.6 (a): Effect of initial concentration on degradation of CR(Experimental Condition: $[\text{BaBiO}_3] = 1.25\text{gL}^{-1}$; $\text{pH}=5.0$; $\text{Temp.}=308\text{K}$).

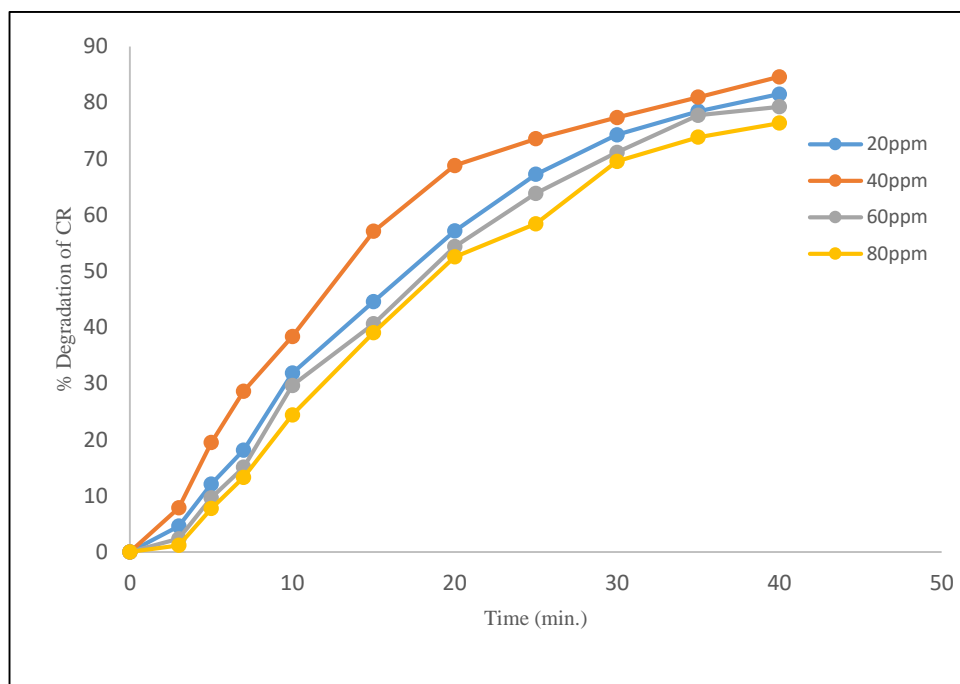
Dye Concentration	20 mgL^{-1}	40 mgL^{-1}	60 mgL^{-1}	80 mgL^{-1}
Time (min)	%Degradation	%Degradation	%Degradation	%Degradation
0	0	0	0	0
3	2.27	4.06	1.18	1.63
5	10.68	14.17	7.73	6.32
7	15.67	17.71	14.39	13.11
10	28.00	34.27	24.40	19.74
15	42.18	50.76	39.06	34.89
20	56.07	64.82	52.55	45.58
25	62.31	68.59	58.45	54.00
30	70.58	75.58	69.54	63.44
35	77.29	77.69	73.85	69.35
40	80.17	82.36	76.35	75.26
∞	80.18	82.37	76.36	75.36



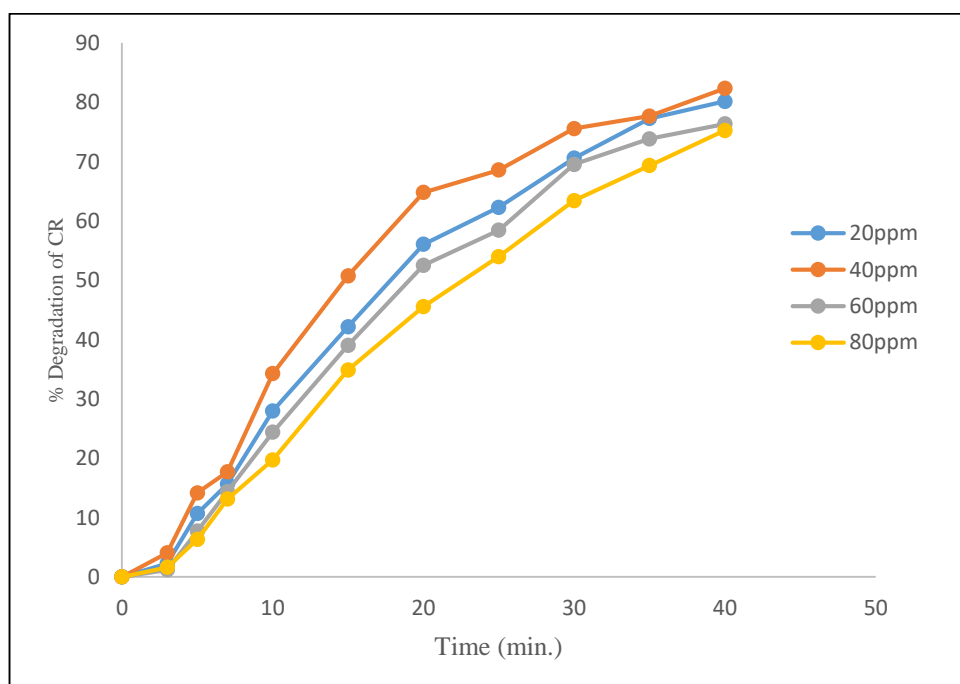
(A)



(B)



(C)



(D)

Figure 6.7 (a): Effect of concentration of CR on its visible light degradation in BaBiO_3 [(A) Catalyst dose: 0.25gL^{-1} ; (B) Catalyst dose: 0.75gL^{-1} ; (C) Catalyst dose: 1.00gL^{-1} ; (D) Catalyst dose: 1.25gL^{-1} , $\text{pH}=5.0$, $\text{Temp.}=308\text{K}$].

The photodegradation kinetics of initial dye concentration is illustrated in **Figure 6.8(a)**, which depicts the dark adsorption-desorption equilibrium and the additional decrease in CR concentration caused by visible light irradiation at optimum catalyst dose i.e. 0.75gL^{-1} .

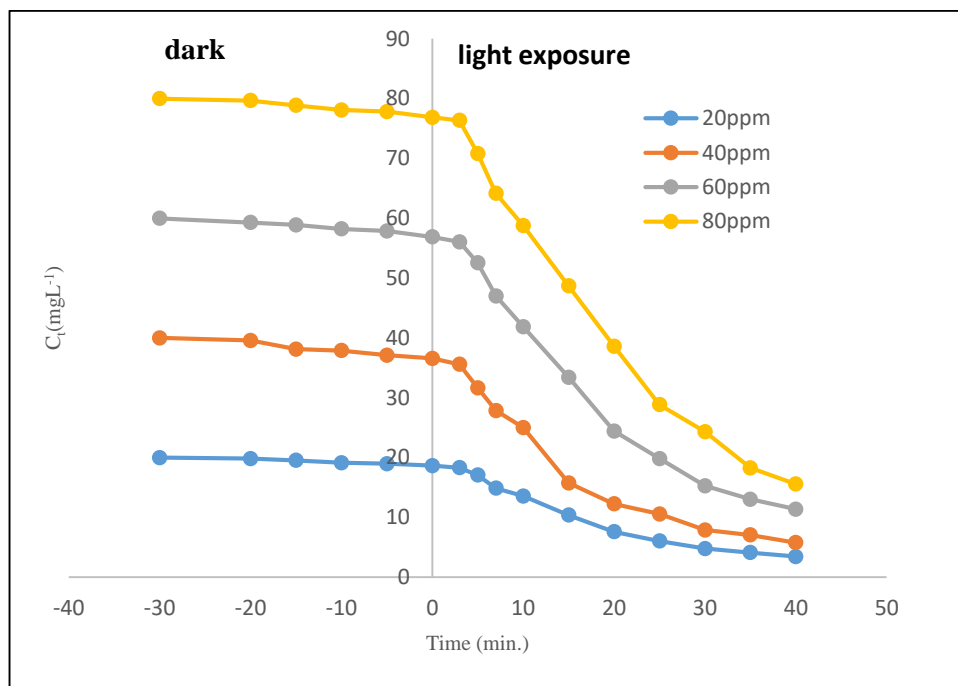


Figure 6.8(a): Variation of dye concentration versus time for different CR initial concentration. (Experimental condition: $\text{BaBiO}_3 = 0.75\text{gL}^{-1}$; $\text{pH} = 5.0$, $\text{Temp.} = 308\text{K}$).

With respect to initial concentration, the rate expression is given by equation:

$$\frac{-d[C]_o}{dt} = K_{app}[C]_o \quad \text{--- (6.12)}$$

Integration of the above equation yields:

$$\ln \frac{C_o}{C_t} = K_{app} \cdot t \quad \text{--- (6.13)}$$

Where, K_{app} is a pseudo first order rate constant (min^{-1}). $[C]_o$ is the equilibrium concentration of the CR dye solution after adsorption, and it is taken as the concentration of the dye solution at visible light irradiation time ' $t=0$ ' for kinetic analysis.

Initial rate (r_o) is determined by the following equation

$$r_o = K_{app}[C]_o \quad \text{--- (6.14)}$$

Where, r_o is initial rate ($\text{mgL}^{-1}\text{min}^{-1}$).

The plot of $\ln C_t/C_o$ versus t with different initial concentration of CR is shown in **Figure 6.9(a)**. The figure shows that the photocatalytic degradation follows perfectly the pseudo-first order kinetic with respect to CR concentrations.

It is found that a plot between $\ln C_t/C_o$ versus time represents a straight line, the slope of linear regression equals the apparent first order rate constant K_{app} which is consistent with the reported first order reaction [66].

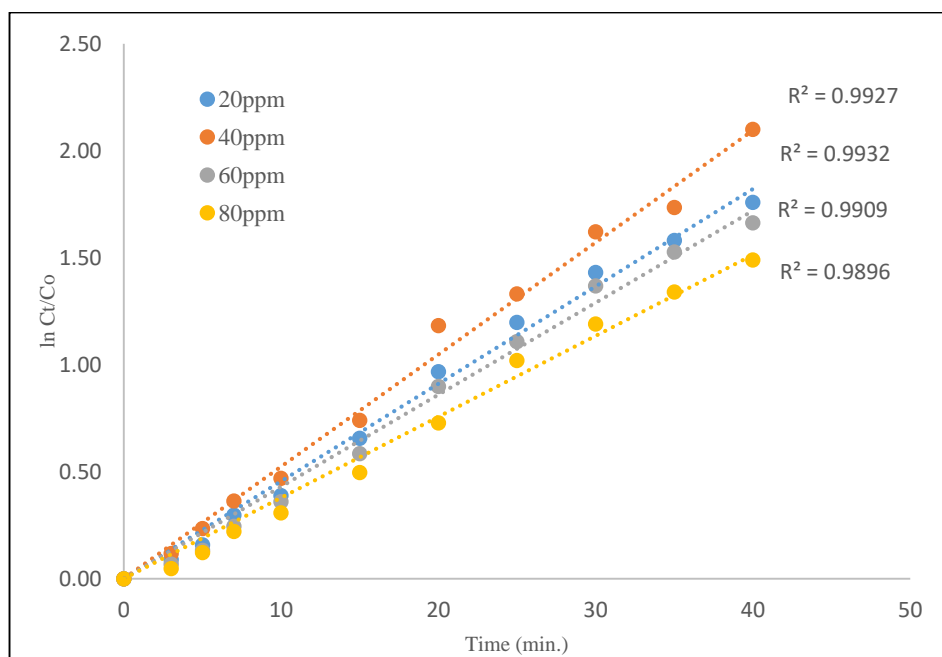


Figure-6.9: (a) Linear variation of $\ln C_t/C_o$ versus time for the photocatalytic degradation of CR dye at different initial concentration. (Experimental condition: $[BaBiO_3] = 0.75gL^{-1}$; $pH=5.0$ Temp. = 308K).

The values of rate constants K_{app} , which corresponds to different initial concentration, along with the initial rate (r_0) and corresponding regression constants, are listed in **Table 6.7(a)**.

Table 6.7 (a): Pseudo-first order apparent rate constant and initial rate values for the different initial concentration of dye.

(Experimental condition: $[BaBiO_3] = 0.75gL^{-1}$; $pH = 5.0$; Temp. = 308K).

S. No.	Initial concentration (mgL^{-1})	Rate constant K_{app} (min^{-1})	Initial rate $r_0 \times 10^{-3}$ ($mgL^{-1}min^{-1}$)	R^2
1	20	0.045	0.90	0.993
2	40	0.058	2.32	0.992
3	60	0.032	1.92	0.990
4	80	0.012	0.96	0.989

The rate of degradation increases with the initial concentration of CR dye then finds a tendency towards independent values with the higher initial concentrations.

According to the **equation 6.9** the plot of $1/r_0$ versus $1/C_0$ represented in **Figure 6.10(a)** shows a linear variation, confirming the Langmuir-Hinshelwood relationship for the initial rates of photodegradation. The values of K_r and K_{LH} calculated from the intercept ($1/K_r \cdot K_{LH}$) and the slope ($1/K_r$) of the straight line ($R^2=0.95$) are $K_r = 0.259 \text{ mgL}^{-1}\text{min}^{-1}$ and $K_{LH} = 4.09 \text{ Lmg}^{-1}$ respectively.

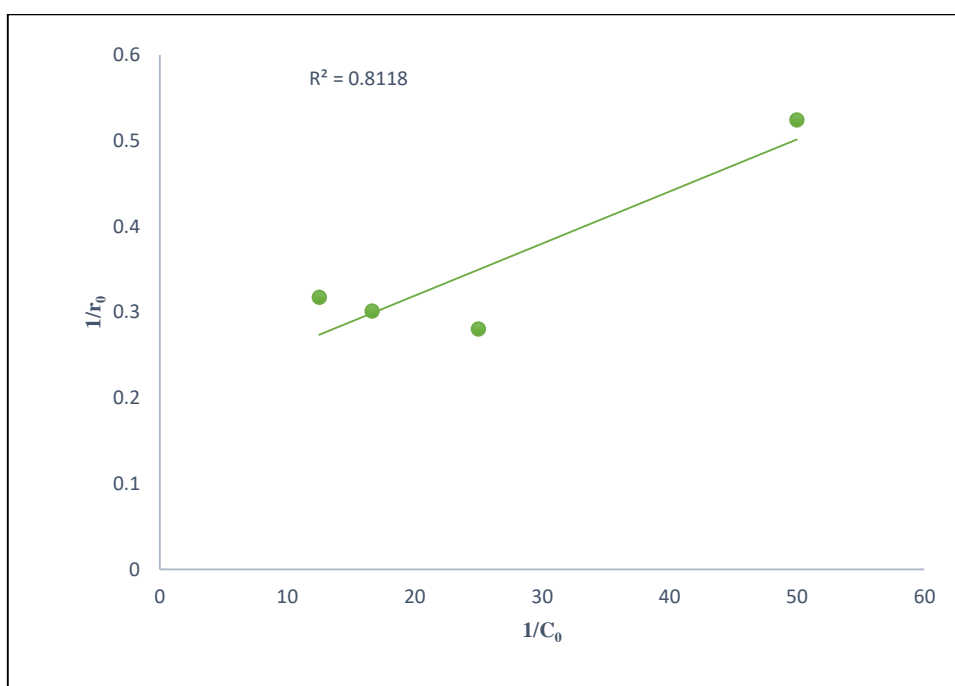


Figure-6.10(a): Langmuir-Hinshelwood plot for visible light photodegradation of CR dye by BaBiO_3 photocatalyst. (Experimental condition: $[\text{BaBiO}_3] = 0.75 \text{ gL}^{-1}$; $\text{pH} = 5.0$; $\text{Temp.} = 308 \text{ K}$).

(b) Results with $\text{Ba}_{0.6}\text{K}_{0.4}\text{BiO}_3$

The experimental results shows that the rate of photocatalytic degradation increases with increase in concentration of dye up to 40 mgL^{-1} . The rate of reaction was then, found to decrease with further increase in the concentration of dye. It is clear from the **Table 6.3 (b)** to **6.6(b)**, initially % degradation of dye increases rapidly and thereafter slowly attains the limiting value.

Figure 6.7.b. (A-D) shows the plots of change in % degradation with time for various concentration of dye at various amount of catalyst.

Table 6.3 (b): Influence of initial concentration on degradation of CR(Experimental Condition: $[\text{Ba}_{0.6}\text{K}_{0.4}\text{BiO}_3] = 0.25\text{gL}^{-1}$; pH=5.0; Temp.= 308K)

Dye Concentration	20 mgL ⁻¹	40 mgL ⁻¹	60 mgL ⁻¹	80 mgL ⁻¹
Time (min)	% Degradation	% Degradation	% Degradation	% Degradation
0	0.00	0.00	0.00	0.00
3	3.79	6.98	3.73	2.99
5	7.21	8.98	6.85	4.99
7	18.82	16.21	18.57	7.76
10	26.94	31.91	22.21	18.40
15	41.66	45.74	38.62	27.68
20	49.76	62.46	48.19	35.42
25	60.92	70.89	61.11	50.74
30	70.74	75.45	66.29	61.81
35	75.40	79.32	72.76	66.76
40	78.04	81.13	75.02	74.13
∞	78.04	81.14	75.02	74.14

Table 6.4 (b): Influence of initial concentration on degradation of CR(Experimental Condition: $[\text{Ba}_{0.6}\text{K}_{0.4}\text{BiO}_3] = 0.75\text{gL}^{-1}$; pH=5.0; Temp.= 308K)

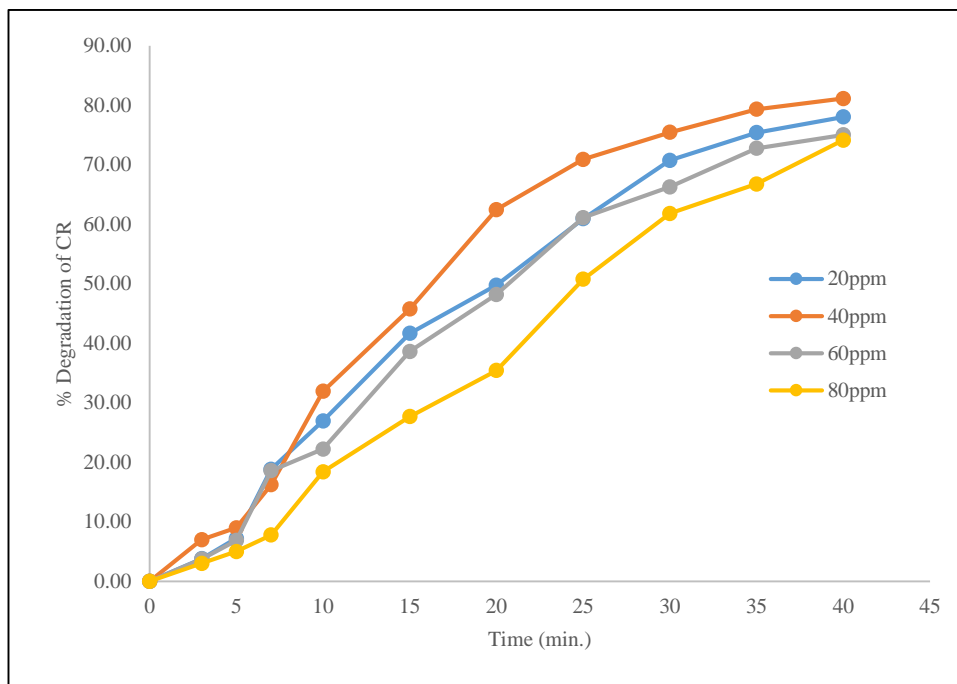
Dye Concentration	20 mgL ⁻¹	40 mgL ⁻¹	60 mgL ⁻¹	80 mgL ⁻¹
Time (min)	% Degradation	% Degradation	% Degradation	% Degradation
0	0.00	0.00	0.00	0.00
3	6.79	15.91	5.89	6.02
5	20.03	28.25	16.40	13.17
7	19.82	32.98	22.37	23.19
10	41.49	44.00	39.35	30.36
15	50.02	64.23	52.13	40.85
20	68.85	72.43	63.65	53.51
25	73.68	76.86	70.49	67.16
30	78.12	81.38	75.77	70.94
35	80.70	85.69	84.42	80.26
40	86.00	88.68	85.33	84.42
∞	86.01	88.69	85.34	84.43

Table 6.5 (b): Influence of initial concentration on degradation of CR(Experimental Conditions: $[\text{Ba}_{0.6}\text{K}_{0.4}\text{BiO}_3] = 1.00\text{gL}^{-1}$; pH=5.0; Temp.= 308K)

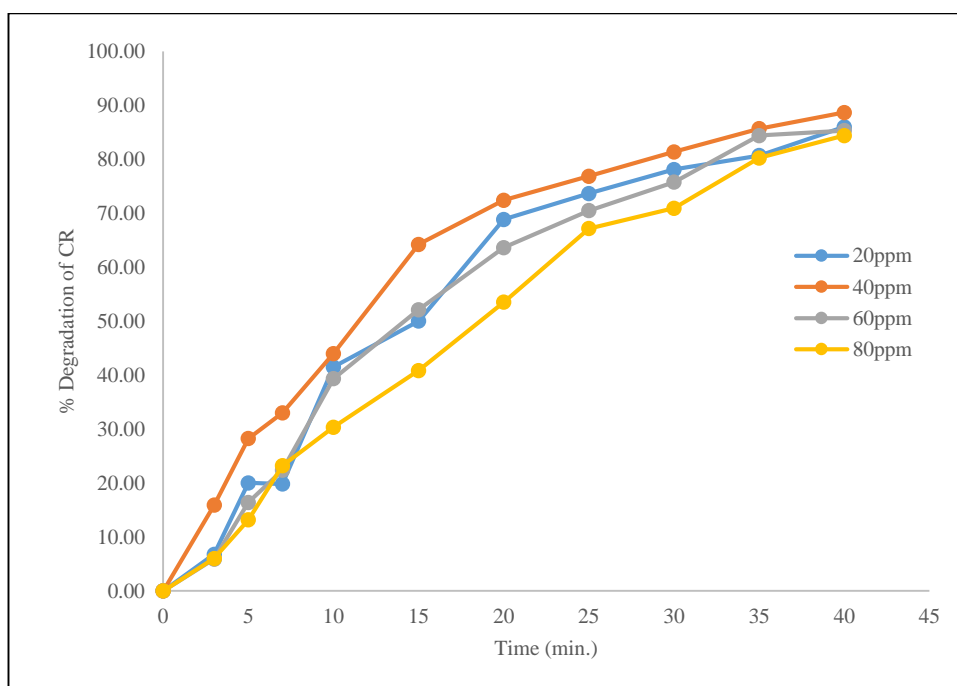
Dye Concentration	20 mgL ⁻¹	40 mgL ⁻¹	60 mgL ⁻¹	80 mgL ⁻¹
Time (min)	% Degradation	% Degradation	% Degradation	% Degradation
0	0	0	0	0
3	7.24	10.84	5.17	3.80
5	18.77	23.08	11.79	14.08
7	19.95	31.28	20.30	18.43
10	34.34	41.41	31.93	27.27
15	48.26	60.74	44.36	38.57
20	60.80	71.18	59.46	50.96
25	70.25	73.87	67.90	60.03
30	78.40	78.96	74.92	70.78
35	83.57	83.25	79.85	77.36
40	83.76	86.29	82.26	81.14
∞	83.77	86.30	82.27	81.14

Table 6.6(b): Influence of initial concentration on degradation of CR(Experimental Conditions; $[\text{Ba}_{0.6}\text{K}_{0.4}\text{BiO}_3] = 1.25\text{gL}^{-1}$; pH=5.0; Temp. =308K)

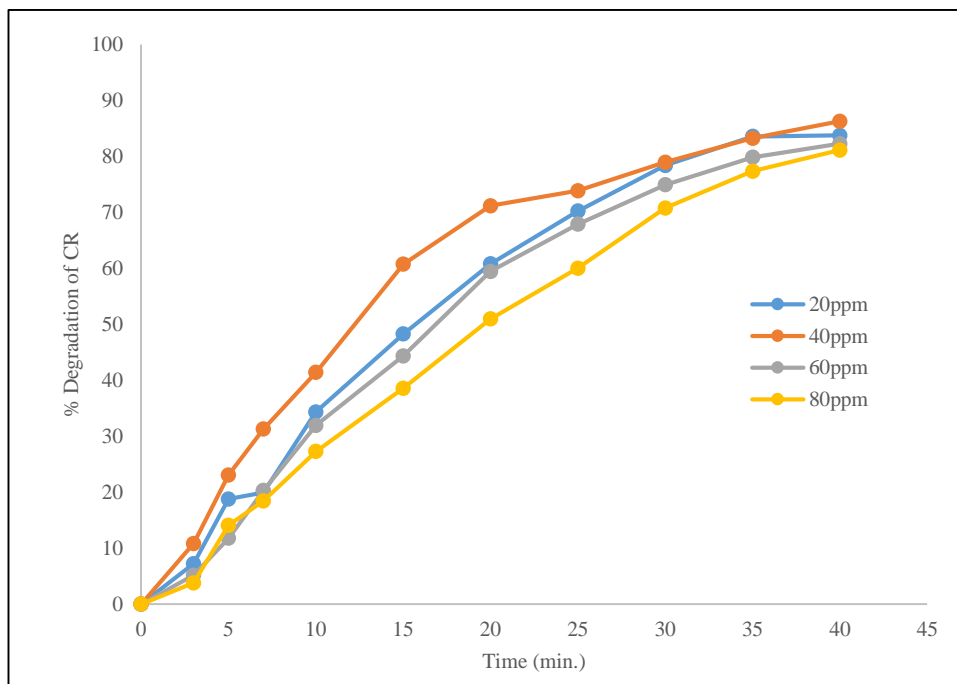
Dye Concentration	20 mgL ⁻¹	40 mgL ⁻¹	60 mgL ⁻¹	80 mgL ⁻¹
Time (min)	% Degradation	% Degradation	% Degradation	% Degradation
0	0	0	0	0
3	4.10	6.70	4.09	3.65
5	12.76	16.98	9.59	11.62
7	21.15	23.56	19.57	18.79
10	34.19	36.84	26.65	22.80
15	44.40	51.81	40.46	36.41
20	59.72	67.77	57.42	48.57
25	65.99	71.96	62.79	58.19
30	72.10	76.98	72.76	67.02
35	74.52	79.43	75.44	70.60
40	79.85	83.58	77.48	76.72
∞	79.86	83.59	77.49	76.72



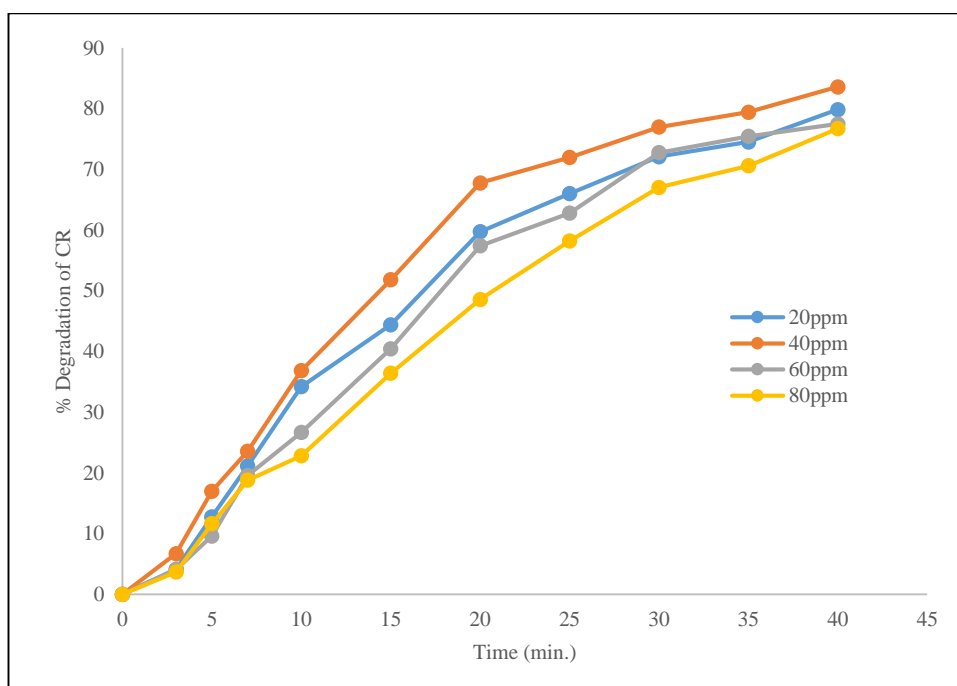
(A)



(B)



(C)



(D)

Figure 6.7(b): Effect of concentration of CR on its visible light degradation in $Ba_{0.6}K_{0.4}BiO_3$ [(A) Catalyst dose: $0.25gL^{-1}$; (B) Catalyst dose: $0.75gL^{-1}$; (C) Catalyst dose: $1.00gL^{-1}$ (D) Catalyst dose: $1.25gL^{-1}$; $pH=5.0$; $Temp. =308K$].

The photodegradation kinetics of initial dye concentration is illustrated in **Figure 6.8(b)**, which depicts the dark adsorption-desorption equilibrium and the additional decrease in CR concentration caused by visible light irradiation at optimum catalyst dose i.e. 0.75gL^{-1} .

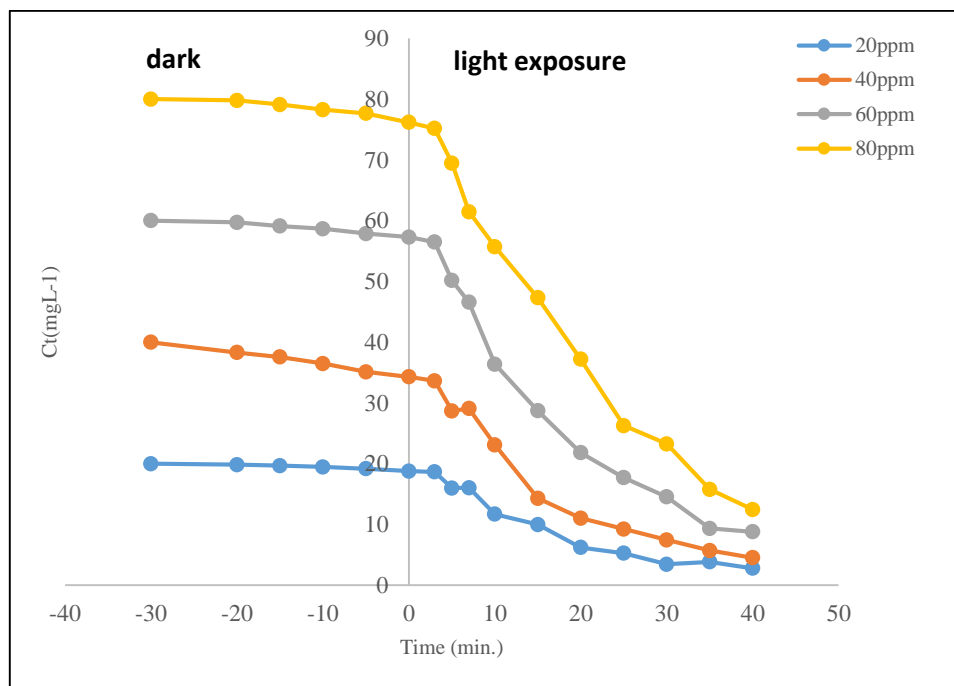


Figure 6.8(b): Variation of dye concentration versus time for different CR initial concentration. (Experimental condition: $[\text{Ba}_{0.6}\text{K}_{0.4}\text{BiO}_3] = 0.75\text{gL}^{-1}$; $\text{pH}=5.0$; $\text{Temp.}=308\text{K}$).

Keeping the rate expression with respect to initial concentration given in **equation 6.12** to **6.14** in mind, graphs are plotted between $\ln C_t/C_0$ and time.

The plot of $\ln C_t/C_0$ versus t with different initial concentration of CR is shown in **Figure 6.9(b)**. The figure shows that the photocatalytic degradation follows perfectly the pseudo-first order kinetic with respect to CR concentrations.

It is found that a plot between $\ln C_t/C_0$ versus time represents a straight line, the slope of linear regression equals the apparent first order rate constant K_{app} which is consistent with the reported first order reaction [66].

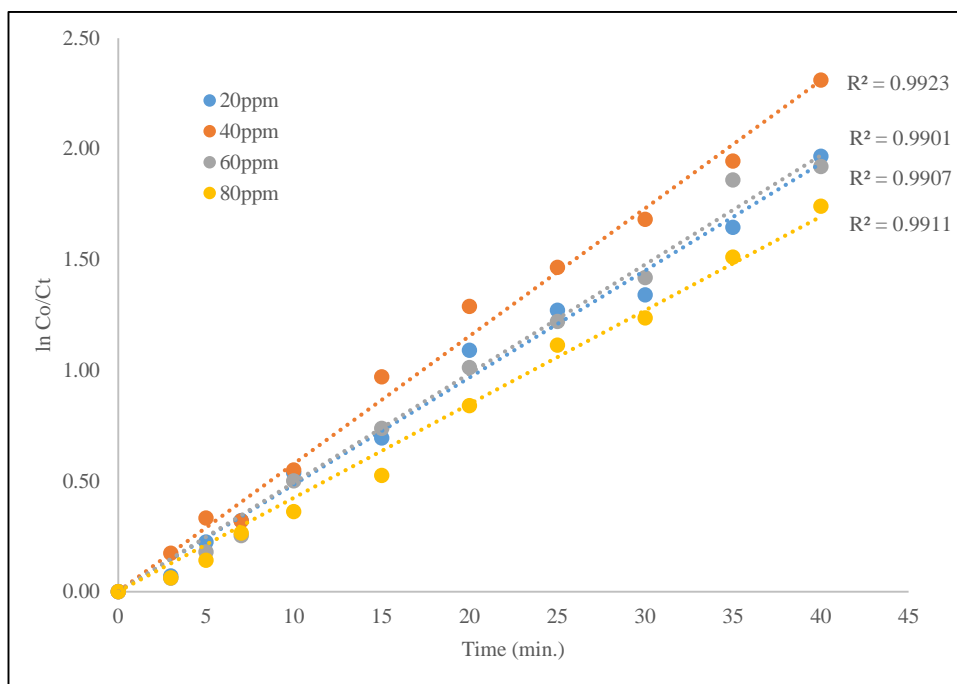


Figure 6.9(b): Linear variation of $\ln C_t/C_0$ versus time for photocatalytic degradation of at different initial dye concentration. (Experimental condition: $[BaBiO_3] = 0.75gL^{-1}$; $pH=5.0$ Temp. = 308K).

The values of rate constants K_{app} , which corresponds to different initial concentration, along with the initial rate (r_0) and corresponding regression constants, are listed in **Table 6.7(b)**.

Table 6.7 (b): Pseudo-first order apparent constant values for the different initial dye concentration of dye

(Experimental condition: $[Ba_{0.6}K_{0.4}BiO_3] = 0.75gL^{-1}$; $pH = 5.0$; Temp. = 308K).

S.No.	Initial concentration (mgL^{-1})	Rate constant K_{app} . (min^{-1})	Initial rate $r_0 \times 10^{-3}$ ($mgL^{-1}min^{-1}$)	R^2
1	0.02	0.049	0.98	0.990
2	0.04	0.063	2.52	0.992
3	0.06	0.022	1.32	0.990
4	0.04	0.013	1.04	0.991

According to **equation 6.9**, the plot of $1/r_0$ against $1/C_0$ as shown in **Figure 6.10(b)** gives linear relationship between $1/r_0$ and $1/C_0$ confirming the Langmuir-Hinshelwood relationship for the initial rate of photodegradation. The values of K_r and K_{LH} calculated from the slope ($1/K_r$) and intercept ($1/K_r \cdot K_{LH}$) of the above figure are found to be, $1.254 mgL^{-1}min^{-1}$ and $6.45 Lmg^{-1}$, respectively.

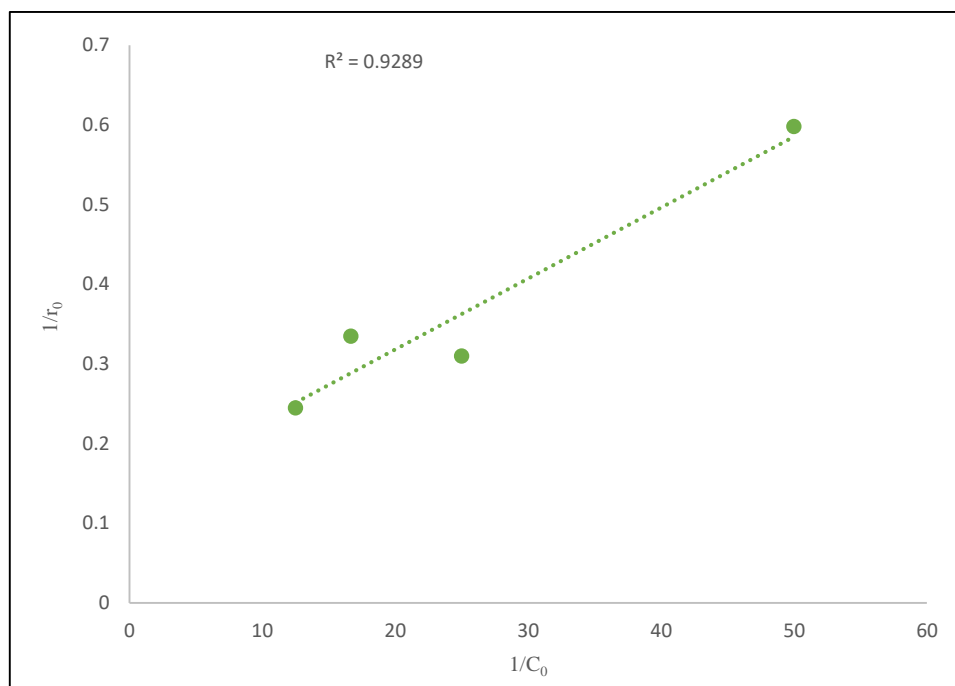


Figure-6.10(b): Langmuir-Hinshelwood plot for visible light photodegradation of CR dye by $Ba_{0.6}K_{0.4}BiO_3$. (Experimental condition: $[Ba_{0.6}K_{0.4}BiO_3] = 0.75 gL^{-1}$; $pH=5.0$; $Temp. = 308K$).

Here, for both the catalysts adsorption equilibrium constant i.e. K_{LH} obtained from the linearization of inverse of initial rate ($1/r_0$) and initial concentration ($1/C_0$), is different to the constant obtained from the dark adsorption (b). This is due to the photo adsorption and very rapid photoreaction of the dyes on the catalyst surface. These results are consistent with the earlier studies on photodegradation of dyes [67].

6.3.4.2 Effect of catalyst dose on photocatalytic degradation of CR

The optimization of catalyst dose is an important issue that is significant for avoiding the use of excessive catalyst and ensuring the maximum absorption of photon light. Hence, a series of experiments is carried out by varying the amount of both the catalysts from 0.25 to 1.25 gL^{-1} at pH 5.0 and 40 mgL^{-1} CR dye concentration at 308K. The degradation is studied till the maximum degradation is achieved.

It is observed that for both the cases, up to 0.75 gL^{-1} doses of photocatalysts, degradation rate increases and then with further increase in dose, the rate decreases.

The enhancement of removal rate may be due to the increase in the availability of active sites on the surface of the photocatalysts, which in turn increases the adsorption of dye species and, hence, the proportion of the excited species by the incoming photons. Larger amount of the catalyst favours the degradation efficiency due to the generation of free radicals O_2° and OH° [68]. Therefore, the rate of degradation increases with the increase of catalysts from 0.25 to 0.75gL^{-1} . A further increase in catalyst dose beyond the optimum will result in non-uniform light intensity distribution, so that the reaction rate would, indeed, be lowered with increased catalyst dosage. The tendency toward agglomeration (particle-particle interaction) increases at high solids concentration, resulting in a reduction in surface area available for light absorption and hence a drop in photocatalytic degradation rate. Although the number of active sites in solution will increase with catalyst dose, a point will be appeared to reach where light penetration is to be compromised because of excessive particle concentration. Thus, the balance between these two opposite phenomena results in an optimum catalyst dose for the photocatalytic reaction [69]. Since, the maximum degradation of CR dye is observed with 0.75gL^{-1} , the other experiments are performed using the same catalyst dose. Similar results have been obtained in the earlier reports on photodegradation of dyes [70,71]. The corresponding results with both the catalysts (BaBiO_3 and $\text{Ba}_{0.6}\text{K}_{0.4}\text{BiO}_3$) have been elaborated below:

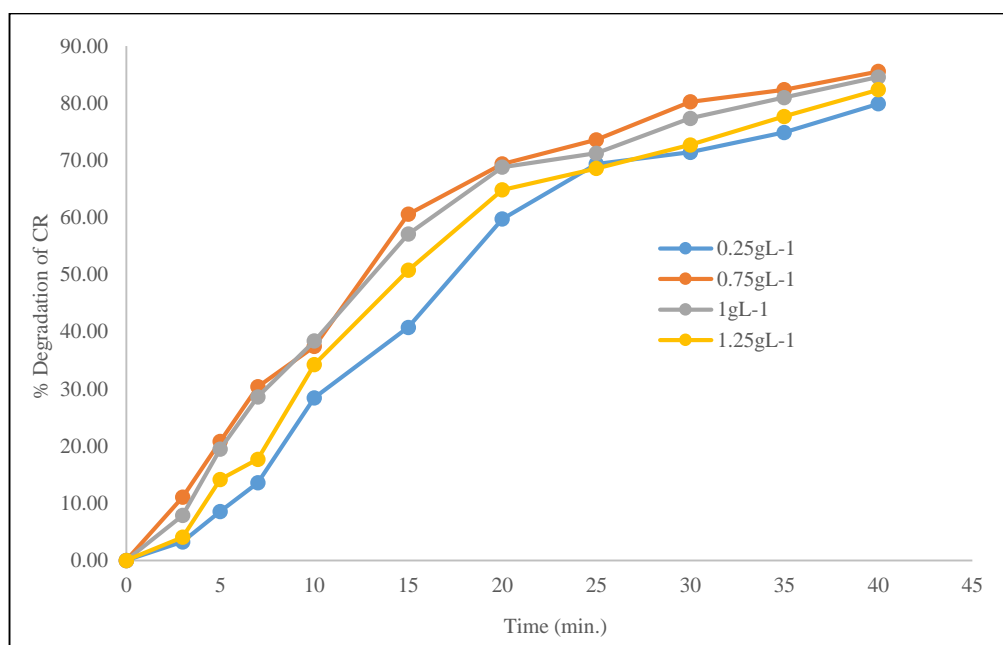
(a) Results with BaBiO_3

A series of experiments is carried out by varying the amount of catalyst from 0.25 to 1.25gL^{-1} at pH 5.0 and 40mgL^{-1} CR dye concentration. The degradation is studied till the maximum degradation is achieved.

Table 6.8(a) shows the influence of the catalyst dose on the % photodegradation of CR under visible light irradiation and the corresponding graphs is shown in **Figure 6.11(a)**.

Table 6.8 (a): Influence of BaBiO₃ dose on degradation of CR**(Experimental Conditions: [CR] = 40mgL⁻¹; pH=5.0; Temp.=308K).**

Catalyst dose	0.25gL ⁻¹	0.75gL ⁻¹	1.00gL ⁻¹	1.25gL ⁻¹
Time (min)	% Degradation	% Degradation	% Degradation	% Degradation
0	0.00	0.00	0.00	0.00
3	3.24	11.05	7.85	4.06
5	8.57	20.84	19.48	14.17
7	13.57	30.39	28.62	17.71
10	28.46	37.44	38.38	34.27
15	40.76	60.57	57.10	50.76
20	59.74	69.36	68.80	64.82
25	69.37	73.59	71.25	68.59
30	71.40	80.24	77.36	72.69
35	74.89	82.36	80.98	77.69
40	79.89	85.55	84.58	82.36
∞	79.90	85.56	84.59	82.37

**Figure 6.11(a): Influence of BaBiO₃ dose on visible light degradation of CR dye.**
(Experimental condition: [CR] = 40mgL⁻¹; pH=5.0, Temp. =308K)

The photodegradation kinetics at different catalyst loading is illustrated in **Figure 6.12(a)**, which depicts the dark adsorption-desorption equilibrium and the additional decrease in CR concentration caused by visible light irradiation.

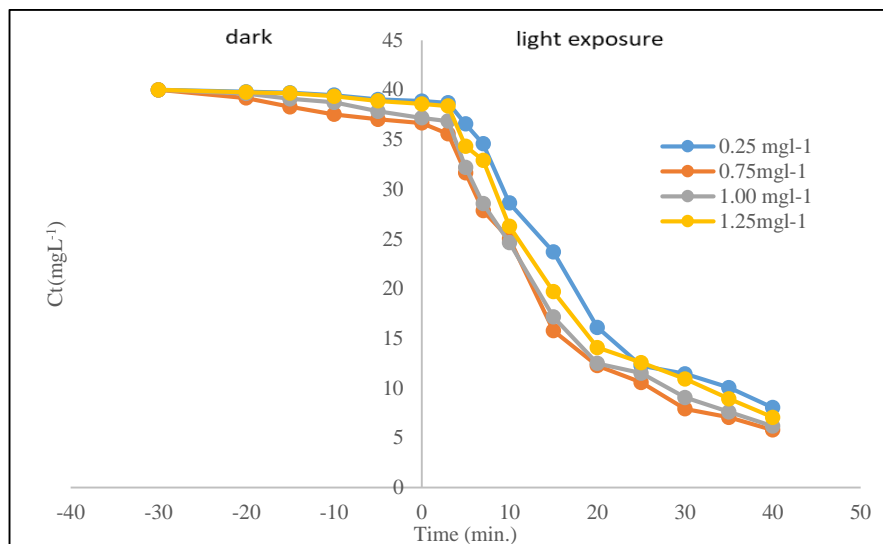


Figure 6.12(a): Variation of residual dye concentration at different BaBiO_3 . (Experimental conditions: $[\text{CR}] = 40 \text{ mgL}^{-1}$; $\text{pH}=5.0$; $\text{Temp.} = 308\text{K}$).

For the calculation of the rate constant (K_{app}) the logarithm of remaining concentration of CR is fitted to the Langmuir Hinshelwood kinetic model (given by **equation 6.11**) by plotting $\ln C_t/C_0$ against the irradiation time at different catalyst dose, which has been shown in **Figure 6.13(a)**.

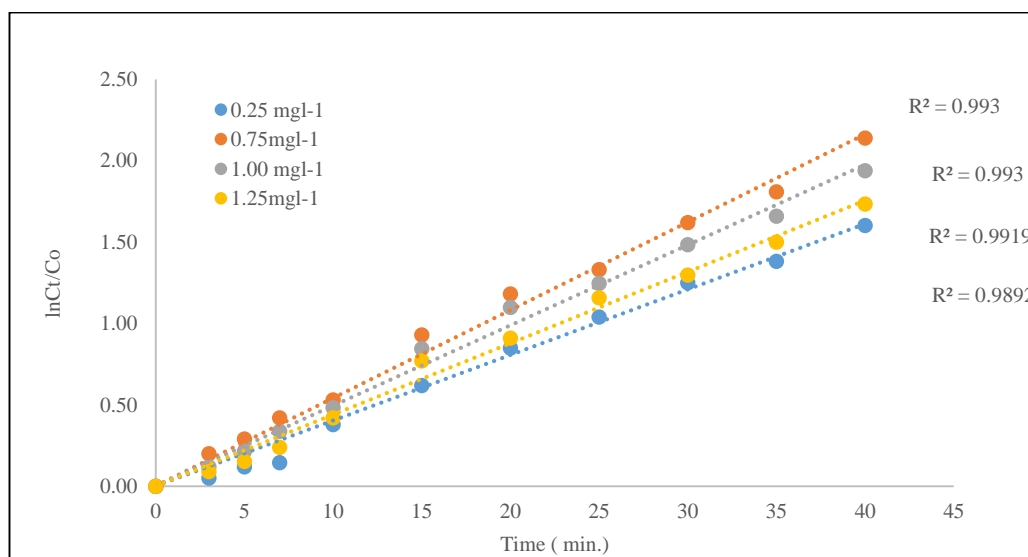


Figure 6.13(a): Linear variation of $\ln C_t/C_0$ versus time for photocatalytic degradation of CR dye at different BaBiO_3 loading. (Experimental condition: $[\text{CR}] = 40\text{mgL}^{-1}$; $\text{pH}=5.0$; $\text{Temp.} = 308\text{K}$).

The pseudo-first-order rate constants, K_{app} (Min^{-1}), are calculated from the slopes of the above **Figure 6.13(a)** and are listed in **Table 6.9(a)**.

Table 6.9(a): Pseudo-first order apparent constant values for the different BaBiO_3 dose

(Experimental condition: $[\text{CR}] = 40\text{mgL}^{-1}$; $\text{pH} = 5.0$; $\text{Temp.} = 308\text{K}$).

S.No.	Catalyst Dose (gL^{-1})	Rate Constant K_{app} (min^{-1})	R^2
1	0.25	0.046	0.993
2	0.75	0.054	0.993
3	1.00	0.032	0.991
4	1.25	0.019	0.989

An empirical relationship between the catalyst dose and initial dye concentration has been reported by Galindo et al ($r_o \alpha [\text{catalyst}]^n [\text{dye}]$), where n is an exponent less than 1 for all the dyes studied relative to low concentration of catalyst [72].

Figure 6.14(a) shows the log-log plots of rate constant against the catalyst dose which results in a straight line with a slope of 0.08 (equal to reaction order with respect to photocatalyst and intercept of -3.043. {**Figure 6.14(a)**} thus the initial degradation rate can be expressed by **equation 6.15**.

$$r_o \alpha [\text{BaBiO}_3]^{0.08} [\text{CR}] \quad \text{--- (6.15)}$$

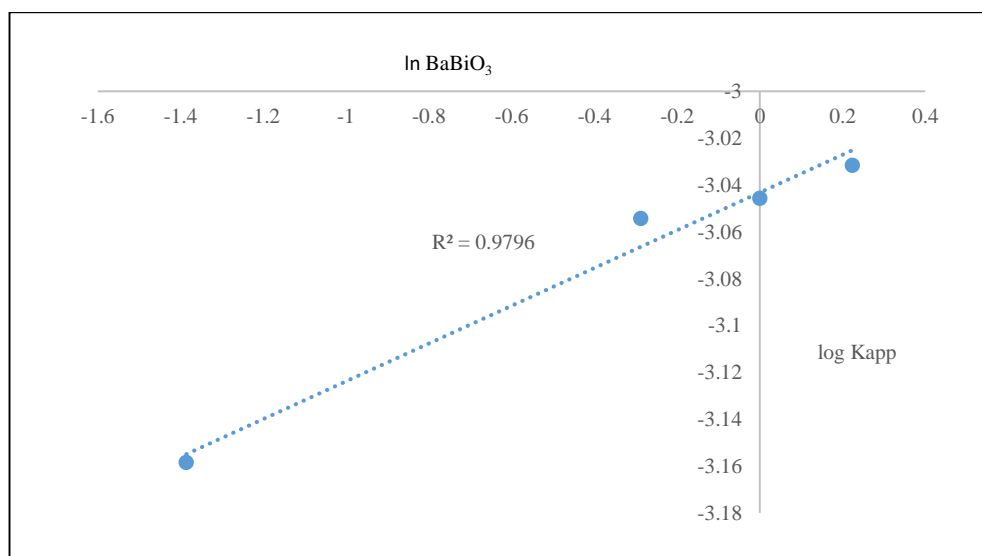


Figure 6.14(a): Relationship between $\ln K_{app}$ and the amount of BaBiO_3 . (Experimental condition: $[\text{CR}] = 40\text{mgL}^{-1}$; $\text{pH} = 5.0$; $\text{Temp.} = 308\text{K}$).

(b) Results with Ba_{0.6}K_{0.4}BiO₃

The catalyst loading was varied from 0.25gL⁻¹ to 1.5gL⁻¹ with an initial dye concentration of 40mgL⁻¹, initial pH 5.0 at 308K. The degradation is studied till the maximum degradation is achieved. **Table 6.8(b)** shows the influence of the catalyst dose on the % photodegradation of CR under visible light irradiation and the corresponding graphs is shown in **Figure 6.11(b)**.

Table 6.8 (b): Influence of Ba_{0.6}K_{0.4}BiO₃ dose on degradation of CR

(Experimental Conditions: [CR] = 40mgL⁻¹; pH=5.0; Temp.=308K).

Catalyst dose	0.25gL ⁻¹	0.75gL ⁻¹	1.00gL ⁻¹	1.25gL ⁻¹
Time (min)	% Degradation	% Degradation	% Degradation	% Degradation
0	0.00	0.00	0.00	0.00
3	5.69	15.91	10.84	6.70
5	7.16	28.25	23.08	16.98
7	16.21	27.28	31.28	20.26
10	31.91	42.21	41.41	36.84
15	45.74	64.23	60.74	51.81
20	62.46	72.43	71.18	67.77
25	70.89	76.86	73.87	71.96
30	75.45	81.38	78.96	74.20
35	79.32	85.69	83.25	79.43
40	81.13	88.68	86.29	83.58
∞	81.14	88.67	86.30	83.59

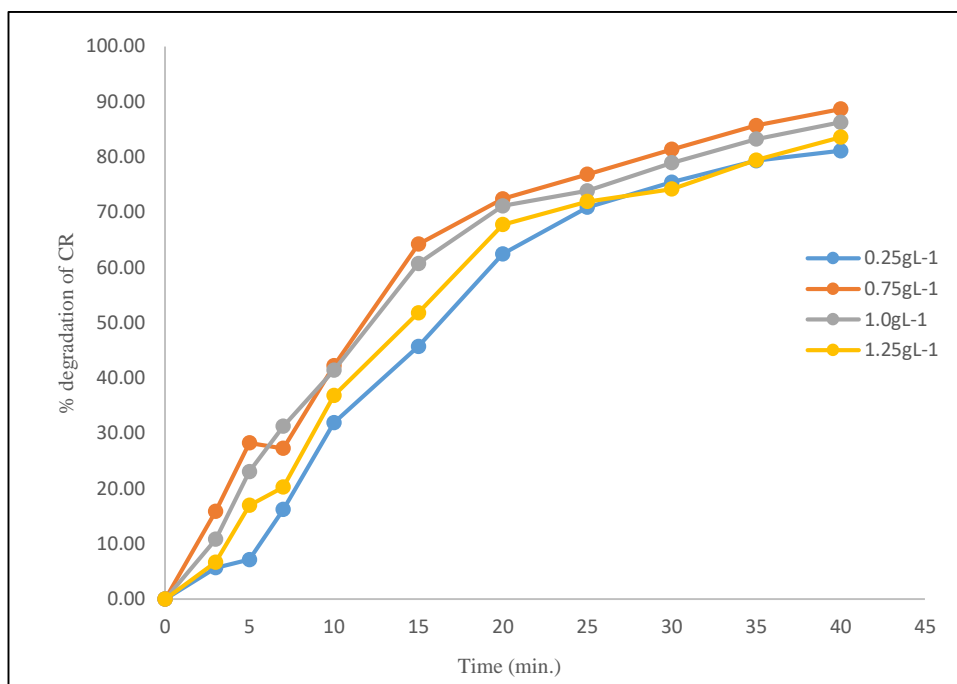


Figure 6.11(b): Influence of $Ba_{0.6}K_{0.4}BiO_3$ dose on visible light degradation of CR dye. (Experimental condition: $[CR] = 40\text{mgL}^{-1}$; $pH=5.0$; $Temp. =308\text{K}$).

The photodegradation kinetics at different catalyst loading is illustrated in **Figure 6.12(b)**, which depicts the dark adsorption-desorption equilibrium and the additional decrease in CR concentration caused by visible light irradiation.

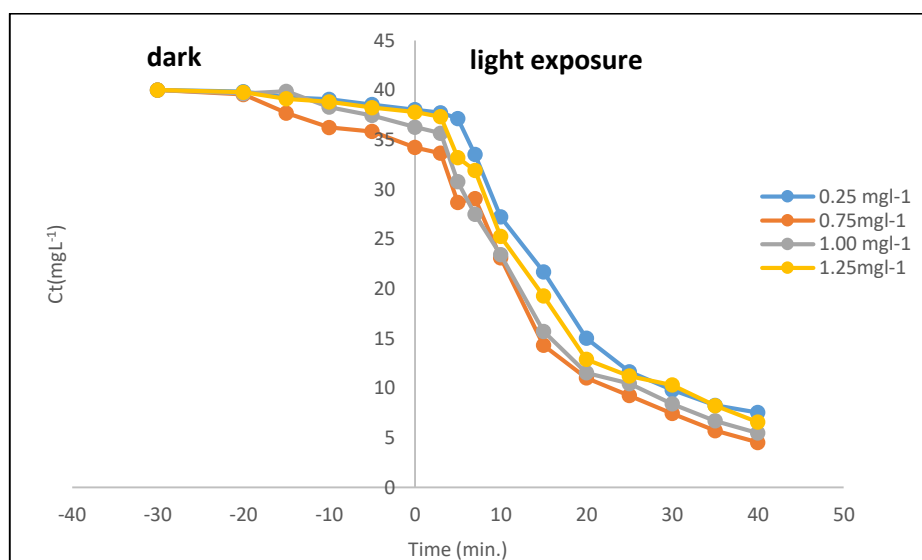


Figure 6.12(b): Variation of residual dye concentration at different $Ba_{0.6}K_{0.4}BiO_3$. (Experimental conditions: $[CR] = 40\text{mgL}^{-1}$; $pH=5.0$, $Temp. =308\text{K}$).

For the calculation of the rate constant (K_{app}) the logarithm of remaining concentration of CR is fitted to the Langmuir Hinshelwood kinetic model by plotting $\ln C_t/C_0$ against the irradiation time at different catalyst dose, which has been shown in **Figure 6.13(b)**.

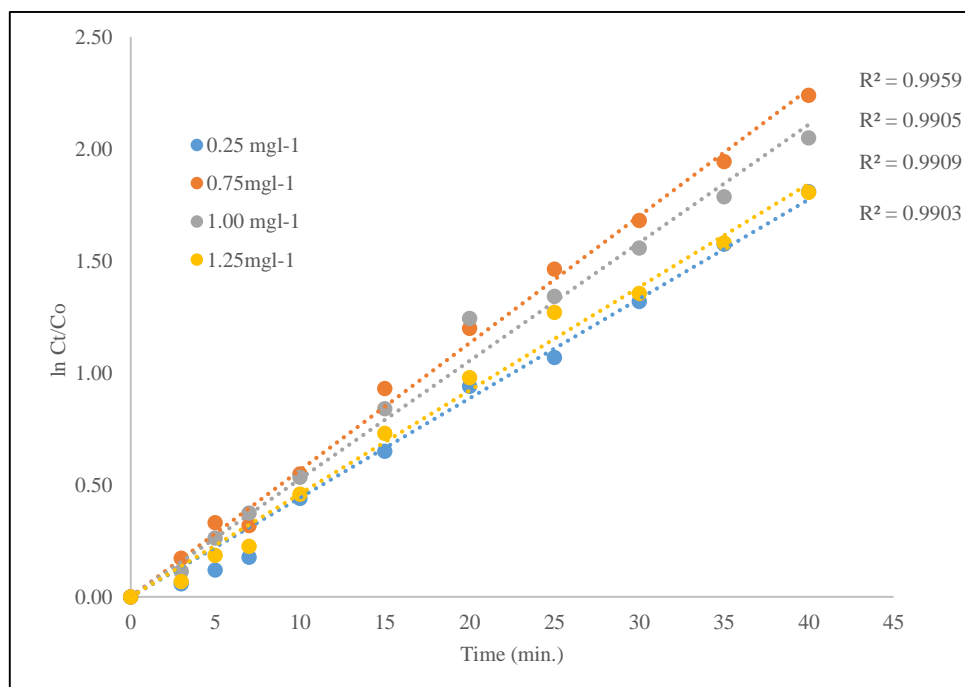


Figure 6.13(b): Linear variation of $\ln C_t/C_0$ versus time for photocatalytic degradation of CR dye at different $Ba_{0.6}K_{0.4}BiO_3$ loading (Experimental condition: $[CR] = 40\text{mgL}^{-1}$; $\text{pH}=5.0$; $\text{Temp.}=308\text{K}$).

The pseudo-first-order rate constants, K_{app} (min^{-1}), are calculated from the slopes of the above **Figure 6.13(b)** and are listed in **Table 6.9(b)**.

Table 6.9(b): Pseudo-first order apparent constant values for the different $Ba_{0.6}K_{0.4}BiO_3$ dose

(Experimental condition: $[CR] = 40\text{mgL}^{-1}$; $\text{pH} = 5.0$; Temperature = 308K).

S.No.	Catalyst Dose gL^{-1}	Rate Constant K_{app} (min^{-1})	R^2
1	0.25	0.048	0.990
2	0.75	0.056	0.995
3	1.00	0.036	0.990
4	1.25	0.029	0.990

Also, an empirical relationship between the initial dye concentration has been reported by Galindo et al ($r_o \alpha [\text{catalyst}]^n [\text{dye}]$), where n is an exponent less than 1 for all the dyes studied relative to low concentration of catalyst [72].

Figure 6.14(b) shows the log-log plots of rate constant against the catalyst dose which results in a straight line with a slope of 0.09 (equal to reaction order with respect to photocatalyst) and intercept of -2988. {**Figure 6.14(b)**} thus the initial degradation rate can be expressed by equation 6.16.

$$r_o \alpha [\text{Ba}_{0.6}\text{K}_{0.4}\text{BiO}_3]^{0.09} [\text{CR}] \quad \text{--- (6.16)}$$

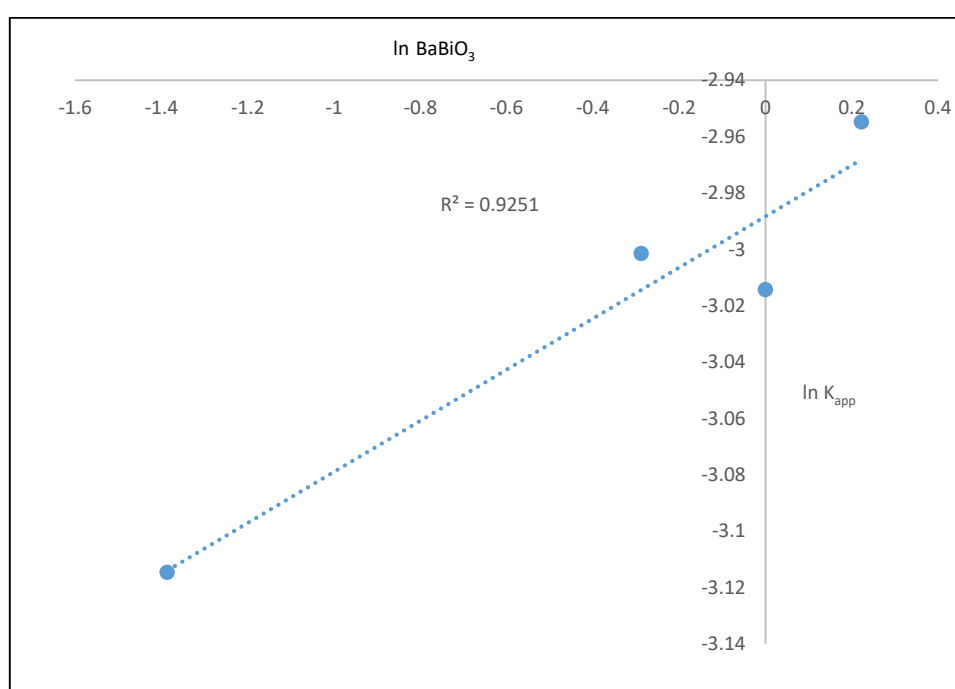


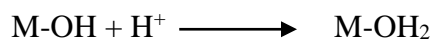
Figure 6.14(b): Relationship between $\ln K_{app}$ and the amount of $\text{Ba}_{0.6}\text{K}_{0.4}\text{BiO}_3$. (Experimental condition: $[\text{CR}] = 40\text{mgL}^{-1}$; $\text{pH} = 5.0$; $\text{Temp.} = 308\text{K}$).

From the experimental results, it was observed that the increase in catalyst dose from 0.25gL^{-1} to 0.75gL^{-1} increased the rate and with further increase in the catalyst dose the reaction rate decreases which is the characteristics of heterogeneous photocatalysis and results are in a good agreement with the earlier studies [73]. In order to have a better dye removal efficiency, we used 0.75gL^{-1} BaBiO_3 or $\text{Ba}_{0.6}\text{K}_{0.4}\text{BiO}_3$ suspension concentration for the rest of the experimental runs. The photocatalytic destruction of other organic pollutants has also exhibited the same dependency over the catalyst dose [74,75].

6.3.3.3 Effect of initial pH on photocatalytic degradation of CR dye

The pH effects both the surface state of catalyst and the ionization state of dye molecule. Organic compounds in wastewater differ greatly in several parameters, particularly in their speciation behaviour, solubility in water and hydrophobicity. While some compounds are uncharged at common pH conditions typical of natural water or wastewater, other compounds exhibit a wide variation in speciation (or charge) and physico-chemical properties. Besides, because of the amphoteric behaviour of most semiconductor oxides, an important parameter governing the rate of reaction taking place on semiconductor particle surfaces is the pH of the dispersions [76,77]. Since, pH influences the surface-charge-properties of the photocatalysts; therefore, the effect of pH on the rate of degradation needs to be considered. Most considerably, it is related to the acid base property of the metal-oxide surface as explained above on the basis of their amphoteric nature [78].

In the present research work also, both the catalysts despite having status of p-type (BaBiO_3) and n-type ($\text{Ba}_{0.6}\text{K}_{0.4}\text{BiO}_3$) semiconductor are supposed to be electrically neutral, making them amphoteric in nature [79,80]. It is known that the metal oxide particles suspended in water behave similarly to diprotic acids. The adsorption of water molecules at sacrificial metal sites is followed by the dissociation of OH^- charged groups leading to coverage with chemically equivalent metal hydroxyl group (M-OH) due to amphoteric behaviour of most metal hydroxides, the following 2 equilibrium reactions are considered [81]:



Experiments are carried out at pH values in the range 4.0-8.0, using 40mgL^{-1} CR solution and 0.75gL^{-1} BaBiO_3 dose. For CR, the extent of photocatalysis increases with increase in pH up to 5.0 and with further increase in pH the degradation efficiency decreases. Nevertheless, at higher pH values, CR anions are generally repelled away from the negatively charged surface of photocatalyst particles, so degradation rate decreases.

Similar results have been obtained in the earlier reports of photodegradation of dyes by semiconductor photocatalysts [82,83].

(a) Results with BaBiO₃

The influence of the initial pH of the solution on the % photocatalytic degradation of CR is depicted in **Table 6.10(a)** and corresponding graphs are shown in **Figure 6.15(a)**.

Table 6.10 (a): Influence of solution pH on degradation of CR
(Experimental Conditions: [CR]= 40mgL⁻¹; [BaBiO₃] =0.75 gL⁻¹; Temp.=308K).

pH	pH=4.0	pH=5.0	pH=6.0	pH =7.0	pH = 8.0
Time (min)	% Degradation				
0	0	0.00	0	0	0
3	2.66	11.05	8.96	7.59	6.24
5	12.96	20.84	18.13	17.09	15.23
7	24.51	30.39	28.78	27.41	26.52
10	34.32	42.33	39.74	38.47	37.44
15	53.80	60.57	58.92	57.47	56.56
20	63.10	69.36	68.22	67.08	65.57
25	65.52	74.29	72.29	71.19	68.98
30	72.13	80.24	79.00	75.37	74.84
35	74.69	82.36	80.62	79.21	77.95
40	75.27	85.55	82.33	78.65	77.17
∞	75.28	85.56	82.34	78.66	77.18

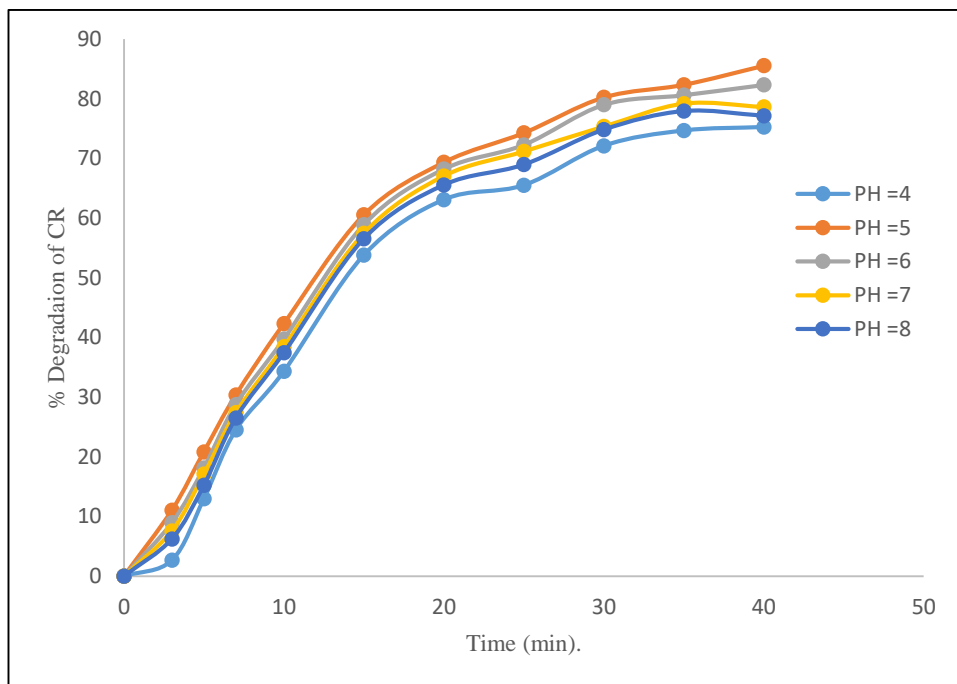


Figure 6.15(a): Effect of initial pH on % degradation of CR. (Experimental condition: $[CR] = 40 \text{ mg L}^{-1}$; $[BaBiO_3] = 0.75 \text{ g L}^{-1}$; $Temp. = 308 \text{ K}$).

The photodegradation kinetics of different pH loading is illustrated in **Figure 6.16(a)**, which depicts the dark adsorption-desorption equilibrium and the additional decrease in CR concentration caused by visible light irradiation.

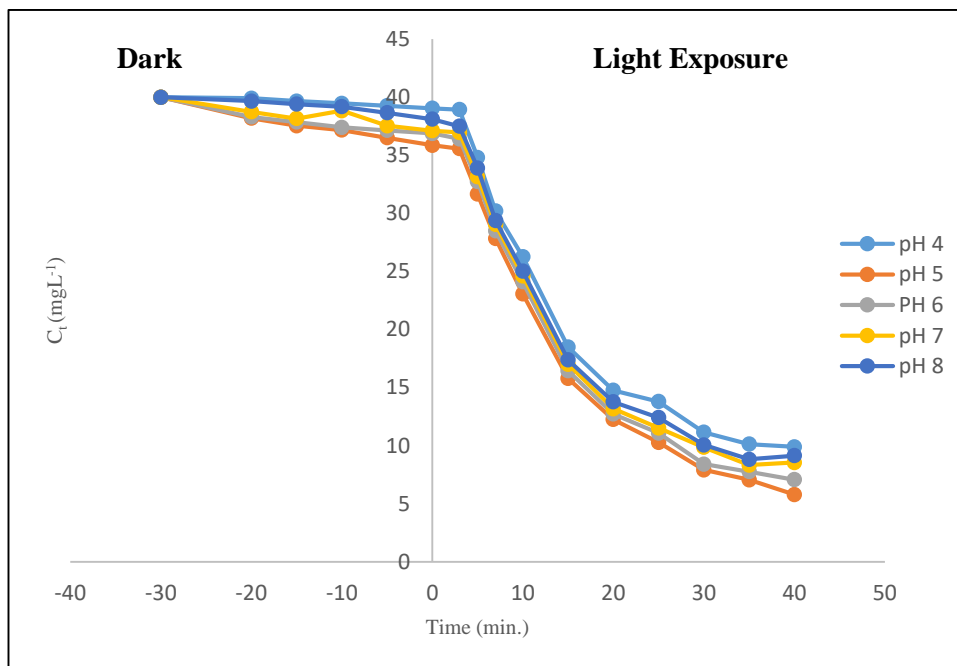


Figure 6.16 (a): Effect of pH on the residual dye concentration. (Experimental conditions: $[CR] = 40 \text{ mg L}^{-1}$; $[BaBiO_3] = 0.75 \text{ g L}^{-1}$; $Temp. = 308 \text{ K}$).

The photocatalytic degradation of CR under a wide range of pH values was fitted to the Langmuir-Hinshelwood model by plotting $\ln(C_t/C_0)$ versus irradiation time which has been shown in **Figure 6.17(a)**.

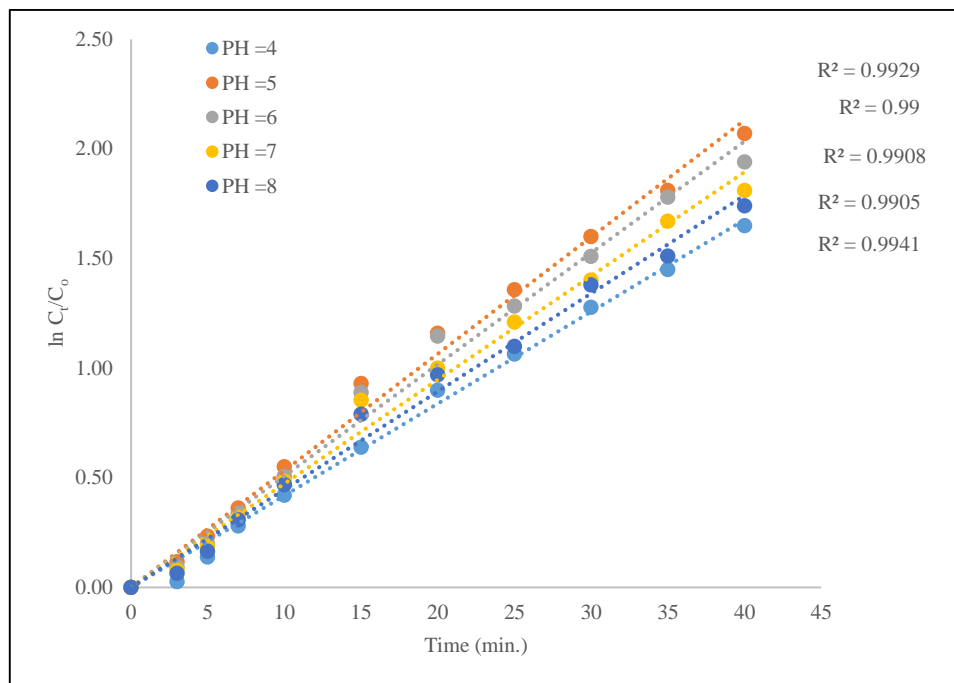


Figure 6.17 (a): Linear variation of $\ln C_t/C_0$ versus time for photocatalytic degradation of CR dye at different initial solution pH. (Experimental condition: $[CR] = 40\text{mgL}^{-1}$; $[BaBiO_3] = 0.75\text{gL}^{-1}$; Temp. = 308 K).

The pseudo-first-order rate constant, K_{app} (min^{-1}), are calculated from the slopes of the plots {**Figure 6.17(a)**} and are presented in **Table 6.11(a)**.

Table 6.11(a): Pseudo-first order apparent constant values for the photodegradation of CR at different solution pH

(Experimental condition: $[CR] = 40\text{mgL}^{-1}$; $[BaBiO_3] = 0.75\text{gL}^{-1}$ Temp. = 308 K)

S.No.	pH	Rate Constant K_{app} (min^{-1})	R ²
1	4.0	0.041	0.997
2	5.0	0.053	0.992
3	6.0	0.050	0.990
4	7.0	0.047	0.990
5	8.0	0.044	0.990

The pseudo-first-order rate constant (K_{app}) values of dye degradation obtained by performing photodegradation reactions under different initial pH are reported in **Figure 6.18(a)**. These K_{app} values indicate that the highest degradation is achieved at neutral pH i.e. pH 5.0.

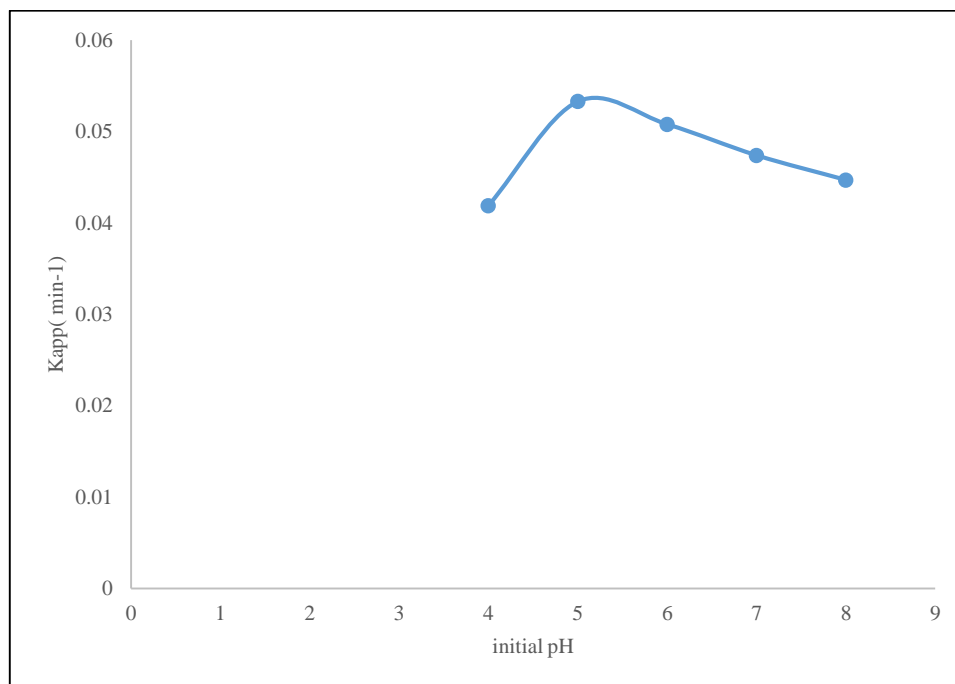


Figure 6.18 (a): Effect of the pH on the reaction rate constant for CR dye degradation (Experimental condition: $[CR] = 40\text{mgL}^{-1}$; $[BaBiO_3] = 0.75\text{gL}^{-1}$; Temp. = 308K).

(b) Results with $Ba_{0.6}K_{0.4}BiO_3$

The influence of the initial pH of the solution on the % photocatalytic degradation of CR is depicted in **Table 6.10(b)** and corresponding graphs are shown in **Figure 6.15(b)**. For CR dye degradation, the extent of photocatalysis increases with increase in pH up to 5.0 and with further increase in pH the degradation efficiency decreases.

Table 6.10(b): Effect of solution pH on degradation of CR

(Experimental Conditions: $[CR] = 40 \text{ mgL}^{-1}$; $[Ba_{0.6}K_{0.4}BiO_3] = 0.75\text{gL}^{-1}$; Temp.= 308K).

pH	pH=4.0	pH =5.0	pH=6.0	pH=7.0	pH = 8.0
Time (min)	% Degradation				
0	0	0.00	0	0	0
3	7.77	15.91	14.43	12.40	11.00
5	16.80	24.48	23.24	20.82	20.33
7	20.08	27.28	25.86	23.45	23.62
10	34.24	42.21	41.01	38.91	37.82
15	56.42	64.23	62.90	60.48	60.06
20	64.99	72.43	71.05	68.58	68.32
25	69.77	76.86	75.70	73.41	72.89
30	73.32	81.38	80.33	77.99	77.25
35	78.14	85.69	84.19	82.04	81.15
40	80.94	88.68	87.42	85.27	84.44
∞	80.95	88.68	87.43	85.28	84.45

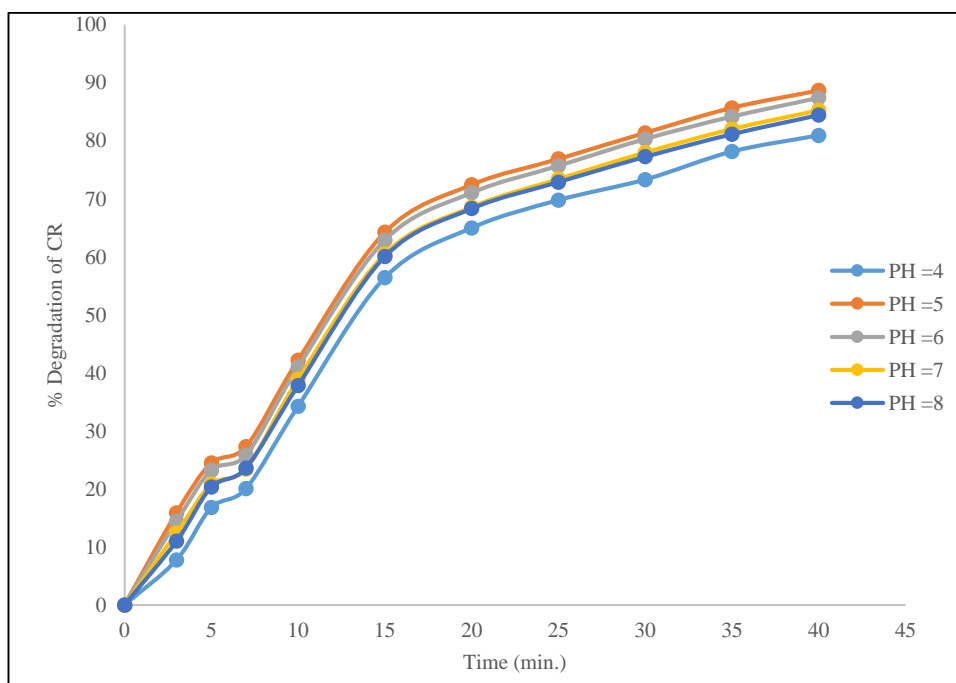


Figure 6.15 (b): Influence of solution pH on % degradation of CR. (Experimental condition: $[CR] = 40 \text{ mg L}^{-1}$, $[Ba_{0.6}K_{0.4}BiO_3] = 0.75\text{gL}^{-1}$, Temp. =308K).

The photodegradation kinetics of different pH loading is illustrated in **Figure 6.16 (b)**, which depicts the dark adsorption-desorption equilibrium and the additional decrease in CR concentration caused by visible light irradiation.

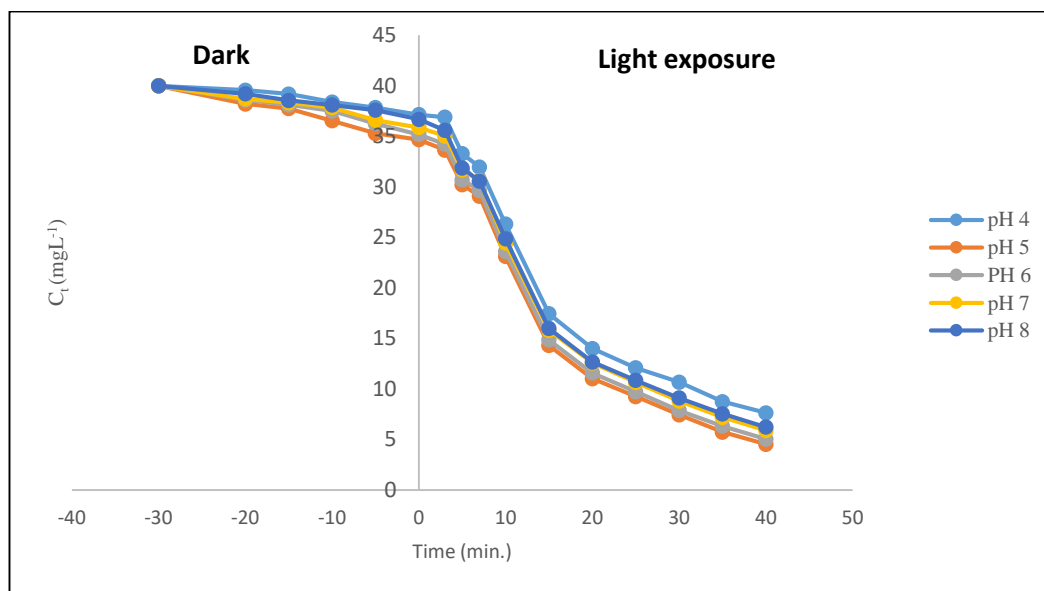


Figure 6.16 (b): Effects of solution pH on the residual dye fractions. (Experimental conditions: $[CR] = 40 \text{ mgL}^{-1}$; $[Ba_{0.6}K_{0.4}BiO_3] = 0.75 \text{ gL}^{-1}$ Temp. = 308K).

A plot between $\ln(C_t/C_0)$ versus irradiation time (t) was fitted to the Langmuir–Hinshelwood model. The pseudo-first-order rate constants, K_{app} (min^{-1}), are calculated from the slopes of the plots {**Figure 6.17(b)**}.

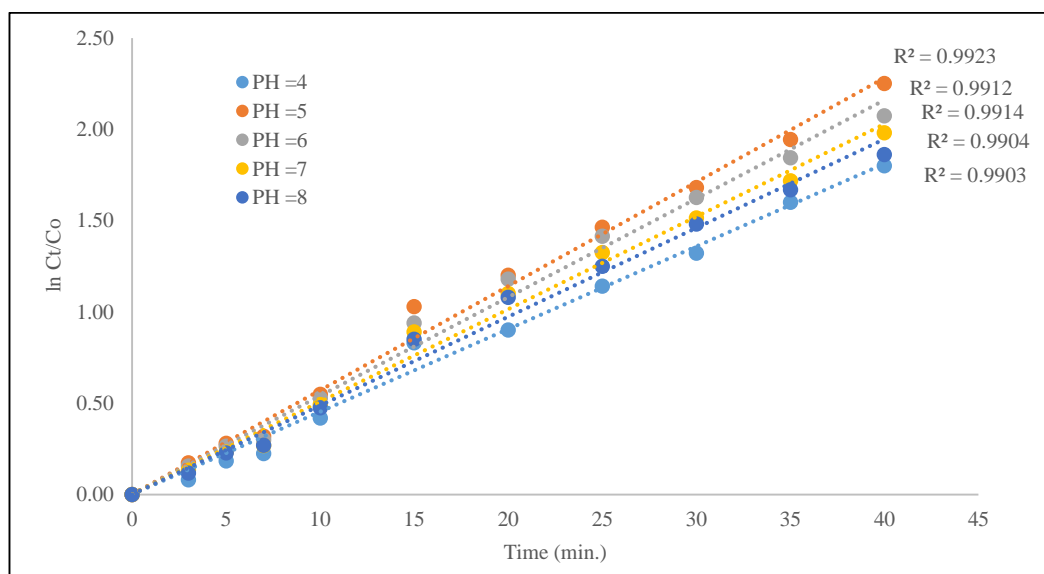


Figure 6.17 (b): Linear variation of $\ln C_t/C_0$ versus time for photocatalytic degradation of CR dye at different initial pH. (Experimental condition: $[CR] = 40 \text{ mgL}^{-1}$; $[Ba_{0.6}K_{0.4}BiO_3] = 0.75 \text{ gL}^{-1}$; Temp. = 308K)

The pseudo-first-order rate constant, K_{app} (min^{-1}), are calculated from the slopes of the plots { **Figure 6.17(b)** } and are presented in **Table 6.11(b)**.

Table 6.11(b): Pseudo-first order apparent constant values for the photodegradation of CR at different solution pH

(Experimental condition: $[\text{CR}] = 40\text{mgL}^{-1}$; $[\text{Ba}_{0.6}\text{K}_{0.4}\text{BiO}_3] = 0.75\text{gL}^{-1}$; Temp. = 308K).

S.No.	pH	Rate Constant K_{app} (min^{-1})	R^2
1	4.0	0.048	0.990
2	5.0	0.057	0.992
3	6.0	0.054	0.991
4	7.0	0.050	0.991
5	8.0	0.045	0.990

The pseudo-first-order rate constant (K_{app}) values of dye degradation obtained by performing photodegradation reactions under different initial pH are reported in **Figure 6.18(b)**. These K_{app} values indicate that the highest degradation is achieved at neutral pH i.e. pH 5.0.

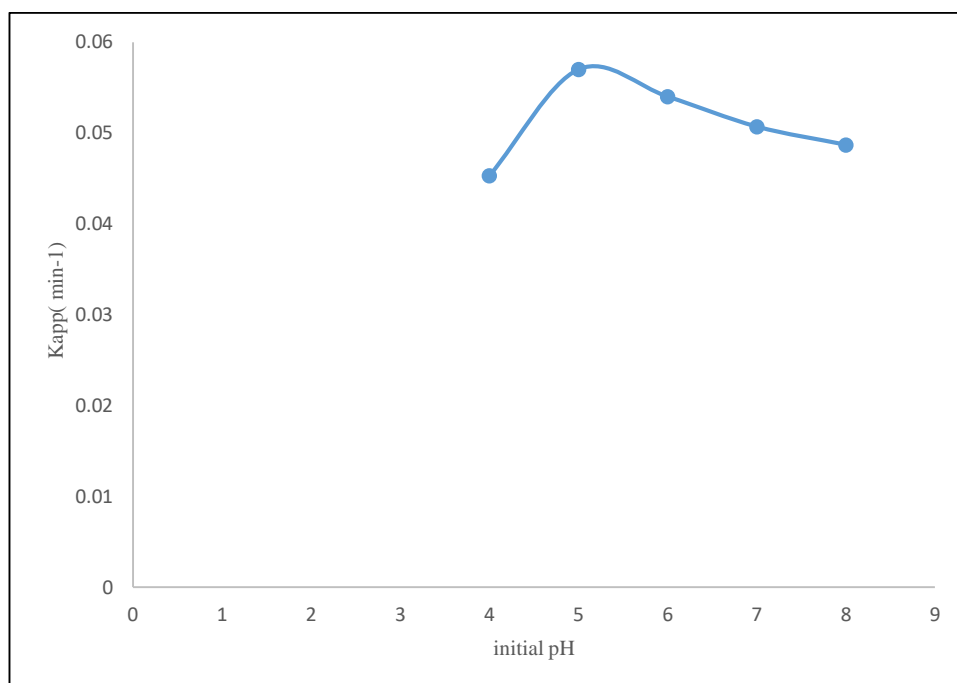


Figure 6.18(b): Effect of the initial pH on the reaction rate constant for CR dye degradation (Experimental condition: $[\text{CR}] = 40\text{mgL}^{-1}$; $[\text{Ba}_{0.6}\text{K}_{0.4}\text{BiO}_3] = 0.75\text{gL}^{-1}$; Temp. = 308K).

6.3.4.4 Effect of temperature on photocatalytic degradation of CR dye

Generally, photocatalysis is not temperature dependent. However, an increase in temperature can affect the amount of adsorption and helped the reaction to complete more efficiently with e^-h^+ recombination [84,85]. An increase in temperature helps the reaction to compete more efficiently with e^-/h^+ recombination as a result of increased collision frequency of molecules; leading to an enhancement of the degradation activity [86]. Several previous research work indicate that the rate of the photocatalytic degradation is temperature dependent and is favoured with the increase of solution temperature [87]. The apparent activation energy (E_a) has been calculated from the **Arrhenius equation** [88]:

$$K_{app} = A \exp. \left[-\frac{E_a}{RT} \right] \quad \text{--- (6.17)}$$

Where, A is a temperature independent factor (min^{-1}), E_a is the apparent activation energy of the photocatalytic degradation (J/mol), R is the gas constant (8.31 J/K mol) and T is the solution temperature. The linear transform of $\ln(K_{app}) = f(1/T)$, gives a straight line whose slope is equal to $-E_a/R$.

The effect of temperature was investigated by studying the photocatalytic degradation at different solution temperatures (298-308 K) under the same operating conditions i.e. $[\text{CR}] = 40\text{mgL}^{-1}$; Catalyst dose = 0.75gL^{-1} and initial $\text{pH}=5.0$.

(a) Results with BaBiO_3

The influence of solution temperature on the % photodegradation of CR dye as a function of time is depicted in **Table 6.12(a)** and the corresponding graph is shown in **Figure 6.19(a)**. The figure indicates that the rate of the photocatalytic degradation is temperature dependent and is favoured with the increase of solution temperature.

Table 6.12 (a): Influence of temperature on degradation of CR

(Experimental condition: $[CR] = 40\text{mgL}^{-1}$; $[BaBiO_3] = 0.75\text{gL}^{-1}$; $\text{pH}=5.0$; $\text{Temp.}=308\text{K}$).

Temperature	298K	303K	308K
Time (min)	%Degradation	%Degradation	%Degradation
0	0.00	0.00	0.00
3	2.31	5.76	11.05
5	10.21	13.71	20.84
7	21.62	25.29	30.39
10	27.84	34.58	42.33
15	52.57	55.30	60.57
20	59.06	62.81	69.36
25	65.22	68.50	73.59
30	66.61	73.72	80.24
35	74.45	77.23	82.36
40	76.77	79.78	85.55
∞	76.78	79.79	85.56

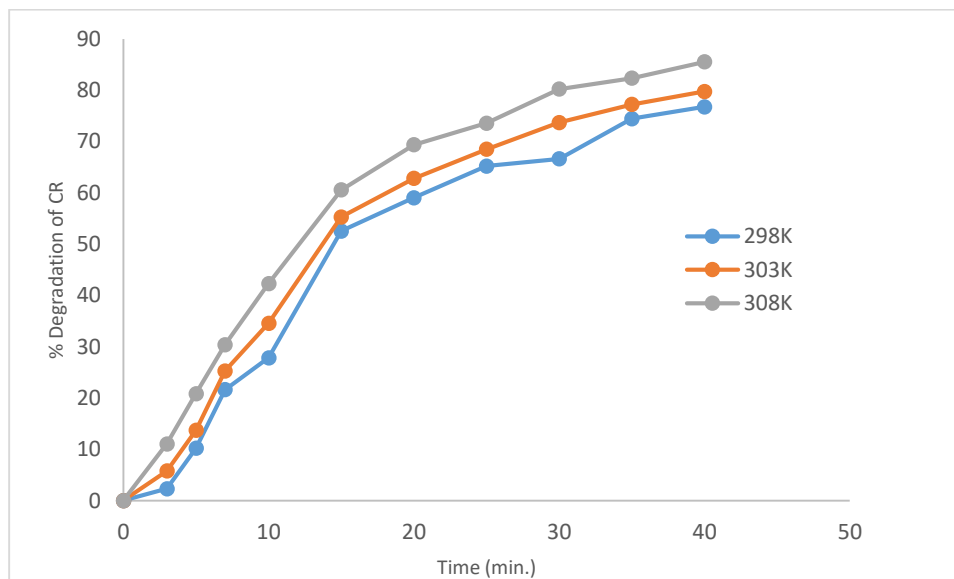


Figure 6.19 (a): Influence of temperature on % degradation of CR. (Experimental condition: $[CR] = 40\text{ mg L}^{-1}$, $[BaBiO_3] = 0.75\text{gL}^{-1}$, $\text{pH}=5.0$).

The photodegradation kinetics at different temperature is illustrated in **Figure 6.20(a)**, which depicts the dark adsorption-desorption equilibrium and the additional decrease in CR concentration caused by visible light irradiation.

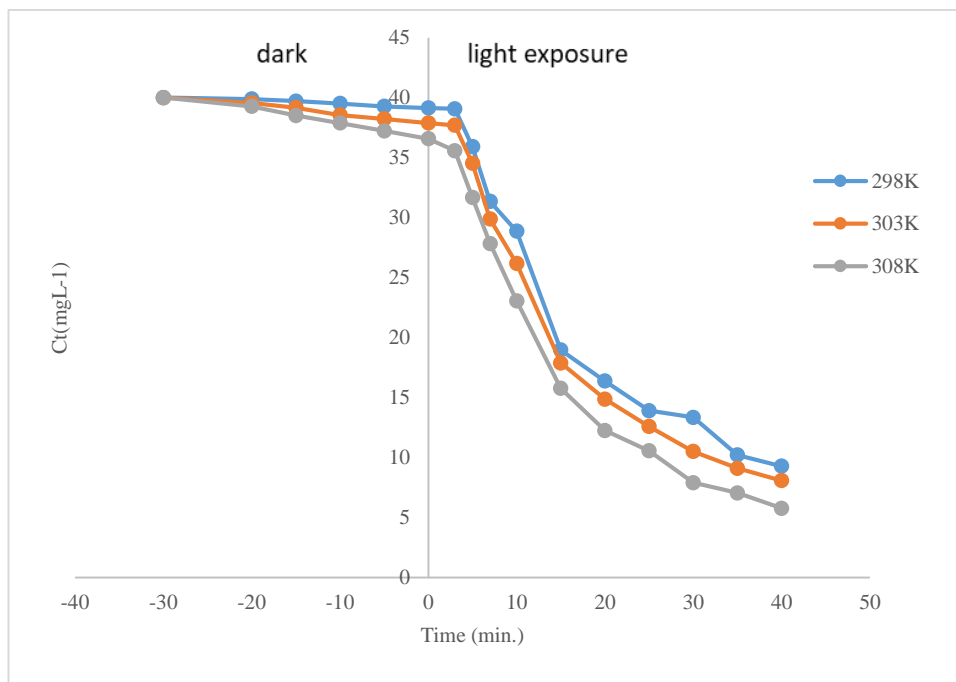


Figure 6.20(a): Effects of Temperature on the residual dye fractions. (Experimental conditions: $[CR] = 40 \text{ mgL}^{-1}$; $[BaBiO_3] = 0.75 \text{ gL}^{-1}$; $pH = 5.0$).

The photodegradation of CR dye at different temperature was fitted to Langmuir Hinshelwood model by plotting $\ln C_t/C_0$ versus time, which has been shown in **Figure 6.21(a)**.

The pseudo-first-order rate constants, $K_{app} \text{ (min}^{-1}\text{)}$, are calculated from the slopes obtained by the curves plotted between $\ln C_t/C_0$ and irradiation time at different temperatures {**Figure 6.21(a)**} and are presented in **Table 6.13(a)**.

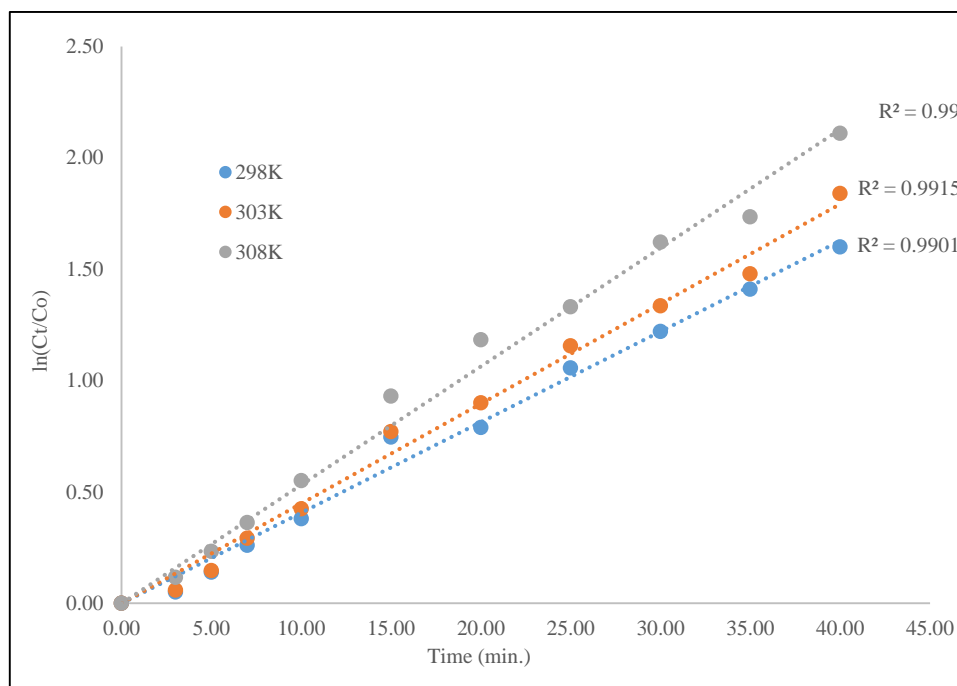


Figure 6.21 (a): Linear variation of $\ln C_t/C_o$ versus time for photocatalytic degradation of CR dye at different temperature. (Experimental condition: $[CR] = 40 \text{ mg L}^{-1}$, $[BaBiO_3] = 0.75 \text{ g L}^{-1}$, $pH = 5.0$).

Table 6.13 (a): Pseudo-first order apparent constant values for the different temperatures.

(Experimental condition: $[CR] = 40 \text{ mg L}^{-1}$; $[BaBiO_3] = 0.75 \text{ g L}^{-1}$; $pH = 5.0$).

S. No.	Temperature (K)	Rate Constant $K_{app} (\text{Min}^{-1})$	R^2
1	298	0.040	0.990
2	303	0.044	0.990
3	308	0.053	0.991

Figure 6.22(a) shows the plot of $\ln K_{app}$ versus Temperature, gives a linear relationship whose slope gives the apparent activation energy which equals to $20.41 \text{ kJ mol}^{-1}$. This apparent energy represents the total activation energy of both adsorption and photocatalytic degradation of dye. [89].

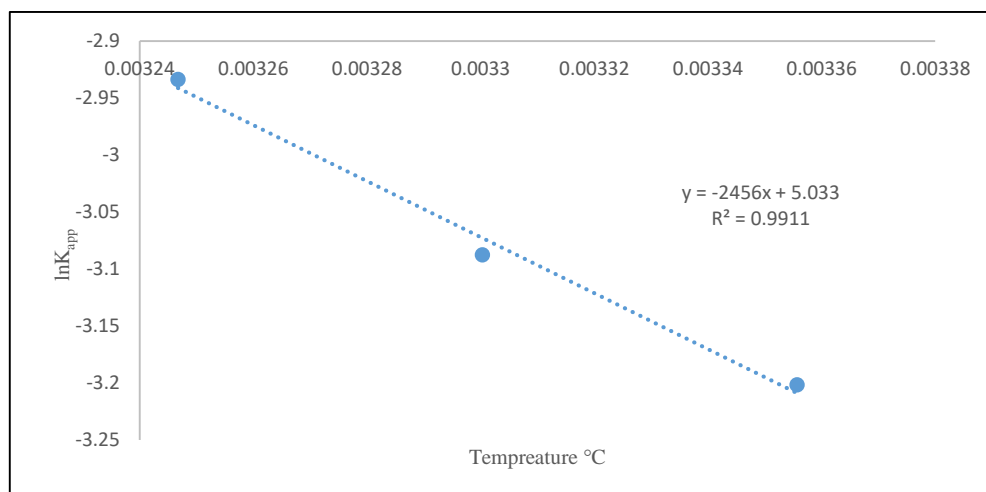


Figure 6.22 (a): Plot of $\ln K_{app}$ versus inverse of temperature (Experimental condition: $[CR] = 40 \text{ mg L}^{-1}$; $[BaBiO_3] = 0.75 \text{ g L}^{-1}$; $pH = 5.0$).

(b) Results with $Ba_{0.6}K_{0.4}BiO_3$

The influence of solution temperature on the % photodegradation of CR dye as a function of time is depicted in **Table 6.12(b)** and the corresponding graphs is shown in **Figure 6.19(b)**. The figure indicates that the rate of the photocatalytic degradation is temperature dependent and is favoured with the increase of solution temperature

Table 6.12(b): Influence of temperature on degradation of CR

(Experimental conditions: $[CR] = 40 \text{ mg L}^{-1}$; $[Ba_{0.6}K_{0.4}BiO_3] = 0.75 \text{ g L}^{-1}$; $pH=5.0$).

Temperature	298K	303K	308K
Time (min)	% Degradation	% Degradation	% Degradation
0	0.00	0.00	0.00
3	2.65	6.73	15.91
5	11.85	19.28	24.48
7	16.37	20.95	27.28
10	31.98	35.76	42.21
15	48.26	54.83	64.23
20	60.76	66.35	72.43
25	63.86	69.81	76.86
30	65.30	72.31	81.38
35	76.26	79.97	85.69
40	73.64	80.61	88.68
∞	73.65	80.62	88.69

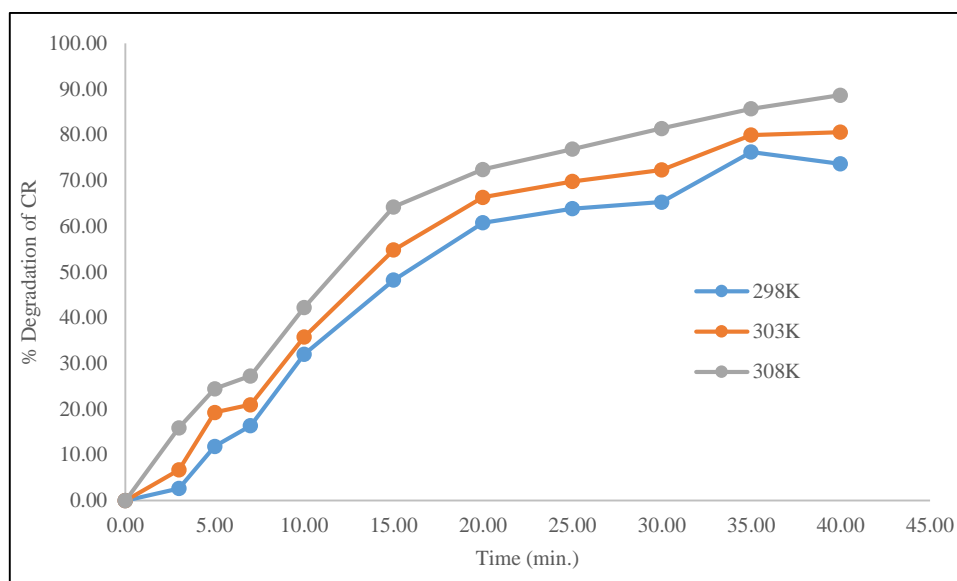


Figure 6.19 (b): Influence of temperature on % degradation of CR. (Experimental condition: $[CR] = 40 \text{ mg L}^{-1}$; $[Ba_{0.6}K_{0.4}BiO_3] = 0.75 \text{ g L}^{-1}$; $pH = 5.0$).

The photodegradation kinetics at different temperature is illustrated in **Figure 6.20 (b)**, which depicts the dark adsorption-desorption equilibrium and the additional decrease in CR concentration caused by visible light irradiation.

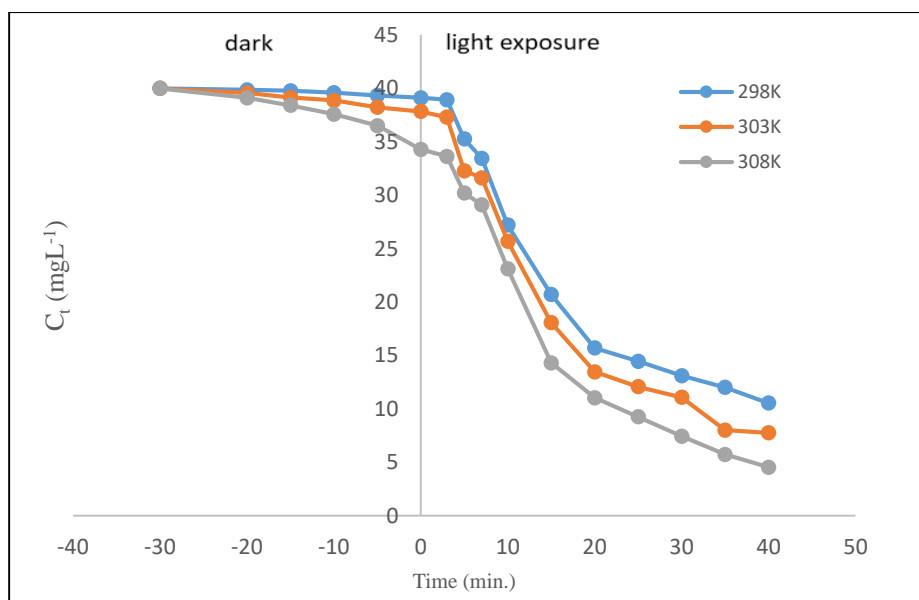


Figure 6.20 (b) Variation of CR dye concentration versus time at different temperature. (Experimental condition: $[CR] = 40 \text{ mg L}^{-1}$; $[Ba_{0.6}K_{0.4}BiO_3] = 0.75 \text{ g L}^{-1}$; $pH = 5.0$).

The photodegradation of CR dye at different temperature was fitted to Langmuir Hinshelwood model by plotting $\ln C_t/C_0$ versus time, which has been shown in **Figure 6.21(b)**.

The pseudo-first-order rate constants, K_{app} (min^{-1}), are calculated from the slopes obtained by the curves plotted between $\ln C_t/C_0$ and irradiation time at different temperatures { **Figure 6.21(b)** } and are presented in **Table 6.13(b)**.

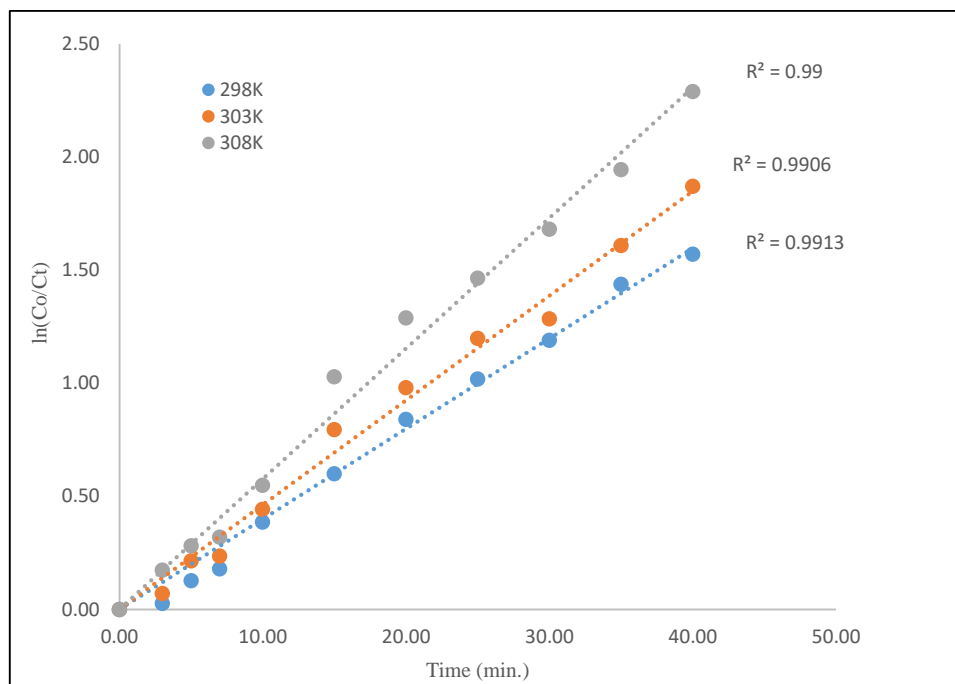


Figure 6.21 (b): Linear variation of $\ln C_t/C_0$ versus time for photocatalytic degradation of CR dye at different temperature. (Experimental condition: $[CR] = 40 \text{ mg L}^{-1}$; $[Ba_{0.6}K_{0.4}BiO_3] = 0.75 \text{ g L}^{-1}$; $pH=5.0$).

Table 6.13 (b): Pseudo-first order apparent constant values for the different temperatures.

(Experimental condition: $[CR] = 40 \text{ mg L}^{-1}$; $[Ba_{0.6}K_{0.4}BiO_3] = 0.75 \text{ g L}^{-1}$; $pH = 5.0$).

S. No.	Temperature (K)	Rate Constant K_{app} (Min^{-1})	R^2
1	298	0.039	0.991
2	303	0.046	0.990
3	308	0.057	0.990

Figure 6.22(b) shows the plot of $\ln K_{app}$ versus Temperature, gives a linear relationship whose slope gives the apparent activation energy equals to 28.31 kJmol^{-1} . This apparent energy represents the total activation energy of both adsorption and photocatalytic degradation of dye [89].

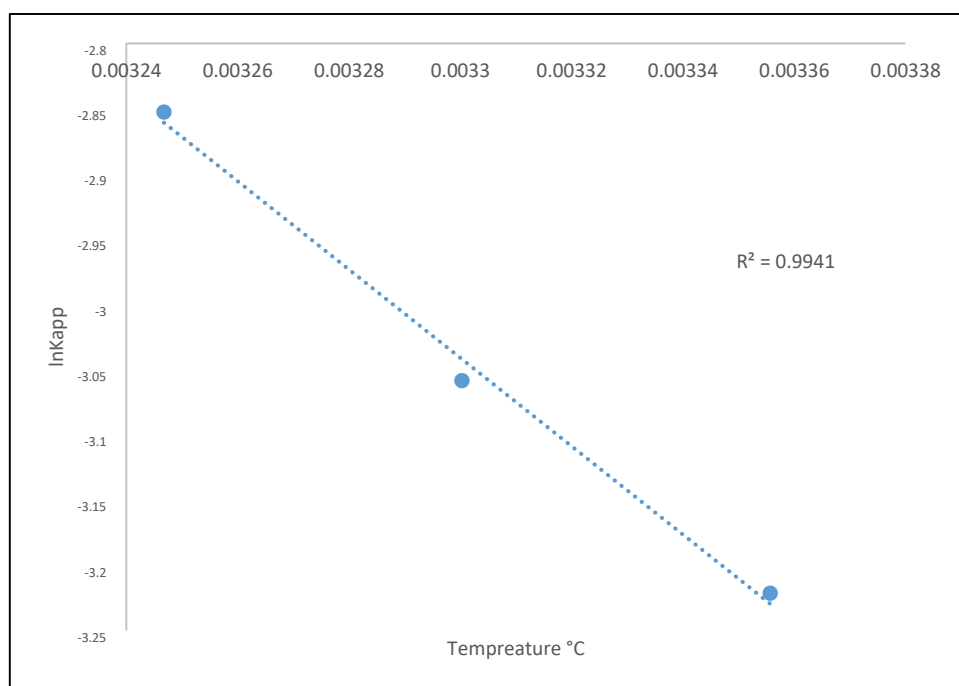


Figure 6.22 (b): Plot of $\ln K_{app}$ versus inverse of temperature. (Experimental condition: $[CR] = 40 \text{ mg L}^{-1}$; $[Ba_{0.6}K_{0.4}BiO_3] = 0.75 \text{ g L}^{-1}$; $pH=5.0$).

6.3.4.5 Regeneration of photocatalysts

Photocatalysis is a clean technology, which normally does not involve any waste disposal problem. The catalyst can be recycled. The economy of the photocatalytic process depends upon how many times a catalyst can be reused without sacrificing its efficiency and the type of regeneration it requires [90].

To evaluate the stability of the as prepared, three recycling experiments are performed. The used catalyst was regenerated by treating it with boiling distilled water till a colourless filtrate was obtained and then by drying in a hot air oven at a temperature of 90° to 100°C . After this, the catalyst was heated in a muffle furnace at about 500°C . As shown in **Figure 6.23**, after being used 3 times for CR dye degradation, the % degradation of dye declined from % to for $BaBiO_3$ and to % for

$\text{Ba}_{0.6}\text{K}_{0.4}\text{BiO}_3$ under the same experimental condition i.e. ($[\text{CR}] = 40\text{mgL}^{-1}$, $[\text{Ba}_{0.6}\text{K}_{0.4}\text{BiO}_3/\text{BaBiO}_3] = 0.75\text{gL}^{-1}$, $\text{pH}=5.0$, $\text{Temp.}=308\text{K}$).

These results indicate that as prepared catalyst is photo-stable during the photocatalytic degradation. The slight decrease in the efficiency of the recycled catalyst may be attributed to the deposition of photo-insensitive hydroxides on the catalyst surface, blocking its active sites [91].

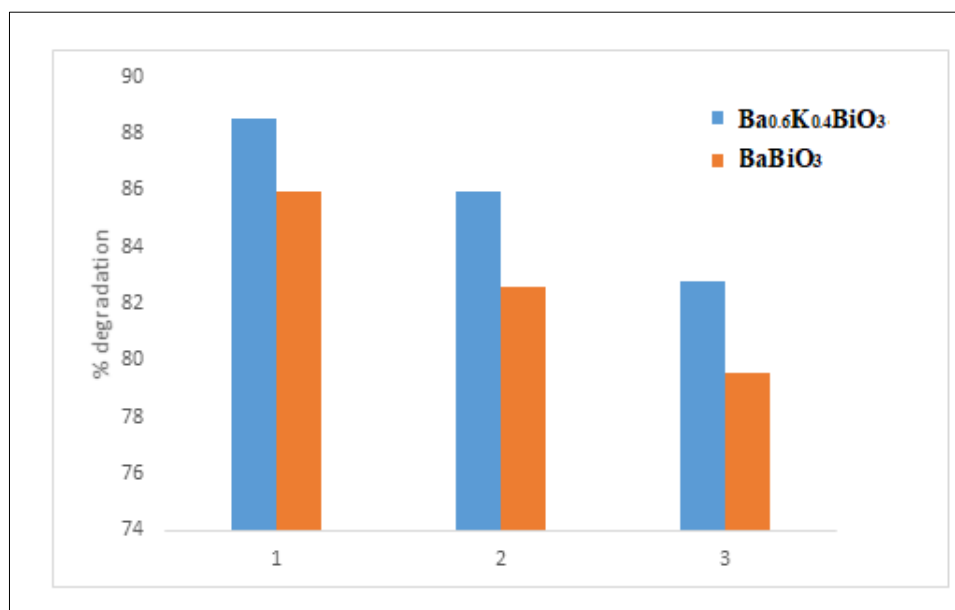


Figure 6.23: Regeneration of photocatalyst. (Experimental condition: $[\text{CR}] = 40\text{mgmL}^{-1}$, $[\text{Ba}_{0.6}\text{K}_{0.4}\text{BiO}_3]/[\text{BaBiO}_3] = 0.75\text{gL}^{-1}$; $\text{pH}=5.0$; $\text{Temp.}=308\text{K}$).

6.4 Comparison of BaBiO_3 and $\text{Ba}_{0.6}\text{K}_{0.4}\text{BiO}_3$ with Degussa p-25 TiO_2

Effectiveness of BaBiO_3 and $\text{Ba}_{0.6}\text{K}_{0.4}\text{BiO}_3$ has been compared with commercially available under above mentioned identical optimum experimental conditions (i.e. $[\text{CR}] = 40\text{mgL}^{-1}$, $[\text{Catalyst}] = 0.75\text{gL}^{-1}$, $\text{pH}=5.0$, $\text{Temp.}=308\text{K}$). As shown in **Figure 6.24**, photocatalytic degradation potential of the as synthesized photocatalysts is found to be much better than the commercially available TiO_2 owing to their much narrower band gap in comparison to the $\sim 3.2\text{eV}$ band gap of TiO_2 [92]. Also, Degussa p-25 adsorbs more CR dye than BaBiO_3 and $\text{Ba}_{0.6}\text{K}_{0.4}\text{BiO}_3$. As the amount of dye absorbed increases, thereby the active sites are

covered with dye ions, thus decreases the formation of $^{\circ}\text{OH}$ ions which further decreases the degradation efficiency.

Thus, it proved the worth of this research work in the direction of tailoring new visible light active photocatalysts.

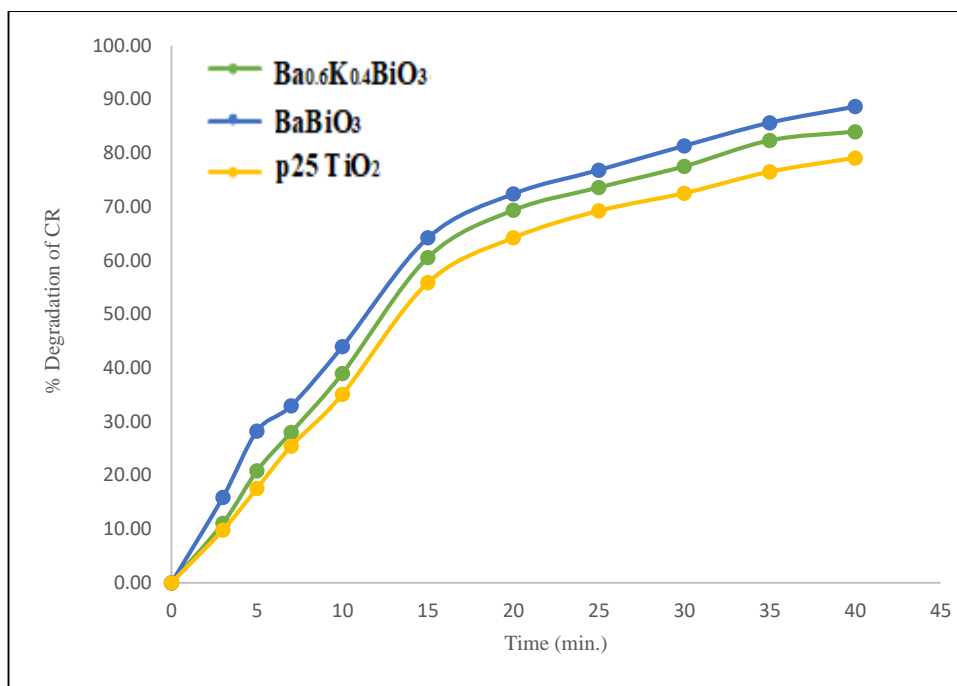


Figure 6.24: Comparison of photocatalytic efficiency of as prepared with p25 TiO₂ under visible light irradiation (Experimental condition: [CR] = 40 mg L⁻¹; [Ba_{0.6}K_{0.4}BiO₃]/ [BaBiO₃]/ [p25 TiO₂] = 0.75 g L⁻¹; pH = 5.0; Temp. = 308 K).

6.5 Visible spectral changes of CR dye

The degradation of CR dye is monitored by UV/vis. Spectrophotometry. Figure 6.25 shows typical UV-vis. Spectrum of CR dye obtained by the degradation of dye in presence of BaBiO₃, Ba_{0.6}K_{0.4}BiO₃ and p25 TiO₂ photocatalysts under visible light irradiation.

In aqueous solution Congo red shows two bands 510 nm ($\pi \rightarrow \pi^*$) and at 338 nm ($n \rightarrow \pi^*$) electron shifting related to azo group [93]. It was observed that the intensity of the band decreased after the experimental run. The reduction in intensity of the band around 502 nm can be attributed to bond cleavage of azo linkage. This decrease is accompanied by the reduction in intensity of band around 338 nm is assigned of the breakage of naphthalene ring [94].

The **Figure 6.25** also indicates that CR dye has been effectively degraded by BaBiO_3 and $\text{Ba}_{0.6}\text{K}_{0.4}\text{BiO}_3$ after 40min. of visible light irradiation. No new absorption bands are appeared in the spectrum, indicating the total mineralization of CR dye. It is clear from the **Figure 6.25** that the maximum degradation efficiency is shown by $\text{Ba}_{0.6}\text{K}_{0.4}\text{BiO}_3$ owing to its lowest band gap value (1.87eV) in comparison to BaBiO_3 (2.07eV) {as discussed in Chapter 3}. P-25TiO_2 has shown least degradation efficiency which is due to its highest band gap among the three catalysts.

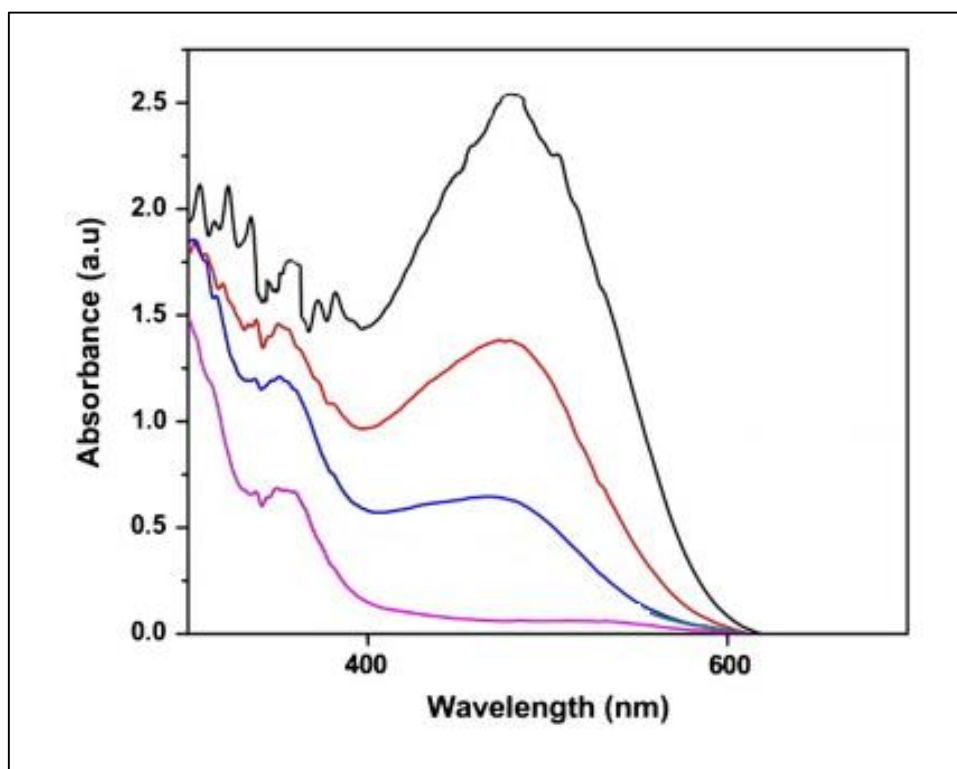


Figure 6.25: UV-vis absorbance spectra of CR solution after photocatalytic degradation over as prepared catalysts. Experimental Conditions: $[\text{CR}] = 40\text{mgL}^{-1}$; $[\text{Ba}_{0.6}\text{K}_{0.4}\text{BiO}_3]/ [\text{BaBiO}_3] / [\text{p25TiO}_2] = 0.75\text{gL}^{-1}$, $\text{pH} = 5.0$, $\text{Temp.} = 308\text{K}$.

6.6 TOC analysis

The complete mineralization of the studied dye is confirmed from the analysis of total organic carbon (TOC) content. The CR dye degradation comprises the oxidative cleavage of azo linkage, benzoic and naphthalene rings. These oxidative reactions result in the creation of primary reaction by-products which are then oxidized and eventually yielding carbon di oxide and water as end products [95]. The TOC concentration is of importance as it is the best parameter to indicate

the final mineralization of the target compound. **Figure 6.26** shows the TOC reduction of CR dye by as prepared BaBiO_3 and $\text{Ba}_{0.6}\text{K}_{0.4}\text{BiO}_3$ at optimum reaction conditions. It can be seen that the % TOC removal values for $\text{Ba}_{0.6}\text{K}_{0.4}\text{BiO}_3$ is higher than BaBiO_3 . As shown in **Figure 6.26**, %TOC removal for photodegradation (following adsorption) in the presence of as prepared photocatalysts is higher than that obtained by the commercially available p25 TiO_2 , thus indicating the greater reactivity of synthesized photocatalysts (BaBiO_3 and $\text{Ba}_{0.6}\text{K}_{0.4}\text{BiO}_3$).

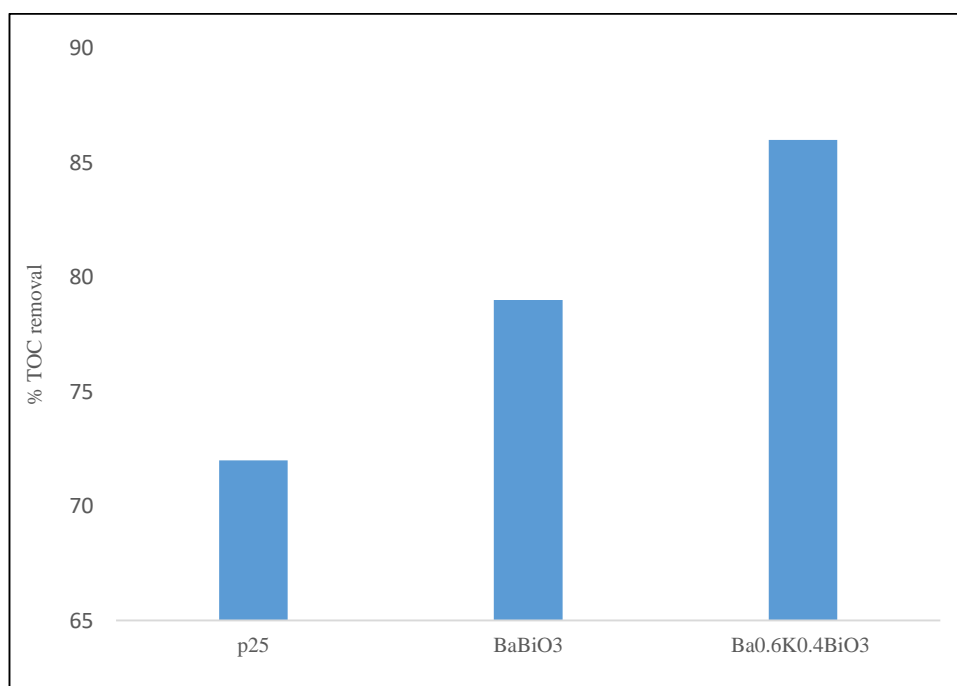
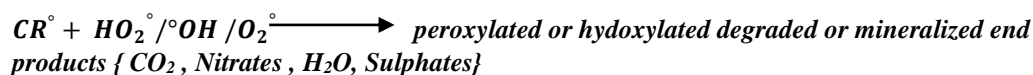


Figure 6.26: TOC removal in CR dye solution obtained by photodegradation by as prepared catalysts. (Experimental Conditions: $[\text{CR}] = 40\text{mgL}^{-1}$; catalyst dose= 0.75gL^{-1} , $\text{pH}=5.0$, Temp. = 308K). (a) for p25 TiO_2 (b) for BaBiO_3 (c) for $\text{Ba}_{0.6}\text{K}_{0.4}\text{BiO}_3$).

6.7 Proposed mechanism of CR dye photodegradation

Organic pollutants like dyestuffs have the ability to absorb visible light. Initially the dye molecules are adsorbed on catalyst surface and get excited through the absorption of light. Thus excited dye (Dye^*) injects an electron to the conduction band of the photocatalyst where it is scavenged by O_2 to form active oxygen radicals. The consequence of electron-ejection into the conduction band results in the charge separation and thus e-hole pairs are generated. Holes are generated in conduction band while e^- are generated in valence band. These electron-hole pair are responsible of generating other reactive species like $^{\circ}\text{OH}$, HO_2 , H_2O_2 and $^{\circ}\text{O}_2^-$.

These active radicals carry out photodegradation or mineralization of organic compounds. Proposed mechanism of CR dye degradation by BaBiO₃ and Ba_{0.6}K_{0.4}BiO₃ under visible light irradiation is as follows:



6.8 Conclusion

In summary, BaBiO₃ and Ba_{0.6}K_{0.4}BiO₃ successfully synthesized by Pechini method resulted in the formation of, mono phase crystalline nano-sized particles which proved their potential in visible light owing to their low band gap (2.07eV and 1.87eV respectively). The feasibility of adsorption and photocatalytic degradation of CR dye using BaBiO₃ and Ba_{0.6}K_{0.4}BiO₃ as in the form of aqueous suspension under visible light irradiation has been investigated. Since, the photocatalytic degradation is directly related to the adsorbed quantities of the pollutant, the adsorption properties of CR on to BaBiO₃ and Ba_{0.6}K_{0.4}BiO₃ are also discussed in terms of Langmuir and Freundlich adsorption isotherms. The photocatalytic degradation was expressed in terms of LH kinetic model, and the subsequent rate constants are also determined. The effect of different operational parameters such as initial dye concentration, catalyst dose, solution pH and temperature on the rate of photo degradation is studied. Moreover, reusability of these catalysts is studied. Furthermore, to estimate the degree of mineralization, measurements of total organic carbon has also been conducted In the present studies, the percentage removal of CR through photocatalytic degradation by BaBiO₃ and Ba_{0.6}K_{0.4}BiO₃ was also compared with the one through TiO₂ (Degussa P-25).

Controlled experiments (photolysis) demonstrated that both visible light and catalyst are needed for the effective destruction of dye. The data obtained from the adsorption experiments are fitted into Langmuir and Freundlich isotherms. They are found to be linear, indicating the formation of mono layer of adsorbate on the outer surface of adsorbent. Langmuir adsorption model is found to be fit for both the catalysts. Thus, obtained results argue that a slow adsorption is noticed on both the catalyst surface, followed by strong photocatalytic degradation.

The study of parameters influencing the degradation process allowed us to find the operating conditions for achieving the highest CR dye degradation rate. The optimization studies revealed the optimum operating conditions: pH value 5.0, catalyst concentration 0.75gL^{-1} , dye concentration 40mgL^{-1} .

The dependence of catalyst concentration on the reaction rate can be explained as $r_0\alpha[\text{BaBiO}_3]^{0.08} [\text{CR}]$ and $r_0\alpha[\text{Ba}_{0.6}\text{K}_{0.4}\text{BiO}_3]^{0.09} [\text{CR}]$ for BaBiO_3 and $\text{Ba}_{0.6}\text{K}_{0.4}\text{BiO}_3$, respectively, when the catalyst concentration is less than 1gL^{-1} .

The Langmuir–Hinshelwood kinetic model showed a good agreement for the initial rates of degradation with the appropriate reaction rate constant (K_r) and the substrate adsorption constant (K_{LH}) values. Here, $K_r = 0.259\text{mgL}^{-1}\text{min}^{-1}$ and $K_{\text{LH}} = 4.09\text{Lmg}^{-1}$ are found for BaBiO_3 while for $\text{Ba}_{0.6}\text{K}_{0.4}\text{BiO}_3$ they are: $K_r = 1.245\text{mgL}^{-1}\text{min}^{-1}$ and $K_{\text{LH}} = 6.45\text{Lmg}^{-1}$. The value of adsorption coefficient (K_{LH}) in kinetic model is found to be different to that found in dark (b) due to the photo-adsorption and very rapid photoreaction of CR dye on the catalyst surface.

The photocatalytic degradation was temperature dependent with apparent activation energy for CR dye of 20.41kJmol^{-1} and 28.13kJmol^{-1} while using BaBiO_3 and $\text{Ba}_{0.6}\text{K}_{0.4}\text{BiO}_3$ as photocatalyst, respectively.

Good reusability of our photocatalyst is obtained after separation from the reaction solution by filtration and washing followed by re-calcination without an obviously reduced photocatalytic activity for at least 3rd run.

Thus, it can be concluded that both BaBiO_3 and $\text{Ba}_{0.6}\text{K}_{0.4}\text{BiO}_3$ are efficient recoverable in CR dye degradation. The complete mineralization of the studied dye is confirmed from the analysis of total organic carbon (TOC) content. On analysing

the UV–vis spectrum of CR dye degradation in the presence of both the catalysts under visible light irradiation leads to prominent decrease in the characteristic band of CR dye at 510nm after 40 minutes. The proposed mechanism indicates the participation of various active species like $^{\circ}\text{OH}$, HO_2 , H_2O_2 and $^{\circ}\text{O}_2^-$ in the degradation of CR dye.

Our results prove that the photocatalytic efficiency of $\text{Ba}_{0.6}\text{K}_{0.4}\text{BiO}_3$ is shown to be greater than that of BaBiO_3 in degradation of CR dye. The higher activity of $\text{Ba}_{0.6}\text{K}_{0.4}\text{BiO}_3$ was attributed to its narrower band gap in comparison to the parent compound (BaBiO_3).

The photocatalytic degradation potential of the as synthesized photocatalysts is found to be much better than the commercially available Degussa P-25 TiO_2 owing to their much narrower band gap in comparison to the wider band gap ($\sim 3.2\text{eV}$) of the later.

Therefore, exploring higher catalytic activity of such perovskite structures may pave the way for designing useful photocatalytic material.

Reference

- [1] R.H. Bustamante, G.M. Branch, S. Eekhout, B. Robertson, P. Zoutendyk, M. Schleyer, A. Dye, N. Hanekom, D. Keats, M. Jurd, C. Mcquaid, *Oecologia* 102, (1995), 189.
- [2] J. D. Parker, J.E. Duffy, R.J Orth, *Mar. Ecol.* 224, (2001), 55.
- [3] H.M. Pinheiro, E. Touraud, O. Thomas, *Dyes Pigm.* 61, (2004), 121.
- [4] T. Robinson, G. McMullan, R. Marchant, P. Nigam, *Bioresour. Technol.* 77, (2001), 247.
- [5] T. Robinson, B. Chandran, P. Nigam, *Water Res.* 36, (2002), 2824.
- [6] A. Gottlieb, C. Shaw, A. Smith, A. Wheatley, S. Forsythe, *J. Biotechnol.* 101, (2003), 49.
- [7] C.-C. Hsueh, B.-Y. Chen, C.-Y. Yen, *J. Hazard. Mater.* 167, (2009), 995.
- [8] L.V.G. Gutiérrez, G.G. Alatorre, E.M.E. Silva, *World J. Microbiol. Biotechnol.* 25, (2009), 415.
- [9] A. Pandey, P. Singh, L. Iyengar, *Int. Biodeterior. Biodegrad.* 59, (2007), 73.
- [10] Böttiger P. Deutsches Reichs, *German Imperial Patent* No. 28753. August 20, 1884.
- [11] H. Patel, R.T. Vashi, *J. Saudi Chem. Soc.* 16, (2012), 131.
- [12] W.C. Wanyonyi, J.M. Onyari, P.M. Shiundu, *Energy Procedia* 50, (2014), 862.
- [13] S. L. Mera, J. D. Davies, *J. Histochem.* 16, (1984), 195.
- [14] T. R. D. Costa, C. F. Rodrigues, A. Meir, M. S. Prevast, A. Redzej, M. Trokter, G. Waksman, *Nature Rev. Microbiol.* 13, (2015), 343.
- [15] D. Morgan, D. M. Diamond, P. E. Gottschall, K. E. Urgan, C. Dickey, J. Hardy, K. Duff, P. Jantzen, G. D. Carlo, D. Wilcock, K. Connor, J. Hatcher, C. Hope, M. Gordon, G. W. Arendash, *Nature* 408, (2000), 982.

-
- [16] M.H. Zamora, F.M. Jerónimo, E.C. Urbina, R.O.C. Villanueva, *Ecotoxicol.* 25, (2016), 1832
- [17] S. S. Babu, C. Mohandass, A. S. Vijayaraj, M. A. Dhale, *Ecotoxicol. Environ. Saf.* 114, (2015), 52.
- [18] H. Rudyk, S. Vasiljevic, R.M. Hennion, C.R. Birkett, J. Hope, I.H. Gilbert, *J. Gen. Virol.* 81, (2000), 1155.
- [19] D. M. Wilcock, M. N. Gordon, D. Morgan, *Nat. Protoc.* 1, (2006), 1591.
- [20] A. Maiti, M.K. Purkait, D. Gupta, *J. Hazard. Mater.* 145, (2007), 287.
- [21] E. Forgacs, T. Cserhádi, G. Oros, *Environ. Int.* 30, (2004), 953.
- [22] R.L. Singh, P.K. Singh, R.P. Singh, *Int. Biodeterior. Biodegrad.* 104, (2015), 21.
- [23] G. Crini, *Bioresor. Technol.* 97, (2006), 1061.
- [24] L. Bilińska, M. Gmurek, S. Ledakowicz, *Chem. Eng. J.* 306, (2016), 550.
- [25] A. R. Ribeiro, O. C. Nunes, M. F. R. Pereira, A. M. T. Silva, *Environ. Int.* 75, (2015), 33.
- [26] M. Cheng, G. Zeng, D. Huang, C. Lai, P. Xu, C. Zhang, Y. Liu, *Chem. Eng. J.* 284, (2016), 582.
- [27] G. Ruppert, R. Bauer, G. Heisler, *Chemosphere* 28, (1994), 1447.
- [28] A. Ajmal, I. Majeed, R.N. Malik, H. Idriss, M.A. Nadeem, *RSC. Adv.* 4, (2014), 37003
- [29] R.K. Wahi, W.W. Yu, Y. Liu, M.L. Mejia, J.S. Falkner, W. Nolte, V.L. Covlin, *J. Mol. Catal. A: Chem.* 242, (2005), 48.
- [30] H. Dong, G. Zeng, L. Tang, C. Fan, C. Zhang, X. He, Y. He, *Water Res.* 79, (2015), 128.
- [31] S. – Y. Lee, S. – J. Park, *J. Ind. Eng. Chem.* 19, (2013), 1761.

-
- [32] V. Etacheri, C. D. Valentin, J. Schneider, D. Bahnemann, S. C. Pillai, **J. Photochem. Photobiol. C: Photochem. Rev.** 25, (2015), 1.
- [33] K. Nakata, T. Ochiai, T. Murakami, A. Fujishima, **Electrochimia Acta.** 84, (2012), 103.
- [34] K. I. Kobayashi, T. Kimura, H. Sawada, K. Terakura, Y. Tokura, **Nature** 395, (1998), 677.
- [35] Y. Moritomo, A. Asamitsu, H. Kuwahara, Y. Tokura, **Nature** 380, (1996), 141
- [36] W. – J. Yin, T. Shi, Y. Yan, **Adv. Mater.** 26, (2014), 4653.
- [37] J. - S. Zhou, J. B. Goodenough, **Phys. Rev. B.** 77, (2008), 132104.
- [38] P. Kanhere, Z. Chen, **Molecules** 19, (2014), 19995.
- [39] J. Shi, L. Guo, **Prog. Natural Sci. Mater. Int.** 22, (2012), 592.
- [40] H. Kato, H. Kobayashi, A. Kudo, **J. Phys. Chem. B.** 106, (2002), 12441.
- [41] R. Asahi, T. Morikawa, T. Ohwaki, K. Aoki, Y. Taga, **Science**, 293, (2001), 269.
- [42] D. Wang, T. Kako, J. Ye, **J. Am. Chem. Soc.** 130, (2008), 2724.
- [43] M. Amir, Z. H. Shah, M. Sher, A. Iqbal, N. Revaprasadu, M. A. Malik, J. Akhtar, **Mater. Sci. Semiconduct. Process.** 63, (2017), 6.
- [44] S. M. H. Qaid, M. S. A. Sobaie, M. A. M. Khan, I. M. Bedja, F. H. Alharbi, M. K. Nazeemuddin, A. S. Aldwayyan, **Mater. Lett.** 164, (2016), 498.
- [45] H. G. Kim, D. W. Hwang, J. S. Lee, **J. Am. Chem. Soc.** 126, (2004), 8912.
- [46] H. Zangeneh, A. A. L. Zinatizadeh, M. Habibi, M. Akia, M. H. Isa, **J. Ind. Eng. Chem.** 26, (2015), 1.
- [47] D. H. Mohsin, A. M. Juda, M. S. Mashkour, **Int. J. Eng. Technol.** 13, (2013), 34.
- [48] S. Balaz, S.H. Porter, P.M. Woodward, L.J. Brillson, **Chem. Mater.** 25, (2013), 3337.

-
- [49] G. Zhang, G. Liu, L. Wang, J.T.S Irvine, *Chem. Soc. Rev.* 45, (2016), 5951.
- [50] D. Kamel, A. Sihem, C. Halima, S. Tahar, *Desalination* 247, (2009), 412.
- [51] N. Soltani, E. Saion, M.Z. Hussein, M. Erfani, A. Abedini, G. Bahmanrokh, M. Navasery, P. Vaziri, *Int. J. Mol. Sci.* 13, (2012), 12242.
- [52] W. Feng, D. Nansheng, Z. Yuegang, *Chemosphere* 39, (1999), 2079.
- [53] Elaziouti, N. Laouedj, B. Ahmed, *J. Chem. Eng. Process Technol.* 2, (2011), 1.
- [54] M.T. Yagub, T.K. Sen, S. Afroze, H.M. Ang, *Adv. Coll. Interface Sci.* 209, (2014), 172.
- [55] V.K. Gupta, Suhas *J. Environ. Manag.* 90, (2009), 2313.
- [56] S. Jain, R. Yamgar, R.V. Jayaram, *Chem. Eng. J.* 148, (2009), 342.
- [57] K.A. Adegoke, O.S. Bello, *Water Resor. Indus.* 12, (2015), 8.
- [58] S. Dawood, T.K. Sen, *Water Res.* 46, (2012), 1933.
- [59] C. Namasivayam, N. Muniasamy, K. Gayari, M. Rani, K. Ranganatan, *Bioresour. Technol.* 57, (1996), 37.
- [60] C. Namasivayam, D.J.S.E. Arasi, *Chemosphere* 34, (1997), 401.
- [61] K.V. Kumar, K. Porkodi, *Appl. Catal. B: Environ.* 79, (2008), 108.
- [62] I.K. Konstantinou, T.A. Albanis, *Appl. Catal. B: Environ.* 49, (2004), 1.
- [63] G. Silvalingam, K. Nagaveni, M.S. Hegde, G. Madras, *Appl. Catal. B: Environ.* 45, (2003), 23.
- [64] U.G. Akpan, B.H. Hameed, *J. Hazard. Mater.* 170, (2009), 520.
- [65] M.A. Rauf, M.A. Meetani, S. Hisaindee, *Desalination* 276, (2011), 13.
- [66] L. Karimi, S. Zohoori, M.E. Yazdanshenas, *J. Saudi Chem. Soc.* 18, (2014), 581.
- [67] H.S. Wahab, H.M. Haidi, *Int. J. Environ. Sci. Technol.* 14, (2017), 2135.

-
- [68] K. Tanaka, K. Padermpole, T. Hianaga, *Water Res.* 34, (2000), 327.
- [69] V.A. Sakkas, M.A. Islam, C. Stalikas, T.A. Albanis, *J. Hazard. Mater.* 175, (2010), 33.
- [70] H-X. Guo, K-L. Lin. Z-S. Zheng, F-B. Xiao, S-Xli, *Dyes Pigm.* 92, (2012), 1278.
- [71] S. Erdemoğlu, S.K. Aksu, F. Sayilkan, B. İzgi, M. Asiltürk, H. Sailkan, F. Frimmel, Ş. Güçer, *J. Hazard. Mater.* 155, (2008), 469.
- [72] C. Galindo, P. Jacqueus, A. Kalt, *Chemosphere* 45, (2001), 997.
- [73] A. Akyol, M. Bayramoğlu, *J. Hazad. Maer.* 124, (2005), 241.
- [74] V.K. Gupta, R. Jain, A. Mittal, M. Matur, *J. Colloid Interface Sci.* 309, (2007), 464.
- [75] L.B. Reutergådh, M. Iangphasuk, *Chemosphere* 35, (1997), 585.
- [76] N. Sobana, M. swaminathan, *Sep. Purif. Technol.* 56, (2007), 101.
- [77] H. Lachheb, E. Puzenat, A. Houas, M. Ksibi, E. Elaloui, C. Guillard, J.M. Herrmann, *Appl. Catal. B: Environ.* 39, (2002), 75.
- [78] N.J. Bejarno-Perez, M.F. Suarez-Herrera, *Ultrason. Sonochem.* 14, (2007), 589.
- [79] D. Bhatnagar, R.Chatterjee, *Adv. Mater. Lett.* 7, (2016), 604.
- [80] B. A. Baumert, *J. Supercond.* 8, (1995), 175.
- [81] C. Guillard, H. Lachheb, A. Houas, M. Ksibi, E. Elaloni, J.M. Herrmann, *J. Photochem. Photobiol. A: Chem.* 158, (2003), 27.
- [82] M. Movahedi, A.R. Mahjoub, S.J. Darzi, *J. Iran. Chem. Soc.* 6, (2009), 570.
- [83] M. Bagheria, A.R. Mahjoub, A.A. Khodadadi, Y. Mortazavi, *RSC Adv.* 4, (2014), 33262.
- [84] R. Jain, S. Sikarwar, *Int. J. Environ. Pollut.* 27, (2006), 158.

-
- [85] M.R. Sohrabi, M. Ghavami, *J. Hazard. Mater.* 153, (2008), 1235.
- [86]
- [87] Y. Ye, Y. Feng, H. Bruning, D. Yntema, H.H.M. Rijnaarts, *Appl. Catal. B: Environ.* 220, (2018), 171.
- [88] N. Daneshvar, M. Rabbani, N. Modirshala, M. A. Behnajady, *J. Photochem. Photobiol. A: Chem* 168, (2004), 39.
- [89] N.Verma, S. Bhatia, R.K. Bedi, *Int. J. Pure Appl. Phys.* 13, (2017), 118.
- [90] T. Ohhno, L. Bai, T. Hisatomi, K. Maeda, K. Domen, *J. Am. Chem. Soc.* 134, (2012), 8254.
- [91] L. Cao, Z. Gao, S.L. Suib, T.N. Obee, S.O. Hay, J.D.. Freihaut, *J. Catal.* 196, (2002), 253.
- [92] K. Nagaveni, M.S. Hegde, N. Ravishankar, G.N. Subbabnna, G. Madras, *Langmuir* 20, (2004), 2900.
- [93] R.E. Sladewski, A.M. Shafer, *Spectrochim Acta A Mol. Biol. Spectrosc.* 65, (2006), 985.
- [94] T. Lindaa, S. Muthupoongodib, X. S. Shajan, S. Balakumar, *Mater Today Proc.* 3, (2016), 2035.
- [95] S. Mozia, M. Tomaszewska, A.W. Morawski, *Appl. Catal. B: Environ.* 59, (2005), 131.

Chapter 7

Conclusion and Future Work

7.1 Outcome of the Present Research Work

Dyes cover an important part of waste water effluents, as they are discharged in abundance by many manufacturing industries. The environmental and health concern of these potentially carcinogenic pollutants in the water has drawn the attention. Due to the stability of modern dyes various biological and physical methods are ineffective for their degradation. In this regard in recent years advanced oxidation process based on the generation of very reactive radical species which are capable of mineralizing organic pollutant into harmless inorganic substances under moderate condition are studied widely. Despite the significant progress that has been made, even today the development of photocatalyst for the photocatalytic degradation of the contaminated water; which are economical, eco-friendly, and sustainable for long time, is very much desired. Hence, in the present study, the preparation of perovskite materials along with their photocatalytic activity for dye degradation is explored.

In summary, pure and doped barium bismuthate nanoparticles (i.e. BaBiO_3 and $\text{Ba}_{0.6}\text{K}_{0.4}\text{BiO}_3$ respectively) were successfully synthesized at comparatively low temperature (800°C and 720°C , respectively) by Pechini method using ethylene glycol, citric acid and metal nitrates as raw materials. The structural, morphological and optical characteristics of the synthesized nanoparticles were studied by Thermo Gravimetric Analysis (TGA), powder X-ray diffraction, Fourier Transform Infra-Red spectroscopy, UV-Vis Diffuse Reflectance Spectroscopy (UV DRS) and Scanning Electron microscopy (SEM).

The XRD patterns suggest that BaBiO_3 crystallizes in the distorted monoclinic structure while $\text{Ba}_{0.6}\text{K}_{0.4}\text{BiO}_3$ crystallizes in the cubic structure. The distortion in the monoclinic structure of BaBiO_3 is attributed to the coexistence of two different types of Bi-O bond. Further, by the incorporation of K, the resulting material gets transformed to perfect cubic structure with more intense peaks. The strong and sharp peaks in the diffractograms indicate the crystalline nature and phase purity of the prepared samples. The phase evolution of both the catalysts

with increasing temperature was done by DT-TGA. The TGA curves show that above final calcination temperatures (800°C for BaBiO_3 and 720°C for $\text{Ba}_{0.6}\text{K}_{0.4}\text{BiO}_3$), no weight loss is observed, hence it is concluded above this temperature, the perovskite are stable. FTIR spectrum shows the presence of the bands around 465cm^{-1} in both the catalysts confirming the metal-oxygen bond formation, which is the characteristic property of perovskite materials. The SEM studies show that both the samples are homogeneous uniform nanoparticles, having 520nm size for BaBiO_3 and $45\text{-}101\text{nm}$ for $\text{Ba}_{0.6}\text{K}_{0.4}\text{BiO}_3$. SEM images reveal the nano rod type structure for BaBiO_3 and plate like layered structure for $\text{Ba}_{0.6}\text{K}_{0.4}\text{BiO}_3$. The diffuse reflectance spectroscopy showed that the catalysts have a broad absorbance in visible region of light. The onset optical absorption edge was around 600 and 660 nm for barium bismuthate and K doped barium bismuthate respectively. The band gap calculation was done by Tauc plots through the converted KM functions. The band gap of BaBiO_3 and $\text{Ba}_{0.6}\text{K}_{0.4}\text{BiO}_3$ was found to be 2.07eV and 1.87eV , respectively. Owing to the low band gap, the catalysts were supposed to be promising in displaying their activity in photocatalysis under visible light irradiation. Incorporation of K ion partially at Ba site (in BaBiO_3) creates a new level between highest occupied molecular orbitals (HOMO) and lowest unoccupied molecular orbitals LUMO of the parent BaBiO_3 which further decreases the band gap of $\text{Ba}_{0.6}\text{K}_{0.4}\text{BiO}_3$.

The photocatalytic activity of as-synthesized BaBiO_3 and $\text{Ba}_{0.6}\text{K}_{0.4}\text{BiO}_3$ nanoparticles was demonstrated over degradation of dyes viz. Crystal violet, Malachite green and Congo red under visible light irradiation. The adsorption trends of studied dyes at various initial concentrations followed the Langmuir and Freundlich adsorption isotherm trends. Since the R^2 values are fairly close to 1, both the models describe the system well but Langmuir isotherm model is considered to be best fit owing to its higher R^2 value. Controlled experiments (photolysis) demonstrated that both visible light and catalyst were needed for the effective destruction of dye.

The dependence of the photodegradation rate on various parameters such as initial dye concentration, catalyst dose, pH and temperature is also studied. The

study of parameters influencing the degradation process allowed us to find the operating conditions for achieving the highest dye degradation rate for each dye. The degradation studies of all three dyes reveal that for all the dyes, the experimental conditions are nearly same except solution pH, which is 5.5 for CR while 6.0 for both CV and MG dye. The other optimum operating conditions are catalyst concentration 0.75gL^{-1} , dye concentration 40mgL^{-1} and 308K temperature.

In order to assess the rate of photocatalytic degradation of dyes over BaBiO_3 and $\text{Ba}_{0.6}\text{K}_{0.4}\text{BiO}_3$, the observed dye degradation results are kinetically analyzed by Langmuir-Hinshelwood kinetic equation, within the experimental range. This pseudo-first-order kinetic model is used to fit all data sets (dye concentration, photocatalyst dose, initial pH solution, and temperature). The Langmuir-Hinshelwood kinetic model showed a good agreement for the initial rates of degradation for all the three studied dyes with the appropriate reaction rate constant (K_r) and the substrate adsorption constant values (K_{LH}).

Further It was observed that the photocatalytic degradation efficiency of both the catalysts for the studied dyes is in the order: $\text{CV} > \text{MG} > \text{CR}$. It is to be noted here that all the three studied three dyes differ in their molecular structure and functional group as well as in the extent of ionization in aqueous solution. Malachite green and Crystal violet are cationic dyes (basic dyes) while Congo red is an anionic (acidic dye), they are expected to behave differently in the photocatalytic processes as observed from our results.

During photodegradation studies, the behavior of MG dye is found to be similar as that of CV dye, due to their almost similar chemical structure. The initial colour removal rate of Malachite green was found lesser than CV dye, because, MG has only two out of three phenyl rings substituted with dimethyl amino groups, allowing the generation of less radicals which further decreases the efficiency of photo degradation. The overall degradation of CV is higher than MG, this is due to the presence of three dimethyl amino group in CV, which results in the generation of more methyl radicals which further oxidize the adsorbed water molecule and thus create the more OH^\bullet radicals which is the principle oxidizing agent in

photodegradation reaction in comparison to two dimethyl amino group present in MG dye.

It was noticed that CR dye is least susceptible towards photodegradation among the three studied dyes which may be due to more complex structure of the dye, which include biphenyl, sulfoxide, naphthol and azoic groups. Besides that, the solvation energy is higher for acidic dyes. As we know that every group which tends to decrease the solubility of molecule in water will decrease the photodegradation process, hence, lower degradation rate was observed for CR dye.

The photodegradation results of all the studied dyes showed a similar trend of photocatalytic activity with both the catalysts. Each dye degradation follows a first order mechanism w.r.t initial concentration.

For Crystal violet, a basic dye, extent of degradation was 95.90% with BaBiO_3 and 99.90% with $\text{Ba}_{0.6}\text{K}_{0.4}\text{BiO}_3$, used as photocatalysts, within 40 minutes of visible light irradiation. 95.29% and 98.75% degradation was achieved for Malachite green, again a basic dye under similar duration of visible light exposure with BaBiO_3 and $\text{Ba}_{0.6}\text{K}_{0.4}\text{BiO}_3$ respectively. As far as Congo red, an acidic dye, is concerned comparatively lowered degradation was observed i.e. 85.56% and 88.69% after 40 minutes of visible light irradiation while using above mentioned photocatalysts BaBiO_3 and $\text{Ba}_{0.6}\text{K}_{0.4}\text{BiO}_3$ respectively.

Hence, it is concluded that $\text{Ba}_{0.6}\text{K}_{0.4}\text{BiO}_3$ photocatalysts has shown its higher degradation potential in comparison to the parent compound i.e. BaBiO_3 . The higher activity of $\text{Ba}_{0.6}\text{K}_{0.4}\text{BiO}_3$ was attributed to narrower band gap in comparison to the BaBiO_3 catalyst.

Thus, heterogeneous photocatalysis, the subject of present research work, is a low-cost, feasible, environmentally benign treatment technology for photodegradation of organic pollutants. The photo activity of regenerated catalysts shows that after being used 3 times for dye degradation, the % degradation of all the three studied dyes declined slightly for both the prepared photocatalysts. It

shows that as prepared photocatalysts are quite photo-stable and recoverable during the photocatalytic degradation of acidic and basic dyes. The complete mineralization of the studied dye is confirmed from the analysis of total organic carbon (TOC) content. The total mineralization of the pollutant dyes is further confirmed by the almost disappearance of the characteristic peak at the end of the experimental run in UV-vis spectrum of all the studied dyes.

In addition, a comparison study was conducted using BaBiO₃, Ba_{0.6}K_{0.4}BiO₃ and commercially available p-25 TiO₂ photocatalysts. It was found that the as-synthesized nanoparticles exhibited superior photocatalytic activity compared to commercially available p-25 TiO₂ due to their lower band gap in comparison to the 3.2 eV for TiO₂ photocatalyst which is further confirmed by their higher % TOC removal in comparison to p25 TiO₂ photocatalyst.

Thus, heterogeneous photocatalysis, the subject of present research work, is a low-cost, feasible, environmentally benign treatment technology for photodegradation of organic pollutants and has proved its efficiency in handling the hazardous toxic organic pollutants into harmless end products at ambient temperature. The results evolved out of the research may encourage the application of this technique in treating other toxic industrial effluents also. Further, this research has contributed to developing visible light active photocatalyst to utilize solar energy more efficiently.

7.2 Future Recommendations

Upon completion of the present research work, several fundamental aspects should be paid attention to in future photocatalytic studies.

- We plan to further test the synthesized photocatalyst using solar light irradiation as the light source. As solar light is an abundant, free and clean source it would be beneficial for the photocatalysis technology.
- In addition, this research work will be applied using real textile wastewater as mixtures of dyes are present in the wastewater. As waste water may contain various pollutants along with the dyes, therefore, the effect of

various additives like H_2O_2 , persulphate along with the common anion additive which are known to play an important role in accelerating or inhibiting the degradation of organic pollutants due to formation of OH^- , SO_4^{2-} , Cl^- ions and various other active species will also be studied.

- Further the determination of degradation pathway will be systematically studied by chromatographic techniques to identify the intermediates formed during the degradation processes.
- Morphology and particle size of these photocatalysts can be fine-tuned to study multi-morphological features such as thin films, nano stars, nano flowers, nano wires and nano tubes in order to achieve better photocatalytic performance in degradation of organic pollutants.
- Further understanding of the crystal and electronic structural factors behind photocatalytic activity will be helpful for the future development of efficient visible light-driven photocatalyst materials.
- Such efforts would certainly pave the pathway and tailoring photocatalysts and enhancing their photocatalytic activity in environmental remediation.

Annexure I
Summary of Thesis

*Adsorption and Degradation Kinetics of Dyes in Perovskite
Dispersion under Visible Light Irradiation*

Summary of Thesis

For the

Award of Ph.D. Degree



Submitted by

Kavita Sharma

Under the Supervision of

Dr. (Mrs) Ultra Chandrawat

Department of Chemistry,

Government College Kota, Kota

Submitted to

UNIVERSITY OF KOTA, KOTA-2017

Adsorption and Degradation Kinetics of Dyes in Perovskite Dispersion under Visible Light Irradiation

SUMMARY

Heterogeneous photocatalysis as the innovative wastewater technology attracts many attention, because it is able to generate highly reactive transitory species for total degradation of organic compounds, water pathogens and disinfection by-product. Semiconductor as photocatalyst have demonstrated their efficiency in degrading a wide range of organics into readily biodegradable compounds, and eventually mineralized them to innocuous carbon dioxide and water, and hence, unlike several other treatment methods, avoids the secondary pollution challenges [1,2].

Among various photocatalysts that have been investigated, **perovskite** based photocatalysts have attracted much interest because of their high photocatalytic activities [3,4]. Many Bi based compounds have narrow band gaps which exhibit good photocatalytic activity under visible light. This is because of their unique band structure which make them ideal candidates for photodegradation processes [5,6]. Despite the significant progress that has been made, further efforts are still needed to be accomplished on various aspects to further advance the use of bismuth related photocatalyst as efficient visible light photocatalysts.

Therefore, in this study, perovskite photocatalysts BaBiO_3 and $\text{Ba}_{0.6}\text{K}_{0.4}\text{BiO}_3$ were prepared by **Pechini method** [7,8] and investigated to explore the possible application in the removal of dyes from contaminated water. The main objective of this study is to investigate the heterogeneous photocatalytic degradation of organic compounds in the presence of as prepared BaBiO_3 and $\text{Ba}_{0.6}\text{K}_{0.4}\text{BiO}_3$ photocatalysts. The structural and morphological characteristics of the photocatalysts are studied by different characterization techniques.

Objectives of the research work:

Three dyes, namely Crystal violet, Malachite Green and Congo red are selected as model pollutants to be degraded by prepared photocatalysts under visible light. The objectives of this research are:

- 1.** To synthesize BaBiO₃ and Ba_{0.6}K_{0.4}BiO₃ using Pechini method.
- 2.** To characterize the synthesized BaBiO₃ and Ba_{0.6}K_{0.4}BiO₃ photocatalyst using Thermo gravimetric analysis (TGA), X-Ray Diffraction (XRD), Fourier Transform Infra-Red spectroscopy (FTIR), Ultraviolet-Visible Diffuse Reflectance Spectroscopy (UV-Vis DRS) and Field Emission Scanning Electron Microscope (FESEM) analyses.
- 3.** To determine the effect of parameters such as, initial dye concentration, catalyst dose, initial solution pH and temperature on the photocatalytic degradation of dyes under visible light irradiation.
- 4.** To test the reusability of these catalysts, and to compare their photocatalytic activity with commercially available p-25 TiO₂ photocatalyst.
- 5.** To apply Langmuir and Freundlich adsorption isotherms and Langmuir-Hinshelwood kinetic model for adsorption and photo degradation process, respectively.

Structure of thesis:

The present work includes issues related to the synthesis, characterization and application of nanostructured oxide powders in wastewater treatment. From the structural point of view, the thesis consists of seven chapters in the following manner:

Chapter 1: Introduction and Literature Survey

This chapter introduces the background of the thesis work along with the scope and contributions to the related field. This chapter summaries all the relevant aspects of the photocatalysis and different photocatalysts used in the waste water treatment and general introduction to the subject of remediation and chemical

oxidation of water pollutants. It also explains the background information needed to understand the chemistry behind photocatalysis, with perovskite oxides as the subject of interest. The properties of perovskite in terms of their ability to degrade organic pollutants are also discussed. This chapter also summarises different synthesis techniques for perovskite materials, focusing on Pechini synthesis.

Chapter-2: Material and Method

In this chapter, a detailed description of the experimental procedures implemented for the present research work are presented. This chapter provides the experimental-related issues, including the lists of chemicals and apparatus employed during catalyst preparation and characterization as well as reaction studies. Moreover, the theoretical fundamentals and operational dealings of the catalyst characterization instruments are also discussed. Finally, a detailed description of procedure for studying adsorption and photodegradation kinetics is also presented.

Synthesis of photocatalysts:

Barium bismuthate and potassium doped barium bismuthate are prepared from highly pure polymeric precursors using the method proposed by Pechini.

The chemical reaction of the synthesis procedure can be written as follows
Metal nitrates \rightarrow $C_6H_8O_7 \cdot H_2O$ \rightarrow *metal citrate solution* \rightarrow $C_2H_6O_2$ \rightarrow
metal nitrate – CA/EG polyester network \rightarrow $BaBiO_{3.5}/Ba_{0.6}K_{0.4}BiO_{3.5} + xH_2O_g +$
 $xCO_{2g} + xNO_{2g}$

Photodegradation studies of dyes:

The photocatalytic degradation is performed using a cylindrical glass reactor, accommodating a central glass tube in which a 500W Xe arc lamp (intensity=137mWcm⁻²) is placed to irradiate the dye solution. At the bottom of the reactor, a magnetic stirrer is placed for homogenization of reaction solution. Only in experiments dealing with the effect of pH on the dye degradation, initial pH was adjusted with buffer solutions and measured with pH meter. The visible light illumination is started following a dark period (without light illumination) of 30 minutes to attain an adsorption equilibrium between dye and photocatalyst. Blank

experiment (without photocatalyst) is also carried out. The dye samples are collected at regular time interval following centrifugation and filtration and then subsequently analysed for the residual concentration using a UV-vis spectrophotometer at the characteristic wavelength for each individual dye with a calibration curve based on Beer Lambert's law. Finally, the photocatalytic activities are determined using the following relation:

$$\%degradation = \frac{C_0 - C_t}{C_0} \times 100 \quad (1)$$

Where, C_0 = concentration of dye solution after adsorption-desorption equilibrium (mgL^{-1}), C_t = concentration of dye solution after photo irradiation (mg L^{-1}). A series of experiments are carried out to study the effect of the initial dye concentration, amount of photocatalyst, pH and temperature on the photocatalytic degradation of dyes.

In order to assess the rate of photocatalytic degradation of dyes over BaBiO_3 and $\text{Ba}_{0.6}\text{K}_{0.4}\text{BiO}_3$, the observed dye degradation results are kinetically analysed by **Langmuir-Hinshelwood kinetic equation** [9]. Langmuir-Hinshelwood kinetic equation describes the relationship between the initial rate constant and initial concentration of the organic substrate.

$$r_o = -\frac{dC}{dt} = \frac{K_r K_{LH} \cdot C_o}{1 + K_r \cdot C_o} \quad (2)$$

$$r_o = \frac{1}{K_r} + \frac{1}{K_r K_{LH} C_o} \quad (3)$$

Where C_o is the initial concentration of organic substrate (mgL^{-1}), r_o is initial rate ($\text{mgL}^{-1}\text{min}^{-1}$), K_{LH} is the Langmuir-Hinshelwood adsorption equilibrium constant (Lmg^{-1}) and K_r is the rate constant of surface reaction ($\text{mgL}^{-1}\text{min}^{-1}$).

The degradation of organic pollutants over catalysts follows the pseudo-first-order kinetics with respect to the initial concentration of the pollutant.

$$r_o = -\frac{dC}{dt} = K_{app} \quad (4)$$

Following equation was used to determine the initial rate by multiplying the apparent first-order rate constant K_{app} with the initial concentration of dye, C_o

$$\ln\left(\frac{C_t}{C_o}\right) = K_{app} \cdot C_o \quad (5)$$

In which K_{app} is the apparent pseudo-first-order rate constant in min^{-1} . The apparent reaction rate constant K_{app} (min^{-1}) is given by the slope of the graph of $\ln C_t/C_o$ versus time (min).

Chapter-3: Synthesis Methodology and Characterization Techniques

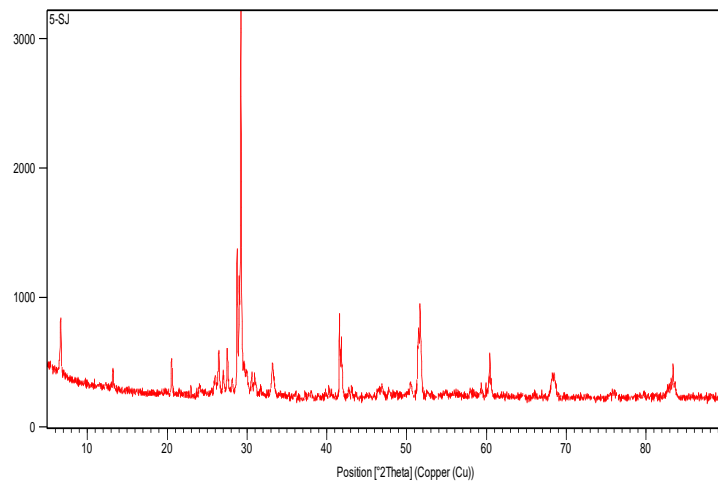
This chapter deals with the synthesis and structural & morphological characterization of prepared compounds. The novel visible light active perovskite materials BaBiO_3 and $\text{Ba}_{0.6}\text{K}_{0.4}\text{BiO}_3$ are synthesized through Pechini method. Furthermore, different photochemical and physical properties of as synthesized compounds are studied in details by means of different characterization techniques.

Here, both the catalysts are prepared under identical conditions except the calcination temperature. Stoichiometric amounts of analytical grade metal nitrates are dissolved in distilled water while bismuth nitrate is dissolved in dil. HNO_3 solution under continuous stirring. Weighed amounts of citric acid, in a 4:1 molar ratio with respect to the total amount of cations, and ethylene glycol in a 3:2 molar ratio with respect to citric acid is added to the above solution under constant strong stirring. Thus obtained solution is transferred to a hot plate where it is heated up to 90°C resulting in the formation of brown resin.

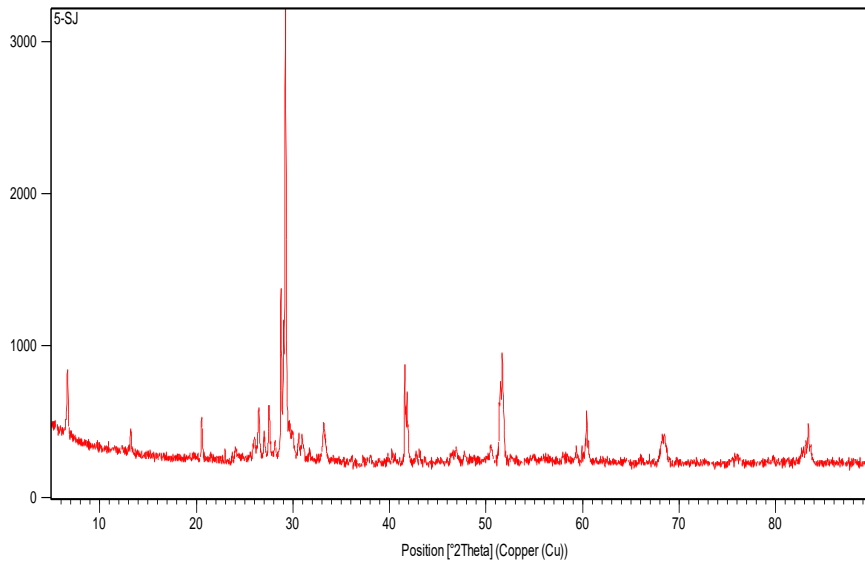
After this, resin is pulverized at 350°C . Thus obtained precursor material is powdered with an agate mortar. Further, to fully evaporate highly combustion species in the mass and to burn down most of the organic constituents, the powder is calcined in a furnace at different temperatures (6 hours at 600°C and 12 hours at 850°C for BaBiO_3 ; 6 hours at 650°C and 12 hours at 720°C for $\text{Ba}_{0.6}\text{K}_{0.4}\text{BiO}_3$). The structural and morphological characteristics of the products were studied by Thermo Gravimetric Analysis (TGA), powder X-ray diffraction, Fourier Transform Infra-Red spectroscopy, UV-Vis Diffuse Reflectance Spectroscopy (UV DRS) and Scanning Electron microscopy (SEM).

The TGA curves show that above final calcination temperatures (800°C for BaBiO_3 and 720°C for $\text{Ba}_{0.6}\text{K}_{0.4}\text{BiO}_3$), no weight loss is observed, hence it is concluded above this temperature, the perovskite are stable. The XRD patterns

suggest that BaBiO_3 crystallizes in the distorted monoclinic structure while $\text{Ba}_{0.6}\text{K}_{0.4}\text{BiO}_3$ crystallizes in the cubic structure {Figure-1(a&b)}. FTIR spectrum shows the presence of the bands around 465cm^{-1} in both the catalysts confirming the metal-oxygen bond formation, which is the characteristic property of perovskite materials {Figure-2(a&b)}. The onset optical absorption edge was around 600 and 660 nm for barium bismuthate and K doped barium bismuthate respectively. The band gap of BaBiO_3 and $\text{Ba}_{0.6}\text{K}_{0.4}\text{BiO}_3$ was found to be 2.07eV and 1.87eV, respectively. Owing to the low band gap, the catalysts were supposed to be promising in displaying their activity in photocatalysis under visible light irradiation. Incorporation of K ion partially at Ba site creates a new level between HOMO and LUMO of the parent BaBiO_3 which further decreases the band gap of $\text{Ba}_{0.6}\text{K}_{0.4}\text{BiO}_3$ {Figure-3(a&b)}. The SEM studies show that both the samples are homogeneous uniform nanoparticles, having 520nm size for BaBiO_3 and 45-101nm for $\text{Ba}_{0.6}\text{K}_{0.4}\text{BiO}_3$. SEM images reveal the nano rod type structure for BaBiO_3 and plate like layered structure of $\text{Ba}_{0.6}\text{K}_{0.4}\text{BiO}_3$ {Figure-4(a&b)}

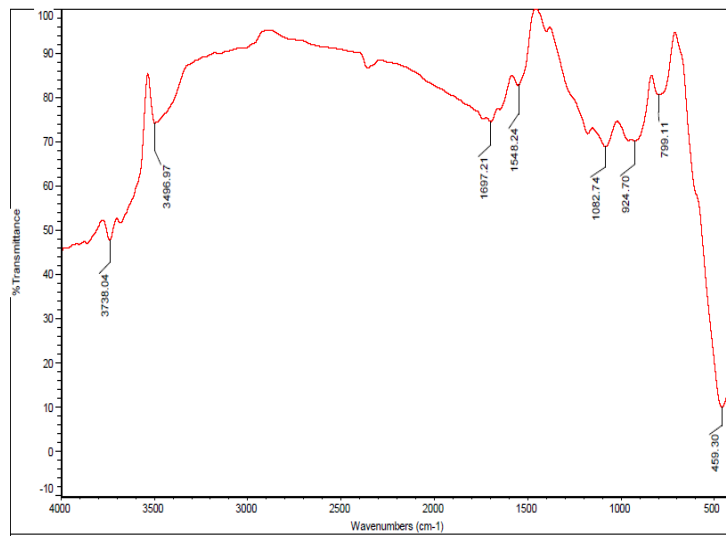


(a)

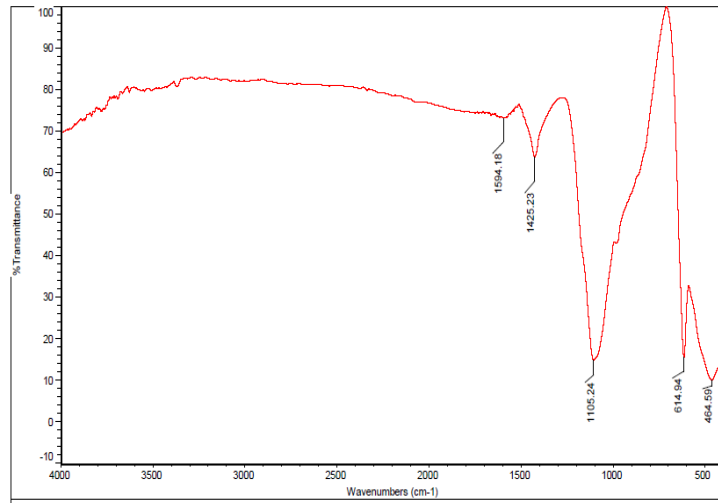


(b)

Figure 1: XRD pattern of (a) $BaBiO_3$ calcined at $800^\circ C/12h$ (b) $Ba_{0.6}K_{0.4}BiO_3$ calcined at $720^\circ C/12h$.

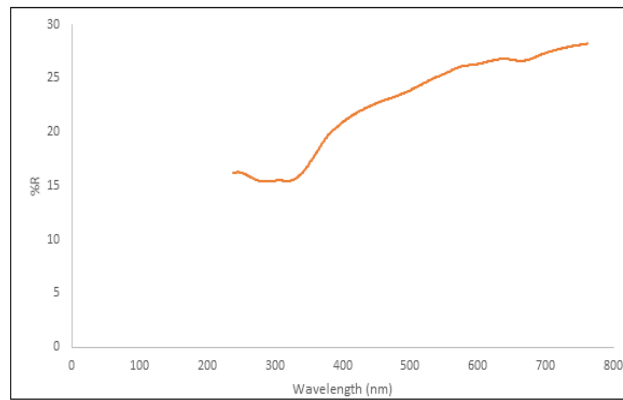


(a)

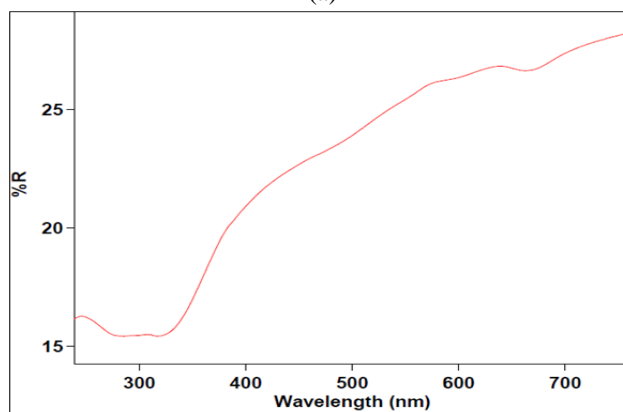


(b)

Figure 2: FTIR spectra of (a) BaBiO₃ calcined at 800°C/12h (b) Ba_{0.6}K_{0.4}BiO₃ calcined at 720°C/12h.

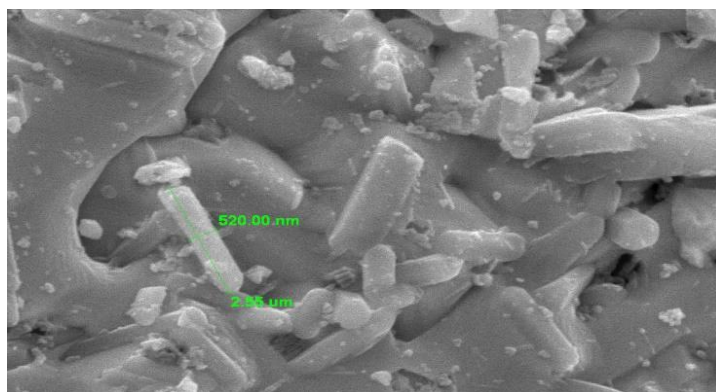


(a)

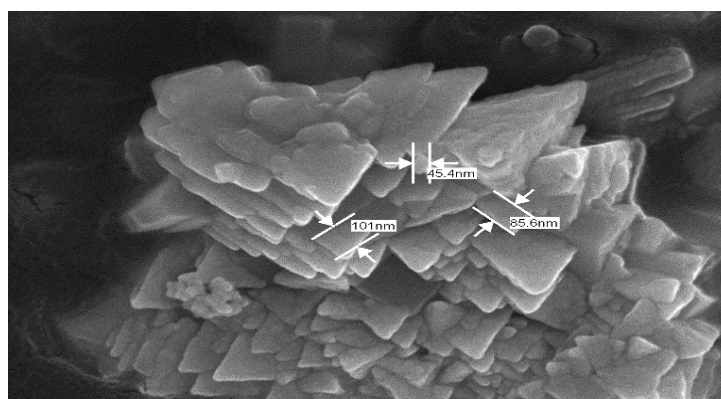


(b)

Figure 3: Reflectance spectrum of (a) BaBiO₃ calcined at 800°C/12h (b) Ba_{0.6}K_{0.4}BiO₃ calcined at 720°C/12h.



(a)



(b)

Figure 4: Scanning electron micrograph of (a) $BaBiO_3$ calcined at $800^\circ C/12h$ (b) $Ba_{0.6}K_{0.4}BiO_3$ calcined at $720^\circ C/12h$.

Chapter 4: Photocatalytic Degradation of Crystal Violet Dye Using $BaBiO_3$ and $Ba_{0.6}K_{0.4}BiO_3$ photocatalysts.

This chapter comprises the study of the photo-chemical degradation of Crystal violet dye, using as prepared $BaBiO_3$ and $Ba_{0.6}K_{0.4}BiO_3$ photo. Herein, the dependence of the photodegradation rate on various parameters such as initial dye concentration, catalyst dose, pH and temperature is studied.

Controlled experiments (photolysis) demonstrated that both visible light and catalyst are needed for the effective destruction of dye. The adsorption trends of Crystal violet at various initial concentrations followed the **Langmuir** and **Freundlich** adsorption isotherm trend [10,11]. Table 1 gives the constants of Langmuir and Freundlich for Crystal violet dye on both the prepared catalysts.

Table-1: Adsorption constants for Crystal violet dye on BaBiO₃ and Ba_{0.6}K_{0.4}BiO₃ photocatalysts.

Adsorbent catalyst	Langmuir Constants			Freundlich Constants		
	Q ₀ (mgg ⁻¹)	b (Lmg ⁻¹)	R ²	K _f (Lg ⁻¹)	n	R ²
BaBiO ₃	0.052	0.05	0.977	1.97	2.975	0.8677
Ba _{0.6} K _{0.4} BiO ₃	0.0307	1.325	0.929	7.74	1.68	0.717

As shown in Table 1, since the R² values are fairly close to 1, both the models describe the system well but Langmuir isotherm model is considered to be best fit because for this model R² is higher as comparison to Freundlich isotherm.

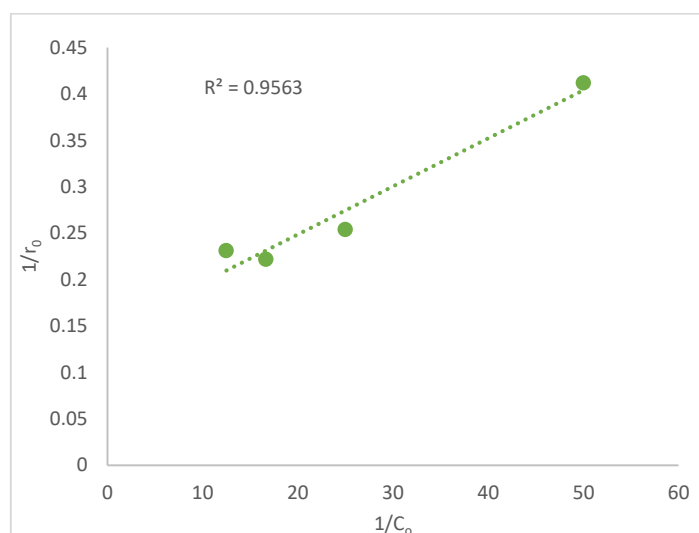
The effect of the initial dye concentration of dye on the rate of degradation is studied by varying the initial dye concentration from 20 to 80mgL⁻¹ initial pH 6.0, with a constant catalyst dose of 0.75gL⁻¹(for both the catalysts) at 35°C. It is observed that up to 40mgL⁻¹ the degradation efficiency increases due to the greater availability of dye molecules for excitation and consecutive degradation; hence there is an increase in the rate. After this, as the dye concentration is increased, the equilibrium adsorption of dye on catalyst surface increases; hence competitive adsorption of OH⁻ on the same site decreases, which further decreases the rate of formation of OH[•] radical, which is the principal oxidant necessary for a high degradation efficiency. Our results are in accordance with the earlier research work [12].

A series of experiments is carried out by varying the amount of both the catalysts from 0.25 to 1.25 gL⁻¹ at pH 6.0 and 40mgL⁻¹ Crystal violet dye concentration at 35°C. The degradation is studied till the maximum degradation is achieved. It is observed that for both the cases up to 0.75 gL⁻¹ doses of photocatalyst, degradation rate increases and then with further increase in dose, the rate decreases. The enhancement of removal rate may be due to the increase in the availability of active sites on the surface of the, which in turn increases the adsorption of dye species and, hence, the proportion of the excited species by the incoming photons. Larger amount of the catalyst favours the degradation efficiency due to the generation of free radicals O₂[•] and OH[•]. Therefore, the rate of degradation increases with the increase of from 0.25 to 0.75gL⁻¹. A further increase in catalyst

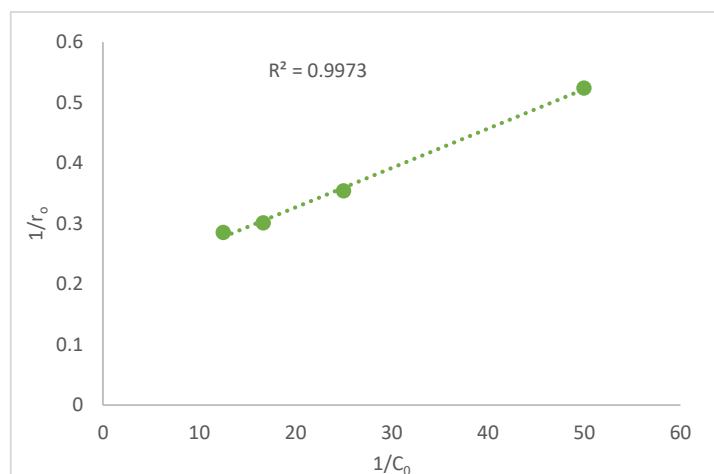
dose beyond the optimum will result in non-uniform light intensity distribution, so that the reaction rate would indeed be lowered with increased catalyst dosage [13].

Experiments are carried out at pH values ranging 4.0-8.0 of using 40mgL^{-1} Crystal violet solution and 0.75gL^{-1} BaBiO_3 dose at 35°C . For Crystal violet, the extent of photocatalysis increases with increase in pH up to 6.0 and with further increase in pH the degradation efficiency decreases. An increase in the rate of degradation with increase in the pH is due to the generation of more OH^- ions. These ions loose an electron to the hole generated at the semiconductor surface and OH^\bullet free radicals are formed. These formed free radicals cause oxidation of the dye. On further increase in pH above 6.0, a decrease is observed because at very high pH Crystal violet becomes negatively charged and so it repels negatively charged OH^- ions thereby restricting the approach of OH^- ions to the surface of catalyst and free radical generation is retarded. A similar effect of the pH on the photodegradation of dyes have been obtained in the earlier reports by semiconductor photocatalysts [14].

The Langmuir–Hinshelwood kinetic model showed a good agreement for the initial rates of degradation with the appropriate reaction rate constant and the substrate adsorption constant values of $K_r = 6.90\text{ mgL}^{-1}\text{min}^{-1}$ and $K_{LH} = 2.76\text{ Lmg}^{-1}$ for BaBiO_3 and for $\text{Ba}_{0.6}\text{K}_{0.4}\text{BiO}_3$ $K_r = 7.14\text{ mgL}^{-1}\text{min}^{-1}$ and $K_{LH} = 1.5\text{ Lmg}^{-1}$ {Figure 5 a&b}.



(a)



(b)

Figure 5: Langmuir-Hinshelwood plot for visible light photodegradation of Crystal violet dye (a) by BaBiO₃ (b) by Ba_{0.6}K_{0.4}BiO₃. (Experimental condition: [Catalyst] = 0.75gL⁻¹; pH=6.0 Temp. = 35°C).

The study of parameters influencing the degradation process allowed us to find the operating conditions for achieving the highest Crystal violet dye degradation rate. The optimization studies revealed the optimum operating conditions: pH value 6.0, catalyst concentration 0.75gL⁻¹, dye concentration 40mgL⁻¹ at 35°C.

The dependence of catalyst concentration on the reaction rate can be explained as $r_0 \propto [\text{BaBiO}_3]^{0.62} [\text{CV}]$ and $r_0 \propto [\text{Ba}_{0.6}\text{K}_{0.4}\text{BiO}_3]^{0.82} [\text{CV}]$ for BaBiO₃ and Ba_{0.6}K_{0.4}BiO₃, respectively. The photocatalytic degradation was temperature dependent with apparent activation energy for Crystal violet dye of 34.89kJmol⁻¹ and 44.55 kJmol⁻¹ while using BaBiO₃ and Ba_{0.6}K_{0.4}BiO₃ as photocatalyst respectively.

Chapter 5: Photocatalytic Degradation of Malachite Green Dye using BaBiO₃ and Ba_{0.6}K_{0.4}BiO₃ photocatalyst.

This chapter comprises the study of the photo-chemical degradation of Malachite green dye, using as prepared BaBiO₃ and Ba_{0.6}K_{0.4}BiO₃ photocatalysts. Herein, the dependence of the photodegradation rate on various parameters such as initial dye concentration, catalyst dose, pH and temperature is studied.

The adsorption trends of Malachite green dye at various initial concentrations followed the Langmuir and Freundlich adsorption isotherm trends.

Table 2 gives the constants of Langmuir and Freundlich for Malachite green dye on both the prepared catalysts.

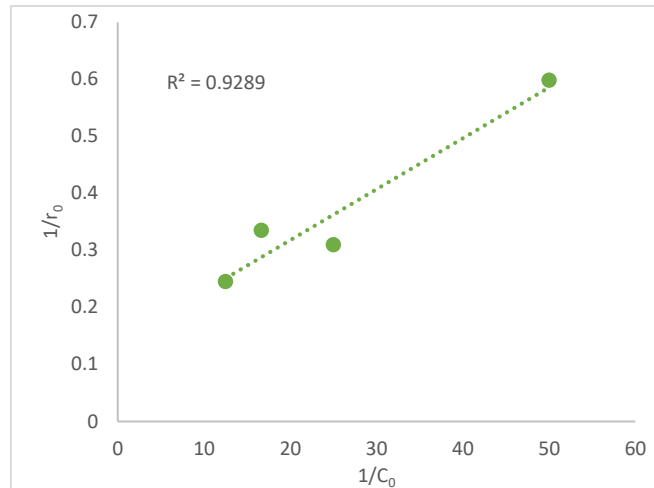
Table-2: Adsorption constants for Malachite green dye on BaBiO₃ and Ba_{0.6}K_{0.4}BiO₃ photocatalysts.

Adsorbent catalyst	Langmuir Constants			Freundlich Constants		
	Q ₀ (mgg ⁻¹)	b (Lmg ⁻¹)	R ²	K _f (Lg ⁻¹)	n	R ²
BaBiO ₃	2.633	0.0349	0.955	1.77	2.313	0.875
Ba _{0.6} K _{0.4} BiO ₃	3.3058	0.0268	0.941	0.313	1.147	0.870

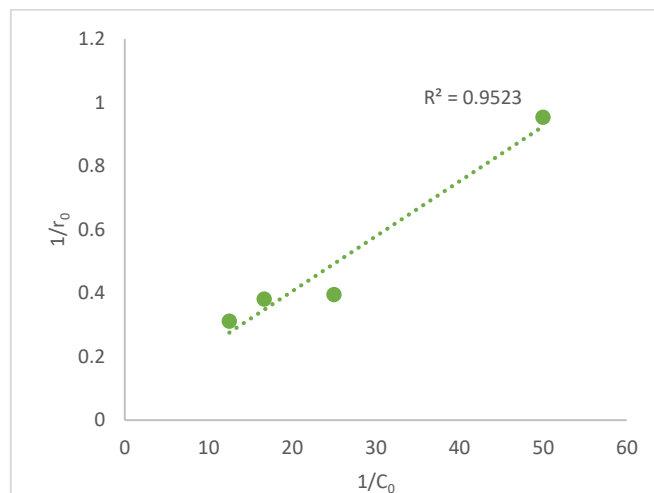
As shown in Table 2, since the R² values are fairly close to 1, both the models describe the system well but Langmuir isotherm model is considered to be best fit because for this model R² is higher as comparison to Freundlich isotherm. It is to be noted that while studying the influence of various process parameters such as initial dye concentration, catalyst dose and pH on the rate of photodegradation of Malachite green dye, the trend of results of degradation efficiency are found to be similar to those ones as described in Chapter 4.

The study of parameters influencing the degradation process allowed us to find the optimum operating conditions for achieving the highest Malachite green dye degradation rate.

The **Langmuir–Hinshelwood** kinetic model showed a good agreement for the initial rates of degradation with the appropriate reaction rate constant and the substrate adsorption constant values of K_r = 1.1 mgL⁻¹min⁻¹ and K_{LH} = 4.5 Lmg⁻¹ for BaBiO₃ and for Ba_{0.6}K_{0.4}BiO₃ K_r = 5.06 mgL⁻¹min⁻¹ and K_{LH} = 3.2 Lmg⁻¹ {Figure 6 a&b}.



(a)



(b)

Figure 6 : Langmuir-Hinshelwood plot for visible light photodegradation of Malachite green dye (a) by BaBiO₃ (b) by Ba_{0.6}K_{0.4}BiO₃. (Experimental condition: [Catalyst] = 0.75gL⁻¹; pH=6.0 Temp. = 35°C).

The study of parameters influencing the degradation process allowed us to find the operating conditions for achieving the highest Malachite green dye degradation rate. The optimization studies revealed the optimum operating conditions: pH value 6.0, catalyst concentration 0.75gL⁻¹, dye concentration 40mgL⁻¹ at 35°C.

The dependence of catalyst concentration on the reaction rate can be explained as $r_0 \propto [\text{BaBiO}_3]^{0.48} [\text{MG}]$ and $r_0 \propto [\text{Ba}_{0.6}\text{K}_{0.4}\text{BiO}_3]^{0.75} [\text{MG}]$ for BaBiO₃ and Ba_{0.6}K_{0.4}BiO₃, respectively. The photocatalytic degradation was temperature dependent with apparent activation energy for Malachite green dye of 33.34kJmol⁻¹.

¹ and 38.77 kJmol⁻¹ while using BaBiO₃ and Ba_{0.6}K_{0.4}BiO₃ as photocatalyst respectively.

Chapter 6: Photocatalytic Degradation of Congo Red Dye using BaBiO₃ and Ba_{0.6}K_{0.4}BiO₃

This chapter comprises the study of the photo-chemical degradation of Congo red dye, using as prepared BaBiO₃ and Ba_{0.6}K_{0.4}BiO₃ photocatalysts. Herein, the dependence of the photodegradation rate on various parameters such as initial dye concentration, catalyst dose, pH and temperature is studied.

The adsorption trends of Congo red dye at various initial concentrations followed the Langmuir and Freundlich adsorption isotherm trends. Table 3 gives the constants of Langmuir and Freundlich for Congo red dye on both the prepared catalysts.

Table-3: Adsorption constants for Congo red dye on BaBiO₃ and Ba_{0.6}K_{0.4}BiO₃ photocatalysts.

Adsorbent catalyst	Langmuir Constants			Freundlich Constants		
	Q ₀ (mgg ⁻¹)	b (Lmg ⁻¹)	R ²	K _f (Lg ⁻¹)	n	R ²
BaBiO₃	2.237	0.0367	0.972	1.258	1.68	0.843
Ba_{0.6}K_{0.4}BiO₃	0.0315	1.644	0.983	1.807	1.578	0.798

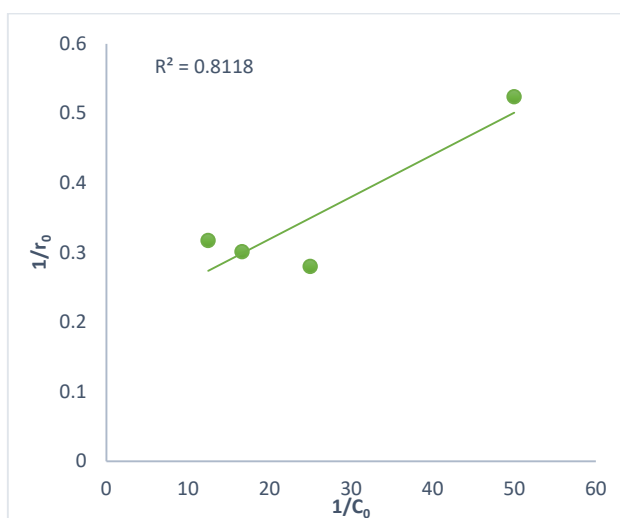
As shown in Table 3, since the R² values are fairly close to 1, both the models describe the system well but Langmuir isotherm model is considered to be best fit because for this model R² is higher as comparison to Freundlich isotherm.

It is to be noted that while studying the influence of various process parameters such as initial dye concentration, catalyst dose, pH and temperature on the rate of photodegradation of Congo red dye, the trend of results of degradation efficiency are found to be similar to those ones as described in Chapter 4.

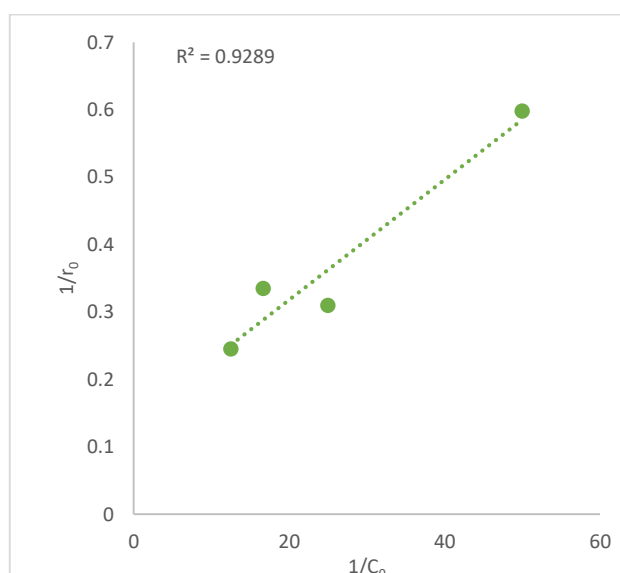
The study of parameters influencing the degradation process allowed us to find the optimum operating conditions for achieving the highest Congo red dye degradation rate. The optimization studies revealed the optimum operating conditions: pH value 5.0, catalyst concentration 0.75g/L⁻¹, dye concentration

40mgL⁻¹ at 35°C. Similar trends have been observed in the earlier reports of photodegradation of dyes by semiconductor photocatalysts [17].

The **Langmuir–Hinshelwood** kinetic model showed a good agreement for the initial rates of degradation with the appropriate reaction rate constant and the substrate adsorption constant values of $K_r = 0.259 \text{ mgL}^{-1}\text{min}^{-1}$ and $K_{LH} = 4.09 \text{ Lmg}^{-1}$ for BaBiO₃ and for Ba_{0.6}K_{0.4}BiO₃ $K_r = 1.254 \text{ mgL}^{-1}\text{min}^{-1}$ and $K_{LH} = 6.45 \text{ Lmg}^{-1}$ {Figure7 a &b}.



(a)



(b)

Figure 7: Langmuir-Hinshelwood plot for visible light photodegradation of Congo red dye (a) by BaBiO₃ (b) by Ba_{0.6}K_{0.4}BiO₃. (Experimental condition: [Catalyst] = 0.75gL⁻¹; pH=5.0 Temp. = 35°C).

The study of parameters influencing the degradation process allowed us to find the operating conditions for achieving the highest Congo red dye degradation rate. The optimization studies revealed the optimum operating conditions: pH value 5.0, catalyst concentration 0.75gL^{-1} , dye concentration 40mgL^{-1} at 35°C . The dependence of catalyst concentration on the reaction rate can be explained as $r_o \propto [\text{BaBiO}_3]^{0.08} [\text{CR}]$ and $r_o \propto [\text{Ba}_{0.6}\text{K}_{0.4}\text{BiO}_3]^{0.09} [\text{CR}]$ for BaBiO_3 and $\text{Ba}_{0.6}\text{K}_{0.4}\text{BiO}_3$, respectively.

The photocatalytic degradation was temperature dependent with apparent activation energy for Congo red dye of 20.41kJmol^{-1} and 28.13kJmol^{-1} while using BaBiO_3 and $\text{Ba}_{0.6}\text{K}_{0.4}\text{BiO}_3$ as photocatalyst.

The photocatalytic degradation potential of the as synthesized catalysts is found to be much better than the commercially available Degussa P-25 TiO_2 owing to their much narrower band gap in comparison to the wider band gap ($\sim 3.2\text{eV}$) of the later [18].

The photo activity of regenerated catalysts shows that after being used 3 times for dye degradation, the % degradation of all the three studied dyes declined slightly for both the prepared photocatalysts. It shows that as prepared photocatalysts are quite photo-stable during the photocatalytic degradation processes.

The complete mineralization of the studied dye is confirmed from the analysis of total organic carbon (TOC) content. %TOC removal for photodegradation of all the three dyes in the presence of as prepared photocatalysts is higher than that obtained by the commercially available p25 TiO_2 which shows the greater reactivity of synthesized photocatalysts (BaBiO_3 and $\text{Ba}_{0.6}\text{K}_{0.4}\text{BiO}_3$). The total mineralization of the pollutant dyes is further confirmed by the almost disappearance of the characteristic peak at the end of the experimental run in UV-vis spectrum of all the studied dyes.

Chapter 7: Conclusion and Future work

This chapter comprises the findings of the present research work. It can be concluded that both BaBiO_3 and $\text{Ba}_{0.6}\text{K}_{0.4}\text{BiO}_3$ are efficiently recoverable photocatalyst in acidic and basic dye degradation. Our results prove that the photocatalytic efficiency of $\text{Ba}_{0.6}\text{K}_{0.4}\text{BiO}_3$ greater than that of BaBiO_3 in degradation of dyes. The higher activity of $\text{Ba}_{0.6}\text{K}_{0.4}\text{BiO}_3$ was attributed to narrower band gap in comparison to the parent compound i.e. BaBiO_3 .

It is to be noted here that all the three studied three dyes differ in their molecular structure and functional group as well as in the extent of ionization in aqueous solution. The structure of the dye plays the most significant crucial role as it determines the effectiveness with which the photocatalytic material can attack the functional groups in order to disrupt the aromatic ring of the dye. Therefore, the rate of degradation of the dye is very much dependent on the structure of the dye.

Malachite green and Crystal violet are cationic dyes (basic dyes) while Congo red is an anionic (acidic dye), they are expected to behave differently in the photocatalytic processes as observed from our results that among the three studied dyes, Crystal violet suffers degradation with highest rate followed by Malachite green and then by Congo red in the end. It seems that the triphenyl amine structure of Crystal violet dye is more susceptible to degradation in photocatalytic reaction in comparison to Malachite green having two dimethyl amino group and Congo red having a bulky ensemble, including one central biphenyl group and two symmetric amino substituted naphthalene group [19].

This chapter shows the significance and scope of the present study in view of the increasing pollution day by day. This chapter also describes some recommendations for future work in the field of photocatalysis which will enhance the application of green chemistry.

References:

1. V. Gupta, *J. Environ. Manage.* 90, (2009), 2313.
2. T. Y. Mustafa, T.K. Sen, S. Afroze, H.M. Ang, *Adv. Coll. Inter. Sci.* 209, (2014), 172.
3. P. Kanhere, Z. Chen, *Molecules* 19, (2014), 19995-20022.
4. W. Zhou, Z Y. Zhao, *Chin. Phys. Soc.* 25, (2016), 37102(1).
5. S. Keith, M.R. Dutter, D.J. Lawrence , B. A. Reisner, T.C. Devore, *J. Photonics Energy* 4, (2014), 41598.
6. H. Huang, Y. He, Z. Lin, L. Kang, Y. Zhang, *J. Phys. Chem. C* 117, (2013), 22986.
7. M. Pechini, U.S. patent No. 3.330.697 (11 July 1967).
8. J.D.G. Fernandes, D.M.A. Melo, L.B. Zinner, C.M. Salustiano, Z.R. Silva, *Mater. Lett.* 53, (2002), 122-125.
9. M. Montazerzohori, M.H. Habibi, S. Johari, V. Khodadostan, *Annali di chimica* 97, (2007), 1015.
10. G. Mckay, *J. Chem. Technol. Biotechnol.* 32 (1982), 759.
11. S.P. Kodal, Z. Aksu, *Environ. Technol.* 38, (2017), 2551.
12. K. Yu, S. Yang, C. Liu, H. Chen, H. Li, C. Sun, S.A. Boyd, *Environ. Sci. Technol.* 46, (2012), 7318.
13. M. A. Habib, M. Muslim, M. T. Shahadat, M. N. Islam, I. M. I. Islam, T. S. A. Islam, A. J. Mahmood, *J. Nanostructures Chem.* 3,(2013),1.
14. C. Sahoo, A. K. Gupta, A. Pal, *Dyes Pigm.* 66, (2005), 189.
15. C. C. Chen C. S. Lu, Y.C. Chung, J. L. Jan, *J. Hazard. Mater.* 141, (2007), 520.
16. J. V. Tolia, M. Chakraborty, Z. V. P. Murthy, *Polish J. Chem. Technol.* 14, (2012), 16.
17. S. Erdemoğlu, S. K. Aksu, F. Sayilkan, B. İzgi, M. Asiltürk, H. Sayilkan, F. Frimmel, S.Güçer, *J. Hazard. Mater.* 155, (2008), 469.

18. T. Kako, Z. Zou, M. Katagiri J. Ye, *Chem. Mater.* 19, (2007), 198.
19. C. Hachem, F. Bocquillon, O. Zahraa, M. Bouchy, *Dyes pigm.* 49, (2001), 117.

Kavita Sharma

(Research Scholar)

Supervisor

Dr. (Mrs.) Uttra Chandrawat

Department of Chemistry,

Government College Kota, Kota

Annexure-II

List of Publications

- BaBiO₃ Assisted Photodegradation of Malachite Green Dye Under Visible Light Irradiation: Adsorption and Degradation Kinetics, Kavita Sharma, Seema Jain, Ultra Chandrawat, *Iranica Journal of Energy and Environment* 7(4): 375-381, 2016.
- Preparation and Characterization of Ba_{0.6}K_{0.4}BiO₃ Nano Particles with High Visible Light Photo Catalytic Activity Seema Jain, **Kavita Sharma**, Ultra Chandrawat, *Iranica Journal of Energy and Environment* 7(1): 64-71, 2016.
- Photocatalytic Degradation of Anti-inflammatory Drug on Ti Doped BaBiO₃ Nanocatalyst under Visible Light Irradiation, Seema Jain, **Kavita Sharma**, Ultra Chandrawat, *Iranica Journal of Energy and Environment* 7(3): 274-281, 2016.
- Low Temperature Synthesis, Characterization and Photocatalytic Activity of Nanorods BaBiO₃ Perovskite under Visible Light Irradiation, Seema Jain, **Kavita Sharma**, Ultra Chandrawat, *International Journal of Innovative Research in Science, Engineering and Technology* 3(7), 2014, 14405-14411.

List of Seminar/ Conference Attended:

- Participated in 5th National Academic workshop on **Organic Reaction Mechanism & Analytical Techniques used in Chemical Sciences** held on 21-25 October 2013 at University of Kota, Kota.
- Paper presentation as co-author and won “Best Presented Award” in 3rd International Conference on **Advance Trends in Engineering, Technology and Research (ICATETR- 2014)** held on 22-24 December 2014 at Bal Krishna Institute of Technology, Kota.
- Poster Presentation in National conference on **Organic Chemistry in Sustainable Development: Recent Advances and Future Challenges** held on 29-30 August 2016 at Birla Intitute of Technology & Science Pilani, Pilani.

Publications



BaBiO₃ Assisted Photodegradation of Malachite Green Dye Under Visible Light Irradiation: Adsorption and Degradation Kinetics

K. Sharma*, S. Jain and U. Chandrawat

Department of Chemistry, Govt. P.G. College, Kota 324001, India

PAPER INFO

Paper history:

Received 24 February 2016

Accepted in revised form 30 March 2016

Keywords:

BaBiO₃

Malachite Green dye

Pechini Method

Perovskites

Photocatalytic degradation

A B S T R A C T

Nano sized BaBiO₃ is prepared through Pechini method and characterized by SEM, XRD, FTIR, DT-TGA and UV DRS. The kinetic studies of adsorption and degradation phenomena involved in the photocatalytic degradation of Malachite Green dye using a batch reactor under visible light were investigated. Experiments were performed in a suspended BaBiO₃ photocatalyst system. The effect of catalyst loading, solution pH and initial dye concentration on dye degradation is investigated. In addition, adsorption experiment is also performed which indicates that adsorption pattern follows Langmuir model. The decomposition of Malachite Green dye follows pseudo first order kinetics and the Langmuir-Hinshelwood mechanism is found to be valid. Different kinetic parameters for adsorption and photocatalytic degradation of dye are also determined.

doi: 10.5829/idosi.ijee.2016.07.03.10

INTRODUCTION

The industrial and textile wastewater is a considerable source of non-aesthetic pollution in the environment and can create dangerous byproducts through oxidation, hydrolysis or other chemical reactions that take place in the wastewater phase [1-2]. The presence of small amount of dyes is clearly visible and considerably influences the water ecosystem.

Amongst the different pollutants from the textile industry, Malachite Green (MG) is the one of the main disastrous pollutant[3-4]. The use of this dye has been banned in several countries and is not approved by US Food and Drug Administration; it is still being used in many parts of the world due to its low cost, ready availability and efficacy [5].

MG degradation has been studied by various biological and physiochemical methods [6-7]. However, these treatment methods only provide separation of the dyes without any dye degradation, creating a waste disposal problem with the large quantities of sludge production. To resolve this problem, advanced oxidation processes based on heterogeneous catalysis techniques

are being used for the degradation of MG. In several studies TiO₂ is used predominantly due to its low cost and non toxicity [8-9]. However, photochemical efficiency of TiO₂ is limited to UV region only, due to its wide band gap [3.2eV]. Various modifications including cation and anion doping, coupling with semiconductors have been used to enhance photoabsorption ability of TiO₂ in visible region[10-11]. These modified samples of TiO₂ show good photocatalytic activity in visible region, but their activity is not high enough for practical application because of their less stability [12]. Also, sometimes these modifications may cause the distortion of band structure and these additional elements act as a scattering centre which further leads to decrease in photocatalytic activity [13]. Therefore, developing a visible light active photocatalytic material is essential for practical application of photocatalytic technology at wide range. The energy gap of perovskite [14-15] is usually less than 3.0 eV hence it shows good photocatalytic activity in visible light region. Recently, Bismuth based visible light active perovskites such as LiBiO₃[16], KBiO₃ [16], AgBiO₃ [17] are prepared by hydrothermal synthesis and solvent thermal synthesis respectively. In this paper, we

* Corresponding author: Kavita Sharma
E-mail: kavi21089.sharma@gmail.com
Tel- +919461391230

present a simple Pechini type [18] polymerizable complex route, based on polyesterification between citric acid and ethylene glycol that has been successfully used to synthesize several other compounds with perovskite structure [19-20]. Sol-Gel method is advantageous compared to other processing methods, as it allows control over size, calcinations temperature and also it provides chemically uniform powders. The prepared catalyst is characterized by XRD, SEM, UV-DRS, FTIR for structural determination. The photocatalytic activity of thus prepared sample has been evaluated via the degradation of MG dye in aqueous solution under visible irradiation. The initial rates of the reaction are calculated for various initial dye concentrations. The Langmuir-Hinshelwood model [21-22] is found suitable for interpreting the initial rate data and for the development of a rate equation for degradation of MG dye. An adsorption study of BaBiO₃ has also been discussed.

MATERIAL AND METHODS

Materials

In this study all chemicals used are of analytical reagent grade. Barium nitrate, Bismuth nitrate, citric acid and ethylene glycol are purchased from Merck (India). Malachite green is obtained from SDS Fine Chem. (P.) Ltd.(India). Deionised water purified with a milli-Q-water ion exchange system (Millipore Co.) is used throughout the study. Chemical structure of malachite green dye is depicted below-

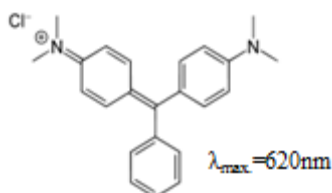


Figure 1. Structure of Malachite Green dye

Preparation of BaBiO₃ perovskite

BaBiO₃ perovskite is prepared by the sol-gel route [Pechini method][17]. Barium nitrate and bismuth nitrate are firstly dissolved in doubly distilled water and dil HNO₃ respectively to get 1.0M solution each. These two are used as starting materials. Both the above solutions are mixed and then magnetically stirred to get a uniform solution. After addition of 1M citric acid [CA] to above solution stirring is performed up to 30 minutes followed by addition of ethylene glycol [EG]. Here, CA and EG are used as complexing agents. The molar ratio among Barium, Bismuth cations is 1:1. The CA/metal ratio is fixed at 4.0 while keeping the CA/EG ratio as 60/40. Thus obtained solution is transferred to a hot plate where it is heated upto 90°C resulting in the formation of brown

resin. This resin is pulverised and then calcined at 850°C for 12 hours to obtain BaBiO₃ Perovskite.

Characterization

Ex-star 6300 thermal analyzer is used to make thermogravimetric (TGA) and differential thermoanalytic (DTA) measurements in air flow (200 mL min⁻¹) in the temperature range 31-900 °C with a heating rate of 5 °C min⁻¹. The structural characterization is done by X-ray diffraction using a X-ray diffractometer [Siemens D500] equipped with a high intensity CuK α radiation, and operated at 45kV and 40mA accelerating voltage and the applied current, respectively. A scan rate of 5° min⁻¹ were used for 0-90° 2 θ values. The morphology and particle size are analyzed using Scanning electron microscope [HitachiX650, Japan]. Fourier transform infrared (FTIR) [Spectrum 100, Perkin Elmer] is utilized to identify chemical bonds existed in the powder. UV-DRS spectrum is carried out using Shimadzu Lambda 900 Spectrophotometer. The spectrum is recorded at 240-800 nm wavelengths.

Catalytic activity

The adsorption experiments in dark are carried out in order to evaluate the equilibrium constant of adsorption. Stock solutions of the different initial dye concentration (C₀) are prepared. A fixed amount of the adsorbent (0.1gram) is added to the 100 mL of above solution. The flasks are then agitated simultaneously for 2h at room temperature. The suspension is centrifuged in order to remove BaBiO₃ catalyst. The amount of adsorbate uptake q_e (mgg⁻¹) can be calculated as-

$$q_e = (C_0 - C_e) V / W \times 100 \quad (1)$$

where C₀ is the initial adsorbate concentration (mgL⁻¹); C_e is the equilibrium concentration in solute on (mgL⁻¹); V is the volume of solution (L); W is the mass of the adsorbent (g); and q_e is the amount adsorbed(mgg⁻¹).

The visible light irradiation experiments are carried out in an indigenously prepared immersion type photocatalytic reactor. A 500W Xe arc lamp (intensity=137 mWcm⁻²) is used as a visible light source. This lamp is placed in a quartz tube which is sealed from one side. This tube is then immersed in a cylindrical borosilicate reactor (capacity 1 L). In this, mixture of catalyst and dye solution are taken following which the mixture is placed in a water bath circulated at a constant speed to keep the above suspension homogenous. Different dye solutions of various concentrations are made from the stock solution (100 mgL⁻¹) by appropriate dilutions. Before irradiation, the suspensions are magnetically stirred in the dark for 20 minutes to get an adsorption-desorption equilibrium between the catalyst and dye solution. The equilibrium concentration of the dye (C_{eq}) in contact with the catalyst, instead of that of

the feed dye solution, represents the true dye concentration in solution at the start of irradiation. For this reason C_{eq} has been used as C_0 for the photodegradation kinetics. The pH of the solutions is adjusted using 0.1N NaOH and 0.1N HCl.

The decrease in absorbance of the dye solution at the characteristic wavelength is observed by taking out the samples at regular intervals throughout the complete experimental run. The aliquots are centrifuged and filtered through Whatman filter paper (No. 42) to remove the catalyst.

The residual dye concentration in the samples are determined using a Systronics double beam UV-VIS spectrophotometer 2203. After that, the absorbance corresponding to the $\lambda_{max} = 620\text{nm}$ are converted to the residual concentration using the predetermined calibration curves for MG dye. Also, the degradation efficiency of the dye at any time t is calculated using the following formula

$$\text{Degradation \%} = \frac{C_0 - C_t}{C_0} \times 100 \quad (2)$$

where $C_0 =$ concentration of dye solution before photoirradiation (mg L^{-1}), $C_t =$ Concentration of dye solution after photoirradiation (mg L^{-1}).

Blank experiments with the pure dye solution (no addition of catalyst) with constant stirring under visible light irradiation for 30 minutes, are conducted prior to the photocatalytic experiments. No significant degradation of the solution is observed indicating that the direct photolysis of the dye is negligible.

RESULTS AND DISCUSSION

Characterization of catalyst

Fig. 2 shows the DTA-TG analysis curves of the BaBiO_3 precursor resin. It can be seen that the decomposition of BaBiO_3 precursor resin takes place in three distinct steps. The first weight loss region ($31\text{--}185^\circ\text{C}$) corresponds to the loss of physio-absorbed water and accompanied by 8.9% weight. The second weight loss (60.80%) region is in temperature range of $186\text{--}416^\circ\text{C}$, which can be attributed to the pyrolysis and combustion of organic compounds and the degradation of intermediate species formed during the polymerisation process. The next weight loss around 13.0% lies in the range of $417\text{--}440^\circ\text{C}$ and can be attributed to the decomposition of nitrates and nitrites residue. The DTA curve shows three weak exothermic peaks at 200, 259, 292 $^\circ\text{C}$ and one strong exothermic peak at 456°C , which are correlated to the weight loss mentioned above and subsequent crystallization of the residual amorphous phase. This observation is supported by powder X-ray diffraction (XRD) of the sample obtained from calcinations of the precursor at 350, 650 and 800°C . (Fig. 3)

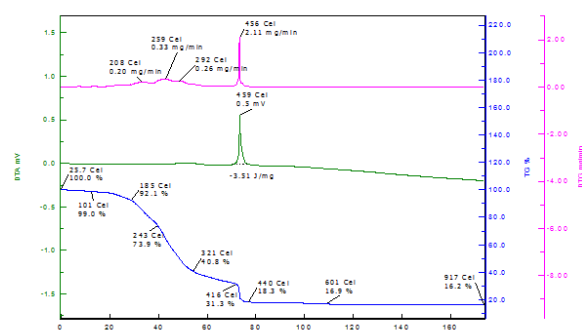


Figure 2. TGA/DTA curves showing thermal decomposition of precursor to a stable BaBiO_3

Fig. 3 shows XRD patterns of the samples which were calcined at different temperature 300°C (a), 600°C (b) and 800°C (c). The XRD pattern (a) at 350°C is found to be amorphous in nature as no sharp peak is observed in the diffraction pattern. At 600°C , the crystalline perovskite type structure of BaBiO_3 started to form and the degree of crystallinity increased with increasing the calcinations temperature as shown in Fig. 3 (b). It is evident from Fig. 3 (c) that at 800°C fully crystallized single-phase oxide BaBiO_3 with well pronounced perovskite crystal structure has formed and its diffraction peaks corresponds to a monoclinic structure with the lattice parameters $a = 6.183 \text{ \AA}$, $b = 6.13 \text{ \AA}$, $c = 8.666 \text{ \AA}$. (JCPDS 35-1020). The main diffraction peaks are observed at $2\theta = 29.23^\circ, 45.00^\circ, 51.67^\circ$ and 59.90° , which is similar to the previously reported data for BaBiO_3 [23].

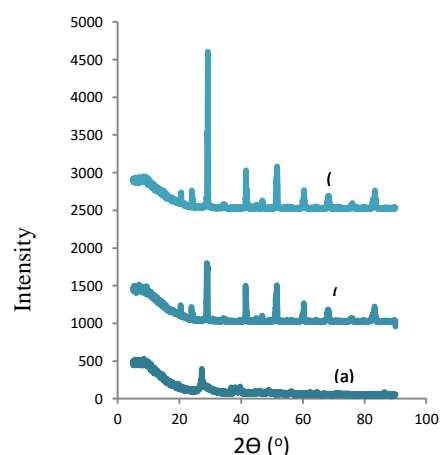


Figure 3. XRD patterns of BaBiO_3 (a) at 350°C (b) at 600°C (c) at 800°C

The diffuse reflectance spectra of BaBiO_3 (Fig. 4) shows a strong fundamental absorption edge at 600nm , which indicates the photocatalytic activity in the visible light as well as the solar light. Further, the optical band gap E_g was determined from Tauc's formula, i.e.

$$(\alpha E)^2 = A (E - E_g) \quad (3)$$

where $\alpha = 4\pi\kappa/\lambda$ is the absorption coefficient, E is the photon energy, and A is a constant. The E_g values are determined by extrapolating the linear portion of the plot relating $(\alpha hv)^2$ [Kubelka-Munk Function] [24] versus hv to $(\alpha hv)^2 = 0$ [Kubelka- Munk conversion spectrum]. The optical band gap is estimated to be about 2.07 eV from the onset of the absorption edge.

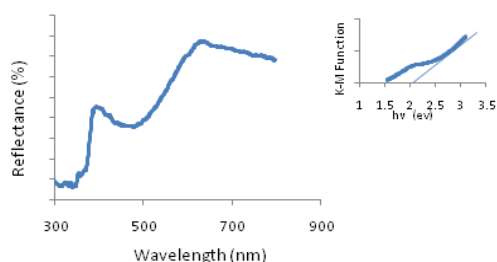


Figure 4. Kubelka-Munk conversion spectrum of BaBiO₃. The inset shows an estimation of band gap energy by extrapolation method.

SEM micrographs of BaBiO₃ (Fig. 5) show that the nanorods with average width 520nm and length as small as 2.55 μ m are synthesized by the calcination at 800°C. This nanosize is further confirmed by the small width of XRD peaks (Fig. 3 c)

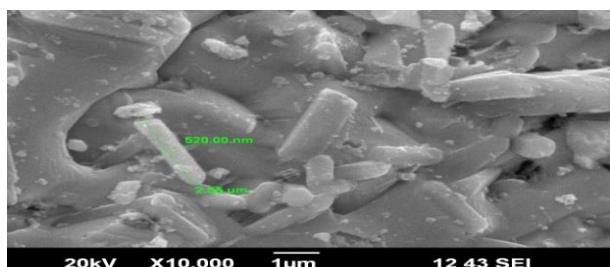


Figure 5. SEM micrographs of BaBiO₃ at 1 μ magnification

Fig.6 shows the FTIR spectra of the BaBiO₃ powder in the range of 400-3500 cm⁻¹, calcined at 800°C. The FTIR is similar to the most other ABO₃-type perovskite compounds which have common BO₆ oxygen-octahedral structure. [25]The band at nearly 468 cm⁻¹ is related to Bi-O bending vibrations.[26] A less intense peak around 850 cm⁻¹ is attributed to the bending vibration of Ba-O bond. [27] The calcined sample shows an absorption around 1446 cm⁻¹, which is due to the adsorption of atmospheric CO₂ during drying processes.

Adsorption studies

Since, the photo-assisted degradation of the dyes occurs predominantly on the photocatalyst surface,

studies on the adsorption of the dyes from aqueous solution onto

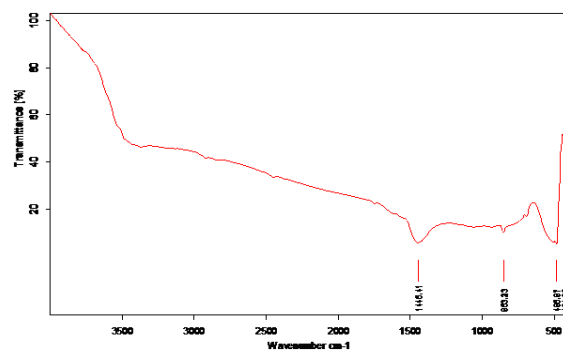


Figure 6. FTIR spectra of BaBiO₃ perovskite

BaBiO₃ nanoparticles are relevant and important. Equilibrium adsorption data collected in the study are fitted on Langmuir adsorption isotherm[28]. Here in, we used the Langmuir model by assuming the monolayered adsorption phenomenon due to the presence of limited active adsorption sites. The linear form of Langmuir Isotherm is represented by the following equation:

$$\frac{C_e}{q_e} = \frac{1}{Q_0 b} + \frac{C_e}{Q_0} \quad (4)$$

where C_e is the concentration of the adsorbate (mgL⁻¹) at equilibrium. q_e is the amount of adsorbate per unit mass of adsorbent at equilibrium in mgg⁻¹. Q_0 is the maximum adsorption at monolayer coverage in mgg⁻¹, b is the Langmuir adsorption constant in Lmg⁻¹. The plots of C_e/q_e versus C_e are linear and presented in Fig. 7. Langmuir adsorption constant (b) and the maximum adsorbable dye quantity (Q_0) are calculated from the intercept and slopes of this figure as 0.055 mgmL⁻¹0.334 mgg⁻¹, respectively. The correlation coefficient was found to be 0.917.

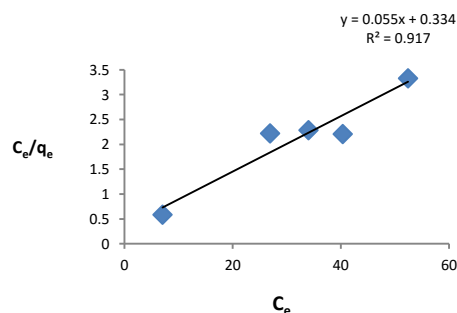


Figure 7. Linear transform of Langmuir isotherm [BaBiO₃=0.75gL⁻¹; pH=6.0]

Effect of catalyst loading

In order to avoid the use of excess catalyst, it is desirable to find out an optimum catalyst loading for efficient degradation. A series of experiments is carried out by

varying the amount of catalyst from 0.25 to 1.25 gL⁻¹ at pH 6.0 and 50 mgL⁻¹ MG concentration. It is observed that up to 0.75 gL⁻¹ loading of photocatalyst degradation rate increases and then with further increase in loading, the rate decreases. The enhancement of removal rate may be due to the increase in the availability of active sites of the photocatalyst. When the concentration of BaBiO₃ catalyst increased above the limiting value the degradation rate decreased, due to the disruption of light by the suspension. Our results are in agreement with the earlier reports [8] Fig. 8 shows a plot of the degradation rate constant (K_{app}) as a function of the BaBiO₃ concentration at the fixed MG concentration (50 mgL⁻¹) and pH 6.0. Also, an empirical relationship between the initial dye concentration has been reported by Galindo et al ($r_0\alpha[\text{catalyst}]^n [\text{dye}]$), where n is a exponent less than 1 for all the dyes studied relative to low concentration of catalyst [29] As it can be seen in Fig. 9, the dependence of the BaBiO₃ concentration on the initial decolorization rate of MG follow a similar relationship

$$r_0\alpha[\text{BaBiO}_3]^{0.72} [\text{MG}] \quad (5)$$

when the BaBiO₃ concentration is less than 1gL⁻¹

Effect of pH

The effect of pH on the rate of degradation of dyes solution is investigated in the pH range 4.0-8.0 with

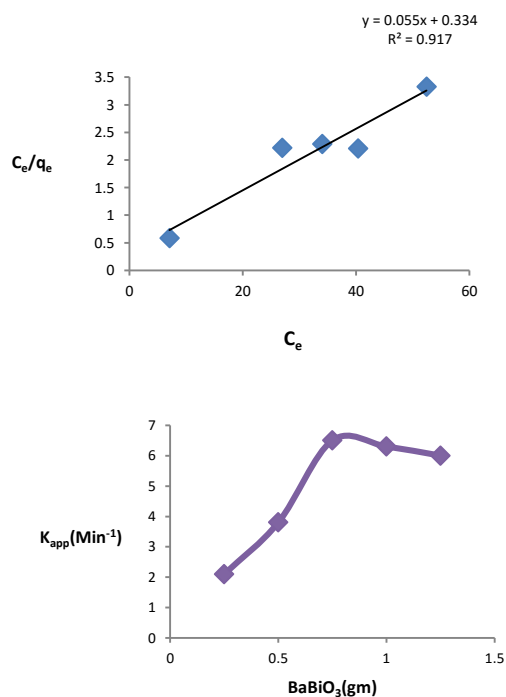


Figure 8. Effect of BaBiO₃ loading on the degradation rate [MG=50mgL⁻¹; pH=6.0]

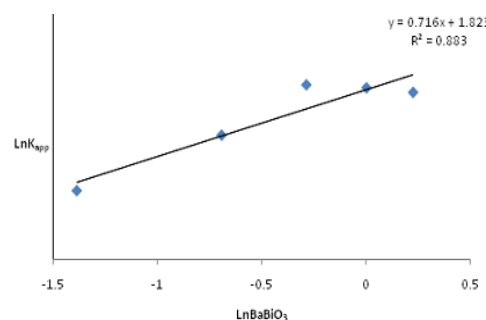


Figure 9. Relationship between $\text{Ln}K_{app}$ and the amount of BaBiO₃ [MG=50mgL⁻¹; pH=6.0]

constant catalyst loading of 0.75 gL⁻¹ and 50 mgL⁻¹ MG concentration. It is observed that the degradation efficiency increases with increase in pH upto 6.0 and with further increase in pH the degradation efficiency decreases. An increase in the rate of degradation with increase in the pH is due to the generation of more OH⁻ ions. These ions loose an electron to the hole generated at the semiconductor surface and OH[•] free radicals are formed. These formed free radicals cause oxidation of the dye. On the further increase in pH above 6.0, a decrease is observed because at very high pH MG becomes negatively charged and so it repels negatively charged OH⁻ ions. This repulsive force does not allow the approach of OH⁻ ions to the surface of catalyst and free radical generation is retarded. Fig. 10 shows a plot of the degradation rate constant (K_{app}) as a function of the pH .

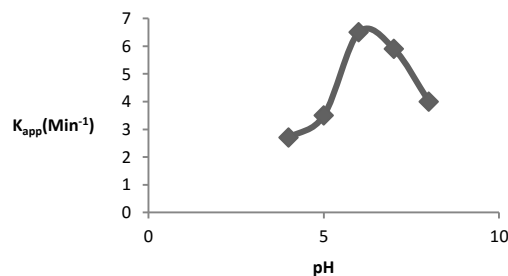


Figure 10. Effect of pH on the degradation rate [BaBiO₃=0.75gL⁻¹; MG=50mgL⁻¹]

Effect of initial dye concentration

The effect of the initial dye concentration of dye on the rate of degradation is studied by varying the initial dye concentration from 20 to 80mgL⁻¹ at pH 6.0, with a constant catalyst loading of 0.75gL⁻¹. It is observed that up to 50mgL⁻¹ the degradation efficiency increases due to the greater availability of dye molecules for excitation and consecutive degradation, hence there is an increase in the rate. After this as the dye concentration is increased, the equilibrium adsorption of dye on catalyst surface increases; hence competitive adsorption of OH⁻ on the same site decreases, which further decreases the rate of

formation of OH^{*} radical, which is the principal oxidant necessary for a high degradation efficiency. On the other hand, considering Beer-Lambert law, as the initial dye concentration increases, the path length of photon entering the solution decreases, resulting in the lower photon adsorption on the catalyst particles and consequently a lower photodegradation rate [8].

In this work, we employed Langmuir-Hinshelwood model [21-22] to describe the total degradation of MG. L-H model covers both adsorption and photocatalytic phenomenon for explanation of dye degradation kinetics. The first order relationship for photocatalytic decomposition of dye can be represented as:

$$-\ln(C_0/C_t) = K_{app} \cdot t \quad (6)$$

where C_0 , C_t and K_{app} are the initial dye concentration, concentration at time 't' and K_{app} is the apparent pseudo first order rate constant. The plots of $\ln(C_0/C_t)$ versus 't' with different initial concentration are shown in Fig. 11. The value of K_{app} is calculated by the slope of the above curves.

The value of initial degradation rate (r_0) is obtained by the multiplying the K_{app} values to the corresponding initial dye concentration, as follows;

$$r_0 = K_{app} \cdot C_0 \quad (7)$$

A linear expression can be conventionally obtained by plotting the reciprocal of initial rate ($1/r_0$) constant against reciprocal of initial concentration ($1/C_0$) (Fig. 12). The linear form of Langmuir-Hinshelwood kinetics can

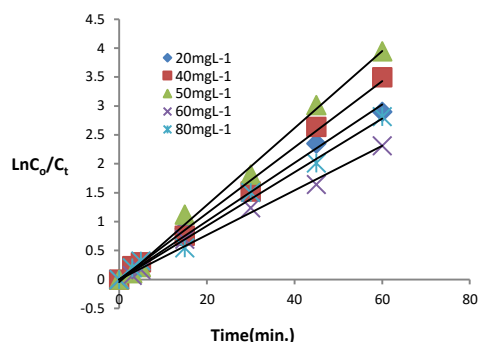


Figure 11. Effect of initial dye concentration on photodegradation of MG dye [$BaBiO_3=0.75gL^{-1}$; $pH=6.0$]

also be given by the following expression

$$1/r_0 = 1/K_r + 1/K_r \cdot K_{LH} \cdot C_0 \quad (8)$$

here, K_r is the reaction rate constant and K_{LH} is the adsorption coefficient of the reactant also known as Langmuir-Hinshelwood constant. Table 1 summarizes all the kinetic parameters calculated using the Langmuir-Hinshelwood model for dye degradation on using $BaBiO_3$ photocatalyst. K_r and K_{LH} values are $25.64 mgL^{-1}min^{-1}$, $1.42 Lmg^{-1}$ respectively. It is noteworthy that the Langmuir adsorption constant ($b=0.055 Lmg^{-1}$) obtained from the dark experiments are different from that determined by Langmuir-Hinshelwood equation ($K_{LH}=1.42 Lmg^{-1}$). This is due to the photoadsorption and very rapid photoreaction of the dyes on the catalyst surface [31].

Table 1. Influence of various parameters on visible light degradation of MG in $BaBiO_3$ suspension:

[MG]	$BaBiO_3$	pH	$K_{app} \times 10^{-2}$	r_0	K_r	K_{LH}
mgL^{-1}	gL^{-1}		Min^{-1}	$mgL^{-1}Min^{-1}$	$mgL^{-1}Min^{-1}$	Lmg^{-1}
50	0.25	6.00	2.1	1.05	25.64	1.42
	0.5		3.8	1.9		
	0.75		6.5	3.25		
	1		6.3	3.15		
	1.25		6	3		
20	0.75	6.00	5.1	1.02		
40			5.7	2.28		
50			6.5	3.25		
60			4.6	2.76		
80			3.5	2.8		
50	0.75	4.00	2.7	1.35		
		5.00	3.5	1.75		
		6.00	6.5	3.25		
		7.00	5.9	2.95		
		8.00	4	2		

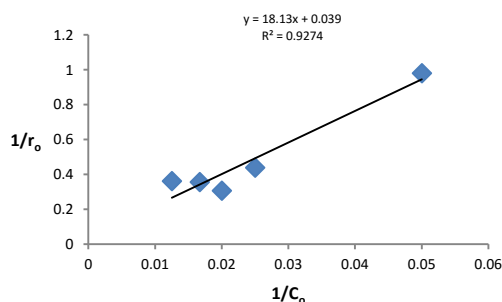


Figure 12. Langmuir-Hinshelwood plot of visible light degradation of MG in BaBiO₃ [BaBiO₃=0.75gL⁻¹; pH=6.0]

CONCLUSION

The synthesis of BaBiO₃ through Pechini method resulted in the formation of nanosized, mono phase crystalline material which has proved its potential as a photocatalyst in visible light owing to its low band gap of 2.07 eV. The photocatalytic activity and the corresponding degradation kinetics shows that it can efficiently degrade MG dye in the aqueous suspension under visible light irradiation. The dependence of the BaBiO₃ concentration on the initial degradation rate can be explained as $(r_0 \propto [\text{BaBiO}_3]^{0.72} [\text{MG}])$, when the BaBiO₃ concentration is less than 1 gL⁻¹. The Langmuir adsorption constant (b) and the maximum adsorption at monolayer coverage Q₀ are calculated as 0.055 Lmg⁻¹ and 0.334 mgg⁻¹ respectively. The photocatalytic degradation of MG by BaBiO₃ is nicely fitted to a Langmuir-Hinshelwood kinetic model. The calculated values of the reaction rate constant (K_r) and Langmuir-Hinshelwood adsorption constant (K_{LH}) are 25.64 mgL⁻¹min⁻¹ and 1.42 Lmg⁻¹ respectively. Therefore, this simple technology of degradation of the colored effluents has the potential to improve the quality of the wastewater from textile and other industries.

Acknowledgements

Authors are thankful to Department of Chemistry, Government P.G. College, Kota for providing the necessary facilities during the research work. We would also like to thank STIC (Sophisticated Test and Instrumentation Centre), Cochin University of Science & Technology for providing experimental support for characterization of the synthesized catalyst.

REFERENCES

- Galindo, C., P. Jacques and A. Kalt, 2001. Photochemical and Photocatalytic Degradation of an Indigoid Dye: A Case Study of

- Acid Blue 74 (AB74). *Journal of Photochemistry and Photobiology. A: Chemistry*, 141(1): 47-56.
- Rao, K. V. K., 1995. Inhibition of DNA Synthesis in Primary Rat Hepatocyte Cultures by Malachite Green: a New Liver Tumor Promoter. *Toxicology Letters*, 81 (2-3), 107-113.
- Alderman, D. J. and R. S. C. Hadley, 1993. Malachite Green: a Pharmacokinetic Study in Rainbow Trout, *Oncorhynchus Mykiss* (Walbaum). *Journal of Fish Diseases*, 16: 297-311.
- Culp, S. J., F. A. Beland, R. H. Heflich, R. W. Benson, L. R. Blankenship, P. J. Webb, P. W. Mellick, R. W. Trotter, S. D. Shelton, K. J. Greenlees and M. G. Manjanatha, 2002. Mutagenicity and Carcinogenicity in Relation to DNA Adduct Formation in Rats Fed Leucomalachite Green, *Mutation Research*, 506/507: 55-63.
- Schnick, R. A. 1988. The Impetus to Register New Therapeutics for Aquaculture. *The Progressive Fish-Culturist*, 50(4): 190-196.
- Paninutti, L., N. Mouso and F. Forchiasini, 2006. Removal and Degradation of the Fungicide Dye Malachite Green from Aqueous Solution Using the System Wheat Bran-Fomes Sclerodermeus. *Enzyme and Microbial Technology*, 39: 848-853.
- Mittal, A., D. Kaur and J. Mittal, 2009. Batch and Bulk Removal of a Triphenyl Methane Dye, Fast Green FCF, from Wastewater by Wastewater by Adsorption over Waste Materials, *Journal Hazardous Materials*, 163(2-3): 568-577.
- Chen, C. C.; C. S. Lu, Y. C. Chung, J. L. Jan, 2007. UV Light Induced Photodegradation of Malachite Green on TiO₂ Nanoparticles. *Journal of Hazardous Material*, 141: 520-528.
- Suresh, T. and G. Annadurai, 2013. Synthesis, Characterization and Photocatalytic Degradation of Malachite Green Dye Using Titanium Dioxide Nanoparticles. *International Journal of Research in Environmental Science and Technology*, 3(3): 71-77.
- Barakat, M. A., H. Schaeffer, G. Hayes and S. I. Shah, 2004. Photocatalytic Degradation of 2-Chlorophenol by Co-Doped TiO₂ Nanoparticles. *Applied catalysis B: Environmental*, 57: 23-30.
- Sahoo, C., A.K. Gupta and A. Pal, 2005. Photocatalytic Degradation of Crystal Violet (C.I. Basic Violet 3) on Silver Ion Doped TiO₂. *Dyes and Pigments*, 66(3): 189-196.
- Mrowetz, M. W. Balcerski, A. J. Colussi and M. R. Hofmann, 2004. Oxidative Power of Nitrogen-Doped TiO₂ Photocatalysts Under Visible Illumination. *Journal of Physical Chemistry B*, 108(45): 17269-17273.
- Mrowetz, M., W. Balcerski, A. J. Colussi and M. R. Hafmann, 2004. Oxidative Power of Nitrogen Doped TiO₂ Photocatalysts Under visible Light Illumination. *Journal of Physical Chemistry B*, 108(45): 17269-17273.
- Kim, H. G., D. W. Hwang and J. S. Lee, 2004. An Undoped, Single-phase Oxide Photocatalyst Working under Visible Light. *Journal of American Chemical Society*, 126: 8912-8913.
- Kudo, A., K. Omori and H. Kato, 1999. A Novel Aqueous Process for Preparation of Crystal from Controlled and Highly Crystalline BiVO₄ Powder. *Journal of American Chemical Society*, 121(49): 11459-11467.
- Ramchandran, R., M. Sathiyaa, K. Ramesha, A. S. Prakash, G. Madras and A.K. Shukla, 2011. Photocatalytic Properties of KBiO₃ and LiBiO₃ with Tunnel Structures. *Journal of Chemical Sciences*, 123(4): 517-524.
- Yu, K., S. Yang, C. Liu, H. Chen, H. Li, C. Sun and S. A. Boyd, 2012. Degradation of Organic Dyes via Bismuth Silver Oxide Initiated Direct Oxidation Coupled with Sodium Bismuthates Based Visible Light Photo Catalysis. *Environmental Science and Technology*, 46, 7318-7326.
- Pechini, M. U. S. Patent No. 3.330.697 (11 July 1967).
- Alemi, A., E. Karimpour, H. Shokri. 2008. Preparation, Characterization and Luminescent Properties of Europium Oxide Doped Nano LaMn_{0.9}Zn_{0.1}O_{3+d} by Sol-gel Processing. *Bulletin of Material Science*, 31: 967-973.
- Sverre M., G. Wang, M. A. Einarsrud and T. Grande, 2007. Decomposition and Crystallization of a Sol-gel-derived PbTiO₃ Precursor. *Journal of American ceramic society*, 90(8): 2649-2652.

21. Kumar, K. V., K. Porkodi, A. Selvaganapathi, 2007. Heterogeneous Photocatalytic Decomposition of Crystal Violet in UV Illuminated Sol-Gel Derived Nanocrystalline TiO₂ Suspension. *Dyes and Pigment*, 75: 246-249.
22. Senthilkumaar, S., and K. Porkodi, 2005. Heterogeneous Photocatalytic Decomposition of Crystal Violet UV-illuminated Sol-gel Derived Nanocrystalline TiO₂ Suspensions. *Journal of Colloid and Interface Science*. 288: 184-189.
23. Sunarso, J., S. Liu, Y. Lin and J.D. da Costa, 2009. Oxygen Permeation Performance of BaBiO_{3-δ} Ceramic Membranes. *Journal of Membrane Science*, 344(1): 281-287.
24. Tang J, Zou Z, Jinhu Y, 2007. Efficient Photocatalysis on BaBiO₃ Driven by Visible Light. *Journal of Physical Chemistry C*, 111(34): 12779-12785.
25. Zhu, D. and Y. H. Zhang, 2002. Hydrothermal Synthesis of Single-Crystal La_{0.5}Sr_{0.5}MnO₃ Nanowire Under Mild Conditions. *Journal of Physics: Condensed Matter*, 14(27): 519–524.
26. Lee, C. Y., K. Y. Song and R. P. Sperline, 1996. Molecular Dynamics Simulation and Far Infrared Measurements of Ba_{0.6}K_{0.4}BiO₃. *Korean Journal of Materials Research*, 6(6): 555-560.
27. LAZAREVIĆ, Z. Ž, N. Ž. ROMČEVIĆ, J. D. BOBIĆ, 2009. Study of Ferroelectric BaBi₄Ti₄O₁₅ Obtained Via Mechanochemical Synthesis. *Optoelectronics and Advanced Materials – Rapid Communications*, 3(7): 700 -703
28. Mckay, G. 1982. Adsorption of Dye stuff from Aqueous Solution with Activated Carbon: Equilibrium and batch Contact Time Studies. *Journal of Chemical Technology and Biotechnology*, 32: 759-772.
29. Galindo, C., P. Jacques and A. Kalt, 2001. Photooxidation of the Phenylazonaphthol AO₂₀ on TiO₂: Kinetic and Mechanistic Investigations. *Chemosphere*, 45(6-7):997-1005.

Persian Abstract

DOI: 10.5829/idosi.ijee.2016.07.03.10

چکیده

نانو ذره BaBiO₃ با روش Pechini آماده شده و خصوصیات آن با آنالیزهای UV DRS و SEM, XRD, FTIR, DT- TGA مشخص شد. مطالعات سنیتیکی جذب و پدیده تجزیه، در تجزیه فوتو کاتالیستی رنگ سبز مالاکیت (Malachite) با استفاده از راکتور بسته تحت نور مرئی، بررسی شد. آزمایش ها در یک سیستم فوتو کاتالیستی BaBiO₃ معلق انجام شدند. اثر بارگذاری کاتالیست، pH محلول و غلظت رنگ اولیه روی تجزیه رنگ بررسی شده اند. علاوه بر آن، همچنین آزمایش جذب انجام شده است که نشان داده الگو جذب از مدل Langmuir پیروی می کند. تجزیه رنگ سبز مالاکیت (Malachite) از شبه سنیتیک درجه اول پیروی می کند و مکانیسم Langmuir-Hinshel Wood معتبر شناخته شد. پارامترهای سنیتیکی مختلف برای جذب و تجزیه فوتو کاتالیستی رنگ همچنین تعیین شد.



Preparation and Characterization of Ba_{0.6}K_{0.4}BiO₃ Nano Particles with High Visible Light Photo Catalytic Activity

K. Sharma*, S. Jain and U. Chandrawat

Department of Chemistry, Govt. P.G.College, Kota 324001, India

P A P E R I N F O

Paper history:

Received 05 May, 2016

Accepted in revised form 15 October 2016

Keywords:

Ba_{0.6}K_{0.4}BiO₃

Malachite Green dye

Pechini Method

Perovskites

Photocatalytic degradation

A B S T R A C T

Herein, we report the synthesis of a novel nano-structured photo catalyst Ba_{0.6}K_{0.4}BiO₃ by Pechini method. Prepared catalyst is characterized using simultaneous thermogravimetric differential thermal analysis (TG-DTA), ray diffraction (XRD), Scanning electron microscopy (SEM), Ultra Violet Diffuse reflectance spectroscopy (UV-DRS) and Fourier-transform infrared spectroscopy (FT-IR). The XRD pattern suggests that Ba_{0.6}K_{0.4}BiO₃ crystallizes in the cubic structure. The formation of perovskite phase can be confirmed by the presence of metal-oxygen band in the FTIR spectrum. SEM image reveals the nano sized plate like structure of Ba_{0.6}K_{0.4}BiO₃ with particle size in the range of 10-45 nm. The band gap is calculated from the DRS and is found to be 1.8eV. The band gap and crystalline nature suggest that this material can be used as a photo catalyst. The photo catalytic activity of Ba_{0.6}K_{0.4}BiO₃ is evaluated for degradation of Malachite Green dye under visible light irradiation. The results reveal that 0.75 gL⁻¹ Ba_{0.6}K_{0.4}BiO₃ with initial concentration of Malachite Green 40 mgL⁻¹ irradiated for 30 minutes shows the highest photo catalytic activity. According to Langmuir-Hinshelwood kinetic model, the photo catalytic degradation of Malachite green dye follows pseudo-first-order kinetics.

doi: 10.5829/idosi.ijee.2016.07.04.08

INTRODUCTION

Today, the top global issues are concerned with ensuring a clean environment and a sustainable supply of clean energy at reasonable cost. For these reasons many researchers are studying advanced materials and processes for the removal of waste or photocatalytic cracking of toxic wastes efficiently at low cost and with less energy consumption and advanced materials. These processes for the production of clean and renewable energy are used for photocatalytic and photoelectrocatalytic water splitting, and also the photocatalytic reduction of organic waste material.

Malachite green chloride (*N*-[4-[[4-(dimethylamino) phenyl]phenylmethylene]-2,5-cyclohexadien-1-ylidene]-*N*-methylmethaminium chloride, is a triphenyl methane dye worldwide used in aquaculture. It is extensively used as biocide in the global aquaculture industry, and is highly effective against important protozoan and fungal infections. It is also used as a food colouring agent, food additive, medical

disinfectant and anthelmintic as well as a dye in the silk, wool, jute, leather, cotton, paper and acrylic industries [1-2]. The US Food and Drug Administration has nominated malachite green (MG) as a priority chemical for carcinogenicity test. There is a concern about the fate of MG and its reduced form, leucomalachite green in aquatic and terrestrial ecosystem science, as they occur as contaminants and are potential human health hazards [3-4]. Considering the potential adverse effects of MG, it should be removed from the environment. Although the use of MG has been banned in several countries; it is still being used in many parts of the world due to some benefits like low cost, ready availability and appreciable efficacy. Photocatalytic degradation of dyes and organic pollutants is of fundamental importance in waste water treatment and other related problems of environmental interest. Recently many new perovskite-based semiconductor materials are being used as visible-light-active photocatalysts [5-6]. Several features associated with oxygen deficiency like band gap energy, cation vacancy and surface area influence the performance of

* Corresponding author: K. Sharma

E-mail: kavi21089.sharma@gmail.com; Tel- +919461391230

material used in photo catalytic degradation. When semiconductor is irradiated with the photons whose energy is greater than or equal to the band gap energy of the semiconductor; the hole-electron pairs are generated. These hole-electron pairs are responsible for generation of other reactive oxidising species like O_2^- , HOO° , HOO^\cdot , HO° etc. which further react with adsorbed dye molecule, leading to the formation of dye radical anions and finally the degradation of the dye occurs [7-8].

The perovskite type oxides ABO_3 own special physical and chemical features because of their stable crystal structure, electromagnetic behaviour, magneto resistive properties and high catalytic activity. They have been applied in environmental protection and industrial catalysis [9-10]. Most of the metal cations are known to be stably incorporated in the perovskite structure. One of the major characteristics of perovskites is the possibility for substitutions at the position of cations. As a result, there are large groups of compounds with different cations in A position $\{A_yA'_{1-y}BO_3\}$ [11-12] and with different cations in B position $\{AB_yB'_{1-y}O_3\}$ [13-14] and with substitution in positions of both the cations $\{A_xA'_{1-x}B_yB'_{1-y}O_3\}$ [15-16]. Potassium doped $BaBiO_3$ perovskite semiconductor material was discovered by Mattheiss et al. in 1988 [17]. Conventionally, potassium doped $BaBiO_3$ powders have been prepared by a traditional solid state reaction [18] and powder sintering technique [19] which needs high temperature and may lead to the presence of impure phases like Bi_2O_3 in the prepared catalyst [18]. In order to overcome these disadvantages, we used Pechini method (sol-gel technique) [20] which is simple and economical, low processing temperature and wide range of possibility to change the properties by varying the composition of the solution [21].

In the present study, $Ba_{0.6}K_{0.4}BiO_3$ nano structured material is prepared by Pechini method and the structural properties of $Ba_{0.6}K_{0.4}BiO_3$ are examined by various characterization techniques. The photo catalytic activity of thus prepared material is evaluated by the degradation of MG using Langmuir-Hinshelwood kinetic model [22-23]. To the best of our knowledge $Ba_{0.6}K_{0.4}BiO_3$ has never been used as a photo catalyst.

MATERIAL AND METHODS

Materials

Barium nitrate, bismuth nitrate, potassium nitrate, citric acid and ethylene glycol are purchased from Merck (India). The MG dye is purchased from SDS Fine Chem. (P) Ltd., India. Deionised water further purified with a milli-Q-water ion exchange system (Millipore Co.) is used throughout the study. Chemical structure of MG dye is shown in Fig. 1. All chemicals are of analytical grade and are used as received.

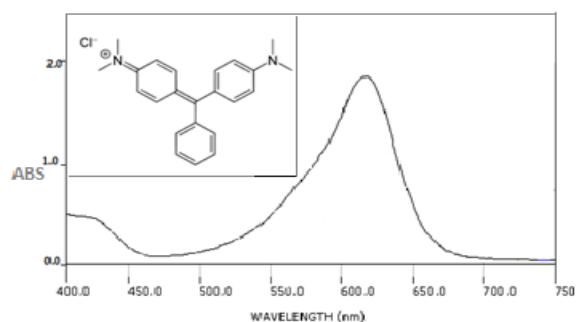


Figure 1. Molecular structure of Malachite Green dye ($\lambda_{max}=620nm$).

Preparation of $Ba_{0.6}K_{0.4}BiO_3$ perovskite

Pechini method,²⁰ which is used to prepare mixed metal oxide powders, it is used here to synthesize $Ba_{0.6}K_{0.4}BiO_3$. This process is based on metallic citrate polymerization with the use of ethylene glycol. A hydro carboxylic acid (such as citric acid), is used to chelate cations in aqueous solution. Polymerization is promoted by heating the mixture, and it results in the formation of homogeneous resin in which metal ions are uniformly distributed.²¹ There are some complicating factors experienced during other conventional methods some of which have been discussed in our previous research work.^{24,25} In the present study, for the preparation of $Ba_{0.6}K_{0.4}BiO_3$ particles, barium nitrate, potassium nitrate and bismuth nitrate are used as starting materials. Atomic ratio of barium nitrate, potassium nitrate and bismuth nitrate is 3:2:5. First, barium nitrate and potassium nitrate are dissolved in deionised water under stirring condition. Bismuth nitrate is separately dissolved in minimum amount of dilute HNO_3 to avoid precipitation of Bi ions; then, it is added dropwise to the barium nitrate and potassium nitrate solution. Citric acid is then added proportionally to the above metal solution, followed by the addition of ethylene glycol as a chelating agent. The citric acid/ethylene glycol ratio is kept at 3:2. The solution thus prepared, while being stirred with a magnetic stirrer, is heated up to $90^\circ C$ to remove excess water and subsequently to accelerate poly esterification reaction between citric acid and ethylene glycol. During the evaporation of solvent, reddish brown gas corresponding to NO_2 comes out of the solution. This produces a viscous, bubbly mass that forms a resin upon cooling. This precursor is burned at $350^\circ C$ for 2 hours. Further, to fully evaporate highly combustion species in the mass and to burn down most of the organic constituents, the powder is calcined in a furnace at different temperatures (6 hours at $650^\circ C$ and 12 hours at $720^\circ C$). The calcination removes most of the residual carbon and thus cubic phase perovskite is finally obtained. Experimental conditions for catalyst loading $0.75gL^{-1}$, pH 5.5 (natural pH), absorbance is recorded at

$\lambda_{\text{Max}} = 620 \text{ nm}$, light intensity 137 mWcm^{-2} , continuous stirring, temperature 35°C .

Characterization

To determine the best calcination temperature, simultaneous thermogravimetric (TG) and differential thermoanalytic (DTA) measurements are achieved in flowing air (200mL/Min.) with heating rate of $5^\circ\text{C}/\text{min}$ upto 900°C using a Netzsch STA449 system. The structural characterization is done by X-ray diffraction using a X-ray diffractometer [Siemens D500] equipped with a high intensity $\text{CuK}\alpha$ radiation, and operated at 45kV and 40mA accelerating voltage and the applied current, respectively. A scan rate of $5^\circ/\text{min}$ was used for 0° - 90° two-theta values. The morphology and particle size are analyzed using Scanning electron microscope [HitachiX650, Japan]. Fourier transform infrared (FTIR) [Spectrum 100, Perkin Elmer] is utilized to identify chemical bonds existing in the powder. UV-DRS spectra is carried out using Shimadzu Lambda 900 spectrophotometer. The spectra is recorded at 240-800 nm wavelength.

Photocatalytic activity

The photocatalytic degradation is performed using a cylindrical glass reactor, accommodating a central glass tube in which an 500W Xe arc lamp (intensity= 137mWcm^{-2}) is placed to irradiate the dye solution. At the bottom of the reactor, a magnetic stirrer is placed for homogenization of reaction solution. The visible light illumination is started following a dark period (without light illumination) of 15 minutes to attain an adsorption equilibrium between dye and photocatalyst. Blank experiment (without $\text{Ba}_{0.6}\text{K}_{0.4}\text{BiO}_3$ photocatalyst) is also carried out. The samples are collected at regular time interval and subsequently analyzed for the residual concentration using a UV-VIS spectrophotometer at the wavelength of 620nm. Finally, the photocatalytic activities are determined using the following relation:

$$\text{Degradation \%} = \frac{C_0 - C_t}{C_0} \quad (1)$$

where, C_0 (mgL^{-1}) and C (mgL^{-1}) are the initial concentration and concentration after photocatalytic degradation, respectively. A series of experiments are carried out to study the effect of the amount of photocatalyst and initial dye concentration on the photocatalytic degradation of MG dye at natural pH (5.5) and 35°C temperature.

RESULTS AND DISCUSSION

Simultaneous TG and DTA investigations are carried out to evaluate the crystallization temperature. Fig. 2 shows DTA-TGA curve of polymeric resin for $\text{Ba}_{0.6}\text{K}_{0.4}\text{BiO}_3$

indicating evolution of perovskite phase with increasing temperature. TGA curve shows a four step decomposition of resin precursor to form the perovskite material. We observed a slight weight loss of $\sim 6\%$ upto 200°C accompanied by a weak exothermic peak at 190°C . This weight loss is caused by elimination of residual water adsorbed due to the storage of the preheated sample in ambient atmosphere. The second weight loss region (42%) is observed in the range of 210 - 300°C is because of combustion of light organic matter and acetates as indicated by an exothermic peak around 240°C in DTA curve. The third weight loss around 23% in the temperature range of 310 - 580°C corresponds to decomposition of the nitrates and nitrites residue. This observation is supported by the well resolved exothermic peak at 550°C in DTA curve. The final small weight loss on the TGA curve observed above 560°C to 900°C corresponds to the crystallization and formation of perovskite phase (at 720°C) which is also confirmed by XRD (Fig. 3) and FTIR (Fig. 4) analysis. The total weight loss of this powder is 72.51%.

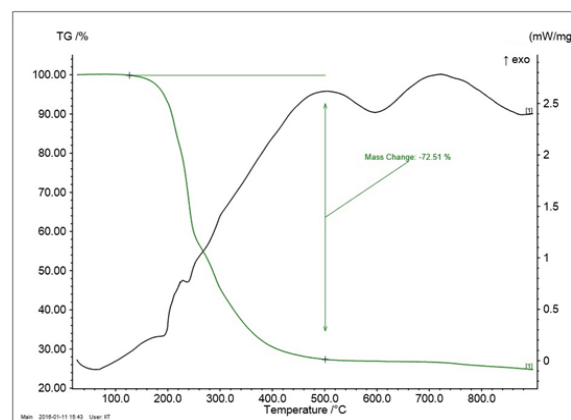


Figure 2. TGA/DTA curves showing thermal decomposition of precursor to a stable $\text{Ba}_{0.6}\text{K}_{0.4}\text{BiO}_3$.

Fig. 3 shows the XRD patterns of the $\text{Ba}_{0.6}\text{K}_{0.4}\text{BiO}_3$ compound. The patterns reveal that the sample burned at 350°C is amorphous in nature. Upon calcination at 650°C the sample becomes more crystalline (inset of Fig. 3). The sample calcined at 720°C is highly crystalline with predominantly perovskite structure. Though, its JCPDS card is not available, it could be seen that the diffraction peaks can be well indexed to cubic phase $\text{Ba}_{0.6}\text{K}_{0.4}\text{BiO}_3$ (pm3m space group and lattice parameter of 4.284\AA) which are in accordance with the earlier studies reported by Flemming et al. [18]. In the Fig. 3 main diffraction peaks are observed at 20.53° , 29.33° , 36.66° , 42.74° , 51.33° , 60.41° , 68.28° , 76.04° and 83.37° which can be assigned to 100, 110, 111, 200, 201, 220, 310 and 321 planes, respectively. Diffraction peak related to Bi_2O_3 are not observed in XRD pattern confirming the purity of the synthesized compound.

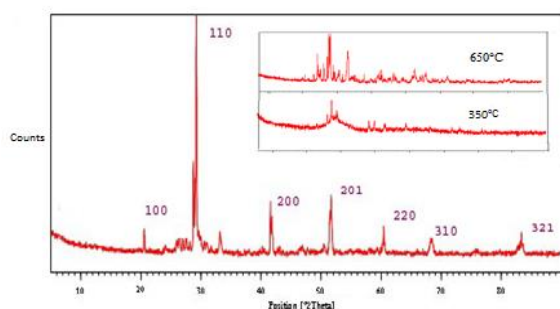


Figure 3. XRD pattern of $Ba_{0.6}K_{0.4}BiO_3$ calcined at $720^\circ C$ for 12h. The inset shows the XRD pattern of precalcined samples.

Fig. 4 shows the FTIR spectra of $Ba_{0.6}K_{0.4}BiO_3$. The band at nearly 465cm^{-1} is related to Bi-O bending mode vibrations. The strong peak at 615cm^{-1} is related to anisotropic oxygen motions, which depends on the potassium ion distribution in the crystal lattice [26]. For the Pechini method, as ethylene glycol is used for polyesterification with citric acid to form a rigid polymer network, a strong band around 1105cm^{-1} is attributed to the C-C-O structure confirming the polymerisation process [27]. The FTIR results thus confirms that complex formation between citric acid and metallic ions occurred in the sol-gel route and that polyesterification of ethylene glycol and citric acid and complexation with metallic ions occurred in the Pechini Method. It is seen from the Fig. 2 that the peak at 1425cm^{-1} is attributed to Ba-O bending vibrations [28]. Thus, the bands at 615cm^{-1} and 1425cm^{-1} are due to creation of new active sites in the photocatalyst, which results in the higher activity of $Ba_{0.6}K_{0.4}BiO_3$ photocatalyst.

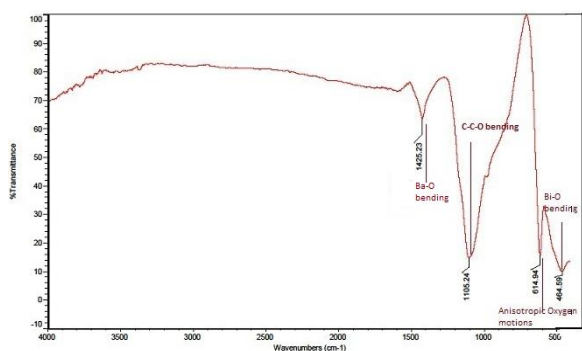


Figure 4. FTIR spectra for $Ba_{0.6}K_{0.4}BiO_3$.

As shown in Fig. 5 the prepared $Ba_{0.6}K_{0.4}BiO_3$ sample is sensitive to visible light and can absorb a wide range of light irradiation up to maximum 663 nm , almost covering the region from UV through all strong visible light under indoor lamp irradiation. This indicates that the prepared $Ba_{0.6}K_{0.4}BiO_3$ sample can be utilized as visible light active catalyst for degrading the dye pollutants. The band edge calculations verifying the

oxidative potential of prepared photocatalyst done by using $E=hc/\lambda$ where h , c and λ are Planks constant (Joule-sec), speed of light (meter/sec) and cut of wavelength (meters) respectively. During the band gap energy calculations $1\text{eV}=1.6\times 10^{-19}$ joules are taken as conversion factor. The optical band is estimated to be 1.87eV , which is in good agreement with reported value [29] of 1.4eV for cubic $Ba_{0.6}K_{0.4}BiO_3$.

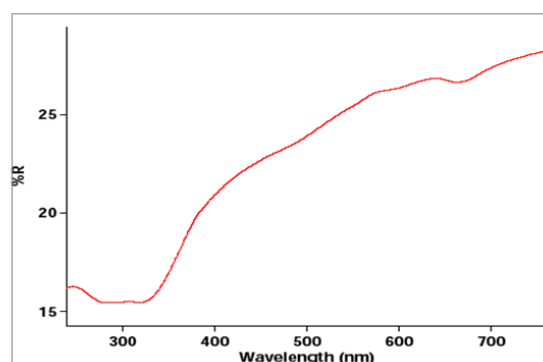


Figure 5. UV-vis diffuse reflectance spectra of $Ba_{0.6}K_{0.4}BiO_3$.

Fig. 6 is the SEM micrograph of $Ba_{0.6}K_{0.4}BiO_3$ powder as prepared at $720^\circ C$. SEM shows well packed plate-like layered grains of variable sizes. The layered plate-like morphology is a characteristic feature of the bismuth containing compounds [30]. The encircled area in Fig. 4 shows weakly bound agglomeration process, which is attributed to Vander-Waals forces. In order to reduce the surface energy, the primary particles tend to form agglomerates with a minimum surface to volume ratio. This type of structure is common in oxides, ferrites, and titanate ceramics prepared by sol gel procedure [22,31]. The nanoparticles have an average size in the range of $45\text{-}101\text{ nm}$

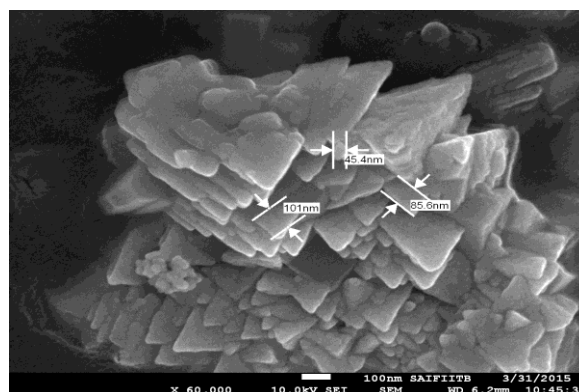


Figure 6. SEM micrograph of $Ba_{0.6}K_{0.4}BiO_3$

The effect of initial concentration of dye on degradation rate can be determined by varying the initial concentration from 20 mgL^{-1} to 60 mgL^{-1} at constant

catalyst loading (0.75gL^{-1}). As seen in Fig. 7, degradation efficiency increases with increase in the dye concentration up to 40mgL^{-1} after this the degradation efficiency decreases. This effect can be explained as follows; as the dye concentration increased, more molecules of dye are available for excitation and degradation. Above optimum concentration, the dye starts acting like a filter for the incident light. Considering the Beer-Lambert law, at higher concentration of dye, the path length of photons entering the solution decreases, resulting in the lower photon adsorption on catalyst particles and consequently, lowering the photo degradation rate. The observation is consistent with previous studies done by Chen *et al.* [5, 32-33].

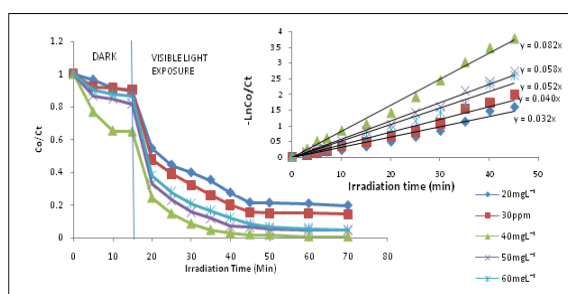


Figure 7. Effect of initial dye concentration on photochemical degradation of MG following dark adsorption with $\text{Ba}_{0.6}\text{K}_{0.4}\text{BiO}_3$ under visible light irradiation. Inset shows the plot of $-\ln C_0/C_t$ versus irradiation time.

From both mechanistic and application point of view, studying the dependence of the photocatalytic reaction rate on amount of the $\text{Ba}_{0.6}\text{K}_{0.4}\text{BiO}_3$ in the MG dye degradation is important. Hence, the effect of photocatalyst concentration on the photodegradation rate of the MG dye is studied by varying the catalyst loading from 0.5gL^{-1} to 1.0gL^{-1} with initial dye concentration 40mgL^{-1} . As shown in Fig. 8, dye degradation is faster for catalyst dose of 0.75gL^{-1} than 0.5gL^{-1} and 1.0gL^{-1} . At lower catalyst loading number of active site are lesser so, initially when the amount of catalyst increases, the number of active sites increase which further increases the degradation rate. After exceeding the optimal catalyst loading, the suspended catalyst reduces the penetration of the light in the solution and decrease in the rate of photocatalytic degradation of dye is observed.

The overall rate of the photocatalytic degradation can be represented as $R=R_1+R_2$, where R , R_1 and R_2 are net degradation, rate of photolysis and rate of photo catalysis, respectively. Though, it should be noted that no dye degradation is observed in the blank experiments, this reveals that there is a negligible effect with the visible light alone. Accordingly, the decrease in the

concentration of dye is due to the effect of both the catalyst and visible light [34].

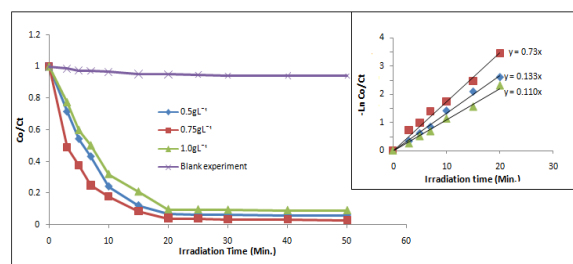


Figure 8. Influence of the catalyst concentration on the photodegradation of MG. Inset shows the plot of $-\ln C_0/C_t$ versus irradiation time.

Heterogeneous photo catalysis process, takes place over the catalyst surface. Therefore, reactant adsorption on catalyst surface is regarded as an important initial process. Fig. 7 also shows adsorption of MG on $\text{Ba}_{0.6}\text{K}_{0.4}\text{BiO}_3$ surface as a function of time. The result indicates that concentration of MG is decreased by 3%. The concentration of the dye after the 15 minutes dark adsorption is taken as the initial concentration (C_0).

The photocatalytic degradation of MG dye on the surface of $\text{Ba}_{0.6}\text{K}_{0.4}\text{BiO}_3$ nanoparticles follows a pseudo-first-order kinetic law and can be expressed by equation

$$\ln C_0/C_t = K_{app} * t \quad (2)$$

The curves of $-\ln C_0/C_t$ against 't' are recorded and fitted linearly; the value of pseudo-first order rate constant (K_{app}) is extracted from the slope of the straight line (inset of Fig. 7). Thus obtained K_{app} is multiplied by respective initial dye concentration to calculate initial reaction rate (R_0). According to numerous works, the kinetics of the photocatalytic degradation is described by using the Langmuir-Hinshelwood (LH) model [22-23].

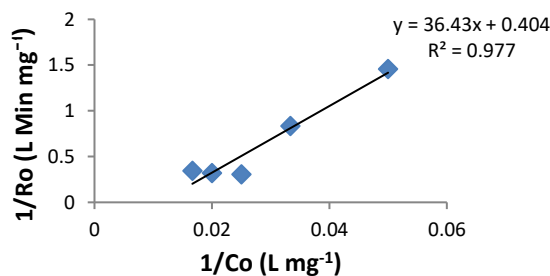


Figure 9. Langmuir-Hinshelwood plot of visible light degradation of MG in $\text{Ba}_{0.6}\text{K}_{0.4}\text{BiO}_3$ suspension.

The linear form of LH model is given by the following expression:

$$1/R_0 = 1/kr + 1/kr.KLH.Co \quad (3)$$

here, k_r and K_{LH} are the reaction rate constant and adsorption constant (Langmuir-Hinshelwood constant), respectively. Fig. 9 shows the graph between R_o^{-1} and C_o^{-1} , giving a straight line, with a slope of $(k_r \cdot K_{LH})^{-1}$ and intercept of k_r^{-1} . k_r and K_{LH} values are $0.011 \text{ mgL}^{-1} \text{ min}^{-1}$, 2.475 Lmg^{-1} , respectively.

CONCLUSION

$\text{Ba}_{0.6}\text{K}_{0.4}\text{BiO}_3$ nanostructured powder is prepared by Pechini method. The X-ray pattern indicates the cubic structure for the prepared catalyst. SEM image of calcined powder shows plate like nanostructured grain in range of 45-101 nm. The diffuse reflectance spectrum shows that the catalyst has a broad absorbance around 663nm with band gap of 1.8eV. Due to the low band gap, the catalyst is tested for the photo catalytic activity in the visible light exposure. The study confirms that the degradation of MG dye can be achieved by photo catalysis in the presence of an aqueous suspension of $\text{Ba}_{0.6}\text{K}_{0.4}\text{BiO}_3$. The degradation process is strongly influenced by the initial dye concentration and catalyst dose. The best degradation results are obtained at catalyst loading 0.75 gL^{-1} and initial concentration of the dye solution of 40 mgL^{-1} at natural pH (5.5) and 35°C temperature. Moreover, degradation kinetics of MG dye can be well described by Langmuir-Hinshelwood model and this process follows pseudo-first-order kinetics. Finally, it is concluded that the $\text{Ba}_{0.6}\text{K}_{0.4}\text{BiO}_3$ nanoparticle can be utilized as photo catalyst for the degradation of wastewater containing dyes and other organic compounds.

Acknowledgements

The authors are thankful to Gardas research group IIT Madras for discussion and guiding, IIT Gandhinagar, IIT Bombay and STIC, Cochin University (Sophisticated Test and Instrumentation Centre) for analytical analysis.

REFERENCES

- Schnick, R. A. 1988. The Impetus to Register New Therapeutants for Aquaculture. *The Progressive Fish-Culturist*, 50(4): 190-196.
- Culp, S. J., F. A. Beland, 1996. Malachite green: a Toxicological Review. *Journal of the American College of Toxicology*, 15: 219-238.
- Rao, K. V. K., 1995. Inhibition of DNA Synthesis in Primary Rat Hepatocyte Cultures by Malachite Green: a New Liver Tumor Promoter. *Toxicology Letters*, 81 (2-3), 107-113.
- Nelson, C. R., R. A. Hites, 1980. Aromatic Amines in and Near the Buffalo River. *Environmental Science and Technology*, 14:147-149.
- Chen, C. C.; C. S. Lu, Y. C. Chung, J. L. Jan, 2007. UV Light Induced Photodegradation of Malachite Green on TiO_2 Nanoparticles. *Journal of Hazardous Material*, 141: 520-528.
- Kako, T., Z. Zou, M. Katagiri, J. Ye, 2007. Decomposition of Organic Compounds Over NaBiO_3 Under Visible Light Irradiation. *Journal of Hazardous Materials*, 19: 98-202.
- Tang, J., Z. Zou, Y. Jinhu, 2007. Efficient Photocatalysis on BaBiO_3 Driven by Visible Light. *Journal of Physical Chemistry C*, 111(34): 12779-12785.
- Yu, K., S. Yang, C. Liu, H. Chen, H. Li, C. Sun and S. A. Boyd, 2012. Degradation of Organic Dyes via Bismuth Silver Oxide Initiated Direct Oxidation Coupled with Sodium Bismuthates Based Visible Light Photo Catalysis. *Environmental Science and Technology*, 46, 7318-7326.
- Dong, B., Z. Li, Z. Li, X. Xu, M. Song, W. Zheng, C. Weng, S. S. A. Deyab, M. E. Newehy, 2010. Highly Efficient LaCoO_3 Nanofibers Catalysts for Photocatalytic Degradation of Rhodamine B. *Journal of American Ceramic Society*. 93: 3587-3590.
- Gupta, R. K., I. J. Choi, Y. S. Cho, H. L. Lee, S. H. Hyun, 2008. Characterization of Perovskite-Type Cathode, $\text{La}_{0.75}\text{Sr}_{0.25}\text{Mn}_{0.95-x}\text{Co}_x\text{Ni}_{0.05}\text{O}_{3+d}$ ($0.1 \leq x \leq 0.3$), for Intermediate-Temperature Solid Oxide Fuel Cells. *Journal of Power Sources*. 187: 371-327.
- Kumar, K. V., K. Porkodi, A. Selvaganapathi, 2007. Heterogeneous Photocatalytic Decomposition of Crystal Violet in UV Illuminated Sol-Gel Derived Nanocrystalline TiO_2 Suspension. *Dyes And Pigment*, 75: 246-249.
- Lemos, F. C. D., E. Longo, E. R. Leite, D. M. A. Melo, A. O. Silva, 2004. Synthesis of nanocrystalline Ytterbium Modified PbTiO_3 . *Journal of Solid State Chemistry*. 177: 1542-1548.
- Alemi, A., E. Karimpour, H. Shokri, 2008. Preparation, Characterization and Luminescent Properties of Europium Oxide Doped Nano $\text{LaMn}_{0.9}\text{Zn}_{0.1}\text{O}_{3+d}$ by Sol-gel Processing. *Bulletin of Material Science*, 31: 967-973.
- Lou Y., X. Li, X. Liu, 2009. NTCR Behaviour of La-doped BaBiO_3 Ceramics. *Advances in Material Science and Engineering*. 383842: 1-4.
- Shao, J., Y. Tao, J. Wang, C. Xu, W. G. Wang, 2009. Investigations of Precursors in the Preparation of Nanostructured $\text{La}_{0.6}\text{Sr}_{0.4}\text{Co}_{0.2}\text{Fe}_{0.8}\text{O}_{3-\delta}$ Via a Modified Combined Complexing Method. *Journal of Alloy and Compounds*. 484: 263-267.
- Kaur, A., A. Singh, A. Asokan, L. Singh, 2014. Structural and Optical Properties of Iron Doped Barium Strontium Titanate. *International Journal of Education and Applied Research*, 4: 26-28.
- Mattheiss, L. F., D. R. Hamann, 1988. Electronic Structure of the High-Tc Superconductor $\text{Ba}_{1-x}\text{K}_x\text{BiO}_3$. *Physical Review Letters*, 60:2681-2684.
- Flemming, R. M., P. Marsh, R. J. Cava, J. J. Krajewski, 1988. Temperature Dependence of the Lattice Parameters in the 30-K Superconductor $\text{Ba}_{0.6}\text{K}_{0.4}\text{BiO}_3$. *Physical Review B*, 38:7026-7028.
- Kim, H. G., D. W. Hwang and J. S. Lee, 2004. An Undoped, Single-phase Oxide Photocatalyst Working Under Visible Light. *Journal of American Chemical Society*, 126: 8912-8913.
- Pechini, M. U. S. Patent No. 3.330.697 (11 July 1967).
- Fernandes, J. D. G., D. M. A. Melo, L. B. Zinner, C. M. Sulustiano, Z. R. Silva, A. E. Martinelli, M. Cerqueira, C. A. Junior, E. Longo, M. I. B. Bernardi, 2002. Low-Temperature Synthesis of Single-Phase Crystalline LaNiO_3 Perovskite via Pechini Method. *Materials Letters*. 53: 122-125.
- Kumar, K. V., K. Porkodi, A. Selvaganapathi, 2007. Heterogeneous Photocatalytic Decomposition of Crystal Violet in UV Illuminated Sol-Gel Derived Nanocrystalline TiO_2 Suspension. *Dyes and Pigment*. 75: 246-249.
- Kumar, K. V., K. Porkodi, F. Rocha, 2008. Langmuir-Hinshelwood Kinetics – A Theoretical Study. 9: 82-84.
- Jain, S., K. Sharma, U. Chandrawat, 2014. Low-Temperature Synthesis, Characterization and Photocatalytic Activity of Nanorods BaBiO_3 Perovskite under Visible Light Irradiation. *International Journal of Innovative Research in Science, Engineering Tecnology*. 3:14405-14411.
- Jain, S., K. Sharma, U. Chandrawat, 2016. Photocatalytic Degradation of Anti-Inflammatory Drug on Ti Doped BaBiO_3

- Nanocatalyst Under Visible Light Irradiation. Iranica Journal of Energy and Environmental. 7 (1): 64-71.
26. Lee, C. Y., K. Y. Song and R. P. Sperline, 1996. Molecular Dynamics Simulation and Far Infrared Measurements of Ba_{0.6}K_{0.4}BiO₃. Korean Journal of Materials Research, 6(6): 555-560.
 27. Gupta, M., P. Yadav, W. Khan, A. Azam, A. H. Naqvi, R. K. Kotlana, R.K. 2012. Low Temperature Synthesis and Magneto Resistance Study of Nano La_{1-x}Sr_xMnO₃ (x= 0.3, 0.33 and 0.4). Advanced Materials Letters, 3:220-225.
 28. Legesse, F., K. Sreenu, S. Kena, K. Legesse, 2015. Synthesis and Characterization of BaBiO₃ Perovskite Through Chemical Route. Science Technology and Arts Research, 4:80- 83.
 29. Jung, D., E. Choi, 1999. Differences of Structural and Electronic Properties in Ba_{1-x}K_xBiO₃ (x= 0, 0.04 and 0.4). Bulletin of Korean Chemical Society, 20:1045-1048.
 30. Martín-González, M.S., J. García-Jaca, E. Moran, M. Á. Alario-Franco, 1998. Synthesis of BaBiO₃ and Ba_{1-x}K_xBiO₃ Films via an Electrodeposition Processes. Physica C, 297:185-191.
 31. Marcos, F. R., J. J. Romero, J. F. Fernandez, 2012. Effect of the Temperature on the Synthesis of (K, Na)NbO₃-Modified Nanoparticles by a Solid State Reaction Route. Journal of Nanoparticle Research, 12: 2495-2502.
 32. Simões, A. Z., E. C. Aguiar, A. H. M. Gonzalez, J. Andrés, E. Longo, J. A. Varela, 2008. Strain Behaviour of Lanthanum Modified BiFeO₃ Thin Films prepared via Soft Chemical Method. Journal of Applied Physics, 104:104115-1-1041156-6.
 33. Alahiane, S., S. Qourzal, M. E. Ouardi, A. Abamrane, A. Assabbane, 2014. Factors Influencing the Photocatalytic Degradation of Reactive Yellow 145 by TiO₂-Coated Non-Woven Fibers. American Journal of Analytical Chemistry, 5:445-454.
 34. Zhang, D., 2012. Heterogeneous Photocatalytic Removal and Reaction Kinetics of Rhodamine-B Dye With Au Loaded TiO₂ Nanohybrid Catalyst. Polish Journal of Chemical Technology, 14: 42-48.

Persian Abstract

DOI: 10.5829/idosi.ijee.2016.07.04.08

چکیده

در این تحقیق سنتز یک نانو ذره جدید به عنوان فتو کاتالیست با استفاده از روش پچینی مورد مطالعه قرار گرفت. کاتالیست تولید شده با استفاده از XRD، SEM، TGA، UV-DRS و FT-IR مورد بررسی قرار گرفت. آنالیز XRD ساختمان کریستالی کاتالیست تولیدی را اثبات کرد. سایز نانو ذره تولیدی با استفاده از آنالیز SEM 45 نانومتر تعیین شد. مقدار ۱/۸ الکترون ولت به عنوان فاصله پیوند تعیین شد. خواص نانو ذره در از بین بردن مالاویت سبز مورد بررسی قرار گرفت.
